

**Transition and Rare-Earth Metal Oxides Coatings:
Surface Characterization, Thermo-mechanical Properties, and
Chemical Reactivity**

This thesis submitted for the degree of
Doctor of Philosophy in Physics

Hussein A. Miran, BSc, MSc



MURDOCH
UNIVERSITY

PERTH, WESTERN AUSTRALIA

School of Engineering and Information Technology,

Murdoch University, Western Australia

2018

Declaration

I declare that this thesis is my own work and includes nothing which is the outcome of work previously done. This thesis has no part of work submitted for any qualification or a degree at either higher education institution.

.....

Hussein A. Miran

2018

Supervisory Statement

It is to certify that the work embodied in the thesis entitled “Transition and Rare-Earth Metal Oxides Coatings: Surface Characterization, Thermo-mechanical Properties, and Chemical Reactivity” by Hussein A. Miran has been carried out under my supervision and that this work has not been submitted elsewhere for a degree at any tertiary education institution.

Dr. Mohammednoor Altarawneh

Dr. Zhong-Tao Jiang

Dr Jean-Pierre Veder

Dr. M Mahbubur Rahman

Abstract

This thesis describes a number of scientific studies investigating different interesting properties of rare earth metal oxides desired in different applications via combined experimental measurements and accurate density functional theory (DFT) calculations. The electronic, structural, mechanical and thermodynamic properties of cubic lanthanide sesquioxides are first reported, with a particular focus on the most common dioxide in the lanthanide family, ceria (CeO_2). This is followed an investigation into the effect of Hf and Zr dopants on the reduction energies of pure ceria. The reduction enthalpies of $\text{Ce}_{1-x}\text{Hf}_x\text{O}_2$ and $\text{Ce}_{1-x}\text{Zr}_x\text{O}_2$ and $\text{Ce}_{1-2x}\text{Hf}_x\text{Zr}_x\text{O}_2$ solid solutions are computed as a function of the reduction extent (x). Alloying with Hf and Zr is found to systematically reduce the energies required to remove oxygen atoms from bulk of ceria. The computed coefficients in the Born-Huang criterion infer a mechanical stability of all cubic lanthanide sesquioxides. Acquired electronic parameters encompass Bader's atomic charges and Partial Density of States (PDOS).

An important part of the thesis focuses on the catalytic capacity of CeO_2 in acting as a stand-alone environmental catalyst toward the decomposition of a series of chlorinated volatile organic compounds, namely chloroethene, chloroethane and chlorobenzene. Guided by recent experimental measurements, the pyrolytic and oxidative decomposition of selected chlorinated compounds have been modelled on the most stable ceria surface, CeO_2 (111). Dissociative addition (surface-assisted fission of the C-Cl bond) and direct elimination pathways (departure of a stable hydrocarbon entity with the co-adsorption of H and Cl atoms on the surface) assume comparable importance. Fission of the C-Cl bond over oxygen vacancies systematically necessitates lower energy barriers in reference to perfect surfaces. We have illustrated that observed catalytic deactivation in the experiment is attributed to the profound stability of adsorbed hydrocarbon adduct. Decomposition of an adsorbed phenyl moiety proceeds via addition of oxygen molecules to partially reduced surfaces. A simplified kinetic model plots the temperature-conversion profiles for the three compounds against corresponding experimental profiles, where a reasonable agreement has been attained.

Surfaces of terbium dioxide (TbO_2) possess an important catalytic feature in that they are capable of producing hydrogen by splitting water molecules. We have computed a large array of thermo-mechanical properties including heat capacities, bulk modules and thermal expansions of bulk TbO_2 as a function of temperatures and pressures based on the quasi-harmonic approximation (QHA) approach. Our calculated lattice constant and band gap were in good agreement with analogous experimental findings. A surface truncated along the (111), terminated with O atoms and with oxygen vacant site (111): $\text{O}+1\text{V}_\text{o}$ incurs a higher thermodynamic stability across all values of oxygen chemical potential. Nonetheless, in the vicinity of the lean-limit of chemical potential the surface terminated with Tb atoms (111): Tb becomes more stable. The implications of these geometries on OH-H fission reactions have been discussed.

Magnetron sputtered CeO_2 films as optically transparent materials, deposited onto crystalline silicon substrates at various oxygen-argon mixture gas, have been intensively studied and characterized by correlating their structural and chemical bonding states. All the thin films exhibit a polycrystalline character with cubic fluorite – structure for cerium dioxide along (111), (200) and (222) orientations. The XPS survey scans of the CeO_x coatings revealed that Ce, O, C elements are present in all of the obtained spectra of the studied films. XPS analysis demonstrated that the atomic percentages of Ce and O atoms increase as oxygen-argon mixture increases. Two oxidation states of CeO_2 and Ce_2O_3 are present in the films prepared at lower oxygen/argon flow ratios; whereas the films are completely oxidized into CeO_2 as the oxygen/argon flow ratio increase. Reflectance data obtained from UV-Vis examinations were utilized to calculate the optical constants such as absorption coefficient (α), the real and imaginary parts of the dielectric function (ϵ_1 , ϵ_2), the refractive index (n) and the extinction coefficient (k). Our analysis indicates that the CeO_2 films display indirect optical band gaps residing in the range of 2.25 - 3.1 eV. We utilized DFT calculations to estimate optical constants of a CeO_2 cluster at ground state. The computed electronic density of states (DOSs) of the optimized unit cell of CeO_2 yields a band gap that agrees well with the corresponding experimental value. The measured and DFT-computed absorption coefficient (α) exhibit a similar trend with similar values in the wavelength range from 100 to

2500 nm. Overall, a satisfactory correlation between the theoretical and experimental findings is demonstrated.

Spinel oxides of $\text{Cu}_x\text{Co}_{3-x}\text{O}_4$ thin films as one of metal mixed oxide systems, synthesized by sol-gel method and annealed at various temperatures ranging from $^{\circ}200$ to $^{\circ}500$ with interval 100, are deeply studied and characterized by various structural and optical characterization techniques. XRD data indicates that as annealing progresses, all the coatings possess a crystalline phase of $\text{Cu}_{0.56}\text{Co}_{2.44}\text{O}_4$ (ICSD 78-2175) with preferential orientation along (400) reflection plane. Optical analysis reveals that the solar selectivity of the studied films improves as the annealing progresses. Bader's charge analysis calculated by DFT implemented in VASP code points out that the Cu and Co atoms in all the stoichiometries hold positive charges whereas the O atoms are linked with negative charges. Our model reveals a covalent character for Cu-Co bond in all the system and ionic characteristics for Cu-O and Co-O bonds.

Finally, the influence of the variation in the Hubbard parameter U on the activation and reaction energies on CeO_2 -catalyzed reactions is studied. This has been achieved by surveying the change in activation and reaction energies for reactions underpinning the partial and full hydrogenation of acetylene over the CeO_2 (111) surface. A positive correlation between the U values and reaction and activation energies reported. It is suggested that kinetic modeling against experimental profiles of products could be used as an approach to optimize the U value.

Dedication

This thesis is dedicated to my family for the unconditional love and support....

Acknowledgements

Over my doctoral study years, I received support and guidance from many people in the school of engineering and information technology at Murdoch University (Australia).

Firstly, I would like to give my sincere thanks to my supervisors, Dr. Mohammednoor Altarawneh, Dr.Zhong-Tao Jiang, Dr.Jean-Pierre Veder, and Dr. M Mahbubur Rahman, for keeping me going when times were tough, offering insightful discussions, and invaluable advice. Their continued support and encouragement enabled this thesis to see the light.

I am giving my sincere appreciation and respect to my parents who provide me with their emotional support all my study time long. I strongly believe that the blessings of their prayers were behind my success in achieving such a hard task.

I am wholeheartedly expressing my thanks to Dr. Hantarto Widjaja, Zainab N. Jaf, and all of my research group members for their appreciable assistance and support.

My very special gratitude goes to the Iraqi government for the funding of my study expense. I am also very thankful to the Pawsey Supercomputing Center in Perth and the National Infrastructure (NCI) for the computational time grants.

Finally, but most importantly, many thanks go again to my family represented by the greatest supportive person in my life, my wonderful wife, Zainab Jaf for her, love, encouragement and prayers, and my three princesses, my daughters, Zahraa, Noor and the little cute one “Fatima” for their support and patience.

Hussein

December 2018

Table of Contents

Title	i
Declaration	ii
Supervisory Statement	iii
Abstract.....	iv
Dedication	vii
Acknowledgements	viii
Table of Contents.....	ix
List of Publications	xv
Conference Papers.....	xvii
Statement of Contribution	xviii
Symbols and Abbreviations	xxiii
List of Figures	xxvii
List of Tables	xliii
Chapter 1 : Introduction and Overview	1
1.1 Introduction	1
1.2 Objectives and Thesis Outline.....	4
Chapter 2 : Literature review.....	7
2.1 Rare Earths Metal Oxides	7
2.2 Structural Characteristics of Stoichiometric and Non- Stoichiometric Cerium Dioxide	10
2.3 CeO₂-Included Solid Solutions	11
2.4 CeO₂- Metal oxide Solid Solutions	13
2.5. Influence of the reduction energies of CeO₂	15
2.6 Well-Known Catalytic Applications of CeO₂	18
2.6.1 Three Way Catalysts (TWCs) in Automotive Cars.....	18
2.6.2 Dehalogenation by CeO ₂ -Based Materials	18
2.6.3 Oxidation of Volatile Organic Compounds.....	19
2.6.4 Chlorinated Volatile Organic Compounds (CVOCs).....	23
2.6.5 Total Hydrogenation of Ethyne over CeO ₂ (111).....	25
2.6.6 Ceria Surface Reactions with Inorganic Molecules	27
2.6.6.1 H ₂ , O ₂ and H ₂ O	27
2.6.7 Ceria Surface Reactions with Sulfur dioxide (SO ₂)	35

2.6.8 Formation of H ₂ , SO ₂ and H ₂ O on Stoichiometric Ceria	37
2.6.9 Ceria Surface Reactions with CO and CO ₂ Molecules	39
2.6.10 Ceria Surface Reactions with nitrogen oxide (NO).....	41
2.6.11 Ceria Surface Reactions with Hydrocarbons.....	44
2.6.12 Ceria Surface Reactions with Methanol.	45
2.6.13 Catalytic performance of Ceria Surface on Phenol.	46
2.7 Thin Film Applications of Ceria	51
2.8 Spinel - Structured Oxides.....	53
2.9 Previous Studies Based on Density Functional Theory (DFT)	54
2.10 Gaps in current knowledge:	57
Chapter 3 : Methodology	59
3.1 Reaearch Plan and Methodology	59
3.2 Sol-Gel Deposition Technique	60
3.3 Magnetron Sputtering.....	60
3.3.1 Unbalanced Magnetron Sputtering	61
3.4 Characterization Techniques	62
3.4.1 X-Ray Diffraction.....	62
3.4.2 X-Ray Photoelectron Spectroscopy (XPS).....	64
3.4.3 Fourier-Transform Infrared Spectroscopy (FTIR)	65
3.4.4 UV-Vis Spectroscopy	66
3.4.5 Field Emission Scanning Electron Microscopy (FESEM).....	67
3.4.6 Atomic Force Microscopy (AFM).....	68
3.5 Theoretical Background	69
3.5.1 The Many-Body Problem	69
3.5. 2 Born-Oppenheimer Approximation.....	71
3.5.3 Density Functional Theory (DFT)	71
3.5.4 The Hohenberg-Kohn Theorems	71
3.5.5 The Kohn–Sham Equations	72
3.5.6 Pure Density Functional Theory Methods.....	73
3.5.6.1 Local Density Approximation (LDA)	73
3.5.6.2 Generalized gradient approximation (GGA).....	74
3.5.7 Hybrid Density Functional Theory Methods.....	74
3.5.8 The DFT + U Approach.....	75
3.5.9 Pseudopotentials	76
3.5.10 Modelling program based on DFT	76
3.5.10.1 DMol ³	78

3.5.10.2 VASP	78
3.5.10.3 CASTEP	79
3.5.10.4 PHONOPY	79
3.5.11 Transition state theory	79
3.5.12 Ab-initio atomistic thermodynamics	81

Chapter 4 : Thermo-mechanical Properties of Cubic Lanthanide Oxides..... 84

4.1 Abstract	84
4.2 Introduction	85
4.3 Computational Details.....	89
4.3.1 Structural Optimization	89
4.3.2 Charge Distribution Analysis	90
4.3.3 Mechanical Properties	90
4.3.4 Calculations of ΔG (T) for Redox Reactions	92
4.4 Results & Discussions.....	92
3.4.1 Electronic and Structural Properties of Ln_2O_3	92
4.4.2 Mechanical Properties of Ln_2O_3	99
4.4.3 The Reduction Energy of Lanthanide Dioxides	102
4.5 Conclusions.....	112

Chapter 5 : Decomposition of Selected Chlorinated Volatile Organic Compounds on CeO_2 113

5.1 Abstract	113
5.2 Introduction	114
5.3 Computational Details.....	117
5.4 Results and Discussion	121
5.4.1 Decomposition in the Gas Phase	121
5.4.2 Catalytic Decomposition of Chloroethene and Chloroethane Over the Stoichiometric CeO_2 (111) Surface	123
5.4.3 Decomposition of Chloroethene Over CeO_2 (111) _{Vo} Surface.....	128
5.4.4 Removal of Adsorbed Vinyl and Ethyl Moieties via Surface Hydrogen Reactions.....	132
5.4.5 Decomposition of Chlorobenzene Over CeO_2 (111) and CeO_2 (111) _{Vo} Surfaces	134
5.4.6 Formation of 1,4-Dichlorobenzene	139
5.4.7 Kinetic Analysis.....	141
5.5 Conclusions.....	148

Chapter 6 : Structural, electronic and thermodynamic properties of bulk and surfaces of TbO₂.....	149
6.1 Abstract	149
6.2. Introduction	150
6.3. Computational details	151
6.3.1. Structural optimization of TbO ₂	151
6.3.2. Quasi-harmonic approximation for thermodynamic properties	153
6.2.3. Ab initio atomistic thermodynamics calculations	153
6.3. Results and discussion.....	154
6.3.1. Bulk properties of TbO ₂	154
6.3.2. Thermo-elastic properties of TbO ₂	155
6.3.3. Optimized geometries of low - index surfaces of TbO ₂	160
6.3.4. Stability phase diagrams for TbO ₂ surfaces	168
6.4. Conclusions and future directions	173
Chapter 7 : Influence of DC magnetron sputtering reaction gas on structural and optical characteristics of Ce-oxide thin films.....	174
7.1 Abstract	174
7.2 Introduction	175
7.3 Experimental and modelling	177
7.3.1 Thin film deposition process	177
7.3.2 XRD measurements	178
7.3.3 XPS measurements	179
7.3.4 FESEM imaging	179
7.3.5 UV-Vis and FTIR measurements	180
7.3.6 Density functional theory-based calculations.....	180
7.4 Results and Discussion	181
7.4.1 Structural analysis of Ce-oxide coatings	181
7.4.2 Optical reflectance and Urbach energy studies	186
7.4.3 Optical properties – the dispersion parameters	190
7.4.4 Dielectric analysis.....	192
7.4.5 Simulation analysis	197
7.5 Conclusions.....	201

Chapter 8 : Structural and Optical Characteristics of Pre- and Post-annealed Sol-gel Derived CoCu-oxide Coatings

.....	203
8.1 Abstract	203
8.2 Introduction	204
8.3 Experimental.....	206
8.3.1 Deposition of coatings	206
8.3.2 Crystal Phase Structure and Rietveld Refinement	207
8.3.3 XPS Analysis	207
8.3.4 Film Surface Feature via FESEM Analysis.....	207
8.3.5 Film Surface Feature via AFM Analysis.....	208
8.3.6 UV-Vis Reflectance Studies	208
8.3.7 FTIR Reflectance Studies	209
8.3.8 Theoretical Charge Distribution Analysis via Density Functional Theory (DFT).....	209
8.4 Results and Discussion	210
8.4.1 XRD Analysis	210
8.4.2 XPS Analysis	214
8.4.3 FESEM Analysis of the Coatings.....	221
8.4.4 AFM Analysis of the Coatings	223
8.4.5 Solar Selectivity Studies	224
8.4.6 Bader's Charge Analysis	228
8.5 Conclusions.....	228

Chapter 9 : Influence of the variation in the U parameters in the DFT + U methodology on activation and reaction energies.....

9.1 Abstract	229
9.2 Introduction	230
9.3 Methodology.....	231
9.4 Results and Discussions.....	232
9.5 Conclusions.....	239

Chapter 10 : Conclusions and Future Research Directions

.....	240
References.....	245

Appendices.....	286
Appendix A.....	286
Coating Deposition Techniques.....	286
Chemical Vapor Deposition (CVD)	286
Physical Vapor Deposition (PVD)	287
Appendix B	288
Appendix C.....	311
Appendix D.....	314

List of Publications

[1] **Miran, H.A.**, Altarawneh, M., Widjaja, H., Jaf, Z.N., Rahman, M.M., Veder, J.P., Dlugogorski, B.Z. and Jiang, Z-T (2018) Thermo-mechanical properties of cubic lanthanide oxides. *Thin Solid Films*, 653 . pp. 37-48.

[2] **Miran, H.A.**, Altarawneh, M., Jiang, Z-T, Oskierski, H., Almatarneh, M. and Dlugogorski, B.Z. (2017) Decomposition of selected chlorinated volatile organic compounds by ceria (CeO₂). *Catalysis Science & Technology*, 7 (17). pp. 3902-3919.

[3] **Miran, H.A.**, Altarawneh, M., Jaf, Z.N., Dlugogorski, B.Z. and Jiang, Z-T (2018) Structural, electronic and thermodynamic properties of bulk and surfaces of terbium dioxide (TbO₂). *Materials Research Express*, 5 (8).

[4] **Miran, H.A.**, Jiang, Z-T, Altarawneh, M., Veder, J-P, Zhou, Z-F, Rahman, M.M., Jaf, Z.N. and Dlugogorski, B.Z. (2018) Influence of DC magnetron sputtering reaction gas on structural and optical characteristics of Ce-oxide thin films. *Ceramics International*, 44 pp. 16450-16458.

[5] **Miran, H.A.**, Rahman, M.M., Jiang, Z-T, Altarawneh, M., Chuah, L.S., Lee, H-L, Mohammadpour, E., Amri, A., Mondinos, N. and Dlugogorski, B.Z. (2017) Structural and optical characteristics of pre- and post-annealed sol-gel derived CoCu-oxide coatings. *Journal of Alloys and Compounds*, 701 . pp. 222-235.

[6] **Miran, H.A.**, Jiang, Z-T, Jaf, Z.N., Rahman, M.M. and Altarawneh, M. Influence of the Variation in the Hubbard Parameter (U) on Activation Energies of CeO₂-Catalysed Reactions, Submitted to *Computational Condensed Matter*, November (2018).

- [7] Widjaja, H., **Miran, H.A.**, Altarawneh, M., Oluwoye, I., Lim, H.N., Huang, N.M., Jiang, Z-T and Dlugogorski, B.Z. (2017) DFT + U and ab initio atomistic thermodynamics approach for mixed transitional metallic oxides: A case study of CoCu₂O₃ surface terminations. *Materials Chemistry and Physics*, 201 . pp. 241-250.
- [8] Rahman, M.M., **Miran, H.A.**, Jiang, Z-T, Altarawneh, M., Chuah, L.S., Lee, H-L, Amri, A., Mondinos, N. and Dlugogorski, B.Z. (2017) Investigation of the post-annealing electromagnetic response of Cu–Co oxide coatings via optical measurement and computational modelling. *RSC Advances*, 7 (27). pp. 16826-16835.
- [9] Jaf, Z.N., Altarawneh, M., **Miran, H.A.**, Jiang, Z.T and Dlugogorski, B.Z. (2017) Mechanisms governing selective hydrogenation of acetylene over γ -Mo₂N surfaces. *Catalysis Science & Technology*, 7 (4). pp. 943-960.
- [10] Jaf, Z.N., Jiang, Z-T, **Miran, H.A.** and Altarawneh, M. (2016) Thermo-elastic and optical properties of molybdenum nitride. *Canadian Journal of Physics*, 94 (9). pp. 902-912.
- [11] Jaf, Z.N. , Altarawneh, M., **Miran, H.A.**, Jiang, Z-T, Dlugogorski, B.Z.(2018) Hydrodesulfurization of Thiophene over γ -Mo₂N catalyst. *Molecular Catalysis*. 449. pp. 21-30.
- [12] Jaf, Z.N., Altarawneh, M., **Miran, H.A.**, Jiang, Z-T. (2018) Geometries, electronic properties and stability of molybdenum and tungsten nitrides low-index surfaces. *Materials Research Express*, 5 (12).
- [13] Jaf, Z.N., Jiang, Z-T., Altarawneh, M., Veder, J-P, Manickam Minakshi, **Miran, H.A.**, Zhou, Z-F, H. N. Lim, N. M. Huang, Dlugogorski, B.Z. “Physico-chemical properties of CrMoN coatings - combined experimental and computational studies” Under review, *Thin Solid Films*. September 2018.
- [14] Jaf, Z.N. , Altarawneh, M., **Miran, H.A.**, Jiang, Z-T, Almatarneh, M., Dlugogorski, B.Z.(2018) Catalytic Hydrogenation of p-chloronitrobenzene to p-chloroaniline Mediated by γ -Mo₂N *ACS Omega*, 3 (10). pp. 14380-14391.

Conference Papers

[1]**Miran, H.A.**, Altarawneh, M., Jaf, Z.N., Widjaja, H., Veder, J.P. and Jiang, Z-T (2017) Electronic properties, mechanical stability and reduction reaction energies for cubic lanthanide oxide composites: A computational modelling approach. In: 9th International Conference on Materials for Advanced Technologies (ICMAT) 2017, 18 - 23 June 2017, Suntec Singapore.

[2]**Miran, H.A.**, Jiang, Z-T, Veder, J.P., Rahman, M.M., Jaf, Z.N. and Altarawneh, M. (2017) Influence of reaction gases on the structural and optical characteristics of Ce-oxide thin film coatings. In: Australian Institute of Physics WA Postgraduate Student Conference, 16 November 2017, University of Western Australia, Perth.

[3]**Miran, H.A.**, Jiang, Z-T, Veder, J.P., Jaf, Z.N. and Altarawneh, M. (2017) Influence of reaction gases on the structural and optical characteristics of Ce-oxide thin film coatings. In: 13th International Conference and Exhibition on Advanced Materials and Nanotechnology, 26 - 28 October 2017, Osaka, Japan.

[4]**Miran, H.A.**, Altarawneh, M., Widjaja, H., Jaf, Z.N. and Jiang, Z-T (2016) Dissociation of chlorobenzene (C_6H_5Cl), Chloroethane (C_2H_5Cl) and isopropyl chloride (C_3H_7Cl) on ceria (CeO_2) 111 surfaces. In: Australian Institute of Physics (AIP) WA. Postgraduate Conference, 13 October 2016, University of Western Australia, Perth.

[5]Jaf, Z.N., Altarawneh, M., **Miran, H.A.** and Jiang, Z-T (2017) Mechanisms and kinetics of thiophene hydrodesulfurization over $\gamma-Mo_2N$ catalyst. In: Australian Institute of Physics WA Postgraduate Student Conference, 16 November 2017, University of Western Australia, Perth.



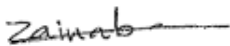

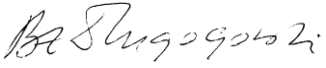
[6]Jaf, Z.N., Altarawneh, M., **Miran, H.A.** and Jiang, Z-T (2017) An atomistic approach of thiophene hydrodesulfurization over $\gamma-Mo_2N$ catalyst. In: 13th International Conference and Exhibition on Advanced Materials and Nanotechnology, 26 - 28 October 2017, Osaka, Japan.

[7]Jaf, Z.N., Altarawneh, M., **Miran, H.A.** and Jiang, Z-T (2016) Selective hydrogenation of Acetylene over $\gamma-Mo_2N$ (100) catalytic surface. In: Australian Institute of Physics (AIP) WA Postgraduate Conference, 13 October 2016, University of Western Australia, Perth.




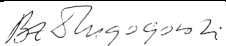
Statement of Contribution

Journal Publications


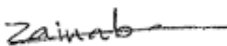
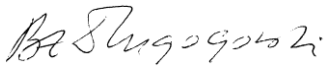
[1] Miran, H.A., Altarawneh, M., Widjaja, H., Jaf, Z.N., Rahman, M.M., Veder, J.P., Dlugogorski, B.Z. and Jiang, Z-T (2018) *Thermo-mechanical properties of cubic lanthanide oxides*. Thin Solid Films, 653. pp. 37-48.

Author's name	Contribution	Overall Percentage (%)	Signature
Miran, H.A.	Computational modeling, data collection and analysis, writing the manuscript and revision	70	
Altarawneh, M.	Project leader, discussions, manuscript preparation and revision	30	
Widjaja, H.	Discussions and manuscript preparation		
Jaf, Z.N.	Discussions and manuscript preparation		
Rahman, M.M.	Discussions		
Veder, J.P.	Manuscript preparation		
Dlugogorski, B.Z.	Manuscript preparation		
Jiang, Z-T	Discussions and manuscript preparation		



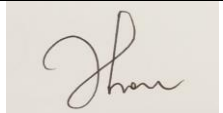
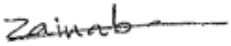
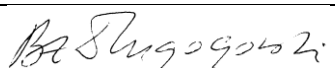
[2] Miran, H. A., Altarawneh, M., Jiang, Z-T, Oskierski, H., and Dlugogorski, B.Z. (2017) *Decomposition of selected chlorinated volatile organic compounds by ceria (CeO₂)*. Catalysis Science & Technology, 7 (17). pp. 3902-3919.

Author's name	Contribution	Overall Percentage (%)	Signature
Miran, H.A.	Computational modeling, data collection and analysis. Writing the manuscript and revision	70	
Altarawneh, M.	Project leader, data analysis , discussions and manuscript preparation	30	
Jiang, Z-T	Project design and manuscript preparation		
Oskierski, H.	manuscript preparation		
Almatarneh, M.	manuscript preparation		
Dlugogorski, B.Z.	manuscript preparation		


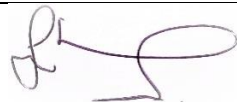
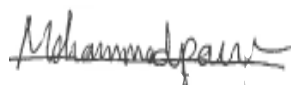
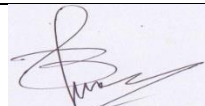

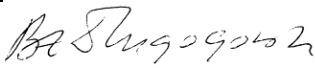
[3] Miran, H.A., Altarawneh, M., Jaf, Z.N., Dlugogorski, B.Z. and Jiang, Z-T (2018)
Structural, electronic and thermodynamic properties of bulk and surfaces of terbium dioxide (TbO₂). Materials Research Express, 5 (8)

Author's name	Contribution	Overall Percentage (%)	Signature
Miran, H.A.	Computational modeling, data collection and analysis. Writing the manuscript and revision	70	
Altarawneh, M.	Project leader, discussions , manuscript preparation and revision	30	
Jaf, Z.N.	Discussions and manuscript preparation		
Dlugogorski, B.Z	manuscript preparation		
Jiang, Z-T	Project design, discussions and manuscript preparation		

[4] Miran, H.A., Jiang, Z-T, Altarawneh, M., Veder, J-P, Zhou, Z-F, Rahman, M.M., Jaf, Z.N. and Dlugogorski, B.Z. (2018) *Influence of DC magnetron sputtering reaction gas on structural and optical characteristics of Ce-oxide thin films*. *Ceramics International* .

Author's name	Contribution	Overall Percentage (%)	Signature
Miran, H.A.	Computational modeling, materials characterizations, data collection, treatment and analysis. Writing the manuscript and revision	65	
Jiang, Z-T	Project leader, material design, manuscript preparation, discussions and revision	35	
Altarawneh, M.	discussions and manuscript preparation		
Veder, J-P	Materials characterization using XPS and manuscript preparation		
Zhou, Z-F	Materials fabrication and manuscript preparation		
Rahman, M.M.	Discussions		
Jaf, Z.N.	Discussions and manuscript preparation		
Dlugogorski, B.Z.	manuscript preparation		

[5] Miran, H.A., Rahman, M.M., Jiang, Z-T, Altarawneh, M., Chuah, L.S., Lee, H-L, Mohammadpour, E., Amri, A., Mondinos, N. and Dlugogorski, B.Z. (2017) *Structural and optical characteristics of pre- and post-annealed sol-gel derived CoCu-oxide coatings*. Journal of Alloys and Compounds, 701. pp. 222-235.

Author's name	Contribution	Overall Percentage (%)	Signature
Miran, H.A.	Computational modeling, data collection, materials characterization, data analysis and manuscript preparation and revision	60	
Rahman, M.M.	Material fabrication and characterizations, manuscript preparation and revision	40	
Jiang, Z-T	Project leader, material design, manuscript preparation and revision		
Altarawneh, M.	Discussion and manuscript preparation		
Chuah, L.S.	Material characterizations and manuscript preparation		
Lee, H-L	Material characterizations and manuscript preparation		
Mohammadpour, E.	Data analysis and discussions		
Amri, A.	Manuscript preparation		
Mondinos, N.	Discussion and manuscript preparation		
Dlugogorski, B.Z.	Discussion and manuscript preparation		

Symbols and Abbreviations

TMs	Transition metals
MO	Metal oxide
Ln	Lanthanide
SIC	Self-interaction-corrected
Å	Angstrom (10^{-10} m)
B	Bulk modulus
ν	Poisson's ratio
G	shear modulus
b.c.c.	Body-centred cubic
TWCs	Three-way catalysts
DFT	Density functional theory
DFPT	Density- functional perturbation theory
QHA	Quasi-harmonic approximation
ΔC^{QHA}	Difference between quasi harmonic heat capacities
$\Delta\mu_O$	Oxygen chemical potential difference
C_P	Pressure-constant heat capacities
C_V	Volume-constant heat capacities
V_o	Equilibrium volume
CFUBMSIP	closed field unbalanced magnetron sputter ion plating
DOS	Density of states
PDOS	Partial density of states
E	Young's modulus
E_f	Enthalpy of formation
F(V,T)	Helmholtz free energy
f.c.c.	Face -centred cubic
G(T,P)	Gibbs free energy
VOCs	Volatile organic compounds
CVOCs	Chlorinated volatile organic compounds
PCDD/Fs	Polychlorinated dibenzo-p-dioxins and dibenzofurans

BET	Brunauer–Emmett–Teller
GHSV	Gas hourly space velocity
OSC	Oxygen-storage capacity
OBC	Oxygen buffering capacity
GGA	Generalized gradient approximations
CE	Chloroethene
CA	Chloroethane
CB	Chlorobenzene
TCE	Trichloroethylene
TOC	Total organic carbon
CWAO	Catalytic wet air oxidation
TPR	Temperature-Programmed Reduction
MC	Micro- ceria
h	Planck's constant (6.63×10^{-34} J.s)
C	Speed of light
K	Thermal conductivity
k _B	Boltzmann constant (1.38×10^{-23} m ² kg.s ⁻² K ⁻¹)
LDA	Local-density approximations
LSDA	Local spin-density approximation
ECP	Effective core potential
P	Pressure
PVD	Physical vapor deposition
CVD	Chemical vapor deposition
LPCVD	Low-pressure chemical vapor deposition
PECVD	Plasma enhanced chemical vapor deposition
LECVD	laser-enhanced chemical vapor deposition
E _B	Binding energy
E _k	kinetic energy
EM	Electromagnetic
T	Temperature
V	Volume
XPS	X-ray photoelectron spectroscopy

XRD	X-ray diffraction
UV-Vis	Ultra violet visible
FTIR	Fourier-transform infrared
AFM	Atomic force microscopy
UHV	Ultra-high vacuum
TPD	Temperature Programmed Desorption
REs	Rare earths
d_{T-S}	Target-substrate distance
OER	Oxygen evolution reaction
H	Hamiltonian Operator
$E_{HK}[\rho(r)]$	Hohenberg-Kohn energy functional
$V_{eff}(r)$	Effective potential
$V_{xc}(r)$	Exchange-correlation potential
CASTEP	Cambridge serial total energy package
VASP	Vienna Ab initio Simulation Package
λ	Wavelength
Θ_D	Debye temperature
QMC	Quantum Monte Carlo
RPA	Random Phase Approximation
NEB	Nudged elastic band
LST/QST	Linear Synchronous and Quadratic Synchronous Transit
MEPs	Minimum Energy Points
PES	Potential Energy Surface
BDE	Bond dissociation energies
STM	Scanning tunnelling microscopy
nc-AFM	Non-contact atomic force microscope
TPSD	Temperature-programmed surface desorption
PFR	Plug flow reactor
FBR	Fluidised bed reactor
E_{vac}	Vacancy formation energy
sccm.	standard cubic centimeter per minute
Ar	argon

D_g	Crystallite size
n	Refractive index
k	Extinction coefficient
$\epsilon_1(\omega)$	Real part of the complex dielectric function
$\epsilon_2(\omega)$	Imaginary part of the complex dielectric function
$\tan\delta$	Loss tangent
V_{el}	Volume energy loss function
S_{el}	Surface energy loss function
FWHM	Full width at half maximum
SSS	Solar selective surface
SEI	Secondary electron imaging
R_a	Mean roughness
R_q	rms value
h_i	Surface roughness value
\bar{h}	Mean surface roughness
PMT	Photo multiplier tube
ϵ_z	Component of strain normal to the surface
QMC	Quantum Monte Carlo
RPA	Random phase approximation

List of Figures

Figure 1.1 : Applications of transition metal oxides.	2
Figure 1.2: The position of rare earth elements in the periodic table.....	3
Figure 1.3 : The overall layout of the thesis.	6
Figure 2.1: Unit cells of Ln_2O_3 (a) A-type (hexagonal), (b) B-type (monoclinic), and C-type (cubic).....	7
Figure 2.2: Adopted cubic fluorite structure of the lanthanide dioxide (LnO_2), CeO_2 , PrO_2 and TbO_2	8
Figure 2.3: Experimental and calculated lattice parameters of fluorite-structure CeO_2 solid solution containing variant rare earth sesquioxides. Reproduced from ref. [15].	13
Figure 2.4: Phase diagram study of CeO_2 - ZrO_2 system with different CeO_2 concentration as a function of temperature. Reproduced from ref. [20].	14
Figure 2.5: Side and top views of CeO_2 (111) slab, doped with a dopant. (a) Removal of oxygen neighboring in the doped slab. (b) Removal of furthest oxygen in the doped slab. Reproduced from ref. [28].	16
Figure 2.6 : Variation of oxidation enthalpies (ΔH) per O_2 with the reduction extent (y) in $\text{Ce}_{0.81}\text{Zr}_{0.19}\text{O}_{2-y}$ and CeO_2 systems. Reproduced from ref.[34].	17

Figure 2.7: Schematic illustration of the CO oxidation over CeO₂(110) surface via Mars – Van Krevelen mechanism [44]. 19

Figure 2.8: Temperature dependencies of methane oxidation over different catalysts of PdO/Ce_{0.64} Zr_{0.16}Ni_{0.2}O₂/γ-Al₂O₃, PdO/Ce_{0.72} Zr_{0.18}Ni_{0.1}O₂/γ-Al₂O₃, PdO/Ce_{0.8} Zr_{0.2}O₂/γ-Al₂O₃ and PdO/Ce_{0.64} Zr_{0.16}Bi_{0.20}O₂/γ-Al₂O₃. Reproduced from ref. [63]. 22

Figure 2.9: Temperature dependencies of trichloroethylene oxidation over CeO₂ catalysts calcined at different temperature. Reproduced from [72]. 25

Figure 2.10: Reaction energy diagram for total hydrogenation of acetylene on CeO₂ (111) catalyst. Energies are computed as a reference to the energy of H₂ and C₂H₂ in the gas phase, and the clean CeO₂ (111) slab. Black line shows the routes of partial hydrogenation of acetylene to ethylene through R5, light brown displays the partial hydrogenation via dissociative acetylene adsorption, and red line represents the full hydrogenation to C₂H₆. The asterisk denotes a clean CeO₂ (111) surface. Reactants, intermediates, and products that are followed by an asterisk correspond to the adsorbed species. Reprinted from ref. [73]. 26

Figure 2.11: O 1s core level spectra from water adsorbed on oxidized CeO₂ (111) and CeO₂ (100) at 180 K. Reproduced from ref. [92]. 30

Figure 2.12: TPD measurements of water adsorption on fully oxidized CeO₂ (111) and CeO₂ (100) at 180 K. Reproduced from ref. [92]. 31

Figure 2.13 : Active sites on CeO ₂ (111) surface; (a) side and top views of perfect CeO ₂ (111) surface; (b) side and top views of reduced CeO ₂ (111) surface.	32
Figure 2.14: O 1s core level spectra from water adsorbed on reduced CeO _{1.7} (111) and CeO _{1.7} (100) at 180 K. Reproduced from ref. [92].	33
Figure 2.15: TPD measurements of water adsorption on reduced CeO _{1.7} (111) and CeO _{1.7} (100) at 180 K. Reproduced from ref. [92].	34
Figure 2.16: H ₂ O and H ₂ reactions on the defect and perfect ceria (111) surfaces. Reproduced from ref. [81].	35
Figure 2.17: Energy diagram of the reaction routes forming H ₂ O, SO ₂ and H ₂ (a). Intermediate structures (b) for the reaction pathways displayed in (a). These represent the adsorption of H ₂ S (E1), first de-hydrogenation (E2), second de-hydrogenation (E3), water formation (E4), SO ₂ formation (E5) and H ₂ formation (E6). Reproduced from ref [100].	39
Figure 2.18 : CO ₂ TPD measurements following exposure at 180 K on fully oxidized CeO ₂ (100) (black) and deficient CeO _{1.7} (100) (blue). Reproduced from ref. [139].	41
Figure 2.19: TPD measurements following exposure of NO on (a) fully oxidized CeO ₂ (111) and (b) sputter reduced CeO _{2-y} (111). On the oxidized	

surface the NO was exposed at 90 K. On the reduced surface the NO was exposed at different temperatures as indicated and then the sample was cooled to 90 K before the TPD. Reproduced from ref. [143].43

Figure 2.20: Temperature Programed Desorption following methanol adsorption at 180K on oxidized CeO₂ (111) and CeO₂ (100). Reproduced from ref. [155].....46

Figure 2.21: XRD patterns of different prepared CeO₂ catalysts. Reproduced from ref. [157].....47

Figure 2.22: O₂-TPD of CeO₂ catalysts. Reproduced from ref. [157].....49

Figure 2.23: H₂-TPR of CeO₂ catalysts. Reproduced from ref. [157].....50

Figure 2.24: Influence of temperature on the CWAO of phenol with and without addition of type A CeO₂. Phenol content amounts to 400 mg/L with oxygen pressure of 0.5 MPa and catalyst loading of 2 g/L. Reproduced from ref. [157].....51

Figure 2.25: Calculated surface free energy of different plausible CeO₂ (100) and CeO₂ (110) orientations with regards to the change in oxygen chemical potential $\Delta\mu_{\text{O}}$ along with their corresponding pressure bar lines at T=600, 900, and 1200 K. Reproduced from ref. [187].....55

Figure 2.26: Calculated surface free energy of different plausible CeO₂ (100) and CeO₂ (111) orientations with regards to the change in oxygen chemical potential $\Delta\mu_{\text{O}}$ along with their corresponding pressure bar lines at T=600, 900, and 1200 K. Reproduced from ref. [187].....56

Figure 3.1 : Flow diagram of the methodology procedure.59

Figure 3.2: diagram of target configuration in closed field unbalanced magnetron sputter ion plating (CFUBMSIP) system.....62

Figure 3.3: D8 DISCOVER XRD manufactured by Bruker AXS.63

Figure 3.4: Kratos AXIS Ultra DLD X-ray photoelectron spectroscopy instrument.....65

Figure 3.5: PerkinElmer Spectrum 100 FTIR Spectrometer, USA.66

Figure 3.6: UV-670 JASCO, USA double beam spectrophotometer.67

Figure 3.7: Zeiss Neon 40EsB FESEM.68

Figure 3.8: A high resolution atomic force microscopy (AFM).69

Figure 3.9: The variation of Ce₂O₃ band gap with Hubbard parameter (U) using LDA+U and GWO approaches. Reproduced from ref. [267].76

Figure 3.10: Flow diagram of the computational work by DFT.77

Figure 3.11: Transition state diagram. ΔG signifies the activation energy.80

Figure 4.1: (a) The unit cell of bulk Ln_2O_3 , light green and red colors stand for Ln and O atoms respectively. (b) The unit cell of bulk CeO_2 , white and red spheres denote Ce and O atoms, respectively.....90

Figure 4.2: Calculated (PBE values) and fitted (to the Birch-Murnaghan’s equation of state; BM EoS) energies (in eV) versus volumes of unit- cell volume (in \AA^3) for selected C-type lanthanide sesquioxides. Calculated bulk modulus (B) from the BM EoS are inserted.93

Figure 4.3: Variation of band gaps of Ce_2O_3 with Hubbard parameters. Dashed line represents the experimental value.....97

Figure 4.4: Total and partial density of states DOS and PDOS for bulk Ce_2O_3 calculated at U_{eff} of 6.5 eV.....98

Figure 4.5: The variation of Gibbs free energy change per oxygen molecule for the reduction reaction with temperature. Dashed line represents the experimental value, ref. [303].....104

Figure 4.6: Variation of reduction enthalpies of CeO_δ with O/Ce atomic ratio.105

Figure 4.7: $2 \times 2 \times 2$ lattice structures of CeO_2 , $\text{Ce}_{1-x}\text{Zr}_x\text{O}_2$, $\text{Ce}_{1-x}\text{Hf}_x\text{O}_2$ and $\text{Ce}_{1-2x}\text{Hf}_x\text{Zr}_x\text{O}_2$, $x = 0.25$. White, red, blue and light blue spheres symbolize Ce, O, Zr and Hf atoms, respectively.....106

Figure 4.8: Reduction enthalpy for CeO_δ with different concentrations of Hf and Zr element as a function of the atomic ratios at $T=0$ K and $P=0$ atm. Reduction enthalpy for $Ce_{1-x}Hf_xO_\delta$ system; Reduction enthalpy for $Ce_{1-x}Zr_xO_\delta$ system; Reduction enthalpy for $Ce_{1-2x}Hf_xZr_xO_\delta$ system. The Y-axis signifies energies in the unit of kilo joule per mole O_2 (kJ/mol- O_2)..... 107

Figure 4.9: Reduction enthalpy for $Ce_{1-x}Zr_xO_\delta$ solid solution system in the range of O/Ce atomic ratios of between 2-1.8. Experimental values [316] are measured at $T= 973$ K..... 108

Figure 4.10: The relative change (V/V_0) of CeO_δ volume to the stoichiometric volume for undoped and doped CeO_δ with different concentrations of Hf and Zr element as a function of the atomic ratios. V/V_0 for $Ce_{1-x}Hf_xO_\delta$ stoichiometry; V/V_0 for $Ce_{1-x}Zr_xO_\delta$ stoichiometry; V/V_0 for $Ce_{1-2x}Hf_xZr_xO_\delta$ stoichiometry. 109

Figure 4.11: Variation of lattice parameters with Hf and Zr concentrations doping CeO_2 , fitted values are from ref. [15]. 110

Figure 5.1: Stoichiometric and partially reduced CeO_2 (111) surfaces. Oxygen atoms are represented as red spheres. 120

Figure 5.2: Optimized geometries of the three selected CVOCs. Values represent BDH in $kJ\ mol^{-1}$. Experimental [337] values are in parenthesis. Green spheres signify chlorine atoms. 122

Figure 5.3: Reaction pathways operating in the interaction of chloroethene and CeO₂(111) surface (a) and direct elimination of Cl₂ from 1,2-dichloroethene (b). Values in (a) are in reference to the initial configuration, M1. All values are in kJ mol⁻¹.....125

Figure 5.4: Reaction pathways operating in the interaction of chloroethane and the CeO₂(111) surface. Values (in kJ mol⁻¹) are in reference to the initial configuration, M5.....126

Figure 5.5: Decomposition of chloroethene over the CeO₂ (111)_{Vo} surface. Values (in kJ mol⁻¹) are in reference to the reactant in each step. ^a ref.[353]...130

Figure 5.6: Hirshfeld's atomic charges and $f^{-1}(r)$ indices for stoichiometric and partially reduced CeO₂(111) surfaces.131

Figure 5.7: Surface hydrogen transfer reactions from HO₁ and H-V_o sites to adsorbed C₂H₃ (a), C₂H₅ (b) and C₆H₅ (c) adducts. All values are in kJ mol⁻¹.133

Figure 5.8: Reaction pathways operating in the interaction of chlorobenzene and the CeO₂(111) surface. (a) and (b) describe direct fission of C-Cl and C-H bonds, respectively. (c) illustrates fission of the C-Cl bond over a V_o site. All values are in kJ mol⁻¹.136

Figure 5.9: Surface reactions of an adsorbed phenol moiety and a surface hydroxyl group, HO_{ads} (a), and between an adsorbed chlorobenzene and HO_{ads}. All values are in kJ mol⁻¹(b). Oxygen atoms in the HO_{ads} group is blue coloured to distinguish them from oxygen lattice in red.137

Figure 5.10: Reactions initiated from the adsorbed phenyl moiety and an oxygen molecule adsorbed at a V_o site. All Values are in reference to the reactant in each step. Also, all values are in kJ mol⁻¹. Oxygen atoms originating from oxygen molecules are yellow colored to distinguish them from oxygen lattice in red.....139

Figure 5.11: Formation of 1,4-dichlorobenzene initiated by hydrogen abstraction by an O⁻ surface anion followed by chlorine transfer from the surface to the vacant para-site. Values are in kJ mol⁻¹ in reference to the initial reactant, M39.140

Figure 5.12: Formation of 1,4-dichlorobenzene over a per-chlorinated CeO₂(111)_{Cl} surface Values are in kJ mol⁻¹ in reference to the initial reactant, M42.143

Figure 5.13: Reaction rates for the decomposition of the selected CVOCs over the stoichiometric CeO₂(111) surface based on 1000 ppm of reactants and a full coverage of the active sites.146

Figure 5.14: Comparison between predicted and experimental conversion values [70, 336, 370] for the decomposition of chloroethene (a), chloroethane (b) and chlorobenzene (c) over the stoichiometric CeO ₂ (111) surface.	147
Figure 6.1: Total density of state (DOS) for bulk Tb ₂ O ₃	152
Figure 6.2: Optimized TbO ₂ unit cell. Light blue and red spheres signify Tb and O atoms, respectively.	155
Figure 6.3: Values of ΔC^{QHA} for fluorite-structure.	156
Figure 6.4: Calculated free energies in eV as a function of unit- cell volume in Å ³ for bulk TbO ₂	156
Figure 6.5: Phonon density of states for bulk TbO ₂	157
Figure 6.6: Variation of Bulk modulus of TbO ₂ with temperature and pressure.	158
Figure 6.7: Heat capacities in J/mol.K per mol of TbO ₂ at different pressures as a function of temperature in K.	158
Figure 6.8: Thermal expansion of terbium dioxide as a function of temperature and pressure.	159
Figure 6.9: Dependence of V/V_0 on temperatures and pressures.	159

Figure 6.10: Side and top views of different terminations of TbO_2 (100) surface: (a) and (b) are $\text{TbO}_2(100) : \text{O}$, (c) and (d) are $\text{TbO}_2(100) : \text{O}$ with 50% surface oxygen vacancies, (e) and (f) are $\text{TbO}_2(100) : \text{O}$ with 25% surface oxygen vacancies, (g) and (h) represent $\text{TbO}_2(100) : \text{O}$ with one surface oxygen vacancy, (i) and (j) are $\text{TbO}_2(100) : \text{O}$ with one subsurface terbium vacancy, (k) and (l) correspond to $\text{TbO}_2(100) : \text{Tb}$, (m) and (n) symbolize $\text{TbO}_2(100) : \text{Tb}$ with one surface terbium vacancy. Light blue and red spheres denote Tb and O atoms, respectively. 161

Figure 6.11: Side and top views of different optimized terminations of TbO_2 (110) surface. Light blue and red spheres denote Tb and O atoms, respectively. 162

Figure 6.12: Side and top views of different terminations of TbO_2 (111) surface: (a) and (b) are $\text{TbO}_2(111)$, (c) and (d) represent $\text{TbO}_2(111) : \text{O}$, and (e) and (f) are $\text{TbO}_2(111) : \text{Tb}$. (g) and (h) are $\text{TbO}_2(111)$ with 50% surface oxygen vacancies, (i) and (j) are $\text{TbO}_2(111)$ with 25% surface oxygen vacancies, (k) and (l) represent $\text{TbO}_2(111)$ with one surface oxygen vacancy, (m) and (n) are $\text{TbO}_2(111)$ with one subsurface terbium vacancy, (o) and (p) correspond to $\text{TbO}_2(111) : \text{O}$ with 0.5 surface oxygen vacancies, (q) and (r) signify $\text{TbO}_2(111) : \text{O}$ with 0.25 surface oxygen vacancies, (s) and (t) symbolize $\text{TbO}_2(111) : \text{O}$ with one surface oxygen vacancy, (u) and (v) are $\text{TbO}_2(111) : \text{O}$ with one

subsurface terbium vacancy,. Light blue and red spheres denote Tb and O atoms, respectively.....163

Figure 6.13: Calculated surface free energy of different TbO₂ (100) and TbO₂ (110) surfaces as a function of the change in oxygen chemical potential $\Delta\mu_o$ with the analogue pressure bar lines at different temperatures of T of 800, 1000, 2000 and 2500 K, and with corresponding temperature bar lines at different pressures of $P= 1$ atm and 10^{-12} atm..... 170

Figure 6.14: Calculated surface free energy of different TbO₂ (111) surfaces as a function of the change in oxygen chemical potential $\Delta\mu_o$ 170

Figure 6.15: Calculated surface free energy for the most stable cases of the three plausible TbO₂ surfaces as a function of the change in oxygen chemical potential $\Delta\mu_o$ 171

Figure 7.1: XRD pattern of CeO_x thin films deposited on the silicon substrate at various oxygen/argon flow ratios..... 182

Figure 7.2: XPS High resolution of Ce 3d spectra. 184

Figure 7.3: Cross sectional FESEM images of Ce-oxide coatings prepared with various oxygen/ argon gas mixtures. 185

Figure 7.4: FTIR spectra of CeO_x films deposited on c-silicon substrate as a function of oxygen/argon flow ratios..... 187

Figure 7.5: Optical reflectance spectra of CeO_x films deposited on c-silicon substrate as a function of oxygen/argon flow ratios.188

Figure 7.6: Variation of absorption coefficient with wavelength for CeO_x films deposited on c-silicon at different oxygen/argon flow ratios.188

Figure 7.7: Plots of $(\alpha E)^{1/2}$ versus (E) of CeO_x deposited on c-silicon substrate at various oxygen/argon flow ratios.....189

Figure 7.8: Variation of refractive index with wavelength for CeO_x films deposited on c-silicon substrate as a function of oxygen/argon flow ratios..191

Figure 7.9: Variation of extinction coefficient with wavelength for CeO_x films deposited on c- silicon at different oxygen/argon flow ratios.191

Figure 7.10: Real part of dielectric constant vs photon energy of CeO_x films deposited on c-silicon at different oxygen/argon flow ratios.193

Figure 7.11: Imaginary part of dielectric constant vs photon energy of CeO_x films deposited on c-silicon at different oxygen/argon flow ratios.193

Figure 7.12: Variation of loss angle with wavelength for CeO_x deposited on c-silicon at different oxygen/argon flow ratios.194

Figure 7.13: Variation of energy loss functions, (a) volume energy loss and (b) surface energy loss of CeO_x deposited on c-silicon substrate at various oxygen/argon flow ratios.196

Figure 7.14: Conventional unit cell of Ce-oxide (CeO_2) structure. Gray and red spheres refer to cerium and oxygen atoms, respectively.197

Figure 7.15: Total density of states of Ce-oxide (CeO_2) clusters.....198

Figure 7.16: Simulated absorption spectrum of CeO_2 clusters.....199

Figure 7.17: Simulated real and imaginary parts of dielectric constants of CeO_2 clusters.....200

Figure 7.18: Simulated refractive index (n) and extinction coefficient (k) spectra of Ce-oxide coatings.....201

Figure 8.1: XRD spectra of CuCo-oxide coatings before annealing and after being annealed at 200-500°C in steps of 100°C.....211

Figure 8.2: Rietveld refinement of XRD spectra of CuCo-oxide coatings before annealing and after being annealed at various temperatures.212

Figure 8.3: XPS survey spectra of CuCo-oxide coatings before and after annealing.214

Figure 8.4: Decoupling of high resolution XPS spectra of $\text{Cu}2p_{3/2}$ peak of CuCo-oxide coatings (a) before annealing, and annealed at: (b) 200°C, (c) 300°C, (d) 400°C, and (e) 500°C.....216

Figure 8.5: Decoupling of high resolution XPS spectra of Co2p_{3/2} peak of CuCo-oxide coatings (a) before annealing, and annealed at: (b) 200°C, (c) 300°C, (d) 400°C, and (e) 500°C.....218

Figure 8.6: Decoupling of high resolution XPS spectra of O1s peak of CuCo-oxide coatings (a) before annealing, and annealed at: (b) 200°C, (c) 300°C, (d) 400°C, and (e) 500°C.....220

Figure 8.7: FESEM images of CuCo-oxide coatings (a) before annealing, and annealed at: (b) 200°C, (c) 300°C, (d) 400°C, and (e) 500°C.....222

Figure 8.8: AFM images of CuCo-oxide coatings (a) before annealing, and annealed at: (b) 200°C, (c) 300°C, (d) 400°C, and (e) 500°C.....223

Figure 8.9: UV-Vis reflectance and absorptance spectra of CuCo-oxide coatings before annealing and after being annealed at different temperatures.226

Figure 8.10: FTIR reflectance spectra of CuCo-oxide coatings before annealing and after being annealed at different temperatures.....226

Figure 9.1: Energy profile for the first hydrogenation step in the partial hydrogenation route of acetylene over the CeO₂ (111) surface at different U values. Values of activation barrier (tilted) and reaction energy are in kcal/ mol with respect to the initial reactant. Red cream, gray, and white stand for atoms, oxygen, cerium, carbon, and hydrogen, respectively.235

Figure 9.2: Energy profile for the second hydrogenation step in the partial hydrogenation route of acetylene over the CeO_2 (111) surface at different U values. Values of activation barrier (tilted) and reaction energy are in kcal/mol with respect to the initial reactant.236

Figure 9.3: Energy profile for the first hydrogenation step in the full hydrogenation route of acetylene over the CeO_2 (111) surface at different U values. Values of activation barrier (tilted) and reaction energy are in kcal/mol with respect to the initial reactant.237

Figure 9.4: Energy profile for the second hydrogenation step in the full hydrogenation route of acetylene over the CeO_2 (111) surface at different U values. Values of activation barrier (tilted) and reaction energy are in kcal/mol with respect to the initial reactant.238

List of Tables

Table 2.1: Bulk modulus B , its pressure derivative B' , and the phase transition pressure for the complete series of Ln_2O_3 . Reproduced from ref. [3]. Results are reported for two DFT functionals, i.e., LDA and GGA + U.	9
Table 2.2: Stoichiometric and non- Stoichiometric structural properties of CeO_2	11
Table 2.3 : Summary of the most important catalysts used for VOCs Catalytic Combustion.	21
Table 4.1: The lattice parameters with their space groups, molar volume per formula unit and calculated energy band gaps for all the C -type Ln_2O_3 in equilibrium states.	94
Table 4.2: Bader's charges (in e) on lanthanide (Ln) and O atoms.	99
Table 4.3: The elastic constants C_{ij} (C_{11} , C_{12} , C_{44}), bulk modulus B , shear modulus G , Young's modulus E , Poisson's ratio ν of lanthanide sesquioxides with cubic structure. All elastic properties except ν are in GPa. S : stable.	100
Table 4.4: Heat of formation for the selected dioxides and sesquioxides.	103
Table 4.5: Variation of charge transfer of cerium with dopants (Hf and/or Zr) contents.	111

Table 5.1: Imaginary frequencies for located transition strictures (in cm^{-1}). ..	121
Table 5.2: Comparison between energy requirements for gas phase dehydrohalogenation and an analogous process assisted by the CeO_2 (111) surface. Numbers in parenthesis refer to the experimental gas phase values (obtained based on the standard enthalpies of formation of species sourced from ref. [337]). All values are in kJ mol^{-1}	123
Table 5.3: Arrhenius parameters obtained from fitting the conversion-temperature profiles to a PFR model.	143
Table 5.4: Calculated reaction rate constants (in $\text{cm}^5 \text{mol}^{-2} \text{s}^{-1}$) for the dissociative adsorption of the selected CVOCs over the stoichiometric CeO_2 (111) surface.	144
Table 6.1: Deviations of interlayer spacing of the topmost two layers in the relaxed slabs in reference to their analogous bulk values Δd_{ij}	165
Table 6.2: Calculated Bader's charges in electron (e) on the Tb and O atoms in TbO_2 surfaces.	167
Table 6.3: Gibbs free energy γ (T, P), in $\text{eV}/\text{\AA}^2$, for all surfaces at oxygen- lean and oxygen- rich limits.	172
Table 7.1: Sputtering parameters for the deposition of CeO_x coatings.	178
Table 7.2: Thickness of CeO_2 films.	180

Table 7.3: Details of the elemental compositions of CeO_x prepared under different oxygen/argon flow ratios as acquired from XPS measurements.	183
Table 8.1: Variation of crystallite size, lattice parameters, residual stress and microstrain of CuCo-oxide coatings with annealing temperatures.	212
Table 8.2: Elemental compositions of CuCo-oxide coatings before and after annealing in air.	215
Table 8.3: The deconvolution results of high resolution XPS spectra at Cu2p photoelectron line and its satellite.	217
Table 8.4: The deconvolution results of high resolution XPS spectra at Co2p photoelectron line and its satellite.	219
Table 8.5: The deconvolution results of high resolution XPS spectra at O1s photoelectron line and its satellite.	221
Table 8.6: Surface roughness parameters of CuCo-oxide coatings before and after annealing.	224
Table 8.7: Solar absorbance, thermal emittance and solar selectivity values of CuCo-oxide coatings before annealing and after annealing at different temperatures in air for 1 hr.	227
Table 8.8 : Bader's charges on Cu, Co and O atoms in e on $Cu_xCo_{3-x}O_4$ ($x = 0, 0.75, 1.5, 2.25$ and 3) coatings.	228

Table 9.1: Variation of activation barriers and reaction energies of acetylene hydrogenation into ethane over the CeO_2 (111) surface. Corresponding values by Carrasco et al. [73] are highlighted.....234

Chapter 1 : Introduction and Overview

1.1 Introduction

Transition metals (TMs) are a class of elements in the periodic table with distinguished electronic structures. They differ from other materials in that their valence electrons can occupy more than one shell, affording them with a number of possible oxidation states. This is clearly displayed in acquiring different electronic characteristics, spanning insulating, conducting, as well as including superconducting behaviors. In addition, owing to paired and unpaired electrons in their orbitals, they also exhibit unique magnetic properties such as paramagnetism, ferromagnetism and diamagnetism.

Transition metals and their oxides have emerged as promising materials in a wide array of applications, most notably in catalysis, lighting, electronics and automobile industries. These applications stem from the unique properties of transition metal oxides as materials incurring excellent mechanical and optical properties. Owing to their favorable properties, some TMs are deployed in the improvement of optical and mechanical characteristics of materials. A great deal of experimental and theoretical work in the last decade has provided accurate measurements of optical and mechanical properties for several TMs, a better understanding of electronic reasoning behind these properties, and the variation of thermo-mechanical characteristics with the relative loads of TMs. Figure 1.1 depicts some of the main applications of transition metal oxides.

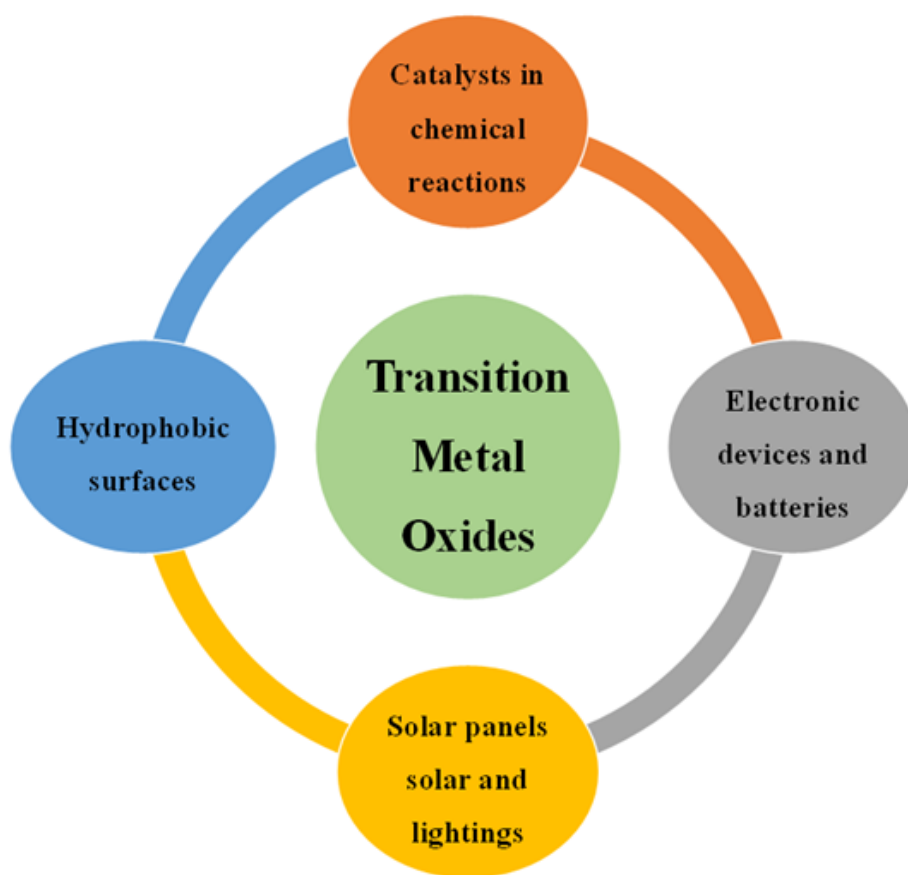


Figure 1.1 : Applications of transition metal oxides.

Rare earth metals, as a part of transition metal family, and their oxides have displayed remarkable features and characteristics suitable to many important industrial fields, especially in automobile and electronic industries. Figure 1.2 depicts the position of rare earth metals in the periodic table of elements.

1 H																	2 He
3 Li	4 Be											5 B	6 C	7 N	8 O	9 F	10 Ne
11 Na	12 Mg											13 Al	14 Si	15 P	16 S	17 Cl	18 Ar
19 K	20 Ca	21 Sc	22 Ti	23 V	24 Cr	25 Mn	26 Fe	27 Co	28 Ni	29 Cu	30 Zn	31 Ga	32 Ge	33 As	34 Se	35 Br	36 Kr
37 Rb	38 Sr	39 Y	40 Zr	41 Nb	42 Mo	43 Tc	44 Ru	45 Rh	46 Pd	47 Ag	48 Cd	49 In	50 Sn	51 Sb	52 Te	53 I	54 Xe
55 Cs	56 Ba	57-71 Lanthanoids	72 Hf	73 Ta	74 W	75 Re	76 Os	77 Ir	78 Pt	79 Au	80 Hg	81 Tl	82 Pb	83 Bi	84 Po	85 At	86 Rn
87 Fr	88 Ra	89-103 Actinoids	104 Rf	105 Db	106 Sg	107 Bh	108 Hs	109 Mt	110 Ds	111 Rg	112 Cn	113 Uut	114 Fl	115 Uup	116 Lv	117 Uus	118 Uuo

Figure 1.2: The position of rare earth elements in the periodic table.

Their application to the abovementioned industrial fields is due to the unique properties rare metal oxides possess, such as oxidation resistance and water repellent surfaces. This crucial role in extending lifetime of the coatings, enhancing their hardness, and increasing their thermal stability under harsh operating environment. It has previously been shown that the oxides of rare earth metals, such as Ce, La, Y, and Zr, enhance the high temperature oxidation resistance of various metal alloys up to 1000 °C. Investigations of structural, thermal, optical and mechanical properties of films, purely consisting of transition metal oxides, have been a central research theme. Experimentally, the aforementioned properties of these films have been probed using a combination of characterization techniques such as X-ray photoelectron spectroscopy (XPS), X-ray diffraction (XRD), field emission scanning electron microscopy (FESEM), atomic force microscopy (AFM), ultra violet visible (UV-vis), Fourier transform infrared spectroscopy (FTIR) and nanoindentation. From theoretical point of view, attempts have been made to underpin various structural and electronic features of rare earth metal oxides based on accurate density functional theory (DFT) calculations. Covered aspects encompass: geometries and thermodynamic stability of their surfaces; chemical reactions with prominent species such as hydrogen and water molecules; and predicting their thermo-mechanical properties. Literature also presents comprehensive DFT accounts on thermal stability of transitional metal oxide surfaces and their chemical reactivity towards fragmentation or forming chemical species. Furthermore, computational studies

have also simulated experimentally-measured various optical and mechanical properties of transition metal; including rare earth oxide coatings.

1.2 Objectives and Thesis Outline

Rare earth metals and their oxides are now widely deployed in electronic devices such as electrodes in batteries, and anti-reflection coating material in solar selective surfaces, catalysts ingredients in partial hydrogenation reactions, and in oxidative decomposition of halogenated pollutants. The major objective of this dissertation is to build a comprehensive and reliable framework for the various characteristic properties of the lanthanide family and mixed metal oxides (spinal metal oxides). The underlying aim is to acquire a detailed atomic-based understanding that enables improvement of the unique mechanical, optical and catalytic application of this family of compounds.

This dissertation is arranged as follows: **Chapter 2** surveys literature pertinent to techniques utilized in the synthesis of transition metal oxides with a focus on the rare earth metal oxides. The electronic, geometric, thermo-mechanical and optical properties of these compounds are also examined, along with their catalytic capacity toward prominent chemical applications.

Chapter 3 highlights the preparation techniques deployed in **Chapters 7** and **8** in this thesis, as well as the techniques utilized to characterize the investigated films. Specifically, the physical principles underpinning the operation of these characterization techniques have been described. Apart from experimental instruments, this chapter also presents a brief background on utilized theoretical approaches in the thesis, most notably, the DFT formalism, the transition state theory, the software used throughout chapters of the thesis, and the ab initio atomistic thermodynamics approach that is typically utilized to construct thermodynamic stability diagram of surfaces.

Chapter 4 reports on the electronic and mechanical properties for the bulk of rare earth oxides (lanthanide series) as well as the thermodynamic properties of the most important compound in this family, ceria (CeO_x). We found in this chapter that alloying CeO_x phases with Zr and Hf atoms systematically reduces reduction energies with respect to pure ceria.

For the first time, this chapter provides Bader's charge distribution for all structures in this family. **Chapter 5** presents a theoretical investigation of the catalytic performance of both pristine and reduced CeO₂ (111) surface in destroying some chlorinated volatile organic compounds; namely chloroethene (CE), chloroethane (CA) and chlorobenzene (CB). We found that the C-Cl bond in the three studied compounds is broken over CeO₂ (111) via modest activation barriers. Dehalogenation of CE and CA molecules (*i.e.*, release of HCl molecules) occurs via a dissociative addition pathway rather than via a direct elimination route. **Chapter 6** explores both perfect and defect surfaces of terbia (TbO₂); a material that is widely deployed in electronic and chemical applications. Findings from ab initio atomistic thermodynamic calculations indicate that surfaces with Tb atoms and surfaces with oxygen atoms and oxygen vacant sites truncated along the (111) direction incur higher thermodynamic stabilities than other surfaces across a wide range of oxygen chemical potentials. **Chapter 7** presents a combined theoretical and experimental study on the structural and optical properties of thin film samples of CeO_x deposited on Si substrates. The XPS survey scans of the CeO_x coatings reveal that the Ce: O ratio between 14% and 56% oxygen/argon flow ratios is largely consistent with the CeO₂ stoichiometry. Introducing oxygen pressure into the system enhances the antireflection characteristics of the films in the visible regions. In **Chapter 8**, a theoretical and experimental investigation is presented to report on the electronic, structural and optical properties of mixed metal oxides coatings such as CoCu-oxides. In this chapter, we have also computed Bader's charges of various forms of CoCu-oxides. Our results indicate that the solar selectivity of the studied films improves with an increase in the annealing temperature. The success of the DFT +*U* approach to precisely calculate the reduction energies of bulk CeO₂ in **Chapter 4** motivated the investigation of the influence of the variation of *U* value on the activation and reaction energies for well-studied catalytic systems, that is partial and fully hydrogenation of acetylene over the CeO₂(111) surface. Calculations in **Chapter 9** disclose that reaction barriers for prominent hydrogenation step correlates positively with the utilized value of *U*. In addition to the very demanding computational frameworks, it is suggested in this chapter that optimization of the *U* value could also be achieved via kinetic modelling against experimental profiles of products. We have shown that the barrier and reaction energies positively increase with the *U* values. Finally, **Chapter 10** summarizes the most important findings in this thesis along with suggestions for future directions. Figure 1.3 presents an overall layout of the thesis with an emphasis on the synergy between experimental measurements and accurate DFT calculations.

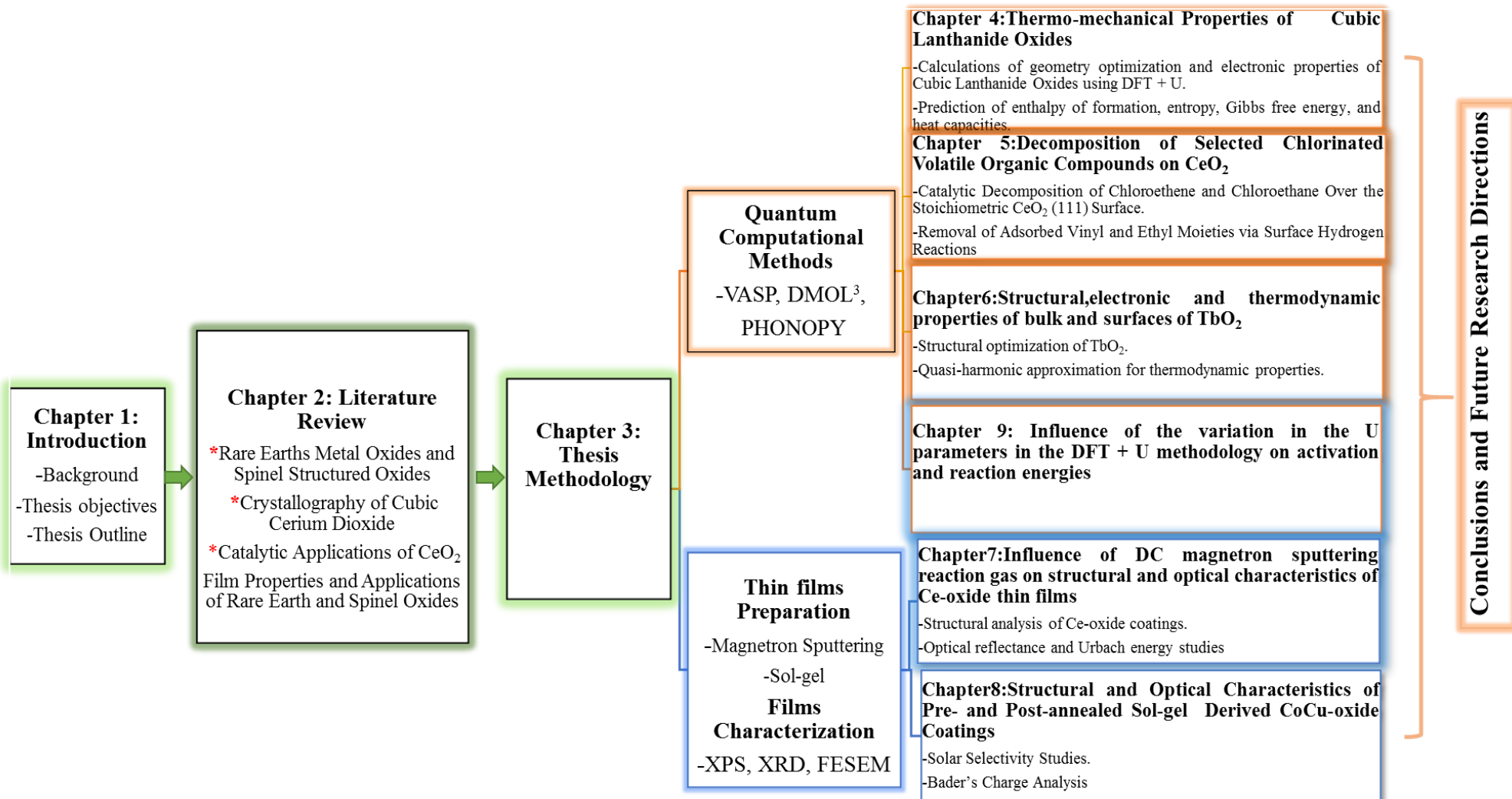


Figure 1.3 : The overall layout of the thesis.

Chapter 2 : Literature review



2.1 Rare Earths Metal Oxides

A great deal of experimental and theoretical research has been devoted towards studying the properties of rare earth metals (lanthanide metals) and their oxides (Ln_2O_3). These materials are widely deployed in a diverse range of applications encompassing catalysis, lighting, electronics and automobile industries. Depending on the operational temperature and pressure, Ln_2O_3 species can adopt three distinct phases at temperatures below 2000 °C. The light rare earth elements Ln_2O_3 oxides (A-type, space group of $P3m1$, no.164) feature a hexagonal structure as depicted in Figure 2.1.

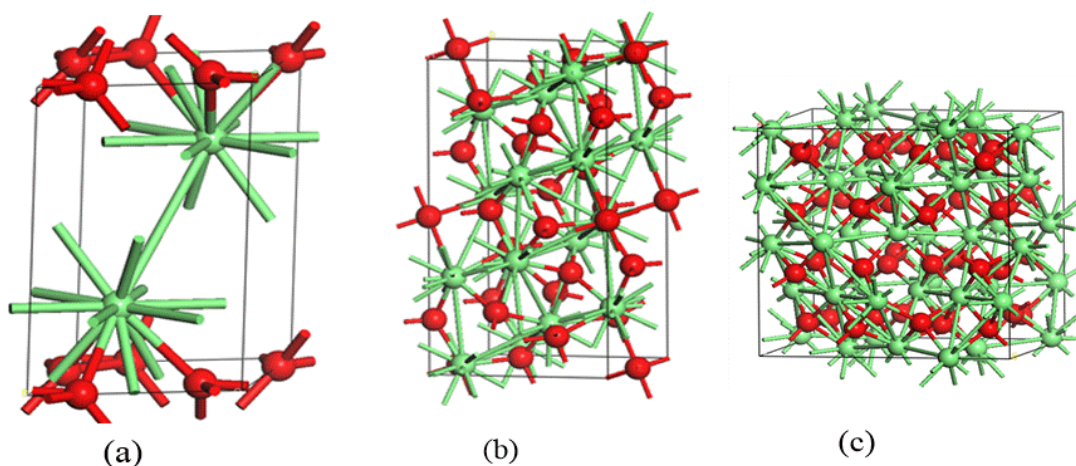


Figure 2.1: Unit cells of Ln_2O_3 (a) A-type (hexagonal), (b) B-type (monoclinic), and C-type (cubic).

The heavy rare earth elements oxides Ln_2O_3 (C-type, space group of $Ia3$, no. 206) are known to adopt cubic structures (Figure 2.1), whilst the remaining rare earth elements oxides generally crystallize in either C-type structure, or B-type structure (monoclinic crystallography) [1]. All of the rare earth elements oxidize readily, but to a varying extent and oxidation state. In the presence of air for instance, cerium (Ce) oxidizes to ceria (CeO_2) which possesses a fluorite structure (Figure 2.2). On the other hand, Praseodymium (Pr) occurs naturally as Pr_6O_{11} , whilst terbium (Tb) is found as Tb_4O_7 . Both of these oxides transform into PrO_2 and TbO_2 under oxygen pressure. The three aforementioned dioxides are crystallized as cubic fluorite face-centered structures. However, the rest of the lanthanide oxides are found in nature as sesquioxides (Ln_2O_3) [2]. It is worth mentioning that most of

rare earth oxides are thermally stable and expected to be highly active against H₂O and CO₂. The most common oxidation state they have is that of a trivalent state, but they can also switch to either divalent or a tetravalent oxidation state.

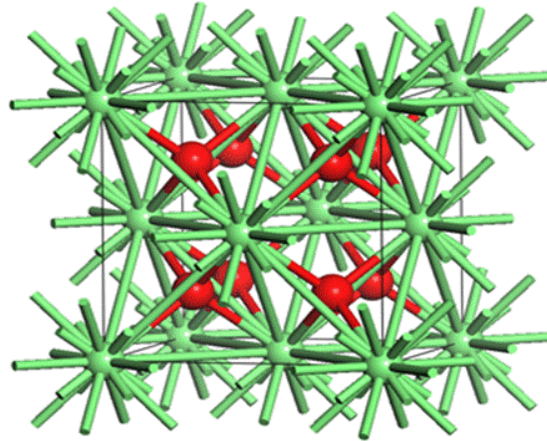


Figure 2.2: Adopted cubic fluorite structure of the lanthanide dioxide (LnO₂), CeO₂, PrO₂ and TbO₂.

The geometric, electronic and mechanical properties of rare earth sesquioxides, and the phase transition pressure from cubic (*C*-type) to hexagonal (*A*-type) have been extensively investigated by means of first-principle calculations' predominantly based on the density functional theory (DFT)- formalisms [3]. Richard *et al.* [3] calculated and validated their theoretical findings on structural and mechanical properties along with the pressure at which phase transition from cubic to hexagonal occurs against corresponding experimental values. Favorable agreement was obtained between the theoretical and empirical studies for the investigated properties. Their study reported that inclusion Hubbard parameter *U* in the methodology resulted in a noticeable correction to the structural properties. The calculated bulk moduli *B*, its pressure derivative *B'*, and the phase transition pressures are depicted in Table 2.1.

Table 2.1: Bulk modulus B , its pressure derivative B' , and the phase transition pressure for the complete series of Ln_2O_3 . Reproduced from ref. [3]. Results are reported for two DFT functionals, *i.e.*, LDA and GGA + U .

Compound	Method	A-phase		C-phase		$P_{C \rightarrow A}$ (GPa)
		B (GPa)	B'	B (GPa)	B'	
La_2O_3	LDA	155.2	4.34	133.9	4.15	0.0
	GGA + U	142.8	4.39	124.4	4.18	
Ce_2O_3	LDA	166.8	4.45	148.5	5.62	-2.6
	GGA + U	142.0	4.29	135.5	4.00	
Pr_2O_3	LDA	170.6	4.38	148.2	4.46	-3.9
	GGA + U	152.3	4.00	157.9	4.00	
Nd_2O_3	LDA	173.5	4.43	150.5	4.38	-3.7
	GGA + U	155.1	3.62	122.0	5.45	
Pm_2O_3	LDA	176.2	4.50	153.8	4.50	-2.7
	GGA + U	156.1	4.01	129.0	4.00	
Sm_2O_3	LDA	177.4	4.42	153.4	4.22	-1.0
	GGA + U	147.0	4.49	138.3	4.29	
Eu_2O_3	LDA	177.7	4.39	156.1	4.33	0.5
	GGA + U	134.3	4.00	143.1	4.17	
Gd_2O_3	LDA	178.1	4.32	158.3	4.42	-0.7
	GGA + U	160.7	4.39	144.7	4.24	
Tb_2O_3	LDA	179.5	4.22	158.6	4.31	-0.3
	GGA + U	159.9	4.53	139.0	4.67	
Dy_2O_3	LDA	180.9	4.24	159.9	4.37	1.5
	GGA + U	160.4	4.64	148.9	5.14	
Ho_2O_3	LDA	180.9	4.63	161.6	4.50	3.4
	GGA + U	179.1	3.71	152.0	4.48	
Er_2O_3	LDA	180.4	4.64	161.2	4.46	5.7
	GGA + U	173.6	4.51	157.2	3.98	
Tm_2O_3	LDA	178.5	4.56	161.6	4.40	7.0
	GGA + U	168.4	4.65	157.7	4.36	
Yb_2O_3	LDA	177.8	4.61	161.6	4.52	7.5
	GGA + U	178.7	4.33	160.9	4.27	
Lu_2O_3	LDA	198.8	4.33	179.4	4.30	7.7
	GGA + U	179.9	4.29	163.0	4.29	

This dissertation in Chapters 4 and 6 investigates the cubic crystallographic type of the rare earth oxide with a special focus on Cerium (Ce) and Terbium (Tb).

2.2 Structural Characteristics of Stoichiometric and Non-Stoichiometric Cerium Dioxide

The oxidation of cerium metal is known to result in the formation of many different phases of cerium oxide ranging from CeO₂ (IV) to Ce₂O₃ (III). The oxidation processes of these two extreme oxidations are exothermic by -1796 and -1089 kJ mol⁻¹ respectively at temperature of 298 K. Between these two phases, partially oxidized phases (CeO_{2-y}), prevail depending on the temperature and oxygen pressure. Ceria (CeO₂) exhibits a fluorite structure crystallized as a centred cubic face (*f.c.c.*) with the space group of *Fm-3m* ($a = 0.541134$ nm, JCPDS 34-394), comprising of a cubic close-packed combination of metal atoms with tetrahedral holes filled by oxygen atoms. Reduced CeO_{2-y} forms by releasing oxygen atoms from the cluster leaving oxygen vacancies behind. The Kröger-Vink notation governs the process of creation of vacancies as expressed [4],



Where Ce and O denote cerium and oxygen atoms, respectively, and $V_{O^{\cdot\cdot}}$ signifies oxygen vacancy.

On the basis of the notation above, the exact nature of the resultant phase relies on the amount of the oxygen released from CeO₂. X-ray diffraction (XRD) was employed to determine the structural parameters of reduced CeO_{2-y} oxides, but this technique exhibits some limitations due to the low scattering power of oxygen. In order to overcome this limitation, the most common approaches to discover the structural phases in the Ce₂O₃-CeO₂ phase diagram are neutron or electron diffraction techniques [5-7]. As Table 2.2 portrays, at temperatures over 685 °C and low oxygen pressure, CeO₂ exhibits several forms of non-stoichiometric oxidation states (CeO_{2-y}). With y ranging from 0 to 0.286, a disordered structure of fluorite-related system termed as the α phase evolves [5, 6]. All phases in this oxidation range adopts a fluorite-type structure but with an ordered arrangement. Formed phases include [7-10] Ce₆O₁₁ (the β phase, monoclinic) [10], Ce₁₁O₂₀ (the δ phase, triclinic) [11], and Ce₇O₁₂ (rhombohedral) [11, 12]. When y increases to exceed 0.286, a new phase termed as the σ phase emerges. The σ phase exists as a body-centred cubic (*b.c.c.*) structure. The C-type sesquioxide Ce₂O₃ formed in the bixbyite structure (space group Ia-3) is the

compositional final member of the σ phase which is related to the *f.c.c.* - structure of CeO_2 . The lattice parameters of the *C*-type Ce_2O_3 are nearly twice that of CeO_2 . This is attributed to the two cation groups being nearly identical, with oxygen anions residing in all tetrahedral sites in the *f.c.c.* structure, whereas only three-quarters exist in the *b.c.c.* structure in an ideally ordered array. Due to the high reactivity of the cubic sesquioxide structure (*C*-type Ce_2O_3) [13] with atmospheric oxygen, the final crystal structure, called the θ phase, is formed. This phase is well known as the *A*-type Ce_2O_3 which is crystallized in a hexagonal structure form, belonging to the $P32/m$ space group ($a = 0.389$ nm, $c = 0.607$ nm; JCPDS 23-1048) [14].

Table 2.2: Stoichiometric and non- Stoichiometric structural properties of CeO_2 .

Material	oxidation extent, y	Temperature ($^{\circ}\text{C}$)	Thermal treatment	Structural phase
CeO_{2-y}	0	< 685	-	Fluorite structure with a face-centred cubic (f.c.c)
CeO_{2-y}	$0 < y < 0.286$	> 685	-	α phase (disordered fluorite structure)
CeO_{2-y}	0.166	> 685	Thermally treated	β phase (ordered fluorite, monoclinic structure)
CeO_{2-y}	0.181	> 685	Thermally treated	δ phase (triclinic structure)
CeO_{2-y}	0.285	> 685	Thermally treated	Rhombohedral structure
CeO_{2-y}	>0.286	> 685	-	σ phase (<i>C</i> -type Ce_2O_3 , body-centred cubic

2.3 CeO_2 -Included Solid Solutions

It is well known that fluorite structure of CeO_2 has the capability of forming solid solution systems with a wide array of oxides. The lattice dimensions of the solid solution typically obey the Vegard's rule; *i.e.*, a linear relation between lattice constant and solute concentration. It must be emphasized that the term 'dopant' should be utilized for cases involving the

introduction of a foreign cation in the ceria lattice, as opposed to situations in which two oxides are mixed [4].

Kim [15] reported an empirical equation clarifying the relationship between the lattice parameters of the solid solution, along with the ionic radius and the cation charge of the dopant introduced into the CeO₂ and fluorite-like oxide structures.

The relation is expressed as,

$$a = 0.5413 + \sum_k (0.0220\Delta r_k + 0.00015\Delta z_k)m_k \quad 2.2$$

where a in nm signifies the unit cell constant of the solid solution containing CeO₂, $\Delta r_k = r_k - r_{Ce(IV)}$ in nm corresponds to the variance between the K_{th} dopant' and Ce (IV) ionic radii, $\Delta z = z_k - z_{Ce(IV)}$ in nm denotes the charge variance of the K_{th} dopant and Ce (IV) and m_k signifies the molar focus of the K_{th} dopant. Kim indicated that the solubility of either oxide material into the fluorite crystallographic structure of CeO₂ relies on the elastic energy per ion present into the unit cell due to the variance in ionic radius. Therefore, a greater magnitude of Δr_k drives a higher elastic energy and a lower solubility limit. The greatest soluble cations possess a radius that corresponds to the matching radius, r_m , the one results in Vegard's slope=0. According to Kim's equation, r_m has to have a value of 0.097 nm for tetravalent dopant cations, 0.1038 nm for trivalent dopants, and 0.1106 nm for divalent dopants. Similar amounts were reported in previous works [16, 17]. Below, Figure 2.3 displays the measured and computed lattice parameters of fluorite-structure CeO₂ solid solutions formed with different rare earth oxides.

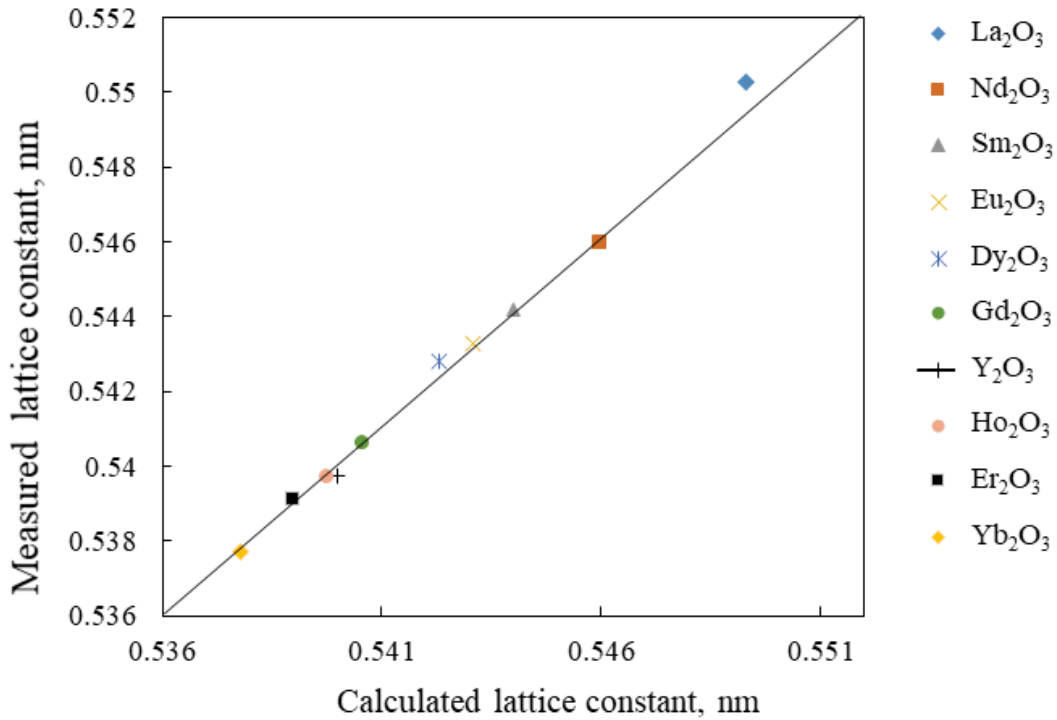


Figure 2.3: Experimental and calculated lattice parameters of fluorite-structure CeO₂ solid solution containing variant rare earth sesquioxides. Reproduced from ref. [15].

Building on the aforementioned discussions, the dopant concentrations display a clear impact on the structural properties of CeO₂-included solid solutions (i.e. lattice dimensions). Thus, Chapter 4 in this dissertation investigates the influence of introducing certain loads of transition metals such as hafnium (Hf) and zirconium (Zr) into the structure CeO₂- on the reduction energy and structural properties of CeO_x systems.

2.4 CeO₂- Metal oxide Solid Solutions

CeO₂-ZrO₂ mixed oxides have received significant attention in literature because of their wide deployment in the so-called three ways catalysts (*TWCs*). As such, the structural properties of CeO₂-based solid solutions have been thoroughly investigated. The difference in ionic radius of Zr⁴⁺ (0.084 nm for a 8-fold coordination) [18] and that of Ce⁴⁺ (0.097 nm) is only 15%.

Yashima and coworkers previously conducted studies on the CeO₂- ZrO₂ solid solution annealed in a Na₂B₂O₇-NaF atmosphere. They studied the properties of the system below 1000 °C using XRD analysis, displaying the entire equilibrium phase diagram of the CeO₂-

ZrO₂ solid solution. Analysis of their phase diagram reveals three crystalline structures depending on the temperature [19], namely cubic phase with CeO₂ high percentage and tetragonal or monoclinic phases with ZrO₂ high percentage. The balanced compositions of the tetragonal, monoclinic and cubic phases, as can be seen from Figure 2.4, occurs at $x=0.112, 0.009$ and 0.84 in Ce_xZr_{1-x}O₂ [19], respectively at temperature of 1055 °C.

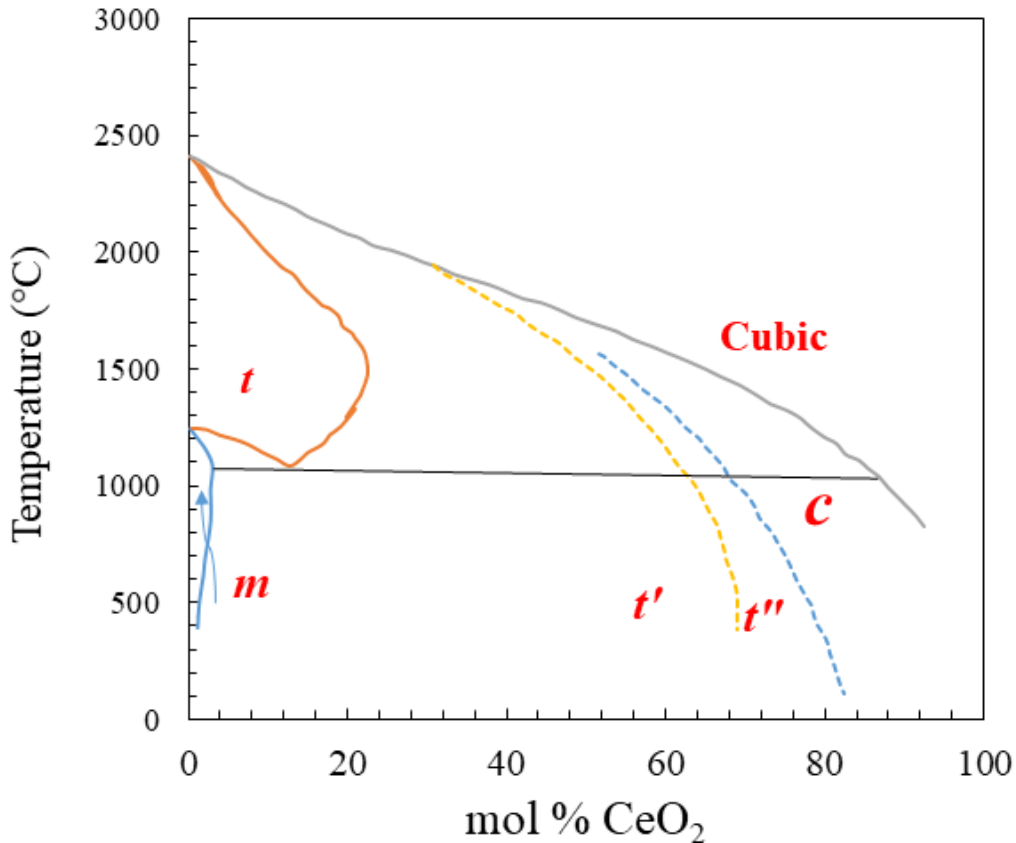


Figure 2.4: Phase diagram study of CeO₂-ZrO₂ system with different CeO₂ concentration as a function of temperature. Reproduced from ref. [20].

Detailed interpretation of the phase diagram is that a monoclinic crystalline phase belonging to the $P2_1/c$ space group is obtained for ZrO₂ and Ce_xZr_{1-x}O₂ system at x values lower than 0.12. With the increase of CeO₂ concentration in the system, the a_m (m refers monoclinic) value approaches that of b_m and the angle β_m lessens indicating a distortion of the monoclinic phase and all approaching those of the tetragonal structure [21, 22]. It must be noted that the phase boundary of $x=0.12$ is substantially affected by some parameters such as preparation of the sample and the grain size. These two parameters in turn affect the nucleation, growth, and kinetics of the transformation [22]. The three tetragonal phases denoted as t, t' and t'' [20-24] are crystallized when the oxygen content becomes higher than 0.12. The t phase is

stable at elevated temperature and for lower CeO₂ concentrations. As the CeO₂ content increases, the other two metastable phases of t' and t'' are formed. For the t and t' form, the c/a ratio is slightly higher than 1, whereas for the ratio of the t'' phase belonging to the $P4_2/nmc$ space group equals 1.

According to the vacancy formation energy in a CeO₂ cluster calculated via DFT, for systems with dopant amounts of ~ 3 mol%, tetravalent dopants such as Ti, Zr, and Hf (IVb in the periodic table) can insert into the bulk of CeO₂. On the contrary, other elements such as C, Si, Ge, Sn, and Pb (IVb in the periodic table) are segregated on the surface [25]. It is found that the vacancy creation energy of 4.035 eV per vacancy calculated by LDA functional and 3.097 eV per vacancy obtained by PBE functional reduce with increasing dopant size, reaching the best size that matches the Ce⁴⁺ ions.

CeO₂-HfO₂ samples have been the subject of extensive structural investigations. Findings obtained from these studies revealed similar structures to that observed for CeO₂-ZrO₂ system. On the basis of XRD studies [26] for samples annealed at 1400 °C for 48 h and cooled down slowly, stable Ce_xHf_{1-x}O₂ solid solutions with $x > 0.85$ (CeO₂-rich materials) are crystalized with cubic fluorite structure. Meanwhile, when $x < 0.15$ (HfO₂-rich materials) solid solutions are formed with monoclinic structure. The samples characterized by a combination of XRD and Raman analysis [27] adopted the metastable tetragonal phases (t' as well as t'').

2.5. Influence of the reduction energies of CeO₂

It is of significant importance to investigate the redox properties of a catalyst by calculating its reduction/oxidation energy. This in turn helps to predict the capability of that material in performing catalytic oxidation reactions. This investigation is carried out by calculating the vacancy formation energy E_{vac} needed to remove oxygen from the system for oxidation and hence creating a vacancy. An improvement by lowering the reduction energies of oxides is achieved via replacing the cations of the catalyst with others [28-30]. DFT investigations undertaken by Hu and Metiu [28] studied the influence of the addition of various cations to CeO₂ catalyst on its reduction energy. In this study, authors survey the effect of adding some dopants such as Pt, Ru, Zr, Ta, Mo, and W dopants in CeO₂ (111) on the neighboring oxygen or distant ones (see Figure 2.5). For the neighboring oxygen atoms, the calculated energies of

oxygen vacancy creation caused by the added cations (added dopants) were found to be almost identical. By contrast, the effect of these dopants has not been recorded on the reduction energy of the distant oxygen. Figure 2.5 displays the removal of oxygen atoms from different position in the CeO_2 (111) slab as a result of introducing dopants.

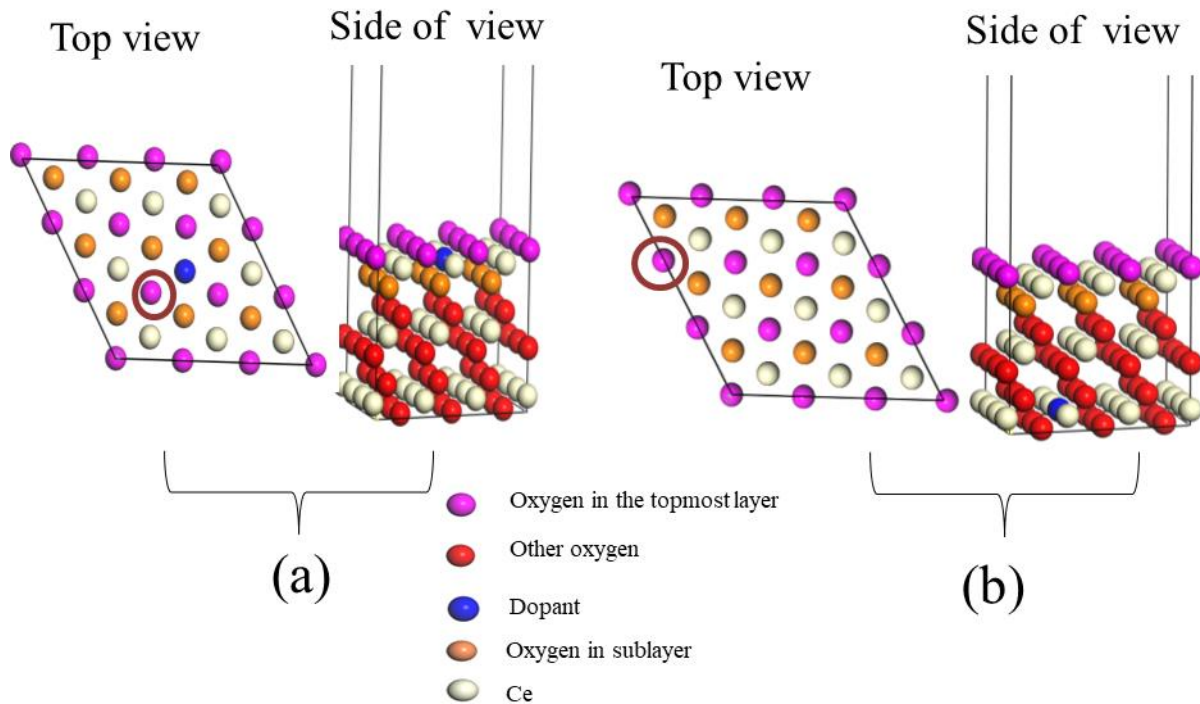


Figure 2.5: Side and top views of CeO_2 (111) slab, doped with a dopant. (a) Removal of oxygen neighboring in the doped slab. (b) Removal of furthest oxygen in the doped slab. Reproduced from ref. [28].

In another instance, first-principle calculations reported by Yang *et al.* [31] surveyed the impact of introducing Zr into a CeO_2 system on the redox properties of CeO_2 . They reported that the reduction energy to remove a neighboring oxygen atom reduced by 0.6 eV in reference to undoped- CeO_2 . In separate work, Yang and his collaborators [32] evaluated the vacancy formation energy of Pd –alloyed CeO_2 . They concluded that introducing Pd atoms into the ceria system lowered the vacancy formation energy from 3.0 eV to 0.6 eV.

To acquire an accurate understanding about the role of trivalent and tetravalent cations such as Zr^{4+} , La^{3+} , and Eu^{3+} incorporated into the ceria lattice, DFT calculations by Vinodkumar *et*

al. [33] concluded that alloyed ceria materials exhibit a better efficiency than unalloyed ceria for soot oxidation and this is attributed to an enhancement in the oxygen defects, specific surface area, and redox properties. Under the exposure of air under tight contact conditions, trivalent-alloyed CeO_2 were proven to be more efficient than tetravalent -alloyed ceria for soot combustion. Finally, Eu^{3+} -doped CeO_2 has been demonstrated to be catalytically more active than La^{3+} -doped CeO_2 and this was ascribed to higher surface area and an increase in oxygen vacancies.

Kim *et al.* [34] assessed the thermodynamic characteristics of $\text{Ce}_{1-x}\text{Zr}_x\text{O}_{2-y}$ solid solutions. As Figure 2.6 displays, the CeO_{2-y} and $\text{Ce}_{0.81}\text{Zr}_{0.19}\text{O}_{2-y}$ solid solution systems have been investigated in terms of the influence of the reduction extent on their redox properties. The figure shows that the reduction energy of ceria-zirconia solid solutions is much lower than that of pure ceria.

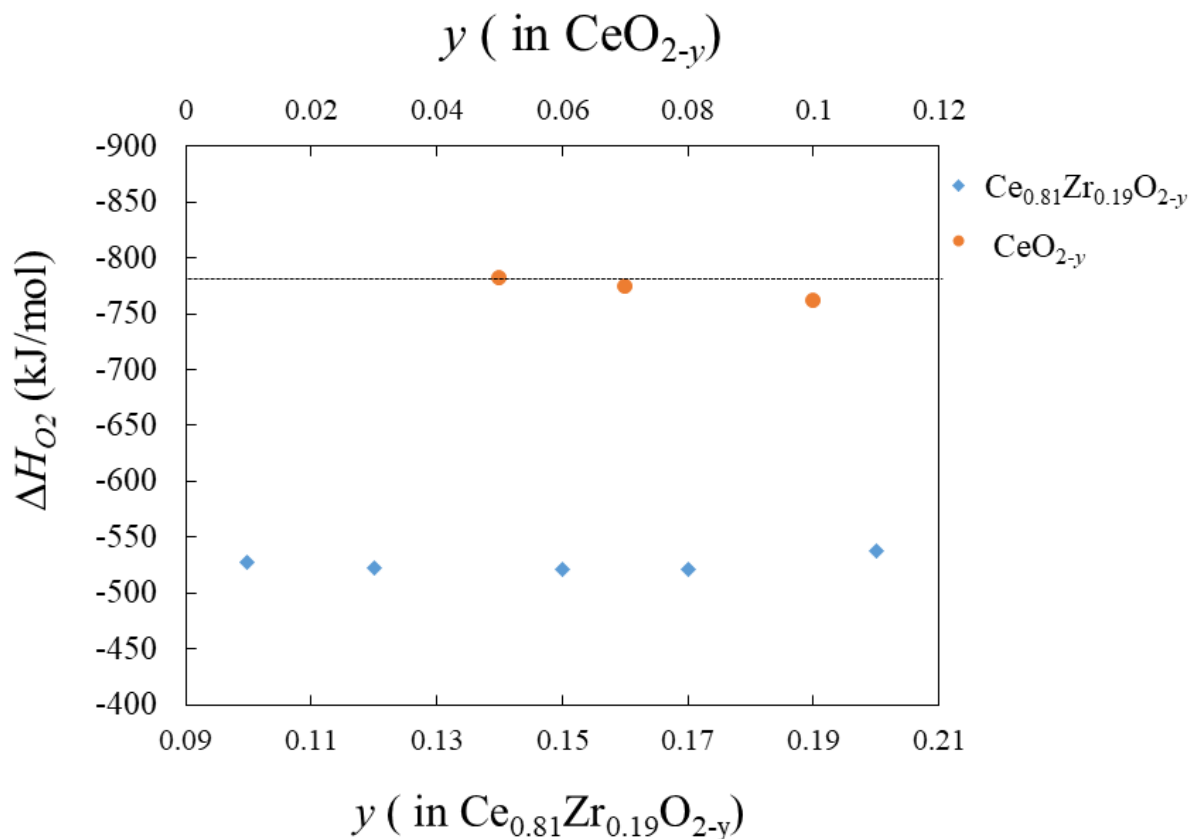


Figure 2.6 : Variation of oxidation enthalpies (ΔH) per O_2 with the reduction extent (y) in $\text{Ce}_{0.81}\text{Zr}_{0.19}\text{O}_{2-y}$ and CeO_2 systems. Reproduced from ref.[34].

2.6 Well-Known Catalytic Applications of CeO₂

2.6.1 Three Way Catalysts (TWCs) in Automotive Cars

The most popular application of cerium dioxide is *TWCs* in which CeO₂ or CeO₂-based materials act as supporters to convert some harmful gases such as CO, HC and NO_x emitted from the automotive vehicles into more benign forms. In this process, CO and HC are oxidized to be converted into CO₂ and H₂O respectively, whereas NO_x is reduced into N₂. In this catalytic technology, the oxidation reactions are supported by some noble elements namely Pt and/or Pd, whereas Rh is required to efficiently catalyze the reduction of NO_x [35]. Non-stoichiometric ceria (CeO_{2-y}) is a good store for oxygen during lean-to-rich transients and hence playing a crucial role to further reduce NO_x molecules. In contrast, stoichiometric ceria (CeO₂) is an excellent provider of the oxygen atoms needed to oxidize CO and HC during rich-to-lean transients [4]. The *TWC* was initially pioneered during 1970s-1980s, fabricated from a combination of CeO₂ and noble metals on doped Al₂O₃ support. Improvements on this design were achieved in the mid-1980s by developing the CeO₂ concentrations and optimizing the CeO₂ distribution on the support alloyed Al₂O₃. Nonetheless, the formation of undesirable CeAlO₃ and the unwanted reaction between CeO₂ and the noble elements is significantly diminished. However, this version of *TWS* could not control the cars pollution because of poor thermal stability. The final generation of *TWCs* convertor is the advanced *TWCs* that are based on CeO₂-ZrO₂ solid solution rather than pure CeO₂ [36]. This version enjoys a high efficiency to remove the pollutant emissions. As stated earlier, introducing ZrO₂ into the CeO₂ lattice enhances the oxygen storage capacity (OSC) of the system needed in the redox cycles, and hence improves the efficiency of the catalyst and reduces emissions at the onset of the engine.

2.6.2 Dehalogenation by CeO₂-Based Materials

CeO₂ and CeO₂-based materials have been employed as economic alternatives to RuO₂ - based catalysts to oxidize and decompose HCl, a harmful by- product produced by industrial processes such as polycarbonates production from dehydroxylated organics and organic chlorination reactions. The chlorine molecule Cl₂ is found to be the predominant industrial output for HCl removal [37]. CeO₂ -based catalysts were noted to be active in O₂-rich feeds (O₂/HCl > 0.75), whereas the deactivation of the catalysts was explored in O₂-poor feeds

($O_2/HCl < 0.25$). High Cl coverage hinders the formation of oxygen vacancies. Hence in order for the original activity to be restored, the samples should be exposed to an excess of oxygen, indicating a reversible deactivation due to the chlorination [38]. Lastly, CeO_2 - ZrO_2 solid solution as improved catalyst exhibits a prolonged stability (700 h on stream) as well as lessening the chlorine uptake with reference to undoped CeO_2 [39].

2.6.3 Oxidation of Volatile Organic Compounds

CeO_2 and CeO_2 -based compounds have served as oxidizing agents for volatile organic compounds VOCs based on the Mars-van Krevelen Mechanism. In general, the Mars-van Krevelen-type mechanism governs the reaction in which CeO_2 acts as the oxygen provider, whilst at the same time being re-oxidized by the gas phase oxygen [40, 41]. High surface area CeO_2 materials have been well known as promoters for noble metals (Pd, Pt, and Au). CeO_2 is now being deployed as a low-temperature catalyst in the decomposition of VOCs. This is because of the increase of metal dispersion and CeO_2 participation in the reaction [42, 43]. Figure 2.7 illustrates Mars-Van Krevelen Mechanism of CeO_2 (110) surface towards oxidizing CO.

Mars-Van Krevelen Mechanism

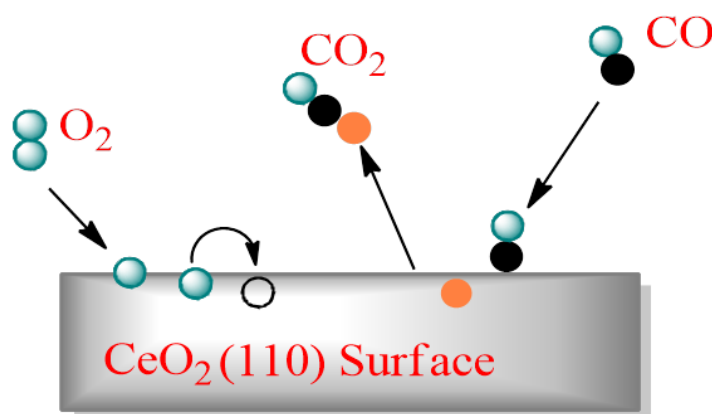


Figure 2.7: Schematic illustration of the CO oxidation over $CeO_2(110)$ surface via Mars – Van Krevelen mechanism [44].

Methane (CH₄), as one of VOCs, is known to pose a number of issues such as its potential impact on the global warming and its major contribution to ozone depletion [45, 46]. The combustible nature of CH₄ adds further challenges in any process aimed at tackling its removal/conversion. The catalytic efficiency of a CeO₂-ZrO₂ solid solution synthesized by urea hydrolysis toward methane was demonstrated to depend on the Ce:Zr fraction. The most active composition was observed in Ce_{0.75}Zr_{0.25}O₂ and gradual drop in the activity was recorded when Zr content decreased due to the phase change and modification of redox properties. Although these systems have been recognized to possess high thermal stability traits [35, 36], they suffer from a general catalytic deactivation during light off experiments. Liotta and coworkers suggested that the strong electron transfer between Ce₃O₄ and CeO₂ resulted in enhanced redox properties and improved methane oxidation [47]. This enhancement has also been observed with CuO/CeO₂ catalysts by optimizing the CuO dispersion, metal loading, and the electronic interaction with ceria; Resulting ultimately in an improved catalytic activity for the system. Despite the excellent efficiency of the CuO/CeO₂ solid solution, a noticeable decrease of the activity was observed due to the existence of H₂O [48]. In a Ce_{0.9-x}Cu_{0.1}Ca_xO_{2-y} system, a remarkable improvement was observed following the introduction of Ca as a result of the formation of oxygen vacancies. This system loses its activity over time due to the migration of Ca atoms to the surface, thereafter forming calcium carbonate species [49]. Finally, the incorporation of La in La_xCe_{1-x}O_{2-y/2} solid solutions led to the enhanced reducibility of ceria and, at the same time, an increase in the formation of oxygen vacancies and surface super oxide ions. In fact, these solid solutions were explored to be crystallized in very small sizes as the ratio of Ce/(Ce + La) was kept in the range from 1.0 to 0.2 [50].

The addition of noble metals such as Pt to different compositions of Ce_xZr_{1-x}O₂ catalysts has been previously investigated as a means to produce thermally stable structures. Among the investigated systems, Pt/Ce_{0.67}Zr_{0.33}O₂ was found to be the most thermally stable and the best active catalysts at 1000 °C. Also, Pt/Ce_{0.67}Zr_{0.33}O₂ catalysts were found to be much more active than that of Pt/Al₂O₃ [4]. Several important catalyst systems, along with a summary of their synthesis and other operational information (BET surface area, gas hourly space velocity (GHSV) and temperature), are tabulated in Table 2.3.

Table 2.3 : Summary of the most important catalysts used for VOCs Catalytic Combustion.

Catalyst	Synthesis technique	BET surface area ($\text{m}^2 \text{g}^{-1}$)	VOC	GHSV ($\text{mL g}^{-1} \text{h}^{-1}$)	VOC concentration	T_{50}^b ($^{\circ}\text{C}$)	Ref.
$\text{Ce}_{0.75}\text{Zr}_{0.25}\text{O}_2$	Sol-gel	108.4	methane	60000	2%	545	[51]
5wt% Cu/CeO ₂	hydrothermal	22.6	methane	27000	1%	540	[52]
1 wt % Cu/CeO ₂	thermal decomposition	68.7	methane	54000	1%	540	[52]
$\text{Ce}_{0.85}\text{Cu}_{0.1}\text{Ca}_{0.05}\text{O}_{2-\delta}$	Citric acid complexation combustion	31.3	methane	30000	1%	478	[49]
Ce(0.6)-La-O	Sol-gel	52.4	methane	13500	0.2%	505	[50]
$\text{Co}_3\text{O}_4\text{-CeO}_2$	Coprecipitation	31	methane	60000	0.3%	471	[47]
2wt%Pt/Ce _{0.67} Zr _{0.33} O ₂	Impregnation	79	methane	12800	1%	550	[53]
CeO ₂	Sol-gel	3	toluene	200000	1000 ppm	430	[54]
5 wt % CeO ₂ /Al ₂ O ₃	impregnation	156	toluene	54000	1400 ppm	275	[55]
$\text{Ce}_{0.9}\text{Zr}_{0.1}\text{O}_2$	Sol gel	56	toluene	20000	1000 ppm	221	[56]
$\text{Ce}_{0.9}\text{Zr}_{0.1}\text{O}_2$	Sol gel	56	ethanol	20000	1000 ppm	207	[56]
$\text{CuO-CeO}_2/\gamma\text{-Al}_2\text{O}_3$	impregnation	156	propane	2300	5.9%	350	[57]
$\text{Cu}_{0.13}\text{Ce}_{0.87}\text{O}_2$	combustion	27	acetone	60000	1000 ppm	200	[58]
$\text{MnO}_x\text{-CeO}_2$	Sol gel	22.2	formaldehyde	60000	580 ppm	160	[59]
$\text{MnO}_x\text{-CeO}_2$	Modified coprecipitation	124	benzene	30000	200 ppm	260	[59]
3wt%Ag/MnO _x -CeO ₂	deposition precipitation	124.0	formaldehyde	30000	580 ppm	70	[60]
0.5 wt % Pt/CeO ₂	impregnation	3	toluene	200000	1000 ppm	180	[54]
1.5 wt % Au/CeO ₂	deposition precipitation	79	propene	35000	1000 ppm	230	[61]
0.25 wt % Pt/23 wt % CeO ₂ /Al ₂ O ₃	Sol gel	95	acetic acid	30000	1000 ppm	175	[62]

^bLight-off temperature at which conversion of VOC is 50%.

Figure 2.8 portrays the methane conversion on several catalysts such as PdO/Ce_{0.64}Zr_{0.16}Ni_{0.2}O₂/γ-Al₂O₃, PdO/Ce_{0.72}Zr_{0.18}Ni_{0.1}O₂/γ-Al₂O₃, PdO/Ce_{0.8}Zr_{0.2}O₂/γ-Al₂O₃ and PdO/Ce_{0.64}Zr_{0.16}Bi_{0.20}O₂/γ-Al₂O₃ as a function of temperature. Apparently, the increase of Ni concentration leads to a reduction in the temperature required for methane conversion. Furthermore, a reduction in the BET specific surface area is also evident.

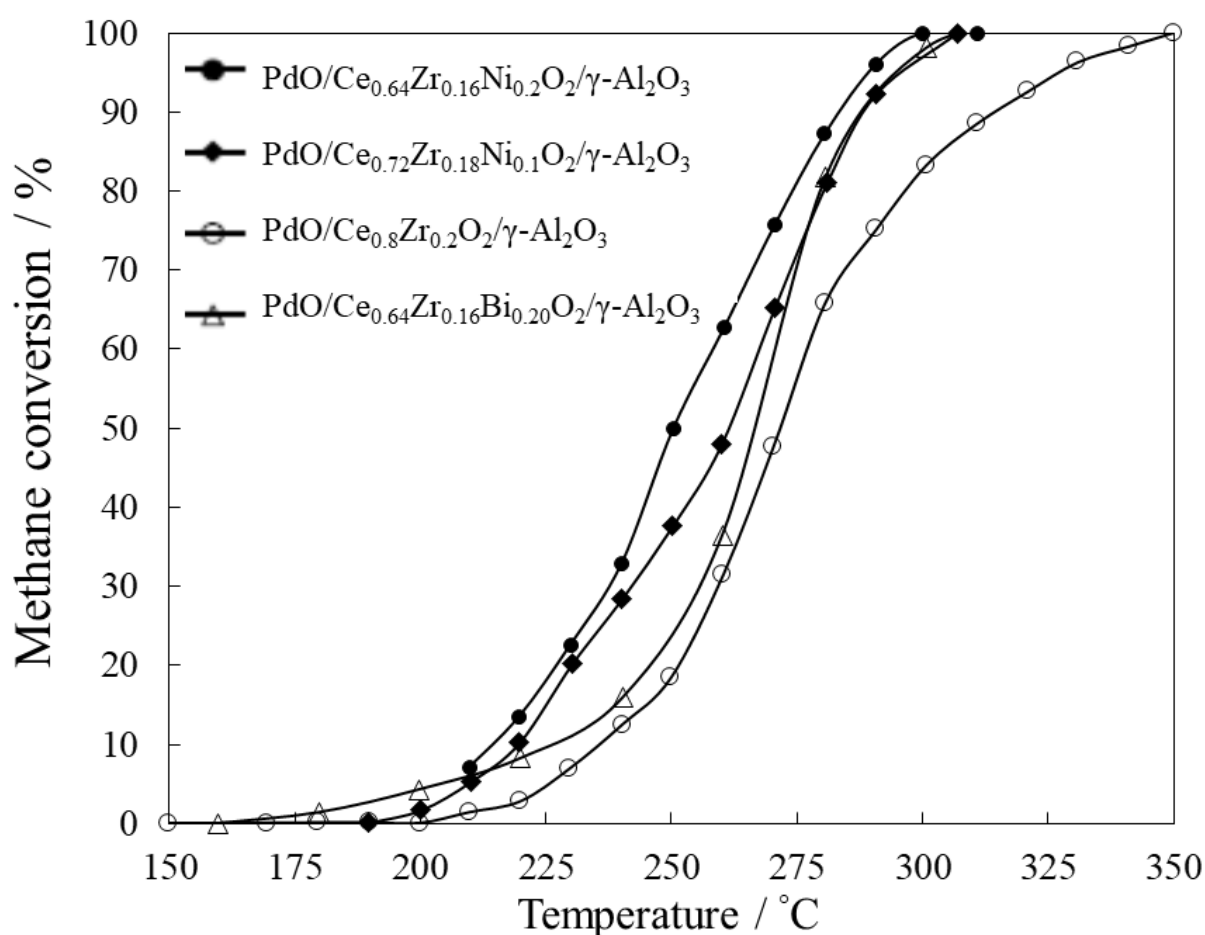


Figure 2.8: Temperature dependencies of methane oxidation over different catalysts of PdO/Ce_{0.64}Zr_{0.16}Ni_{0.2}O₂/γ-Al₂O₃, PdO/Ce_{0.72}Zr_{0.18}Ni_{0.1}O₂/γ-Al₂O₃, PdO/Ce_{0.8}Zr_{0.2}O₂/γ-Al₂O₃ and PdO/Ce_{0.64}Zr_{0.16}Bi_{0.20}O₂/γ-Al₂O₃. Reproduced from ref. [63].

In relation to non-methane gases, $Ce_{1-x}Zr_xO_2$ ($x = 0-0.3$) exhibits a very good catalytic efficiency towards the oxidation of some of these gases, especially benzene and toluene. The $Ce_{1-x}Zr_xO_2$ solid solution has been proven to be more efficient than unalloyed CeO_2 in the combustion of these harmful molecules. For instance, the $Ce_{0.9}Zr_{0.1}O_2$ solid solution demonstrated higher catalytic performance toward oxidizing benzene and toluene than pure CeO_2 at temperature of 100 °C lower than light-off temperature, the temperature at which 50% of conversion (T_{50}) is done [64].

In a similar context, MnO_x-CeO_2 mixed oxides exhibit excellent catalytic performance for the formaldehyde combustion. The synthesis method of such a mixed oxide is an important factor in tuning its catalytic performance. The improvement is due to the formation of a higher oxidation state of manganese and more oxygen on the surface resulting in an enhancement in the energy barrier for the oxygen transfer mechanism [59].

2.6.4 Chlorinated Volatile Organic Compounds (CVOCs)

CVOCs are toxic materials that are emitted from industrial waste gases and contribute significantly in air pollution nowadays. These compounds are emitted from thermal processes whenever a trace of chlorine co-exists with hydrocarbon entities. Among these pollutants are the notorious poly chlorinated dibenzo-*p*-dioxins and dibenzofurans [65, 66]. As a result, significant attention has been devoted to control the emission of these pollutants via the development of novel and efficient catalysts. Catalytic oxidative decomposition is currently deployed as alternative for the commonly deployed high temperature operations. Initially, noble metals such as Pt and Pd catalysts or catalysts supported noble metals have been extensively employed to decompose VOCs [67-69]. These catalysts are very active in the catalytic destruction of chlorinated VOCs, however, they can be readily poisoned by emitted HCl and Cl_2 gases [70]. Transition metal oxide catalysts have now emerged as a cost-effective alternative candidate to noble metals to carry out deep catalytic oxidation for CVOCs. Although they are somewhat less active than noble metals, they are preferred because of their low price and resistance to HCl/ Cl_2 poisoning [71].

Many studies have utilized ceria as an environmental catalyst in the oxidative decomposition of Chlorinated volatile organic compounds. This is predominantly due to some of its excellent catalytic properties relating to its capability to exist within the two oxidation states of Ce^{4+}/Ce^{3+} as well as its high oxygen-storage capacity (OSC). CeO_2 has been examined for the catalytic combustion of trichloroethylene (TCE) whereby Dai *et al.* investigated the catalytic performance in destroying some chlorinated VOCs. They concluded that CeO_2 demonstrates an effective catalytic capacity in decomposing Cl-VOCs at low operating temperatures. They found that the catalytic removal of chloroalkanes over the CeO_2 catalyst is easier than that of chlorinated alkenes [70].

Dia *et al.* [72] studied the trichloroethylene combustion at a broad range of reaction temperatures over CeO_2 systems. Figure 2.9 displays the temperature dependencies of trichloroethylene oxidation over CeO_2 calcined at temperature of 550 °C, 450 °C, 650 °C and 800 °C. The Figure clearly depicts that CeO_2 calcined at 550 °C achieves 90% trichloroethylene decomposition at 350 °C. Dia *et al.* attribute the lower efficiency of the CeO_2 calcined at 650 and 800 °C, in reference to that at 550 °C, to a diminution in BET surface area and an increase in crystallite size. The lower catalytic efficiency for CeO_2 calcined at 450 °C is attributed to a fewer basic sites and active oxygen species.

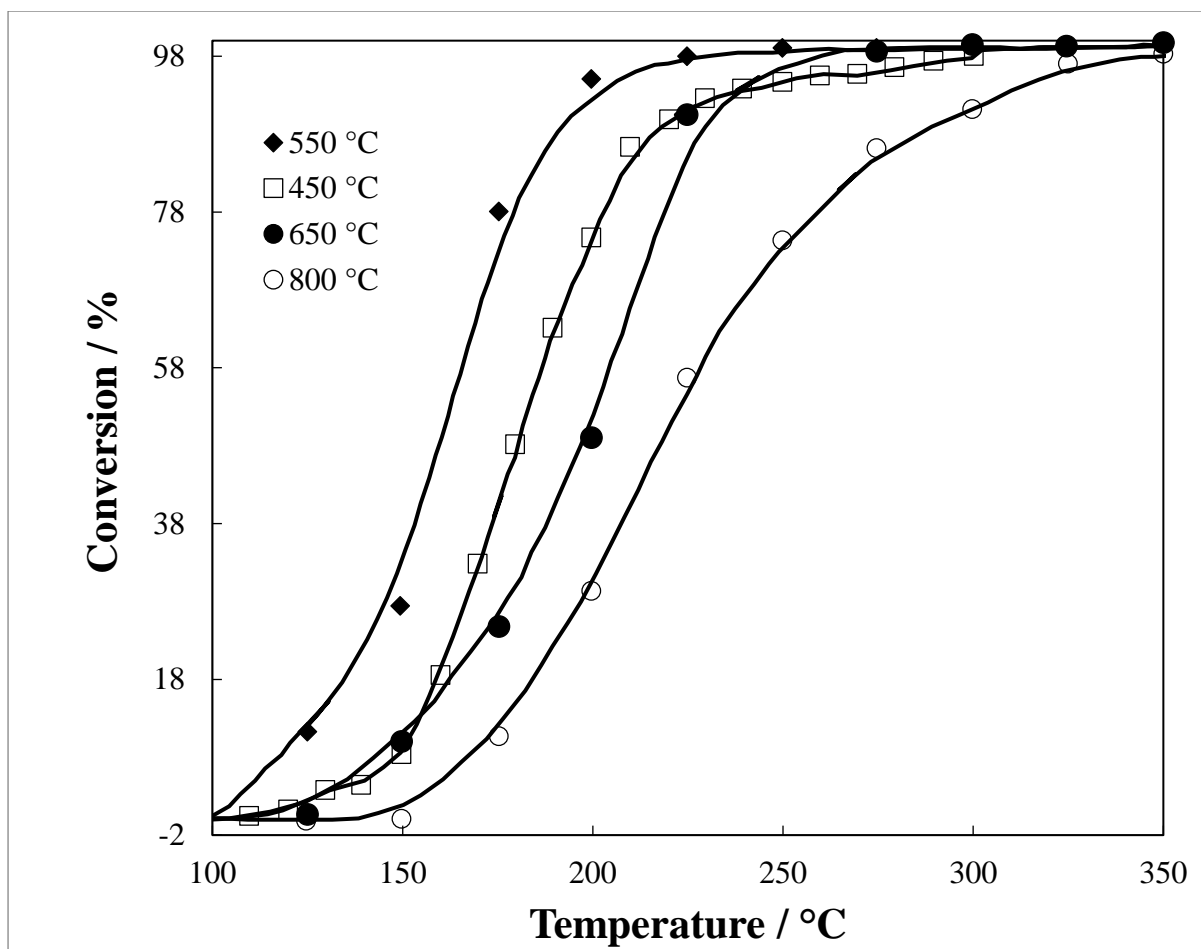


Figure 2.9: Temperature dependencies of trichloroethylene oxidation over CeO_2 catalysts calcined at different temperature. Reproduced from [72].

Chapter 5 investigates the catalytic efficiency of CeO_2 towards oxidation of three of chlorinated VOCs, namely chloroethene, chloroethane and chlorobenzene.

2.6.5 Total Hydrogenation of Ethyne over CeO_2 (111)

The overall hydrogenation process of acetylene (C_2H_2) to ethane (C_2H_6) has been reported experimentally. A plausible hydrogenation mechanism was suggested based on DFT calculations [73]. The entire energy landscape and primary reaction steps along with all intermediate configurations are depicted in Figure 2.10.

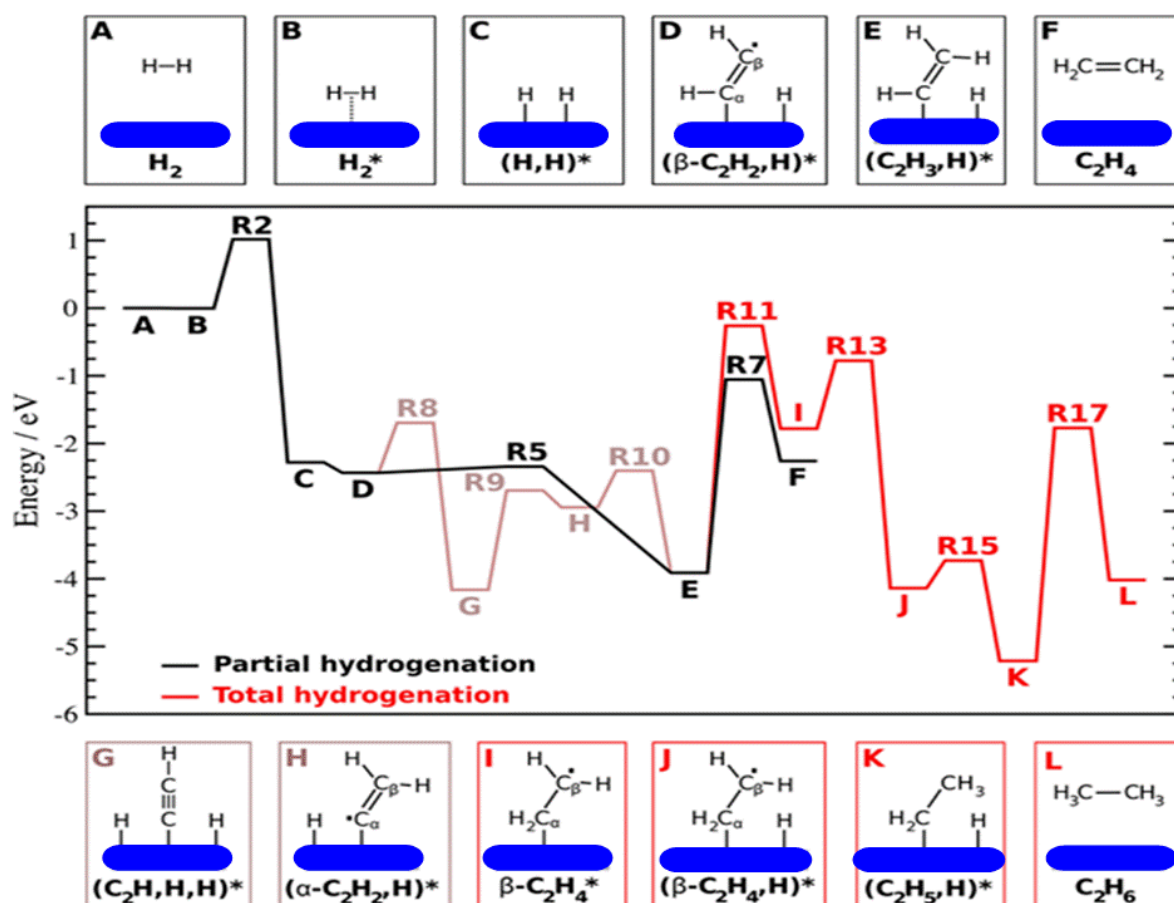


Figure 2.10: Reaction energy diagram for total hydrogenation of acetylene on CeO₂ (111) catalyst. Energies are computed as a reference to the energy of H₂ and C₂H₂ in the gas phase, and the clean CeO₂ (111) slab. Black line shows the routes of partial hydrogenation of acetylene to ethylene through R5, light brown displays the partial hydrogenation via dissociative acetylene adsorption, and red line represents the full hydrogenation to C₂H₆. The asterisk denotes a clean CeO₂ (111) surface. Reactants, intermediates, and products that are followed by an asterisk correspond to the adsorbed species. Reprinted from ref. [73].

Carrasco *et al.* [73] suggest that geometry optimizations for the adsorption of each of the investigated species preferentially occurs over the surface O atoms. Hydrogen molecule adsorption and its subsequent dissociative adsorption on the surface are supposed to be the starting steps rather than the adsorption of a gas-phase C₂H₂ molecule. As a result, the reaction initiates with the molecular adsorption of H₂ followed by homolytic dissociative

adsorption to leave two H^* species and liberate 2.35 eV. The two H atoms adsorb over two closest neighboring surface O atoms to produce two hydroxyl groups and two Ce^{3+} . This primary step necessitates an activation energy of 1.00 eV [74]. The step to separate the two closest adjacent H^* species resulting in two separated species, $(H, H)^* \rightarrow H^* + H^*$, is energetically unfavorable by 0.07 eV. The reaction continues with the adsorption of an acetylene molecule close to one hydroxyl group to form $(\beta-C_2H_2, H)^*$ (step D in Figure 2.10). Subsequently, the radical can easily react with the adjacent hydroxyl groups to produce $C_2H_3^*$ and liberate 1.48 eV. Notably, this process involves only a very small energy barrier of 0.09 eV. In the subsequent step, an adsorbed hydrogen atom migrates to the radical centre in the $C_2H_3^*$ forming an ethene molecule. The fate of the ethene molecule is dictated by two competing channels, desorption into the gas phase or subsequent two hydrogenation steps toward the formation of an ethane molecule; *i.e.*, full hydrogenation route.

2.6.6 Ceria Surface Reactions with Inorganic Molecules

2.6.6.1 H_2 , O_2 and H_2O

Hydrogen molecules (H_2) have been reported in many studies as a reducing agent for CeO_2 powders at high temperature and at the atmospheric pressure [75, 76]. Results obtained by experimental work revealed that H_2 cannot adsorb nor react with CeO_2 surfaces under UHV conditions [77-79]. DFT studies have provided potential energy surfaces for the dissociative uptake of hydrogen molecules over CeO_2 (111) and CeO_2 (110) surfaces via exothermic reactions [80, 81]. It has been proven that at low exposure of non-reduced $CeO_2(111)$ to D atoms at 115 K, surface O-D are formed [79]. As a consequence of this reaction, Ce^{4+} states are reduced to Ce^{3+} states. On the basis of XPS analysis at exposure greater than 50 L of water, a high-resolution of O 1s photoelectron suggested that D(g) adsorbed on the surface react with OD to produce chemisorbed D_2O . The surface OD group reacts with D on the surface to form $D_2O(g)$ between 200 K and 600 K. It is demonstrated that the chemisorbed $D_2O(g)$ molecules are desorbed at temperature close 200 K, whereas D_2 desorbs between 400 K and 500 K. Exposing reduced $CeO_{2-y}(111)$ to D(g) formed OD on the surface, but the trend of producing D_2O at higher exposure lessens with further reduction of the surface. It has been observed that the stability of the OD formed on reduced $CeO_{2-y}(111)$ is greater than that of pristine $CeO_2(111)$. For the different $CeO_{2-y}(111)$ configurations, water and D_2 were found to desorb at 570 K. From a theoretical standpoint, DFT studies on the adsorption of $H_2(g)$ on CeO_2 surfaces have reported that dissociative uptake of $H_2(g)$ O sites in $CeO_2(111)$

and CeO₂ (110) surfaces result in the partial reduction of neighboring Ce cations [82]. Another theoretical approach of ultra-accelerated quantum chemical molecular dynamic simulations demonstrated a mechanisms for the release of water molecules following adsorption of H₂ molecules [83].

The high oxygen storage of ceria renders it a favorable material for wide deployment in the TWC technology in vehicles [84]. As stated earlier, CeO₂ acts as an oxidizing agent in fuel-rich/oxygen deficient periods and as a reducing agent in the oxygen-rich periods. Consequently, it is crucial to understand the physisorption and chemisorption reactions of O₂ occurring on CeO₂ surfaces. It has been reported that the oxidation of Ce metal occurs at temperature of 300 K leading to a form of Ce₂O₃ covered by a layer of CeO₂ [85-87]. It was shown that when the polycrystalline structure is heated to 600 K, XPS examinations of the Ce 3d and Ce 4d photoelectrons peak showed complete reduction to Ce₂O₃ [88]. In contrast, reducing a CeO₂ (100) surface by Ar⁺ ion sputtering at 300 K displayed partially re-oxidation as it is annealed to 600 K in vacuum [77]. These two findings indicate that O redistributes between the surface and the bulk below 600 K. Along the same line of enquiry, DFT calculations were used to determine reaction routes for the interaction of O₂ with stoichiometric and reduced ceria surfaces. Dissociative adsorption of oxygen molecules over the CeO₂ (111) surface is predicted to be endothermic with values residing on the range of 0.91-0.98 eV [89]. In another DFT+*U* study, reactions of O₂ with the partially reduced CeO_{2-y} (111) surface promote superoxo species bonded weakly to its surface O-vacancy (-0.30 to -0.38 eV) and peroxo species that are more strongly bonded (-2.80 to -3.25 eV) [90]. In another related study on the partially deficient CeO_{2-y} (110) and CeO_{2-y} (100) surfaces, binding of the peroxo species involves an adsorption energy of -2.0 eV [91].

Water is an integral part in different catalytic reactions. Experimental work on the adsorption of H₂O on CeO₂ (111) and CeO₂ (100) demonstrated that H₂O can be physisorbed and chemisorbed or a mixture of both [79, 92-98] depending on the applied temperature. This is consistent with analogous computational results for CeO₂ (111). For instance, Fronzi *et al.* [99] and Marrocchelli and Yildiz [100] concluded in separate work that H₂O preferentially adopts several physisorbed states on CeO₂(111), whereas Watkins *et al.* [81] states that the water fragmentation into H and OH is a feasible process. Molinari *et al.* [101] studied the

adsorption of water on the most stable surfaces, CeO₂ (111), (100) and (110) employing DFT-GGA-*U* calculations. They reported that H₂O molecules readily dissociate on the studied surface and that the most stable surface towards the chemisorbed H₂O is CeO₂ (111) surface. They further concluded that the molecular adsorption of water becomes more preferable when the water coverage increases. Fernandez-Torre *et al.* used different DFT calculations to estimate energy barriers for the steps governing water adsorption where they reported very similar energy barriers for the different steps [74].

Data derived by high-resolution analysis of O 1s XPS photoelectron has been the first methodology to recognize molecular water from dissociated -OH on the CeO₂ surfaces [79, 92-98]. As seen from Figure 2.11, the adsorption of H₂O on CeO₂ (111) and CeO₂ (100) close to 200 K leads to three O 1s peaks. The analysis reveals that the lowest binding energy at 530.5 eV belongs to the lattice O in CeO₂, whilst the highest binding energy at 534.4 eV is from molecular water. This water is believed to be dissociated water (chemisorbed water) rather than being multilayer/ physisorbed water. The rationale behind this explanation is that the multilayer water desorbs between 150 K and 170 K and these spectra were obtained above 180 K [102]. The intermediate peak recorded at 532 eV is attributed with -OH despite its location also corresponding to chemisorbed H₂O [94] or a mixture of -OH and chemisorbed water [96]. As is clear from Figure 2.11, the O 1s spectra of CeO₂ (111) suggests that the adsorption energies of the molecular water on the surface and the -OH adsorption possess similar binding energies and this finding is in agreement with other accounts that conclude a negligible energy difference between the physisorbed water and -OH adsorption. Further analysis of the O 1s spectra reveals that the H₂O is merely decomposed on this surface confirming the study performed by Molinari *et al.* [101]. From these results, one can conclude that hydroxyls group on oxidized CeO₂ (100) are more stable than on CeO₂ (111).

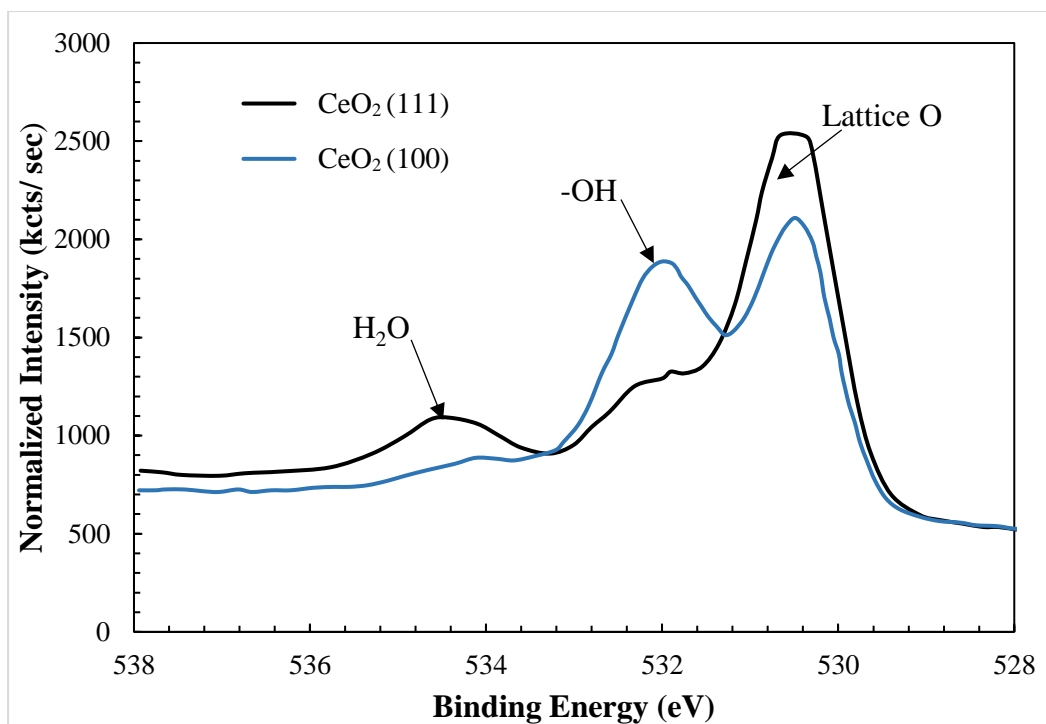


Figure 2.11: O 1s core level spectra from water adsorbed on oxidized CeO₂ (111) and CeO₂ (100) at 180 K. Reproduced from ref. [92].

TPD measurements have been recorded after water adsorption on the fully oxidized CeO₂ (111) and CeO₂ (100) surfaces at a temperature of 180 K. As Figure 2.12 portrays, the water mostly leaves CeO₂ (111) in a single, sharp peak close 200 K [79, 92, 94, 95], whereas water desorption on the CeO₂ (100) takes place from close to 200 K to more than 500 K [92].

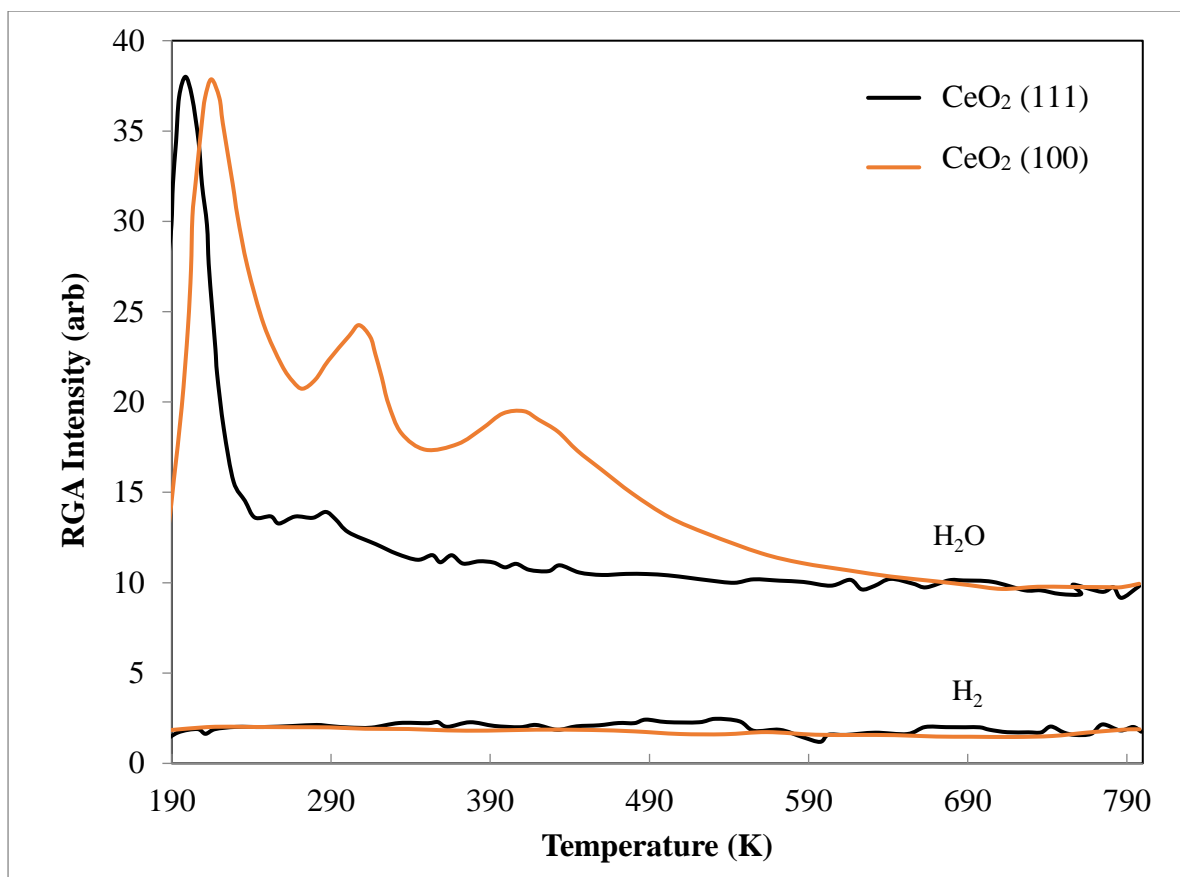


Figure 2.12: TPD measurements of water adsorption on fully oxidized CeO_2 (111) and CeO_2 (100) at 180 K. Reproduced from ref. [92].

Ceria is well-known to swing between two extreme oxidation states of +4 and +3. The reduction of ceria occurs via the releasing of oxygen atoms from CeO_2 . As such, creation of oxygen vacancies as a result of CeO_{2-y} (111) surface undergoing a reduction reaction, leads to the production of Ce cations with two coordination vacancies and a three-fold hollow adsorption sites [103]. Below, Figure 2.13 illustrates the active sites on CeO_2 (111) surface.

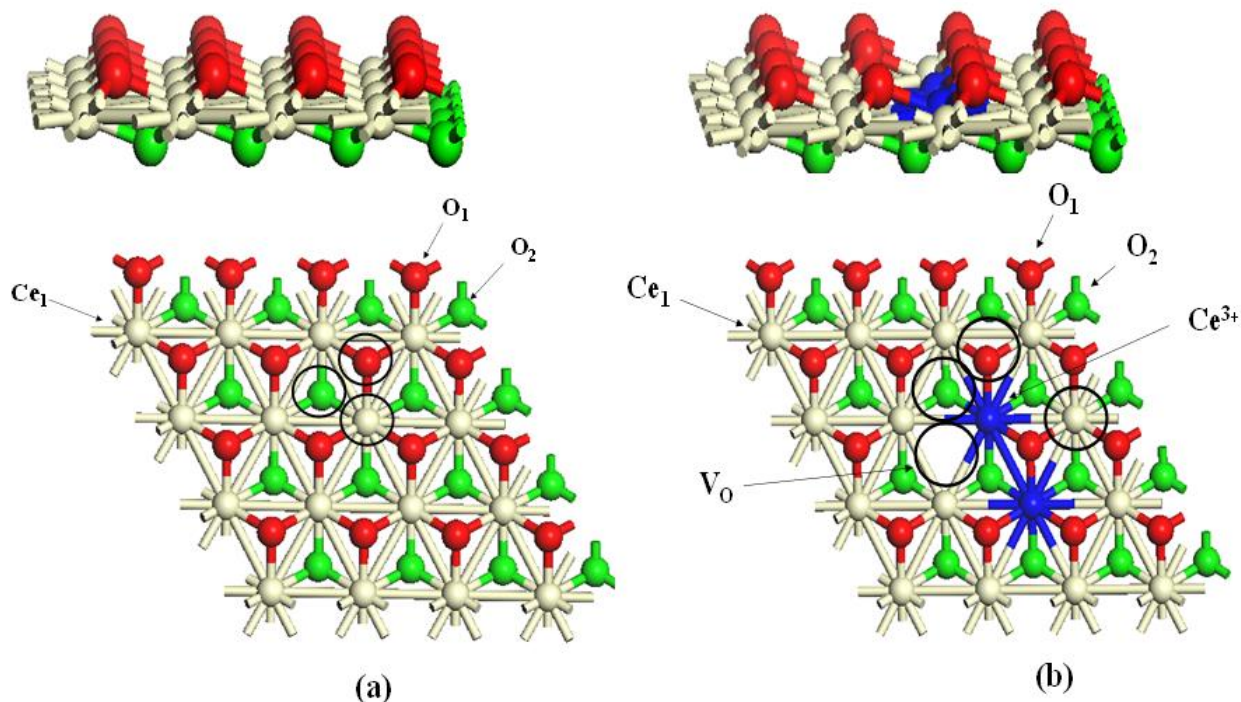


Figure 2.13 : Active sites on CeO₂ (111) surface; (a) side and top views of perfect CeO₂ (111) surface; (b) side and top views of reduced CeO₂ (111) surface.

A number of experimental [79, 92, 104] and computational [81, 99, 100] studies have reached similar conclusions that vacancies created on CeO_{2-y}(111) surface enhance and stabilize the decomposition of H₂O. From Figure 2.14 and 2.15, it is evident that the amount of -OH on CeO_{1.7} (111) is greater than that on CeO₂ (111). A survey of literature suggests that the reaction between -OH on CeO_{1.7} (111) leads to release of H₂ [79, 92, 94]. The high-resolution Ce 3d XPS spectra suggest further reduction of Ce from CeO_{2-y} (111) as a consequence of water adsorption. Nevertheless, Henderson *et al.* [95] did not report any H₂ desorption from the aforementioned face. The difference between the findings reported by Henderson *et al.* and those reported by other studies are attributed to the substrates on which they deposited their CeO_{2-y} (111) films. Henderson *et al.* deposited their films on substrate of yttrium-stabilized ZrO₂ (111) (YSZ), whereas others grew their films on Ru (0001) [92, 94] or Cu (111) [93, 105]. Ferrizz *et al.* [106] suggested that ceria films deposited on YSZ(100) exhibited a larger reducibility than films deposited on α -Al₂O₃(0001). The reason for the improved reducibility on YSZ remains unclear. However, if an analogous influence is taking place on YSZ (111), this promoted reducibility might be indicative of a lower O-vacancy formation energy, and hence generating a smaller driving force in order to re-oxidize a

reduced surface via water destruction. Improved reducibility of CeO_2 (111) deposited on YSZ is most probably the reason why Henderson *et al.* observed a thermal reduction at annealing temperature of 830K, while other researchers could reduce their films at temperatures much higher than 830K [107, 108]. It must be noted that H_2 desorption following adsorption of water on $\text{CeO}_{1.7}$ (111) is contradictory to the desorption from reduced $\text{CeO}_{1.7}$ (100) in which the primary desorption route remains recombination to form water with only a trivial amount of H_2 formation (Figure 2.15). The energy of vacancy creation on CeO_2 (111) is found to be greater than that on CeO_2 (100) [109, 110]. Hence, it is expected that the driving force to fill the vacancy is greatest on CeO_{2-y} (111) surfaces.

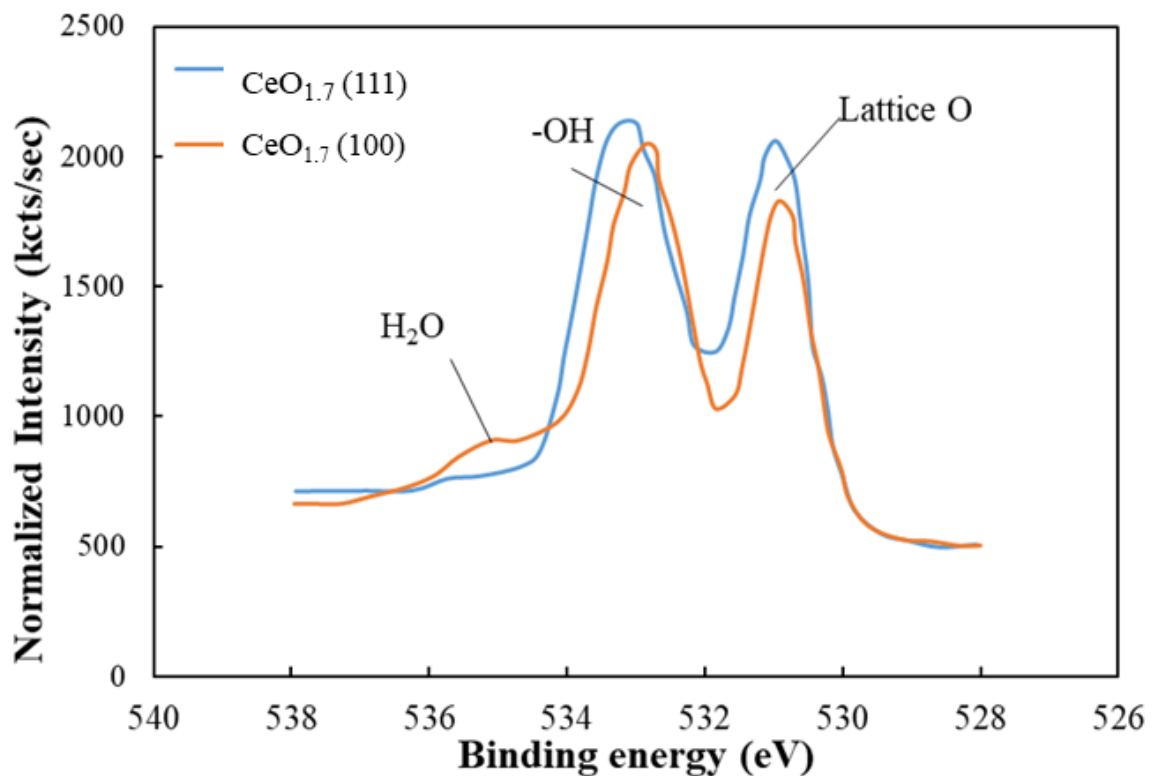


Figure 2.14: O 1s core level spectra from water adsorbed on reduced $\text{CeO}_{1.7}$ (111) and $\text{CeO}_{1.7}$ (100) at 180 K. Reproduced from ref. [92].

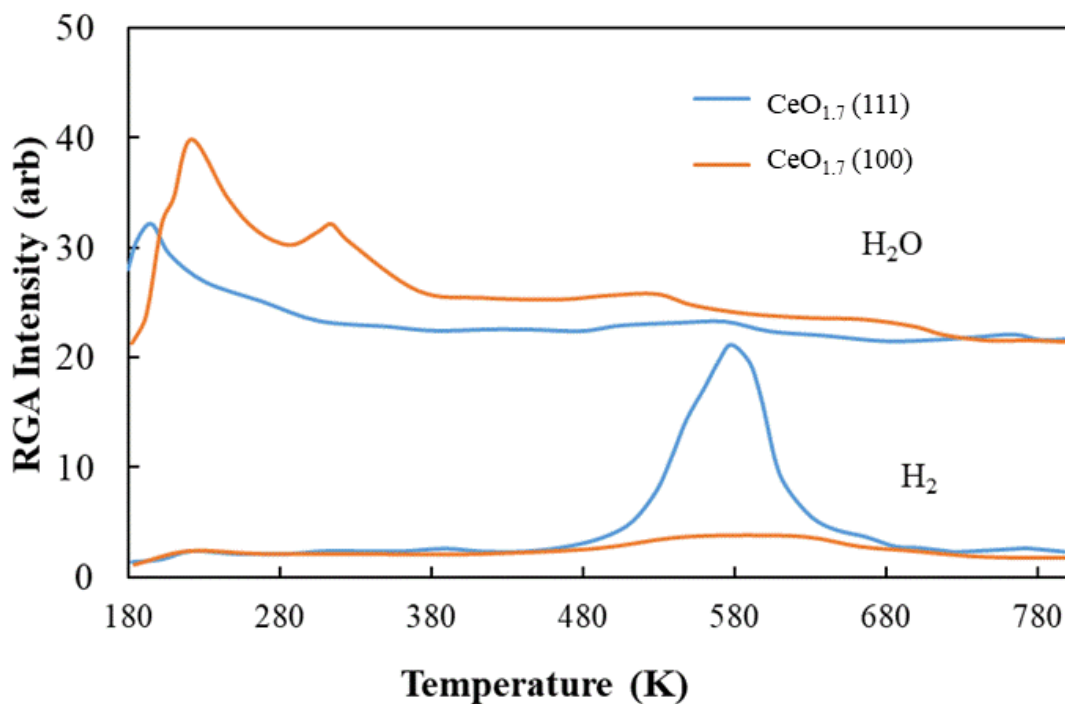


Figure 2.15: TPD measurements of water adsorption on reduced CeO_{1.7} (111) and CeO_{1.7} (100) at 180 K. Reproduced from ref. [92].

Watkins *et al.* [81] assessed by means of DFT+U method the decomposition pathways of H₂O and H₂ on both the pristine and defective ceria (111) surface. The H₂O physisorption reaction is an exothermic process on both configurations (see Figure 2.16); however, physisorption of water is more exothermic on the vacancy site. The dissociation of water on the two studied surfaces results in formation two hydroxyl groups, one in the initial water physisorbed site and the other on a surface oxygen ion. Furthermore, Watkins and co-workers reported a potent exothermic chemisorption reaction for H₂ on the perfect ceria (111) surface, which is ascribed to the low-lying 4*f* states, and thereafter great electron affinity of ceria. Lastly, the study concluded that the decomposition of water is preferred on the perfect surface of ceria (111) due to the formation of a strong hydrogen bond between the OH⁻ and H⁺ moieties created upon decomposition.

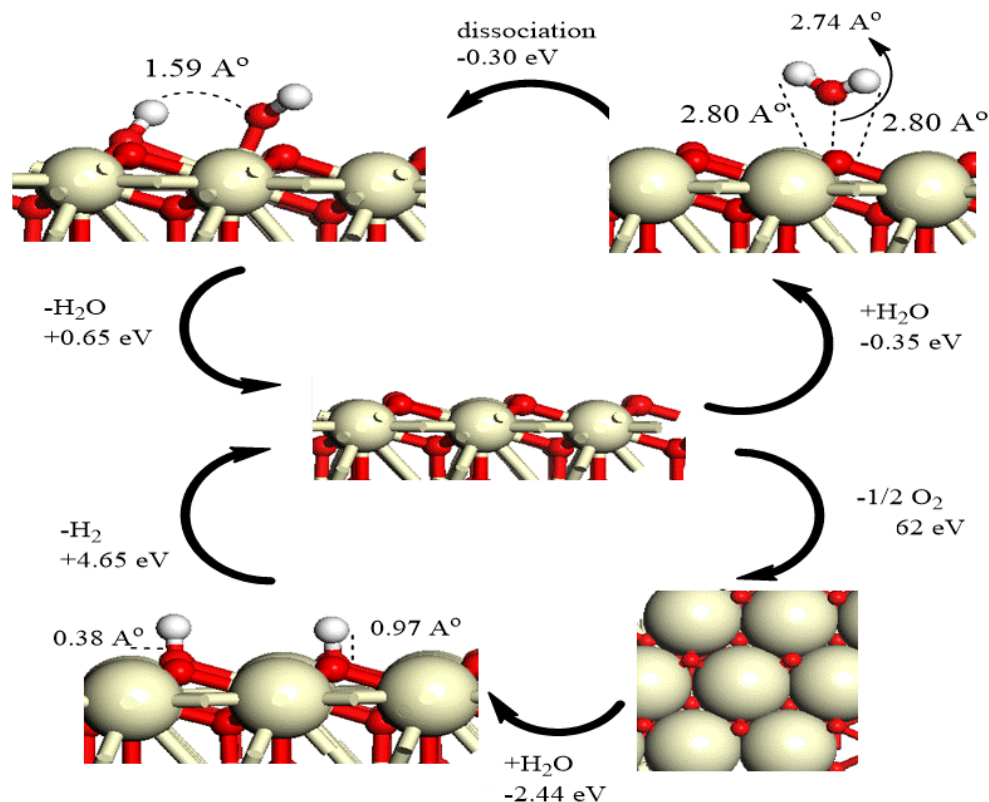


Figure 2.16: H₂O and H₂ reactions on the defect and perfect ceria (111) surfaces. Reproduced from ref. [81].

2.6.7 Ceria Surface Reactions with Sulfur dioxide (SO₂)

It is understood that trace concentration of sulfur-based molecules in fossil fuels results in the production of sulfur oxides (SO_x) in the exhaust. Adsorption of such molecules on ceria has a negative effect on its oxygen storage capacity properties in automotive catalytic converters. However, the high affinity for SO_x can, in principle, be exploited by trapping sulfur in the effluent gases.

SO₂ adsorption on cerium oxide thin films has been investigated by two studies and two different conclusions were reached. Through surface measurements on SO₂- CeO₂ (111)/Ru (0001) system, Overbury *et al.* concluded that that SO₂ is adsorbed as sulfite ion SO₃²⁻ on the stoichiometric surface at temperatures from 100 to 600 K [111]. According to S2p high resolution XPS spectra, the SO₂ adsorbs via a Lewis acid–base interaction at the basic O²⁻ surface sites. SO₂ molecularly desorbs with main desorption peaks close 200 K and 400 K.

There was no evidence to suggest that the oxidation process yield SO_4^{2-} or the reduction process yields SO^{2-} or S^{2-} , which is in agreement a previous study by Waqif *et al.* [112]. Waqif *et al.* utilized vibrational spectroscopy to study CeO_2 powders, observing that only SO_3^{2-} formes after room temperature exposure to SO_2 [113]. Sulfate formation occurs following exposure at 673K and is encouraged by simultaneous exposure to O_2 . Contradictory to these studies, Rodriguez *et al.* Observed that SO_2 was adsorbed almost exclusively as SO_4^{2-} on stoichiometric, polycrystalline CeO_2/Pt (111) [114]. In an attempt to elucidate the contradiction, a number of additional experiments were performed in which different parameters have been assessed. The adsorption of SO_2 on polycrystalline CeO_2 films deposited on Al_2O_3 utilizing an SO_2 pressure of 2.5 mbar has been studied by Smirnov *et al.* [115]. In their study, they demonstrate SO_3^{2-} formation at temperature below 473 K and SO_4^{2-} formation above 573 K. As O_2 gas with an identical pressure was introduced alongside SO_2 exposure, SO_3^{2-} formation was suppressed at the low temperatures but SO_4^{2-} is still apparent at the higher temperatures. Interestingly, the sulfate concentrations are enhanced by the introduction of O_2 at higher temperatures. Likewise, Ferrizz and his co-workers used polycrystalline ceria films deposited on Ta foil by spray pyrolysis to carry out TPD measurement. In their XPS examinations, they utilized a different substrate of Mo (100) to deposit CeO_2 in an O_2 atmosphere synthesized by Ce vapor deposition. After SO_2 introduction at 298 K, a major SO_2 desorption peak was evident at 473K [116]. This is in an agreement studies conducted by Overbury *et al.* [111]. However, by another SO_2 desorption peaks was noted residing in the range of 800 K -1000 K which were not observed by Overbury *et al.* As SO_2 exposure temperature increases to 573 K, the intensity of peaks located at higher temperatures increases, unlike those in the lower temperature range that start to decay. The S2p photoelectron line obtained by XPS suggested that the SO_2 adsorbed mainly as sulfite at 298 K but some of this transformed to sulfate when the sample was annealed. Increasing the exposure temperature to 923 K resulted in more transformation of the sulfate into sulfide. Analogous findings were reported with the pure SO_2 exposure and as a mixture with O_2 .

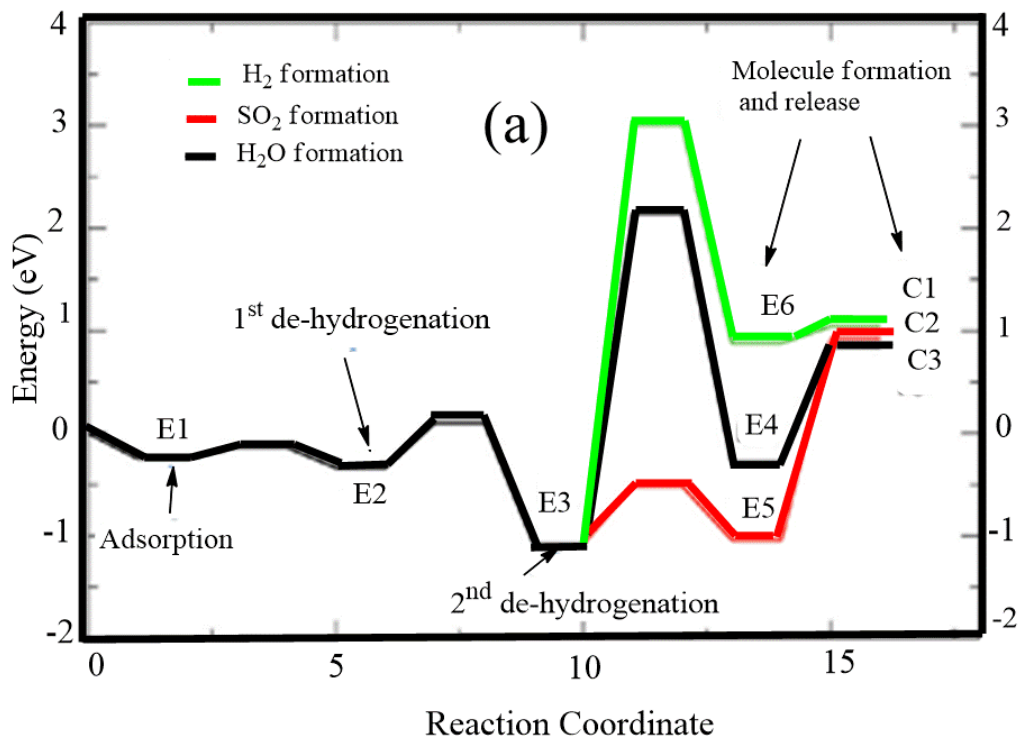
Recently, Happel *et al.* investigated SO_2 adsorption on $CeO_2(111)/Cu$ (111) [117]. Their S 2p XPS analysis suggested that sulfite is the main surface species at 300K. When the sample was annealed, some of the sulfur was reduced to S^0 and S^{2-} . There was no sulfate observed at any temperature.

The physisorption and chemisorption reactions of Sulfur dioxide (SO_2) were investigated on single crystal metal such as Cu [118, 119], Au [120], and Pt [121, 122] and on pure CeO_2 (111) [111, 114, 117], as well as on the metal supported CeO_2 (111) such as Cu-supported [123], Au-supported [123, 124], and Pt-supported CeO_2 [125]. In these previous investigations, SO_2 adsorption and dissociation on CeO_2 (111) doped with Cu, Au, Pt results in different products. For instance, it was found that SO_2 interacts with the surface oxygen on CeO_2 (111) to produce the sulfite ion SO_3^{2-} [111, 117] or sulfate ion SO_4^{2-} [126]. At higher temperatures, SO_3^{2-} SO_4^{2-} were found to be desorbed without dissociating as S^0 or S^{2-} on the catalyst surface. SO_2 weakly adsorbs on Au (111) and desorbs at annealing temperature of 150 K [120]. SO_2 is physisorbed in two different arrangements, standing up and lying down, on the Pt (111) surface [121, 127]. Streber *et al.* found that the SO_2 molecule exists with minimal disruption [121]. In contrast, SO_2 reacts with Cu (111), Cu (100) [128] and Cu (110) faces [119] with some of the SO_2 dissociating to elemental S^0 . In the case of metals-based CeO_2 (111), the reaction of SO_2 occurs spontaneously. At over 250 K, SO_2 has been observed as a molecule on Au/ CeO_2 (111) without decomposing. On Cu/ CeO_2 (111), the dissociation to S^0 is improves by contrast to Cu single crystals. The activity peaks at Cu coverages ranging from 0.5 to 1.0ML, and beyond this the activity decays back [123]. However, the overall reaction of SO_2 on Pt/ CeO_2 (111) catalyst is rather complicated [125]. At a temperature of 150 K, on the CeO_2 (111) surface, SO_2 adsorbs as sulfite standing upright on the Pt nanoparticles depending on the XPS high resolution of S2p photoelectron line. This is in line with those cases of on metal-free CeO_2 (111) [111] and on Pt (111) [121, 127], except for the absence of SO_2 lying flat on the Pt nanoparticles.

2.6.8 Formation of H_2 , SO_2 and H_2O on Stoichiometric Ceria

In an attempt to assess the hydrogen diffusion characteristics in bulk CeO_2 , Marrocchelli and Yildiz [100] investigated the reaction mechanism of H_2O and H_2S molecules on the CeO_2 (111). The presented mechanisms relating to H_2 , SO_2 and H_2O on CeO_2 (111), initiate with adsorption of H_2S on the surface (E1) as displayed in Figure 2.17a. Consequently, two configurations are necessary, the first being dehydrogenation (E2), and second dehydrogenation (E3). After this, three possible routes exist that result in the production and growth of H_2 , H_2O , or SO_2 molecules. The black line in Figure 2.17a portrays the water-producing channel. After the second dehydrogenation step (E3), one of the hydrogens in hydroxyl surface is linked with the adjacent OH^- radical, (E4), producing an adsorbed water

molecule on the surface. This pathway, initiated by the release of the hydrogen from one OH to the other, necessitates activation energy at 3.20 eV -0.28 eV. The desorption of H₂O as a final step entails additional 1.1 eV [100]. The water-forming pathway creates a vacancy on the CeO₂ (111) surface and exhibits an endothermic process of 0.83 eV, in reference to the starting configuration, and an activation energy of 3.20 eV. Placing a sulfur atom on the surface occupies the vacancy, in a process that is associated with trivial exothermicity of -0.31 eV. On the other hand, this route is kinetically unfavorable as its activation energy amounts to 3.2 eV. The SO₂ producing channel is represented by the red curve in Figure 2.17a. Starting from the E3 intermediate, the sulfur atom bound by one covalent bond with adjacent oxygen tends to form one more covalent bond with other neighboring oxygen atoms. A SO₂ molecule is formed in the final step, E5. This formation pathway takes place by *via* a trivial endothermic energy and an accessible energy barrier of 0.83 eV [100]. However, SO₂ desorption is endothermic by 1.96 eV. This configuration results in two vacancies on the ceria surface. In the final route, a hydrogen molecule is formed. In this route, two hydrogen atoms and two surface hydroxyls combine to form a H₂ molecule, weakly linked to Ce cation on the surface. This route necessitates very high activation energy of 4.10 eV, and thus represents a bottleneck for the overall mechanism. Desorption of the hydrogen molecule from the surface demands energy of 0.20 eV.



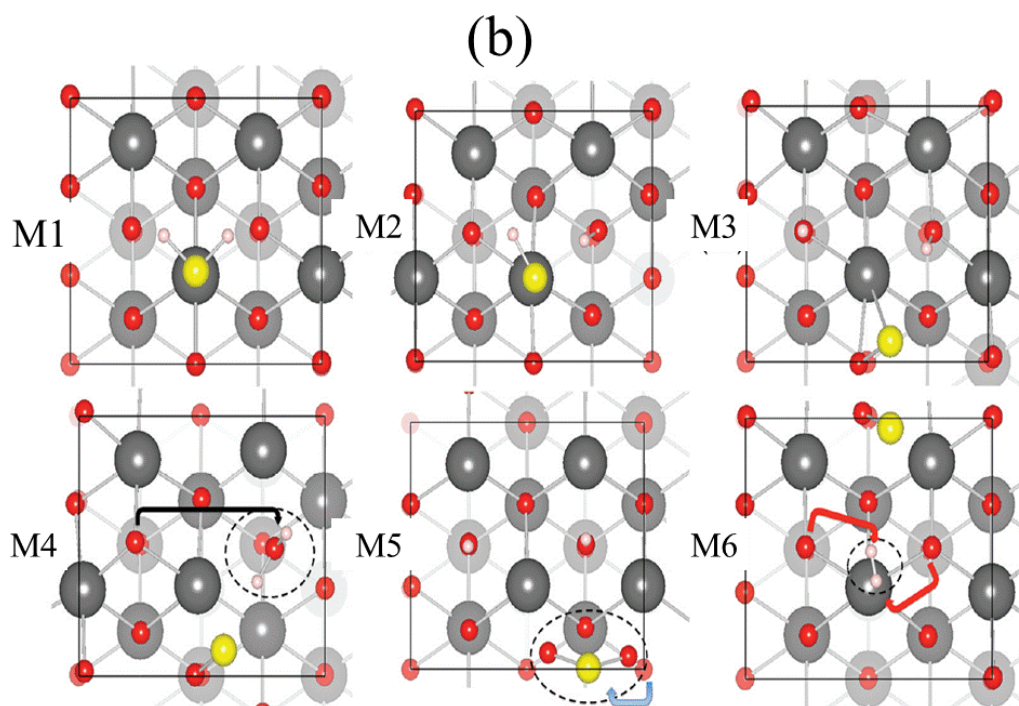


Figure 2.17: Energy diagram of the reaction routes forming H_2O , SO_2 and H_2 (a). Intermediate structures (b) for the reaction pathways displayed in (a). These represent the adsorption of H_2S (E1), first de-hydrogenation (E2), second de-hydrogenation (E3), water formation (E4), SO_2 formation (E5) and H_2 formation (E6). Reproduced from ref [100].

2.6.9 Ceria Surface Reactions with CO and CO_2 Molecules

Ceria powder and nanocrystals are known to effectively reduce CO at high temperature, forming CO_2 and CeO_{2-y} . It is very well-known that the function of ceria when used in the three way catalysis is to oxidize CO gas into CO_2 [84]. Similar to the case of H_2 , the adsorption of CO has not been reported on $\text{CeO}_2(111)$ or $\text{CeO}_2(100)$ under UHV conditions [129-131]. Many studies have reported that the adsorption of CO on ceria surfaces is as very weak with a binding energy at 0.2 eV [132-134]. On the other hand, several studies conclude that the formation of carbonate species on the $\text{CeO}_2(110)$ is an exothermic process with energy > 2 eV. In another study by Nolan and Watson, the formation of carbonate is found to be more exothermic on $\text{CeO}_2(100)$, -3.2 eV, than that on the $\text{CeO}_2(110)$, -1.95 eV [134]. On the contrary, Stubenrauch and Vohs's argued that CO could not be detected in its

physiosorbed state over the CeO₂ (100) surface at 300 K [129]. They demonstrated that 0.1ML of CO potentially adsorbed on the CeO₂(100) at 100 K completely desorbed at 200 K [135].

Senanayake and Mullins [136] explored the weak interaction between CO₂ and CeO₂ (111) and found that at 90 K, the carbon dioxide was adsorbed on the surface, whilst complete desorption was recorded at 150 K. This study further reported that a minor quantity of carbonate species was produced and continued up to 300 K. In another instance, Senanayake *et al.* [98] demonstrated the formation of a small amount of carbonate on non-stoichiometric ceria (CeO_{2-y}) grown on Au (111) substrate. These carbonate molecules persisted until 300 K. In an attempt to re-oxidize the non-stoichiometric CeO_{2-y} (111) deposited on Cu (111) substrate, Lykhach *et al.* [137] and Staudt *et al.* [138] observed a negligible quantity of carbonate and carboxylate in the analyzed C 1s and O 1s curves [137]. However, a considerable concentration of Ce³⁺ was oxidized into Ce⁴⁺.

Very recent work conducted on the adsorption of CO₂ on CeO_x(100) has explored a stronger interaction of CO₂ with the oxidized and reduced surfaces [139]. Figure 2.18 exhibits the CO₂ TPD from fully oxidized CeO₂ (100) and partially oxidized CeO_{1.7} (100) following CO₂ exposure at 180 K. In relation to the fully oxidized CeO₂(100), the CO₂ was seen to be desorbed in a group of peaks at 230 K, 410 K, 510 K and 655 K. The rising part of CeO₂ (100) is indicative of CO₂ desorption from the sample holder. The DFT+*U* approach was utilized to calculate and investigate the most stable sites of CO₂ adsorption on CeO₂ (100) and CeO_{1.7} (100). The carbonate species in tri-dentate form have been found to be the most stable arrangement as a result of the CO₂ adsorption on the surface and the adsorption energy for this species amounts to -1.93 eV [135]. Figure 2.18 demonstrates that the carbonate species on the reduced CeO_{1.7} (100) is strongly stabilized at 765 K, whereas CO₂ desorption was observed at low temperature. To the best of our knowledge, there are no reports on the desorption of CO molecules on the oxidized or reduced surfaces. This is evidenced by the obtained invariant intensity of Ce- 4*f* peak indicating that CeO_{1.7} (100) surface has not been re-oxidized by CO₂.

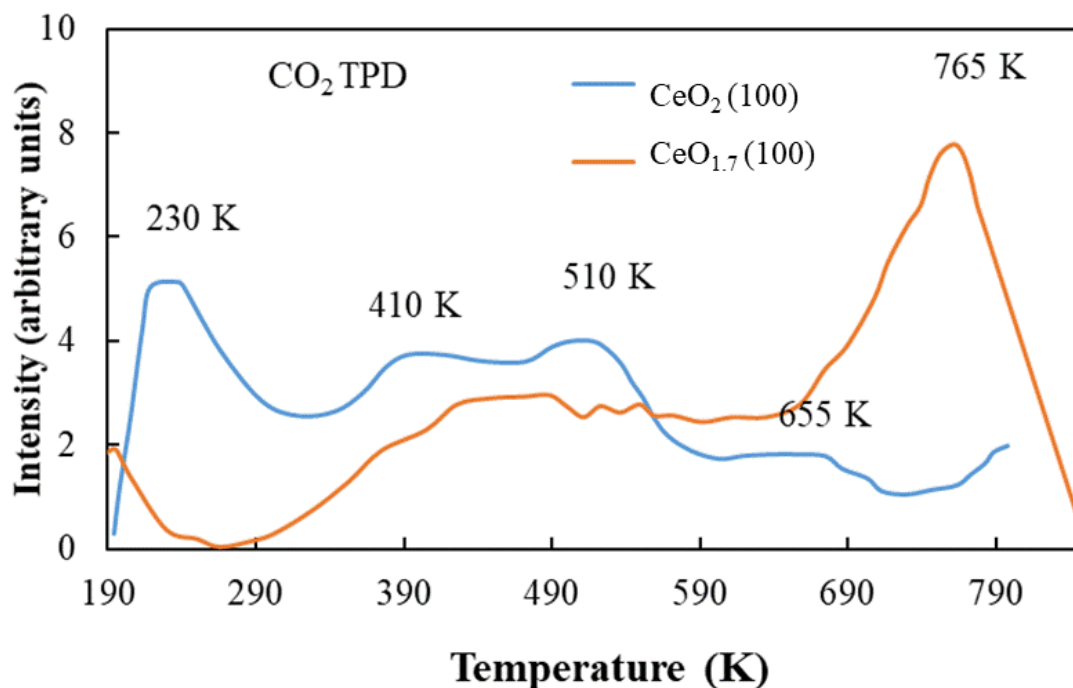


Figure 2.18 : CO₂ TPD measurements following exposure at 180 K on fully oxidized CeO₂ (100) (black) and deficient CeO_{1.7} (100) (blue). Reproduced from ref. [139].

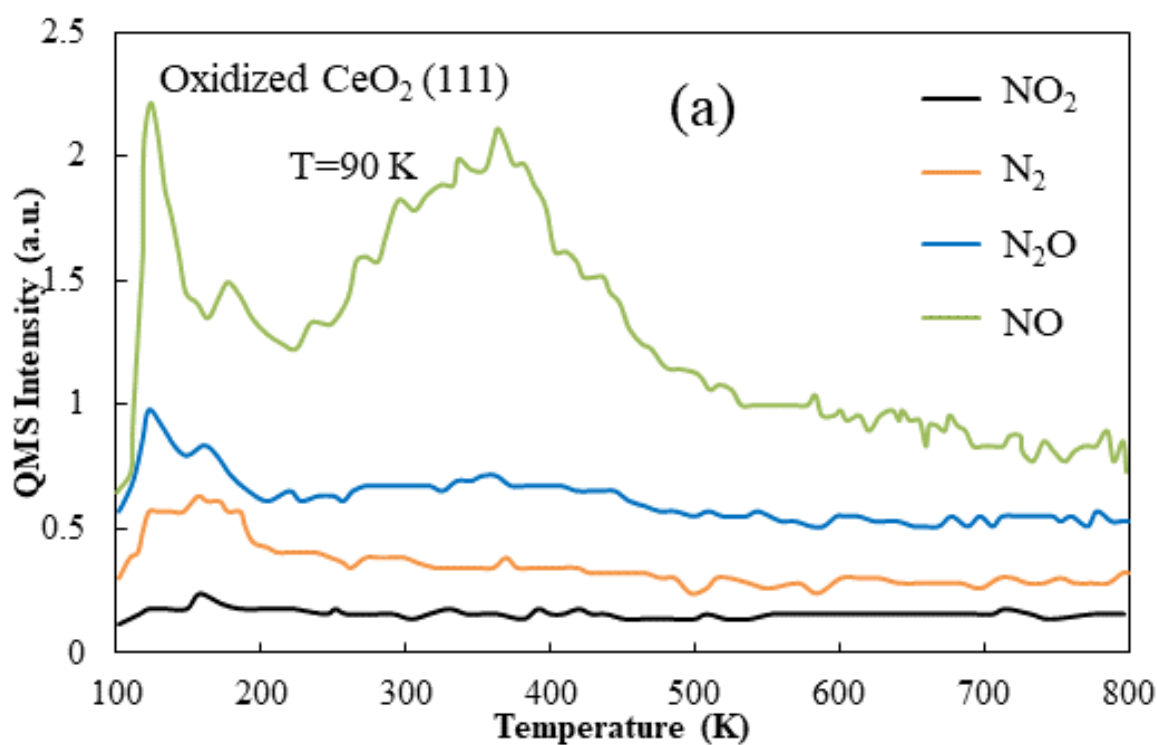
The adsorption of CO₂ on the CeO₂ (111) face has been evaluated by Hahn *et al.* [140] using pure DFT and DFT +*U* approaches. In their simulation, they found that the most stable configuration was a monodentate carbonate species with a weak adsorption energy of nearly -0.3 eV in both approaches. Another DFT+*U* study conducted by Cheng *et al.* [141] investigated the CO₂ adsorption on both stoichiometric and non-stoichiometric CeO_x (110) to reveal a physisorbed reaction between CO₂ molecule and the surfaces with an adsorption energy of -0.26 eV. Carbonate species were not formed in their mechanism.

2.6.10 Ceria Surface Reactions with nitrogen oxide (NO)

Given the importance of ceria's catalytic performance to treat NO_x in automobile exhausts, the adsorption of nitrogen oxide in its forms as N₂O, NO and NO₂ on ceria surfaces have been investigated. Ferrizz *et al.* indicated the non-adsorption of NO at 300 K on the fully oxidized CeO₂ (111) single crystal or on CeO₂ deposited on α -Al₂O₃ (0001) [142]. Overbury *et al.* further reported that NO does not interact with CeO₂ (100) at 160 K or 300 K [77],

however, NO was observed to interact rather weakly at 90 K on stoichiometric CeO₂(111) / Ru (0001) [143].

As clearly seen from Figure 2.19a, NO is physisorbed below 200 K with small amounts of N₂O and N₂ desorbing in the same temperature window. The wide temperature range of NO desorption between 300 K and 400 K was attributed initially to adsorption of NO on the sample holder and on the back of the Ru (0001) substrate. This weak adsorption on the stoichiometric surface is in line with a study by Yang *et al.* [48] that concluded that there was an adsorption of NO over the Ce⁴⁺ cation site on CeO₂(111) with a physisorbed energy amounted to only -0.1 eV. The XPS high-resolution N1s spectra showed that at 90 K, the nitrogen oxide as [NO₂] and N₂O physisorbed on CeO₂(111). These more stable adsorbates were not reported in the study by Yang *et al.*



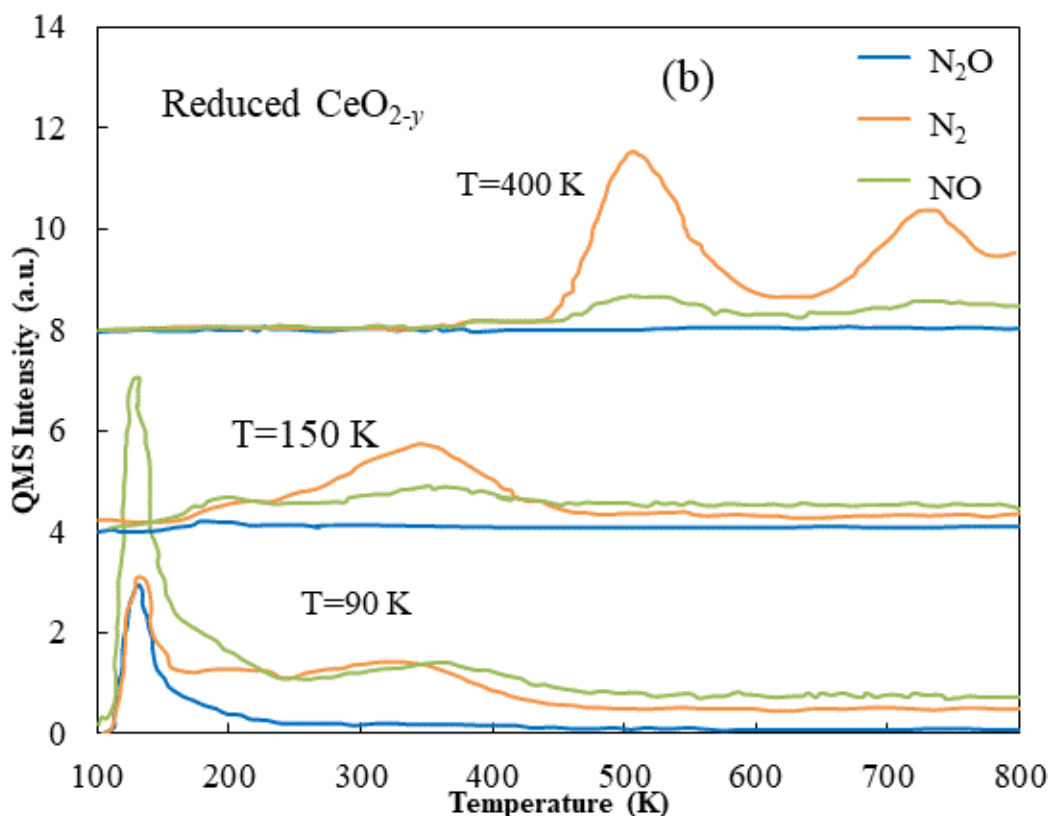


Figure 2.19: TPD measurements following exposure of NO on (a) fully oxidized CeO₂ (111) and (b) sputter reduced CeO_{2-y} (111). On the oxidized surface the NO was exposed at 90 K. On the reduced surface the NO was exposed at different temperatures as indicated and then the sample was cooled to 90 K before the TPD. Reproduced from ref. [143].

In two different studies conducted by Ferrizz *et al.* [142] and Overbury *et al.* [77, 143], NO was shown to adsorb more strongly on non-stoichiometric CeO_{2-y} and these indications are in agreement with work conducted by Daturi *et al.* [144]. These studies linked the so-called “deNO_x” catalytic capacity of ceria with the number of vacancies created on the ceria surface. Ferrizz *et al.* reported that after the NO adsorption at 300 K on non-stoichiometric CeO₂/α-Al₂O₃ (0001), only N₂ molecules were formed and desorbed. The N₂ desorption profile is dependent on the method by which the reduced surface is synthesized. A film that was prepared in a lower O₂ pressure led to a sharp N₂ desorption in the range of 300 K to 400 K. The desorption of N₂ extended from 400 K to 800 K by removing the O from fully oxidized films that were formed because of N₂ desorption. Overbury *et al.* revealed a diversity of desorbed species and the desorbed product distribution was generally affected by the

desorption [143]. As shown in the Figure 2.19b, NO, N₂ and N₂O molecules are formed mainly below 200 K as a consequence of following adsorption at 90 K with the desorption of NO and N₂ in the range of 200 K to 400 K. As the adsorption temperature increases to 150 K, the low temperature desorption diminishes and only additional N₂ desorption is captured at 350 K. As the adsorption temperature rises to 400 K, new desorption characteristics appear with a considerable amount of N₂, in addition to the desorption of NO represented by peaks located at 500 K and 740 K.

2.6.11 Ceria Surface Reactions with Hydrocarbons

When the cerium oxide surfaces are supported by Rh or Pt, ethylene adsorption and dissociation has been observed. Thermal interaction of ethylene on Rh pure crystal faces leads to the formation of gaseous H₂ leaving C on the surface [145-147]. It is found that the hydrogen molecule leaves from the Rh surface between 300K and 500K. If Rh is deposited on an unreactive material such as α -Al₂O₃ (0001), ethylene dissociates in an analogous way and H₂ leaves close 440 K [106]. Ethylene dissociation over Rh/CeO₂ (111) surface [148] or Rh/CeO₂/ α -Al₂O₃ (0001) [106] forms CO and H₂ molecules. CO molecules are formed as a consequence to the reaction between the carbon layer deposited on the Rh particles and O on the ceria's substrate. Over successive cycles of ethylene adsorption the temperature of CO desorption shifts to increasingly higher temperatures in subsequent TPD measurements suggesting that it gets more difficult to eliminate O from an increasingly reduced surface [106]. Aside from CO and H₂ production from decomposition of ethylene on Rh/CeO₂/YSZ (100), CO₂ species were also present [149]. This indicate that the YSZ (100) substrate changes the reactivity of the O in ceria. In particular, H₂O is not recorded in any of these Rh/CeO₂ materials, suggesting that the H atoms produce H₂, leaving the surface instead of interacting with O in the ceria producing water molecules.

An analogous trend is seen for ethylene adsorbed on Pt/CeO₂ (111) catalyst [150]. The high-resolution XPS C1s spectra demonstrated the destruction of the ethylene to C on the Pt at elevated temperatures, with evidence for C atoms being desorbed. It has been shown that when CeO₂ reduces to Ce₂O₃ via interaction of carbon with the surface O, eliminated carbon steadily increases. In the same vein, Pt nanoparticles on CeO₂ (111) surfaces activate the dehydrogenation process of the ethylene at a lower temperature compared to Pt (111).

Methane on Pt/CeO₂ (111) [151, 152] was shown to improve the dehydrogenation activity as well. It has been observed that methane partly dehydrogenates to CH₃ at temperatures close 100 K. Moreover, it has been shown that the methane species dehydrogenates to CH when reacted on Pt nanoparticles on CeO₂ (111). Supported methane activation was also detected for low-surface area Rh, Pt and Pd on CeO₂ during methane steam reforming [153].

2.6.12 Ceria Surface Reactions with Methanol.

In order for organic molecules to interact with ceria surfaces under ultra-high vacuum (UHV) conditions, the presence of a functional group including a heteroatom such as O, N, and S is essential. Yet, literature presents several accounts on the interaction of a wide range of non-functionalized organic molecules with ceria. For instance, it has been demonstrated that ethylene leaves CeO₂ (111) surface as a molecule under 150 K [148]. Furthermore, ethylene was investigated on Rh/CeO₂/YSZ (100) [149], but the authors did not report ethylene's reaction with the vacancy-free ceria surface. Instead, they focused on the interaction between adsorbed ethylene the Rh particles. Vile *et al.* studied the selective hydrogenation of alkynes to olefins at elevated conversion over polycrystalline ceria powders [154]. Carrasco *et al.* conducted computational studies on the selective hydrogenation of acetylene to ethylene over CeO₂ (111) using DFT [73]. In this study, β -C₂H₂ radical species were reported to have adsorbed on the surface of oxygen atoms, subsequently converting to C₂H₃. Formation of this species requires a lower activation energy barrier to convert to gas phase C₂H₄ with reference to the formation of a β -C₂H₄ radical that would result in more highly hydrogenated products.

The TPD measurement of methanol adsorption on CeO₂ (111) and CeO₂ (100) is depicted in Figure 2.20 [155]. Methanol and water were reported to be the initial products on CeO₂ (111), subsequently leaving the surface between 200 K and 300 K (black lines). This is mainly attributed to the reaction between methoxy and hydroxyl co-adsorbed on the surface. It is of significance to note that a competing reaction in this temperature range is the disproportionation of hydroxyls to yield water and a vacancy.

Isotopic labelling experiments of Ce^{18}O_2 (111) proved that water formed close 200 K holds lattice O [156]. Methanol desorption between 200 K and 300 K is in agreement with the reduction of methoxy exposure when the sample is annealed. The disproportionation of methoxy at ca.560 K is found to facilitate other reaction products at higher temperature.

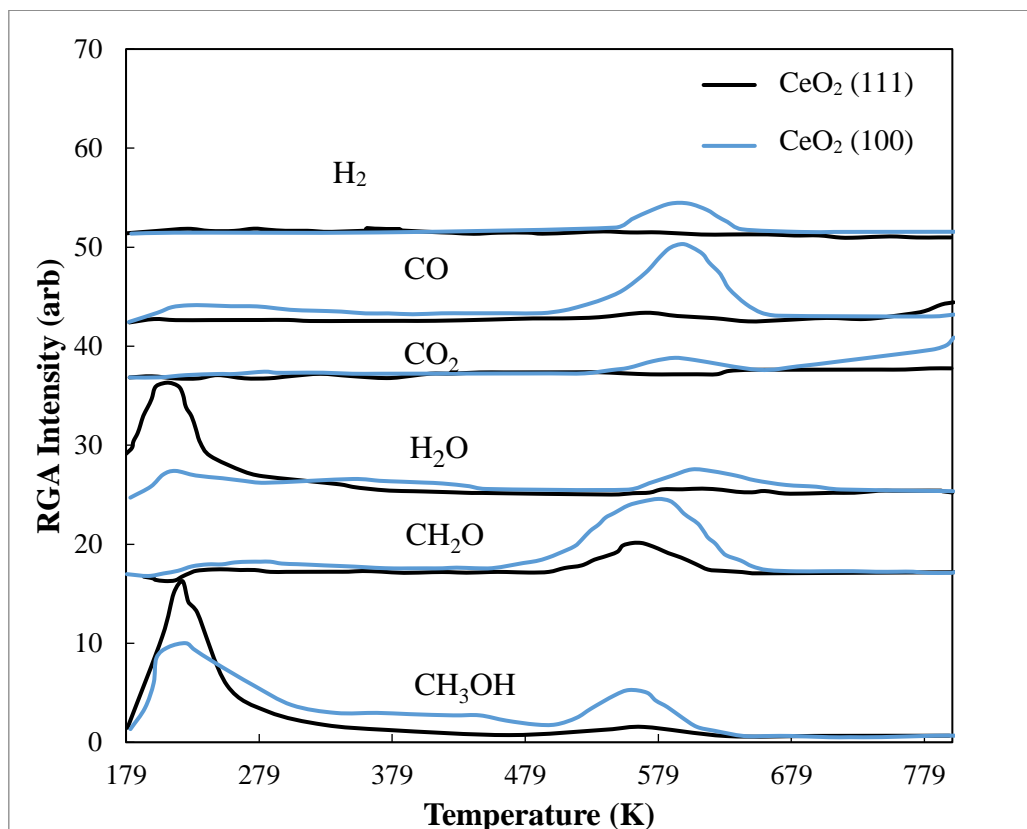


Figure 2.20: Temperature Programed Desorption following methanol adsorption at 180K on oxidized CeO_2 (111) and CeO_2 (100). Reproduced from ref. [155]

2.6.13 Catalytic performance of Ceria Surface on Phenol.

Phenol plays a crucial role as a raw material in many important industrial fields such as the chemical, petrochemical and pharmaceutical industries. Despite the positive use of phenol in the aforementioned applications, researchers have also devoted significant effort to develop methods by which phenol can be efficiently degraded. This is because phenol is viewed as a harmful contaminant, most notably in wastewater even at a content as low as 0.001 mg/L [157]. Furthermore, a phenolic concentration of 50 mg/ L is sufficient to have a bactericidal effect on microorganisms. Lin *et al.*[157] investigated the catalytic efficiency of CeO_2 on phenol conversion and total organic carbon (*TOC*) conversion. They studied using XRD, O_2 -

TPD, and H₂-TPR techniques, the catalytic wet air oxidation (CWAO) of a number of CeO₂ samples calcined under different thermal impacts, classified from the highest thermally calcined to the lowest thermally calcined, *i.e.*, type A, type B, type C and type D. They reported a number of conclusions. Firstly, CeO₂ calcined under different thermal conditions displays variable catalytic efficiency in the CWAO of phenol. The highest thermal impact sample (denoted as A CeO₂) exhibits a less stable structure, more structural oxygen exchange, and more oxidizing capability for the intake of H₂ and conversion of phenol. For the A-type CeO₂, at phenol content in the range of 400 to 2500 mg/L, oxygen pressures between 0.5–1.0 MPa, and temperatures exceeding 160°C phenol conversion amounted to ratios, greater than 90% after 4 h. The elimination process of total organic carbon enhances with the increase in the reaction temperature. Finally, CO₂ selectivity was found to be approximately $\geq 80\%$ after 4 h reaction.

As observed from Figure 2.21, the XRD pattern obtained from the abovementioned catalyst systems demonstrate that Type A prepared with the highest thermal impact has peaks with lowest intensity. This is indicative of the increased number of defects in its structure. In contrast, the CeO₂ catalysts calcined with less thermal impact possesses more structural stability.

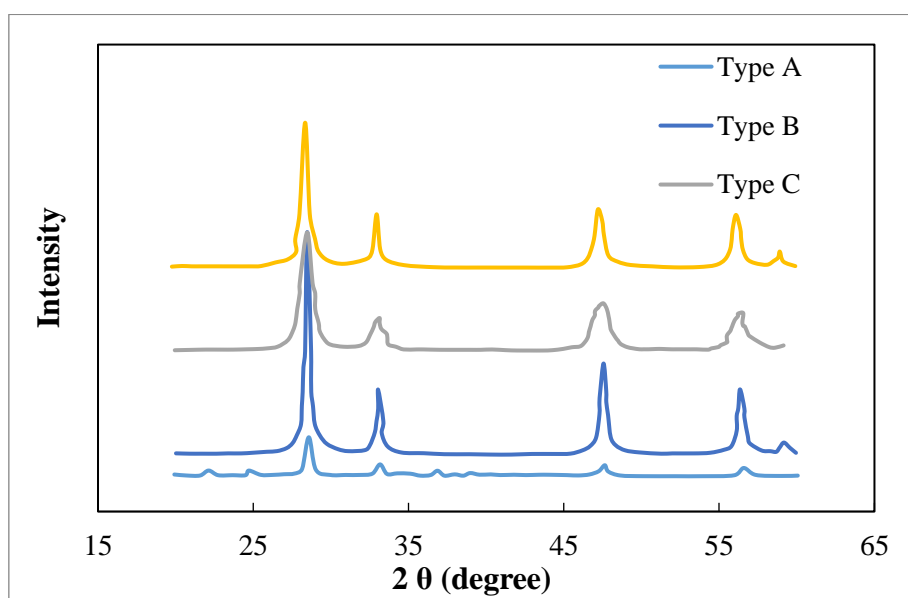


Figure 2.21: XRD patterns of different prepared CeO₂ catalysts. Reproduced from ref. [157].

Yao and co-workers [158] classified three types of oxygen in CeO₂, namely as capping, bulk and shared oxygen. Below 500 °C, capping oxygen forms due to defects in the CeO₂ structure undergoing an elevated thermal impact [158, 159]. This activity of the capping oxygen type is ascribed to its mobility that leads to a facile redox cycle between the two extreme cerium oxidation states of +4 and +3.

The O₂-TPD technique was employed by Lin *et al.* [157] to evaluate the mobility of oxygen in a CeO₂ crystal. From Figure 2.22, it is observed that type B CeO₂ has only one peak, near 120°C. This peak is may belong to the physisorbed oxygen molecule O₂ on the surface. There was no evidence for any other type of oxygen on the CeO₂ structure in the range of investigated temperatures. However, at temperatures exceeding 120°C, other peaks emerged for type A CeO₂, regardless of whether it was pre-treated with O₂ or not. These peaks are attributed to the depletion of capping oxygen inside the bulk structure. Furthermore, at temperatures higher than 120°C, it is found that CeO₂ samples pre-treated with O₂ release an amount of O₂ greater than that without pre-treatment. This suggests diffusion of O₂ in the gas phase into the type A CeO₂ crystal. Hence, Lin *et al.* reach an important conclusion that due to the high ability to undergo redox reaction in type A CeO₂, it can effortlessly exchange its structure oxygen with the O₂ in the gas phase.

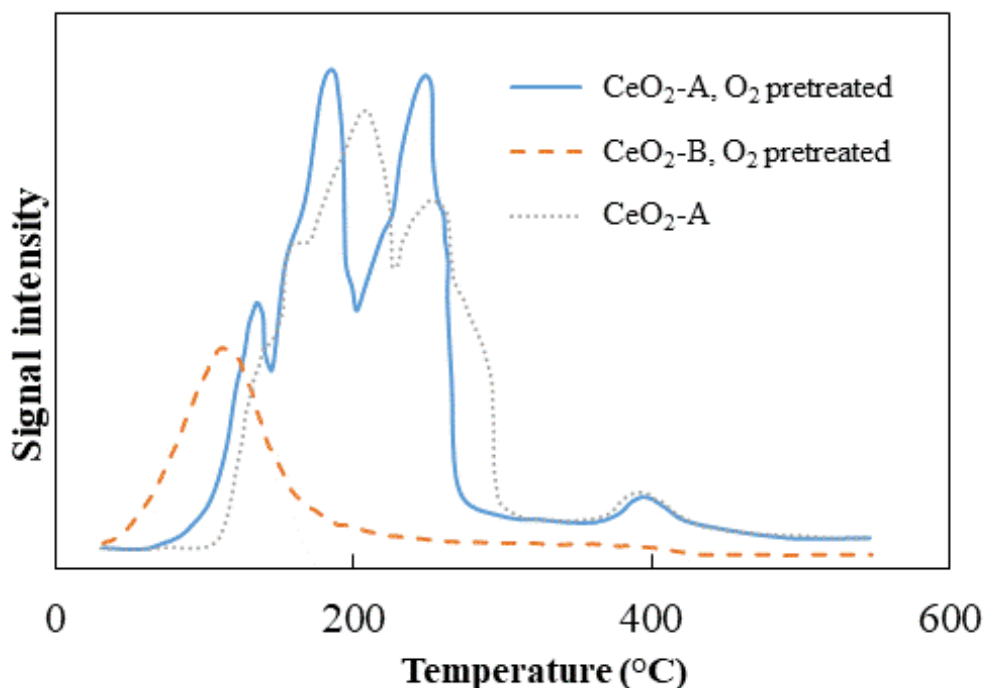


Figure 2.22: O₂-TPD of CeO₂ catalysts. Reproduced from ref. [157].

The high oxidation capability of CeO₂ was further investigated by means of the H₂-TPR technique. The technique is based on the fact that H₂ consumption is indicative of its oxidation by the catalyst. The appearance of the peaks at lower temperatures is indicative of the high stability of the catalyst. Consequently, as displayed in Figure 2.23, the type A CeO₂ performs as the highest oxidizing catalyst among other types (B, C and D). In relation to the peak at approximately 550°C, belonging to type D (regenerated CeO₂), this peak is attributed to the reduction and desorption of reaction residues, most likely polymers, deposited on the CeO₂ surface.

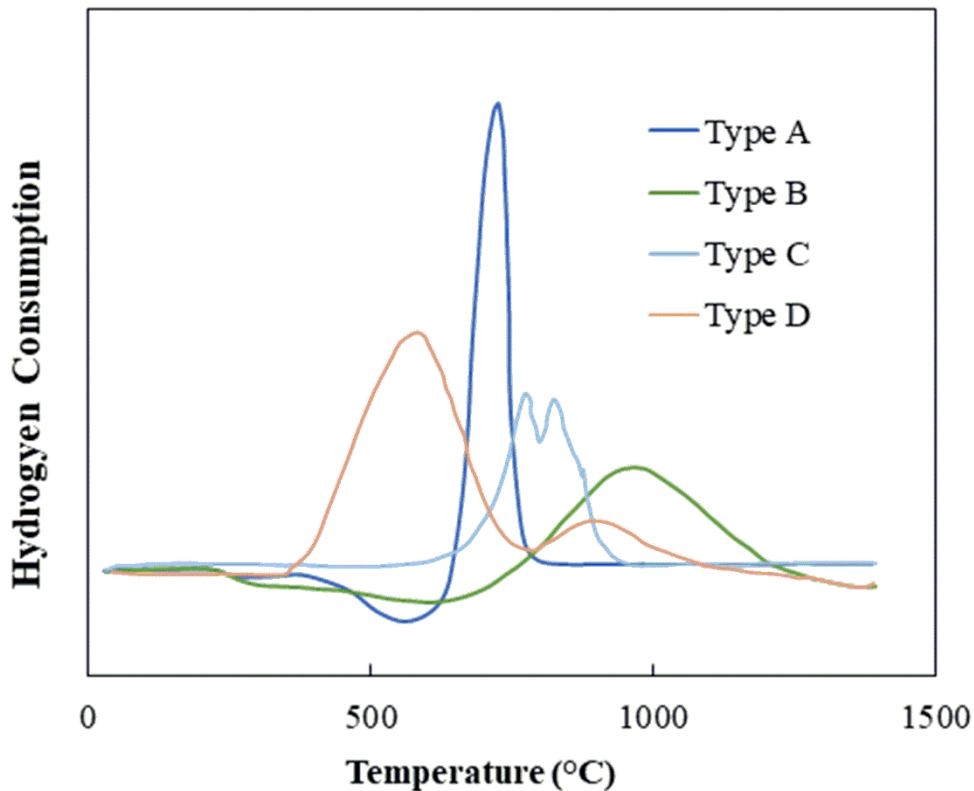


Figure 2.23: H₂-TPR of CeO₂ catalysts. Reproduced from ref. [157].

The catalytic efficiency of type A CeO₂ was further investigated by the *CWAO* of phenol. As Figure 2.24 shows, type A CeO₂ exhibits an excellent efficiency for the *CWAO* of phenol. At 400 mg/L phenol content with 0.5 MPa oxygen molecule pressure, the conversion of phenol was achieved as 95% after 2 and 3 h reaction times at reaction temperatures of 180°C and 160°C, respectively. By contrast, in the absence of a catalyst, the conversion of phenol after 4 h reaction time was only 20% at a temperature of 180°C and 0.5 MPa oxygen pressure. The improvement in phenol conversion is clearly evident in Figure 2.24 with the introduction of type A CeO₂ for a reaction temperature above 140°C.

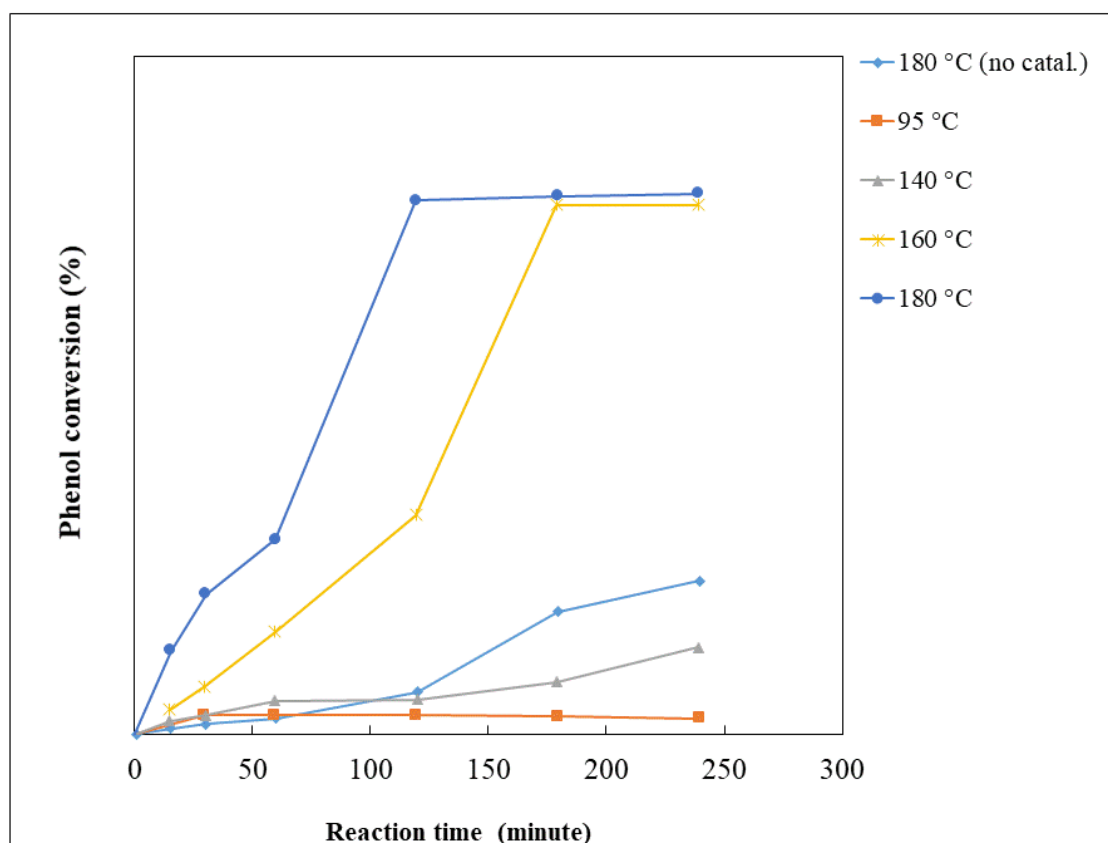


Figure 2.24: Influence of temperature on the CWAO of phenol with and without addition of type A CeO₂. Phenol content amounts to 400 mg/L with oxygen pressure of 0.5 MPa and catalyst loading of 2 g/L. Reproduced from ref. [157].

2.7 Thin Film Applications of Ceria

A consensus of opinions in the literature suggests that some rare earth elements, most notably La, Ce, Zr, and Y or their oxides, induce a net positive effect on improving the high temperature oxidation resistance of alumina- and chromia-producing alloys via an enhancement of their reactive-element effect (REE)[160, 161]. Thanneeru *et al.* [162] coated AISI 304 stainless steel (SS) with nanocrystalline ceria and La³⁺-doped nanocrystalline ceria particles with the aim of studying their high temperature oxidation resistance at 1243 K in dry air for 24 h. Results were then compared to those of similar coatings in the absence of micro-ceria coatings. The nanocrystalline ceria coatings were observed to enhance the oxidation resistance character by 90% compared to those cases of uncoated and micro-ceria coated steels.

Likewise, Fernandes and Ramanathan [163] reported the effect of surface coatings of Ce, La, Pr, and Y oxide gels on the oxidation behavior of a Fe-20Cr alloy at 1000 °C. Alloying small quantities of rare earths (RE) to chromia or alumina forming alloys enhances their high temperature oxidation resistance. Usually, rare earth elements are added or doped with oxides to form a protective layer for chromia and alumina alloys. Different methods can be deployed to coat alloy substrates with rare earth oxides, including the sol-gel process. In addition, it is important to mention that the morphology of RE oxide coatings varies with the nature of RE. For instance, the oxidation rate of RE oxide coated Fe-20Cr was considerably less than that of the uncoated alloy [163].

Huiming *et al.* [164] have studied the impact of nanometric ceria coatings on the oxidation behavior of chromium at 900 °C. They revealed that the ceria film dramatically enhances the oxidation resistance of Cr both in isothermal and cyclic oxidizing experiments. They attributed this improvement to the fact that ceria robustly decreases the growth speed and grain size of Cr₂O₃.

Ceria as a coating material utilized in various electronic and optical applications has been extensively studied in the literature with the aim of enhancing and tuning the preparation parameters that contribute to achieving optimal characteristic properties. Ozar *et al.*, [165] employed a sol-gel spin coating technique to prepare crystalline CeO₂ coatings and investigated the optical and electronic properties of such thin films. Their XPS analyses revealed that the films possess a compositional structure of CeO₂ and their surface topography as examined by scanning electron microscopy (SEM) demonstrated good uniformity and homogeneity. The authors also reported that the CeO₂ films exhibit high electrochemical stability based on the results of the spectroelectrochemical cyclic voltammetry experiments. Moreover, their analysis of spectroelectrochemical cyclic voltammetry experiments confirmed that CeO₂ coatings are a good passive counter electrode material in terms of inserted/ extracted charge and optical response.

Ta *et al.* [166] have previously also studied the epitaxial growth of CeO₂ films deposited on Si (111) by r.f. magnetron sputtering. The films were fabricated under different experimental conditions such as deposition temperature, sputtering power and target-substrate distance. They conclude that the three aforementioned experimental parameters affect the growth rate

of the deposited films, but the deposition temperature parameter was found to have a stronger influence on the improvement of the crystallinity of the deposited layers in the studied films.

The reactive DC magnetron sputtering technique was used by Jain *et al.* [167] to synthesize cerium dioxide thin films deposited onto Si and quartz substrates. The films were prepared as a function of target-substrate distance (d_{T-S}) and characterized by a number of characterization techniques such as XRD, atomic force microscopy (AFM) and UV-Vis spectroscopy. The study revealed that, the structural and optical characteristics of the deposited films are strongly dependent on the target-substrate distance. They also concluded that the synthesized films exhibit good transmittance characteristics in the wavelengths range of 400-1100 nm.

2.8 Spinel - Structured Oxides

Spinel structures have a general formula of AB_2X_4 , in which A and B are cations and X represents anions such as O and sometimes F, S, Se, Te. Three configurations of spinels have been recognized according to their cations distributions. The value of ϕ in the $A_{1-\phi}[A_\phi B_{2-\phi}]X_4$ form specifies the type of the spinel and for that three types are referred to as normal, statistic (completely disordered) and inverse spinels, with ϕ values corresponding to 0, 2/3 and 1, respectively [168].

Spinel oxides have a general form of AB_2O_4 with a cubic close-packed configuration of oxygen ions of the lattice system [169]. The two cations A and B are placed in some or all of octahedral and tetrahedral sites in the crystalline lattice [168]. In the spinel oxide system, the two cations belong to the same elements but possess different valance states. Among the spinel oxide systems, transition metal cobaltite oxide, MCo_2O_4 ($M=Co, Ni, Cu, Zn, Mn, etc$), exhibits excellent electrocatalytic characteristics which make them suitable for use in the oxygen evolution reaction (OER) [170-176]. Several studies have investigated the synthesis, electrocatalytic characteristics, and mechanism for OER of these interesting materials. For instance, some cobaltite spinels such as Co_3O_4 and $NiCo_2O_4$ have been extensively studied in terms of their preparation methods, the electrocatalytic properties, physicochemical properties and the electrocatalytic mechanism of OER. Moreover, some studies attributed a high catalytic performance for Co_3O_4 and $NiCo_2O_4$ in electrochemical applications, including

the oxygen evolution reaction because of its high stability in alkaline solutions. Other studies confirmed the lowest anode over potentials and a high mechanical stability for Co_3O_4 and NiCo_2O_4 [172, 174, 177]. Furthermore, other binary spinel oxides such as copper cobaltite spinel, with the formula of $\text{Cu}_x\text{Co}_{3-x}\text{O}_4$, were evaluated as catalysts to oxidize CO to CO_2 , in alcohol synthesis, in car pollution control, and oxygen evolution [178-182]. Chi and his colleges [183] prepared $\text{Cu}_x\text{Co}_{3-x}\text{O}_4$ spinels with various x values by a hydroxide co-precipitation technique and characterized them using different methods such as TGA, XRD, BET, and SEM. They concluded that the cation distribution depends on the copper concentration x so that with the increase of x from 0.7 to 0.9, more Co^{3+} ions insert into the tetrahedral sites of the system. Furthermore, the interesting conclusion in their work is that the increase of Co^{3+} ions in the tetrahedral sites leads to a strongly enhanced electrocatalytic performance of the spinel system for the oxygen evolution reaction in alkaline water electrolysis. It is also worth noting that spinel oxides with different valence states show electrically conducting or semiconducting characteristics, enabling them to be employed as electrode materials, with electron transfer occurring with relatively low activation barriers between cations of various valences by hopping process. In the case of spinel oxides with the same valence states, they require mixing with graphite to improve their electronic conductivity [184].

2.9 Previous Studies Based on Density Functional Theory (DFT)

From an atomistic point of view, numerous DFT studies have been reported relating to the investigation of the bulk and surface properties of a number of refractory-metal oxynitrides and rare earth oxides. These reflect the ability of first-principles calculations in accurately predicting the chemical bonding, band structures, and thermomechanical properties in agreement with experimental findings. An earlier study conducted by Weinberger and his colleges reported band structure and cohesive properties using ab-initio calculations of 3d, 4d and 5d-transition metal carbides and nitrides in the NaCl structure [185]. The elastic properties of series of early transition metal nitrides and carbides were investigated by Yadav and Singh. In addition, the bulk-modulus of 3d, 4d, and 5d-transition metal mono-nitrides were computed for the NaCl-type (fcc) structure using plasma oscillation theory of solids[186].

Fronzi *et al.* [187] employed an Ab initio atomistic thermodynamics approach to assess relative thermodynamic stability and Wulff constructions of the three low index surfaces of CeO₂, namely, (100), (110), and (111). Among the different plausible studied surfaces, the stoichiometric (111) surface under “oxygen-rich” conditions is predicted to be the most stable surface. Under reducing conditions, the stoichiometric (111) face with subsurface oxygen vacancies becomes the most thermodynamically stable facet. However, near to the O-lean region, the (111) Ce-terminated surface becomes the most stable surface (see Figures 2.25 and 2.26).

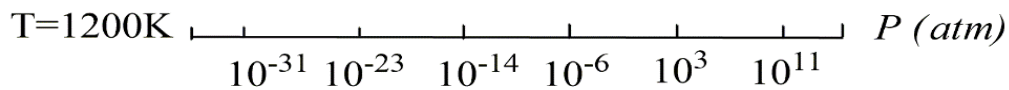
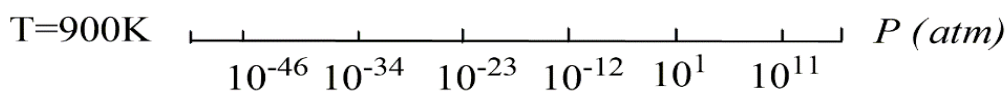
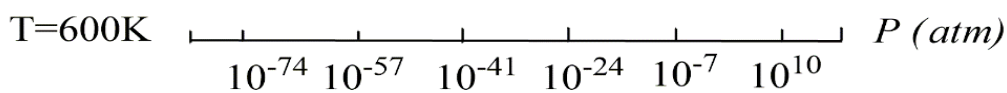
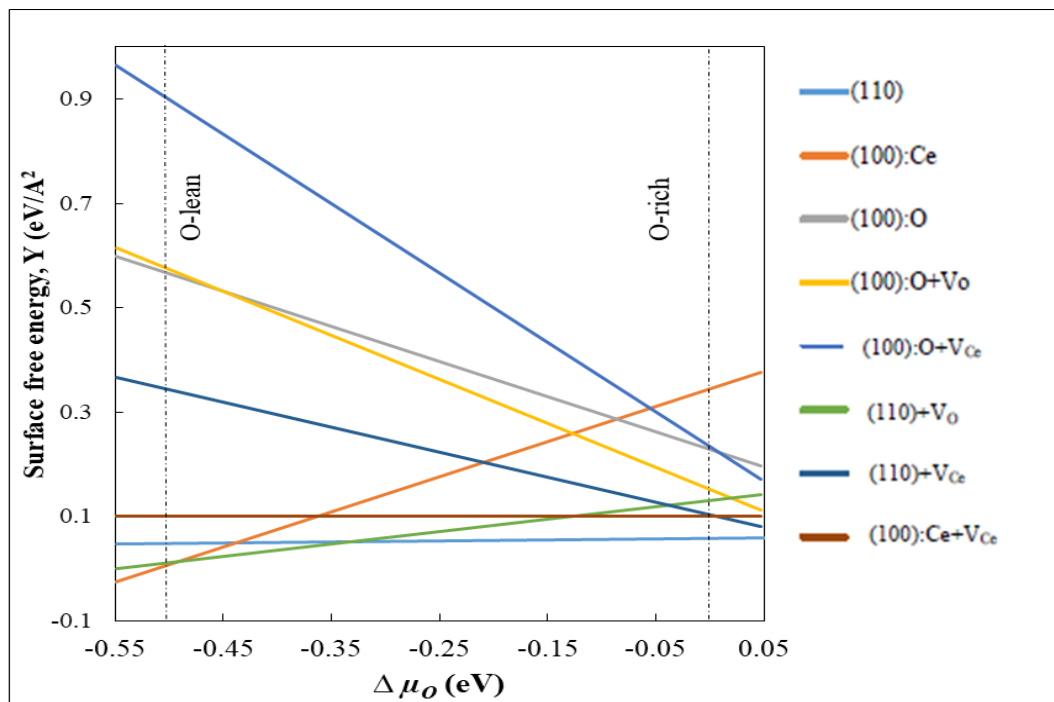


Figure 2.25: Calculated surface free energy of different plausible CeO₂ (100) and CeO₂ (110) orientations with regards to the change in oxygen chemical potential $\Delta\mu_O$ along with their corresponding pressure bar lines at T=600, 900, and 1200 K. Reproduced from ref. [187].

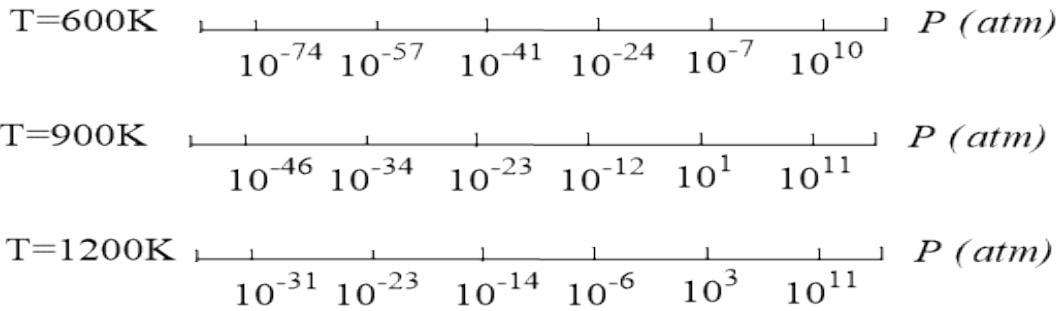
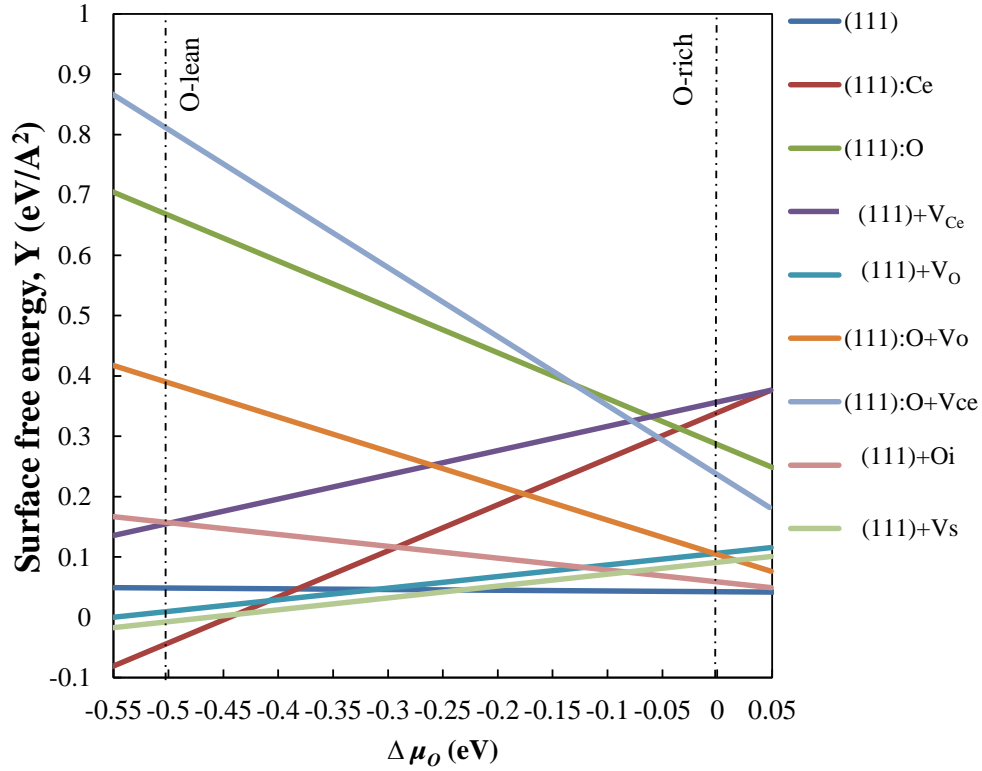


Figure 2.26: Calculated surface free energy of different plausible CeO_2 (100) and CeO_2 (111) orientations with regards to the change in oxygen chemical potential $\Delta\mu_{\text{O}}$ along with their corresponding pressure bar lines at $T=600, 900,$ and 1200 K. Reproduced from ref. [187].

The properties of solid solution systems have also been reported using DFT. Lü, Zhou *et al.* have studied the effects of rare earth elements (Eu and Yb) added to the magnesium solid solution on the structural and mechanical properties using first-principles calculations. They calculated and analyzed the lattice parameters, elastic constants, bulk moduli, shear moduli, Young's moduli and anisotropic parameter of these solid solutions[188]. A combination of DFT results and Monte Carlo simulations were applied by Grieshammer and coworkers in their investigation on the dopant dispersion and its impact on the oxygen ion conductivity of ceria alloyed with rare earth oxides [189]. Tekumalla and his coworkers reviewed the

mechanical properties of rare earths when alloyed with pure magnesium and other Mg alloys [190]. Recently, the electronic and optical properties of rare earth oxides in Gd_2O_3 and Tb_2O_3 compounds have been studied by means of DFT calculations [191]. Grosse et al. [192] investigated the electronic structure of the rare earth sesquioxide and their alloys using DFT functional. In their calculations, the insulating character of Gd_2O_3 could not be re-produced, so they corrected their functional by adding Hubbard parameter within LDA+ U approach. The authors concluded that that the optical band gap of LaLuO_3 layer is higher than that the corresponding Gd_2O_3 .

The three well known dioxides in the lanthanide series, CeO_2 , PrO_2 and TbO_2 were comprehensively investigated by Kanoun and co-workers [193] to simulate their electronic, structural, elastic, optical and magnetic properties. The consensus in literature suggests that an accurate description of the electronic system of CeO_2 requires the inclusion of the U term in the DFT functional. This is primarily due to the fact that pure DFT incorrectly describes ceria as a conducting material. For PrO_2 and TbO_2 , U implementation and the spin-orbit coupling are significant to obtain the proper ferromagnetic insulating behavior of these two materials. The dielectric functions and the reflectivity computed for photon energies up to 12 eV demonstrated excellent optoelectronic properties for PrO_2 and TbO_2 .

2.10 Gaps in current knowledge:

Having surveyed literature pertinent to chemistry and physics of CeO_2 , we can now pinpoint to some gap in our current knowledge:

- The influence of annealing temperature on microstructure on solar selectivity of the CuCo-oxide coatings deserves more experimental investigations. This has been addressed in Chapter 8.
- It is important to address the impact of critical sputtering parameters (O_2/A_2 flow ratio) on optical properties of magnetron sputtered CeO_x films. Chapter 7 in this thesis presents the results of this study.

- Literature presents no theoretical accounts on structural, electronic and optical properties of CuCo-oxide and CeO₂ coatings. Validation of XPS related measurements can be attained by accurate DFT calculations.
- While there are numerous theoretical and experimental studies on CeO₂ bulk and surfaces, analogous literature presents no analogous studies on the seemingly equally important TbO₂ phase. The findings on bulk and surface properties of TbO₂ are shown in Chapter 6.
- As discussed in section 2.6.5, CeO₂-assisted hydrogenation of C₂H₂ into C₂H₄ and C₂H₆ has been theoretically and experimentally investigated, reactions mechanisms for other catalyzed reactions by CeO₂ are yet to be reported; examples include oxidative decomposition of chlorinated volatile organic compounds and hydrogenation of aromatic rings. Chapter 5 reveals a comprehensive study on the catalytic activity of CeO₂ toward destruction of some chlorinated volatile organic compounds.
- Likewise, it is important to provide a theoretical benchmarking of the effect of dopants on the reduction energies of CeO₂ systems. This theoretical benchmarking has been conducted, in detail, in Chapter 4.
- Elucidate the variation influence of Hubbard value, U on the activation and reaction energies of partial and full hydrogenation of CeO₂ (111). Chapter 9 investigates the effect of Hubbard value, U on the activation and reaction energies.

Chapter 3 : Methodology

3.1 Reaearch Plan and Methodology

This chapter reports descriptions about the techniques used in the preparation of the studied films, namely Ce-oxides and CuCo-oxides, as well as it provides explanation about the characterization instruments by which variant electronic, structural, surface morphologies and optical properties can be probed. The physical principles behind these characterization techniques have been depicted. Moreover, this chapter summarizes the deployed theoretical methods utilized in this dissertation, especially, the DFT formalism, the transition state theory, the software utilized throughout the dissertation, and the ab initio atomistic thermodynamics approach by which thermodynamic stability diagram of surfaces can be deeply investigated. Figure 3.1 below systemically displays flow chart of the methodology in this dissertation.

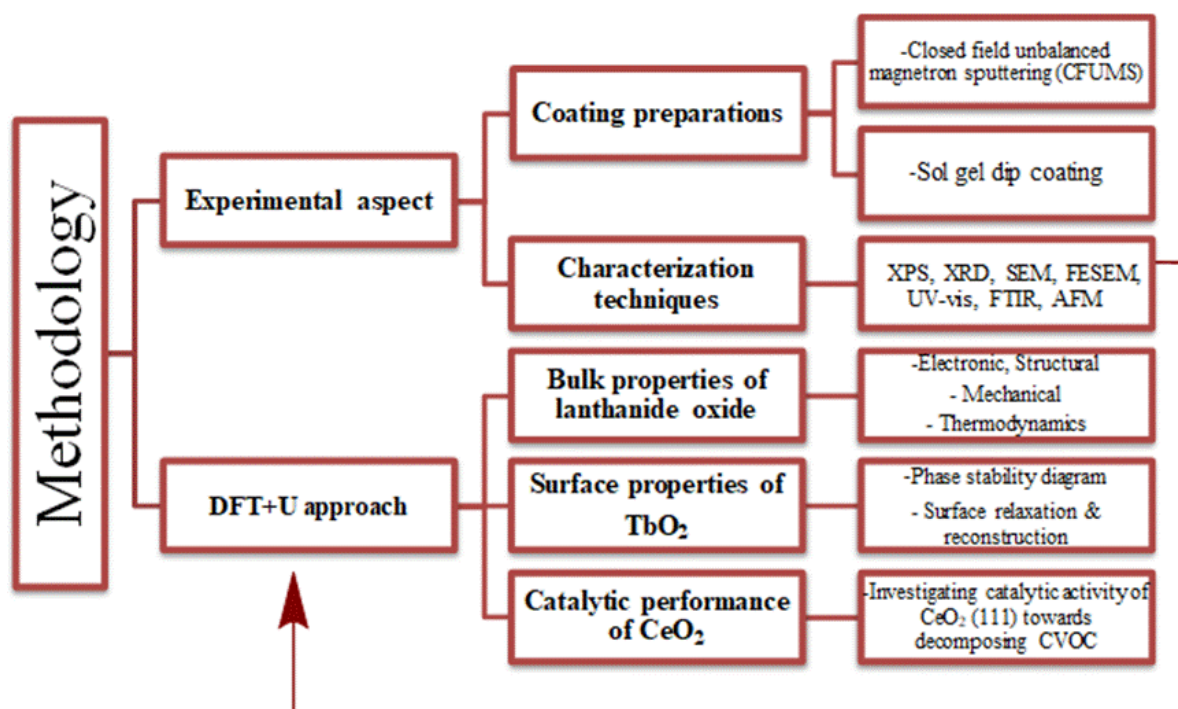


Figure 3.1 : Flow diagram of the methodology procedure.

3.2 Sol-Gel Deposition Technique

Sol-gel technique is a chemical synthesis deposition technique that has long been used to prepare thin film layers of metal oxides utilized as anti-corrosion and to enhance the optical properties of the materials. Sol-gel can be described as a process of material transformation of sol holding properties of fluid to gel with properties of solid. This technique displays several advantages including providing a good adhesion between the coating material and the metallic substrate, fabricating a thick film to enhance the performance of corrosion protection and producing high quality films economically efficient.

There are two most commonly employed coating methods namely, the dip-coating and spin-coating methods. The former is used to coat the double sides of the substrate, while the latter is utilized for coating one side of the substrate. Basically, in dip coating method the substrate is withdrawn from the liquid, whereas in the spin coating process the one side of substrate surface rotates and then the sol gel is poured on. All in all, sol gel technique has been widely used for thin films studied and characterized to get optimum optical properties for optical applications.

3.3 Magnetron Sputtering

Magnetron sputtering is a technique that is used for coating many of various materials. Presently, it is an established tool in industrial important coatings. This technique has attracted a significant attention and been rapidly developed over the last decade [194]. In this process, energetic ions generated in glow discharge plasma bombard the target (or cathode) which is located in front of glow discharge plasma. This process can result, during prolonged ion or plasma bombardment of a material, in significant erosions of material. The ion bombardment also causes generating of secondary electrons from the target surface. However, there are some limitations with this process that are low deposition rate, substrate heating effect, and lower ionization coefficients [195, 196]. In magnetron sputtering device, a magnetic field parallel to the cathode surface is used to keep the secondary electron motion in the vicinity of the target[197]. Due to the magnetic field, the probability of ionizing electron atom collision will increase; this in turn results in increasing the density of plasma near to the target region and finally, leading to the increased ion bombardment of the target which then gives higher deposition rate at the substrate. Therefore, secondary electrons emitted from the target play a key role in magnetron sputtering device.

Intensive research using magnetron sputtering was done on the study of the properties of deposited films[198, 199]. Furthermore, many experimental and theoretical studies have been done, especially on the physical properties of magnetron discharge and its dependence on process parameters like gas pressure, substrate biasing, electrical power *etc.*[200].

3.3.1 Unbalanced Magnetron Sputtering

Recently, limitations with magnetron sputtering have been overcome by the development of magnetron sputtering and, more recently, unbalanced magnetron sputtering. In an unbalanced magnetron the outer ring of magnets is relatively stronger than the central pole. As a result of this, not all the field lines are closed between the central and outer poles in the magnetron, but some will direct towards the substrate. Also, some secondary electrons will be able to follow these field lines. Consequently, the plasma is no longer strongly confined to the target region but is also allowed to flow out towards the substrate. Therefore, high ion currents can be extracted from the plasma without the need to externally bias the substrate[200]. This type of unbalanced magnetron discussed above was termed Type-2. There is another type of unbalanced magnetron, namely Type-1. In this type the central pole is strengthened relative to the outer pole. In this case the field lines which do not close on themselves are directed towards the chamber walls and the plasma density in the substrate region is low. This design is not commonly used, because of the resulting low ion currents at the substrate [201]. Figure 3.2 shows the arrangement of the positions of the four targets used in the system. This instrument also uses argon gas (Ar_2) as a working gas as well as the vacuum pump utilized to control the pressure inside the system. This technique is used to synthesize CeO_2 coatings deposited on Si substrate.

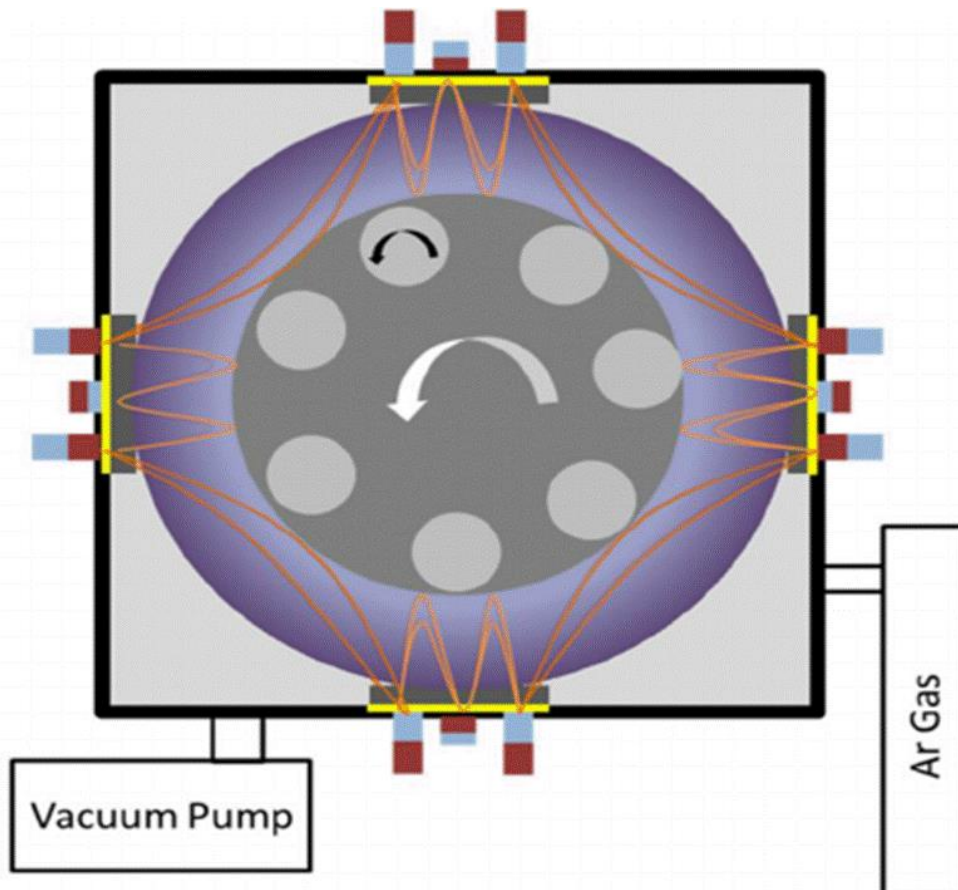


Figure 3.2: diagram of target configuration in closed field unbalanced magnetron sputter ion plating (CFUBMSIP) system.

3.4 Characterization Techniques

3.4.1 X-Ray Diffraction

X-ray diffraction is one of the structural techniques by which crystalline phases of a solid material can be determined. It is very well-known that each solid system has its own characteristic x-ray pattern which represents a fingerprint for its identification. X-ray diffraction is multi use, non-damaging analytical method for identification and quantitative determination of the different crystalline materials, well known as phases exist in solid compounds and powders. Determination of the present phase of materials is normally performed by contrasting the x-ray spectrum of patterns obtained from the studied samples with an internationally featured database containing reference patterns of the measured phases for the almost materials. Nowadays, all of the diffractometers connected to computers whose codes can utilize routines to measure, record and interpret the unique patterns obtained

by single constituents in even highly complex mixtures. The physical principle governed x-ray technique is Bragg's law stating that as a monochromatic x-ray beam with wavelength λ is incident on a crystal with a lattice planer distance at certain incident angle θ , reflection for the x-rays will occur when the wavelengths of the scattered x-rays interfere constructively. The general formula for Bragg's law is expressed as,

$$n\lambda = 2d \sin \theta \quad 3.1$$

In which n is the entire number of wavelengths or the order of the diffraction, λ denoted the projected wavelength, d corresponds to the spacing between the atomic planes (hkl) in the crystal, and θ stands for the incident angle. The crystallographic phase of the studied samples, in this thesis, is characterized by D8 DISCOVER XRD diffractometer manufactured by Bruker AXS (Figure 3.3).

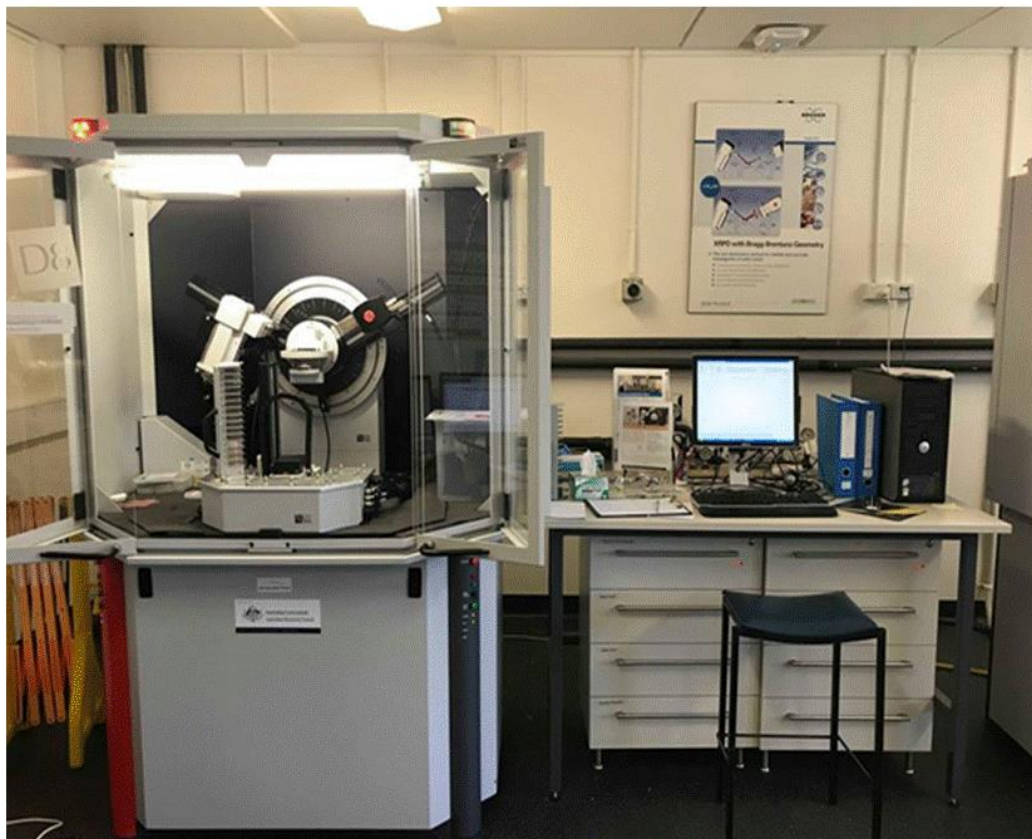


Figure 3.3: D8 DISCOVER XRD manufactured by Bruker AXS.

3.4.2 X-Ray Photoelectron Spectroscopy (XPS)

To obtain good information about surface properties and an elemental status of a solid material, XPS technique is the main instrument that is commonly used to achieve this purpose due to the low energy of the used x-ray that can penetrate approximately 5 nm. The interactions between the atoms of any surface and the elements in the environment lead one to investigating the nature of these interactions and thereafter reporting all the surface characteristics of the system. The physical principle of this structural surface characterization technique (XPS) is the photoelectric effect explored by Hertz in 1887. The spectra obtained by XPS contain photoemission lines belonging each to a specific element defined by its characteristic binding energy of its photoelectron, so these lines act as an indicator of the chemical elements present on the surface of the studied material. XPS measures the binding energy according to the following relationship;

$$E_B = h\nu - E_K - W \quad 3.2$$

Where E_B is the binding energy of the emitted photoelectron in the atomic system, $h\nu$ represents the incident photon energy, E_k denotes the kinetic energy of the photoelectron and W corresponds to the spectrometer work function. Furthermore, chemical bonding states can be provided by XPS. Kratos Axis Ultra X-ray photoelectron spectroscopy XPS (Kratos, Manchester, UK) (Figure 3.4) is operated in this dissertation to obtain the survey and high-resolution spectra of all coating samples and by which all the compositional and surface bonding state can be derived.

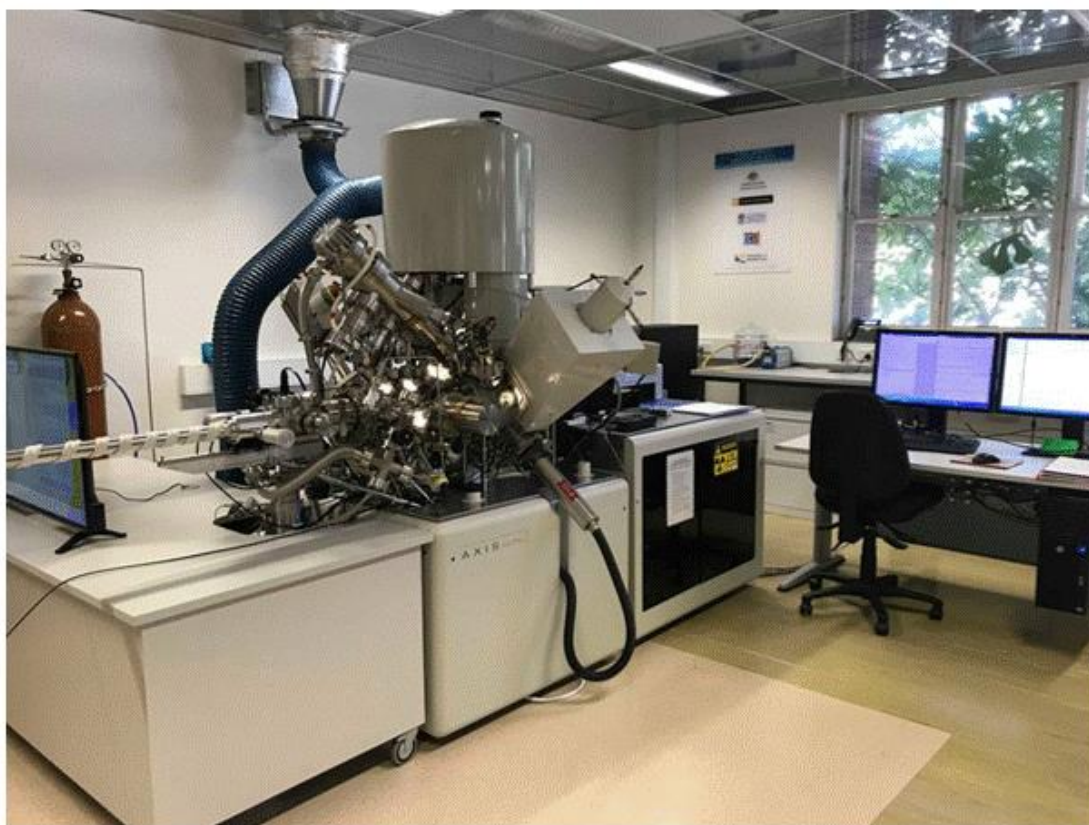


Figure 3.4: Kratos AXIS Ultra DLD X-ray photoelectron spectroscopy instrument.

3.4.3 Fourier-Transform Infrared Spectroscopy (FTIR)

Fourier-transform infrared spectroscopy is an instrument utilized to measure the optical properties of a solid such as the absorptance, reflectance and transmittance in the infrared range. Moreover, in organic chemistry, the infrared (IR) analysis is used to identify the chemical compounds present in the material. As very well known the atoms within the molecules are in movement states and the molecule as a whole in vibration motion. Furthermore, it is well documented that the electromagnetic (EM) waves in the infrared range are able to transfer molecules to their higher vibrational energy level. Consequently, if the frequency of the photon projected on the molecule matches the frequency of the bond energy, absorption occurs for that photon energy resulting in moving to higher vibration energy level. PerkinElmer FTIR spectrometer (Figure 3.5) has been used to measure the solar reflectance of our coating samples in the infrared region.



Figure 3.5: PerkinElmer Spectrum 100 FTIR Spectrometer, USA.

3.4.4 UV-Vis Spectroscopy

Ultraviolet visible spectrometers (as denoted as UV-Vis spectroscopy) are used to quantify the optical properties of a solid material in the ultraviolet and visible wavelength ranges of light. The physical principle of this technique is based on the electron transfers between their ground and excited states. In this technique, the material is exposed to incoming light in the ultraviolet and visible range resulting in exciting the valence electrons such as p or d in the outer orbitals. For more clarity, electrons will absorb the incident photon energies to transfer to higher energy levels of molecules.

The photon energy absorbed by a material is equal to the energy difference between the energetic levels between which the transfers are occurred. The energy difference is expressed as;

$$E = h\nu = \frac{hc}{\lambda}$$

3.3

Where E denotes the photon energy, h stands for Plank constant, ν corresponds to the frequency of the photon, C is the speed of light and λ signifies the wavelength of the photon. Optical data of all the films were acquired by UV-670 UV-Vis spectrophotometer, JASCO, USA double beam spectrophotometer (Figure 3.6).



Figure 3.6: UV-670 JASCO, USA double beam spectrophotometer.

3.4.5 Field Emission Scanning Electron Microscopy (FESEM)

FESEM is an important technique to provide information about the surface topography of materials such as the roughness and smoothness. This instrument is used by many researchers in field such as biology, chemistry and physics to view the nanostructures (1 millimeter = billion of a nanometer). In this imaging microscope, electrons released by a field emission source are projected on entire or fractioned systems. To clarify its function, electrons are liberated from a source and they are accelerated in a high vacuum column. These electrons named primary electrons are concentrated and deflected by electronic lenses

to provide a narrow scan beam that hits the material. As a consequence, secondary electrons are emitted from that system. The secondary electrons will be caught by a detector by which an electronic signal is going to be obtained and amplified and then transferred to a scan image seen on a monitor. Cross-sectional images for determining the thickness of the synthesized films were obtained in this work by Zeiss Neon 40EsB FESEM imaging (Figure 3.7).

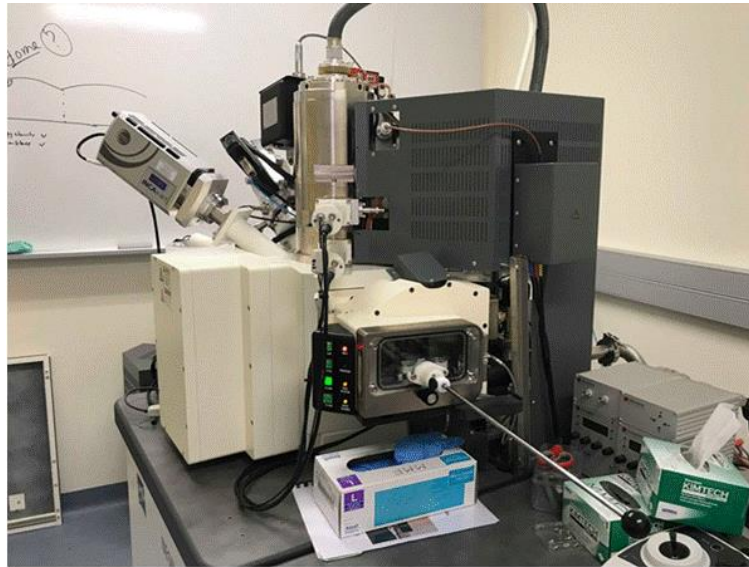


Figure 3.7: Zeiss Neon 40EsB FESEM.

3.4.6 Atomic Force Microscopy (AFM)

Atomic force microscopy (AFM) is an important kind of scanning probe microscopy. This technique is also considered as one of the most commonly microscopes that can provide surface topography information with high resolution ability up to the order of fraction of a nanometer. In nutshell, this machine is composed of a sharp probe with micro-measurements, scanning the surface of interest. The probe is fixed to a horizontal holder, whereas its self is perpendicular on this holder and the surface wanted to be scanned. In this method, laser radiations are projected on the holder being able to move up and down with probe movement and consequently the reflected laser radiation will be picked on a receiver fixed on the holder. Thus, the topography of the surface is determined according to the laser beam reflex movement. Figure 3.8 displays AFM used in this dissertation.



Figure 3.8: A high resolution atomic force microscopy (AFM).

3.5 Theoretical Background

3.5.1 The Many-Body Problem

Understanding and solving the electronic structure of atoms, molecules or any system are the main goal in computational modeling. It is well known that atoms consist of electrons and nuclei, from quantum mechanics perspective; Schrödinger equation is utilized to solve the electronic structure for atoms.

The Schrödinger Equation of any time independent quantum system describes as:

$$H\psi(r) = E\psi(r)$$

3.4

Where, ψ is expressed the wave function, E is the energy of the particle (electrons), and H is the Hamiltonian operator that describes the particle's energy as the summation of potential and kinetic energy and as given below:

$$H = T + V = \frac{1}{2}mv^2 + V \quad 3.5$$

By replacing the classical expressions for kinetic and potential energies with their quantum mechanical operators, we will obtain the quantum mechanical Hamiltonian H

$$H = \frac{\hbar^2}{2m} \frac{\partial^2}{\partial r^2} + V(r) \quad 3.6$$

Where \hbar is reduced Plank's constant (1.05457×10^{-34} Joule second), m is the mass of the particle (electron), V is the potential energy and it refers to the coulomb repulsion between each pair of charged particles. The potential energy term can be written as.

$$V = \frac{1}{4\pi\epsilon_0} \left[\sum_i \sum_{j<i} \left(\frac{e^2}{\Delta r_{ij}} \right) + \sum_I \sum_{J<I} \left(\frac{Z_I Z_J e^2}{\Delta R_{IJ}} \right) - \sum_i \sum_I \left(\frac{Z_I e^2}{\Delta r_{iI}} \right) \right] \quad 3.7$$

Where e and Z represent electron and nucleus charges respectively and r and R are denoted to electrons and nuclei positions respectively. The first term in Equation 3.7 represents electron-electron repulsion, the second term stands for nuclear-nuclear repulsion and the last term describes electron-nuclear attraction [202].

$$H = -\frac{\hbar^2}{2m_e} \sum_i \nabla_i^2 - \sum_{i,I} \frac{Z_I e^2}{|r_i - R_I|} + \frac{1}{2} \sum_{i \neq j} \frac{e^2}{|r_i - r_j|} - \sum_I \frac{\hbar^2}{2M_I} \nabla_I^2 + \frac{1}{2} \sum_{I \neq J} \frac{Z_I Z_J e^2}{|R_I - R_J|} \quad 3.8$$

The equation above refers to the Hamiltonian where m_e and M_I refer to the electron mass and nuclei mass respectively, r_i and R_I are positions of electron and nuclei. Z_I symbolizes the charge of nuclei and e signifies the charge of electron. Due to Coulomb force between charged particles, the electrons and nuclei interact with each other. The first term and fourth term represent the kinetic energy of electrons and nuclei respectively, second term is the attractive interaction between the electron and nuclei, third term is electron-electron repulsion term, and the last term corresponds to the nuclei-nuclei repulsion. Mathematically, it is quite difficult to solve such an equation, so approximations have been emerged to solve the many-body problem[203].

3.5. 2 Born-Oppenheimer Approximation

Born-Oppenheimer approximation is one of the earliest approximations employed to solve the Schrodinger equation. This approximation involves the claim that the nuclei cannot move as much as electron due to its heavy mass compared to electron's, in the other words, the nuclei move very slowly as compared with electrons. Accordingly, the term kinetic energy of nuclei was cancelled, and the electronic energy relies only on the position of the nuclei. Meaning that, this approximation leads to separate nuclear and electronic motions, and now the many-body problem is solved. According to the Born-Oppenheimer approximation, the Hamiltonian is given by [204].

$$H = T^{\text{elec}}(r) + T^{\text{nucl}}(R) + V^{\text{nucl-elec}}(R, r) + V^{\text{elec}}(r) + V^{\text{nucl}}(R) \quad 3.9$$

Where, $T^{\text{elec}}(r) + T^{\text{nucl}}(R)$ refer to the kinetic energy operators for electrons and nuclei, respectively; $V^{\text{nucl-elec}}(R, r)$ describes coulomb interaction between electrons and nuclei, while $V^{\text{elec}}(r) + V^{\text{nucl}}(R)$ represent the repulsive interaction between electrons and between nuclei respectively [204, 205].

3.5.3 Density Functional Theory (DFT)

Density functional theory (DFT) is the most frequently quantum mechanical modeling approach in material science. It has extensively been used for studying different properties of many condensed matter systems involving complex materials such as molecules, proteins, interfaces and nanoparticles. In other words, electronic structure of atoms, molecules, crystals which are considered large and periodic systems can easily be investigated using this method [206].

3.5.4 The Hohenberg-Kohn Theorems

Two theorems were expressed by Hohenberg and Kohn in 1964. They suggested in these theorems that the use of wavefunction can be replaced by electron density when determining the total energy for a system. The first theorem supposes that the external field $V_{\text{ext}}(r)$ of interacting particle can be determined by the ground state density $\rho_0(r)$ [207, 208], and can mathematically express as:

$$E[\rho(r)] = \int \rho(r) V_{\text{ext}} dr + F_{HK}[\rho(r)] \quad 3.10$$

In addition, Hohenberg's and Kohn's second theorem states that the electron density follows variational principle. Consequently, the lowest total energy of the system has to be equal or greater than the ground state energy.

$$E_0 = E[\rho_0(r)] \leq E[\rho(r)] \quad 3.11$$

From the various densities calculated by Equation 3.11, it can be selected the one with lowest energy to be the proper solution. Hohenberg-Kohn energy functional $F_{HK}[\rho(r)]$ in Equation 3.10 should be approximated and this would be a challenging work in DFT. The interaction energy between electrons $E_{ee}[\rho]$ and the kinetic energy $T_e[\rho]$ in $F_{HK}[\rho(r)]$ are given as,

$$F_{HK}[\rho] = E_{ee}[\rho] + T_e[\rho] \quad 3.12$$

The interaction energy E_{ee} equals the Coulomb repulsion $J[\rho]$ plus the component of E_{ncl} resulted from self-interaction, exchange and coulomb correlation contributions.

$$E_{ee} = J[\rho] + E_{ncl}[\rho] \quad 3.13$$

3.5.5 The Kohn–Sham Equations

In attempt to approximately the Hohenberg-Kohn energy functional $F_{HK}[\rho]$, Kohn and Sham found out a method that separates the kinetic energy functional T_e into two kind of energies namely as non- interacting reference system T_s and an unknown part T_c . Because of electron interaction in the actual system, T_c includes the correction. Hohenberg-Kohn functional may be expressed as,

$$F_{HK}[\rho] = T_s[\rho] + J[\rho] + E_{xc}[\rho] \quad 3.14$$

The non-interacting electron kinetic energy. T_s is given as a function of one-particle wave function Φ ,

$$T_s[\rho] = \sum_{i=1}^N \left\langle \Phi_i \left| -\frac{1}{2} \nabla^2 \right| \Phi_i \right\rangle \quad 3.15$$

And $E_{xc}[\rho]$ stands for the exchange-correlation energy defined as,

$$E_{xc}[\rho] = T_e[\rho] - T_s[\rho] + E_{ee}[\rho] - J[\rho] \quad 3.16$$

The difference between the kinetic energies of interacting electron system and non-interacting ones, as well as the repulsion energy between electrons E_{ncl} are described by the exchange-correlation energy. Hence, it can obtain an effective single particle problem instead of many-body problem. As a consequence, the electron density of the actual

interacting system can be regenerated by specifying the one particle wavefunction employing the effective one-particle equation and this results in the Kohn-Sham equation,

$$\left[-\frac{1}{2}\nabla^2 + V_{eff}(r)\right]\Phi_i = \epsilon_i \Phi_i \quad 3.17$$

In which $V_{eff}(r)$ corresponds to the effective potential which includes the external $V_{ext}(r)$, the coulomb and the exchange-correlation $V_{xc}(r)$ potential.

3.5.6 Pure Density Functional Theory Methods

There is a combination of methods used to approximate the exchange-correlation energy per particle $E_{xc}n(r)$. Finding an appropriate approximation (approach) for this term could be of great challenges in DFT. The Starting point for this approximation is from Kohn and Sham approach. Different approximations are proposed to compute the exchange and correlation energy using different DFT methods.

DFT is grouped into two methods which are pure methods and hybrid methods. It can be concluded from their name, pure DFT methods are used just DFT exchange energy functional. Below is a description of some frequently used approximations with pure DFT methods:

3.5.6.1 Local Density Approximation (LDA)

It is considered one of the most commonly used approximation in pure (local) DFT to calculate the exchange-correlation energy proposed by Hohenberg and Kohn. It is assumed that if the variation of the charge density of some regions of a material was slow, the exchange correlation energy at that point can be considered the same as that for a locally uniform electron gas of the same charge density. In this case we can write E_{xc} as;

$$E_{xc}[\rho] = E_{xc}(\rho(r)) \quad 3.18$$

Where E_{xc} is the exchange-correlation energy per particle of the homogeneous electron gas. In other words, LDA aimed to approximate the electron density of the inhomogeneous gas system locally based on the density of the homogeneous electron gas [209]. This approximation is very simple, accurate, and forms the essential approximations of most DFT codes. It is effective even in systems where the charge density is quickly changing. However, it tends to under predict atomic ground state energies and ionization energies, while over predicting binding energies. It is also known to be used in high spin state structures[210]. Meaning that The main error source in the LDA is in the exchange energy[206].

Local spin-density approximation (LSDA) has the same base as LDA with only one difference which is including electron spin that describes as below;

$$E_{xc}[\rho] = \int \rho(r(\rho_{\uparrow}, \rho_{\downarrow}))_{\epsilon_{xc}}(\rho) dr \quad 3.19$$

3.5.6.2 Generalized gradient approximation (GGA)

Efforts have been made to move beyond the LDA through the addition of gradient corrections to be more accurate for complicated systems.

GGA is an extension to LDA approximation, used for the exchange-correlation energy which can be defined as:

$$E_{xc}[\rho] = E_{xc}(\rho(r), \nabla\rho(r)) dr \quad 3.20$$

$E_{xc}[\rho]$ is the exchange-correlation energy in a homogeneous electron gas, the approximation is LDA but the gradient of electron density at the same coordinate is taken into account beside the density. The GGA approximation designed by Perdew and co-workers.[211, 212]. LDA approximation fails to predict exact exchange energy when its density experiences swift changes in molecules, whereas it becomes easily to overcome this limitation using GGA. Finally, various GGA functional were developed such as, Becke (B88), Perdew and Wang (PW91), and Perdew, Burke, and Ernzerhof (PBE). All of these functionals denote to the personal authors' name and the year of publication. PBE is one of widely used forms (functionals) in DFT calculations, belonging to generalized gradient approximation (GGA)[213].

3.5.7 Hybrid Density Functional Theory Methods

In hybrid methods, combinations of DFT and Hartree-Fock exchange energies are utilized to enhance the performance. For more clarity, new types of exchange-correlation energy approximations used in density functional theory due to GGA, LDA and PBE functional are insufficient to treat d and f electrons accurately [203]. To address these limitations new functionals have suggested. Frequently, B3LYP method, which represents Becke, 3-parameter, Lee-Yang-Parr is the widely used one. Moreover, B3P91 - uses Becke's exchange functional with part of the Hartree-Fock exchange mixed in, and a scaling factor on the correlation part.

3.5.8 The DFT + U Approach

Density functional theory (DFT) within both of its approximations, LDA and GGA has been proven to be disabled to treat the self- interaction errors raised in the d - and f - materials and thereafter, resulting in incorrectly describing the electronic and structural properties of such groups of materials [214, 215]. The self-interactions can be explained as the d and f orbitals are localized on each atomic site leading to coulombic repulsion between the electrons [214]. To solve this, the DFT + U approach was established. In this method, the self-interaction errors are addressed by correcting the DFT energy *via* introducing an adjustable parameter $U_{eff} = U - J$ where U signifies the Coulomb self- interaction term and J corresponds to the exchange self-interaction term.

In LDA+ U method, the valance states except d and f states are treated by the pure DFT functional, while for the d and f strongly correlated electron states, Hubbard parameter U is necessarily used. The total energy of a system can be given as [216];

$$E_{LDA+U}[\rho(r)] = E_{LDA}[\rho(r)] + E_{Hub}[\{n_{mm}^{l\sigma}\}] - E_{dc}[\{n^{l\sigma}\}] \quad 3.21$$

In this formalism, E_{LDA} stands for the approximate DFT total energy functional being corrected, E_{Hub} corresponds to the term that contains the Hubbard Hamiltonian to treat correlated states. Due to the additive behavior of this correction, it is of significant importance to remove from the (approximate) DFT functional, E_{LDA} , the part of the interaction energy to be modeled by E_{Hub} . This is achieved by taking away the term E_{dc} (double- counting) that models the contribution of the strongly correlated electrons to the DFT energy as a mean-field approximation of E_{Hub} [216].

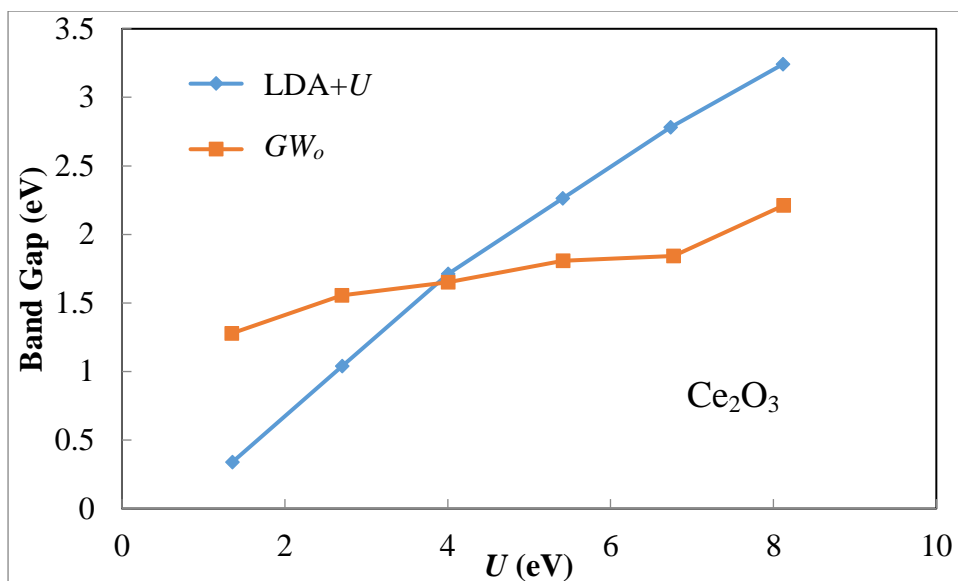


Figure 3.9: The variation of Ce_2O_3 band gap with Hubbard parameter (U) using LDA+ U and GW_0 approaches. Reproduced from ref. [267].

As Figure 3.9 depicts, band gap of Ce_2O_3 varies with the of Hubbard parameter U . Practically, values of Hubbard parameter are optimized by reproducing the corresponding experimental values of the studied materials. In Chapter 4, for instance, U_{eff} of 5 eV was considered because it reproduces the corresponding experimental lattice parameters and the semiconducting nature of all the studied lanthanide sesquioxides except that of Ce_2O_3 . However, a higher U_{eff} value at 6.5 eV was required to acquire the experimentally measured band gap of Ce_2O_3 .

3.5.9 Pseudopotentials

For solid state calculations, a plane-wave basis set is usually the most commonly used basis set. It is well –known that core electrons are generally not included in chemical bonding, so it is important to rid from the complicated effects of the motion of the core electrons by replacing the non-valance electrons of an atom and its nucleus with an effective potential or effective core potential (ECP) [217].

3.5.10 Modelling program based on DFT

The use of computer codes has become indispensable to achieve various kinds of calculations in material science. Different modelling programs based on quantum mechanics, especially

density functional theory DFT such as Quantum Espresso, cambridge serial total energy package (CASTEP), Gaussian, Dmol³, Crystal and Vienna Ab initio Simulation Package (VASP) were released with different operating systems as Windows, Linux, and Macintosh. In this thesis, some of these codes used in solid state systems such VASP, Dmol³ and CASTEP are operating to calculate different material properties such as electronic, structural, mechanical, thermodynamic and optical, as well as investigating the catalytic performance of the most stable surface of the materials. These codes use pseudopotentials and a plane wave basis set in their calculations [218]. Generalized gradient approximation (GGA) is used for the exchange and correlation energy [219]. Below flow chart illustrates steps of the work done by DFT.

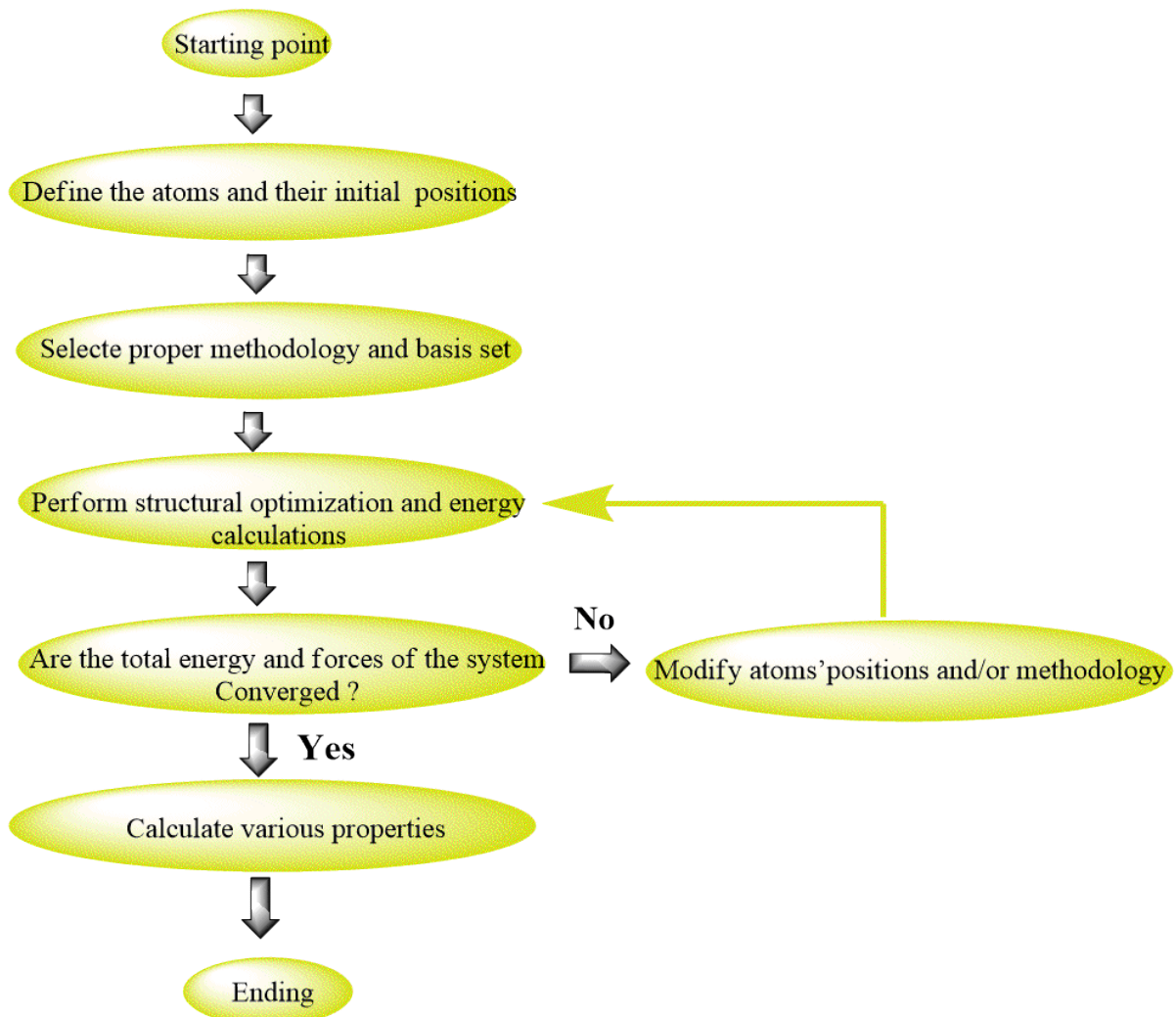


Figure 3.10: Flow diagram of the computational work by DFT.

3.5.10.1 DMol³

DMol³ is a simulation software that is based on DFT along with plane waves basis sets used to obtain model geometry and energy calculations of a gas, liquid and solid systems. DMol³ uses two types of functionals namely as local functional including VWN functional of Vosko *et al.* [220] and PWC of Perdew and Wang[221], and nonlocal functionals such as PW91[222, 223] , BP [222, 223] HCTH [224], RPBE [225], PBE [222] and BLYP [226]. The nonlocal functionals were proven to be more accurate because of its dependency on $/dr$, where, ρ empowers to obtain precise results in terms of energies and geometries characteristics. Furthermore, different basis sets ranging from small sets to large sets are supplied by DMol³ code. These start with the minimal basis set (MIN), double numerical (DN), double numerical plus d-functions (DND) which combines the DN basis set with a polarization *d*-function on all-non-hydrogen atoms, double numerical plus polarization (DNP) which is considered an enhancement to the DND basis set via including a polarization *p*-function on all hydrogen atoms, and triple numerical plus polarization (TNP) where additional polarization functions are applied over the DNP basis set on all atoms.

In relation to the pseudopotentials, DMol³ uses three different methods to process the core electrons; namely as density functional semi-core pseudopotentials (DSPP), effective core potential (ECP), and scalar relativity. The scalar relativity core treatment provides the most precise results, but at the highest computational expenses.

DMol³ can carry out restricted and unrestricted DFT calculations, structural optimization, and transition state search via a combined LST/QST/conjugate gradient method [227, 228].

3.5.10.2 VASP

VASP is one of the DFT code that is employed to carry out quantum-mechanical molecular dynamic calculations. This is achieved by using pseudopotentials or the projector-augmented wave basis set [229, 230]. VASP assesses the electronic ground state at each time step of the molecular dynamics. In VASP, ultra-soft Vanderbilt pseudopotentials (US-PP) or the PAW method describe the interactions between electrons [231, 232]. These two methods can lessen the number of plane-waves per atom significantly at least for transition elements. Using VASP, the forces and stress tensor used for the relaxations into their instantaneous can be easily calculated.

3.5.10.3 CASTEP

CASTEP is a DFT package utilized to perform geometry optimizations and energy calculations. CASTEP uses the plane-wave pseudopotentials method to solve a set of one-electron Schrodinger (Kohn-Sham) [233]. Furthermore, a plane wave basis set is used to expand the wavefunctions. The ab initio pseudopotentials within norm-conserving [234] and ultrasoft [235] describe the electron-ion potential. In order to obtain the electronic wavefunctions, self-consistently and the charge density, CASTEP software utilizes the direct energy minimization Schemes.

3.5.10.4 PHONOPY

PHONOPY is a code used to calculate phonons in a solid-state system via supercell approach. It is commonly combined with other force calculators such as VASP, ABINIT, WIEN2K, *etc.* the ones can calculate forces on atoms in the crystallographic structures. PHONOPY performs phonon calculations through a series of steps summarized as; (1) to relax the selected unit cell, (2) Subsequent to the relaxation process, a supercell has to produce after which displacement calculations are to be run, (3) using any force calculator, the forces on the atoms have to be computed, (4) based on phonon analysis, different characteristic properties such as thermal properties and band structure can be extracted.

3.5.11 Transition state theory

During a path of a chemical reaction, there are some chemical bond between atoms are fractured and some new bonds is formulated. As a consequence, energy-elaborating is occurred. Thus, it is crucial to get the system into a state which permits the bond to fission by giving a certain energy called the activation energy. Activation energy produces a structure, being unstable, temporary state named as transition state which cannot persist for a long time.

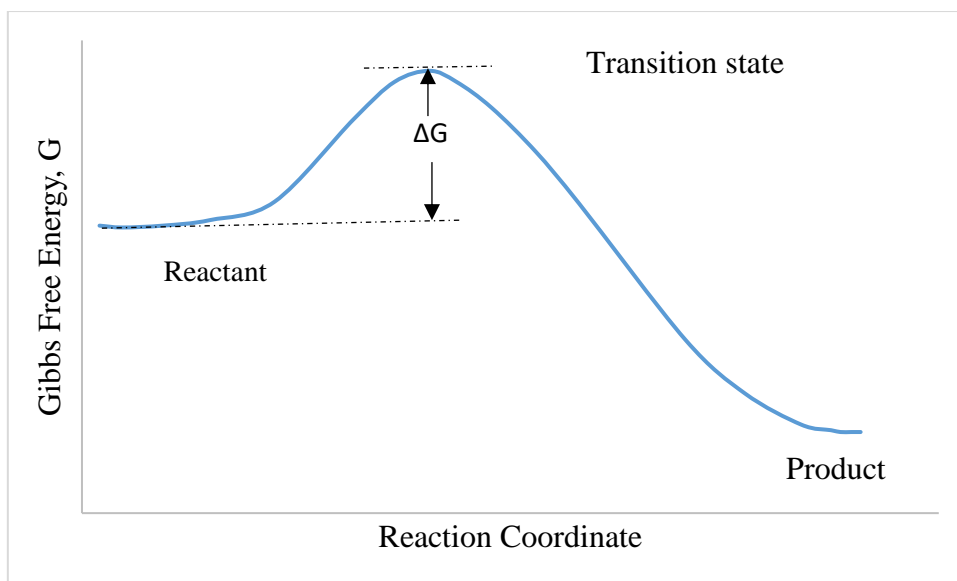


Figure 3.11: Transition state diagram. ΔG signifies the activation energy.

In this dissertation, the linear (LST) [227] and quadratic transit (QST) [227] methods within Dmol³ code have been employed to determine the transition states (LST/QST method). In LST method, the reactants and products are linked to each other by a set of perfect structures. The latter are attained by linear interpolating of the distances between all couples of atoms in the reactants and the products by the following formalism;

$$r_{ab}^i(f) = (1 - f)r_{ab}^R - fr_{ab}^P, \quad 3.22$$

In which r_{ab}^i and r_{ab}^R signify distances between the inter- nucleus of atoms a and b in the reactants and products, respectively, and f correspond to the interpolation parameter having a magnitude in the range of [0,1]. The transit course is specified utilizing molecular geometry, with the distances of inter atoms bring very near to the perfect values that are easily extracted by minimizing the function C written below;

$$C(f) = \frac{1}{2} \sum_{a \neq b} \frac{(r_{ab} - r_{ab}^i(f))^2}{(r_{ab}^i(f))^4} + 10^{-6} \sum_{\zeta=x,y,z} \sum_a (\zeta_a - \zeta_a^i(f))^2 \quad 3.23$$

where ζ_a correspond to the actual and ζ_a^i denotes the interpolated Cartesian site of an atom. Reducing function C detects the geometry of the reactants when $f = 0$ and the geometry of the products when $f = 1$. An estimate of LST maximum has been enhanced by minimizing the geometry with accordance to a constant p giving by;

$$p = \frac{d_R}{d_R + d_P} \quad 3.24$$

d_R symbolizes the reactant distance from any other geometry of the molecule that is given by the following equation

$$d_R^2 = \frac{1}{N} \sum_a (\zeta_a - \zeta_a^R)^2 \quad 3.25$$

N refers the number of the atoms in the molecule.

Then the resulting optimum geometry, pm ($pm = p \text{ opt}$), is employed to carry out QST calculations, in which a quadratic interpolation is achieved via the reactants, products and pm . In QST, each path is produced by substituting Equation 3.22 by the quadratic interpolation expression;

$$r_{ab}^i = \alpha + \beta f + \gamma f^2 \quad 3.26$$

The QST estimation for the transition state represents the maximum energy along this quadratic path.

3.5.12 Ab-initio atomistic thermodynamics

It is well-known that DFT calculates various properties of a material at ground state, zero temperature and zero pressure. In contrast, the catalytic reactions are occurring in elevated practical temperature and pressure. Thus, considering the realistic conditions when investigating the behavior of a catalyst is of significance importance. Temperature, pressure and the surrounding gas phase are the most popular parameters. In order to expand the predictive ability of *ab-initio* calculations to finite temperature and pressures, *ab-initio* atomistic thermodynamics was expressed [236, 237]. The essential purpose is to explicate the DFT results in terms of a thermodynamic potential. If either of the thermodynamic

potentials is already calculated by DFT, then, the other thermodynamics other properties can be computed. It is essential to know that surfaces are supposed to be in equilibrium with their underlying bulk and the gas atmosphere. Also, the individual chemical potentials (μ) are known to be equal if two components are in thermodynamic equilibrium. The bulk of the solid and the gaseous atmosphere are basically dealt as reservoir of particles. The most proper thermodynamic potential for a known (T,P) is Gibbs's free energy (G). In addition, the free energy per formula unit or per particle is denoted as g . Homogeneous and infinite reservoir has g value similar to the chemical potential μ .

For a solid system in a gas atmosphere, the Gibbs free energy of the solid and gas phase as one system can be expressed as:

$$G = G_{solid} + G_{gas} + \Delta G_{surf}. \quad 3.27$$

The contributions are parted into solid, gas and the surface. If the surface is a single crystal surface, then the contribution of the surface will measure with the area A and thereafter presenting the express of surface energy γ as:

$$\gamma = \frac{1}{A}(G - G_{solid} - G_{gas}) \quad 3.28$$

In which γ is defined in terms of the finite portion of the total (infinite) system and G signifies the total energy which concludes the effect resulted from the solid and the gas phase. In Equation 3.28, a deduct process for the effects of G_{solid} , G_{gas} from the total energy G with the aim to exclude only the effect of the surface. If the surface contains N_M metal atoms and N_O oxygen atoms per surface area, then the Equation 3.28 it is possibly given as:

$$\gamma(T, P) = \frac{1}{A}(G(T, P, N_M, N_O) - N_M g_M(T, P) - N_O \mu_O(T, P)) \quad 3.29$$

At this point, it is worthwhile noting that a more negative sign for Gibbs free energy will suggest a more stable configuration of the system. In the explanation of a chemical potential this translates to μ approximating $-\infty$ in the limit of an infinitely dilute gas, because adding a particle will then produce an infinite gain in entropy. As a result, $\gamma > 0$ suggests the cost of producing the surface between the solid bulk phase and the homogeneous gas phase. Alternatively, when discussing the stability of phases that result from adsorbing species at the solid surface, it can be appropriate to pick another zero reference. The surface free energy of the clean surface can be determined via the following formalism,

$$\gamma_{clean}(T, P) = \frac{1}{A}(G(T, P, 0, N_M) - N_M g_M(T, P)) \quad 3.30$$

The Gibbs free energy of a clean surface is importantly calculated to be a reference for the relative stability of the surface.

$$\begin{aligned} \Delta G^{ads}(T, P) &= \gamma_{clean}(T, P, 0, N'_M) - \gamma(T, P, N_O, N_M) = \frac{1}{A}(G(T, P, N_O, N_M) - \\ &G(T, P, 0, N'_M) - N_O \mu_O(T, P) - (N_M - N'_M) g_M(T, P)) \end{aligned} \quad 3.31$$

The final term stands for a possible difference in the number of metals atoms between the reference clean surface and the oxidized surface structural model. Apparently, the most stable surface configuration at certain (T, P) in the gas phase is the one that minimizes the surface free energy, or equivalently the one that results in the most positive Gibbs free energy of adsorption at the corresponding oxygen chemical potential.

Chapter 4 : Thermo-mechanical Properties of Cubic Lanthanide Oxides

Paper I

Miran, H.A., Altarawneh, M., Widjaja, H., Jaf, Z.N., Rahman, M.M., Veder, J.P., Dlugogorski, B.Z. and Jiang, Z-T (2018) Thermo-mechanical properties of cubic lanthanide oxides. *Thin Solid Films*, 653 . pp. 37-48.

4.1 Abstract

This chapter investigates the effect of the addition of the Hubbard U parameter on the electronic structural and mechanical properties of cubic (C -type) lanthanide sesquioxides (Ln_2O_3). Calculated Bader's charges confirm the ionic character of Ln-O bonds in the C -type Ln_2O_3 . Estimated structural parameters (*i.e.*, lattice constants) coincide with analogous experimental values. The calculated band gaps energies at the U_{eff} of 5 eV for these compounds exhibit a non-metallic character and U_{eff} of 6.5 eV reproduces the analogous experimental band gap of cerium sesquioxide Ce_2O_3 . We have thoroughly investigated the effect of the O/Ce ratios and the effect of hafnium (Hf) and zirconium (Zr) dopants on the reduction energies of CeO_x configurations. Our analysis for the reduction energy of CeO_2 , over a wide range of temperatures displays that, shuffling between the two + 4 and + 3 oxidation states of Ce exhibit a temperature-independent behavior. Higher O/Ce ratios necessitate lower reduction energies. Our results on Ce-Hf-Zr-O alloys are in reasonable agreements with analogous fitted values pertinent to lowering reduction energies and shrinkage in lattice parameters when contrasted with pure CeO_2 . Structural analysis reveals that Hf and Zr atoms in the solid solution are shifted towards the nearest vacancies upon reduction. It is hoped that values provided herein to shed an atomic-base insight into the reduction/oxidation thermodynamics of increasingly deployed catalysts for environmental applications.

4.2 Introduction

Over the last two decades, considerable attention has been devoted towards better understanding of properties that drive the unique applications of rare earth metals and their oxides. Lanthanide (Ln) oxides represent an array of materials that enjoy remarkable characteristics, such as high melting points of over 2000 °C, superior mechanical, thermal, optical and magnetic properties [238]. In earth elements, the unfilled $4f$ orbital is shielded from interactions with the adjacent atmosphere by the full octet of electrons in the $5s^2p^6$ outer shell [239]. The series of lanthanide oxides (Ln_2O_3) has emerged as promising materials in a wide range of applications, spanning in catalysis, antireflection coatings, ionic conductor industries [240-242], *etc.* Compounds of Ln_2O_3 have been in the centre of mounting interest as early as 1925 [243-248]. The two forms of cerium oxide (CeO_2 and Ce_2O_3) for instance have been the subject of numerous studies aiming to elucidate chemical and physical characteristics of their bulk and thin films. Cerium oxides have been generally deployed as catalysts in the preparation of active metal nanoparticles [249, 250], as electrolytes or as anode support materials [251]. Naturally, the lanthanide oxides occur in a sesquioxide form; however, in the case of Ce, Pr, and Tb oxides, they can also adapt other structural forms. Metallic Ce and Pr are readily oxidized into CeO_2 (ceria) and PrO_2 , respectively, in air, while under elevated oxygen pressures, Tb is found as Tb_4O_7 , and eventually transforms into TbO_2 [252].

Interestingly, it was revealed that, the Ln_2O_3 series exhibit a well-ordered periodicity in their physical attributes with the gradual filling of the $4f$ -electron shell, increasing from La to Lu. For example, a periodicity of band gap, E_g variation was found across this series [253]. The lattice structure of the sesquioxides at temperatures lower than 2000 °C falls into three distinct polymorphic forms: (a) *A*-type which assumes a hexagonal configuration with the $P-3m1$ space group symmetry, (b) *B*-type occurring in a monoclinic structure with the $C2/m$ space group symmetry, and (c) cubic *C*-type with the $Ia3$ space group symmetry [248, 254].

An early experimental study by Templeton and Dauben [255] measured the lattice parameters of several lanthanide oxide samples with purity of > 99.9% (cubic: Mn_2O_3 type structure)

from powder diffraction patterns with high accuracy. Recently, combinations of structural, mechanical, and optical properties, of rare earth oxides thin films produced by various synthesis techniques have been experimentally investigated. For instance, Dubau *et al.*, [256] fabricated a large surface area cerium oxide films with thickness ≤ 30 nm using RF magnetron sputtering technique. They stated that, the structure and morphology of the deposited films was strongly affected by the oxygen concentration in the working gas utilized for the deposition process. Furthermore, optical and structural properties of Er_2O_3 films prepared by magnetron sputtering system have been studied by Miritello *et al.*, [257]. Likewise, various characterization techniques have been utilized for the bulk and surface analysis of Ln_2O_3 . For instance, FTIR spectroscopy is a widely used characterization technique for the investigations of surface chemistry of lanthanide series using probe molecules such as H_2 and CO [258].

On the theoretical side, density functional theory (DFT) investigation [259] has elucidated an atomic-base insight into structures and electronic properties by of Ln_2O_3 . Studied compounds include the *A*-type hexagonal structure and CeO_2 with the cubic fluorite structure (space group *Fm-3m*). Hirosaki *et al.* [242] attempted to screen the dependency of the volume per unit formula in *A*- and *C*-type structures on atomic numbers establishing an inverse relation. Nonetheless, recent theoretical advances have demonstrated that pure DFT methods utilized by Hirosaki *et al.* [242] are not capable of accurately describing the rather electronically highly correlated system of the Ln_2O_3 series. A very recent DFT investigation has been carried out by Richard *et al.* [254] with a focus on the pressure-induced *C*-type \rightarrow *A*-type phase transition. This study analyzed the crystalline structure, crystal equilibrium volumes, bulk modulus (B) and its first pressure derivative (B') as well as the electronic properties of these two phases. However, the study did not assess the mechanical stability of the Ln_2O_3 species nor utilized the obtained charge distribution to comment on the relative ionicity of the Ln-O bonds.

It has now become apparent that neat DFT methods [260, 261], most notably the generalized gradient (GGA) and local density approximations (LDA), are unable to accurately describe the electronic structure in Ln_2O_3 . This is due to several deficiencies in standard DFT methods, for example, the lack of self- interaction cancellation, which results in reducing or even closing obtained band gaps. On this regard, GGA and LDA often underestimate

corresponding experimental band gaps of Ln_2O_3 [252, 262, 263]. For example, Ce_2O_3 is incorrectly predicted by pure DFT methods as metallic (LDA) or a semiconductor with a small band gap (GGA) [259]. To overcome the severe delocalization of $4f$ electrons in Ln_2O_3 systems by GGA and LDA functionals, an empirical (*i.e.*, *ad hoc*) Hubbard U approach was developed; LDA+ U / GGA+ U [264, 265]. Applying the self-interaction-corrected (SIC) or hybrid DFT approaches [266] provide accurate predictions for the electronic structures of d - and f -electronic systems as well. However, the DFT+ U formalism proves to be a cost-effective approach choice that adequately overcomes the fundamental shortcoming of plain DFT. The empirical Hubbard U potential characterizing the strength of the on-site Coulomb interaction is not a universal value but rather an adjustable parameter, which is practically determined by fitting the calculated DFT+ U values against analogous experimental data [267]. Examples of these fitted values include lattice constants, [248] band gaps [252] and reaction energies [268].

Accruing various fundamental solid-state properties, such as phonon spectra, specific heat, and thermo-elastic quantities is of fundamental importance when attempting to fine-tune characteristics of Ln_2O_3 toward real-life applications. From a chemical point of view, catalytic applications of lanthanide oxides rely on their remarkable capabilities to undergo a redox reaction in which the oxidation state switches from + 4 to + 3. In hydrogenation reactions of alkynes into olefins over CeO_2 , a crucial step is the stabilization of $\beta\text{-C}_x\text{H}_y$ radicals caused by reduction of Ce surface atoms following adsorption of C_xH_y species [73]. The formation of partially reduced ceria surface was also a key mechanistic step in the reduction of SO_2 [269]. It follows that it is of a crucial importance to gain an insight into the thermodynamic feasibility pertinent to the redox cycle of the commonly deployed lanthanide oxides. A GGA + U study by Lutfalla et al. [268] has benchmarked the redox energy of CeO_2 against the corresponding experimental value for different U value, but only at 298.15 K. However, industrial applications of Ln_2O_3 -based catalysts typically occur at elevated temperatures.

It is well-known that cerium oxide CeO_2 plays a crucial role as an oxygen-storage component in many technologies, most notably in the three-way catalytic converters (*TWCs*) of automotive emissions [268]. The catalytic activity of the two stable states of ceria, namely

Ce^{4+} and Ce^{3+} is linked with their ability to undergo a facile redox reaction. This in turn enables Ce-based catalysts to mimic analogous behavior of noble metals [270]. In this regard, Ce-based materials serve as an oxygen buffer in prominent chemical reactions, most notably water-gas shift reactions, hydrocarbon oxidation and NO_x conversion into nitrogen [271, 272]. The thermodynamic feasibility of the redox cycle – as will be demonstrated in section 4.4.3 was shown to strongly depend on the O/Ce ratios as well as on the existence of doped Hf and Zr in the alloys of Ln_2O_3 .

The catalytic interaction of various chemical species with the reduced and stoichiometric low CeO_2 (111) surface has been the subject of many theoretical investigations. For instance, the the DFT + U work by Fernández-Torre, D., *et al.* [74] addressed the dissociation of molecular hydrogen, atomic hydrogen diffusion and clustering on the CeO_2 (111) surface. They found that dissociation of H_2 occurs at reaction barrier of only 1.0 eV (*i.e.*, 96 kJ/mol). Diffusion of an atomic hydrogen adsorbed on a surface oxygen atom to the third layer was found to be noticeably endothermic by ~ 1.8 eV. Chen, *et al.* [80] plotted reaction profiles for the hydrogen cycle over the two stoichiometric and reduced CeO_2 (111) and CeO_2 (110) surfaces. In our very recent work, we establish thermo-kinetic parameters for the dissociative adsorption of three chlorinated volatile organic compounds (CVOCs), namely chloroethene (CE), chloroethane (CA) and chlorobenzene (CB) [273] over the CeO_2 (111) surface. Our findings indicate that direct fission of the Cl-C bonds prevails over surface-assisted elimination of HCl molecules. Likewise, chlorine transfer from the surface into the adsorbed cyclic moieties signifies a viable chlorination route. However, ceria may also play a dual role in the destruction/formation of aromatic pollutants as it strongly fixes phenyl radicals; a crucial step in the surface-mediate formation of dioxin-type compounds [274, 275].

The unique contribution of this study is comprehensive DFT + U accounts into the electronic structures and mechanical properties of C-type lanthanide sesquioxides. The aim of this work is fourfold: (1) to evaluate the effects of the Hubbard U parameter on the electronic and structural properties of C-type lanthanide sesquioxides (Ln_2O_3), (2) to assess the mechanical stability of all C-type lanthanide sesquioxides, (3) to elucidate the thermodynamic feasibility of CeO_2 to undergo a redox reaction at temperatures relevant to catalytic applications, and (4) to underpin the effect of adding Hf and Zr impurities on the reduction energies of CeO_δ

[$\delta=2-1.5$]. To the best of our knowledge, $\Delta G(T)$ values for reduction of any Ln_2O_3 have not been elucidated so far in the literature.

4.3 Computational Details

4.3.1 Structural Optimization

Density functional theory (DFT) within the generalized-gradient approximation (GGA) formalism [276] has been employed to perform structural optimizations for the complete series of the rare earth metal oxides with the *C*-type cubic structure at 0 K as implemented in the Vienna *Ab initio* Simulation Package (VASP) [230]. The PAW-PBE [219] pseudopotentials provide atomic environments. As the next section demonstrates, an effective Hubbard term (*i.e.*, $U_{\text{eff}} = U - J$) has been added to account for the strongly correlated Ln *f*-electrons only, in the title systems. The structures were relaxed without any symmetry constraints at an energy cut-off of 500 eV. Integration of the irreducible part of the Brillouin zone in all structures was achieved via utilizing a $4 \times 4 \times 4$ κ -point grid generated by a Monkhorst Pack scheme [277]. Furthermore, all atoms were allowed to relax until the final energy and the forces on each atom reached 10^{-5} eV and 10^{-2} eV/Å, respectively. Figure 4.1a represents the unit cell structure of the *C*-type lanthanide sesquioxides studied in this work. 16 formula units constitute the unit cell of Ln_2O_3 compounds. Figure 4.1b displays the unit cell of Cerium dioxide (CeO_2). Ceria (CeO_2) exhibits a fluorite structure with space group of *Fm-3m*, comprising a cubic close-packed combination of metal atoms with tetrahedral holes filled by oxygen atoms.

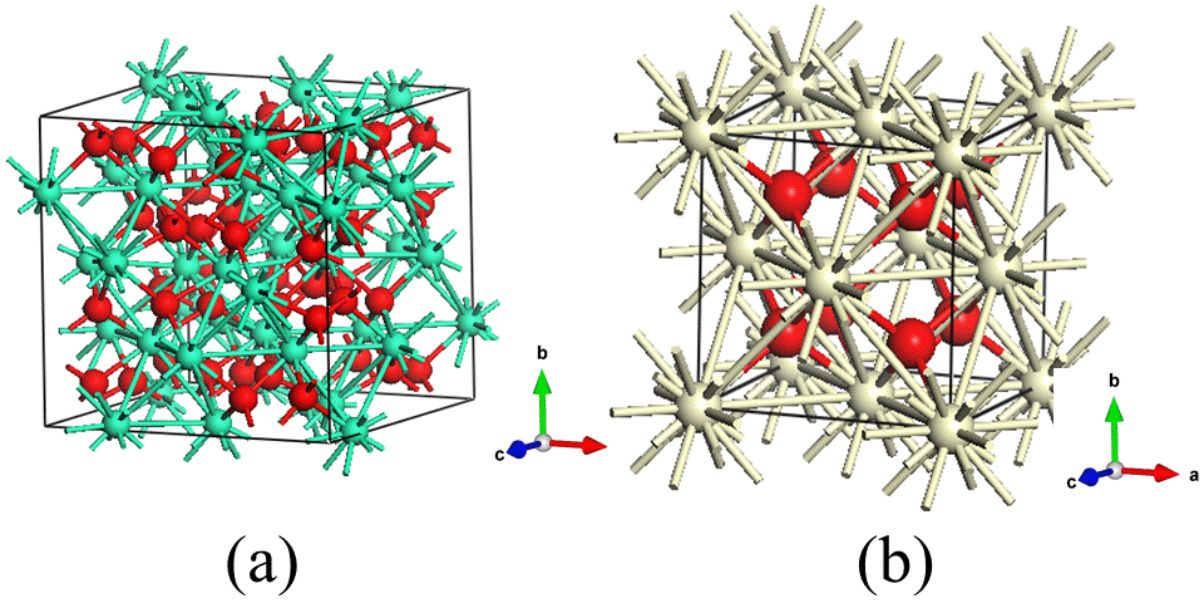


Figure 4.1: (a) The unit cell of bulk Ln_2O_3 , light green and red colors stand for Ln and O atoms respectively. (b) The unit cell of bulk CeO_2 , white and red spheres denote Ce and O atoms, respectively.

4.3.2 Charge Distribution Analysis

Bader's theory [278] is a method to analyze the charge distributions in a crystalline structure. In this theory, the electronic charge density is employed to partition continuous molecular charges into individual atomic charges *via* dividing the space in molecules into volumes (*i.e.* Bader volumes). Electron density maxima exist in these volumes separated from each other by the so-called zero flux surfaces, while the charge density minima are perpendicular to these surfaces:

$$\nabla\rho(r)\cdot\hat{n} = 0 \tag{4.1}$$

in which ρ signifies the electron density per unit surface and n stands for the unit vector perpendicular to the dividing surface.

4.3.3 Mechanical Properties

In order to obtain the elastic constants, a small strain was applied onto the structure. This is followed by calculating the change in energy induced by the stress. For any small variation of strain (ϵ), the total energy $E(V, \epsilon)$ can be expanded as a Taylor series [279]:

$$E(V, \varepsilon) = E(V_0, \varepsilon) + V_0 \sum_{i=1}^6 \sigma_i \varepsilon_i + \frac{V_0}{2} \sum_{i=1}^6 C_{ij} \varepsilon_i \varepsilon_j \quad 4.2$$

where $E(V_0, \varepsilon)$ corresponds to the energy of the unstrained system with the equilibrium volume V_0 . The strain tensor matrix is defined as [279];

$$\varepsilon = \begin{pmatrix} e_1 & \frac{1}{2}e_6 & \frac{1}{2}e_5 \\ \frac{1}{2}e_6 & e_2 & \frac{1}{2}e_4 \\ \frac{1}{2}e_5 & \frac{1}{2}e_4 & e_3 \end{pmatrix} \quad 4.3$$

C_{ij} signifies the elastic stiffness coefficients or elastic constants which determine the response of the crystal to an applied stress. There are 3 tensile and 3 shear components for both stress and strain. The elastic constants comprise a 6×6 symmetric matrix [280].

In relation to cubic lattices (structures), there are three independent elastic constants, namely C_{11} , C_{12} and C_{44} . Moreover, the mechanically stable phases or macroscopic stability can be known through determining the elastic constants. For a stable cubic structure, these elastic constants should satisfy the Born-Huang criteria [276], given by : $C_{44} > 0$, $C_{11} > |C_{12}|$ and $C_{11} + 2C_{12} > 0$. Furthermore, bulk modulus B and shear modulus G are functions of the elastic constants [280].

$$B = \frac{C_{11}+2C_{12}}{3} \quad 4.4$$

$$G = \frac{5(C_{11}-C_{12})C_{44}}{4C_{44}+3(C_{11}-C_{12})} \quad 4.5$$

Young's modulus E and Poisson's ratio ν are functions of B and G , expressed by:

$$E = \frac{9BG}{3B+G} \quad 4.6$$

$$\nu = \frac{3B-2G}{2(3B+G)} \quad 4.7$$

Young's module represents the stiffness of a solid material. The bulk and shear moduli evaluate the substance's resistance against fracturing and plastic deformations, respectively [281, 282]. Poisson's ratio is as a measurement of the stability against shear. A smaller Poisson's ratio indicates more stability against shear.

4.3.4 Calculations of ΔG (T) for Redox Reactions

We estimate the change in Gibbs energies for the redox reactions based on a statistical thermodynamic relations by using the PHONOPY code [283]. We extracted force constants and atomic displacements based on a $1 \times 1 \times 1$ supercell. Obtained phonon frequencies (ω_i) were utilized to obtain G (T) at the equilibrium volume and ambient pressure for the bulk configurations. In this formalism, Helmholtz free energy (F) is computed from the internal energy of the system (U at 0 K) and the summation of all vibrational energies as:

$$F(T) = U(0 \text{ K}) + \sum_i \frac{1}{2} \hbar \omega_i + k_B T \sum_i \ln(1 - e^{-\frac{\hbar \omega_i}{k_B T}}) \quad 4.8$$

Where \hbar is the Planck's constant and k_B correspond to the Boltzmann's constant.

Thermodynamic calculations to assess the impact of the oxidation extent (*i.e.* Ce/O ratio or δ) on the reduction energy for the cerium oxide have been carried out. In these calculations, we consider the stoichiometric CeO_2 as a $2 \times 2 \times 2$ supercell of bulk ceria comprising 32 Ce atoms and 64 O atoms. The reduced CeO_{2-y} phases have been constructed by randomly removing oxygen atoms from the supercell to attain the required y value. The deployed equation for the reduction of CeO_{2-y} phases is thus:



Finally, we turn our attention to theoretically validate the well-known enhancement of the redox cycle of ceria upon alloying it with hafnium (Hf) and zirconium (Zr).

4.4 Results & Discussions

3.4.1 Electronic and Structural Properties of Ln_2O_3

Experimental measurements, mainly by XRD, disclose that, the entire Ln_2O_3 series adapt the two space groups of $Ia-3$ and $I213$. Two lattice structures ($Ia-3$ and $I213$) for C -type lanthanide Ln_2O_3 sesquioxides have been optimized. The lattice parameters and atomic positions of the entire series were initially obtained from their experimental values [242, 284, 285]. The lattice parameters of equilibrium states were calculated using GGA+ U approach with U_{eff} values of 5 eV, and these would be used to obtain the molar volume (volume per formula unit) for each compound at each U_{eff} . Figure 4.2 portrays our calculated energy

versus volume curves for selected Ln_2O_3 along with their analogous curves fitted to the Birch-Murnaghan's [286] equation of state. The obtained results in terms of lattice parameters in \AA with their space groups, molar volume in \AA^3 per unit formula and electronic band gaps are enlisted in Table 4.1.

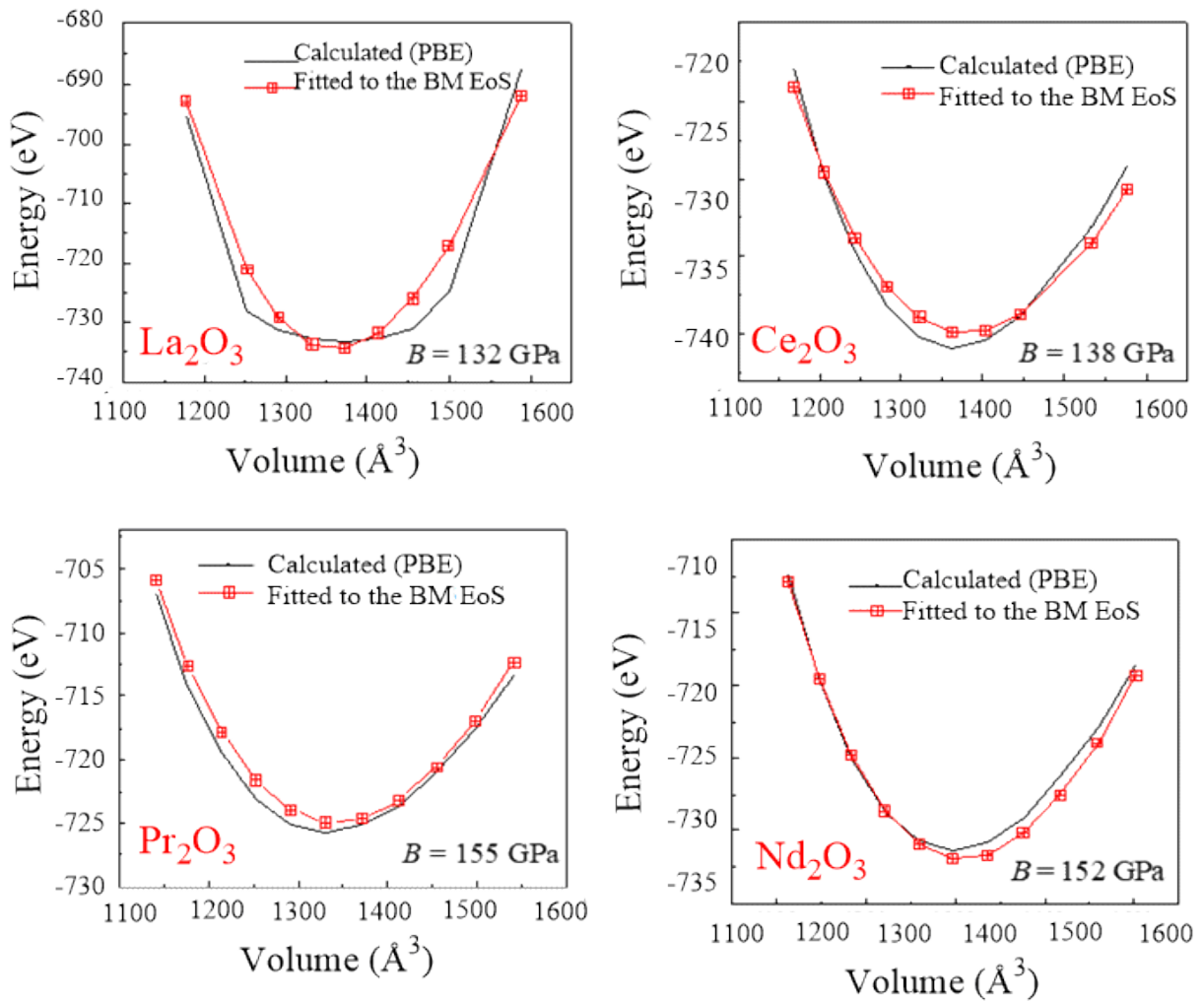


Figure 4.2: Calculated (PBE values) and fitted (to the Birch-Murnaghan's equation of state; BM EoS) energies (in eV) versus volumes of unit-cell volume (in \AA^3) for selected C-type lanthanide sesquioxides. Calculated bulk modulus (B) from the BM EoS are inserted.

Table 4.1: The lattice parameters with their space groups, molar volume per formula unit and calculated energy band gaps for all the C-type Ln₂O₃ in equilibrium states.

Material	Reference	Lattice parameters $a = b = c$ (Å)	Molar volume (Å ³ per formula unit)	Band g_{ab} , E_g (eV)	Space Group
La ₂ O ₃	(GGA+ U_{eff} , $U_{eff}=5$)	11.08	85.01	3.07	Ia-3
	GGA-PW91 [242]	11.392			
	Experimental work	11.360 ^[287]		5.4 ^[288]	
Ce ₂ O ₃	(GGA+ U_{eff} , $U_{eff}=5$)	11.08	85.01	1.6	Ia-3
	GGA-PW91 [242]	11.41			
	Experimental work	11.149 ^[288]		2.49 ^[253]	
Pr ₂ O ₃	(GGA+ U_{eff} , $U_{eff}=5$)	11.00	83.18	3.03	Ia-3
	GGA-PW91 [242]	11.288			
	Experimental work	11.152 ^[288]		3.9 ^[253]	
Nd ₂ O ₃	(GGA+ U_{eff} , $U_{eff}=5$)	10.90	80.93	3.05	Ia-3
	Experimental work	11.077 ^[288]		4.7 ^[253]	
Pm ₂ O ₃	(GGA+ U_{eff} , $U_{eff}=5$)	10.81	78.95	3.14	Ia-3
	GGA-PW91 [242]	11.065			

	Experimental work	10.990 ^[288]			
Sm ₂ O ₃	(GGA+ U_{eff} , $U_{eff}=5$)	10.74	77.42	3.15	I213
	GGA-PW91 [242]	10.995			
	Experimental work	10.932 ^[255]		5.0 ^[288]	
Eu ₂ O ₃	(GGA+ U_{eff} , $U_{eff}=5$)	10.71	76.78	3.49	I213
	Experimental work	10.866 ^[255]		4.5 ^[288]	
Gd ₂ O ₃	(GGA+ U_{eff} , $U_{eff}=5$)	10.59	74.22	3.28	I213
	GGA-PW91 [242]	10.812			
	Experimental work	10.813 ^[255]		5.4 ^[253]	
Tb ₂ O ₃	(GGA+ U_{eff} , $U_{eff}=5$)	10.54	73.18	3.28	I213
	PAW-PBE [217]	10.744			
	Experimental work	10.730 ^[289]		3.8 ^[253]	
Dy ₂ O ₃	(GGA+ U_{eff} , $U_{eff}=5$)	10.48	71.93	3.23	I213
	GGA-PW91 [242]	10.67			
	Experimental work	10.667 ^[255]		4.9 ^[253]	
Ho ₂ O ₃	(GGA+ U_{eff} , $U_{eff}=5$)	10.46	71.52	3.24	I213
	GGA-PW91	10.605			

	[242]				
	Experimental work	10.607 ^[255]		5.3 ^[253]	
Er ₂ O ₃	(GGA+ U_{eff} , $U_{eff}=5$)	10.39	70.10	3.29	I213
	GGA-PW91 [242]	10.544			
	Experimental work	10.547 ^[255]		5.3 ^[253]	
Tm ₂ O ₃	(GGA+ U_{eff} , $U_{eff}=5$)	10.33	68.89	3.31	Ia-3
	PAW-PBE [217]	10.472			
	Experimental work	10.488 ^[255]		5.4 ^[253]	
Yb ₂ O ₃	(GGA+ U_{eff} , $U_{eff}=5$)	10.39	70.10	3.62	I213
	Experimental work	10.439 ^[255]		4.9 ^[253]	
Lu ₂ O ₃	(GGA+ U_{eff} , $U_{eff}=5$)	10.24	67.10	3.41	Ia-3
	GGA-PW91 [242]	10.358			
	Experimental work	10.391 ^[255]		5.5 ^[253]	

As Table 4.1 enlists, calculated lattice constants at the selected U_{eff} value across the C-type series reasonably agree with analogous experimental [255, 287-289] and other theoretically-derived values [217, 242]. This finding is in accords with the literature reported calibration of the U_{eff} value for Ce₂O₃ at 5 – 6 eV based on GGA/LDA + U approaches [290, 291]. Precise description of the electronic structure of Ce₂O₃ is often referred to as a classical case that necessitates a DFT+ U treatment [252, 292]. Figure 4.3 plots the band gap of Ce₂O₃ versus the Hubbard parameter values. It is obvious that band gap value of Ce₂O₃ is sensitive

to the deployed U_{eff} values. Figure 4.4 plots electronic density of states (DOS) and partial density of states (PDOS) of Ce_2O_3 using GGA_PBE + U with the U_{eff} set 6.5 eV. This value has been chosen because it satisfactorily affords the analogous experimental value the band gap [253]. In fact, setting the U_{eff} value at 0 produces a metallic character. By comparing our deployed methodology (PBE+ U) with the LDA+ U approach, it becomes evident that both theoretical frameworks yield essentially the experimentally observed band gap (*i.e.*, 2.7 eV) [57] at very similar U_{eff} values of 6.5 and 6 eV; respectively.

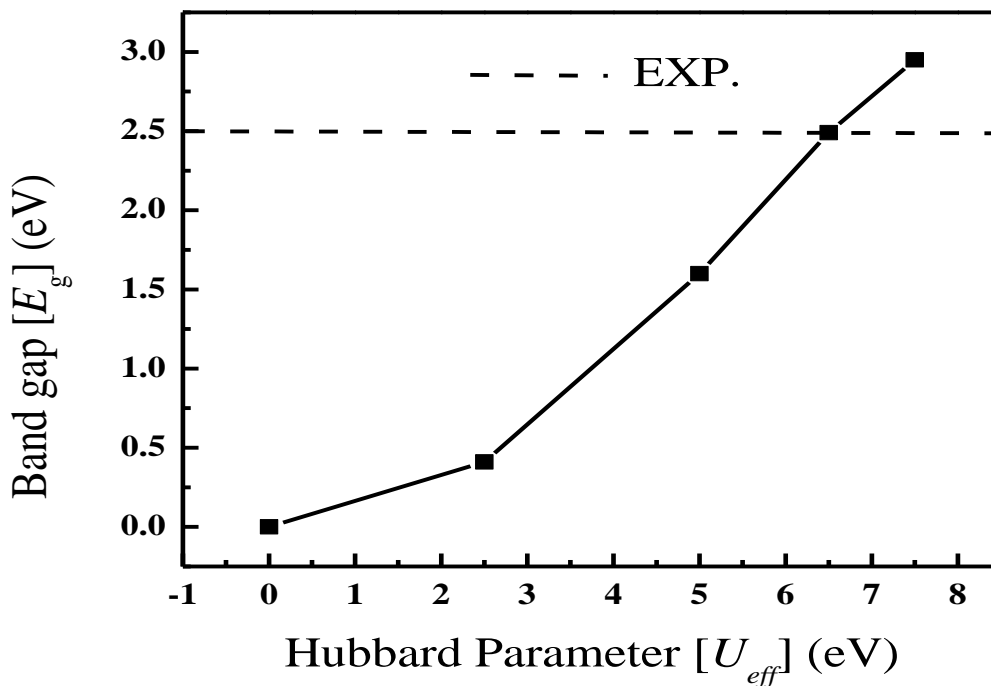


Figure 4.3: Variation of band gaps of Ce_2O_3 with Hubbard parameters. Dashed line represents the experimental value.

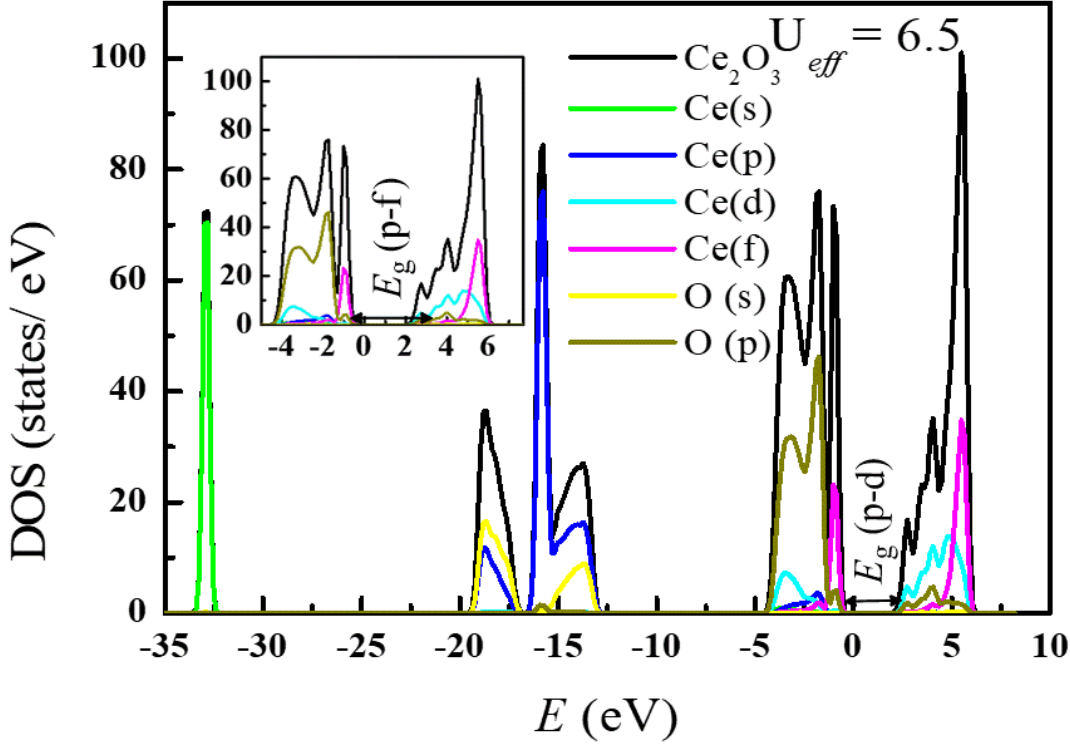


Figure 4.4: Total and partial density of states DOS and PDOS for bulk Ce_2O_3 calculated at U_{eff} of 6.5 eV.

It is evident from Table 4.1 that our approach at the U_{eff} of 5 eV for all Ln_2O_3 demonstrates non-metallic characters. Figure 4.4 displays DOS and PDOS of bulk Ce_2O_3 at U_{eff} of 6.5 eV. The plotted DOS, for this material, exhibits that, the topmost valence band is located at the Fermi level and is predominantly comprised of the O- p orbital with small contributions from Ln- s , Ln- p and Ln- d orbitals. Conduction band mainly originates from the Ln- f orbital with small contribution from Ln- s , O- p , Ln- p and Ln- d orbitals. All of the Ln_2O_3 family members exhibit an insulating character and this conclusion is consistent with the general consensus of opinions from various theoretical studies [252, 254]. Our obtained band gaps also closely match those recently obtained by Richard *et al.* [252] using the LSDA+ U approach. Values of the band gaps in Table 4.1 are also in accordance with the analogous values obtained by using the significantly more expensive Hartree-Fock methods such as HSE03/06[259]. Our finding herein reconfirms the accuracy of the relatively inexpensive GGA+ U approach in describing the electronic structure of Ln_2O_3 .

Bader's theory [293] provides an algorithm to break the continuous charge density into individual atoms. Table 4.2 lists Bader's charges on selected lanthanide elements and oxygen atoms. Values in Table 4.2 show that, all lanthanide atoms in bulk Ln_2O_3 hold positive charges, whereas O atoms are associated with negative charges. Values in Table 4.2 reveal a very comparable ionic character for Ln-O bond in all C-types Ln_2O_3 .

Table 4.2: Bader's charges (in e) on lanthanide (Ln) and O atoms.

Ln_2O_3	Ln	O	Ln_2O_3	Ln	O
La_2O_3	2.085	-1.378	Tb_2O_3	2.197	-1.438
Ce_2O_3	1.966	-1.366	Dy_2O_3	2.161	-1.433
Pr_2O_3	2.085	-1.392	Ho_2O	2.150	-1.428
Nd_2O_3	2.096	-1.391	Er_2O_3	2.218	-1.470
Pm_2O_3	2.089	-1.395	Tm_2O_3	2.213	-1.477
Sm_2O_3	2.102	-1.392	Yb_2O_3	1.553	-1.037
Eu_2O_3	1.551	-1.034	Lu_2O	2.186	-1.460
Gd_2O_3	2.181	-1.441			

4.4.2 Mechanical Properties of Ln_2O_3

Determination of the elastic stiffness coefficients is necessary to assess mechanical stability of materials. As stated in section 4.3.3, for a cubic structure to approach stability, it must satisfy the criteria $C_{44} > 0$, $C_{11} > |C_{12}|$ and $C_{11} + 2C_{12} > 0$. As given in Table 4.3, these elastic stiffness constants meet the criteria mentioned above, suggesting that all of the C-type Ln_2O_3 are mechanically stable at $T = 0$ K.

Table 4.3: The elastic constants C_{ij} (C_{11} , C_{12} , C_{44}), bulk modulus B , shear modulus G , Young's modulus E , Poisson's ratio ν of lanthanide sesquioxides with cubic structure. All elastic properties except ν are in GPa. S : stable.

Material		C_{11} GPa	C_{12} GPa	C_{44} GPa	B GPa	G GPa	E GPa	ν	Stability
La ₂ O ₃	This work LDA WC-GGA	196.22	98.29	79.34	130.93 133.9 ^[254] 125.6 ^[254]	63.57	164.14	0.29	S
Ce ₂ O ₃	This work LDA WC-GGA	283.94	152.02	135.42	196.00 148.5 ^[254] 135.8 ^[254]	95.28	245.99	0.29	S
Pr ₂ O ₃	This work LDA WC-GGA	211.42	108.44	85.52	142.77 148.2 ^[254] 137.0 ^[254]	67.63	175.24	0.29	S
Nd ₂ O ₃	This work LDA	223.76	109.85	91.04	147.82 150.5 ^[254]	73.46	189.06	0.28	S
Pm ₂ O ₃	This work LDA WC-GGA	200.74	97.69	75.53	132.04 153.8 ^[254] 136.0 ^[254]	63.66	164.55	0.29	S
Sm ₂ O ₃	This work LDA WC-GGA EXP.	216.19	116.07	100.12	149.45 153.4 ^[254] 136.5 ^[254] 142(3) ^[294]	71.51	185.03	0.29	S
Eu ₂ O ₃	This work LDA WC-GGA EXP.	132.86	86.35	59.56	101.85 156.1 ^[254] 137.0 ^[254] 115(1) ^[295]	36.66	98.21	0.33	S
Gd ₂ O ₃	This work LDA WC-GGA EXP.	265.41	107.76	113.43	160.31 158.3 ^[254] 139.7 ^[254] 134(6) ^[296]	96.48	241.09	0.24	S
Tb ₂ O ₃	This work	258.48	111.73	110.98	160.65	92.10	231.97	0.25	S

	LDA WC-GGA				158.6 ^[254] 143.7 ^[254]				
Dy ₂ O ₃	This work LDA WC-GGA EXP.	243.98	105.31	99.10	151.53 159.9 ^[254] 145.3 ^[254] 150 ^[297]	84.58	213.93	0.26	<i>S</i>
Ho ₂ O ₃	This work LDA WC-GGA EXP.	249.36	103.86	97.77	152.36 161.6 ^[254] 145.7 ^[254] 178 ^[298]	85.94	217.02	0.26	<i>S</i>
Er ₂ O ₃	This work LDA WC-GGA EXP.	255.41	114.21	105.42	161.27 161.2 ^[254] 146.1 ^[254] 155 ^[299]	88.05	223.48	0.26	<i>S</i>
Tm ₂ O ₃	This work LDA WC-GGA EXP.	266.90	112.97	106.98	164.28 161.6 ^[254] 146.61 ^[254] 54.5(7.5) ^[300]]	92.54	233.74	0.26	<i>S</i>
Yb ₂ O ₃	This work LDA WC-GGA EXP.	160.52	121.57	71.36	134.55 161.6 ^[254] 144.5 ^[254] 181(1) ^[301]	34.54	95.46	0.38	<i>S</i>
Lu ₂ O ₃	This work LDA WC-GGA EXP.	312.78	148.36	60.50	203.16 179.4 ^[254] 164.8 ^[254] 14(6) ^[302]	67.64	182.66	0.35	<i>S</i>

The bulk (*B*), shear (*G*), Young (*E*) moduli and Poisson's ratio *v* of the selected materials have been calculated using Equations 4.4, 4.5, 4.6 and 4.7, respectively. Among these series, Ce₂O₃ displays the highest young's modulus of 245.99 GPa indicating that that Ce₂O₃ is the stiffest bulk in the series. It is also noted from Table 4.3 that Yb₂O₃ has the smallest Young's

modulus of 95.46 GPa. The highest value of bulk modulus is associated with Lu₂O₃, *i.e.*, 203.16 GPa. This indicates that, Lu₂O₃ is the hardest oxide in the series. Overall, calculated bulk modulus agrees reasonably with analogous theoretical and experimental values in the literature [254, 294-302]. As shown in Table 4.3, our results on the structural parameters of the bulk modulus coincide better with LDA-derived values in reference to analogous WC-GGA values that slightly overshoot the corresponding experimental values. Values of B obtained from fitting energy versus volume curves to the Birch–Murnaghan equation of state (Figure 4.2) reasonably match corresponding values B values enlisted in Table 4.3.

4.4.3 The Reduction Energy of Lanthanide Dioxides

Via sophisticated equilibrium oxidation isotherm measurements, the reduction energy of bulk ceria was found to reside in the range of 760 – 800 kJ/mol-O₂. According to the seminal work by Gorte and his collaborators [303], the reduction energy of bulk ceria is almost insensitive to the oxidation extent of ceria, *i.e.*, the y value in CeO_{2-y}. When considering a ceria supported on modified alumina, the reduction energy varies from a near-bulk value (760 kJ/mol-O₂) at high reduction extent (*i.e.*, $y = 0.25$) to 500 kJ/mol-O₂ at low reduction extent (*i.e.*, $y = 0.05$). In their series of studies, Gorte *et al.* [304-308] have illustrated that reduction energy of bulk ceria exceeds that of surface ceria by almost 200 kJ/mol-O₂.

Estimation of reduction energies for ceria (and its solid solution) follows an equilibrium isotherm in which the fugacity of oxygen is in equilibrium with the ceria’s material [309]. However, these measurements have not elucidated the effect of the temperature on the reduction energies. Herein, we investigate the reduction energy $\Delta G(T)$ of the redox reactions for CeO₂ under a wide range of temperature and at an ambient pressure, in relevance to practical conditions encountered in emission systems. The considered reaction is:



As a benchmark for the accuracy of our thermodynamic analysis, we estimate enthalpies of reaction for the two considered earth oxides. We calculate enthalpies of formation of the two cerium oxides based on the following balanced chemical reactions:



Enthalpies of formation have been estimated by calculating the internal energies per formula unit in the ground state for cerium and cerium oxides crystalline lattices. These calculations utilize ground state energy of triplet oxygen molecule at -9.83 eV.

Table 4.4: Heat of formation for the selected dioxides and sesquioxides.

Material	Heat of Formation (kJ/mol).	
CeO ₂	This work	-859
	Exp.[310]	-1090.4
Ce ₂ O ₃	This work	-1906
	Exp. [311]	-1813.1

Table 4.4 lists heat of formation values for CeO₂/Ce₂O₃, in the ground state ($T=0$ and $P=0$ atm). Our results have been compared with the corresponding measured values at T of 298.15 K and they are in accord with those values reported in the literature [310, 311].

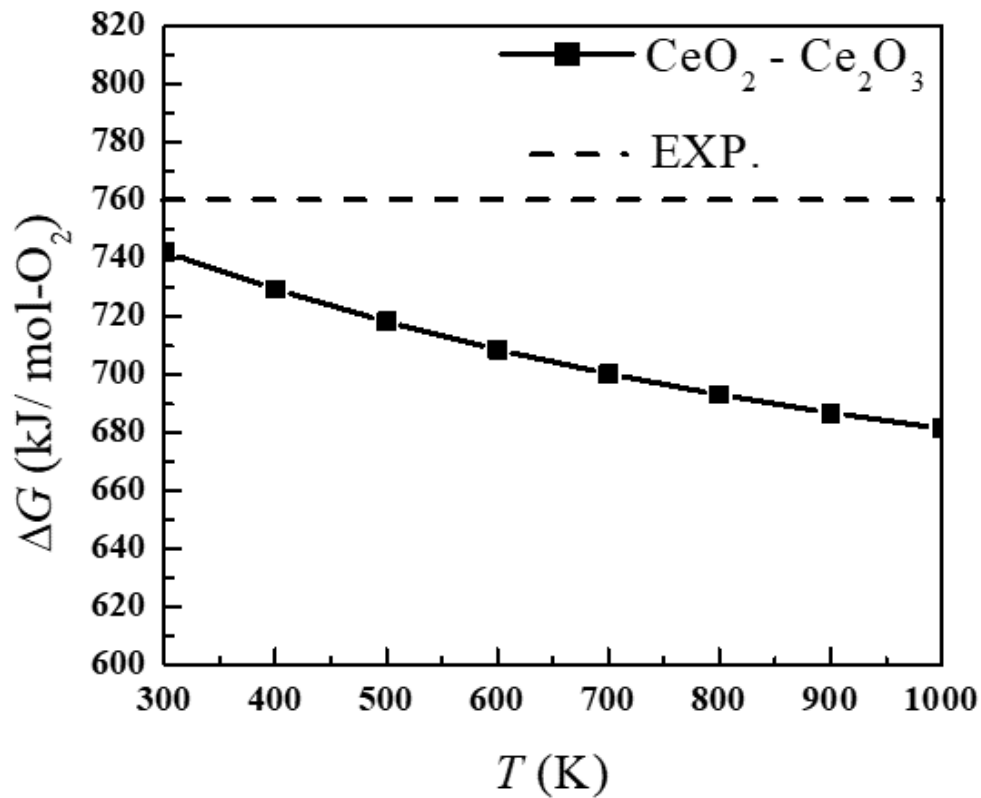


Figure 4.5: The variation of Gibbs free energy change per oxygen molecule for the reduction reaction with temperature. Dashed line represents the experimental value, ref. [303].

Gibbs values for the oxygen molecule have been sourced from thermodynamic JANAF Tables [312] whereas $G(T)$ values for bulk oxides have been determined from phonon frequencies as section 4.3 demonstrates. Figure 4.5 depicts the relationship between the differences in Gibbs free energies (per unit formula) and the considered reaction. The calculations were performed at a U_{eff} value of 5 eV. As Figure 4.5 shows, the reduction energies for Ce oxide exhibit an endothermic nature and this endothermicity of the reduction reaction for cerium oxide slightly reduces with temperature. The $\Delta G(T)$ curve for the reaction exhibits a nearly temperature-independent behavior. Our calculated ΔG for the reduction of ceria is in line with the analogous experimental values that scatter in the range of 700 – 800 kJ/mol- O_2 [313, 314].

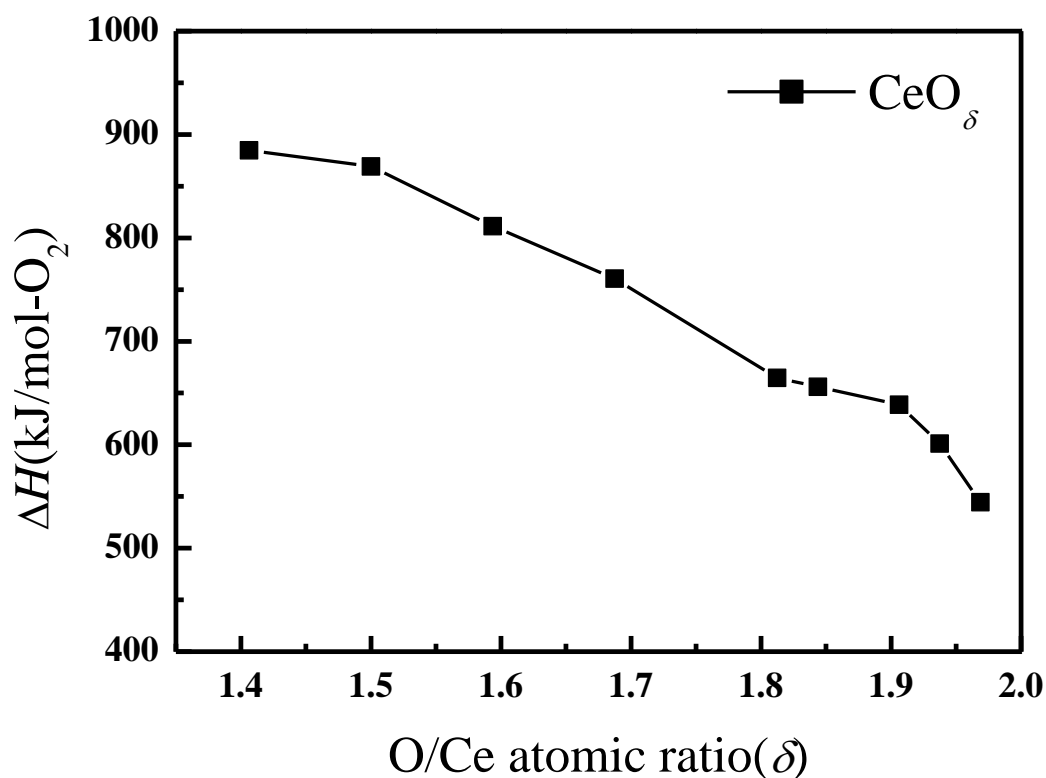


Figure 4.6: Variation of reduction enthalpies of CeO_δ with O/Ce atomic ratio.

It is worthwhile noting that catalytic activity of transitional metal oxides in general does not only depend on their ability to undergo a facile redox reaction; the presence of oxygen vacancies and kinetics factors are also of a crucial importance. For instance, alloying of PrO_2 with Ce/Hf/Zr may overcome its oxidation irreversibility. Clearly, more experimental and theoretical work is needed to underpin the catalytic behavior of other Ln_2O_3 .

In Figure 4.6, we assess the influence of the oxidation extent (*i.e.* Ce/O ratio or δ) on the reduction energy for the cerium oxide. The experimental study by Zhou *et al.* [303] has found that, the reduction energy of pure ceria to vary in a narrow range of 50 kJ/mol- O_2 for δ values between 1.85 and 2.0. Our values in Figure 4.6 slightly overshoot the analogous measurements by Zhou *et al.* but they seem to be in a qualitative agreement with corresponding ΔH curve by Hao *et al.* [313]. Based on data in Figure 4.6, the reduction energy of ceria energy increases by 26 kJ/mol- O_2 upon reduction from $\delta = 1.9$ to $\delta = 1.8$. Reduction energy reported by Hao *et al.* displays a noticeable swing of ~ 150 kJ/mol- O_2 between reduced ceria at $y = 0.2$ and stoichiometric CeO_2 .

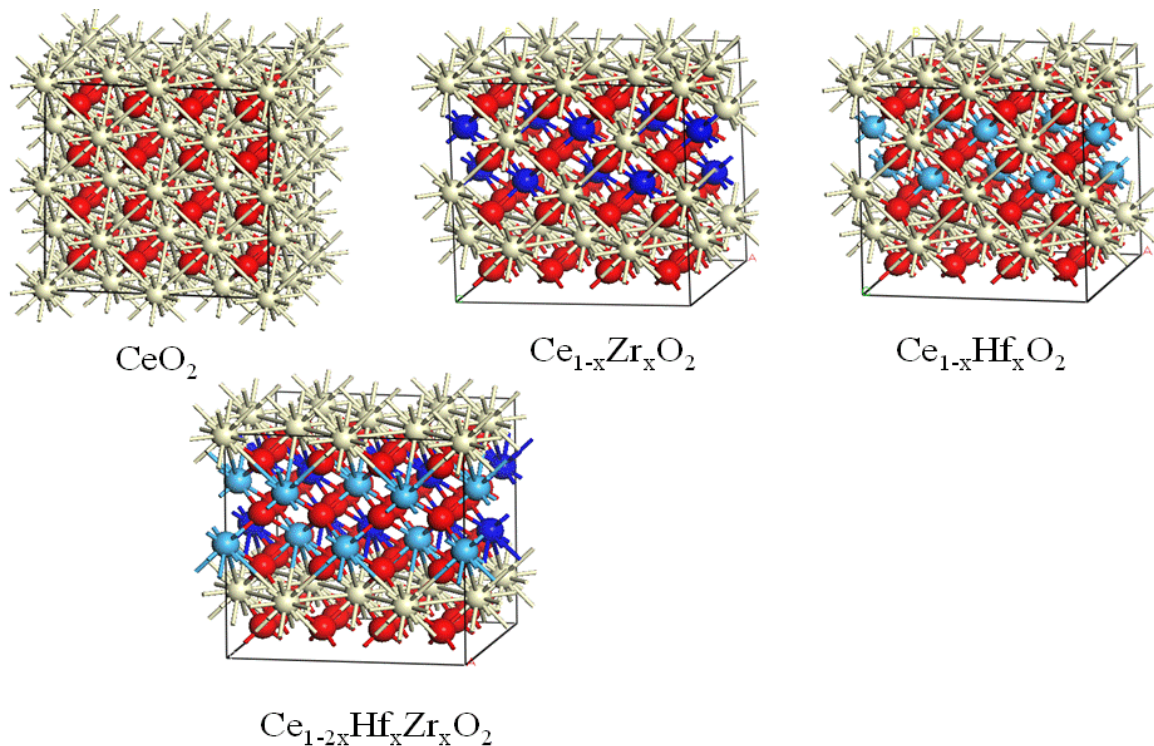


Figure 4.7: $2 \times 2 \times 2$ lattice structures of CeO_2 , $\text{Ce}_{1-x}\text{Zr}_x\text{O}_2$, $\text{Ce}_{1-x}\text{Hf}_x\text{O}_2$ and $\text{Ce}_{1-2x}\text{Hf}_x\text{Zr}_x\text{O}_2$, $x = 0.25$. White, red, blue and light blue spheres symbolize Ce, O, Zr and Hf atoms, respectively.

The reduction energy per O_2 of CeO_2 has been proven to be affected by adding impurities such as Zr, Th, and Hf, which resulted in decreasing the $\text{Ce}^{4+}/\text{Ce}^{3+}$ reduction energy [315]. Effect of introducing various contents of transition metals such as Hf and Zr to CeO_2 on the reduction enthalpies has been further investigated. Figure 4.7 displays crystal structures of pure CeO_2 and CeO_2 alloyed with Hf and Zr elements at the atomic concentration of 0.25. Figure 4.8 displays the variation of reduction enthalpies per O_2 for CeO_2 alloyed with Hf and Zr elements at different concentrations.

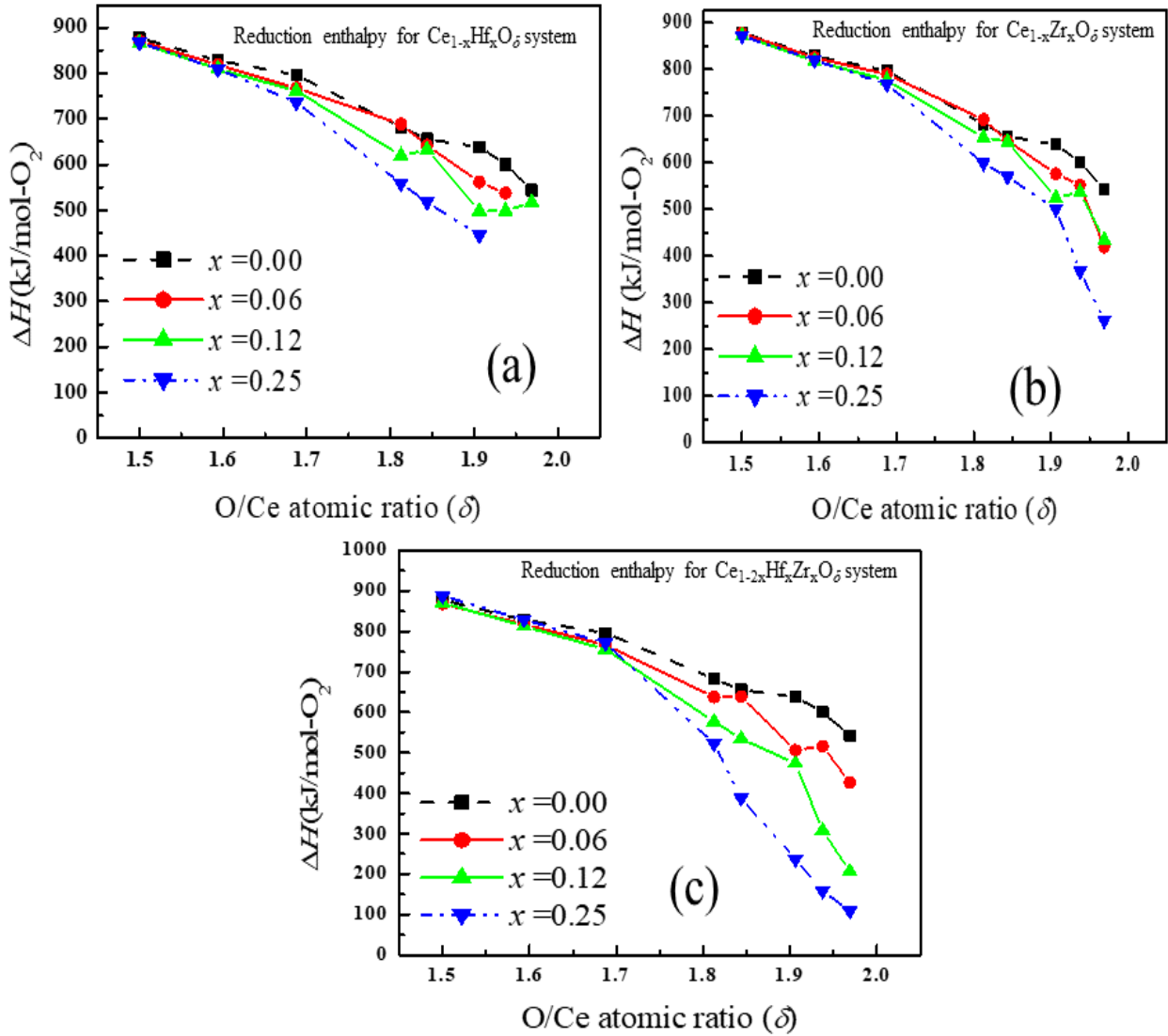


Figure 4.8: Reduction enthalpy for CeO_δ with different concentrations of Hf and Zr element as a function of the atomic ratios at $T=0$ K and $P=0$ atm. Reduction enthalpy for $\text{Ce}_{1-x}\text{Hf}_x\text{O}_\delta$ system; Reduction enthalpy for $\text{Ce}_{1-x}\text{Zr}_x\text{O}_\delta$ system; Reduction enthalpy for $\text{Ce}_{1-2x}\text{Hf}_x\text{Zr}_x\text{O}_\delta$ system. The Y-axis signifies energies in the unit of kilo joule per mole O_2 (kJ/mol-O_2).

As the figures show, adding Hf and Zr elements to the stoichiometry of CeO_2 leads to further lowering of the reduction enthalpies and this is truly in line with what has been reported in the literature [4]. For sake a comparison, our computed reduction energies for $\text{Ce}_{1-x}\text{Zr}_x\text{O}_\delta$ are plotted and compared with experimental estimates at 973 K. As Figure 4.9 depicts, there is a reasonable agreement between our calculated and limited analogous literature values [316].

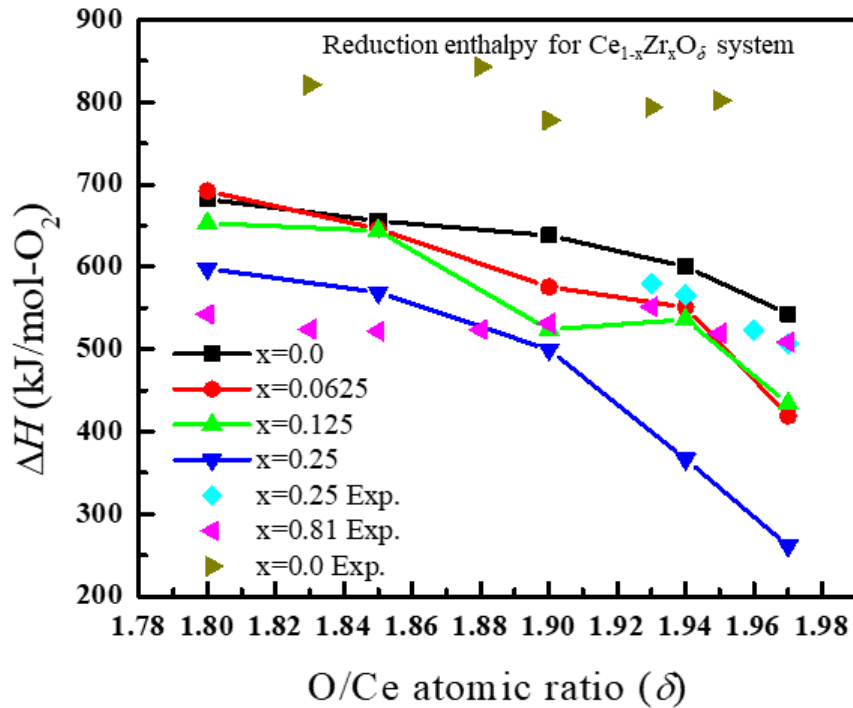


Figure 4.9: Reduction enthalpy for $Ce_{1-x}Zr_xO_\delta$ solid solution system in the range of O/Ce atomic ratios of between 2-1.8. Experimental values [316] are measured at $T=973$ K.

It is well established that introducing Zr or Hf into CeO_2 lattice results in reducing its lattice dimensions [315, 317]. This could be partly sourced from replacing Ce^{4+} ions with Zr^{4+} or Hf^{4+} ; *i.e.*, smaller radii in reference to Ce^{4+} . A study by Bishop and his collaborators attributed the decrease in the lattice constant, in case of adding Zr^{4+} , to a noticeable shift of zirconium ions towards the closest vacancies if compared with cerium ions [318]. Herein, we attempted to computationally investigate the effect of these dopants (Hf^{4+} , Zr^{4+}) on stoichiometric and non-stoichiometric CeO_δ lattice volume.

Figure 4.10 represents the relative change (V/V_0) of CeO_δ volume (V signifies the volume of doped CeO_δ with different concentrations of Hf and Zr element at 0 K and V_0 refers volume of stoichiometric CeO_2 at 0 K, as a function of the atomic ratios (δ)). As can be seen from Figure 4.10, for each concentration of Hf or Zr, the lattice parameters decrease as O/Ce ratio (δ) increases. Adding further contents of Zr or Hf lead to more reduction in the lattice parameters. In accordance with the findings from Bishop and his co-worker's, our analysis

reveals that Hf and Zr atoms in the solid solution are shifted towards the nearest vacancies upon reduction.

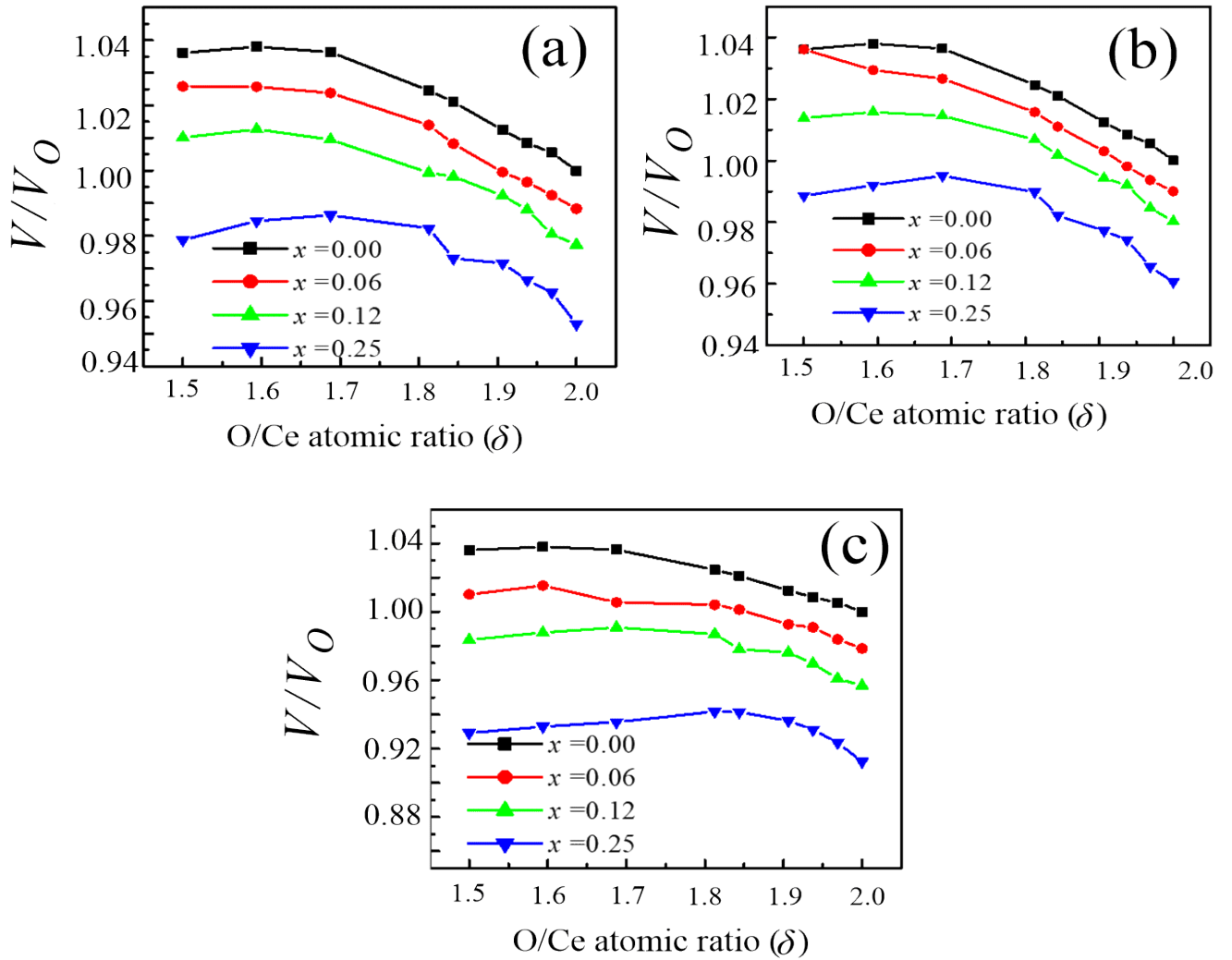


Figure 4.10: The relative change (V/V_0) of CeO_δ volume to the stoichiometric volume for undoped and doped CeO_δ with different concentrations of Hf and Zr element as a function of the atomic ratios. V/V_0 for $\text{Ce}_{1-x}\text{Hf}_x\text{O}_\delta$ stoichiometry; V/V_0 for $\text{Ce}_{1-x}\text{Zr}_x\text{O}_\delta$ stoichiometry; V/V_0 for $\text{Ce}_{1-2x}\text{Hf}_x\text{Zr}_x\text{O}_\delta$ stoichiometry.

Figure 4.11 portrays our theoretical values with the corresponding fitted values calculated by the empirical equation of Kim [15] applied to fluorite – structure oxide solid solutions ;

$$a(\text{\AA}) = 5.413 + \sum_{M=1}^i (r_{M^{4+}} - r_{\text{Ce}^{4+}}) m_M \quad (47)$$

where a signifies lattice parameters in \AA , $r_{M^{4+}}$ and $r_{\text{Ce}^{4+}}$ correspond to the ionic radii (in \AA) of M^{4+} and Ce^{4+} , respectively. m denotes the molar percent of M^{4+} in CeO_x . Ionic radii of Ce^{4+} ,

Hf^{4+} and Zr^{4+} amount to 0.97, 0.83 and 0.84 Å, respectively. From Figure 4.11, it is clearly seen that our modelling values are in an excellent accordance with the corresponding fitted ones obtained by aforementioned empirical equation.

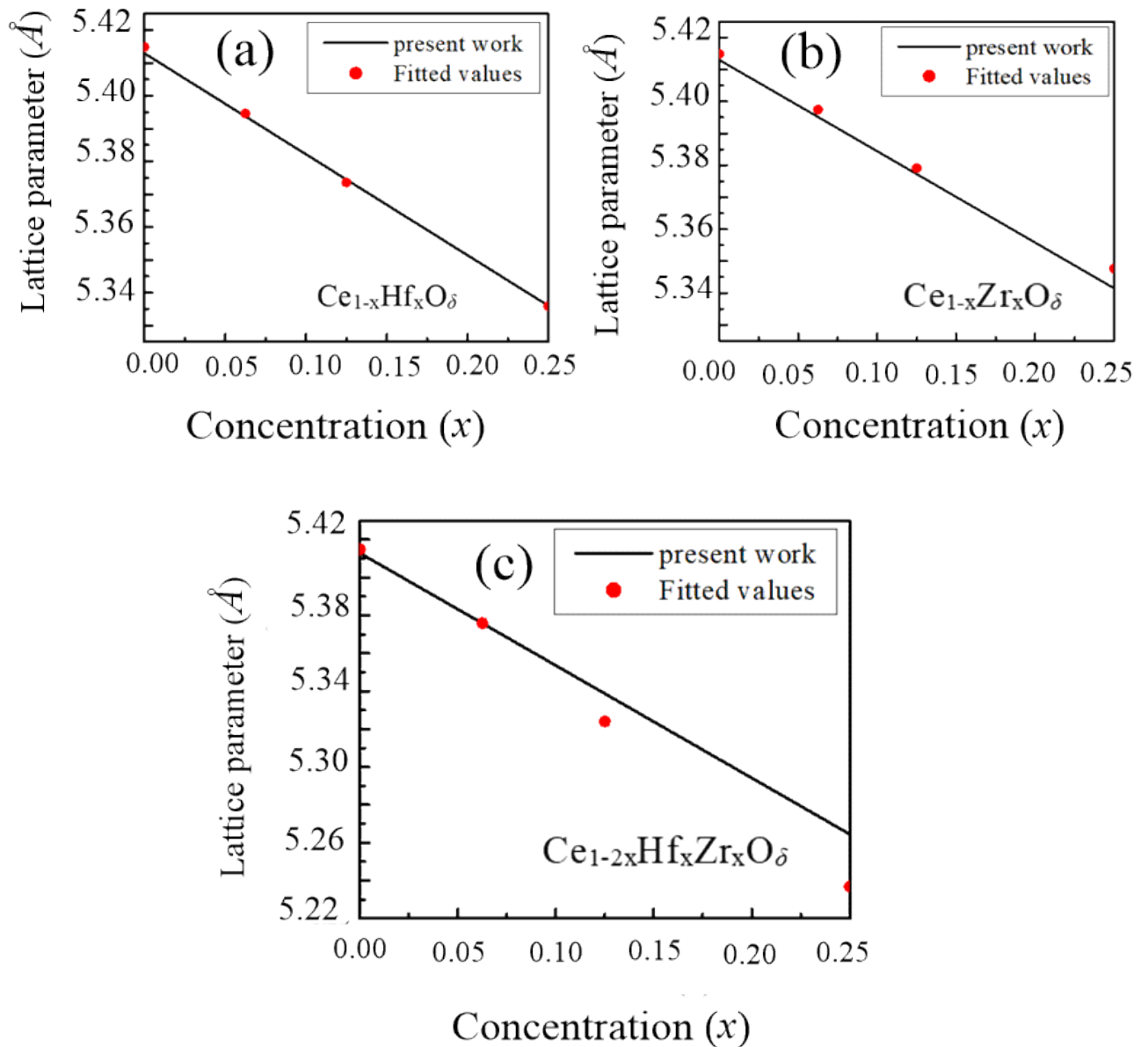


Figure 4.11: Variation of lattice parameters with Hf and Zr concentrations doping CeO_2 , fitted values are from ref. [15].

It is interesting to evaluate the impact of introducing transition metals on net Bader's charge distribution of Ce atoms in the lattice of CeO_δ . Table 4.5 gives the net charge distribution values on cerium atoms in the CeO_δ doped with different contents of Hf and/or Zr metals. It is evidently observed that an increase in Hf and Zr concentrations lead to the rise of the net charge of Ce atoms. Pauling's electronegativity is an effective way to explain this matter. The Pauling's electronegativities for Ce, Hf, Zr and O amount to 1.12, 1.3, 1.33 and 3.44; respectively. Our calculations for all concentration exhibit a net charge transfer from Ce to Hf and Zr. The cause of this particular charge transfer direction warrants further investigation.

Table 4.5: Variation of charge transfer of cerium with dopants (Hf and/or Zr) contents.

Material	Concentration (x)	Charge transfer (e)
CeO_2	0	2.12
$\text{Ce}_{1-x}\text{Hf}_x\text{O}_2$	0.0625	2.19
$\text{Ce}_{1-x}\text{Hf}_x\text{O}_2$	0.125	2.22
$\text{Ce}_{1-x}\text{Hf}_x\text{O}_2$	0.25	2.24
$\text{Ce}_{1-x}\text{Zr}_x\text{O}_2$	0.0625	2.20
$\text{Ce}_{1-x}\text{Zr}_x\text{O}_2$	0.125	2.24
$\text{Ce}_{1-x}\text{Zr}_x\text{O}_2$	0.25	2.26
$\text{Ce}_{1-2x}\text{Hf}_x\text{Zr}_x\text{O}_2$	0.0625	2.24
$\text{Ce}_{1-2x}\text{Hf}_x\text{Zr}_x\text{O}_2$	0.125	2.25
$\text{Ce}_{1-2x}\text{Hf}_x\text{Zr}_x\text{O}_2$	0.25	2.26

4.5 Conclusions

In this chapter, the GGA+ U approach was utilized to study and evaluate the geometric, electronic and elastic properties of C -type Ln_2O_3 series. We found the lattice parameters and band gap values for the studied compounds at $U_{\text{eff}} = 5$ eV to be in a good agreement with the experimental data. An exception to this is Ce_2O_3 for which a $U_{\text{eff}} = 6.5$ eV reproduces the experimental lattice constant and the band gap. Our findings predict an ionic nature for the Ln-O bonds in C -type Ln_2O_3 compounds. Studied lanthanide sesquioxides satisfied Born-Huang criterion for mechanical stability. Gibbs free energies for the reduction energy reaction of CeO_2 to Ce_2O_3 exhibit an endothermic trend. We have also investigated the effect of Hf and Zr on structural, electronic and thermodynamic properties of cerium dioxide. Our findings explain that, adding these metals to the stoichiometric and reduced CeO_2 lattice reduces their reduction enthalpy, and hence displaying an improvement in potential catalytical properties of Hf/Zr- CeO_2 doped materials.

Chapter 5 : Decomposition of Selected Chlorinated Volatile Organic Compounds on CeO₂

Paper II

Miran, H.A., Altarawneh, M., Jiang, Z-T, Oskierski, H., Almatarneh, M. and Dlugogorski, B.Z. (2017) Decomposition of selected chlorinated volatile organic compounds by ceria (CeO₂). *Catalysis Science & Technology*, 7 (17). pp. 3902-3919.

5.1 Abstract

Chlorinated volatile organic compounds (CVOCs) are toxic chemical entities emitted invariably from stationary thermal operations when a trace of chlorine is present. Replacing the high-temperature destruction operations of these compounds with catalytic oxidation has led to the formulation of various potent metal oxides catalysts; among them are ceria-based materials. Guided by recent experimental measurements, this study theoretically investigates initial steps operating in the interactions of ceria surface CeO₂ (111) with three CVOCs model compounds, namely chloroethene (CE), chloroethane (CA) and chlorobenzene (CB). We find that, CeO₂ (111) surface mediates fission of the carbon-chlorine bonds in the CE, CA and CB molecules via modest reaction barriers. As a result of localization of excess electrons left behind after creation of oxygen vacancies, analogous fission over an oxygen vacant surface systematically necessitates lower energy barriers. Dehydrochlorination of CE and CA molecules preferentially proceed via a dissociative addition channel; however, subsequent desorption of vinyl and ethyl moieties requires less energy than the surface assisted β C-H bond breakage. The profound stability of hydrocarbons species on the surface contributes to the observed deactivation of ceria at temperatures as low as 580 K under pyrolytic conditions. Adsorption of an oxygen molecule at an oxygen vacant site initiates decomposition of adsorbed phenyl moiety. Likewise, adsorbed surface hydroxyl groups serve as the hydrogen source in the observed conversion of CB into benzene. A plausible mechanism for the formation of 1,4-dichlorobenzene incorporates abstraction of a para hydrogen in the CB molecule by an O⁻ surface anion followed by chlorine transfer from the surface. Plotted conversion – temperature profiles via a simplified kinetic model against corresponding experimental profiles exhibit a reasonable agreement. The results from this study could be useful in the ongoing efforts to improve the ceria's catalytic capacity in destroying CVOCs.

5.2 Introduction

Chlorinated volatile organic compounds (CVOCs) are toxic materials that are emitted from thermal processing of fuels whenever a chlorine source is present. These compounds are often of an environmentally persistent nature and induce toxic effects to the wildlife as well as to human health. Many efforts have been devoted to controlling emission of these harmful gases by destroying them into smaller fragments. Thermal oxidation at temperature above 1000 K has been widely used to ensure destruction of these compounds in stationary emission sources. However, these operations are very energy intensive and may lead to the formation of highly toxic by-products such as the notorious polychlorinated dibenzo-*p*-dioxins and furan compounds in post-combustion chambers *via* complex homogenous and heterogeneous pathways [275, 319]. Given the aforementioned drawbacks of thermal oxidation, the search for other methods is an urgent demand. An initial improvement in the field started with developing novel and efficient catalysts to oxidize these pollutants. Noble metals such as Pt and Pd catalysts or catalysts supported noble metals were among the first catalysts to be employed in minimizing formation of CVOCs.[320-322]. While these catalysts are very active in the catalytic destruction of CVOCs, their active sites could be readily poisoned by adsorption of HCl and Cl₂, the two main chlorine carriers during oxidation of CVOCs [70].

Beside their high costs, facile deactivation of noble metal-based catalysts has limited their use in catalytic destruction of CVOCs. Alternatively, transition metal oxides such as alumina and alumina-based materials were utilized as potent and relatively low-cost catalysts in destroying CVOCs [323]. However, the use of these oxides in the abatement of CVOCs has been gradually phased out based on two compelling grounds. The presence of Brønsted acidic sites on alumina surfaces prominently mediates the conversion of CVOCs (most notably, chlorophenols) into PCDD/Fs in the temperature window of 500 – 700 K [324]. Decomposition of CVOCs over transition metal oxides forms a carbonaceous film layer, and hence results in the blocking of the catalyst surface toward further uptake of CVOCs. In a nutshell, high cost, facile deactivation and the potential for the formation of PCDD/Fs have limited the use of noble metal and alumina-based catalysts in destroying CVOCs. This has paved the way for employing rare earth metal oxides and group VI transition metal carbides and nitrides as alternative catalysts with collective properties that overcome the drawbacks of

other catalysts. Jujjuri *et al.*,[325] reported higher selectivity toward formation of chlorobenzene from a mixture of 1,3-dichlorobenzene and H₂ (*i.e.*, hydrohalogenation) over *fcc*-Mo₂C and *hcp*-W₂C at 533 K. Similarly, Oxley *et al.*,[326] measured high selectivity into benzene from hydrohalogenation of several aryl halides over Mo₂C and W₂C at 573 – 623 K. However, it must be noted that studies by Jujjuri *et al.* [325] and Oxley *et al.*,[326] deployed high H₂/substrate inlet ratios (*i.e.*, 200:1); an operational scenario that is not typically encountered in real thermal systems of CVOCs. The effective performance of group VI transition metal carbides and nitrides in the hydrohalogenation of aryl and alkene halides stems from their well-documented functionality as highly selective hydrogenation catalysts. However, their corresponding performance at low H₂/substrate exhibited low dechlorination reactivity. Delannoy *et al.*,[327] reported low conversion values (*i.e.*, 5-8%) for H₂(2):chloropentafluoroethane (1) mixture over stoichiometric Mo₂C and W₂C with corresponding rates in the range of 4.7 – 14.7 nmol m⁻² s⁻¹ at ~ 625 K. The obtained conversions over these two metal carbides were lower by more than order of magnitude in reference to Pd-based catalysts. Rapid deactivation as result of polymerization substantially reduces the catalytic activity of Mo₂C and W₂C. Excessive hydrogenation mediated by group VI transition metal nitrides and carbides forms carbonaceous deposits that deteriorate the catalytic activity via reducing the surface area and poisoning the active sites. Over Mo₂N surfaces, we have demonstrated that formation of oligomers (*i.e.*, precursors for green oil) commences[328] with surface-assisted condensation of smaller C₂ cuts into larger fragments.

CeO₂ or CeO₂ – supported materials have emerged as alternative materials to expensive noble metals and are now being widely used in prominent industrial applications [73, 329, 330] spanning hydrogenation [73, 331] and conversion of NO_x into dinitrogen [332]. The Profound catalytic effectiveness of CeO₂ mainly stems from its ability to switch between Ce⁴⁺ and Ce³⁺ oxidation states and its high oxygen-storage capacity (OSC) [4]. The remarkable physiochemical properties of CeO₂ mainly originate from unique electronic configuration induced by its partially occupied 4*f* orbitals [333]. The electronic configuration of CeO₂ characterizes interaction between strongly correlated 4*f* electrons and delocalized valence electrons. Such an interaction is sensitive to the increase of the valence or a variation of the temperature–pressure conditions.

Very recently, mounting experimental evidence has established robust catalytic behavior of CeO₂ toward dechlorinating and degradation of CVOCs under various operating conditions. Via various experimental techniques, Dai *et al.* investigated CeO₂ catalytic performance in decomposing several chlorinated C₁-C₃ species as model compounds for CVOCs [70]. CeO₂ was found to completely decompose tetrachloroethylene and dichloromethane at 533 K and 433 K, respectively. These values are significantly lower than the temperatures needed for the complete destruction of chlorinated olefins over alumina-based catalysts which typically reside above 823 K [320-322]. The major oxidative decomposition products of tetrachloroethylene encompass HCl, Cl₂, CO, CO₂ and C₂HCl. The unclosed chlorine balance in gas phase species prompted authors to carefully investigate surface chlorination leading to the formation of CeCl₃ and CeOCl. Their XPS analysis reveals the appearance of surface-bounded chlorine. Addition of water reduces the catalytic activity at low loads while an enhancement was observed at higher loads. It was postulated that the introduced water releases adsorbed chlorine in the form of HCl, which thereby recovering the catalytic performance of CeO₂ [334].

Similarly, He *et al.* [335] studied oxidation of chlorobenzene over CuMnCeO_{E_x} catalysts reporting the complete oxidation of chlorobenzene into water, HCl and CO₂ at around 523 K. Generally, based on the experimental results of Dai *et al.*, [70, 336] and He *et al.*, [335] the performance of CeO₂ as an environmental catalysts was superior to those of noble metal and transition metal oxide catalysts on two basis; the higher selectivity toward the formation of HCl in reference to Cl₂, and the lower temperature required for the complete destruction of CVOCs. HCl is an inactive chlorinating agent. CeO₂ destroys CVOCs within the temperature window for the heterogeneous formation of PCDD/Fs, 473 – 673 K (*i.e.*, 200 – 400 °C). Over other catalysts, CVOCs survive destruction in this temperature interval, which may enable their condensation into toxic chlorinated aromatic compounds.

While the aforementioned studies have indicated unequivocally the superior functionality of CeO₂ in decontamination of CVOCs, the underlying mechanistic steps are largely unknown. Due to the significant difference in C-Cl and C-H bond dissociation energies, [337] it is intuitively appealing to assume that surface Ce atoms preferentially abstract a chlorine atom from the gas phase molecule releasing a carbon-radical center. The latter could easily be

oxidized by gaseous oxygen molecules or to a lesser extent by adsorption into an oxygen surface lattice. It follows that, direct abstraction of a chlorine atom from CVOCs is a central step in the decomposition mechanism. For this reason, the current study is devoted to investigating theoretically the interaction of model CVOC compounds with the most thermodynamically stable surface of CeO₂, the 111 termination [187]. In order to assess the dependency of the catalytic activity of CeO₂ in promoting fission of C-Cl bonds, we consider three model compounds (chlorobenzene (C₆H₅Cl, termed as CB hereafter), chloroethane (C₂H₅Cl or CA for short) and chloroethene (C₂H₃Cl or CE for short) with distinct C-Cl bond dissociation energies (352 – 400 kJ mol⁻¹) [337]. We elect to study model compounds for alkanes, alkenes and aromatics exclusively as they are the major products from thermal decomposition of major chlorine-containing polymers, *i.e.*, poly vinyl chlorine (PVC) [338]. To this end, this study has a three-fold aim; firstly to map out the reaction pathways operating in the interaction of the three title CVOCs with the CeO₂ (111) surface; secondly to assess the influence of the commonly present surface oxygen vacancy site on mediating rupture of the C-Cl bond; and thirdly to investigate the reactions that led to deactivation/regeneration of the surface active sites. Overall, we found that estimated relatively low activation energies for the carbon-chlorine bond session explain the observed low-temperature oxidation of CVOCs over CeO₂ surfaces.

5.3 Computational Details

In this chapter, DMol³ code [339] performs all spin-polarized structural optimizations and energy calculations based on the Perdew and Wang (PAW) DFT functional within the local density approximation (LDA) for the exchange-correlation potential [223]. The computational methodology comprises a double numerical plus *p* function (DNP) basis set, thermal smearing of 0.05 Ha and a real space cut-off radius at 3.7 Å. A κ points sampling of $1 \times 2 \times 1$ was deployed in the integration of the first Brillion zone. The optimization convergence criteria for the total energy change, maximum force, and maximum displacement for consecutive cycles amount to 1×10^{-6} Ha, 0.004 Ha Å⁻¹, and 0.005 Å, respectively. A 30 Å vacuum separates images of the slab along the *z*-direction.

Fronzi *et al.* [187] demonstrated that the plain DFT-LDA approach (*i.e.*, the employed methodology herein within the DMol³ code) satisfactorily reproduces the experimental values

of the bulk CeO₂, for instance, lattice constant (5.36 Å/5.41 Å), indirect O-2*p*-Ce-4*f* band gap (2.11 eV/3.00 eV), enthalpy of formation (-11.06 eV/ -10.62 eV) and bulk modulus (222.7 GPa/230 GPa). Likewise, the estimated energies for creation of surface and subsurface oxygen vacancies obtained by plain DFT methods closely match the analogous values obtained by DFT + *U* methodologies [340]. This should serve as verification for the accuracy of our adapted DFT-LDA methodology.

The main focus of the current chapter is the kinetic parameters underpinning decomposition of the selected CVOCs. In this regard, a recent comprehensive analysis by Capdevila *et al.*[341] has shown that the thermodynamic and kinetic parameters for CeO₂ systems respond differently to a single *U* value in reference to hybrid DFT methods. They have explained that while the DFT + *U* approach satisfactorily reproduces enthalpies of reaction (with *U* = 4.5 eV, PBE) in reference to the HSE06 results, the activation energies at the optimum *U* value become negative. Using the PBE + *U* (=4.5 eV) approach has led to the complete disagreement between the experimental and calculated activation energies in dissociation of formaldehyde over the CeO₂ (111) surface [341]. Interestingly, activation energies at *U* = 0 (*i.e.*, corresponding to plain DFT methods) were very close to those of the analogous HSE06 results. In a nutshell, while applying the DFT + *U* approach is necessary to reproduce thermochemistry and electronic properties of bulk CeO₂, its analogous performance in the estimation of kinetic parameters has not been thoroughly tested so far.

A 2×1 supercell with three Ce atomic layers (comprising 24 Ce atoms and 48 O atoms) was used in all calculations. A test on one dissociative adsorption structure (the M1 configuration in CE) using four Ce layers has changed its binding energies only marginally by 2.8 % if compared with the analogous values obtained from three Ce layers. Figure 5.1 shows geometries for the stoichiometric CeO₂(111) where three potent adsorption sites can be easily distinguished, top surface Ce (Ce), surface O (O₁), and a subsurface O (O₂). Over the partially reduced CeO₂(111) surface, termed as CeO₂(111)V_o, the surface oxygen vacant site (V_o) is highlighted.

DMol³ achieves transition states calculations through the linear synchronous and quadratic synchronous transit LST/QST method [227, 228]. While the commonly employed nudged elastic band (NEB) method [342] reasonably yield accurate sampling of the potential energy

surface (PES), computational resources are equally directed to all minimum energy points (MEPs) along the PES not only to geometry of the transition state itself. The LST/QST methodology overcomes this problem by directly focusing on accurate locating the transition state. In this method, linear interpolations of distances between all pairs of atoms (n and m) in reactants (r_{nm}^R) and products (r_{nm}^P) firstly produce a series of intermediates (i):

$$r_{nm}^i(f) = (1-f)r_{nm}^R - fr_{nm}^P \quad 5.1$$

The maximum energy structure along the obtained path provides a first estimate for the transition structure. A single refinement in the direction orthogonal to the LST pathway yields a further refined estimate for the transition state geometry. The resultant transition state geometry from the LST pathway is subsequently considered as input for quadratic interpolation between reactant and product. Detailed description of the approach underlying the LST/QST methodology can be found in the studies by Govind *et al.*[227] and Halgren and Lipcomb [228].

Computations of vibrational frequencies confirm the nature of located transition structures as first-order saddle points via the inclusion of an imaginary frequency along the designated reaction coordinate. In calculating vibrational frequencies, we only consider the molecule and the first two atomic layers of the surface. This approach is justified based on the fact that inner atomic layers are not involved in the atomic movements of the transition structures. The Electronic Supporting Information enlists obtained vibrational frequencies whilst Table 5.1 summarizes the negative vibrational frequencies of selected located transition states.

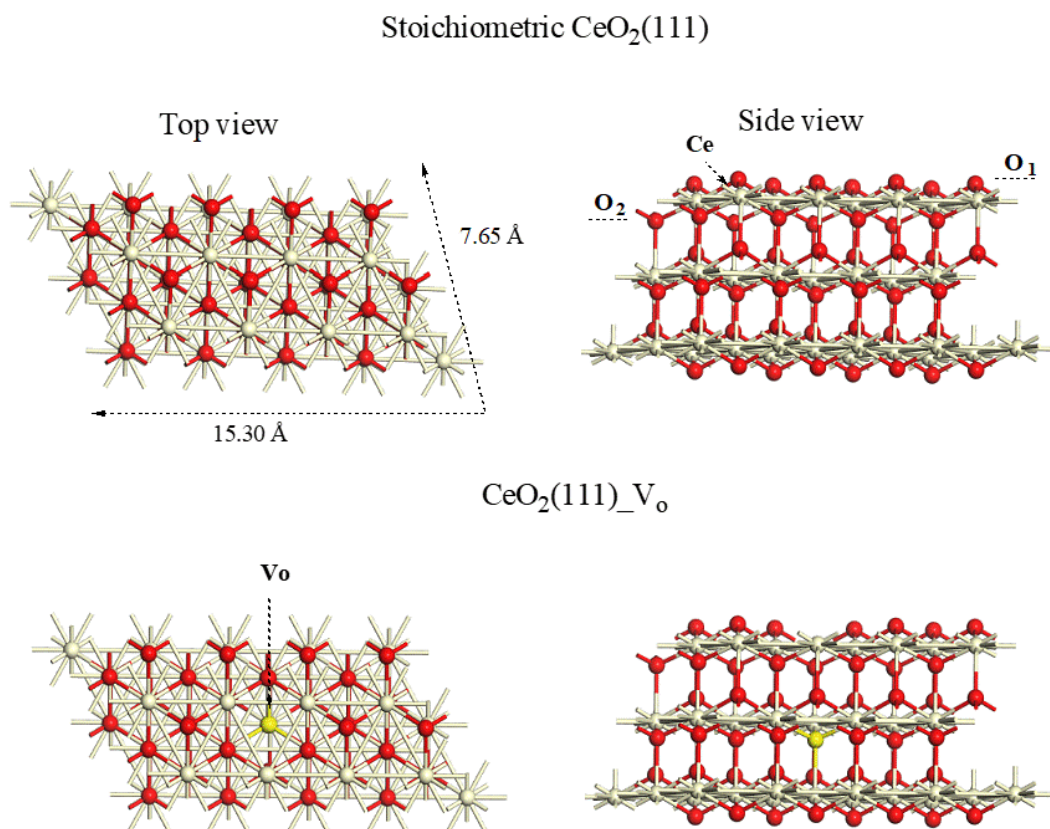


Figure 5.1: Stoichiometric and partially reduced CeO₂ (111) surfaces. Oxygen atoms are represented as red spheres.

Adsorption/desorption energies are calculated based on the energy difference between the non-interacting and the adsorbate systems. The non-interacting system is characterized as a gas phase species positioned at the middle of the vacuum, separated by at least 7.0 Å from both sides of the surface in the periodic image.

We estimate charge transfer and Fukui indices ($f^1(r)$) for electrophilic attack based on the Hirshfeld formalism [343]. $f^1(r)$ [344] is calculated from partitioning of the electron density and provide a robust molecular descriptor for the tendency of an atomic site to undergo addition reaction by an electrophilic agent. We employ the composite chemistry model of CBS-QB3 [345] as implemented in the Gaussian 09 code [346] to estimate energies and activation energies for gas phase reactions (dehydrohalogenation of chloroethane and chloroethene, and carbon-chlorine bond fissions).

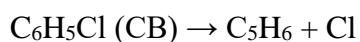
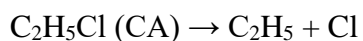
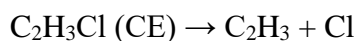
Table 5.1: Imaginary frequencies for located transition structures (in cm^{-1}).

Transition structure	Imaginary frequency	Transition structure	Imaginary frequency
TS1	$269.3i$	TS15	$129.5i$
TS2	$828.6i$	TS16	$370.6i$
TS3	$1056.9i$	TS17	$187.1i$
TS5	$440.4i$	TS19	$39i$
TS6	$716.4i$	TS21	$678.4i$
TS8	$272.4i$	TS22	$388.5i$

5.4 Results and Discussion

5.4.1 Decomposition in the Gas Phase

Scrubbing chlorine off CVOCs is the ultimate goal in thermal recycling of chlorine-containing fuel [347]. Establishing the thermo-kinetic parameters for chlorine removal from CVOCs in homogenous pathways provides a benchmark for the dechlorination catalytic performance. Figure 5.2 shows the optimized geometries for gaseous CE, CA and CB molecules. We commence our analysis by estimating the C-Cl bond dissociation energies (BDE) of the three molecules in the gas phase:



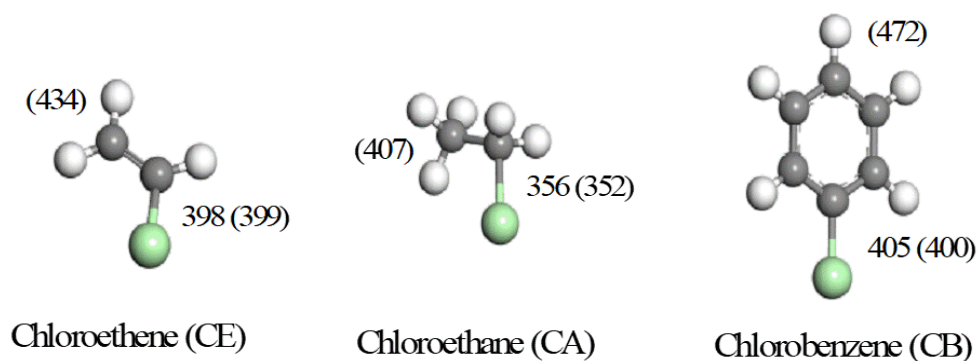


Figure 5.2: Optimized geometries of the three selected CVOCs. Values represent BDH in kJ mol^{-1} . Experimental [337] values are in parenthesis. Green spheres signify chlorine atoms.

Our calculated BDEs for the C-Cl bonds of CE, CA and CB molecules amount to 398 kJ mol^{-1} , 356 kJ mol^{-1} and 405 kJ mol^{-1} ; respectively. These values reasonably match their corresponding experimental values [337] of 399 kJ mol^{-1} , 352 kJ mol^{-1} and 400 kJ mol^{-1} . BDEs for the investigated C-Cl bonds are significantly lower than their corresponding C-H values of 434 kJ mol^{-1} , 407 kJ mol^{-1} and 472 kJ mol^{-1} , in that order. In addition to C-Cl bond fission, direct elimination of HCl represents a major decomposition pathway for chlorinated aliphatic hydrocarbons. In a previous theoretical study;[348] we investigated the effect of various electronic and geometrical factors on the dehydrohalogenation kinetics of the selected ethyl halides. Table 5.2 gives CBS-QB3 calculated values for the activation and reaction energies for HCl elimination from CE and CA molecules. The higher C-Cl BDE in the CE molecule when compared with that of the CA molecule translates into higher activation energy for the former (306 kJ mol^{-1} versus 243 kJ mol^{-1}). The noticeably high activation energy for the reaction $\text{C}_2\text{H}_3\text{Cl} \rightarrow \text{HCl} + \text{C}_2\text{H}_2$ is consistent with the high onset temperature for the oxidative decomposition of gaseous trichloroethene reported by Dai *et al.*,[70] *i.e.* $\sim 800 \text{ K}$. Elimination of the two negatively charged chlorine atoms from a 1,2-dichloroethene molecule to a chlorine molecule occurs through a sizable activation barrier of 517 kJ mol^{-1} . This high barrier coincides with the fact that the main chlorine load in the thermal systems exists as HCl rather than Cl_2 [319]. We find that BDE for C-Cl bond fission in the 1,2-dichloroethene molecule marginally exceeds that of chloroethene by only 5 kJ mol^{-1} in. This discloses that the degree of chlorination is expected to have a little influence on the kinetics for HCl elimination from mono-tri chloroethene. Indeed, we have found previously [349] that the kinetics for HCl elimination from various models mimicking ideal and defect

polyvinylchloride (PVC) is largely independent of the length and degree of chlorination of the aliphatic chain. This indicates that the findings presented herein for the CE molecule should be also applicable for the trichloroethene molecule, whose oxidative catalytic decomposition was investigated by Dai *et al* [70].

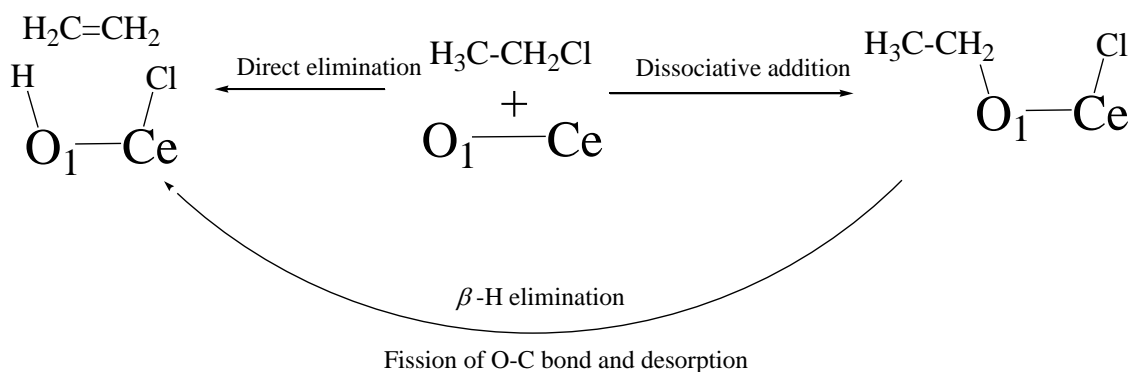
Table 5.2: Comparison between energy requirements for gas phase dehydrohalogenation and an analogous process assisted by the CeO₂ (111) surface. Numbers in parenthesis refer to the experimental gas phase values (obtained based on the standard enthalpies of formation of species sourced from ref. [337]). All values are in kJ mol⁻¹.

	C ₂ H ₂ Cl ₂ → Cl ₂ + C ₂ H ₂	C ₂ H ₃ Cl → C ₂ H ₂ + HCl	C ₂ H ₅ Cl → C ₂ H ₄ + HCl
Activation energy			
Gas phase	517	306	243
CeO ₂ (111) surface	46*	101*	51*
Reaction energy			
Gas phase	231 (229)	111 (122)	68 (72)
CeO ₂ (111) surface	-27	-9	-96

^a Based on the overall barrier of the dissociative addition route with respect to the initial reactant.

5.4.2 Catalytic Decomposition of Chloroethene and Chloroethane Over the Stoichiometric CeO₂ (111) Surface

Molecular non-dissociative adsorption of CE and CA molecules is rather very weak with adsorption energies of - 8 and -6 kJ mol⁻¹, respectively. Mechanistically, two competing routes principally underpin reactions of halogenated compounds with metal oxides, namely dissociative adsorption, followed by β C-H bond breakage, and direct hydrogen halide elimination (with the CE molecule as a model):



The β -hydride elimination reaction often constitutes the rate determining step in the course of dehydrohalogenation of alkyl halogens and olefins on Pt-based and transition metal oxide catalysts. In the CeO_2 (111) structure, the O_1 -Ce surface bond signifies a Lewis-acid/base pair facilitating the occurrence of the dehydrochlorination mechanism. Our recent study [350] on the interaction of a wide range of brominated compounds with α - Fe_2O_3 clusters has indicated that, the dissociative adsorption route largely predominates over the direct elimination pathway. Our conclusion was in accordance with the analogous findings from Biswas *et al.* [351] who investigated the decomposition of chlorinated alkanes over dehydrated alumina (α - Al_2O_3) clusters. Herein, the decomposition of the CE and CA molecules along the dissociative adsorption and direct elimination routes.

In all calculations, we consider the O_1 and Ce sites for the adsorption of the C_xH_y moieties and Cl atoms, respectively. All our attempts to position hydrocarbon radicals on Ce sites converge to O_1 sites. Similarly, it was found that all C_2H_x species during hydrogenation of acetylene over CeO_2 (111) surface occupy O_1 sites [73].

Figure 5.3.a and 5.4 maps out potential energy surfaces for the dissociative adsorption and direct elimination routes for CE and CA molecules, respectively. Fission of the C-Cl bond in the CE and CA molecules demands modest activation barriers of 49 kJ mol^{-1} and 38 kJ mol^{-1} via the transition structures TS1 and TS5, respectively. This trend in activation energies positively correlates with the BDE values of the C-Cl in parent molecules (398 kJ mol^{-1} in CE *versus* 356 kJ mol^{-1} in CA), *i.e.*, in accordance with the Evans–Polanyi principle. In reference to the very endothermic C-Cl bond scission in the gas phase (refer to Table 5.2), the analogous surface-mediated rupture is noticeably exothermic by 178 kJ mol^{-1} (the M2 configuration in Figure 5.3.a, CE) and 139 kJ mol^{-1} (the M6 structure in Figure. 5.3, CA). The highly exothermic nature of the bond fission in the stable molecules over CeO_2 is often

attributed to its high electron affinity derived by low-lying $4f$ states [352]. In an alternate pathway, direct HCl elimination from the CE and CA molecules proceeds *via* a sizable barrier of 229 kJ mol^{-1} (TS2) and 156 kJ mol^{-1} (TS7), respectively. The analogous gas phase reactions barriers overshoot the surface-mediated direct elimination of HCl from CE and CA molecules by 34% and 36%, respectively. Nonetheless, C-Cl bond fission requires significantly lower energy barriers when compared with the direct HCl elimination route. In all dissociative structures, the separated Cl atoms reside at $\sim 3.0 \text{ \AA}$ above surface Ce atoms. This very weak bonding facilitates removal of Cl atoms as chlorine molecules at a very low reaction barrier of only 6 kJ mol^{-1} as determined by Cen *et al.* [353].

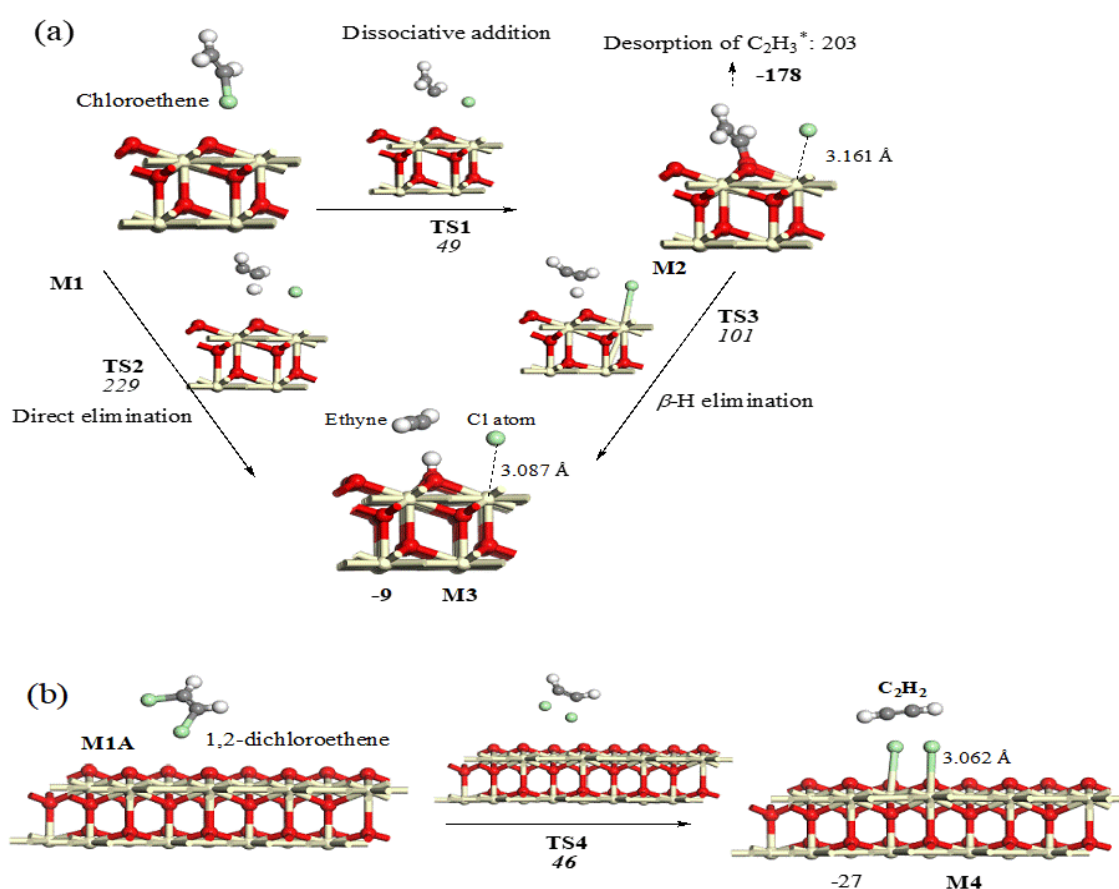


Figure 5.3: Reaction pathways operating in the interaction of chloroethene and $\text{CeO}_2(111)$ surface (a) and direct elimination of Cl_2 from 1,2-dichloroethene (b). Values in (a) are in reference to the initial configuration, M1. All values are in kJ mol^{-1} .

Conversion of chlorinated alkanes into chlorine-free olefins (*i.e.*, alkenes) carries substantial economic value as the latter are the building blocks for the formation of a wide range of commercial polymers, most notably, polyethylene. Producing pure streams of olefins has

been a central theme of catalysis research [354]. Herein, while the main aim of using ceria is to decompose chlorinated alkanes, we assess the kinetic feasibility for the formation of alkenes over the CeO_2 (111) surface *via* a hydrogen transfer from $\beta(\text{C})$ to an O_1 site. The reaction barrier for the β -hydride elimination step increases from only 190 kJ mol^{-1} in case of the adsorbed ethyl radical (the M6 structure in Figure 5.4) to 279 kJ mol^{-1} for H transfer from the adsorbed vinyl (the M2 structure in Figure 5.3.a). When considering barriers in reference to the entrance route, transition structures for the β -hydride elimination step have barriers of only 101 kJ mol^{-1} (CE) and 51 kJ mol^{-1} (CA) above the initial physisorbed states, M1 (CE) and M5 (CA).

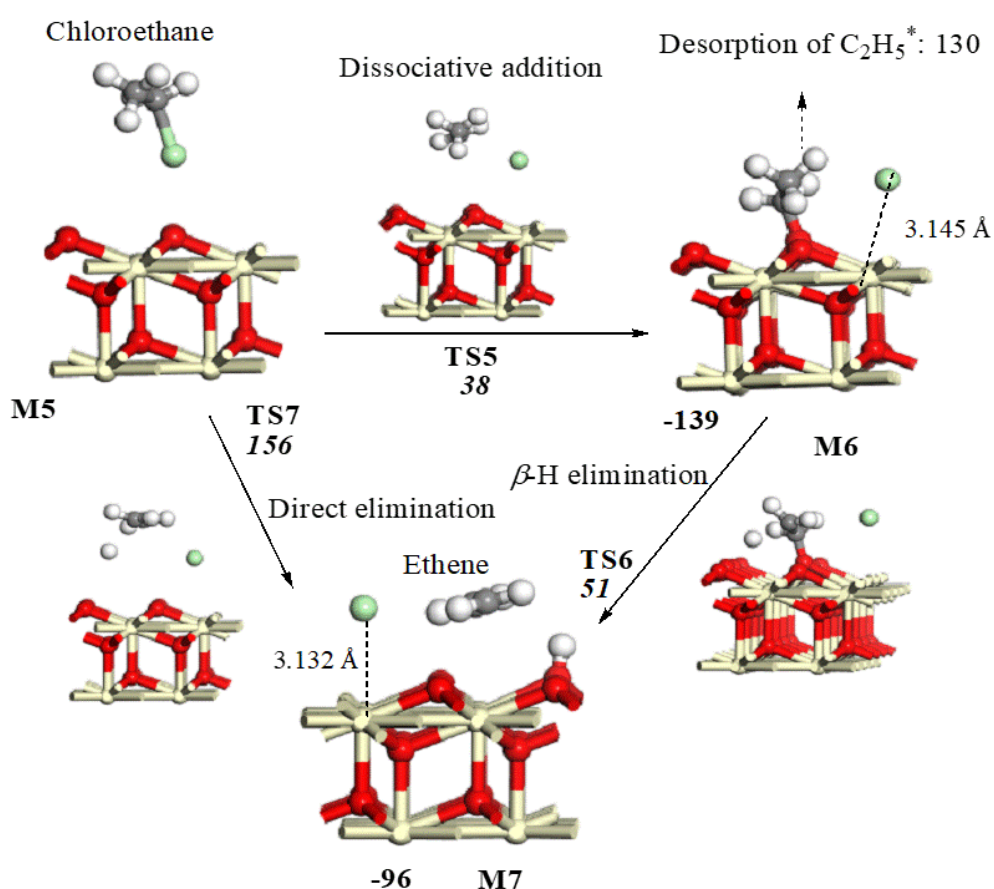


Figure 5.4: Reaction pathways operating in the interaction of chloroethane and the CeO_2 (111) surface. Values (in kJ mol^{-1}) are in reference to the initial configuration, M5.

The significant variation of the reaction barriers associated with β -hydrogen transfer originates from the noticeable difference in the BDE in the parent CE (434 kJ mol^{-1}) and CA (407 kJ mol^{-1}) molecules, refer to Figure 5.2. The two-step dissociative addition and the

direct elimination routes afford the same products: $C_2H_2 + HO_1-ClCe$ (CE) and $C_2H_4 + HO_1-ClCe$ (CA). Inferred from Figure 5.3.a and 5.4 is that the dissociative addition is expected to predominate over the direct HCl elimination route, *i.e.*, 101 kJ mol^{-1} *versus* 229 kJ mol^{-1} (CE) and 51 kJ mol^{-1} *versus* 156 kJ mol^{-1} (CA). Clearly, this finding concurs very well with the general consensus pertinent to the importance of the dissociative addition route over the direct elimination pathway. Analogously, the $\beta(C)H$ transfer reaction often is characterized as a bottleneck step in the dehydrohalogenation of halogenated alkanes over transitional metal oxides. We have found that the $\beta(C)H$ transfer reaction in ethyl adsorbed on $\alpha\text{-Fe}_2\text{O}_3$ cluster proceeds through a sizable barrier of 200.0 kJ/mol [350]. A similar trend has been observed for the dehydrohalogenation of halogenated alkanes by alumina clusters [351]. As will be conveyed in section 5.4.7, the estimated low overall activation barrier for the dehydrochlorination of CA and CE molecules is consistent with the experimentally observed high conversion of chlorinated alkanes and alkenes reported by Dai *et al.*, [70, 336] at relatively low temperature (*i.e.*, $500 - 600 \text{ K}$).

To account for the plausible chlorine molecule elimination from di/tri-chlorinated alkanes (in reference to trichloroethylene for example), we find in Figure 5.3.b that a surface-mediated loss of two chlorine atoms from dichloroethene requires only 46 kJ mol^{-1} . Thus, while Cl_2 elimination from chlorinated aliphatic in the gas phase is a largely negligible route when compared with the dehydrochlorination route (loss of HCl), catalytic decomposition over the $CeO_2(111)$ surface favors the $Cl...Cl$. This becomes evident when comparing the reaction barriers of TS2 (229 kJ mol^{-1}) and TS4 (46 kJ mol^{-1}). Experimental support for these findings stems from the observation of C_2HCl (rather than C_2Cl_2) [70, 336] as the major intermediate from the catalytic oxidative decomposition of C_2HCl_3 . The facile nature for surface-assisted elimination of two chlorine atoms from the dichloroethene molecule is derived by high electron affinity of surface Ce^{4+} cations.

The recyclability of the ceria catalyst and the complete destruction of CVOCs rely on the removal of the adsorbed C_xH_y adduct. Beside the $\beta C(H)$ fission route, O_1-C bond scission and desorption of C_2H_3 and C_2H_5 radicals constitute another exit channel for the adsorbed $C_2H_3^*$ and $C_2H_5^*$ species in structures M2 and M6. The O_1-C distances in adsorbed C_2H_3 (Figure 5.3.a) and C_2H_5 (Figure 5.4) signify genuine chemical bonds of 1.320 \AA and 1.393 \AA , respectively. For example, these distances are within 0.05 \AA from the distances in analogous

gas phase molecules, for example ethyl vinyl ether ($C_2H_3-O-C_2H_5$) and diethyl ether ($C_2H_5-O-C_2H_5$), optimized at the CBS-QB3 level of theory. This has resulted in significant energy penalties for the desorption of vinyl and ethyl radicals at 203 kJ mol^{-1} and 130 kJ mol^{-1} , respectively. Obviously, these two values largely represent adsorption energies of C_2H_3 and C_2H_5 radicals at an O_1 site. The significant difference in desorption energies from the $CeO_2(111)$ surface among the vinyl and ethyl radicals (*i.e.*, 95 kJ mol^{-1}) correlates well with the BDE in gas phase analogous molecules; for example the BDE for the O-C bond in $C_2H_3-OC_2H_5$ exceeds that in $C_2H_5-OC_2H_5$ by $\sim 80 \text{ kJ mol}^{-1}$ [337]. Fronzi *et al.* [355] have systematically investigated adsorption of CH_{1-3} radicals on the $CeO_2(111)$ surface. Their calculated adsorption energy for the methyl (CH_3) radical at an O_1 site amounts to $201.0 \text{ kJ mol}^{-1}$. This value reasonably matches our estimated adsorption energies for the vinyl radical. Concluded from Figure 5.3.a and 5.4 is that the reaction barriers for the $\beta C(H)$ fission route significantly exceed the desorption energies for adsorbed vinyl (203 kJ mol^{-1} *versus* 279 kJ mol^{-1}) and ethyl radicals (130 kJ mol^{-1} *versus* 180 kJ mol^{-1}).

The strong adsorption of adsorbed vinyl and ethyl radicals is anticipated to result in rapid catalytic deactivation by blocking the O_1 active sites. Additionally, this is expected to enable these two radicals to undergo surface-assisted coupling into larger hydrocarbon fragments following an analogous mechanism that we developed for condensation of two adsorbed vinyl radicals into C_4H_5 over the $\gamma-Mo_2N(100)$ surface [328]. Once desorbed, the fate of alkyl and allyl radicals is dictated by the operational conditions. Highly reducing conditions in the gas phase could convert alkyl into their respective alkanes. Similarly, under oxidative conditions, their reactions with gas phase oxygen molecules under oxidative conditions result in their further decomposition into $CO/CO_2/H_2O$. Desorbed alkoxy radicals could be readily oxidized in the gas phase according to well-documented mechanisms [356].

5.4.3 Decomposition of Chloroethene Over $CeO_2(111)_{Vo}$ Surface

The removal of O_1 atoms in CeO_2 initiates its facile redox cycle swinging between Ce^{+4} and Ce^{+3} states. The emerged oxygen vacant sites *via* surface reduction play a crucial role in potent catalytic applications of ceria, most notably, conversion of NO into N_2 , oxidation of hydrocarbons and oxidation of CO into CO_2 [357]. The concentration of surface oxygen vacancies was measured to be as high as $3 \times 10^{20} \text{ cm}^{-3}$ and found to be strongly affected by

the grain size of CeO₂ [358]. Thus, it will be insightful to compare the energetics for the overall decomposition of CVOCs on stoichiometric CeO₂ (111) surfaces *versus* a partially reduced configuration, a surface with a surface oxygen vacant site (V_o); refer to Figure 5.1 for the geometry of the CeO₂ (111)_{V_o} surface. Figure 5.5 shows the decomposition pathways for chloroethene over the CeO₂(111)_{V_o} surface. Fission of the C-Cl bond at a V_o site requires only 11 kJ mol⁻¹ of activation energy *via* the transition structure TS8 and results in the formation of the M9 configuration in which the dissociated chlorine atom occupies a V_o position. In Figure 5.5, we attempt to provide an elucidation into the lower activation barrier for TS8 (over V_o site; 11 kJ mol⁻¹) in reference to TS1 (over O₁ site; 49 kJ mol⁻¹). As a result of localization of excess electrons left behind after a creation of an oxygen vacancy,[359] calculated $f^1(r)$ index for the three Ce atoms adjacent to the V_o site increases to 0.044 when contrasted with the analogous value (0.0355) in the stoichiometric CeO₂(111) surface. This demonstrates an increase in the electron affinity for the Ce atoms adjacent to the surface oxygen vacant site. This in turn is reflected by a lower activation barrier and higher exothermicity for the C-Cl bond fission.

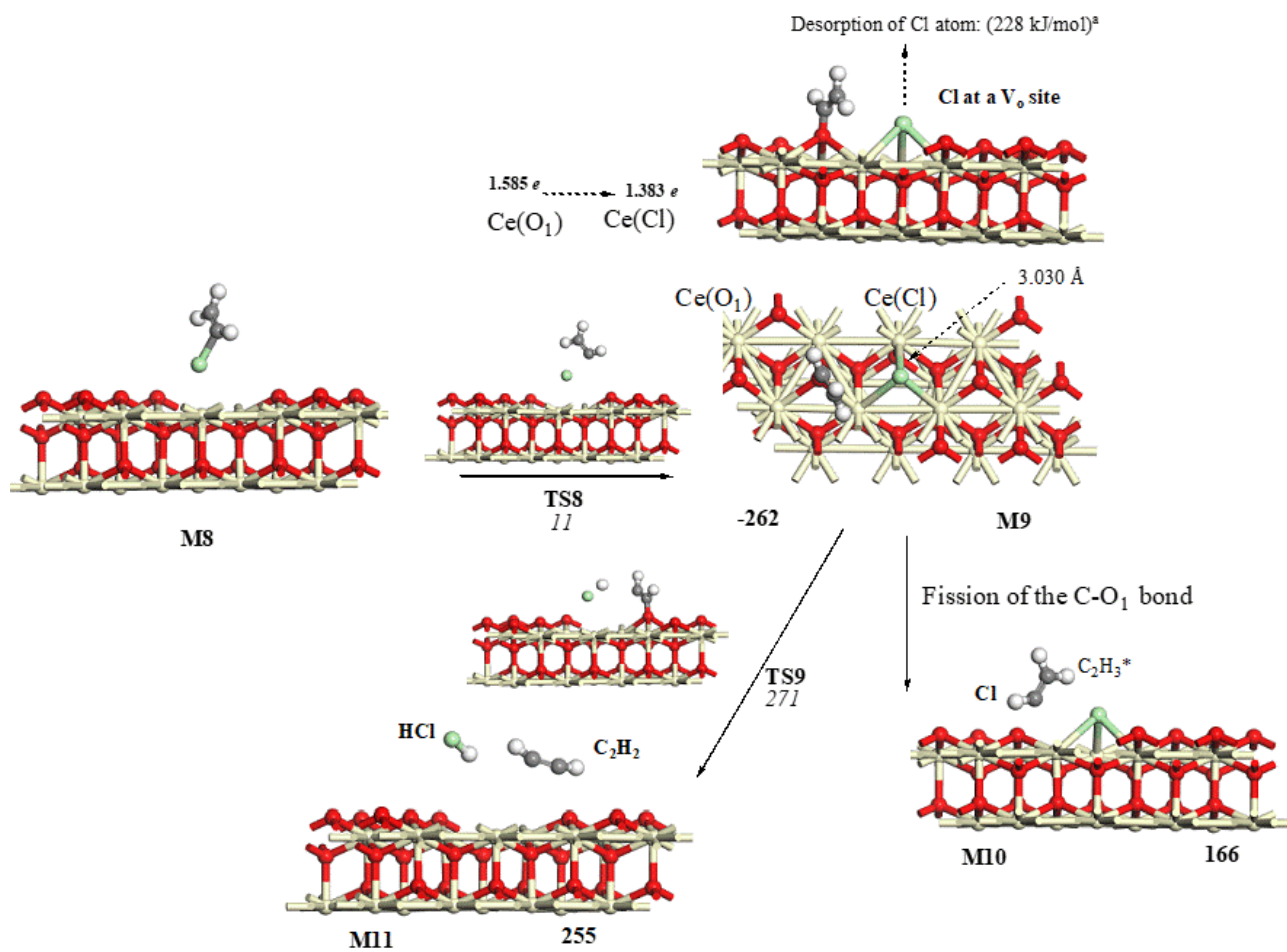


Figure 5.5: Decomposition of chloroethene over the $\text{CeO}_2(111)$ _Vo surface. Values (in kJ mol^{-1}) are in reference to the reactant in each step. ^a ref.[353].

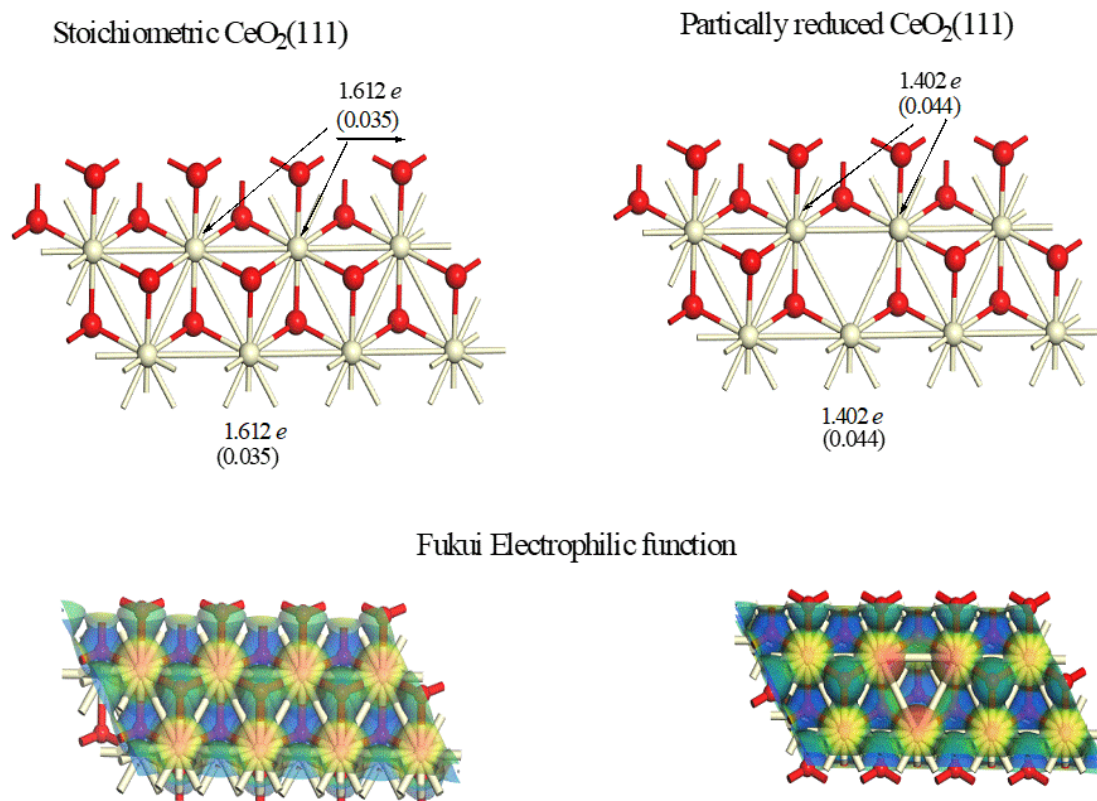


Figure 5.6: Hirshfeld's atomic charges and $f^1(r)$ indices for stoichiometric and partially reduced CeO₂(111) surfaces.

The substituted Cl atom at the V_o site causes partial reduction of the three neighboring Ce atoms from $1.612 e$ to $1.402 e$. Likewise, Cen *et al.*[353] explained that adding a chlorine atom to the V_o site resulted in the complete reduction of an adjacent Ce^{4+} ion to Ce^{3+} . Cen *et al.*, found that removal of the chlorine atom from the V_o site necessitates an energy of 228 kJ mol^{-1} [353]. This strong surface binding of chlorine atom at the V_o position contributes to the calculated higher barrier (271 kJ mol^{-1}) for its removal as HCl along the transition structure TS9. Finally, C-O₁ bond scission liberates the adsorbed vinyl radical in an endothermic process of 166 kJ mol^{-1} .

5.4.4 Removal of Adsorbed Vinyl and Ethyl Moieties via Surface Hydrogen Reactions

In the previous section we have demonstrated that formation of alkenes and alkynes from their respective chloro alkanes and alkenes *via* HCl elimination is expected to be hindered in view of lower desorption energies of vinyl and ethyl radicals when contrasted with the energy barriers for the β -C(H) hydride fission route. Hydrogen transfer from H-O₁ sites to adsorbed hydrocarbon cuts features a key step in selective hydrogenation of alkynes over ceria [73]. Hydroxylated CeO₂(111) surfaces have been characterized by various techniques including Scanning tunneling microscopy (STM) [360] and non-contact atomic force microscope (nc-AFM) [361]. Dissociation of hydrogen molecules over CeO₂(111) surfaces was found to require an accessible energy barrier of only 96 kJ mol⁻¹ [74] and results in the creation of H-O₁ sites. Pyrolysis and oxidation of halogenated pollutants often proceed in a hydrogen-rich environment,[362, 363] and thus it is insightful to investigate the interplay between a hydrogen-bearing CeO₂ surface and catalytic decomposition of CVOCs. In this section, we assess the energetic requirements for surface hydrogen-assisted removal of adsorbed vinyl and ethyl radicals over stoichiometric CeO₂ (111) and CeO₂ (111)_{V_o} surfaces.

Figure 5.7.a and b show the energy requirements for surface hydrogenation of adsorbed vinyl and ethyl radicals, respectively. Hydrogen migration from the HO₁ site into the CH group in the adsorbed vinyl affords an ethene molecule. However, such step requires a very sizable energy barrier of 393 kJ mol⁻¹. Our calculated barrier for the reaction M12 \rightarrow M13 is in a relative agreement with the corresponding barrier reported by Carrasco *et al.*, [73] for the reaction C₂H₃^{*} + H^{*} \rightarrow C₂H₄ obtained through the NEB method at \sim 350 kJ mol⁻¹. Hydrogen adsorbed at V_o sites exhibits greater mobility than hydroxyl group hydrogen. As the reaction barrier of TS11 revealed (284 kJ mol⁻¹), hydrogenation of adsorbed vinyl into ethene commencing from the V_o site demands a lower activation energy by \sim 110 kJ mol⁻¹ when contrasted with hydrogenation by HO₁ site. In Figure 5.7.b, formation of ethane molecules *via* hydrogen transfer from a hydroxyl surface group to a V_o site presents lower activation energies (296 kJ mol⁻¹ and 250 kJ mol⁻¹) than the formation of ethene. Bearing in mind that surface hydrogen diffusion into a neighboring HO₁ site (resulting in water evolution/surface reduction) proceeds *via* only 144 kJ mol⁻¹;^[364] it can be concluded that removal of adsorbed vinyl *via* surface hydrogenation is of negligible practical importance.

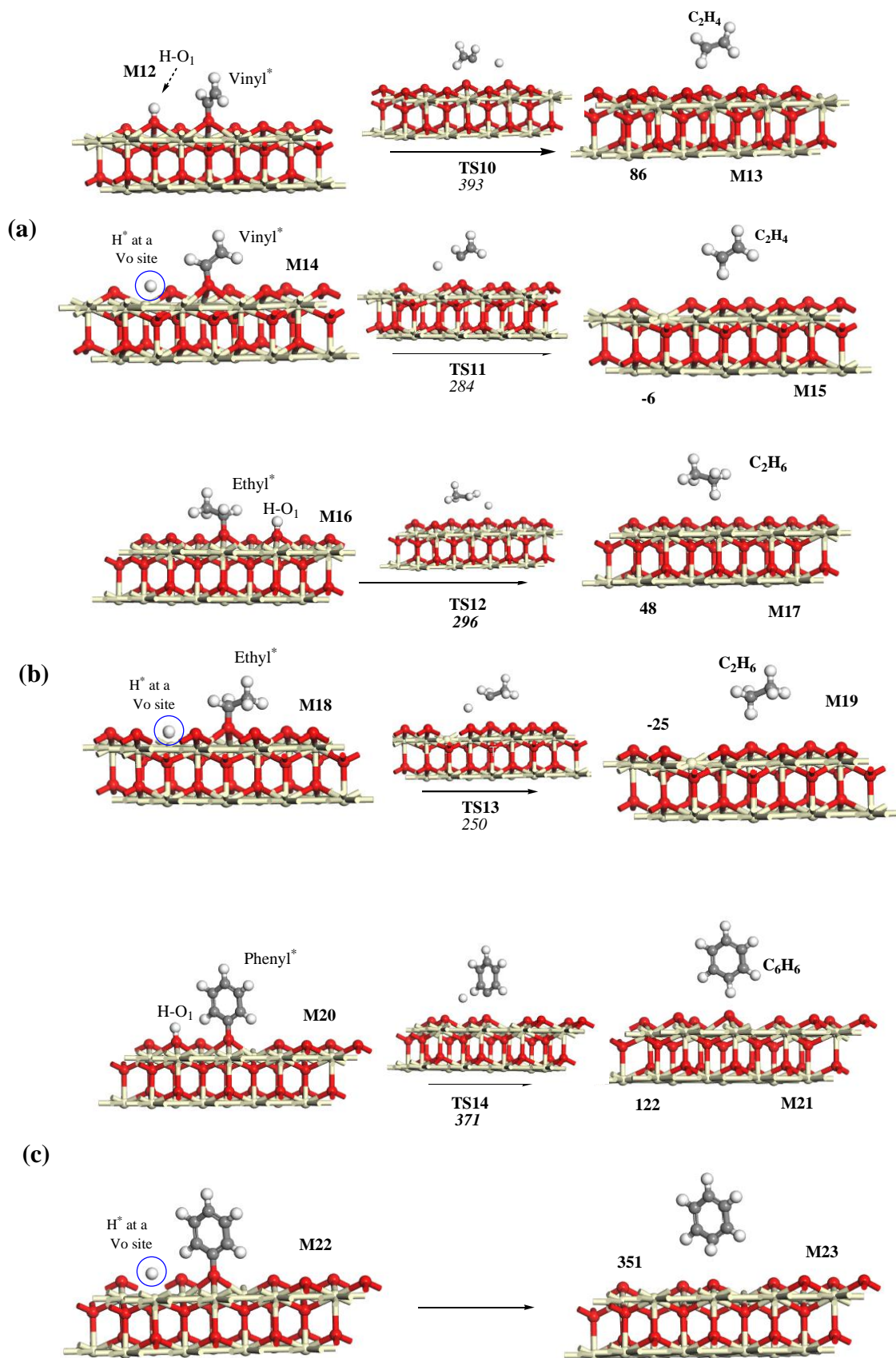


Figure 5.7: Surface hydrogen transfer reactions from HO₁ and H-V_o sites to adsorbed C₂H₃ (a), C₂H₅ (b) and C₆H₅ (c) adducts. All values are in kJ mol⁻¹.

Complete oxidation of adsorbed non-cyclic C_xH_y radicals (into CO/CO₂ and water) over metal oxides generally occurs *via* competing mechanisms that primarily feature the elementary-like reactions i) thermal dehydrogenation (direct fission of C-H bonds), ii) oxidative dehydrogenation operated by surface O* and HO* (*i.e.*, $C_xH_y^* + HO^* \rightarrow C_xH_{y-1}^* + H_2O$), iii) surface oxidation (*i.e.*, $C_xH_y^* + O^* \rightarrow C_xH_yO^*$), and iv) C-C bond cleavage (*i.e.*, $CH_mCH_nO^* \rightarrow CH_m^* + CH_nO^*$) [365, 366]. In a series of studies, Janik and co-authors [367-369] systematically investigated decomposition of methyl and *i*-propyl radicals over pure and doped CeO₂(111) surfaces. Deep catalytic oxidation of these radicals proceeds by successive abstraction of H by surface lattice oxygen atoms and addition of oxygen to radical centres in adsorbed C_xH_y radicals. The final H abstraction along the reaction $HCO^* \rightarrow H^* + CO^*$ was found to be the rate determining step with a reaction barrier of ~68 kJ mol⁻¹. Involved oxygenated intermediates include CH₃O*, CH₃OH*, H₂CO*, H₂COH*, and HCOH*. Oxidative decomposition of larger hydrocarbons radicals (greater than C₁) was shown to follow numerous possible sequences of C-C and C-H bond fission and C-O forming steps leading to formation of H₂O and CO/CO₂. During degradation of *i*-propyl radicals over ceria,[368] four general pathways co-exist; namely, fissions of C-H bonds, C-C bond cleavages; re-oxidizing of the surface and desorption of CO/CO₂ and oxygenated intermediates. The nature of the rate-limiting reaction was shown to vary with the redox conditions in which C-H bond fission and surface re-oxidation prevail under oxidizing and reducing media, respectively.

5.4.5 Decomposition of Chlorobenzene Over CeO₂(111) and CeO₂(111)_{V_o} Surfaces

Via sophisticated temperature-programmed surface desorption (TPSD) and supplementary experimental techniques, Dai *et al.*, [370]. thoroughly investigated decomposition of CB over pure ceria and Ru-doped ceria in various operational environments, including Ar and air with various moisture content. The C-Cl bond fission initiates the degradation of chlorobenzene over ceria-based catalysts; subsequent decomposition/conversion routes of adsorbed phenyl radicals were shown to depend primarily on the combustion medium. In an inert environment, benzene emerges as an important intermediate whereas admitting oxygen into the system increases formation of CO₂, presumably by oxidizing adsorbed phenyl fragments [370]. In this section, we first study fission of the C-Cl/C-H bonds on the CeO₂(111) and

CeO₂(111)_{V_o} surfaces before mapping out the reaction pathways for the removal of surface phenyl radicals by adsorbed OH and O₂. We find that molecular adsorption of chlorobenzene over a V_o site is slightly more stable when contrasted with its adsorption over the stoichiometric surface (-5.2 kJ mol⁻¹ *versus* -8.5 kJ mol⁻¹). The very low adsorption energies of the three considered CVOCs are manifested by that fact that the geometries of the physisorbed states of CE, CA and CB exhibit to large extent corresponding geometries in the gas phase (depicted in Figure 5.2). Figure 5.8.a and b show that surface-assisted ruptures of C-Cl and C-H bonds in chlorobenzene require activation energies of 78 kJ mol⁻¹ (TS15) and 280 kJ mol⁻¹ (TS16). Fission of the C-H bond occurs over two O₁ sites forming a hydroxyl surface group, HO₁. The significant variance in the barriers of TS15 and TS16 stems from the sizable energy difference in the BDE for the aromatic C-Cl bond (400 kJ mol⁻¹) *versus* aromatic C-H bond (472 kJ mol⁻¹); refer to Figure 5.1. Thus, it is expected that decomposition of chlorobenzene proceeds solely through dissociative addition driven by fission of C-Cl bond.

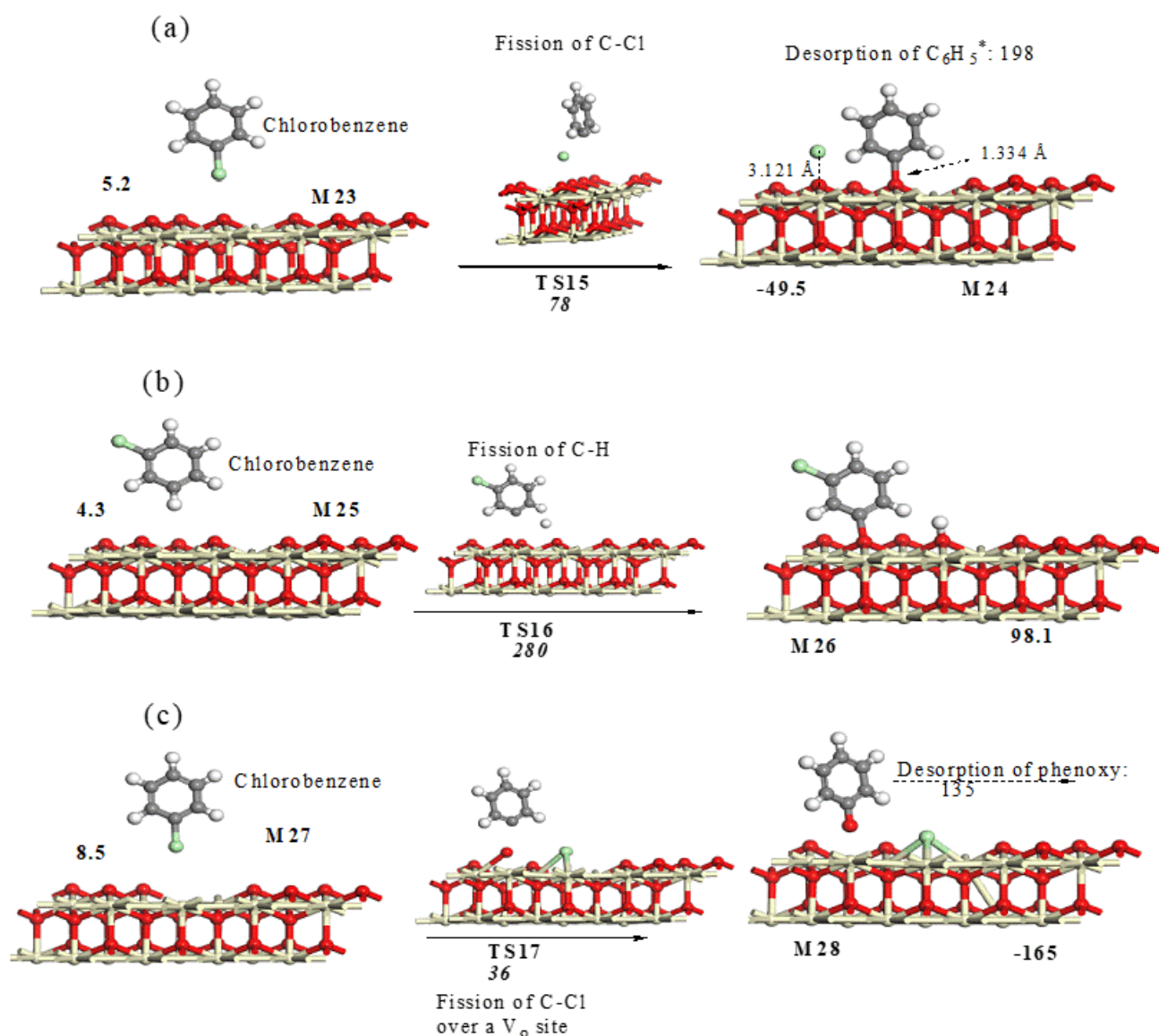


Figure 5.8: Reaction pathways operating in the interaction of chlorobenzene and the $CeO_2(111)$ surface. (a) and (b) describe direct fission of C-Cl and C-H bonds, respectively. (c) illustrates fission of the C-Cl bond over a V_o site. All values are in kJ mol^{-1} .

Fission of the C-Cl bond over a V_o site (Figure 5.8.c) demands a modest reaction barrier of 36 kJ/mol accompanied with an exothermicity of 165 kJ mol^{-1} . Departure of the adsorbed phenyl attached to a lattice oxygen atom affords a phenoxy radical with an energy penalty of 135 kJ mol^{-1} . This process creates another V_o site available for further uptake of chlorobenzene.

Conversion of adsorbed phenyl into benzene entails the presence of a hydrogen source. Dai *et al.*[370] attributed this source to ambient adsorbed hydroxyl groups or to the water produced from decomposition of the parent CB. However, based on the reaction barrier of the aromatic C-H bond fission (280 kJ mol^{-1} , TS16), the latter pathway is predicted to be highly unfeasible. Additionally, Figure 5.7 presents high activation energies for the formation of benzene through hydrogen migrations either from HO_1 site or from a V_o site.

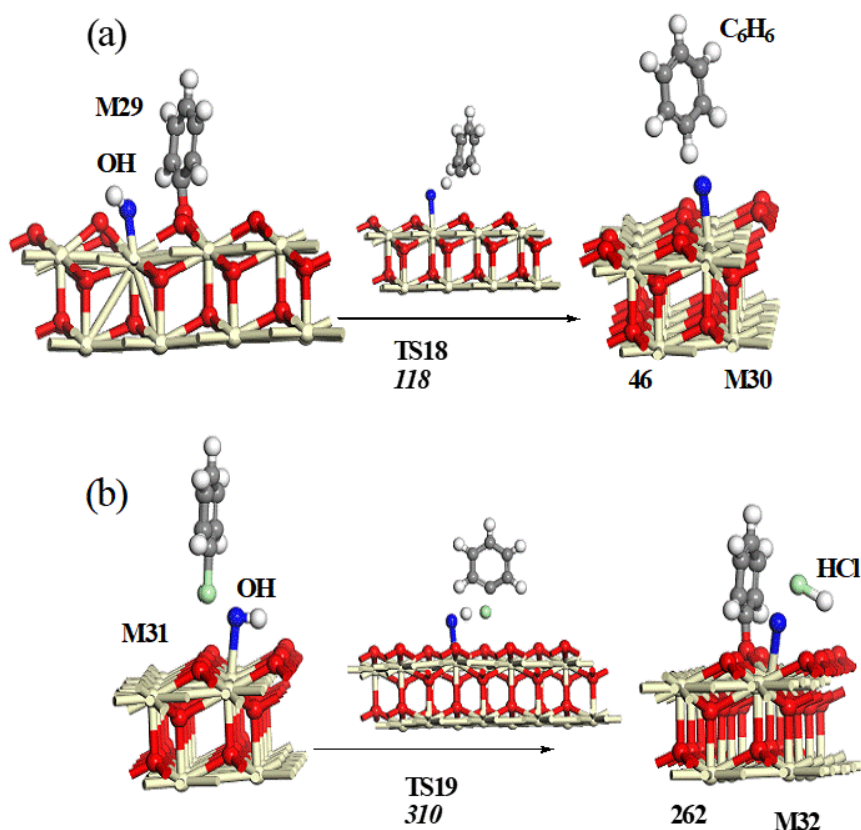


Figure 5.9: Surface reactions of an adsorbed phenol moiety and a surface hydroxyl group, HO_{ads} (a), and between an adsorbed chlorobenzene and HO_{ads} . All values are in kJ mol^{-1} (b). Oxygen atoms in the HO_{ads} group is blue coloured to distinguish them from oxygen lattice in red.

Dissociation of water over CeO_2 was shown to readily yield HO_1 and HO_{ads} -Ce sites[340]. FTIR spectra showed that the resultant Brønsted and Lewis acid sites were found to correspond to 1396 cm^{-1} and 1557 cm^{-1} ; respectively [371]. Figure 5.9.a depicts a pathway for the formation of a benzene molecule *via* hydrogen transfer from a HO_{ads} site to the

adjacently adsorbed phenyl adduct. The emergence of a basic O site and benzene *via* TS18 climbs a moderate reaction barrier of 118 kJ mol⁻¹. The FTIR-TPD experiments by Farra *et al.*[371] have demonstrated an efficient catalytic reactivity of CeO₂ in deriving the so-called Deacon reaction, *i.e.*, conversion/oxidation of HCl into Cl₂ in a process that converts surface HO_{ads} groups into Brønsted acidic sites. In Figure 5.9.b, we found that formation of HCl through the reaction of an incoming chlorobenzene molecule and a surface HO₁ site is hindered by 310 kJ mol⁻¹ (TS19). Concluded from Figure 39 is that surface hydroxyl groups do not mediate the initial decomposition of chlorobenzene and their role is limited to serving as a hydrogen source for the overall conversion of chlorobenzene into benzene.

Dai *et al.*, [370] attributed the rapid deactivation of pure ceria to adsorbed chlorine blocking surface vacant sites in addition to consumption of surface oxygen atoms. The latter observation becomes very evident from the significantly low conversion of chlorobenzene (~20%) even at a temperature as high as 650 K in the absence of oxygen. Additionally, owing to their profound stability, surface phenyl adducts are expected to play a major role in the deactivation of ceria. The O₁-C bond in the adsorbed C₆H₅ moiety is 1.334 Å *i.e.*, it exceeds the equilibrium distance in gaseous phenoxy radicals by only 0.070 Å. This genuine chemical bond makes desorption of the C₆H₅ adduct (from structure M24 in Figure 5.8) to a phenyl radical highly endothermic by 198 kJ mol⁻¹.

The very strong interaction of phenyl with the CeO₂ surfaces results in its deactivation under pyrolytic conditions. Dai *et al.*, [370] found that the catalytic reactivity could readily be recovered by flowing an air stream to replenish surface oxygen sites. Introduced oxygen also acts as an oxidizing agent by decomposing adsorbed phenyl moieties into CO₂ and water. The sharp increase in the yield of CO₂ in air may have partially originated from the oxidative decomposition of surface phenyl groups. Figure 5.10 presents the detailed reaction pathways for the initial decomposition steps of the adsorbed phenyl radical introduced by the adsorption of a gas phase oxygen molecule at a V_o site. The reaction of O₂ with the adjacent phenyl adducts branches into three routes *via* reaction barriers in the range of 30 kJ mol⁻¹ – ~100 kJ mol⁻¹. These three pathways lead to the production oxygenated C₆ rings, namely phenoxy (M38) and *o*-benzoquinone (M36). Decomposition of these oxygen-bearing species through the well-documented ring contraction/CO elimination explains the notable increase

in the yield of CO₂ from the oxidative decomposition of chlorobenzene. Inferred from pathways depicted in Figure 5.10 is that the introduced oxygen molecules readily regenerate the ceria catalytic activity *via* oxidizing adsorbed phenyl moieties as well as by re-oxidizing the partially reduced Ce cations.

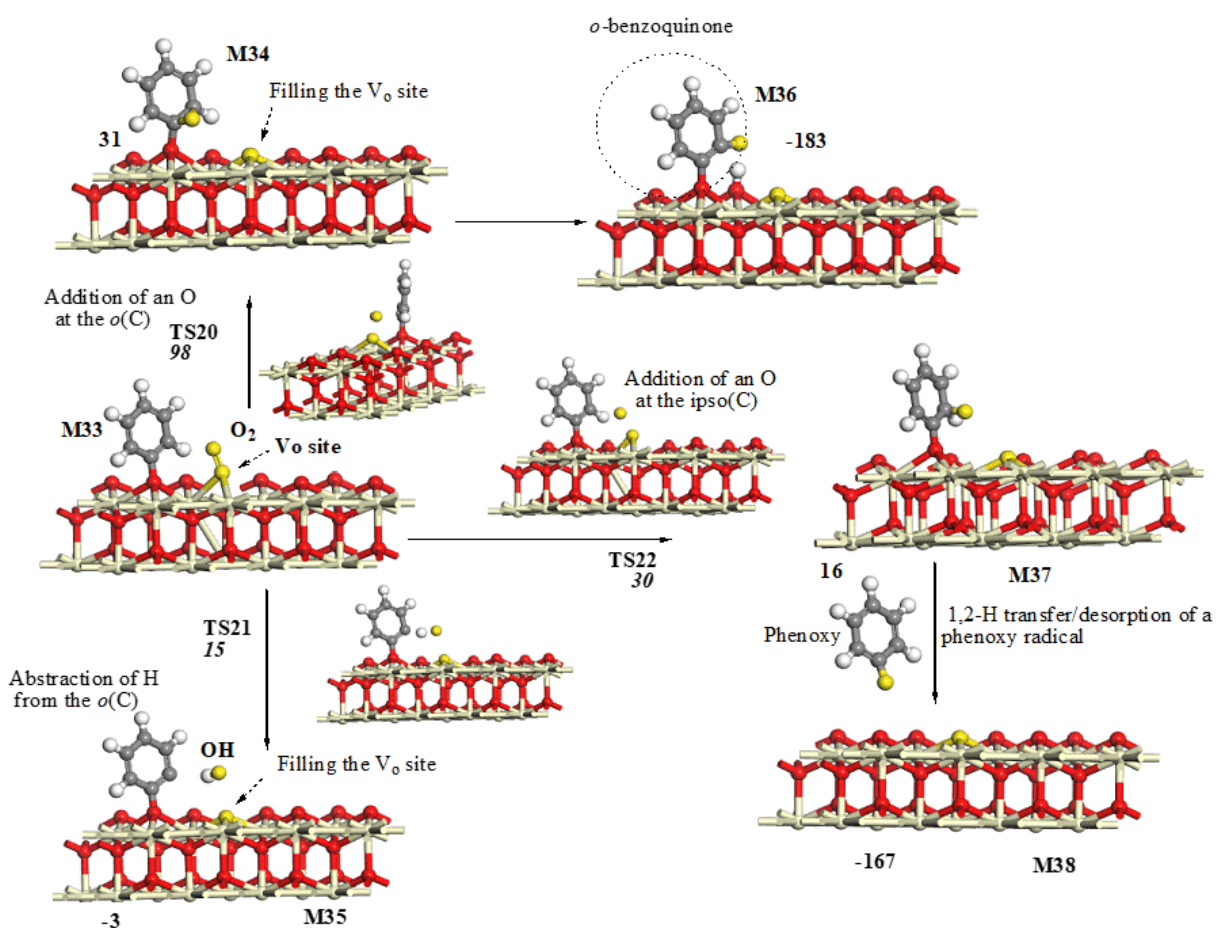


Figure 5.10: Reactions initiated from the adsorbed phenyl moiety and an oxygen molecule adsorbed at a V_o site. All Values are in reference to the reactant in each step. Also, all values are in kJ mol⁻¹. Oxygen atoms originating from oxygen molecules are yellow colored to distinguish them from oxygen lattice in red.

5.4.6 Formation of 1,4-Dichlorobenzene

The potential for the formation of higher chlorinated aromatics often represents a serious drawback in industrial application of the catalytic decomposition of CVOCs. The acidic

nature of transition metal oxides often plays a dual role in destroying CVOCs into smaller fragments on the one hand, and mediating their condensation into polyhalogenated aromatics on the other [324]. Under oxidative condition, the two dichlorobenzene isomers 1,4- and 1,2-dichlorobenzene were the major chlorine-bearing species from oxidative decomposition of CB [370]. Formation of dichlorobenzene congeners entails the occurrence of a surface chlorination mechanism. Chlorination by electrophilic substitution is the most widely discussed catalytic chlorination mechanism [319]. In a recent study,[372] our predicted halogenation sequence of several halogenated aromatics based on the $f^1(r)$ index reproduces their analogous isomers distribution in thermal and environmental matrices.

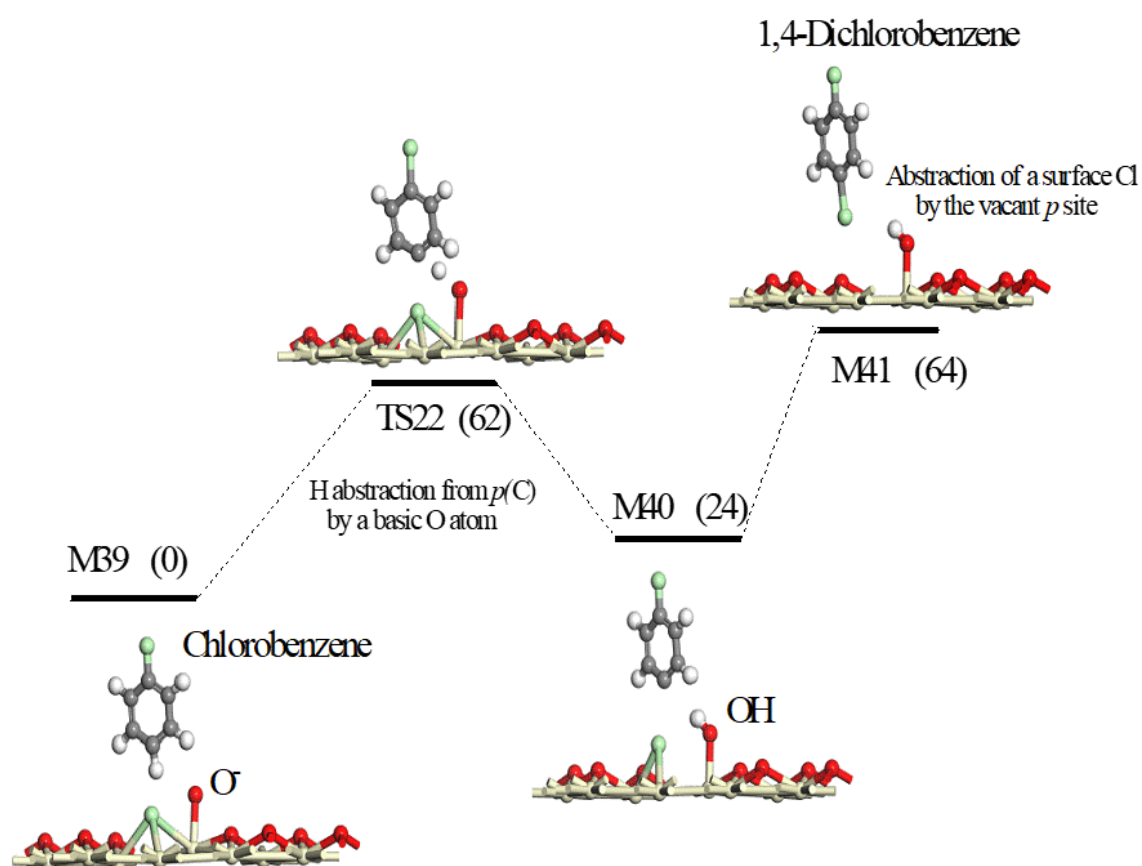


Figure 5.11: Formation of 1,4-dichlorobenzene initiated by hydrogen abstraction by an O⁻ surface anion followed by chlorine transfer from the surface to the vacant para-site. Values are in kJ mol⁻¹ in reference to the initial reactant, M39.

Farra *et al.*[371] found that CeO₂ serves as an efficient catalyst for the conversion of HCl into the potent chlorination agent Cl₂. During the course of HCl oxidation, all lattice O₁ atoms were replaced with chlorine atoms occupying the V_o sites. Along the same line of enquiry, simulations by Cen *et al.* [353] predicted that chlorine surface coverage should not exceed 1/9 ML under conditions encountered in typical catalytic scenarios, *i.e.*, 5 – 10 vol % O₂ and < 100 ppm Cl₂. In addition to the most plausible electrophilic substitution; suggested chlorination mechanisms encompass direct chlorine transfer from a partially or fully chlorinated surface [319]. Figure 5.11 and 5.12 present pathways that account for these two plausible mechanisms. The chlorination mechanism in Figure 5.11 is characterized by *para*-hydrogen abstraction by a surface oxygen anion followed by attack of the vacant phenyl carbon on a chlorine atom positioned at the V_o site. Oxygen surface anions could originate from a loss of hydrogen from the adsorbed OH_{ads} groups (for example *via* the reaction M29 → M30 in Figure 5.9). Abstraction of the *para*-hydrogen atom by O⁻ requires only 62 kJ mol⁻¹ (TS22). Abstraction of a surface chlorine followed by desorption of a 1,4-dichlorobenzene molecule is predicted to be endothermic by 40 kJ mol⁻¹. The accessible energy requirement for chlorination pathway indicates that chlorination of an aromatic ring *via* an oxychloride structure is very feasible. To the best of our knowledge, this is the first mechanistic account for a surface-mediated chlorination pathway of an aromatic molecule.

Figure 5.12 depicts a two-step chlorination mechanism over a pre-chlorinated surface, denoted as CeO₂ (111)_{Cl}. This mechanism proceeds *via* HCl elimination followed by chlorine transfer from the surface. Clearly, the loss of an aromatic H represents a bottleneck for this process with a noticeable activation barrier of 276 kJ mol⁻¹. Nonetheless, such an energy demanding pathway might contribute to chlorination in highly chlorine corrosive environment in the absence of oxygen, the species that drive the Deacon reaction[371] as well as generation of surface O⁻ anions.

5.4.7 Kinetic Analysis

Our calculations on the three title molecules have consistently demonstrated the role of the V_o site in facilitating C-Cl rupture. However, the TPD profile reported by Dai *et al.*,[370] has indicated that the loss of surface lattice oxygen occurs at ~ 820 K, significantly higher than the reported temperature interval for the decomposition of the three title CVOCs (*i.e.*, below

500 K) [70, 336, 370]. This arises the question on whether the decomposition of CVOCs was driven by V_o sites or it merely occurred on surface Ce-O₁ bonds, prior to the creations of V_o sites. Nonetheless, it also must be noted that the V_o sites also exist as structural defects in stoichiometric CeO₂ [373]. An insight into these intriguing competing scenarios could be achieved by contrasting our calculated activation energies for the C-Cl bond fissions over the CeO₂ (111) and CeO₂(111)_{-V_o} surfaces with analogous interpreted experimental values. Fitting the temperature-conversion profiles reported by Dai *et al.* (in their Figure 5.1)[70] [370] by a simplified plug flow reactor (PFR) model (for a first-order reaction without pressure drop) yields the temperature-dependent reaction rate constant; $k(T)$: [374]

$$\begin{array}{ccc}
 & k(T) \text{ versus } T & \\
 \text{exp}_{k(T)=\frac{1}{\tau}\left[\ln\frac{1}{(1-X(T))}\right]} & \xrightarrow{\hspace{2cm}} & \text{exp}_{k(T)=Ae^{\frac{-E_a}{RT}}} \\
 \text{Experimental profiles} & & 5.2
 \end{array}$$

Where τ stands for the residence time under the experimental conditions of Dai *et al.*[70] ($1.8 \times 10^{-8} \text{ s}^{-1}$ based on a gas hourly space velocity of 15000 h^{-1}) and $X(T)$ denotes the measured conversion profiles. Fitting the obtained $k(T)$ values by the Arrhenius equation gives the experimental activation energy (E_a) and the pre-exponential A values. Table 5.3 presents the extracted E_a and A values for the catalytic decomposition for trichloroethylene, dichloroethene and chlorobenzene. Extracted E_a values from the temperature conversion profiles for the decomposition of trichloroethylene, dichloroethane and chlorobenzene attain values of 57 kJ mol^{-1} , 48 kJ mol^{-1} and 74 kJ mol^{-1} . These values are in reasonable agreement with our activation energies for the C-Cl bond fission in the analogous CE, CA and CB molecules of 49 kJ mol^{-1} ; 38 kJ/mol and 78 kJ mol^{-1} , in that order. The fitted experimental E_a values largely deviate from the corresponding activation energies for the C-Cl bond fission in the CE and CB molecules over V_o sites of 11 kJ mol^{-1} and 36 kJ mol^{-1} ; respectively. This finding reveals that the main decomposition of CVOCs over CeO₂ occur over stoichiometric Ce-O bonds prior to the creation of surface vacancies at a significantly higher temperature.

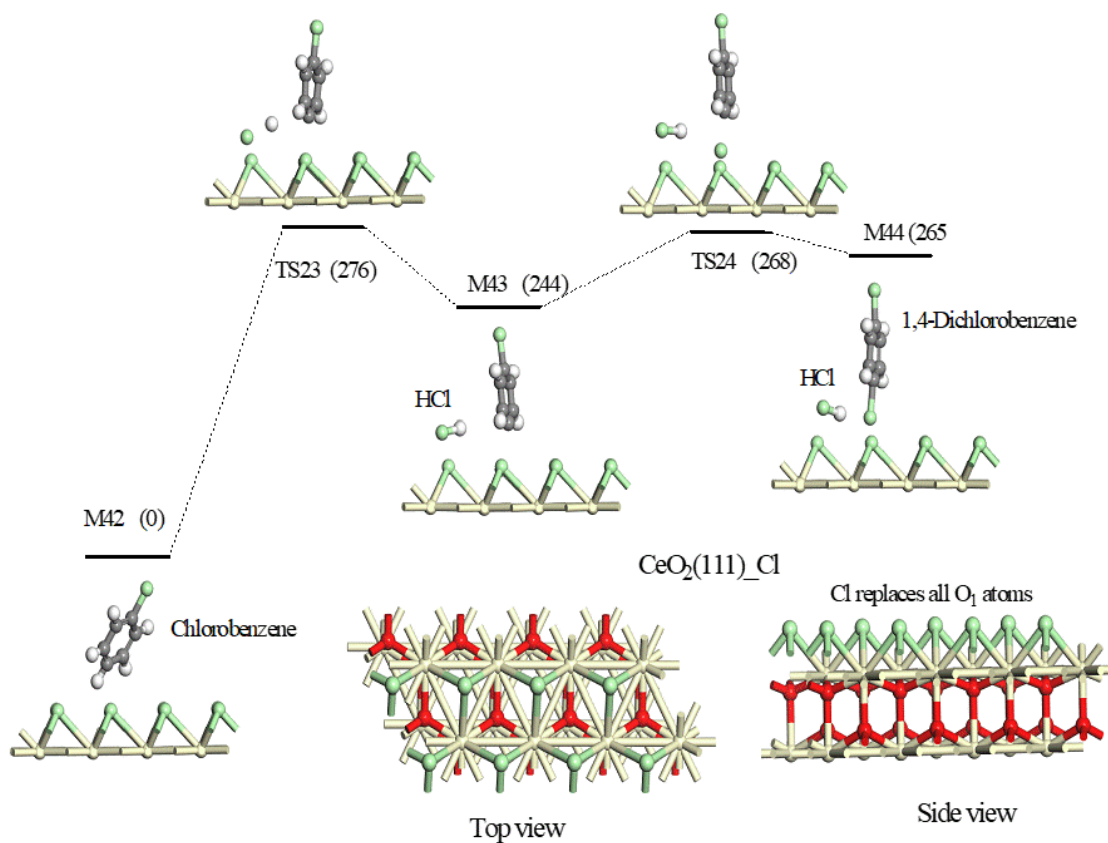


Figure 5.12: Formation of 1,4-dichlorobenzene over a per-chlorinated CeO₂(111)_{Cl} surface. Values are in kJ mol⁻¹ in reference to the initial reactant, M42.

Table 5.3: Arrhenius parameters obtained from fitting the conversion-temperature profiles to a PFR model.

	C ₂ HCl ₃ → Products	C ₂ H ₄ Cl ₂ → Products	C ₂ H ₅ Cl → Products
Experimentally fitted values			
<i>A</i> (s ⁻¹)	2.34 × 10 ¹⁴	1.60 × 10 ¹⁴	5.29 × 10 ¹⁵
<i>E_a</i> (kJ/mol)	57	48	74

Table 5.4: Calculated reaction rate constants (in $\text{cm}^5 \text{mol}^{-2} \text{s}^{-1}$) for the dissociative adsorption of the selected CVOCs over the stoichiometric $\text{CeO}_2(111)$ surface.

T (K)	1,2-Dichloroethene	Chloroethene	Chloroethane	Chlorobenzene
	Cl-Cl elimination	H-Cl elimination	H-Cl elimination	C-Cl bond fission
300	8.13×10^2	1.76×10^{-6}	4.44×10^3	1.75×10^{-2}
340	9.59×10^3	2.09×10^{-4}	4.14×10^4	7.36×10^{-1}
380	6.77×10^4	9.16×10^{-3}	2.43×10^5	1.42×10^1
400	1.56×10^5	4.58×10^{-2}	5.16×10^5	5.01×10^1
440	6.59×10^5	7.38×10^{-1}	1.90×10^6	4.43×10^2
460	1.23×10^6	2.48	3.36×10^6	1.15×10^3
480	2.20×10^6	7.52	5.66×10^6	2.74×10^3
500	3.74×10^6	2.09×10^1	9.17×10^6	6.11×10^3
540	9.65×10^6	1.29×10^2	2.16×10^7	2.55×10^4
560	1.47×10^7	2.91×10^2	3.17×10^7	4.82×10^4
600	3.17×10^7	1.26×10^3	6.35×10^7	1.53×10^5
640	6.20×10^7	4.57×10^3	1.17×10^8	4.19×10^5
660	8.41×10^7	8.20×10^3	1.54×10^8	6.63×10^5
700	1.47×10^8	2.39×10^4	2.56×10^8	1.54×10^6

The surface reaction rate constant can be obtained based on the reaction rate expression of:[375]

$$k_{surf}(T) = \frac{s}{\sigma^2} \sqrt{\frac{RT}{2\pi M}} e^{\frac{-E_a}{RT}} \quad 5.3$$

where σ stands for the active site density of surface oxygen, s denotes the sticking coefficient (assumed to be 1.0), M is the molecular mass of the dissociated molecule and E_a is taken to be our calculated reaction barriers for the corresponding overall barriers for H-Cl elimination from CE/CE, Cl-Cl elimination from 1,2-dichloroethene and for C-Cl bond fission in CB. The rate of dissociative adsorption is then expressed as $-r(T) = k(T)C_s^2P_{gas}$ where P_{gas} is the partial pressure of the gas phase species and C_s represents concentration of available surface sites. Via thermogravimetric measurements coupled to a conductivity cell, Al-Madfa *et al.*, [376] measured the concentration of surface oxygen atoms (O_1) to be $\sim 1.6 \times 10^{15}$ atoms/cm². When considering the upper limit of the surface area of CeO₂ reported by Dai *et al.* at 54.2 m²/g, [70] the concentration of O_1 sites corresponds to 1.44×10^{-3} mol O_1 g_{CeO₂}⁻¹. Table 5.4 lists the calculated values of $k_{surf}(T)$ for the decomposition of the title molecules based on a 1.44×10^{-3} mol O_1 g_{CeO₂}⁻¹ site density. A surface reaction rate or a turnover frequency (TOF) for the overall decomposition of the four CVOCs can then be obtained based on the inlet concentration of the gas phase species and the degree of surface coverage. Upon utilizing 1000 ppm for the initial concentration of the gas phase species (*i.e.*, similar to the experimental conditions of Dai *et al.* [70, 336, 370]) and by assuming a full surface coverage, Figure 5.13 plots the TOFs values for decomposition of CE, /CA (*via* HCl elimination) and CB (*via* C-Cl bond fission) and for 1,2-dichloroethene through Cl₂ elimination from dichloroethene. No analogous TOFs values were reported by Dai *et al.*, [70, 336, 370] and hence we elected to employ our calculated $k_{surf}(T)$ values to predict temperature-dependent conversion profiles *via* a simplified fluidized bed reactor (FBR) model:

$$\frac{dF_{CE}}{dW} = -r_{CE} \quad r_{CE} = k_{surf}C_sC_{gas}^{CE} \quad X = 1 - \frac{F_{CE}}{F_{CE}^0} \quad 5.4$$

This model utilizes 1 mol s⁻¹ for the initial molar flow rate of the gas phase species (*i.e.*, F_{CE}^0) and assumes a full surface coverage (*i.e.*, $\sigma = C_s$ or $\theta = 1$) for a weight (W) of the catalyst at 100 g. The model produces conversion – temperature profiles based on the $k_{surf}(T)$ values given in Table 5.4. Figure 5.14 contrasts the model and experimental conversion-temperature profiles. Conversion profile for trichloroethylene is compared against analogous values

obtained from Cl-Cl elimination from dichloroethylene. The conversion profile of dichloroethane is contrasted with the corresponding conversion values obtained from H-Cl elimination from chloroethane. The profile of chlorobenzene conversion is contrasted against the conversion values obtained from the C-Cl bond fission in chlorobenzene.

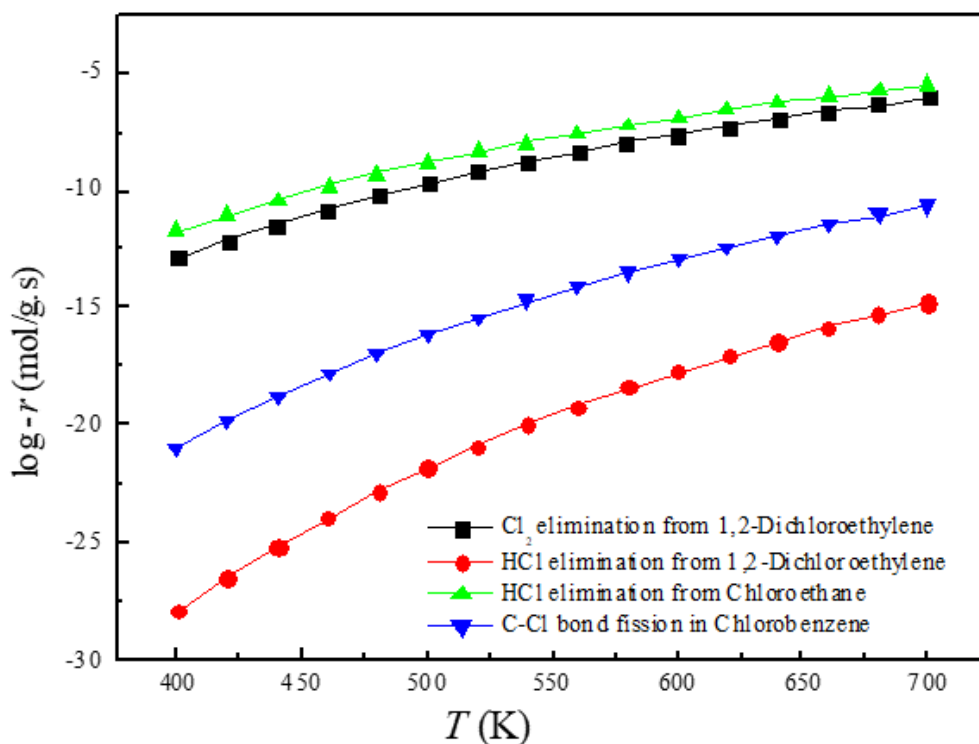


Figure 5.13: Reaction rates for the decomposition of the selected CVOCs over the stoichiometric CeO₂(111) surface based on 1000 ppm of reactants and a full coverage of the active sites.

Our simplified kinetic model reasonably reproduces the general trend of the experimentally obtained conversion profiles. As Figure 5.14.a and b show, our model overshoot measured conversion values [70, 336, 370] by 0.1 – 0.3. The over prediction of conversion profiles in case of dichloroethylene and chloroethane can be rationalized based on the fact that we described the overall decomposition of these two molecules based on H-Cl/Cl-Cl elimination pathways. A better agreement could be obtained if the model accounts for the initial C-Cl bond fission, a step with lower activation energy (*i.e.*, in case of chloroethane 38 kJ mol⁻¹ versus 51 kJ mol⁻¹). As demonstrated in section 5.4.4, desorption of vinyl and ethyl radical is expected to predominate over the β(C)H transfer route. However, the former process may encounter a desorption barrier that increases the overall energy penalty for the desorption pathway. Despite our best attempts, we could not locate a genuine transition state for the

desorption of vinyl, ethyl and phenyl radicals from the surface. The described overall decay based on the H-Cl/Cl-Cl₂ elimination in chlorinated alkanes and alkenes serves as a lower estimate for the overall decomposition of chlorinated aliphatics in reference to accounting for only the first C-Cl bond fission. Another source of discrepancy is the plausible presence of defects and edge terraces on the surfaces of CeO₂; both structural features were not accounted for in the model.

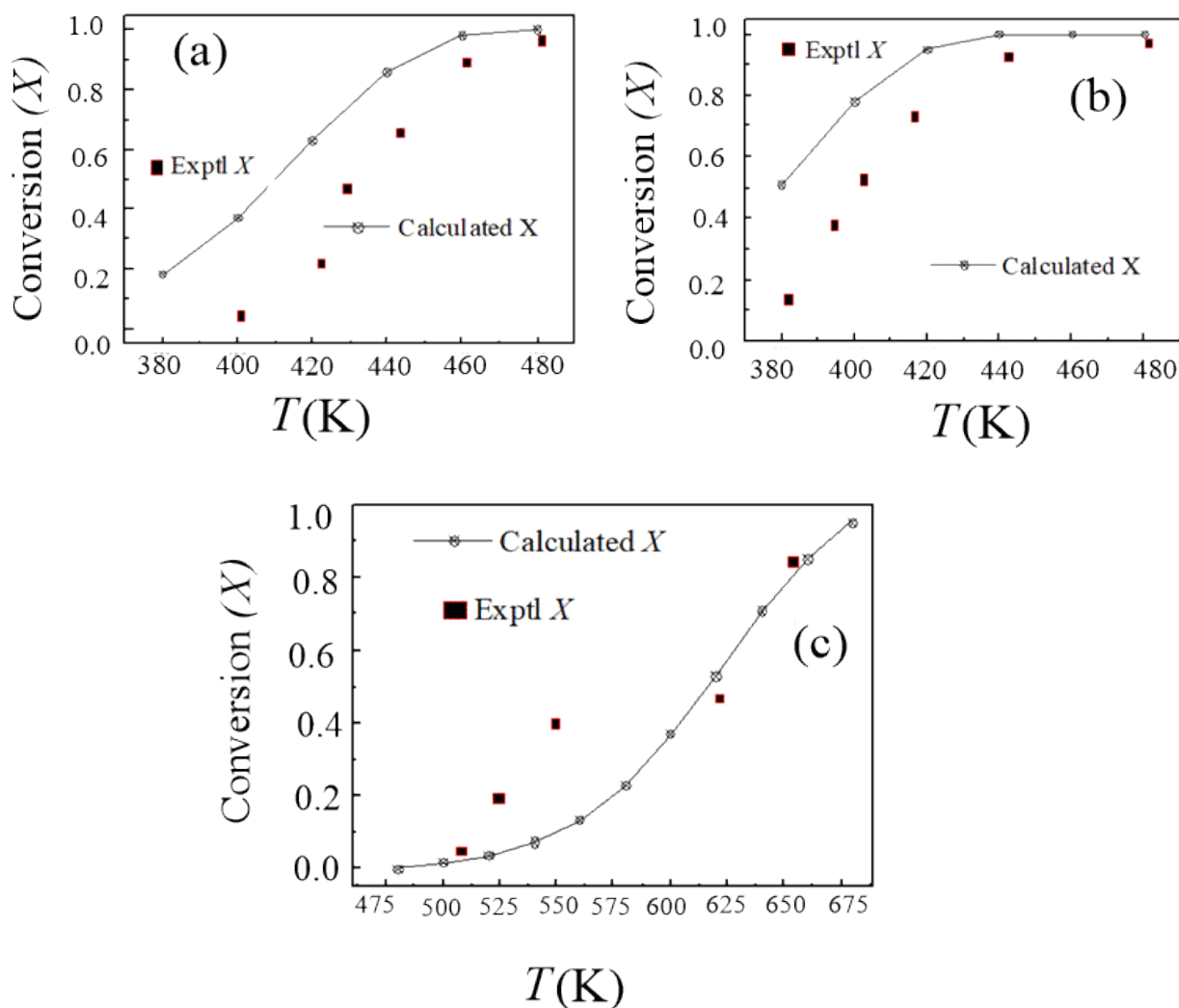


Figure 5.14: Comparison between predicted and experimental conversion values [70, 336, 370] for the decomposition of chloroethene (a), chloroethane (b) and chlorobenzene (c) over the stoichiometric CeO₂(111) surface.

5.5 Conclusions

The three investigated CVOCs assume rather weak molecular adsorption modes over the CeO₂ (111) surface, prior to their exothermic dissociative adsorption. Activation energies interpreted from experimental conversion –temperature profiles reflect very well the calculated activation energies for the C-Cl bond fission in CE, CB and CB molecules over the stoichiometric configuration of CeO₂(111). The large electron affinity of surface Ce atoms facilitates elimination of the two chlorine atoms from the dichloroethene molecule. Dehalogenation of CE and CA molecules (*i.e.*, loss of HCl) proceeds through a two-step mechanism rather than *via* a direct elimination pathway. Surface C_xH_y radicals bind very strongly to O₁ sites, resulting in rapid catalytic poisoning in the absence of oxygen. Removal of adsorbed vinyl, ethyl and phenyl radicals by migration of surface's hydrogen atoms entails very high activation energies. Hydrogen transfer from adsorbed HO_{ads} groups to adsorbed phenyl adducts results in the formation of benzene; *i.e.*, the major product from the pyrolytic catalytic decomposition of CB. Reactions of oxygen molecules adsorbed at the V_o sites recover the catalytic activity of ceria by transforming the adsorbed phenyl into oxygenated species (phenoxy, *o*-benzoquinone) as well as by filling in the oxygen vacant sites. Several contradicting factors seem to contribute to the overall role of vacant oxygen sites in promoting *versus* suppressing the catalytic effect on the decomposition of CVOCs. While we have shown that oxygen vacant sites systematically reduce activation energies required for the C-Cl bond fission (in reference to the surface oxygen sites), fragmented chlorine molecules block these active sites. Furthermore, we have found that decomposition of a chlorobenzene molecule over a per-chlorinated surface has a very high activation barrier. The results from this study shall be helpful to understand the role CeO₂-based catalysts in the destruction of persistent halogenated pollutants.

Chapter 6 : Structural, electronic and thermodynamic properties of bulk and surfaces of TbO₂

Paper III

Miran, H.A., Altarawneh, M., Jaf, Z.N., Dlugogorski, B.Z. and Jiang, Z-T (2018) Structural, electronic and thermodynamic properties of bulk and surfaces of terbium dioxide (TbO₂). Materials Research Express, 5 (8).

6.1 Abstract

This chapter reports a comprehensive investigation into the structural, electronic and thermal properties of bulk and surface terbium dioxide (TbO₂); a material that enjoys wide spectra of catalytic and optical applications. Our calculated lattice dimension of 5.36 Å agrees well with the corresponding experimental value as at 5.22 Å. Electronic density of states configuration of the bulk structure exhibits a semiconducting nature. Thermo-mechanical properties of bulk TbO₂ were obtained based on the quasi-harmonic approximation formalism. Heat capacities, thermal expansions and bulk modulus of the bulk TbO₂ were obtained under a wide range of temperature and pressure. The dependency of these properties on operational pressure is very evident. Cleaving bulk terbium dioxide affords different six terminations. Bader charge distribution analysis for the bulk and the surfaces portrays an ionic character for Tb-O bonds. In an analogy to the well-established finding pertinent to stoichiometric CeO₂ surfaces, the (111):Tb surface appears to be the thermodynamically most stable configuration in the nearness of the lean-limit of the oxygen chemical potential. For the corresponding non-stoichiometric structures, we find that, the (111):O+1V_O surface is the most stable configuration across all values of accessible oxygen chemical potentials. The presence of an oxygen vacant site in this surface is expected enable potent catalytic-assisted reactions, most notably production of hydrogen from water.

6.2. Introduction

Terbium oxide belongs to the lanthanide oxides family and adopts a fluorite-type RO_2 (rare earth dioxide) structure. It exists in different oxygen-deficient phases (TbO_{2-y}). This is due to the facile accessibility to switch between + 3 and + 4 oxidation states. Derived by noticeable ease in changes in terbium oxide's stoichiometry, it has enjoyed prominent optical properties; especially as ingredients in promising thin film materials deployed in antireflection layers, photo-elastic films, in additions to pigments, Fresnel lenses and so on [377]. TbO_2 has also been deployed as a good supporter for cerium oxide in many catalysis technologies, most notably in the s-called three-way catalysts (*TWC*) [378, 379]. In the latter, ceria act as an oxidizing and reducing material for potent pollutants (CO , NO_x , HC) emitted by cars, and subsequently converting them into harmless gases (*i.e.*, CO_2 and N_2). With the aim to develop a new *TWC* system, Bernal and his collaborators conducted a study on CeO_2 doped with Tb and Pt. Based on oxygen buffering capacity (OBC) and oxygen storage capacity (OSC) results, they found that, catalytic performance of Pt/CeTbO_x configurations outperform Pt/CeO_2 solid mixtures in oxidizing mixtures of methane and CO at low operating temperature as well as in oxidizing both methane and carbon monoxide [379].

In another related work, Bernal *et al.* have experimentally demonstrated that addition of 20 mol% of terbia to ceria improves its catalytic capability in *TWC* operations. This has been attributed to profound enhancement in proficiency to diminishing fast oscillations of the oxygen partial pressure [378]. The production of solar hydrogen (H_2) via metal oxide ((MO) has been a central research theme for renewable energy applications. TbO_2 is now being utilized in the production technology of solar thermochemical H_2 by the two-step solar thermochemical water splitting reaction (WS) cycle. In this new technology, TbO_2 is thermally reduced into Tb and O_2 as a first step, while in the second step Tb is oxidized by water splitting reaction resulting in the synthesis of H_2 [380].

To this end, the aim of this study is to provide comprehensive structural, electronic and thermodynamic account for bulk and surfaces of TbO_2 via performing density functional theory (DFT) calculations. Previous DFT studies on TbO_2 have only presented its bulk

electronic structures [193]. It is hoped that computed properties in this study to provide insight into the remarkable catalytic and optical properties of TbO₂. For instance, a profound thermodynamic stability for structures with vacant oxygen sites is expected to facilitate fission of O-H bond in water, *i.e.*, a central step in the WS cycle.

6.3. Computational details

6.3.1. Structural optimization of TbO₂

The plane wave DFT code of Vienna ab initio simulation package (VASP) [381] was used to carry out all structural optimizations and energy calculations, with the spin polarized PAW-GGA functional [382]. Spin polarized calculations within DFT are essential to accurately describe different characteristic properties of ferromagnetic solid materials, including TbO₂, such as the structural, electronic and thermodynamic properties. This is achieved by accounting for the magnetism of itinerant electrons in solid state materials [383]. From our previous publications [384, 385], surfaces are bulks of metal oxides and halides incur less total energies when optimized via spin polarized treatment, in reference to spin unpolarized treatment. A plane wave cut-off energy of 400 eV was used in all calculations. $4 \times 4 \times 4$ and $4 \times 4 \times 1$ mesh of κ -points sampling generated by the Monkhorst-Pack scheme [277] provided sampling for the integration of the irreducible part in the Brillion zones in bulk and surfaces calculations; respectively. All layers were allowed to relax till the energy and force tolerance on each atom converged to less than 10^{-5} eV and 10^{-2} eV/Å; respectively. It is essential to introduce the on-site coulomb interaction correction (DFT+ U) to obtain correct electronic description of the strongly localized f electrons in LnO₂ compounds [386] system. The deployed U value herein at 6 eV followed the suggestion by Kanoun *et al.* [193]. To the best of our knowledge, literature presents no experimental value for the band gap of TbO₂. Hence, we elect to compare the experimental band gap of Tb₂O₃ with its analogous calculated value herein in order to set a benchmark for the accuracy of the adapted methodology. The adapted DFT + U approach satisfactorily reproduces the experimental band gap of Tb₂O₃. A U value of 6 eV yields the experimental band gap of Tb₂O₃ at 3.8 eV [387] as Figure 6.1 depicts.

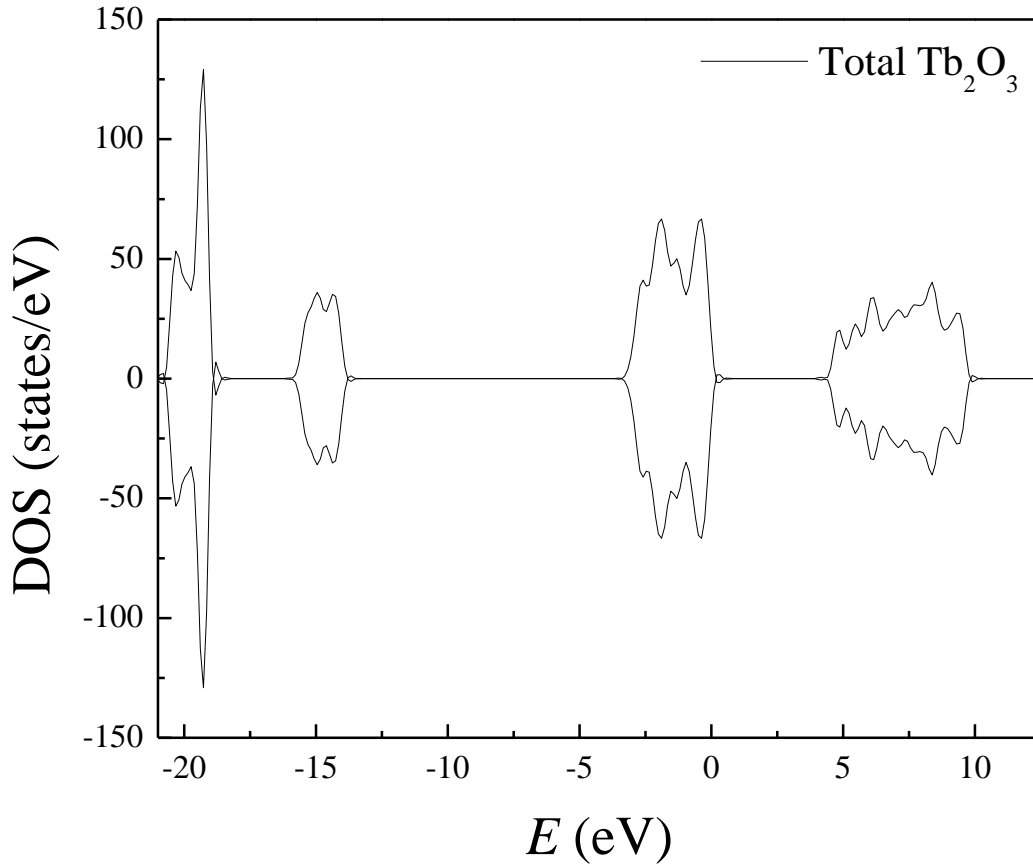


Figure 6.1: Total density of state (DOS) for bulk Tb_2O_3 .

The formation energy per oxygen atom of metal oxides is given by [388];

$$\Delta E_O = \frac{1}{y}E(A_xO_y) - \frac{x}{y}E(A) - \frac{1}{2}E(O_2) \quad 6.1$$

Where ΔE_O is the formation energy, A corresponds to the metal present in the oxide and O is oxygen atom.

Based on Equation 6.1 the enthalpy of formation per oxygen molecule of bulk TbO_2 (ΔH_f) is expressed by the following formalism;

$$\Delta H_f(O_2) = H(TbO_2) - H(Tb) - \frac{y}{2}H(O_2) \quad 6.2$$

in which $H(TbO_2)$ and $H(Tb)$ denote the bulk TbO_2 and bulk Tb energies per unit formula, respectively. $H(O_2)$ corresponds to the enthalpy of an oxygen molecule.

6.3.2. Quasi-harmonic approximation for thermodynamic properties

Thermal properties of bulk TbO_2 have been calculated using the quasi-harmonic approximation method (QHA) as implemented in the PHONOPY code [389]. By deploying the density- functional perturbation theory (DFPT) within the VASP code, force constants and atomic displacements for a $2 \times 2 \times 2$ supercell of TbO_2 were obtained. These calculations deploy $4 \times 4 \times 4$ κ -point grid meshes for the integration over the Brillouin zone. The Vinet's equation of state has been used to fit energy-volume curves [390]. Details on the implementation and equations underlying the QHA are reported elsewhere [389]. In a nutshell, the QHA treats phonon frequencies of a solid to depend only on volume's displacement rather than on temperature's variation. Consequently, the Gibbs free energy is minimized for each volume [391, 392] *via* Helmholtz's free energy $F(T, V)$ term [393]:

$$G(T, P) = \min_V [F(T, V) + PV] \quad 6.3$$

in which T , P and V signify unit cell's' temperature, pressure and volume, respectively. In this formalism, Helmholtz free energy is calculated from the internal energy of a solid at the ground state summed over the vibrational energies phonon [389].

6.2.3. Ab initio atomistic thermodynamics calculations

Thermodynamic stability phase diagrams for all plausible orientations of TbO_2 surfaces have been constructed using the *ab initio* atomistic thermodynamics approach. Detailed descriptions and derivation of this equation can be found elsewhere [394]. In short, surface free energies, $\gamma(T, P)$, at constant temperature T and pressure P is expressed as [385]:

$$\gamma(T, P) = \frac{1}{2A} [G^{surf}(T, P) - N_{Tb} G_{TbO_2}^{Bulk}(T, P) - (N_O - nN_{Tb}) \mu_O(T, P)] \quad 6.4$$

Where $G^{surf}(T, P)$ and $G_{TbO_2}^{Bulk}(T, P)$ represent the Gibbs free energies of TbO₂'s surfaces and bulk TbO₂, respectively, at certain temperature and pressure. N_{Tb} and N_O signify the number of Tb and O atoms in the slab and $\mu_O(T, P)$ corresponds to the chemical potential of oxygen defined as [385]:

$$\mu_O(T, P) = \Delta\mu_O(T, P^0) + \frac{1}{2}KT \ln\left(\frac{P}{P^0}\right) \quad 6.5$$

Oxygen chemical potential difference ($\Delta\mu_O$) values have been sourced from standard thermodynamic tables[395]:

$$\Delta\mu_O(T, P^0) = \frac{1}{2} [H(T, P^0, O_2) - H(0, P^0, O_2)] - \frac{T}{2} [S(T, P^0, O_2) - S(0, P^0, O_2)] \quad 6.6$$

6.3. Results and discussion

6.3.1. Bulk properties of TbO₂

The bulk crystalline structure of TbO₂, as shown in Figure 6.2, exhibits a face-centered cubic (fcc) Bravais lattice with a space group of $Fm-3m$. The bulk structure of TbO₂ is crystallized as a Tb₄O₈. Oxygen atoms are located in the cubic closed packed terbium. It is crucial to establish an accuracy benchmark of our adapted methodology by contrasting computed values with their analogous experimental estimates. For this reason, we elect to reproduce some electronic and structural properties for bulk TbO₂. Our TbO₂ computed lattice parameter of 5.36 Å is in an accord with its analogous measured value at 5.22 Å [396].

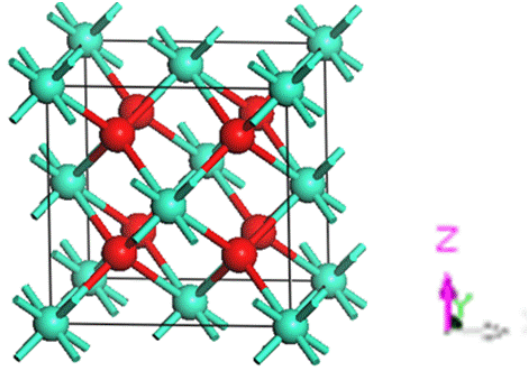


Figure 6.2: Optimized TbO_2 unit cell. Light blue and red spheres signify Tb and O atoms, respectively.

6.3.2. Thermo-elastic properties of TbO_2

The coordination nature of a material is changeable when applying external mechanical and thermal conditions (*i.e.* applied pressures). This has motivated computational materials scientists to compute thermal and mechanical properties at different practical pressures and at a wide range of temperatures. To do so, we applied a quasi-harmonic model to derive thermo-mechanical properties of bulk TbO_2 . The dependency of computed properties on the size of the deployed supercell size must be established first. Detailed description of this supercell size -dependent benchmarking is reported in many recent studies [397, 398]. Figure 6.3 displays the difference between quasi harmonic heat capacities $\Delta C^{QHA} = C_P - C_V$ at $2 \times 2 \times 2$ supercell (96 atoms). Computed values of $\Delta C^{QHA} = C_P - C_V$ at $3 \times 3 \times 3$ supercell (342 atoms) overshoot analogous values obtained based on a $2 \times 2 \times 2$ supercell (96 atoms) within 6%. Thus, we elect to obtain all the thermo-elastic properties of terbium dioxide based on a $2 \times 2 \times 2$ supercell. As another benchmark of accuracy, we calculate total free energies against terbium unit cell's volume (see Figure 6.4) reproducing the experimental lattice constant as explained in section 6.3.1. Thus, all values reported herein are based on $2 \times 2 \times 2$ supercell.

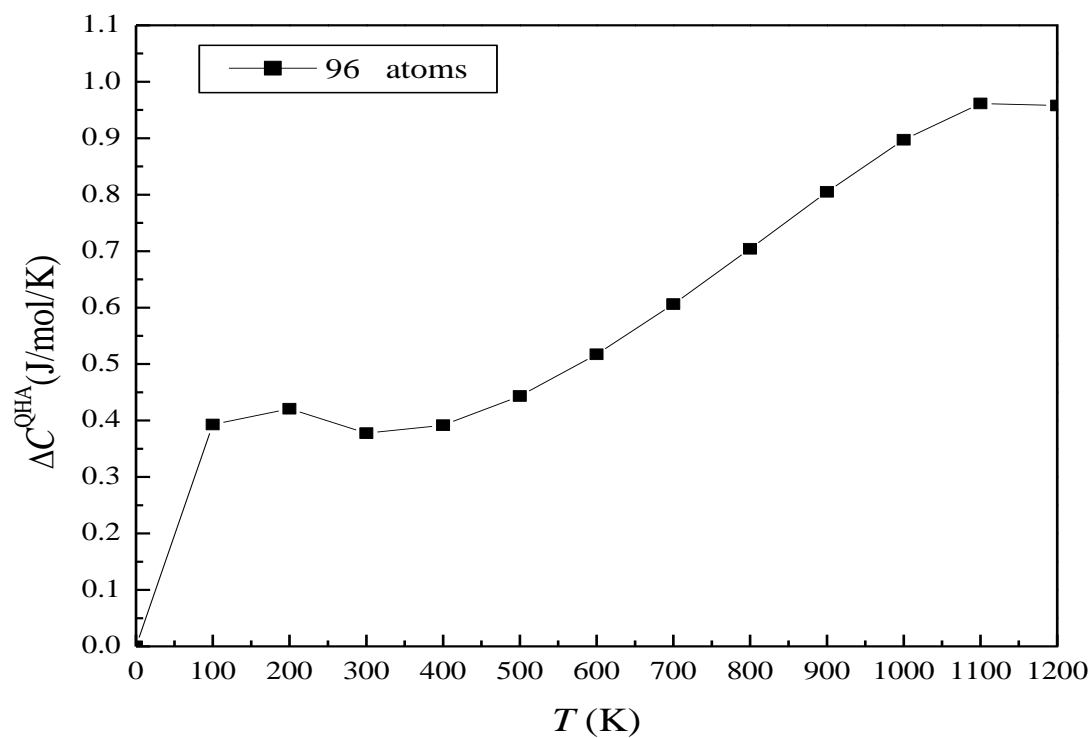


Figure 6.3: Values of ΔC^{QHA} for fluorite-structure.

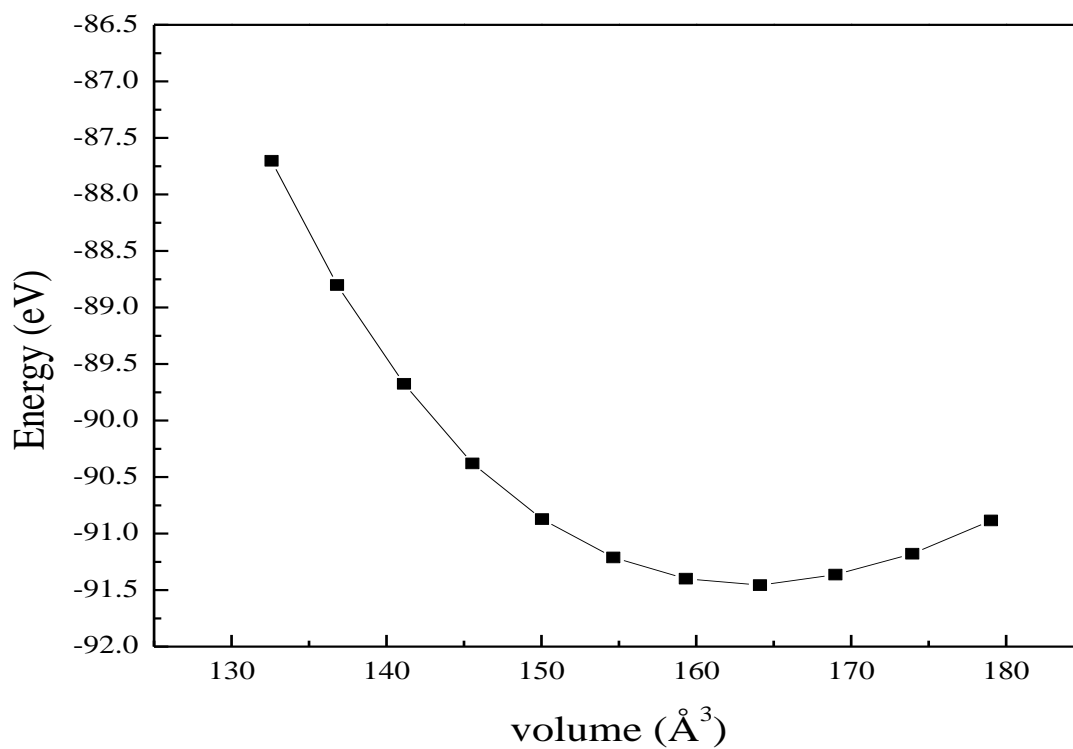


Figure 6.4: Calculated free energies in eV as a function of unit-cell volume in \AA^3 for bulk TbO_2 .

Figure 6.5 shows the calculated phonon dispersion of relaxed TbO_2 structure at ground state (zero temperature and zero pressure). As Figure 6.6 portrays, bulk modulus curves exhibit a T -dependent reducing behavior. Figure 6.7 presents the variation of pressure-constant heat capacities C_P with the temperature at various values of pressures for TbO_2 . By inspection of this Figure, it becomes apparent that C_P values vary rather very slightly with the pressure. Figure 6.8 displays that, calculated thermal expansions of terbium lattice inversely correlate with the applied pressure. Finally, V/V_0 (V_0 corresponds to the equilibrium volume of TbO_2 at T and $P = 0$) has been calculated as a function of temperature and pressure. As expected, the V/V_0 ratios decrease with the applied pressures as evident in Figure 6.9.

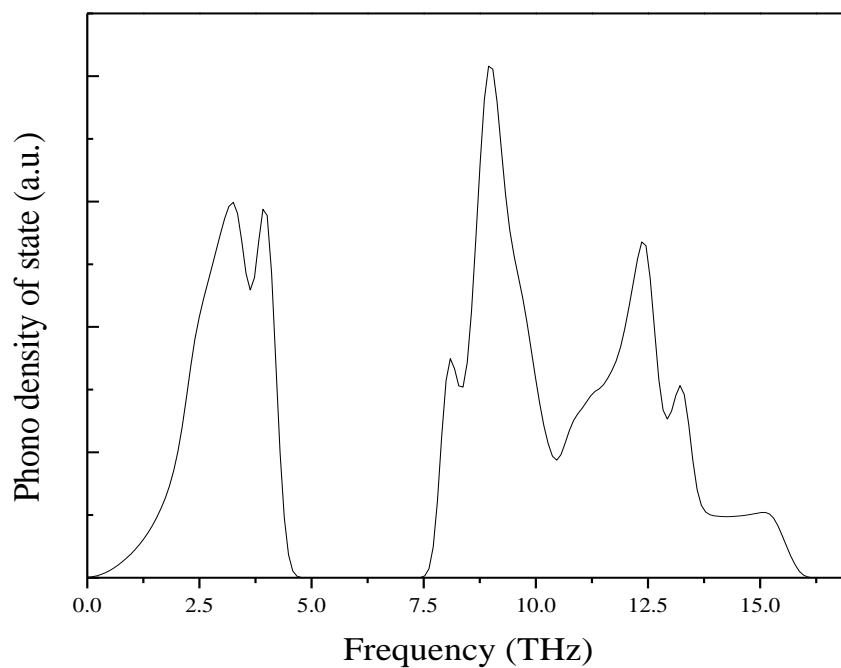


Figure 6.5: Phonon density of states for bulk TbO_2 .

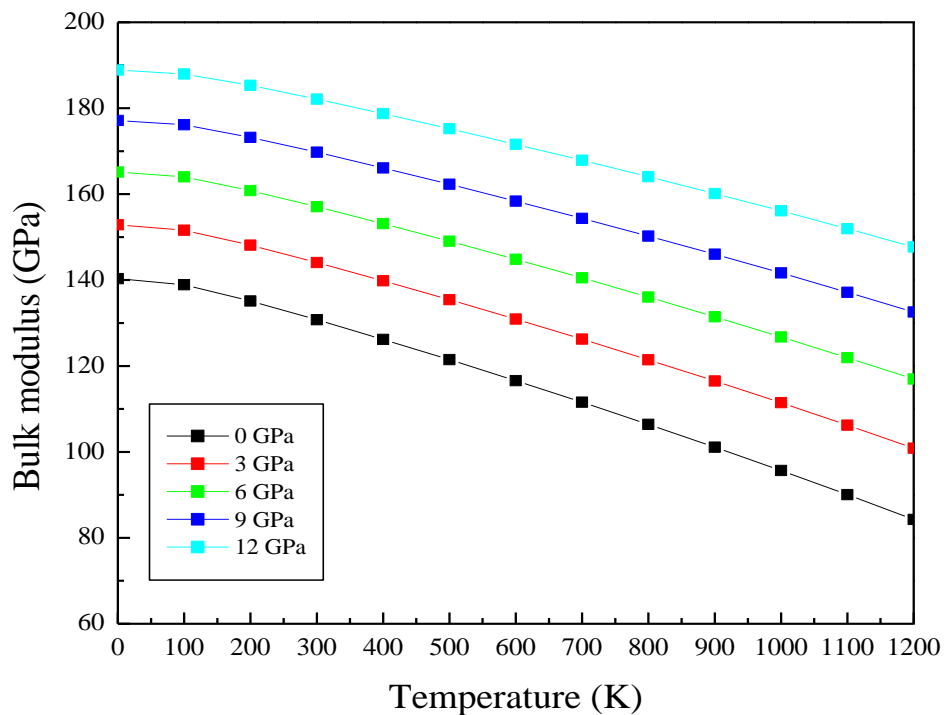


Figure 6.6: Variation of Bulk modulus of TbO₂ with temperature and pressure.

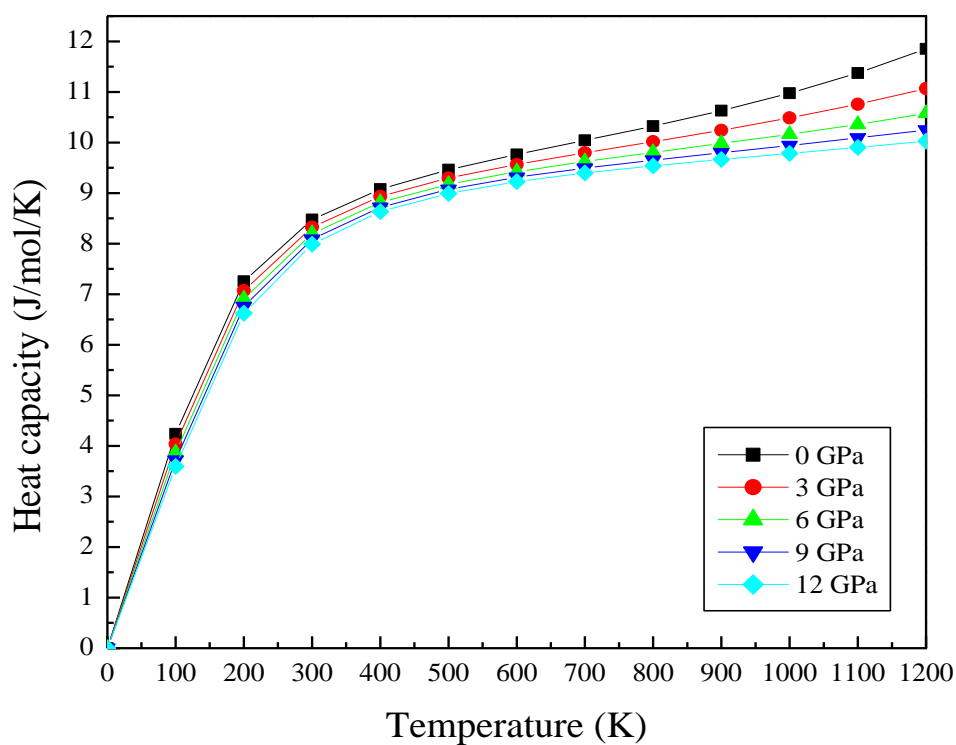


Figure 6.7: Heat capacities in J/mol.K per mol of TbO₂ at different pressures as a function of temperature in K.

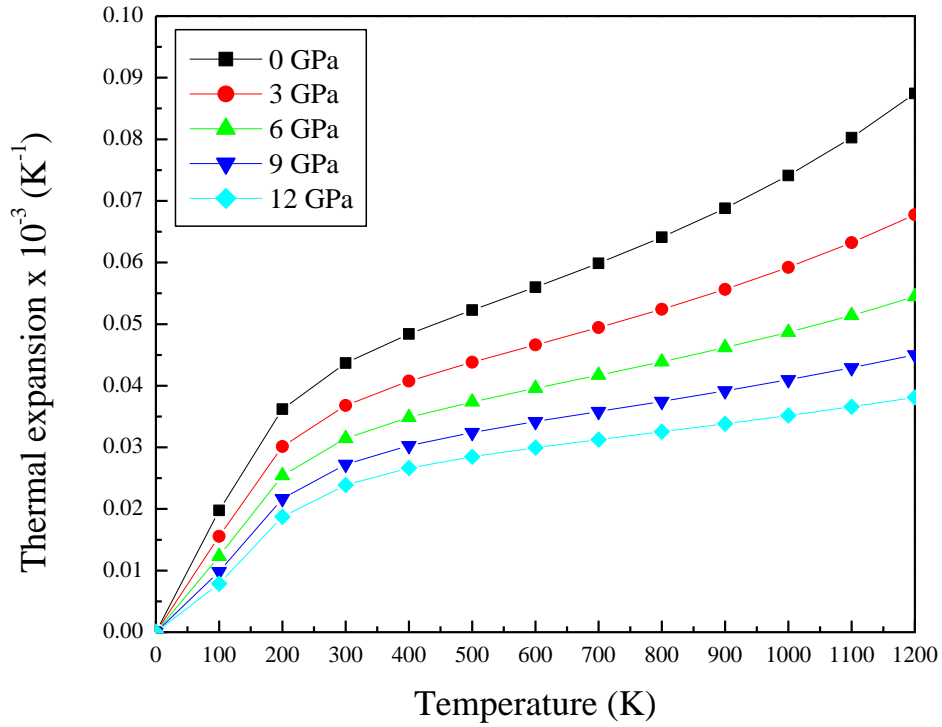


Figure 6.8: Thermal expansion of terbium dioxide as a function of temperature and pressure.

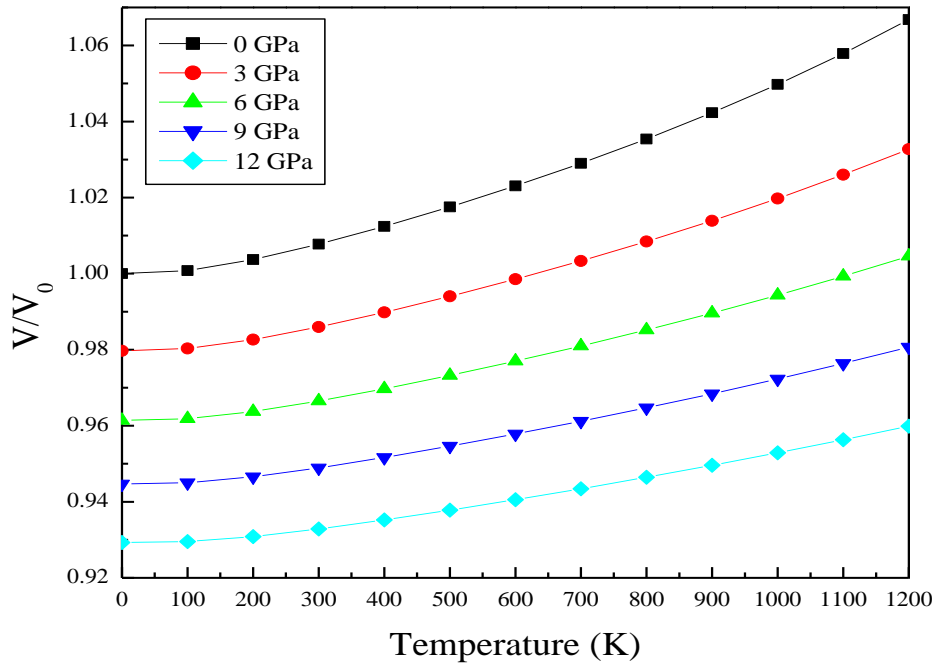


Figure 6.9: Dependence of V/V_0 on temperatures and pressures.

6.3.3. Optimized geometries of low - index surfaces of TbO₂

Three low-index structures (slabs) were created by cleaving the bulk along (100), (110) and (111) directions. (100) orientation exhibits two surface terminations, namely (100):Tb and (100):O (Figure 6.10). On the other hand, the (110) direction displays only one stoichiometric surface termination denoted as a (110):TbO (Figure 6.11). Cutting the bulk of TbO₂ towards (111) direction affords differently three cases of surfaces. A trilayers termination ordered as O-Tb-O is symbolized as (111). The second orientation is terminated with O atoms only and thereafter denoted as the (111):O configuration. The final probable surface is that one terminated with Tb atoms and signified as a (111):Tb (Figure 6.12). Two of the six ideal surface terminations are stoichiometric at the surface; however; the rest are polar planes, having an excess of oxygen or of terbium atoms. Interlayer spacing have been computed as $d = (d_{ij} - d_0) / d_{ij} \times 100 \%$, in which d_{ij} is the interlayer spacing between i^{th} and j^{th} atomic layers (for the (100) and the (110) surfaces) and d_0 is the bulk interlayer spacing. As a special case for (111) surfaces, which their slabs consist of only three trilayers, we consider d_{ij} as the distance between the last sublayer in the first trilayers and the first sublayer in the next trilayers.

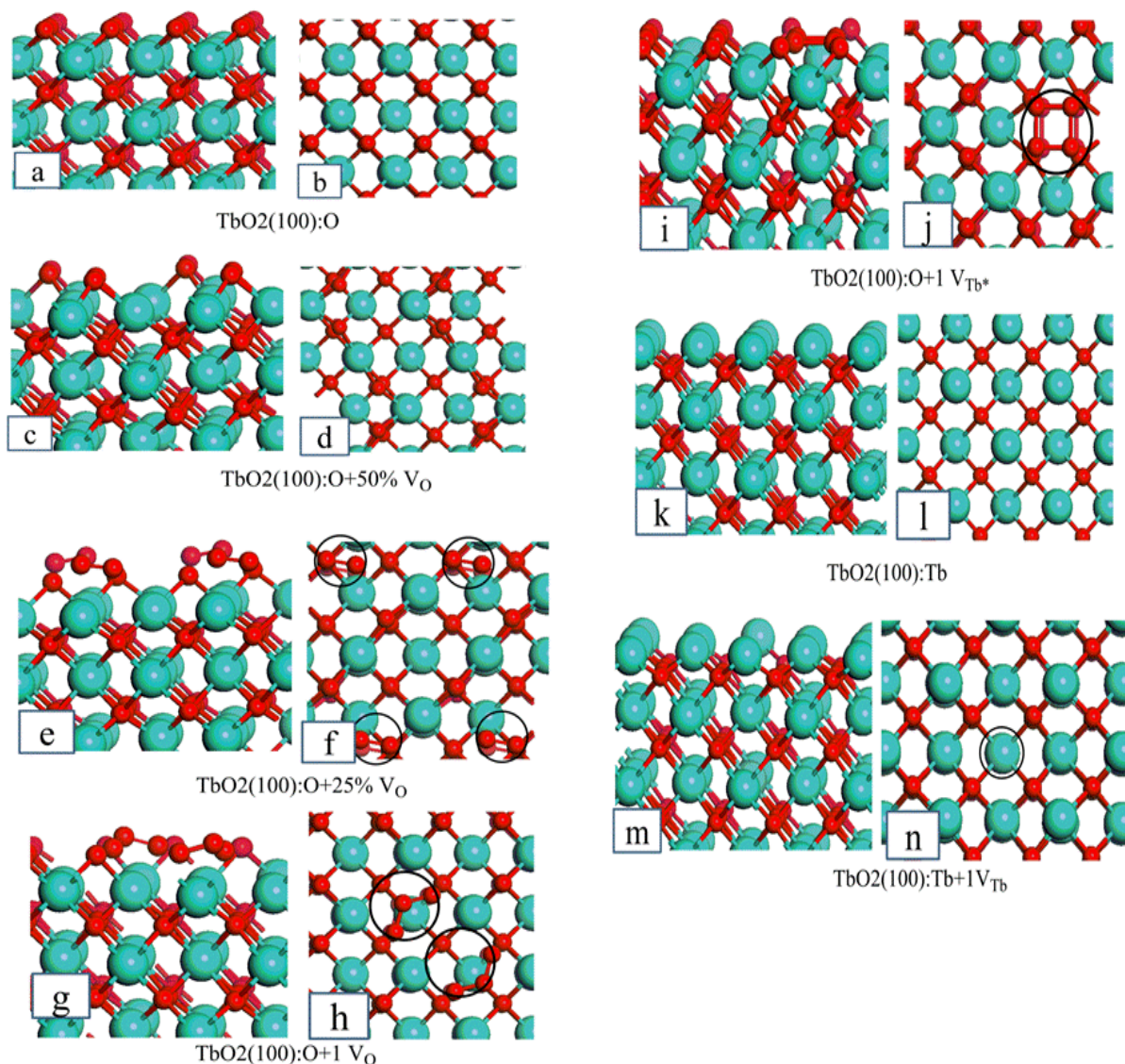


Figure 6.10: Side and top views of different terminations of TbO₂ (100) surface: (a) and (b) are TbO₂ (100) :O, (c) and (d) are TbO₂ (100) :O with 50% surface oxygen vacancies, (e) and (f) are TbO₂ (100) :O with 25% surface oxygen vacancies, (g) and (h) represent TbO₂ (100) :O with one surface oxygen vacancy, (i) and (j) are TbO₂ (100) :O with one subsurface terbium vacancy, (k) and (l) correspond to TbO₂ (100) :Tb, (m) and (n) symbolize TbO₂ (100) :Tb with one surface terbium vacancy. Light blue and red spheres denote Tb and O atoms, respectively.

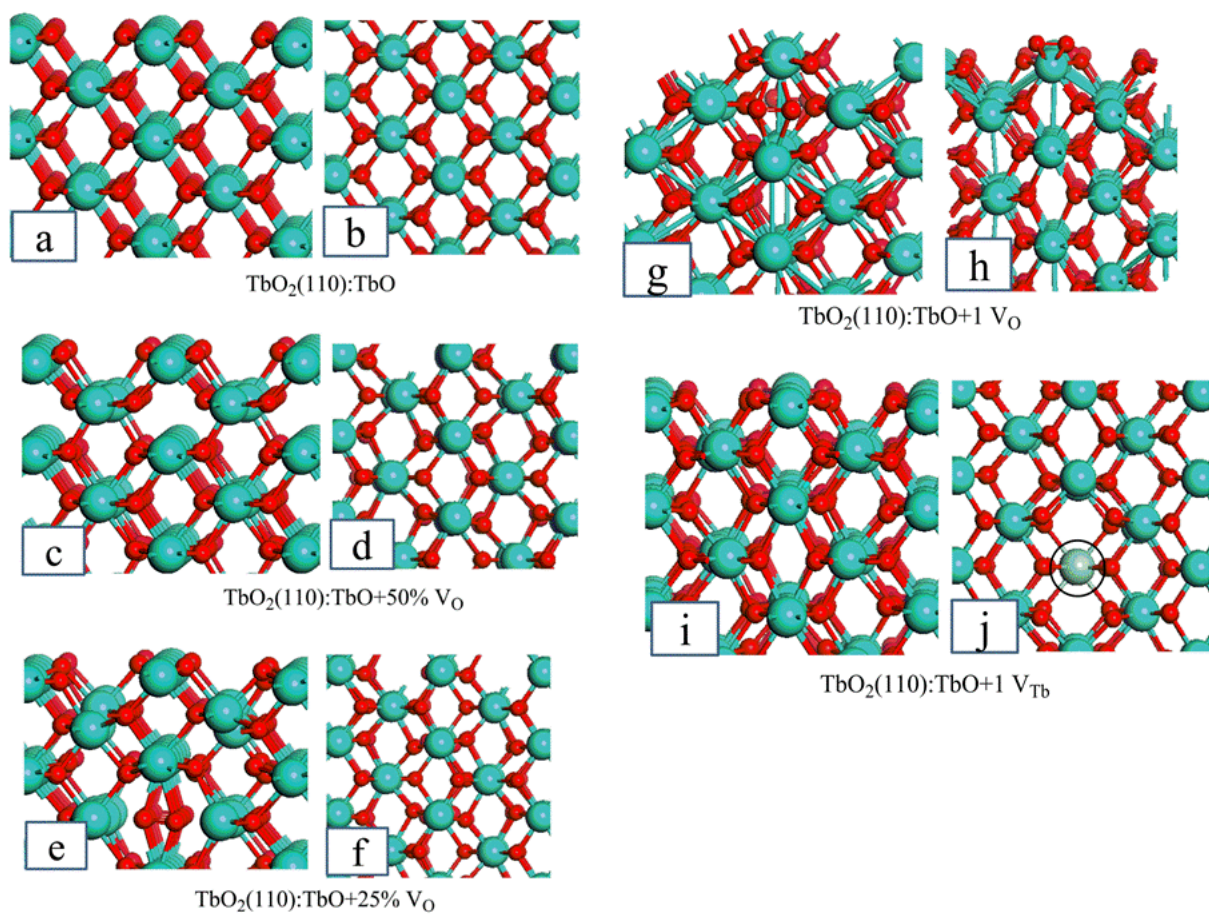


Figure 6.11: Side and top views of different optimized terminations of TbO_2 (110) surface. Light blue and red spheres denote Tb and O atoms, respectively.

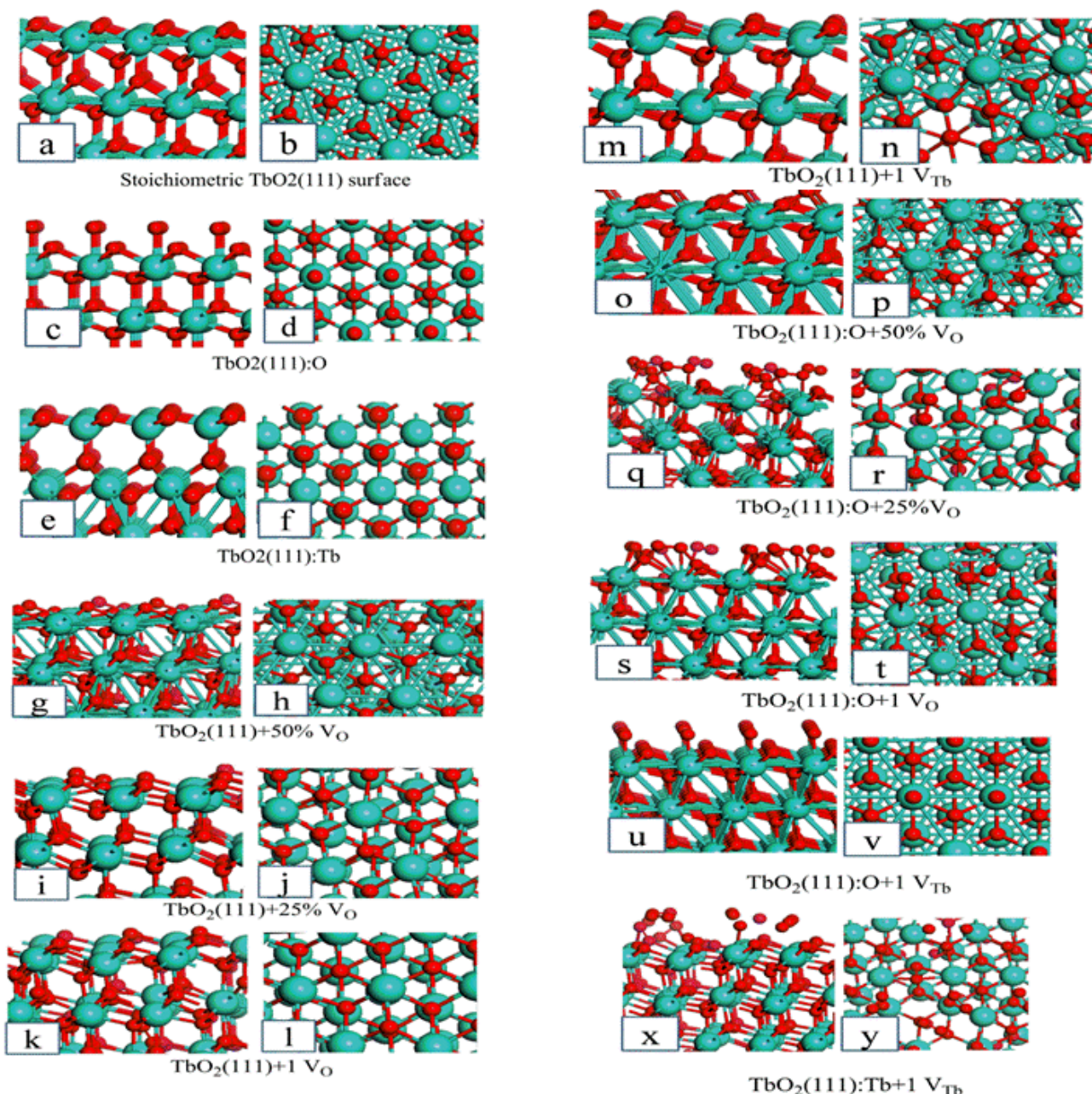


Figure 6.12: Side and top views of different terminations of TbO_2 (111) surface: (a) and (b) are TbO_2 (111), (c) and (d) represent TbO_2 (111):O, and (e) and (f) are TbO_2 (111):Tb. (g) and (h) are TbO_2 (111) with 50% surface oxygen vacancies, (i) and (j) are TbO_2 (111) with 25% surface oxygen vacancies, (k) and (l) represent TbO_2 (111) with one surface oxygen vacancy, (m) and (n) are TbO_2 (111) with one subsurface terbium vacancy, (o) and (p) correspond to TbO_2 (111):O with 0.5 surface oxygen vacancies, (q) and (r) signify TbO_2 (111):O with 0.25 surface oxygen vacancies, (s) and (t) symbolize TbO_2 (111):O with one surface oxygen vacancy, (u) and (v) are TbO_2 (111):O with one subsurface terbium vacancy,. Light blue and red spheres denote Tb and O atoms, respectively.

The analysis of optimized slabs suggested that, the surface structures and their terminations experienced noticed relaxations. For the (110) ideal surface, the Tb-O bond length at the surface is 2.29 Å, largely matching their corresponding bulk values (2.34 Å), whereas the first interlayer spacing is slightly expanded (~ 3%). For both non-reduced (100) surfaces, (100):O and (100):Tb, Tb-O bond distances ($d_{\text{Tb-O}}$) are contracted with regard to their bulk values (2.28 and 2.11 Å for $\text{TbO}_2(100):\text{O}$ and $\text{TbO}_2(100):\text{Tb}$), namely by -1.7 % and -9.2%, respectively. For (111) surfaces, the (111):Tb slab undergoes a significant reconstruction in that it has been cleaved initially to have Tb in the outermost layer whereas the optimized configurations is terminated with only O atoms (Figure 6.12). This behavior mimics the analogous observed trend in case of in its final CeO_2 [386]. This is due to the significant outward displacement of the oxygen atoms in the second layer. Upward displacement for electronegatively charged atoms was also observed in case of CuCl_2 , FeCl_2 and Co_2CuO_3 [394, 399]. Table 6.1 enlists the deviation values of interlayer spacing for all the optimized surface structures from their analogous bulk values. As observed from the table, the relaxed structures are experiencing changes in the interlayer spacing. This is ascribed to the upward and downward displacements occurring at the first three layers in all the optimized slabs.

Table 6.1: Deviations of interlayer spacing of the topmost two layers in the relaxed slabs in reference to their analogous bulk values Δd_{ij} .

Surface	$\Delta d_{12} / \text{\AA}$	$\Delta d_{23} / \text{\AA}$
(100):O	-0.055	-0.003
(100):O+0.50 V_O	0.020	-0.160
(100):O+0.25 V_O	0.221	-0.207
(100):O+ 1 V_O	0.056	-0.075
(100):O+ 1 V_{Tb}	-0.175	0.073
(100):Tb	-0.444	0.146
(100):Tb + 1 V_{Tb}	-0.401	0.079
(110):TbO	0.028	0.042
(110):TbO + 0.50 V_O	-0.069	0.066
(110):TbO + 0.25 V_O	-0.023	0.029
(110):TbO + 1 V_O	0.056	0.059
(110):TbO + 1 V_{Tb}	0.028	0.051
(111)	-0.426	0.162
(111) + 0.50 V_O	0.188	-0.080
(111) + 0.25 V_O	0.080	0.026
(111) + 1 V_O	-0.067	0.106
(111) + 1 V_{Tb}	-0.260	0.148
(111):O	-0.260	0.076
(111):O + 0.50 V_O	-0.830	-0.056
(111):O + 0.25 V_O	-0.675	0.112
(111):O + 1 V_O	-0.244	0.002
(111):O + 1 V_{Tb}	0.098	-0.006
(111):Tb	-0.404	-0.187

Defect surfaces have occupied a growing interest in catalyst-related research [385, 400-402]. This is due to its capability in reference to their perfect surfaces in lowering the dissociation energies of adsorbate species such as volatile organic compounds (VOCs) [403] acting as a surface-host for light dissociated fragments. Consequently, this chapter has also included the

influences of surface defects on the surface stability via removing O and Tb atoms from the first layer in the perfect slabs. Herein, we consider surfaces with 25%, 50% of removed O atoms and one Tb atom in its outermost layer. Figure 6.10 shows optimized geometries for these considered defect surfaces. For instance the (100):O+0.25 V_O denotes a (100):O surface with 25% oxygen surface vacancy. In these defect surfaces, trioxygen (O_3) and oxygen square planar cluster (O_4) have been created by (100):O+1 V_O and (100):O+1 V_{Tb} , respectively.

Bader's theory [404] provides a precise algorithm to calculate partial charge density of individual atoms in molecules. Table 6.2 lists charge density values calculated for selected Tb and O atoms in the first two topmost atomic layers in the slabs. Tb and O atoms carry net charges of +2.21 e and -1.10 e in the bulk TbO_2 structure. Charges values of Tb and O in the second surface layers of all the slabs approach relatively the analogous charges' values in bulk Tb and O atoms. Tb and O atoms in the first layers of structures hold charges deviated from their corresponding ones in the bulk configuration. All in all, high positively and negatively charged for Tb and O atoms in all the slab structures reveal ionic nature of Tb-O bond in the TbO_2 surfaces. This trend of ionic bonding was also observed with Ce-O bond in the cleaved corresponding fluorite- structure CeO_2 [405]. Our analysis on the charge's distributions demonstrates that, the charge densities on the neighboring Tb atoms become more positive as oxygen vacancies are created. However, it shall be noted that creation of vacant oxygen sites requires noticeable activation energies [406, 407]. Estimation of these activation energies and their associated random-access memory in case of TbO_2 will be investigated in a due course.

Table 6.2: Calculated Bader's charges in electron (e) on the Tb and O atoms in TbO₂ surfaces.

Surface	Tb1	Tb2	O1	O2
(100):O	2.14	2.20	-0.51	-1.11
(100):O+0.50 V _O	2.16	2.22	-0.76	-1.25
(100):O+0.25 V _O	2.16	2.22	-0.23	-0.89
(100):O+ 1 V _O	2.21	2.22	-0.44	-0.63
(100):O+ 1 V _{Tb}	2.22	2.17	-0.86	-0.33
(100):Tb	1.81	2.20	-1.36	-1.19
(100):Tb + 1 V _{Tb}	1.87	2.21	-1.33	-1.14
(110):TbO	2.17	2.22	-1.00	-1.21
(110):TbO + 0.50 V _O	2.06	2.18	-1.45	-1.35
(110):TbO + 0.25 V _O	2.16	2.20	-1.23	-1.27
(110):TbO + 1 V _O	2.17	2.22	-1.01	-1.25
(110):TbO + 1 V _{Tb}	2.19	2.23	-0.96	-1.15
(111)	2.21	2.19	-1.30	-0.86
(111) + 0.50 V _O	2.14	2.20	-1.19	-1.39
(111) + 0.25 V _O	2.18	2.15	-1.16	-1.16
(111) + 1 V _O	2.14	2.14	-1.19	-1.26
(111) + 1 V _{Tb}	2.20	2.20	-1.17	-0.82
(111):O	2.21	2.24	-0.20	-0.70
(111):O + 0.50 V _O	2.23	2.23	-0.29	-0.94
(111):O + 0.25 V _O	2.16	2.23	-0.05	-0.37
(111):O + 1 V _O	2.16	2.16	-0.24	-0.75
(111):O + 1 V _{Tb}	2.20	2.23	-0.08	-0.20
(111):Tb	2.04	2.17	-1.42	-1.39

6.3.4. Stability phase diagrams for TbO₂ surfaces

In order to assess the stability of the various oxide surfaces when they are in contact with an oxygen atmosphere, we applied Equations 6.4 and 6.5 (section 6.3) to plot the surface Gibbs free energy against the change of oxygen chemical potential $\Delta\mu_o$. Based on Equation 6.6, we calculate the surface Gibbs free energy $\gamma(T, P)$ as a function of $\Delta\mu_o$ for a wide range of oxygen pressures and temperatures. The values of $\Delta\mu_o(T, P)$ can practically change solely between two limits, namely oxygen-lean and oxygen-rich. These two limits denote the experimental accessible conditions of the chemical potential of oxygen in case of bulk TbO₂. The oxygen-lean limit corresponds to the value of $\Delta\mu_o(T, P)$ at which bulk TbO₂ starts to formulate when it is present in an oxygen gas environment, whereas the oxygen-rich limit refers to the onset of destruction of oxygen gas (O₂) into oxygen atoms. The O-rich and O-lean limits take values of 0.0 and -4.5 eV, respectively. These magnitudes are typically bounded by $\frac{1}{2}\Delta H_f(O_2)(p = 0, T = 0 K) < \Delta\mu_o(pO_2, T) < 0$ [237]. $\Delta H_f(O_2)$ represents the enthalpies of formation values per oxygen molecule for TbO₂ calculated by Equation 53 and it amounts to -9 eV. Table 6.3 tabulates $\gamma(T, P)$ values at the two oxygen limits. The $\gamma(T, P)$ values between these two boundaries. Figures 6.13, 6.14 portray thermodynamic stability lines of TbO₂ perfect surfaces with respect to the change of oxygen chemical potential values $\Delta\mu_o(T, P)$, along with pressure bar lines at different temperatures of T of 800, 1000, 2000 and 2500 K, and with corresponding temperature bar lines at different pressures of $P = 1$ atm and 10^{-12} atm. It is evident that all considered surfaces exhibit T -dependent trends. Figure 6.15 plots surface free energies for the most stable surfaces among all configurations. The (111):O+1V_O surface remains the most stable configuration across the accessible range of oxygen chemical potential while the (111):Tb surface holds more stability in the vicinity of the lean-limit of the oxygen chemical potential. The stability of the latter surface is in accord with the analogous finding pointing to the stability of the (111):Ce surface in case of CeO₂ terminations [187]. Nonetheless, elucidating explanations into the profound stability of the (111):O+1V_O requires careful considerations. In fact, it has been shown that several structural as well as electronic factors contribute to the ordering of chemical thermodynamic stability. The thermodynamic stability of the (111):O+1V_O over other surfaces follow the general consensus that reduced surfaces having an excess of electro negatively charged atoms such as O [384, 408, 409] often hold more thermodynamic stability in reference to stoichiometric surfaces. However, other structural and electronic factors may also contribute

to the thermodynamic stability trend. These factors include surface relaxation, amount of the net charge in the upper layer and the polarity of the surface [384].

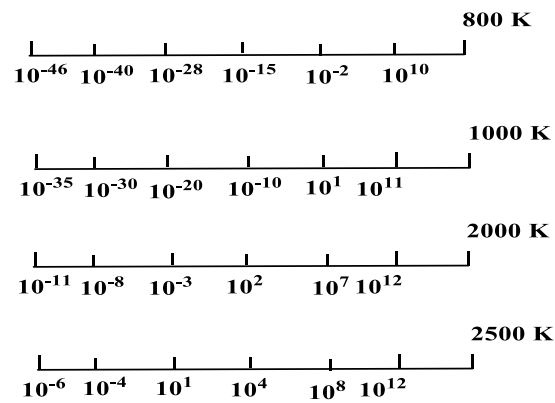
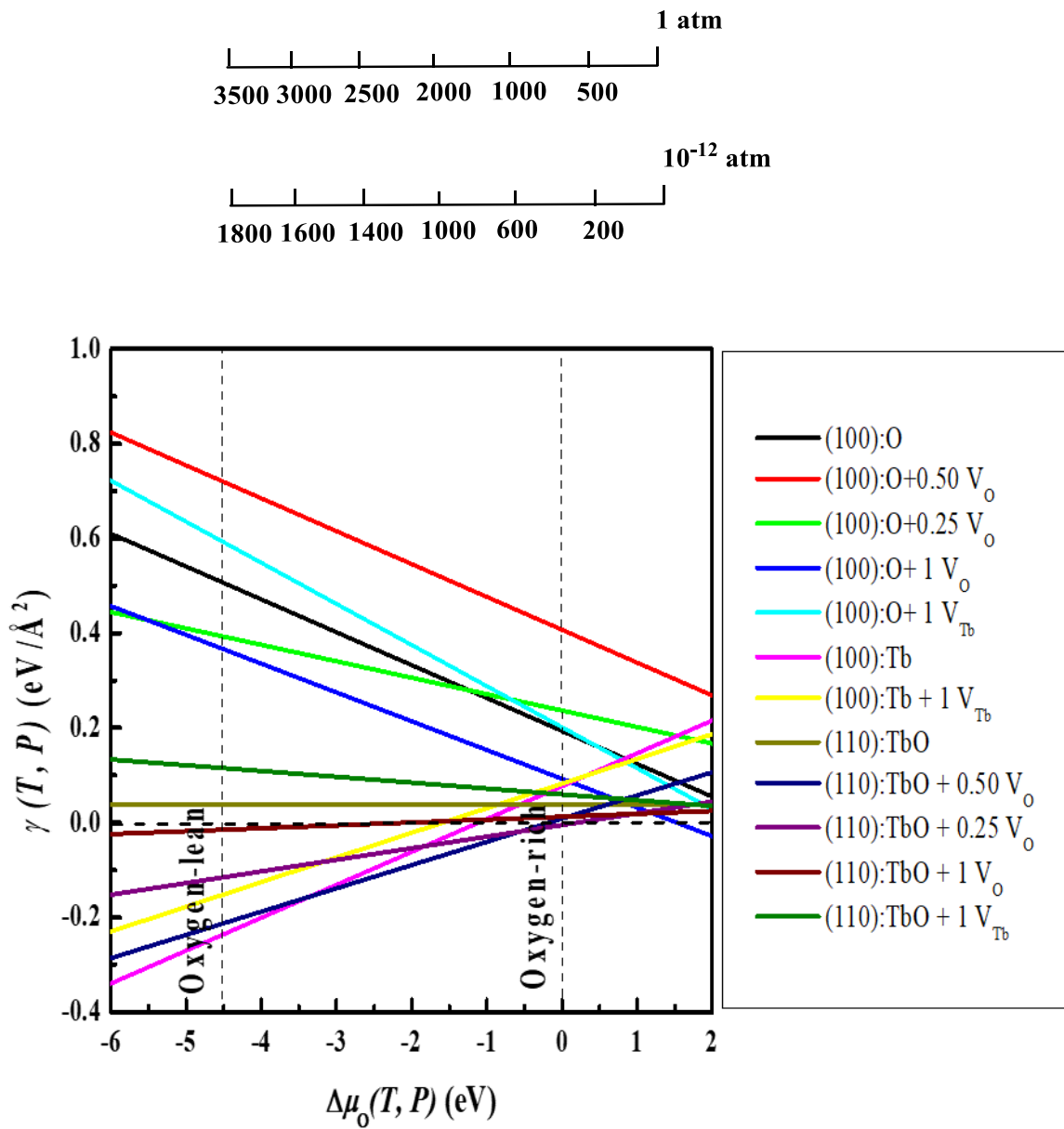


Figure 6.13: Calculated surface free energy of different TbO_2 (100) and TbO_2 (110) surfaces as a function of the change in oxygen chemical potential $\Delta\mu_o$ with the analogue pressure bar lines at different temperatures of T of 800, 1000, 2000 and 2500 K, and with corresponding temperature bar lines at different pressures of $P=1$ atm and 10^{-12} atm.

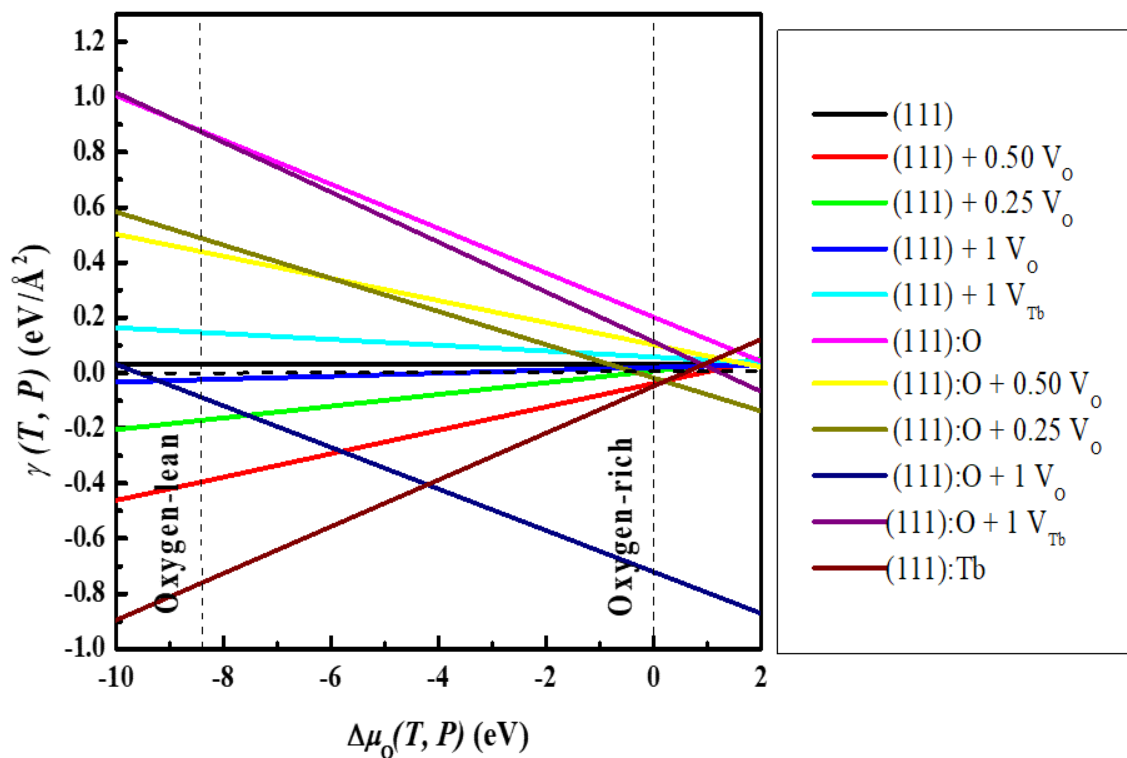


Figure 6.14: Calculated surface free energy of different TbO_2 (111) surfaces as a function of the change in oxygen chemical potential $\Delta\mu_o$.

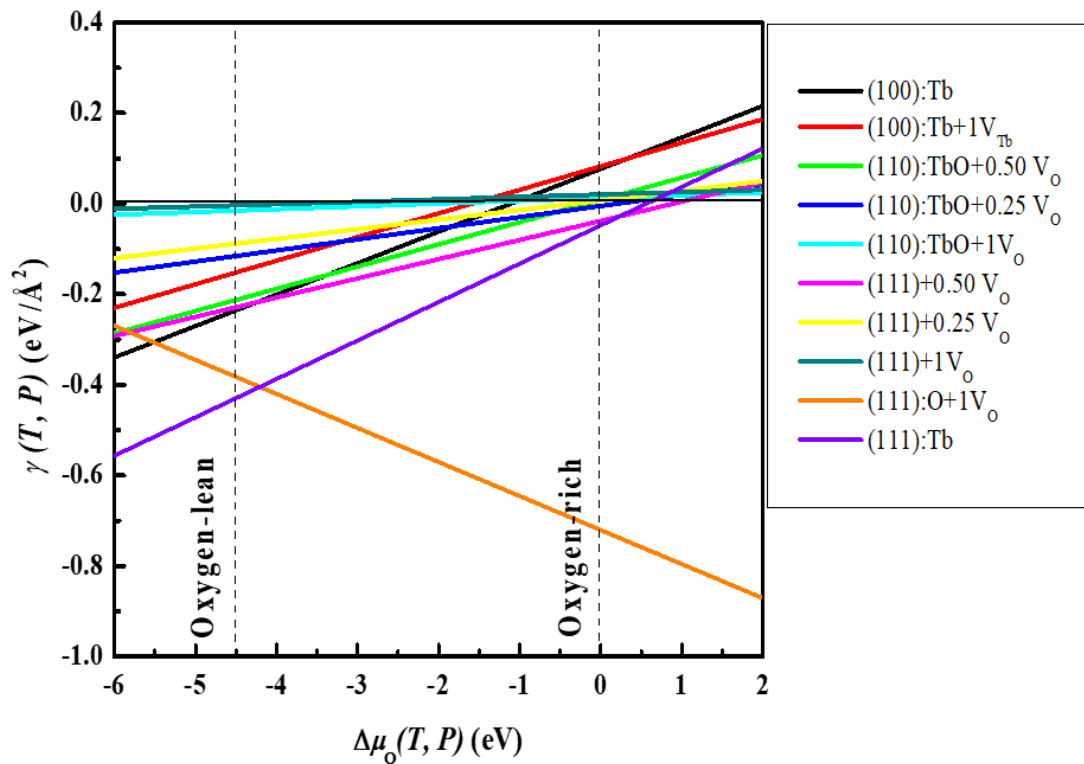


Figure 6.15: Calculated surface free energy for the most stable cases of the three plausible TbO₂ surfaces as a function of the change in oxygen chemical potential $\Delta\mu_o$.

Table 6.3: Gibbs free energy γ (T, P), in eV/ \AA^2 , for all surfaces at oxygen- lean and oxygen- rich limits.

Surface	Oxygen- lean limit	Oxygen- rich limit
(100):O	-0.240	0.19
(100):O+0.50 V_O	-0.215	0.40
(100):O+0.25 V_O	-0.155	0.23
(100):O+ 1 V_O	-0.117	0.09
(100):O+ 1 V_{Tb}	-0.012	0.20
(100):Tb	0.037	0.07
(100):Tb + 1 V_{Tb}	0.120	0.08
(110):TbO	0.365	0.03
(110):TbO + 0.50 V_O	0.390	0.008
(110):TbO + 0.25 V_O	0.500	-0.004
(110):TbO + 1 V_O	0.590	0.01
(110):TbO + 1 V_{Tb}	0.720	0.05
(111)	-0.430	0.031
(111) + 0.50 V_O	-0.380	-0.037
(111) + 0.25 V_O	-0.237	0.007
(111) + 1 V_O	-0.090	0.02
(111) + 1 V_{Tb}	-0.005	0.06
(111):O	0.032	0.20
(111):O + 0.50 V_O	0.105	0.10
(111):O + 0.25 V_O	0.25	-0.01
(111):O + 1 V_O	0.28	-0.72
(111):O + 1 V_{Tb}	0.52	0.11
(111):Tb	0.57	-0.04

6.4. Conclusions and future directions

First-principles DFT calculations combined with quasi harmonic approximation (QHA) are deployed to obtain geometric, electronic and thermo-mechanical properties of terbium oxide (TbO_2). The bulk lattice parameter and electronic density of state configuration are in line with those reported in the literature. Our thermodynamic analysis demonstrates that the supercell of $2 \times 2 \times 2$ suffice to achieve convergence in the optimum adopted size for accurately calculating all the thermos-elastic properties. We reported the structural and electronic properties of the three low-Miller indices surfaces of TbO_2 along with various surface terminations. Bader's charges calculations for the bulk and surface suggested that, the three low-index surfaces retain the ionic nature for the Tb-O bond as they are in the terbia bulk. Stability phase diagram plots indicated that, find out the terbium-terminated surface along the 111 orientation (111):Tb to be the most thermodynamically stable configuration in the closeness of oxygen-lean region, whereas the (111):O+1V_O exhibits a profound stability under a wide range of oxygen chemical potential. The presence of O surface voids may entail excellent catalytic character and the effect of these structural defects on mediating chemical reactions warrants further investigations.

Chapter 7 : Influence of DC magnetron sputtering reaction gas on structural and optical characteristics of Ce-oxide thin films

Paper VI

Miran, H.A., Jiang, Z-T, Altarawneh, M., Veder, J-P, Zhou, Z-F, Rahman, M.M., Jaf, Z.N. and Dlugogorski, B.Z. (2018) Influence of DC magnetron sputtering reaction gas on structural and optical characteristics of Ce-oxide thin films. *Ceramics International*, 44(2018). pp. 16450-16458.

7.1 Abstract

The influence of the reaction gas composition during the DC magnetron sputtering process on the structural, chemical and optical properties of Ce-oxide thin films was investigated. X-ray diffraction (XRD) studies confirmed that all thin films exhibited a polycrystalline character with cubic fluorite structure for cerium dioxide. X-ray photoelectron spectroscopy (XPS) analyses revealed that cerium is present in two oxidation states, namely as CeO₂ and Ce₂O₃, at the surface of the films prepared at oxygen/argon flow ratios between 0-7%, whereas the films are completely oxidized into CeO₂ as the aforementioned ratio increases beyond 14%. Various optical parameters for the thin films (including an optical band gap in the range of 2.25 – 3.1 eV) were derived from the UV-Vis reflectance. A significant change in the band gap was observed as the oxygen/argon flow ratio was raised from 7% to 14% and this finding is consistent with the high-resolution XPS analysis of Ce 3d that reports a mixture of Ce₂O₃ and CeO₂ in the films. Density functional theory (DFT+*U*) implemented in the Cambridge Serial Total Energy Package (CASTEP) was carried out to simulate the optical constants of CeO₂ clusters at ground state. The computed electronic density of states (DOSs) of the optimized unit cell of CeO₂ yields a band gap that agrees well with the experimentally measured optical band gap. The simulated and measured absorption coefficient (α) exhibited a similar trend and, to some extent, have similar values in the wavelength range from 100 to 2500 nm. The combined results of this study demonstrate good correlation between the theoretical and experimental findings.

7.2 Introduction

Rare-earth oxides have emerged as interesting materials in diverse optical and electronic applications. Among this family of materials, Ce-oxide has received particular attention due to it exhibiting a number of remarkable properties stemming from its ability to shuttle between two oxidation states (+4 and +3) of CeO₂ and Ce₂O₃ [270], high oxygen storage capacity [410] and ability to support deviations in its stoichiometry whilst maintaining a fluorite structure[411]. In particular, CeO₂ has garnered significant interest for its application to the fields of catalysis[412], gas, temperature, radiation and humidity sensing [413], along with capacitor devices [414] and field-effect transistors [415]. The desirable properties exhibited by Ce-oxide materials also make them promising candidates in other areas, including: an alternative to silicon in integrated circuits due to the similarity in lattice parameters between CeO₂ and silicon [416]; transparent materials in smart window technologies due to their ability to insert and extract large charge densities [417] ; and also as single and multilayer optical coatings for solar energy applications due to their high refractive index [418-420].

The influence of various synthesis parameters on the resultant properties of Ce-oxide films has been demonstrated in several previous studies. Porqueras and co-authors [421] evaluated the influence of oxygen partial pressure on the structural and optical properties of cerium dioxide (CeO₂) on different substrates using an *e*-beam PVD method. Their structural analysis demonstrated that all of the structural characteristics apart from stoichiometry are sensitive to changes in the oxygen pressure/flow rate. Whilst their investigations for the optical transmittance properties of the samples studied in the visible range of 400 – 800 nm displayed remarkable high values, the study did not include a comprehensive investigation of the influence of other conditions such as deposited rate and substrate temperature nor did assess the loss factors for the selected samples. In separate work, Debnath *et al.* prepared CeO₂ films *via* an *e*-beam evaporation process onto glass substrates at a pressure of 6×10^{-6} Torr and with different film thicknesses from 140 to 180 nm. The studied films in the wavelength ranging from 200 to 850 nm showed excellent transparency properties in the visible region, whilst exhibiting low reflectance values in the ultra-violet region. Furthermore, the optical band gap of the films decrease with the increase of the thickness [422]. Özar *et al.* [165], employed a sol-gel spin coating technique to prepare crystalline CeO₂ coatings and investigated the optical and electronic properties of such thin films. The XPS analyses revealed the films possess a compositional structure of CeO₂ and the surface

topography, examined by scanning electron microscopy (SEM), demonstrated a good uniformity and homogeneity. The authors also reported CeO₂ films exhibit high electrochemical stability based on the results of cyclic voltammetry and spectroelectrochemical experiments. The experimental analyses of the CeO₂ coatings indicated a good passive counter electrode material in terms of inserted / extracted charge and optical response.

In other instances, magnetron sputtering has been investigated and applied as a promising approach to prepare Ce-oxide films. Sundaram *et al.* [423] prepared CeO₂ coatings on glass substrates *via* r.f. magnetron sputtering using a number of sputtering power levels and oxygen pressures. They found that at a 100 W sputtering power level the deposition rate increased with increasing oxygen/argon flow ratio compared to the sputtering power levels of 150, 170 and 200 W which showed minimal change to the deposition rate. In addition, the maximum deposition rate was achieved at O₂/Ar₂ of 0.45 and 0.60. Further increases in the oxygen pressure resulted in decreases in the deposition rate. Jain *et al.* synthesized CeO_x thin films deposited onto Si and quartz substrates by reactive DC magnetron sputtering technique [167]. The films were prepared as a function of target-substrate distance (d_{T-S}) and characterized by a number of characterization techniques such as XRD, atomic force microscopy (AFM) and UV-Vis. The study revealed that the structural and optical characteristics of the deposited films are strongly dependant on the target-substrate distance. They also concluded the synthesized films exhibit good characteristics of transmittance in the wavelengths range of 400 - 1100 nm.

Shi *et al.* [424, 425] previously investigated the surface morphology, wetting behaviour, microstructure, tribological and mechanical properties of CeO_{2-y} films deposited onto Si substrates by reactive unbalanced magnetron sputtering using different oxygen/argon flow ratios and substrate bias voltages. Regarding the influence of the substrate bias voltage, the CeO_{2-y} coatings possessed a hydrophobic nature with water contact of nearly 100 °C. The preferable phase formation of cubic crystalline CeO₂ occurred at bias voltage of -80 V, with significant enhancements to the microstructure evident at higher voltages resulting in an increase in material hardness, yielding a maximum value of -18.0 GPa. For Ce-oxide films prepared as a function of oxygen/argon flow ratio, all coatings exhibited smooth surfaces

with similar wetting characters with a hydrophobic nature. They also concluded that the hydrophobicity lessens with the existence of excess surface lattice oxygen. Furthermore, at 7% oxygen/argon flow ratio, they achieved a maximum hardness, and elastic modulus of -18.1 and -190.2 GPa, respectively; however; these two mechanical properties decrease with subsequent increases to the oxygen/argon flow ratio.

It is apparent from the above discussion that the characteristics of Ce-oxide thin films prepared via different techniques vary somewhat significantly depending on the preparation technique employed. This also opens up the interesting prospect of tuning the properties of Ce-oxide films for certain applications by exploiting the inherent variability that the synthesis parameters have on the resultant film properties. It is also apparent from prior literature that there is scope to improve the optical properties of Ce-oxide coatings. We propose that this can be achieved via a study of the amount of oxygen flow effects on the optical properties of CeO_x, as prepared by DC magnetron sputtering. In this instance, DC magnetron sputtering is the preferred technique to synthesize the thin film materials because the optimal plasma distribution can result in excellent adhesion between the thin films and the substrates. Herein, we investigate the influence of the reaction gas composition using DC magnetron sputtering on the structural, chemical and optical properties of the Ce-oxide thin films, with a view to achieving an enhanced understanding of the tunable nature of Ce-oxide materials.

7.3 Experimental and modelling

7.3.1 Thin film deposition process

CeO_x thin films were deposited onto the Si (100) wafers using a magnetron sputtering system (Teer coating Ltd, UK). A pure Cerium (Ce) target (99.9 % purity) of 300 mm × 100 mm × 5 mm size was used to synthesize the coatings. Ar₂ and O₂ gases with purity of 99.999 % were used as the working gas and reactive gas, respectively, and the flow rates of these gases were controlled by MKS mass flow controllers. The vacuum chamber was pumped down to a background pressure of 4×10^{-5} Pa prior to deposition. The pressure of the working gas was maintained at ~0.3 Pa throughout the sputtering process. The target-to-substrate distance was set as 10 cm and the sputtering process was performed without substrate rotation. In the first stage, the substrate was sputter cleaned by argon plasma at a bias of -400 V (frequency 250

kHz) for 20 min, in order to remove the surface oxide layer or any contaminant. Then the bias voltage was reduced to -60 V at a frequency of 250 kHz for deposition. The target current applied to the Ce target was fixed at 4.0 A, while varying the sputtering power in the range of 700 - 900 W. As the CeO_x films were highly insulating, a pulsed power supply (Pinnacle Plus, Advanced Energy Industries, Inc.) was used to drive the magnetron at a frequency of 350 kHz. CeO_x thin films were deposited at various O₂/Ar₂ ratios by adjusting their flow rates. The O₂/Ar₂ was been chosen as 0/35 (0%), 2.5/32.5 (7%), 5/30 (14%), 10/25 (28%), 15/20 (42%) and 20/15 (56%) with a net flow of 35 sccm. The deposition time was 60 min and there was no external heating to the substrate holder during deposition. The sputtering conditions used in the present work are summarized in Table 7.1.

Table 7.1: Sputtering parameters for the deposition of CeO_x coatings.

No.	Sputtering conditions	Range
1	Target-substrate distance	10 cm
2	Base pressure	4×10^{-5} Pa
3	Sputtering gas	Ar
4	Reactive sputtering gas	O ₂
5	Oxygen/argon flow ratio	0 %, 7 %, 14 %, 28 %, 42 % and 56 %
6	Sputtering pressure	~ 0.3 Pa
7	Sputtering power	700-900 W
8	Deposition time	60 min
9	Substrate temperature	Not heated

7.3.2 XRD measurements

In order to identify the crystallographic phases, present in the deposited films, X-ray diffraction (XRD) measurements were carried out using a Bruker Advance D8 X-ray Diffractometer with Cu- K_{α} radiation ($\lambda = 1.5406 \text{ \AA}$) integrated with a LynxEye detector. The XRD machine was operated at a power of 40 kV and 40 mA. XRD data was collected over the angular range of $20^{\circ} \leq 2\theta \leq 65^{\circ}$ with the step size of 0.015° .

7.3.3 XPS measurements

A Kratos Axis-Ultra X-ray Photoelectron Spectrometer (XPS) was utilized to examine the elemental and chemical state of the sample films. XPS measurements were performed using an Al- K_{α} monochromatic X-ray source possessing photon energy of 1486.6 eV and operating at 150W. All samples were placed onto a stainless-steel sample holder and then positioned in the XPS analyzer chamber which was maintained at an approximate pressure of 3×10^{-9} Torr. The binding energy scale was calibrated using the main adventitious carbon component (C-H/C-C bond) of the $C1s$ spectrum situated at 284.8 eV as a reference [426, 427]. The test area for each measurement was defined by a $700 \times 300 \mu\text{m}$ slot configuration. All survey spectra were collected using pass energy of 160 eV, whilst the high-resolution spectra of Ce $3d$, O $1s$ and C $1s$ were examined by using pass energy of 40 eV. CASA-XPS v.2.3.15 package was used for the determination of chemical composition and deconvolution of high resolution spectra.

7.3.4 FESEM imaging

Field emission scanning electron microscopy (FESEM) is an important characterization technique which provides surface morphological information of the materials under investigations. A Zeiss Neon 40EsB FESEM operated at 15 kV was used to determine the film thickness through a high resolution of cross-section backscattered electron imaging. Samples were prepared by mounting cross-sections in resin and polishing the mounts down to reveal the undamaged film against the substrate. The samples were then coated with approximately 3nm Pt to make the surfaces conductive and subsequently imaged using a backscattered electron detector to highlight the atomic number difference between the film and substrate. EDS was used to verify the elemental differences. Measurements were taken using the FESEM operating software packages. The thickness of each sample was measured at different positions and then the average was calculated and listed in Table 7.2.

Table 7.2: Thickness of CeO₂ films.

No.	Oxygen/argon flow ratio, %	Thickness of the coating (nm)
1	0	390
2	7	1330
3	14	180
4	28	160
5	42	150
6	56	610

7.3.5 UV-Vis and FTIR measurements

A double-beam UV-Vis spectrophotometer (Model: UV-670 UV-Vis spectrophotometer, JASCO, USA) provided with a single monochromatic design covering a wavelength range of 190 to 2500 nm was used to measure the solar absorptance spectra of the CeO₂ films. In order to study the reflectance spectra of the prepared films in the infrared region, a PERKIN Elmer Spectrum 100 FTIR Spectrometer (USA) was used in the wavelength range of 2.5 to 15 μm . By using the UV-Vis reflectance data the optical parameters such as absorption coefficient (α), extinction coefficient (k) and optical band gap (E_g) can easily be calculated [428, 429].

7.3.6 Density functional theory-based calculations

Plane wave density functional theory (DFT) with the generalized-gradient approximation (GGA) [276] implemented in the Cambridge Serial Total Energy Package (CASTEP) software [430] was employed to simulate the structural relaxations and energy calculations of fluorite-structured CeO₂ at ground state (T and $P = 0$). The XRD predicted phase of CeO₂ was modeled using DFT+ U approach proposed by Dudarev *et al.* [214], as the Hubbard parameter (U) is critical when dealing with strongly electron-correlated systems such as f -orbital systems. In our simulation, U of 5 eV could reproduce the measured band gap of cerium dioxide. Structural optimization was performed using plane wave basis sets with a

cut off energy of 370 eV to expand the electronic wave functions, while an energy tolerance of 2×10^{-5} eV/atom and an atomic force tolerance of 0.05 eV/Å were utilized. For the integration over Brillouin Zone, a $4 \times 4 \times 4$ k -point Monkhorst grids [431] were selected. The computation details also include the spin-polarized PAW-PBE function [219].

7.4 Results and Discussion

7.4.1 Structural analysis of Ce-oxide coatings

In order to conduct a computational modelling investigation into the deposited CeO_x materials, XRD measurements were undertaken to provide crystalline structural information which would be used as inputs for the model. The XRD patterns of the CeO_x films deposited using various oxygen/argon flow ratios shown in Figure 7.1 demonstrate a polycrystalline character with cubic fluorite structure of CeO_2 with space group of $Fm-3m$ ($a = 5.410$ Å) along with (111), (200) and (222) reflection planes (PDF-4 card no. 00-001-0800) at 2θ of 29.4, 33.4 and 59.3°, respectively. The cubic fluorite-structure of CeO_2 for our coatings with preferred (111) peaks, as depicted in Figure 7.1, indicates that these coatings have high atomic packing densities resulting in coatings with very low surface energies [432]. The intensity of the (111) peak increases with increasing oxygen pressure and reaches to the maximum at an oxygen/argon flow rate ratio of 28%. Further increases in the oxygen partial pressure results in a gradual reduction in the peak intensities. The increase in the intensity of the (111) peak may be due to the increase in the crystallite size and the decrease in its intensity is associated with the excess oxygen segregation at the grain boundaries of the CeO_2 structures [433]. Notably, small peaks attributed to the (200) and (222) reflection planes are also observed for the 14% and 28% oxygen/argon flow ratios. The Bragg peaks observed at 2θ of 26.3°, 36.7°, 39.1° and 43.4°, belong to tetragonal-structured SiO_2 ($a = b = 4.933$ Å and $c = 6.464$ Å) which results from the contributions of coatings and Si substrate.

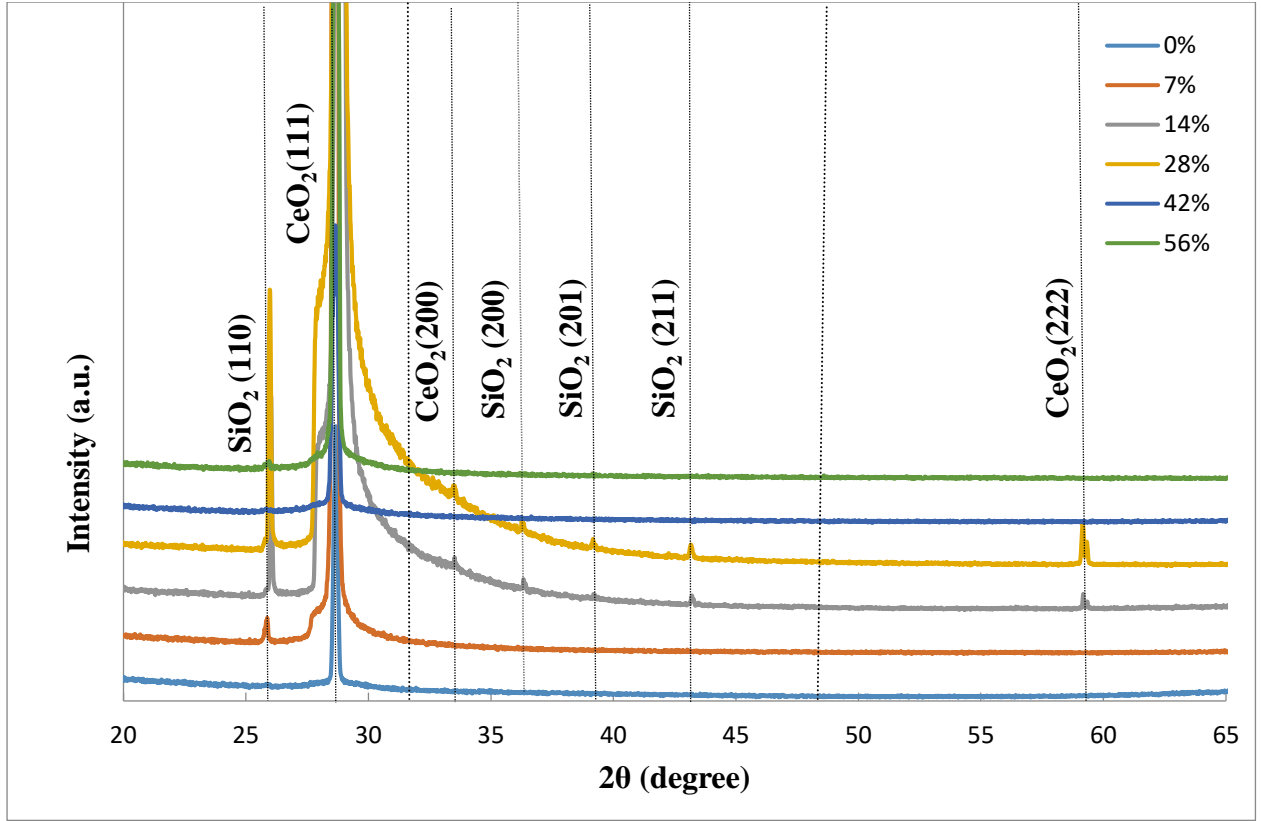


Figure 7.1: XRD pattern of CeO_x thin films deposited on the silicon substrate at various oxygen/argon flow ratios.

The Debye–Scherrer relation was used to estimate the crystallite size of CeO_2 films around the (111) reflection plane,

$$D_g = \frac{k \lambda}{\beta \cos \theta} \quad 7.1$$

where D_g represents the crystallite size, k is the crystallite-shape factor ($k = 0.90$) [434], λ is the X-ray wavelength, β corresponds to full width at half maximum (FWHM) of the most dominant peak, and θ is the Bragg angle. The crystallite size based on (111) plane of the films were found to be 84.9, 123.2, 110.0, 100.6, 57.9, 73.5 nm, respectively. It is obvious that the crystallite size of (111) reflection plane increases from no oxygen pressure to 7% oxygen/argon flow ratio and beyond this ratio the crystalline size reduces. We attribute the change in the crystallite size to the change in deposition rate associated with varying O_2/Ar_2 flow ratios [435].

XPS provides important elemental chemical state information related to the surface of the deposited films. The XPS survey scans of the CeO_x coatings fabricated with various oxygen-argon mixtures are shown in Figure S1 (see Appendix C). As expected, the survey spectra reveal the presence of Ce and O, along with C arising from adventitious carbon (pollutant) which is commonly observed in XPS measurements. The relative atomic concentrations of the elements in each of the samples as calculated from the XPS survey scans (neglecting the contribution from adventitious carbon) are presented in Table 7.3. Whilst the oxygen content initially appears to be in excess to the 1:2 ratio expected for a CeO₂ stoichiometry, it is important to note the presence of oxygen is also expected to arise from functional groups associated with the adventitious carbon also present on the sample (*e.g.* C-O-C, C-OH, O-C=O, etc.). The high-resolution O 1s spectra was deconvoluted in order to determine the proportion of lattice oxygen (*i.e.* Ce-O bonds) present in the sample and the relative atomic concentrations are reported in Table S1 (see also Figure S2). The final column in Table 7.3 uses the information derived from the O 1s spectra to present oxygen content relating to Ce-O bonds. Subsequent examination of the Ce: “adjusted O” ratios demonstrate that at oxygen/argon flow ratios between 14-56% yield thin films with compositions consistent with the expected CeO₂ stoichiometry.

Table 7.3: Details of the elemental compositions of CeO_x prepared under different oxygen/argon flow ratios as acquired from XPS measurements.

Oxygen/argon flow ratio, %	Atomic percentage of the elements		Lattice O
	Ce	Total O	
0	26.1	73.9	44.5
7	28.9	71.1	46.4
14	29.8	70.2	57.7
28	31.5	68.5	57.5
42	31.3	68.7	57.0
56	30.7	69.3	57.8

The Ce 3d spectra (See Figure 7.2) of the two extreme oxidation states of Ce (Ce^{4+} , Ce^{3+}) are generally well understood [436-438]. Typically, the Ce^{4+} oxidation state is differentiated from Ce^{3+} by the existence of three pairs of spin-orbit doublets, whereas Ce^{3+} is characterized by two pairs of spin-orbit doublets [439]. The presence of the satellite peaks at a high binding energy of 916.3 eV confirms the presence of the oxidized phase of CeO_2 [439]. By contrast, the spectrum of non- oxygen partial pressure displays a photoelectron line peaks at binding energies of 884.9 and 903.3 eV indicative of the presence of a mixture of Ce^{3+} [440], and Ce^{4+} oxidation states. Further increases in the oxygen pressure led to a reduction in intensity of these peaks such that they are no longer distinguishable when the oxygen/argon flow ratio is raised to 14%. This suggests that all the Ce beyond this oxygen ratio is completely oxidized to form CeO_2 , which is consistent with the stoichiometry inferred from the analysis of the elemental composition from the survey spectra. Notably, XRD measurements were unable to discern any Ce^{3+} in any of the systems, presumably since it is present merely as a surface enriched species.

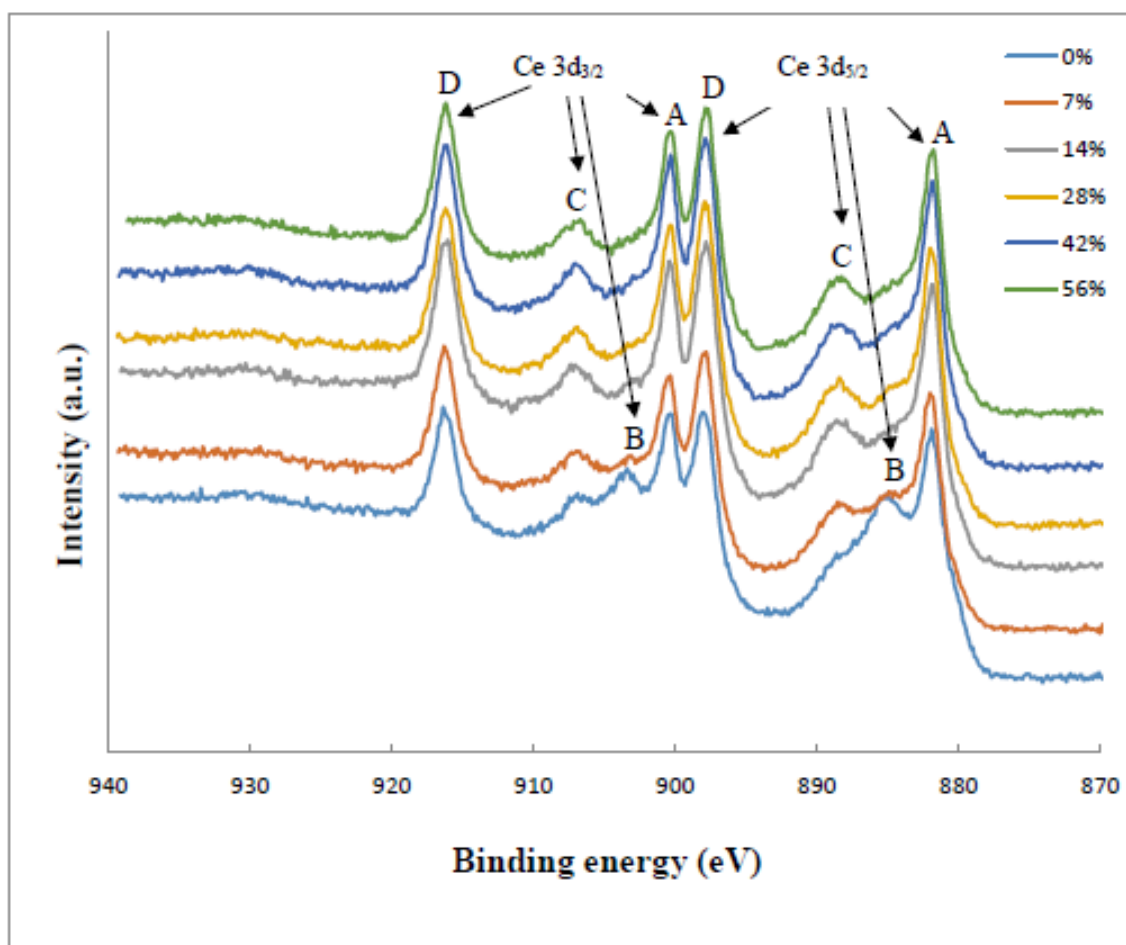


Figure 7.2: XPS High resolution of Ce 3d spectra.

The cross sectional FESEM images shown in Figure 7.3 were used to estimate the thickness of the sputtered CeO_2 films. Several points on each sample were taken to average the accurate thickness of these films. As listed in Table 7.2, the thickness reaches a maximum at 7% oxygen/argon flow ratio and reduces beyond this ratio. This drop in the film thickness is believed to be due to the increasing oxygen content leading to a decrease in the energy of the resultant sputtered particles. Consequently, the number of species reaching the substrate was reduced, resulting in decreased growth rate [441, 442].

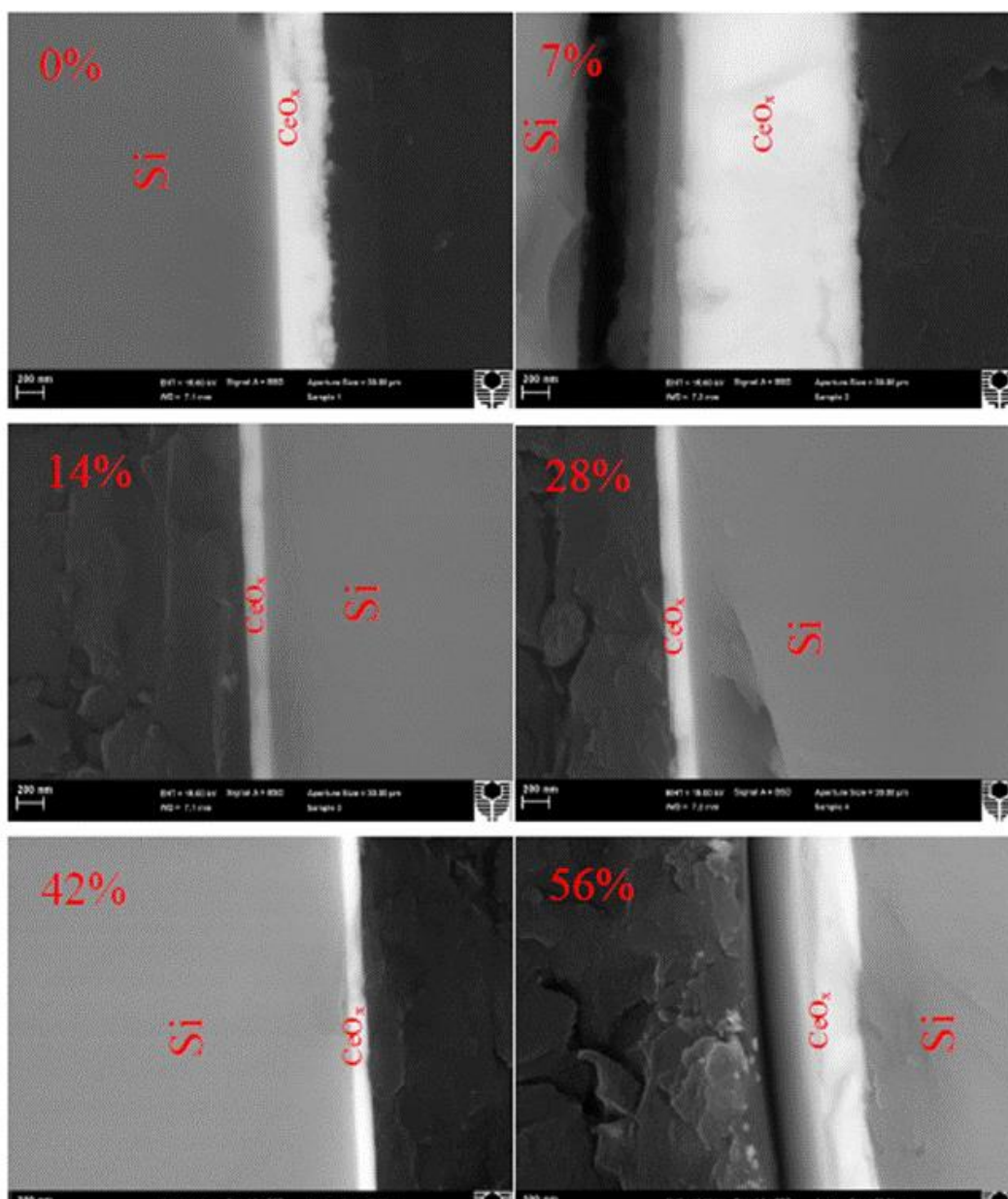


Figure 7.3: Cross sectional FESEM images of Ce-oxide coatings prepared with various oxygen/ argon gas mixtures.

7.4.2 Optical reflectance and Urbach energy studies

The infrared (IR) reflectance spectra of CeO₂ films acquired by FTIR spectroscopy is displayed in Figure 7.4. The IR spectra are aimed to detect the chemical functional groups present in the deposited materials. From Figure 7.4, one observes the absorptions due to carbon-oxygen single bond in the infrared region of 9017.1 - 9041.6 nm demonstrating the presence of (C-O) group in the CeO_x films, consistent with the results obtained *via* XPS. The UV-Vis optical reflectance spectra of CeO_x films at different oxygen/argon flow ratios are shown in Figure 7.5. From Figure 7.5, it can be seen that all the films, apart from that with 0 % oxygen/argon flow ratio, exhibit antireflection properties in the visible regions. This indicates that increases in oxygen/argon result in better antireflection properties in the visible region of the solar spectra. The increase of the reflectance in the visible region, for the CeO_x films prepared without reactive oxygen gas, may be due to its high surface roughness resulting in the loss of intensity of the incident light by scattering [443]. The optical absorption coefficient (α) of CeO₂ films was calculated using the relationship:

$$\alpha = 2.3026 \frac{A}{d} \quad 7.2$$

where A and d are the solar absorption in percentage and thickness of the films, respectively. Figure 7.6 exhibits the variation of the absorption coefficient of CeO_x films at various oxygen/argon flow ratio as a function of incident photon wavelength. The variation of optical absorption coefficient with the photon energy helps to study the band structure and the type of electron transition included in absorption process. The optical band gaps E_g of the studied films were estimated from the calculated absorption coefficient values using the Tauc relation [429, 444] ;

$$\alpha h\nu = A(h\nu - E_g)^n \quad 7.3$$

where, α stands for the absorption coefficient, $h\nu$ is the incident photon energy, h is the Planck's constant, ν corresponds to the frequency of incident photon, A is the probability

parameter for the transition, E_g is the optical band-gap and n is an index that determines the type of optical transition involved in photon absorption process. The index $n = 1/2$ and 2 is for allowed direct and indirect optical transitions, respectively. In practice, the direct transition energy gap (direct band-gap) can be calculated *via* plotting $h\nu$ against $(\alpha h\nu)^2$ and extrapolating the linear portion of the curve to $(\alpha h\nu)^2 = 0$ in the x -axis. Similarly, the indirect energy band-gap can be found by plotting $h\nu$ vs $(\alpha h\nu)^{1/2}$ and extrapolating the linear part of the curve to $(\alpha h\nu)^{1/2} = 0$ along the x -axis.

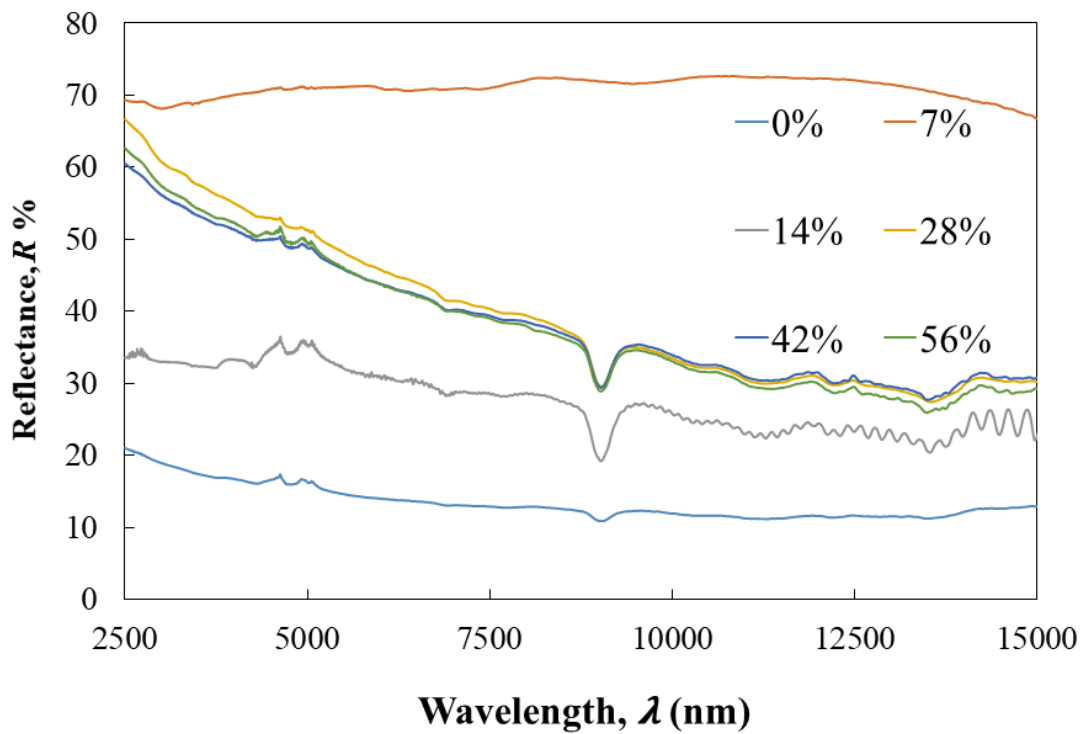


Figure 7.4: FTIR spectra of CeO_x films deposited on c-silicon substrate as a function of oxygen/argon flow ratios.

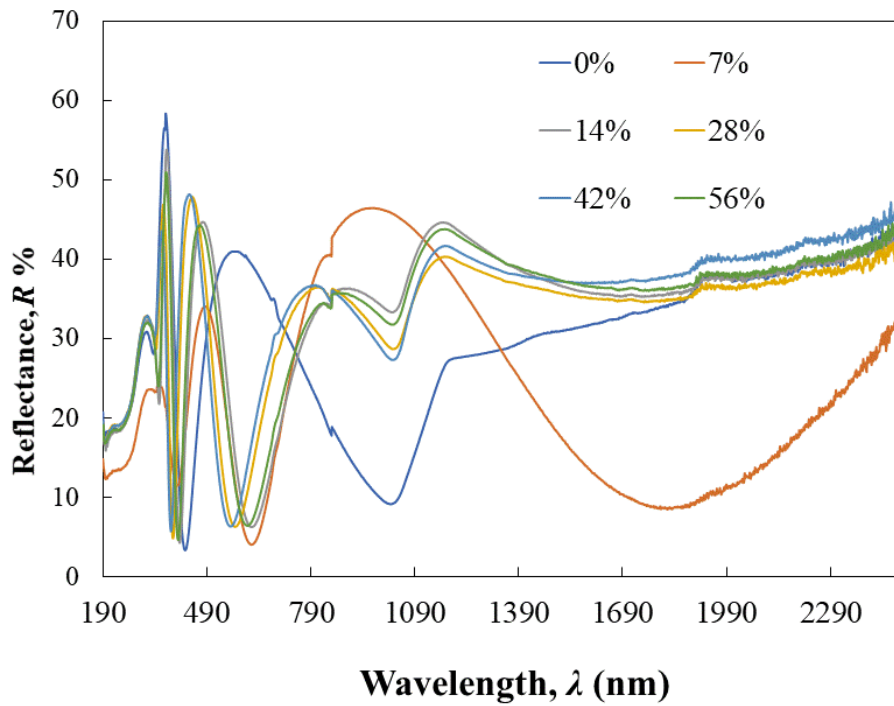


Figure 7.5: Optical reflectance spectra of CeO_x films deposited on c-silicon substrate as a function of oxygen/argon flow ratios.

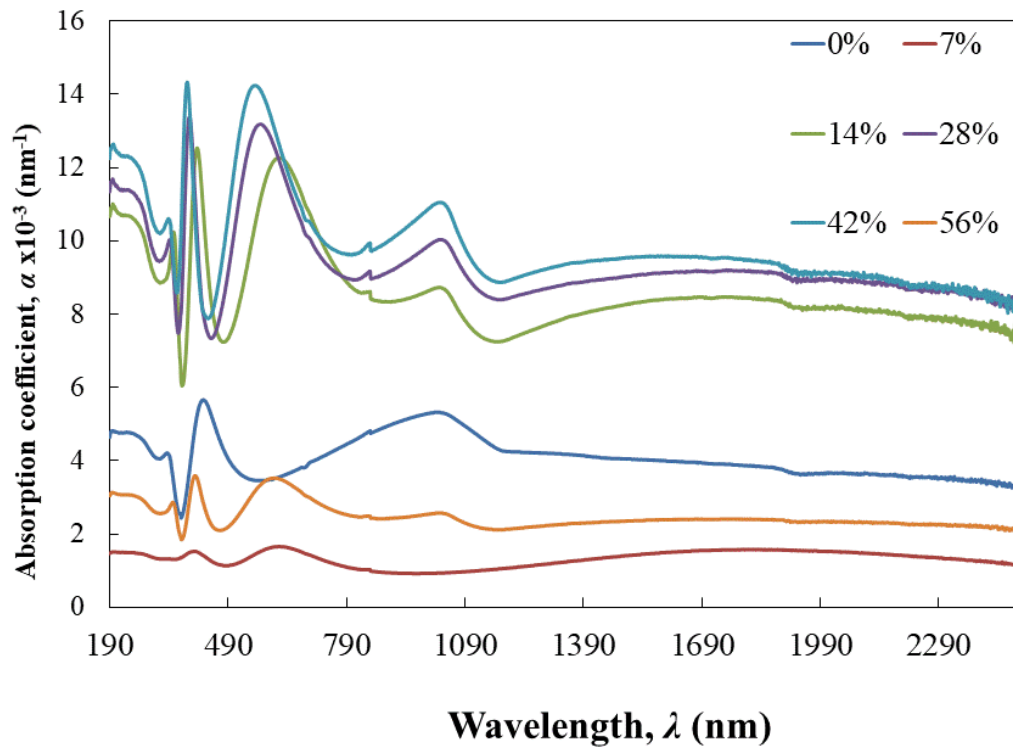


Figure 7.6: Variation of absorption coefficient with wavelength for CeO_x films deposited on c-silicon at different oxygen/argon flow ratios.

Figure 7.7 represents the plots of $(\alpha h\nu)^{1/2}$ against incident photon energy ($h\nu$) of the CeO_x films synthesized at various oxygen/argon flow ratios. According to our measurements, the indirect optical band-gap of the films increased from 2.28 to 3.05 eV with the increase in oxygen flow ratio from 7 % to 14 %. Further increases in the oxygen content into the system results in a reduction in the band-gap to 2.95 eV. This drop in band-gap energy is due to either the excess oxygen reducing the number of grains[445], an alteration to the crystalline structure, or alterations to the crystal orientation due to the strong dependence between oxygen/argon flow ratio and the lattice structure [446]. This is in agreement with XPS results which revealed that at higher levels of oxygen pressure the crystalline structure of Ce_2O_3 is completely oxidized into CeO_2 . This finding is also in accordance with our XRD analysis confirming the increase of (111) orientation from 0% to 28% leading to increase the grains size and beyond this ratio the grain size starts to reduce.

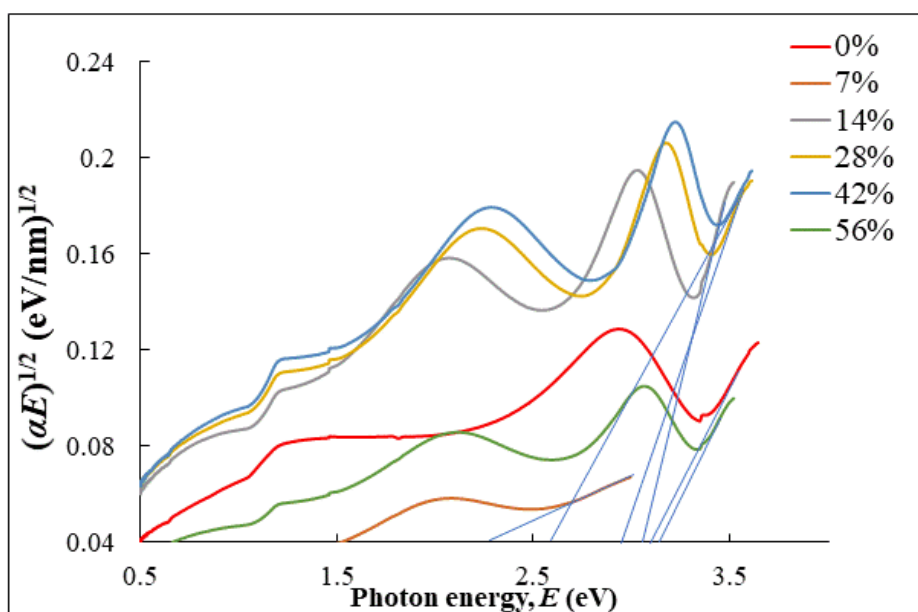


Figure 7.7: Plots of $(\alpha E)^{1/2}$ versus (E) of CeO_x deposited on c-silicon substrate at various oxygen/argon flow ratios.

7.4.3 Optical properties – the dispersion parameters

Studies of refractive index (n) and the extinction coefficient (k) provide important information on the dispersion behaviors of optical materials for a certain incident wavelength. The refractive index and extinction coefficient calculated using the UV-Vis reflectance data, in the wavelength range of 190 – 2500 nm, are shown in Figures 7.8 and 7.9. The complex refractive index is given by the following relation:

$$n^* = n + ik \quad 7.4$$

Where k is the imaginary part of the refractive index known as the extinction coefficient and can be calculated *via* following relation:

$$k = \frac{\alpha\lambda}{4\pi} \quad 7.5$$

The real part of the refractive index, n is obtained using the reflectance data, R and extinction coefficient, k values as:

$$n = \left(\frac{1+R}{1-R} \right) + \sqrt{\frac{4R}{(1-R)^2} - k^2} \quad 7.6$$

Figure 7.8 suggests that all the spectra of refractive index against oxygen gas contents have minimal values in the visible range of the solar spectra. The extinction coefficient plotted in Figure 7.9 exhibits comparatively lower values in the ultra-violet and visible range than the infrared region. This in turn indicates the good quality of the Ce-oxide films that have less dispersion and absorption in the visible range of the solar spectra.

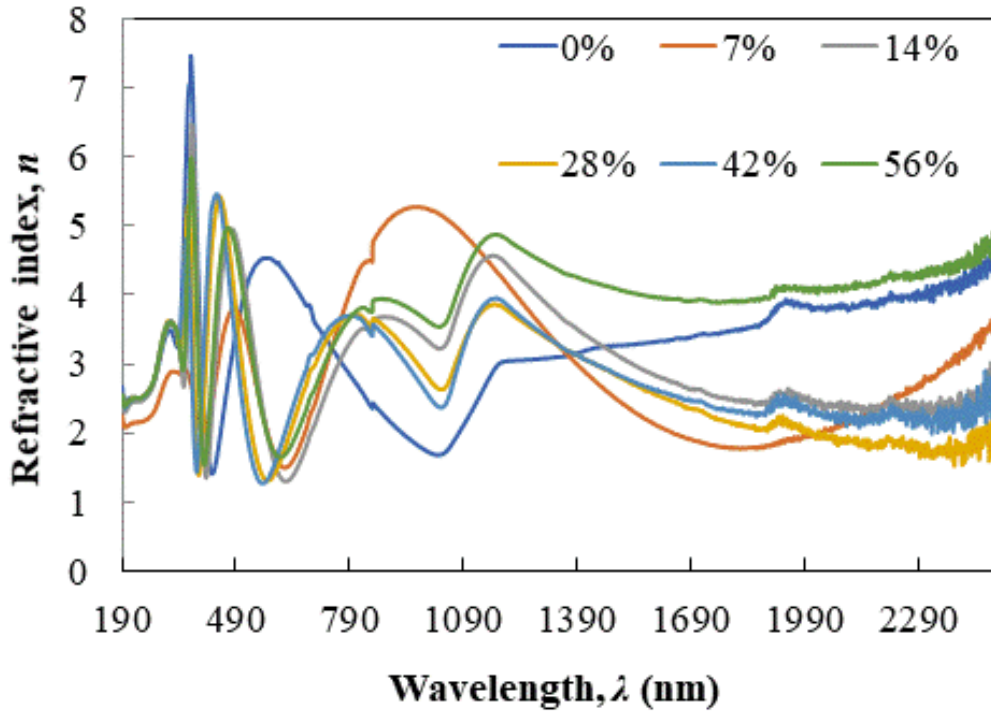


Figure 7.8: Variation of refractive index with wavelength for CeO_x films deposited on c-silicon substrate as a function of oxygen/argon flow ratios.

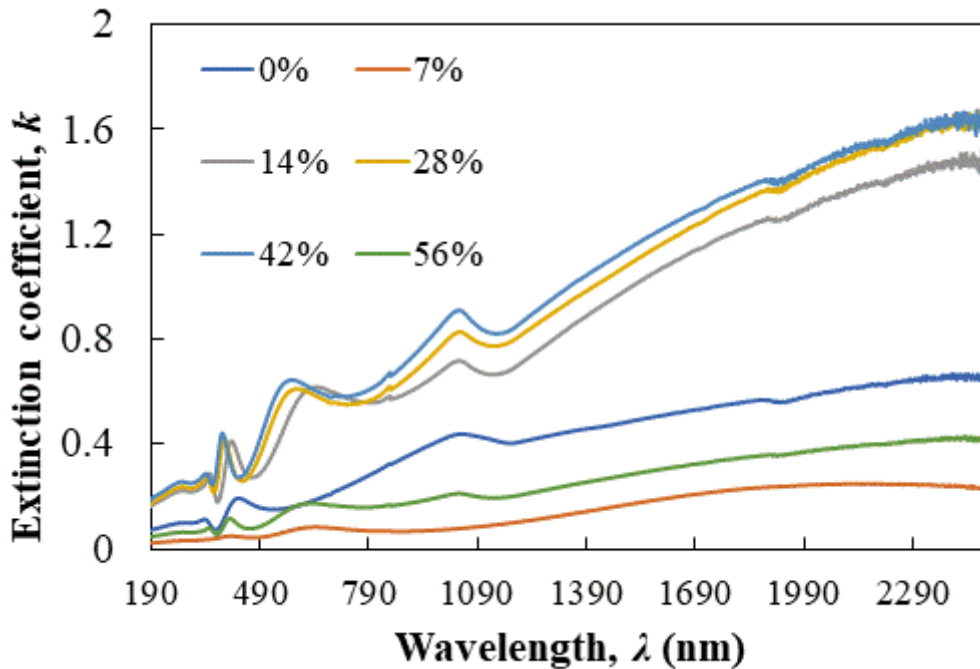


Figure 7.9: Variation of extinction coefficient with wavelength for CeO_x films deposited on c-silicon at different oxygen/argon flow ratios.

7.4.4 Dielectric analysis

The complex dielectric function is expressed as,

$$\varepsilon(\omega) = \varepsilon_1(\omega) + i\varepsilon_2(\omega) = (n(\omega) + ik(\omega))^2 \quad 7.7$$

where $\varepsilon_1(\omega)$ and $\varepsilon_2(\omega)$ corresponds to the real and imaginary part of the complex dielectric function, respectively that are defined by the following relationships [447] ,

$$\varepsilon_1 = n^2 - k^2 \quad 7.8$$

$$\varepsilon_2 = 2nk \quad 7.9$$

$\varepsilon_1(\omega)$ corresponds to the amount of the material that becomes polarized when applying an electric field because of creation of electric dipoles in the material, whereas $\varepsilon_2(\omega)$ represents the absorption in the material and hereafter the loss energy [448]. From Figure 7.10, it clearly shows that the ε_1 spectra exhibit an oscillatory behavior with the photon energy, while ε_2 spectra shown in Figure 7.11 displays energy dependent reducing trend. However, ε_1 and ε_2 curves show small values in the visible range reflecting their least energy loss in this region and thereafter suggesting the high quality of the studied films.

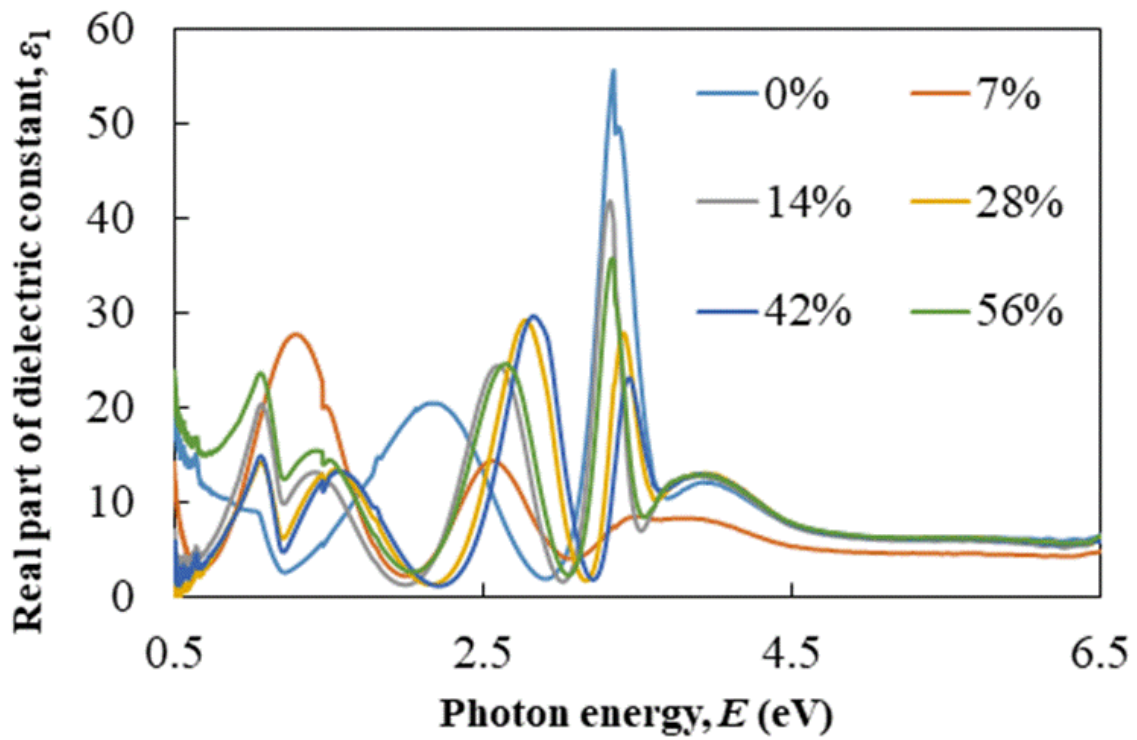


Figure 7.10: Real part of dielectric constant vs photon energy of CeO_x films deposited on c-silicon at different oxygen/argon flow ratios.

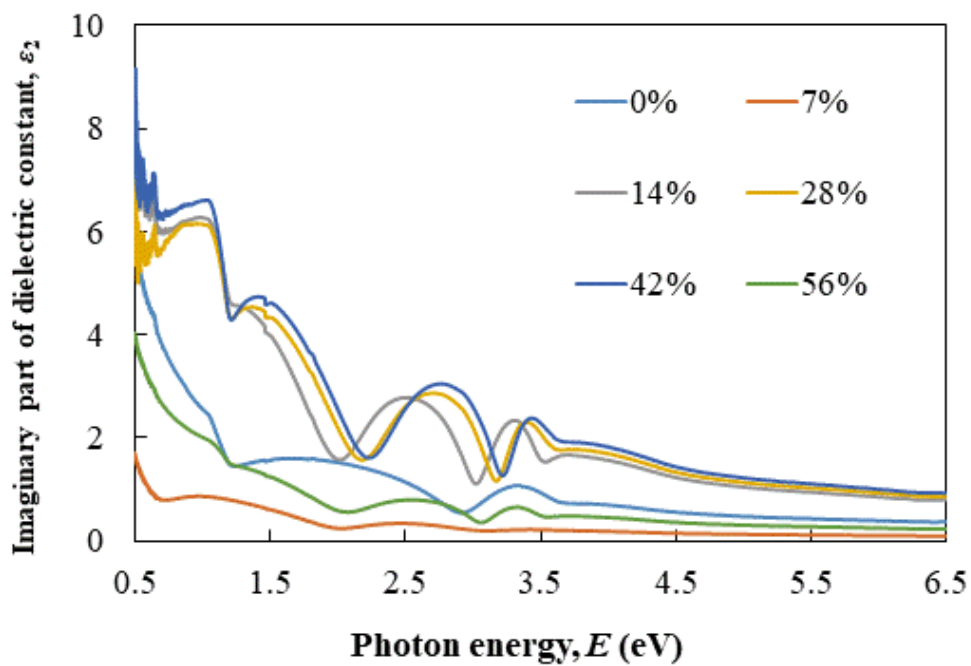


Figure 7.11: Imaginary part of dielectric constant vs photon energy of CeO_x films deposited on c-silicon at different oxygen/argon flow ratios.

This power loss occurs as a result of the inelastic scattering process during the charge transfer and charge conduction mechanisms [429]. The loss factor is defined as,

$$\tan\delta = \frac{\varepsilon_2}{\varepsilon_1} \quad 7.10$$

Figure 7.12 illustrates the variation of the loss tangent, of cerium-oxide films fabricated at different oxygen-argon flow ratios, with the incident photon energy. The variation in loss tangent exhibits the same trend as ε_2 . Since the ε_2 values are lower than that of ε_1 , hence the energy loss of the CeO_x is relatively low.

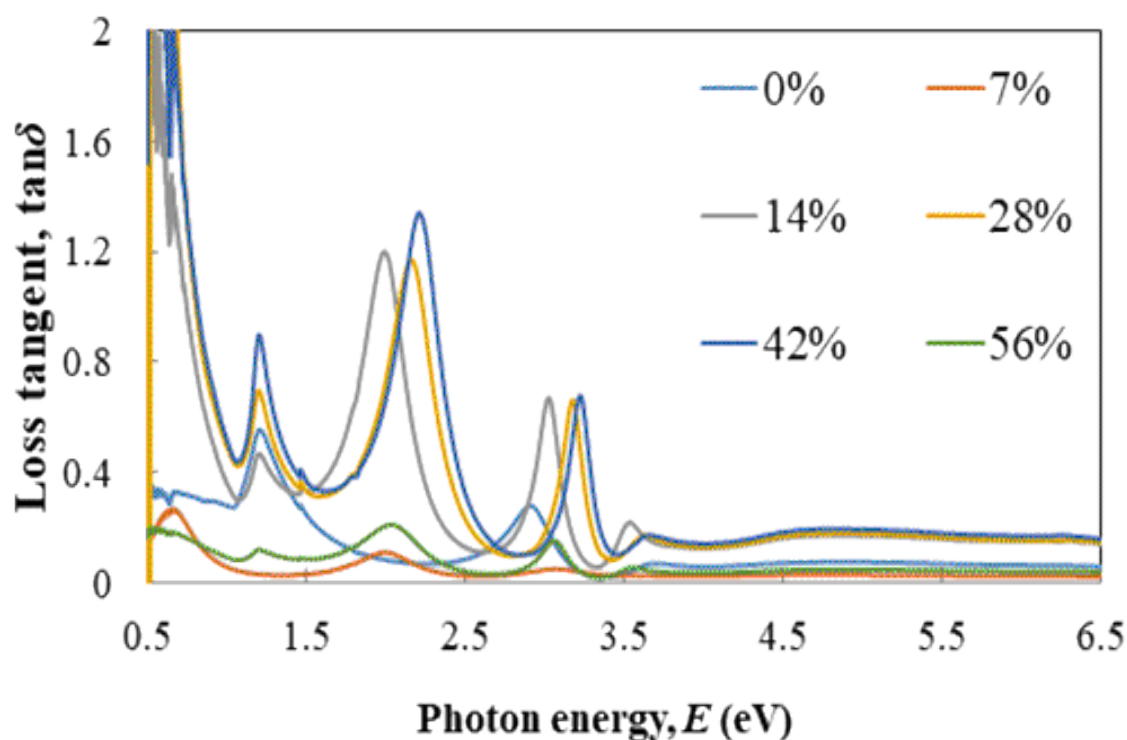


Figure 7.12: Variation of loss angle with wavelength for CeO_x deposited on *c*-silicon at different oxygen/argon flow ratios.

The energy loss functions are classified as volume energy loss function, V_{el} and surface energy loss function, S_{el} [447].

$$V_{el} = \text{Im} \left(-\frac{1}{\varepsilon(\omega)} \right) = \frac{\varepsilon_2}{\varepsilon_1^2 + \varepsilon_2^2} \quad 7.11$$

$$S_{el} = \text{Im} \left(-\frac{1}{\varepsilon(\omega) + 1} \right) = \frac{\varepsilon_2}{(1 + \varepsilon_1)^2 + \varepsilon_2^2} \quad 7.12$$

The energy loss functions that are associated with the optical characteristics of a material *via* real and imaginary parts of dielectric constant of CeO_x films are shown in Figure 7.13. Both V_{el} and S_{el} mimic the same trend as that of loss tangent data displayed in Figure 7.12. It is also noted that the film with 7% oxygen/argon ratio exhibits the lowest energy loss for a wide range of the incident photon energies.

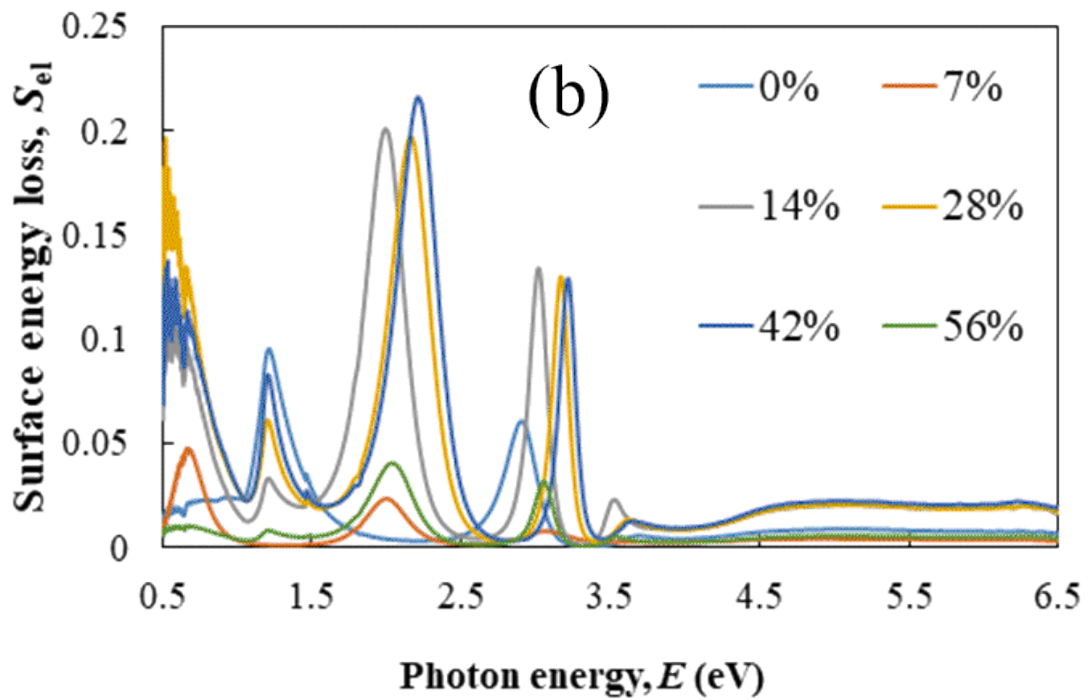
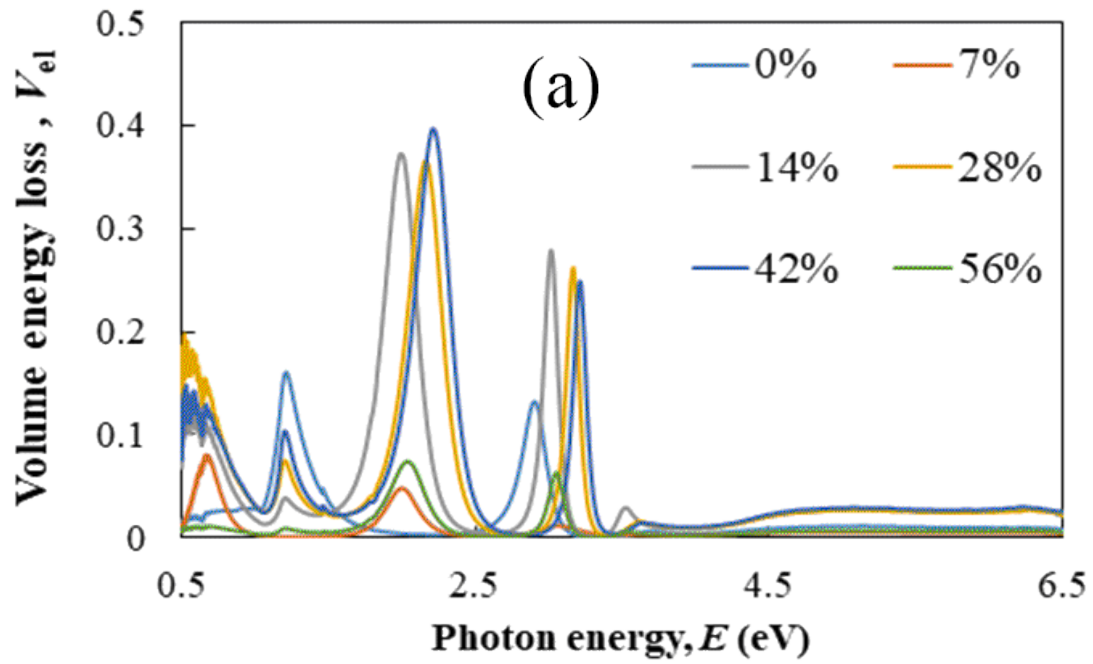


Figure 7.13: Variation of energy loss functions, (a) volume energy loss and (b) surface energy loss of CeO_x deposited on c-silicon substrate at various oxygen/argon flow ratios.

7.4.5 Simulation analysis

Structural optimizations of the CeO₂ lattice were executed *via* computational modeling. The CeO₂ system shows a cubic symmetry in *Fm-3m* space group composed of four formula units in a unit cell. The lattice parameters of CeO₂ in the balanced condition amounts to 5.478 Å as computed *via* theoretical predictions. Our simulated findings of the lattice parameters are in accordance with that of the experimentally measured value of $a = 5.410$ Å (see section 7.4.1). In the present unit cell model of CeO₂, there are 4 Ce and 8 O atoms. The lattice structure was relaxed and is displayed in Figure 7.14.

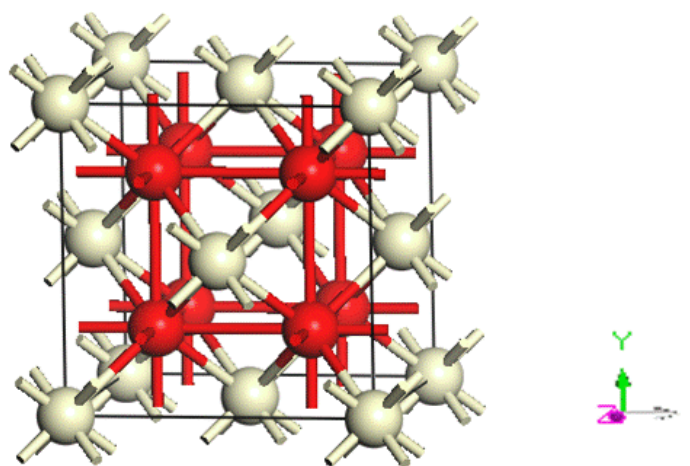


Figure 7.14: Conventional unit cell of Ce-oxide (CeO₂) structure. Gray and red spheres refer to cerium and oxygen atoms, respectively.

Figure 7.15 depicts the electronic density of states (DOSs) of the optimized CeO₂ cluster. The electronic characteristics of CeO₂ structure were determined by calculating the total density of states at the Fermi level. Our results reveal that the CeO₂ cluster exhibits a non-metallic character due to *f*-orbital of Ce which leads to the semiconducting nature. The top most valance band is stretching from -4.30 to 0 eV (Fermi level) and the conduction band is positioned at 3 eV above the Fermi level.

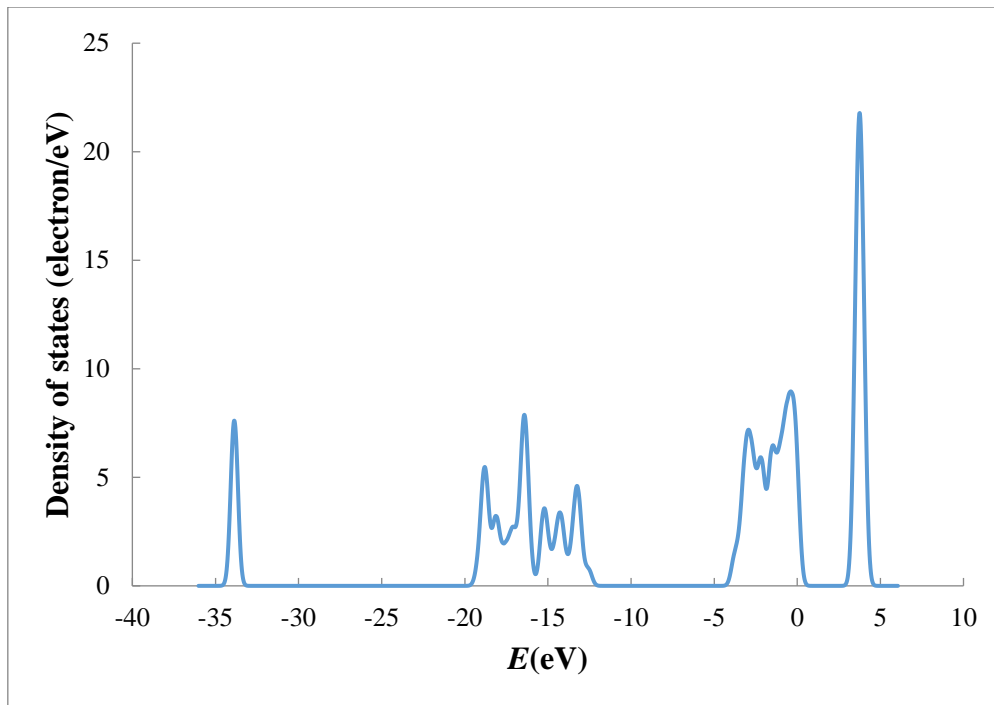


Figure 7.15: Total density of states of Ce-oxide (CeO_2) clusters.

The computed absorption coefficients of CeO_2 films, as a function of wavelength, in the range of 100 – 2500 nm is depicted in Figure 7.16. It is evident that the CeO_2 spectrum shows a good absorption behavior for the incident photons in the ultra-violet region, whereas an opposite trend is observed at visible region. This reveals that CeO_2 is a promising transparent material with superior optical properties applied for electrodes in battery industries and solar panels. Furthermore, the absorption coefficient spectrum confirms the non-metallic character of CeO_2 materials [449].

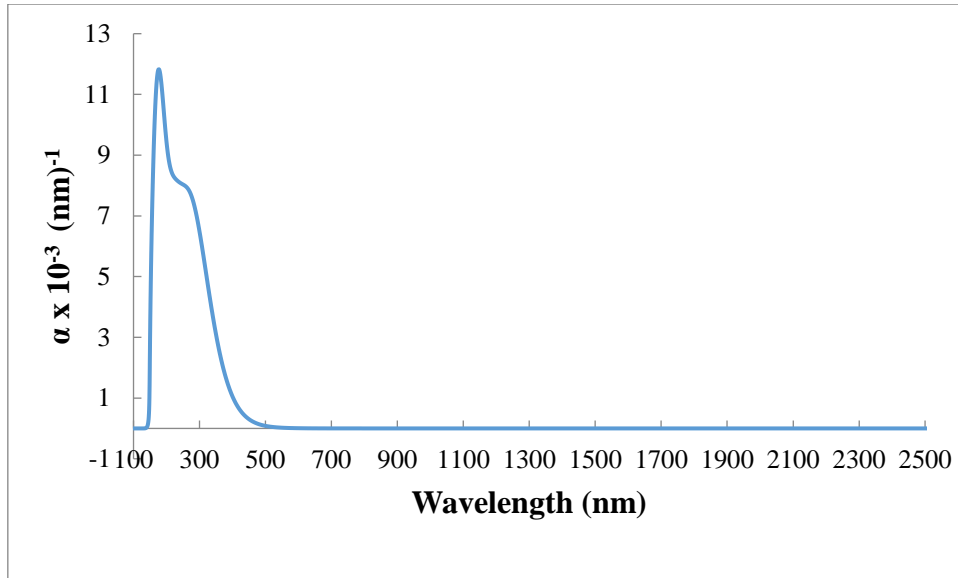


Figure 7.16: Simulated absorption spectrum of CeO₂ clusters.

The dielectric function describes the interaction between the incident photons and electrons in a certain material. The DFT calculated complex dielectric constants of CeO₂ films as a function of the wavelength in the range of 100 to 2500 nm are shown in Figure 7.17. The calculated dielectric function involves the intra-band impacts from free electrons (conduction electron contribution) and intra-band effects (from valance- electron contribution). As observed from Figure 7.17, the dielectric constants (real and imaginary parts) is increased at shorter wavelength regions and become almost invariant in the longer wavelength side. Zero value of ϵ_2 indicates that the material is transparent, while absorption will be represented for nonzero values of ϵ_2 [450]. As seen in Figure 7.17, ϵ_2 values sharply reduces to zero at wavelengths longer than 500 nm indicating a high-quality transparent material for optical applications.

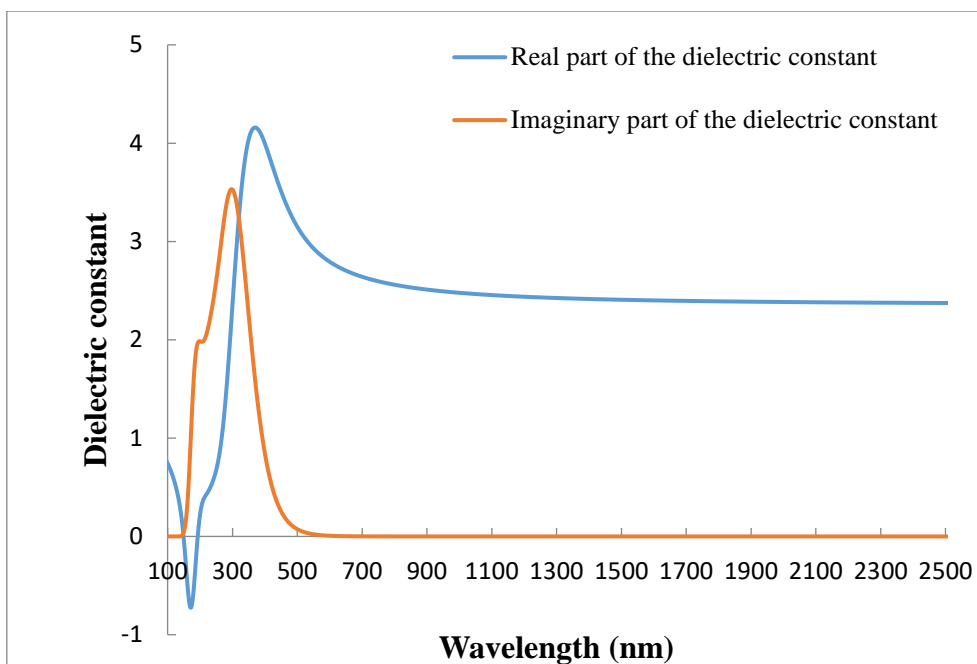


Figure 7.17: Simulated real and imaginary parts of dielectric constants of CeO_2 clusters.

The DFT calculated refractive index (n) and extinction coefficient (k) spectra, in the wavelength range between 100 and 2500 nm, of CeO_2 are illustrated in Figure 7.18. Both refractive index and extinction coefficient spectra exhibit the same trend as the dielectric functions because both of them have peak values in the shorter wavelength regions. The simulated and experimental refractive index has analogous behaviors in the wavelength range from 100 to 2500 nm. Moreover, the computed and measured extinction coefficients have similar trend in the wavelength range of interest.

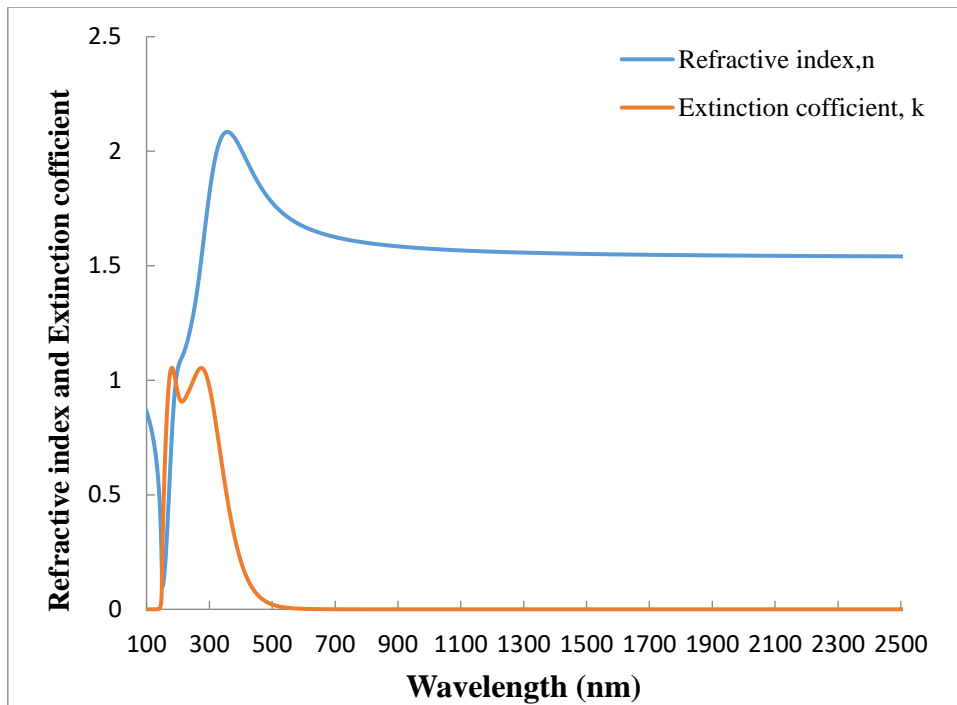


Figure 7.18: Simulated refractive index (n) and extinction coefficient (k) spectra of Ce-oxide coatings.

7.5 Conclusions

Magnetron sputtered CeO_2 films as optically transparent materials, synthesized onto crystalline silicon substrates at various oxygen-argon mixture gas, have been rigorously studied and characterized by correlating their structural and chemical bonding states. All deposited thin films exhibited a polycrystalline character with cubic fluorite structure for cerium dioxide along (111), (200) and (222) orientations. The XPS survey scans of the CeO_x coatings revealed that the Ce:O ratio between 14-56% oxygen/argon flow ratios is largely consistent with the CeO_2 stoichiometry. As revealed from the high-resolution Ce 3d spectra, two oxidation states of CeO_2 and Ce_2O_3 are present in the films prepared at lower oxygen/argon flow ratios; whereas the films are completely oxidized into CeO_2 as the gas ratio is increased. Reflectance data obtained from UV-Vis investigations were utilized to calculate the optical constants such as absorption coefficient (α), the real and imaginary parts of the dielectric function (ϵ_1 , ϵ_2), the refractive index (n) and the extinction coefficient (k). Our analysis indicates that the CeO_2 films have indirect optical band gaps residing in the range of 2.3 - 3.1 eV. The simulated electronic density of states (DOSs) of the optimized structure of CeO_2 films reveals a band gap that agrees well with the experimental optical band gap results. The measured and calculated absorption coefficients display similar trends

and, to some extent, a similar range of values in the observed wavelength range. The excellent agreement between the experimental and theoretical results demonstrates the validity of our computation models. The information gleaned from this study will be of benefit in applications requiring the tunable structural and optical properties of CeO₂ thin films.

Chapter 8 : Structural and Optical Characteristics of Pre- and Post-annealed Sol-gel Derived CoCu-oxide Coatings

Paper V

Miran,H.A., Rahman, M.M., Jiang, Z-T, Altarawneh, M., Chuah, L.S., Lee, H-L, Mohammadpour, E., Amri, A., Mondinos, N. and Dlugogorski, B.Z. (2017) Structural and optical characteristics of pre- and post-annealed sol-gel derived CoCu-oxide coatings. Journal of Alloys and Compounds, 701 . pp. 222-235.

8.1 Abstract

Sol-gel derived CuCo-oxide coatings synthesized onto aluminum substrates and annealed at various temperatures are evaluated as solar selective surfaces by linking their spectral selective behaviors with their structural, chemical bonding states, and surface morphological topographies. As the annealing progressed, all the coatings displayed a preferential orientation of $\text{Cu}_{0.56}\text{Co}_{2.44}\text{O}_4$ (ICSD 78-2175) phase along (400) reflection plane. First principle calculations *via* Rietveld refinement of X-ray diffraction (XRD) data indicated, as the annealing rises, the residual stress and microstrain developed around the coating surfaces are reduced revealing the internal stress release are resulted from reduction of coatings defects. Enhancement of the crystallite size and surfaces roughness of the coatings was confirmed *via* XRD, field emission scanning electron microscopy (FESEM), and atomic force microscopy (AFM) analysis. Optical investigations showed the solar selectivity of the coatings remarkably increases from 3.81 to 24 as the annealing temperature reaches 500°C.

8.2 Introduction

Mixed metal oxide based coatings are versatile materials have received great interest in recent years because of their incredible properties such as a large surface to volume ratio, increased activity, special electronic properties, catalytic properties, and unique optical properties as compared to those of the bulk materials [451, 452] and wide-spread applications in lithium-ion batteries, ion exchange, catalysts, and solar energy transformation, and magnetic semiconductors for recording devices and magnetic sensors due to their capability to interact with ions, atoms, and molecules, not only at the surfaces, but also all the way through the bulk of the material [453-459]. The key factors that determine the potential applications of mixed metal oxide ceramics include stoichiometry and homogeneity of composition, crystal morphology, surface area, and their particle size and shape [460, 461]. In previous reports, the copper-cobalt oxide thin films deposited on aluminum substrate *via* sol-gel dip-coating route displayed unique optical properties with a spectrally selective feature in the visible wavelength of the solar spectrum [456, 462, 463]. Nonetheless, it is realized that temperature change in the synthesis route of CuCo-oxide thin films has considerable impact on their physicochemical, structural, magnetic and electronic behaviors [464]. The CuCo-oxide compounds were found to be stable up to 680 °C, whereupon a phase transformation occurs. The spinel CuCo-oxides lean towards a low crystallized single phase together with a moderately inverted spinel configuration and a minor segregation of copper and cobalt oxide matrices dependent on the Cu/Co ratio and the annealing temperature [465, 466]. The gradual rise in annealing temperature contributed to an increase crystalline phases of CuCo-oxide systems [467].

Solar selective surface is an important component of a solar thermal collector aimed to accumulate solar radiation and transform it into beneficial heat energy for numerous domestic and industrial applications. An ideal solar selective surface (SSS) should, generally, absorb the highest incoming solar radiation in the visible and lowest thermal emittance in the infra-red range of the solar spectrum. Industrial SSSs use metal particles based ceramic cermet structures synthesized *via* vacuum, electroplating, sputtering, and electrochemical procedures [468, 469]. Recently we reported our work on copper-cobalt oxide thin film coatings on the top of highly reflective aluminum substrates using a customized, and yet, cost-effective sol-gel dip-coating method [456, 470]. The new coatings demonstrated distinct optical

properties with promising prospects for solar selective absorber application. Details regarding the metal oxidation states as well as the mechanical properties of these coatings are, nonetheless, rather sketchy and currently lacking even though they are vital for design optimization purposes.

An area of application of which these cobalt-based oxides are comparatively less studied is optical or solar-based coating whereby optical performance of a surface can be manipulated by depositing thin films with varying thicknesses and reflective indices. Incidentally, there are certainly many knowledge gaps that need to be filled in terms of fundamental surface characteristics of these thin films especially in regard to their morphologies, binding states of metal oxides and mechanical strengths. A technical understanding of these characteristics is an essential component in the smart design and engineering context of thin film coatings for optical applications. From an atomistic point of view and apart from the experiment, density functional theory (DFT), a quantum mechanics based computational modelling; provide a powerful tool to analysis various material properties, such as electronic structure, thermal and mechanical properties [37]. Numbers of theoretical studies have been conducted to investigate bulk and surface properties, *e.g.*, bonding, band structures, and thermomechanical properties *etc.*, of Cu-oxide [471, 472] and Co-oxide [473, 474] based materials. An earlier study given by Soon *et al.* reported that the band structures and cohesive properties of copper oxide structure [475].

The physicochemical, optical, magnetic, electrochemical, and thermal properties of these coatings have been extensively studied by several groups which are essential to afford functionalities and enrich application performances of these materials [467, 476-478]. Compared to a large volume of available literature, the post annealing structural features of CuCo-oxide coatings are rarely studied and, till date there are not any integrated experimental reports on temperature dependent structural and optical properties these coatings. Higher degree of thermal stability of a material is an essential condition for its real-world applications. This is also true for metal oxide structures [479]. The particle morphology, crystallite size, grain structure, surfaces roughness and local electronic bonding states of the metal oxides formed *via* powder synthesis and coatings deposition could differ significantly during thermal treatment and could be essentially different from the regularities established in the unannealed coatings. There are, however, many aspects entailing more in-depth analysis

to comprehend the impact of annealing temperatures on the structural, morphological and optical characteristics of these coatings.

Assessing the above facts, this work is aimed at investigating the structural, morphological and local electronic bonding states, and solar selective profile of CuCo-oxide coatings, synthesized before annealing and annealed at 200, 300, 400, 500°C in air for 1 hour, using XRD, FESEM, AFM, X-ray photoelectron spectroscopy (XPS), ultra-violet visible near infrared (UV–Vis–NIR), and Fourier transform infrared (FTIR) spectroscopic methods. Possible charge distribution given by Bader's charge calculation for cluster of $\text{Cu}_{0.75}\text{C}_{2.25}\text{O}_4$ matrix will be used to interpret the electronic structure results from experimental characterization.

8.3 Experimental

8.3.1 Deposition of coatings

Cobalt (II) chloride ($\text{CoCl}_2 \cdot 6\text{H}_2\text{O}$, APS Chemical, >99%), copper (II) acetate monohydrate ($\text{Cu}(\text{OOCCH}_3)_2 \cdot \text{H}_2\text{O}$, Alfa Aesar, >98%), propionic acid ($\text{C}_2\text{H}_5\text{COOH}$, Chem Supply, >99%), and absolute ethanol (E. Mark of Germany, >99%.) were used to synthesize CuCo-oxide coating onto highly-reflective commercial aluminum substrates (Anofol, size 2 cm × 4 cm). Aluminum substrates were cleaned with a hot mixture of Cr(VI)O and phosphoric acid followed by a wash using milli Q water. The cleaned substrates were dried with a flash of N_2 gas. 1.502 gm of cobalt (II) chloride ($\text{CoCl}_2 \cdot 6\text{H}_2\text{O}$, 0.25 mol/L), and 1.273 gm of copper (II) acetate monohydrate ($\text{Cu}(\text{OOCCH}_3)_2 \cdot \text{H}_2\text{O}$) were mixed with absolute ethanol. Propionic acid ($\text{C}_2\text{H}_5\text{COOH}$) was used to make complex solution with the metal ions and to stabilize the solution from unwanted precipitation. After stirring the mixed solution for 2 h, the sol was coated onto aluminum substrates using a dip-coating technique. A dipping and withdrawal rate of 180 mm/min and 60 mm/min, respectively was maintained throughout the synthesis process which was repeated four times to increase the thickness of film with better uniformity. Finally, the coatings were annealed at 200, 300, 400 and 500 °C in air for 1 h. A constant heating rate of 10 °C/min was maintained throughout. More details about the deposition of coatings is reported elsewhere [462].

8.3.2 Crystal Phase Structure and Rietveld Refinement

Rietveld refinement was employed to refine the XRD data as implemented in TOPAS program. We used a pseudo-Voigt peak shape model comprised of Lorentzian and Gaussian components. The difference between the two patterns was minimized through a process of least-squares. A Bruker Advance D8 X-ray Diffractometer equipped with a LynxEye detector was used to carry out the XRD measurements. The XRD machine was operated at 40 kV and 40 mA at room temperature over a 2θ range of 30° to 80° with a step size of 0.01° . The X-rays used to characterize the coatings was a combination of $\text{CuK}\alpha_1$ ($\lambda = 0.15406$ nm) and $\text{CuK}\alpha_2$ ($\lambda = 0.15444$ nm) radiations. The initial crystal structure including atomic positions of CuCo-oxide phases were obtained from ICSD database to model the cubic structure in Fm-3m symmetry group. The background was modelled using a Chebychev polynomial background function with order of 6. The lattice parameter, scale, zero error, sample displacement and background were refined to estimate the lattice parameter, crystallite size (domain size), residual stress, and microstrain of CuCo-oxide coatings before and after annealing.

8.3.3 XPS Analysis

Chemical analysis of the coatings was performed via Kratos Axis-Ultra photoelectron spectrometer. The Kratos XPS machine uses Al- $K\alpha$ monochromatic X-ray source with beam energy of 1486.6 eV at a power of ~ 10 mA and ~ 15 kV. Square size samples (2 mm \times 2 mm) were mounted on steel sample holder. A uniform pressure of 2.9×10^{-9} Torr was maintained in the XPS analyser chamber. The Cu2p, Co2p, O1s, C1s photoelectron lines were recorded with a 2D delay line detector. The photoelectron energy scale was calibrated using C1s (hydrocarbon; C-H) line-at 284.6 eV. CASA-XPS v.2.3.15 software was used for XPS data analysis and deconvolution of the curves.

8.3.4 Film Surface Feature via FESEM Analysis

FESEM is one of the popular techniques to investigate the morphological features of coating materials which gives us essential information concerning the growth mechanism, shape and size of the coating particles. The surface morphology of samples was studied utilizing a field-emission scanning electron microscope (FESEM, Nova NanoSem 450) operating at low voltage (10kV) to minimize charging effects. FESEM digitized micrographs

were obtained with a magnification 50,000 to 100,000×. A secondary electron imaging (SEI) detector was used for this purpose.

8.3.5 Film Surface Feature via AFM Analysis

A high-resolution atomic force microscopy (AFM, Nanomagnetic Instrument Co.) was used to acquire the two and three-dimensional topographical images of the CuCo-oxide coatings. The AFM was operated in tapping mode at the room temperature. A typical rectangular cantilever was employed for the imaging process. This was accomplished by raster scanning the position of the sample with respect to the tip and recording the height of the probe that corresponds to a constant probe-sample interaction. A LabVIEW software was used to analyse the micrographs.

The AFM images are usually quantified by three parameters at the microscopic scale namely, the mean roughness (R_a), rms value (R_q), and z scale. The mean roughness, R_a of an AFM image is estimated from the following relation [480],

$$R_a = \frac{\sum_{i=1}^N |h_i - \bar{h}|}{N} \quad 8.1$$

where h_i indicates the surface roughness value of the coating at 'i', \bar{h} is the mean surface roughness, and N is the number of data points considered for that particular AFM image, but the most common parameter used for estimating the changes in surface topography of a coating is known as the rms value of the surface roughness, R_q . The R_q is a measure of the height deviations taken from the mean data plane and is defined as [480],

$$R_q = \sqrt{\frac{\sum_{i=1}^N |h_i - \bar{h}|^2}{N}} \quad 8.2$$

The z scale gives the vertical distance between the highest and the lowest point of the image [480].

8.3.6 UV-Vis Reflectance Studies

Solar absorptance of the coatings was determined using a double-beam UV-Vis spectrophotometer (Model: UV-670 UV-Vis spectrophotometer, JASCO, USA) with a unique, single monochromator design covering a wavelength range from 190 to 2500 nm.

The monochromator consists of a 1200 grooves/mm grating and a photo multiplier tube (PMT) detector for the UV-Vis measurements.

8.3.7 FTIR Reflectance Studies

The solar reflectance of the thin film coatings were measured using a FTIR spectrometer (Perkin Elmer Spectrum 100 FTIR Spectrometer, USA) in the wavelength of 2.5 to 15.5 μm . The solar absorptance and the thermal emittance of a material can be calculated from measurements of reflectance data from the visible and infrared ranges of the solar spectrum [481]. The total solar absorptance (α) and thermal emittance (ε) of the coatings were estimated via Beckmann-Duffie method as described in Ref. [481]. The solar selectivity (s), the ratio of the solar absorptance (α) to the emittance (ε) [427, 482] (*i.e.*, $s = \frac{\alpha}{\varepsilon}$) of the coatings was also estimated from the UV-Vis and FTIR data of the coatings.

8.3.8 Theoretical Charge Distribution Analysis via Density Functional Theory (DFT)

The charge calculations for $\text{Cu}_{0.7}\text{C}_{2.28}\text{O}_4$ material were initially performed using density functional theory (DFT) as implemented in Vienna ab-initio simulation package (VASP) code [230]. The exchange correlated energies were treated by generalized gradient approximation (GGA) [483]. To improve the simulated results, we have been required to employ the on-site coulomb interaction correction within DFT+ U (where U is the Hubbard parameter) approach by Dudarev *et al.* [214], as this approach can reproduce the corresponding measured band gap for this material. We set Hubbard parameters U and J within ($U_{\text{eff}} = U - J$) at 9.5 and 0.95 eV, respectively. The cut-off energy of 500 eV was used to expand the wave function in a form of plane wave. A $4 \times 4 \times 4$ K-points generated by Monkhorst Pack scheme [484] was used to integrate the Brillouin Zone of selected cluster. All atoms were allowed to relax until their energies reached 10^{-4} eV. Bader's theory [485] was employed to investigate the charge distribution with the structure. Bader's method uses electronic charge density to partition continuous molecular charges into individual atomic charges through dividing the space in molecules into volumes.

$$\nabla \rho(r) \cdot \hat{n} = 0$$

8.3

where $\nabla\rho(r)$ is three-dimensional gradient operator for the electron density at a position r and \hat{n} corresponds to the unit vector perpendicular to the dividing surface.

8.4 Results and Discussion

8.4.1 XRD Analysis

XRD patterns of the CuCo-oxide coatings before and after being annealed at 200, 300, 400 and 500°C are shown in Figure 8.1. Inspecting the peak intensities and d -spacing values for peaks at 38.3° (222), 44.8° (400), 65.2° (440), and 78.3° (622) can be attributed to the $\text{Cu}_{0.95}\text{Co}_{2.05}\text{O}_4$ (ICSD 78-2177), $\text{Cu}_{0.75}\text{Co}_{2.25}\text{O}_4$ (ICSD 78-2176), $\text{Cu}_{0.56}\text{Co}_{2.44}\text{O}_4$ (ICSD 78-2175), and $\text{Cu}_{0.37}\text{Co}_{2.63}\text{O}_4$ (ICSD 78-2174) phases. All these phases have the cubic crystal symmetry and a space group of $Fd\bar{3}m$ (227). According to the XRD data it is seen that the degree of crystallinity of (400) CuCo-oxide phases increases with the rise in annealing temperatures. XRD data revealed that the as-deposited coatings demonstrated as obvious feature of amorphous nature. It was also found that all the annealed coatings had a polycrystalline structure with multiple crystal planes orientations of (222), (400), (440), and (622) respectively. As the annealing progresses, all the coatings shown a preferential orientation along (400) reflection plane together with a significant peak broadening behavior. It is also clearly shown that with the subsequent annealing, intensities of (222) and (400) peaks are gradually enhanced while a reverse phenomenon was identified with (440) reflection plane. It is assumed that the peak broadening behavior was instigated from the diminution of grain size and the presence of residual stress induced around the crystal matrix. Rietveld refinement, of the diffraction patterns of crystallized CuCoO coatings analyzed within the $Fm\bar{3}m$ space group, produced successful fits with approximated $R_{wp}\approx 23\%$ and $R_{exp}\approx 20\%$ (See Figure 8.2). The lattice constant was measured as 0.809 nm at room temperature and slightly increased during the annealing.

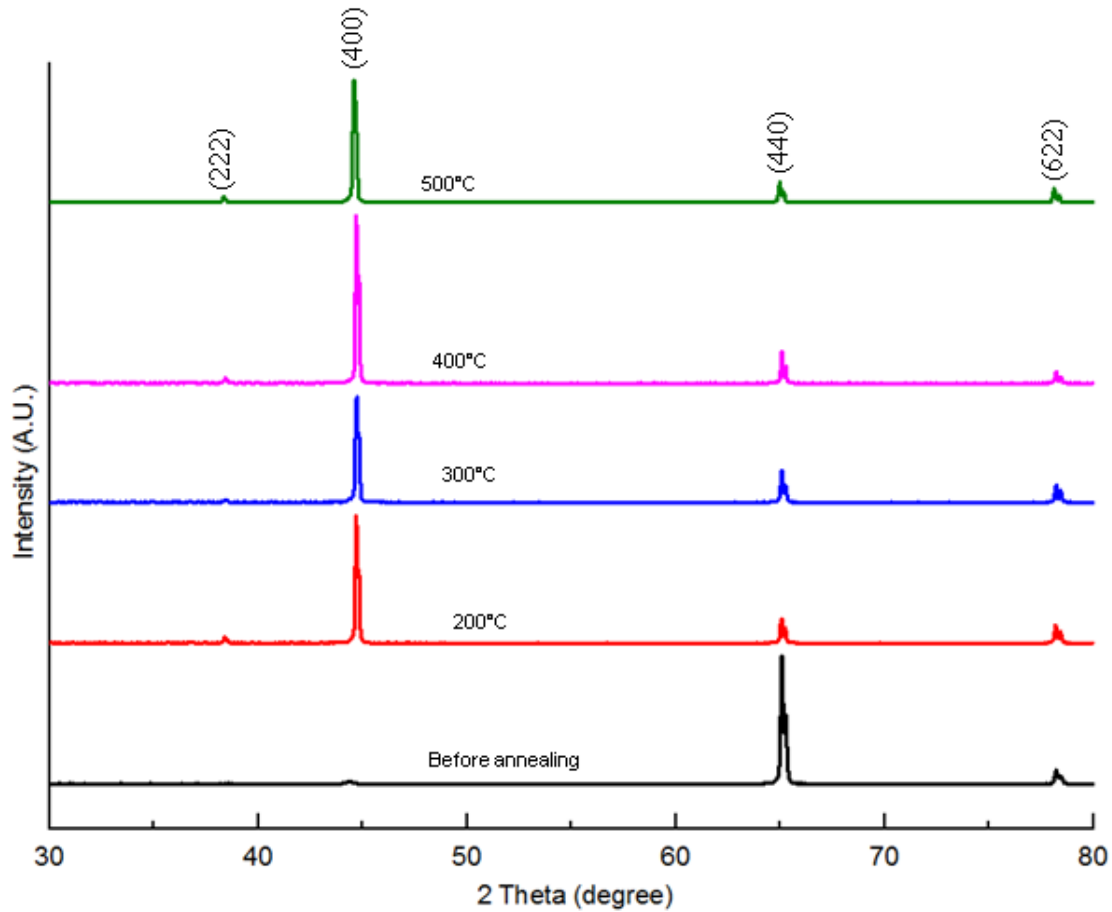


Figure 8.1: XRD spectra of CuCo-oxide coatings before annealing and after being annealed at 200-500°C in steps of 100°C.

Debye–Scherrer formula (Equation 8.4) was employed to estimate the grain size of the coatings. The results presented in Table 8.1 show that as the annealing temperature raises, the crystallite size and lattice parameters of the coatings increases considerably.

$$D_g = \frac{K\lambda}{\beta \cos\theta} \quad 8.4$$

where K is a dimensionless quantity known as the crystallite-shape factor ($K = 0.90$) [486], β is the line broadening at half the maximum intensity (FWHM) measured in radians, and θ is the Bragg angle.

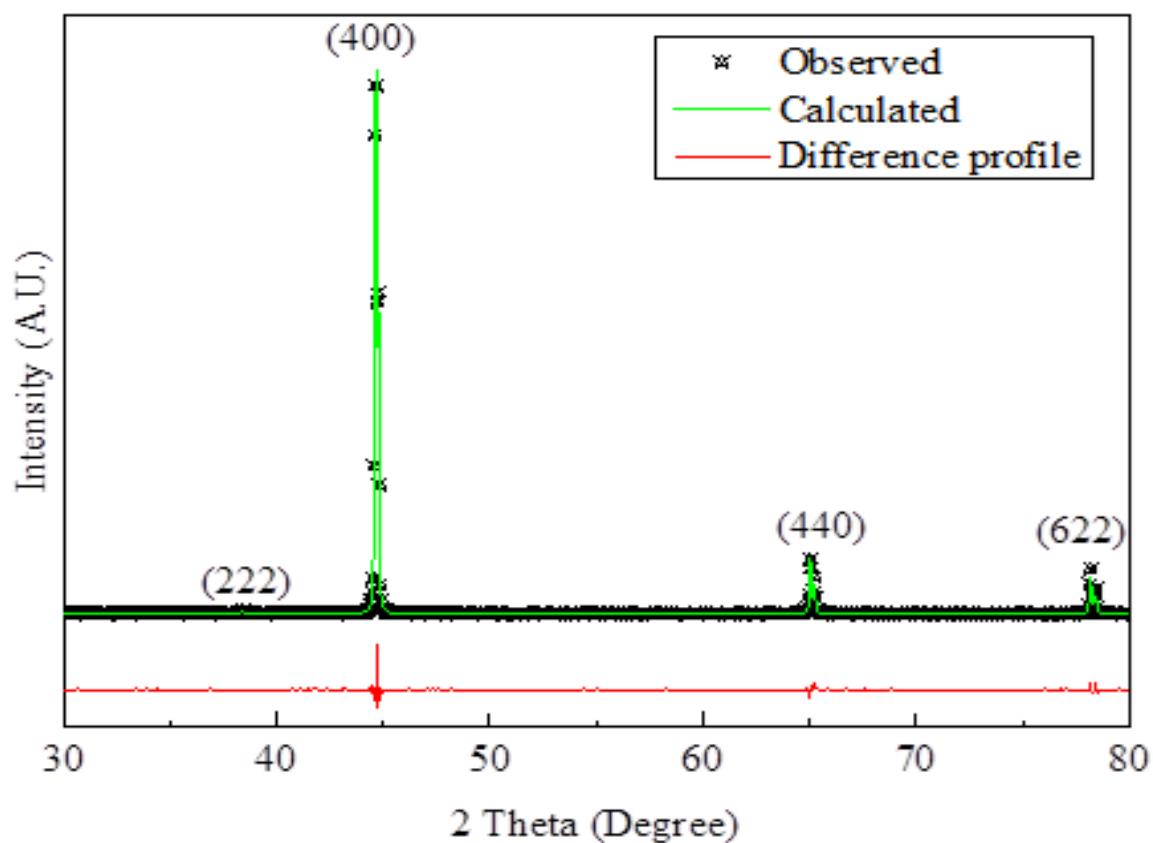


Figure 8.2: Rietveld refinement of XRD spectra of CuCo-oxide coatings before annealing and after being annealed at various temperatures.

Table 8.1: Variation of crystallite size, lattice parameters, residual stress and microstrain of CuCo-oxide coatings with annealing temperatures.

Annealing temperature (°C)	Crystallite size ($\pm 20\%$), D_g (nm)	Lattice constant, a (nm)	Along (400) plane		Along (440) plane		Microstrain σ_x
			2θ	Residual stress, σ_x (GPa)	2θ	Residual stress, (GPa)	
Room temperature	310	0.809	44.74	-1.15	65.12	0.19	0.14
200.00	330	0.810	44.70	0.05	65.07	0.11	0.12
300.00	350	0.810	44.71	0.05	65.08	0.08	0.11
400.00	420	0.811	44.72	0.03	65.09	0.08	0.10
500.00	530	0.812	44.72	0.02	65.09	0.07	0.08

The strain developed within a material can be estimated by evaluating the d -spacing of the crystal planes using X-ray diffraction [487]:

$$\varepsilon_z = \frac{d_n - d_0}{d_0} \quad 8.5$$

where ε_z is the component of strain normal to the surface, and d_n and d_0 are the measured and strain free d -spacing values, respectively. For a coating thickness of $\sim 1 \mu\text{m}$, the residual stress σ_z is, generally, taken to be zero [488]. Thus, the strain component normal to the surface is written as [489],

$$\varepsilon_z = -\nu(\varepsilon_x + \varepsilon_y) = -\frac{\nu}{E} (\sigma_x + \sigma_y) \quad 8.6$$

where ν is Poisson's ratio, E is Young's modulus, and σ_x and σ_y are the stresses along x and y directions, respectively.

Assuming the coating to be isotropic *i.e.*, $\sigma_x = \sigma_y$, and linking Equations 8.5 and 8.6, we attain

$$2\sigma_x = -\frac{E}{\nu} \left(\frac{d_n - d_0}{d_0} \right) \quad 8.7$$

Equation 8.7 is used to estimate the residual stress developed within the CoCu_2O_3 matrix at various annealing temperatures. The average E value (100 GPa) [457] has been used to realize the tendency of stress changing as the annealing progresses. It is interesting to note that the experimental value of E is very promising with those estimated *via* first principle calculations, demonstrating that the actual stress developed in the coatings is also in good agreement. From our analysis, it is clearly shown that the residual stress of CuCo-oxide coatings decreases with the rise in annealing temperature (See Table 8.1). Diffraction patterns of cubic CuCo-oxide coatings before annealing and after being annealed at various temperatures were analyzed within the $Fm-3m$ space group. Rietveld refinement of XRD data produced successful fits with $R_{\text{wp}} \approx 23\%$ and $R_{\text{exp}} \approx 20\%$ (See Fig. 79).

The lattice constant was measured as 0.809 nm at room temperature and slightly increased as the annealing progressed. The preferential growth in the as deposited coating was observed at (440) orientation. The reorientation of the coating film from (440) to (400) took place at 200 °C. The XRD patterns of annealed coatings were dominated by peak broadening and sharpening. The maximum line broadening and peak sharpening occurred to coating annealed at 500 °C. The contribution of crystallite size, lattice constant, residual stress, and

microstrain to the peak broadening were identified using the Lorentzian and Gaussian components of the fitted peaks. Table 8.1 show that the crystallite size and lattice constants of the coatings are systematically increased as the annealing rises. On the other hand, the residual stress and lattice micorstrain are reduced at higher temperatures which indicates the internal stress release in the coating resulted from reduction of defects like dislocations and vacancies.

8.4.2 XPS Analysis

Figure 8.3 shows the XPS survey scans of CuCo-oxide coatings before and after annealing in the binding energy range of 0-1200 eV. Elemental compositions of the coatings before annealing and after annealing as estimated *via* XPS studies are listed in Table 8.2. From Table 8.2, it is evident that annealing has prominent effect on the elemental compositions of metal oxide coatings. The atomic percentages of Cu and Co are reducing with the rise in annealing temperature while the O and C-contents were enriched. This reveals the occurrence of surface oxidation as the annealing progresses. Since the oxygen content is higher at high annealing temperature, the oxidation layer may be thicker and more predominant at the surface. Acquired XPS data were calibrated with respect to the C1s peak at a standard binding energy of 284.6 eV to avoid the charge shift.

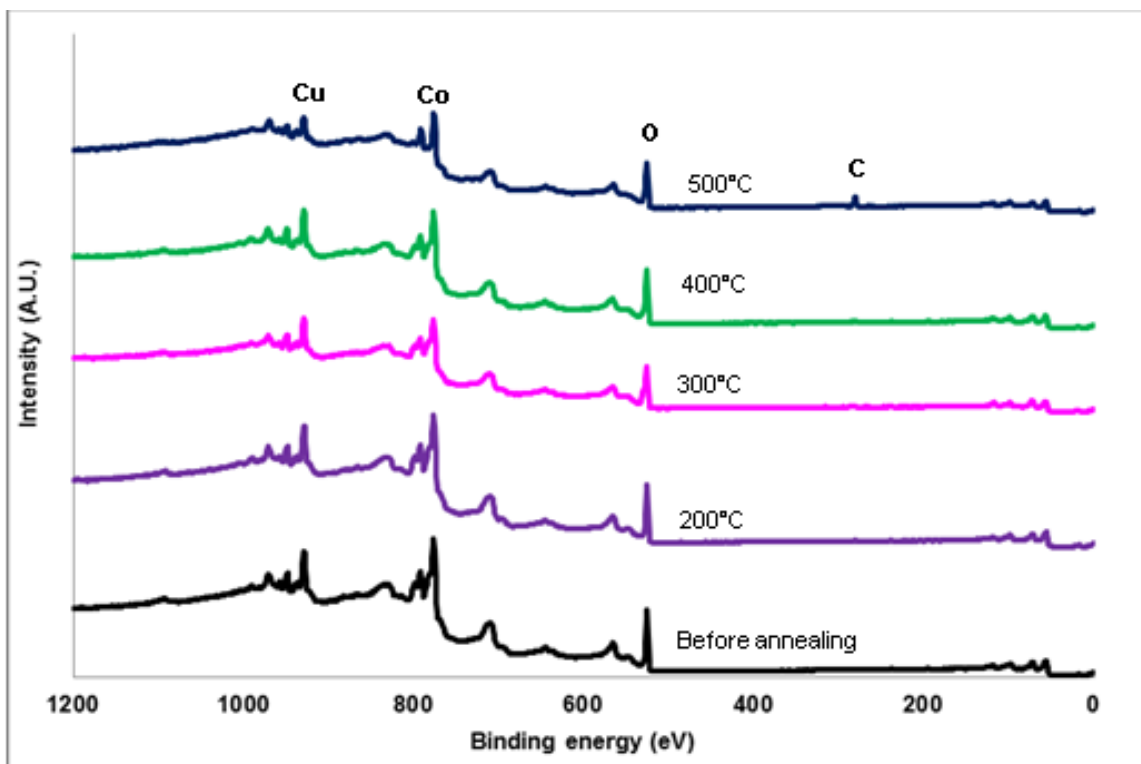


Figure 8.3: XPS survey spectra of CuCo-oxide coatings before and after annealing.

Table 8.2: Elemental compositions of CuCo-oxide coatings before and after annealing in air.

Annealing temperatures (°C)	Atomic percentages of elements			
	Cu	Co	O	C
Before annealing	13.96	24.57	59.32	2.15
200°C	11.99	25.10	60.25	2.67
300°C	11.35	23.89	61.54	3.22
400°C	10.77	17.86	63.67	7.70
500°C	6.43	12.41	53.04	28.13

The deconvolution curve of $\text{Cu}2p_{3/2}$ photoelectron line and its satellite, before and after annealing, of CuCo-oxide coatings is shown in Figure 8.4. The curve-fitting results of all coatings as deduced from XPS data analysis are enumerated in Table 8.3. From Figure 8.4, it is clearly seen that features arising from $\text{Cu}2p_{3/2}$ photoelectron line lies in the binding energy range of 931.7–943.8 eV. It also indicates that gradual increase of annealing temperature does not have significant effect on the copper bonding structure around the coatings surface. $\text{Cu}2p_{3/2}$ feature seen at 931.7–932.6 eV (denoted as ‘i’) is originated from tetrahedral Cu^+ ions. The second component detected at 932.5–933.5 eV (denoted as ‘ii’) can be assigned as the contribution from the octahedral Cu^{2+} ions. The third segment observed at 933.7–934.8 eV are assumed to be originated from a mixture of Cu^+ ions and Cu^{2+} ions. The absence of a component at the low binding energy side of the $\text{Cu}2p_{3/2}$ peak indicates that natural cooling overnight to room temperature inside the closed oven furnace might prevent the reduction of octahedral Cu^{2+} in contrast to the relatively faster cooling outside the furnace.

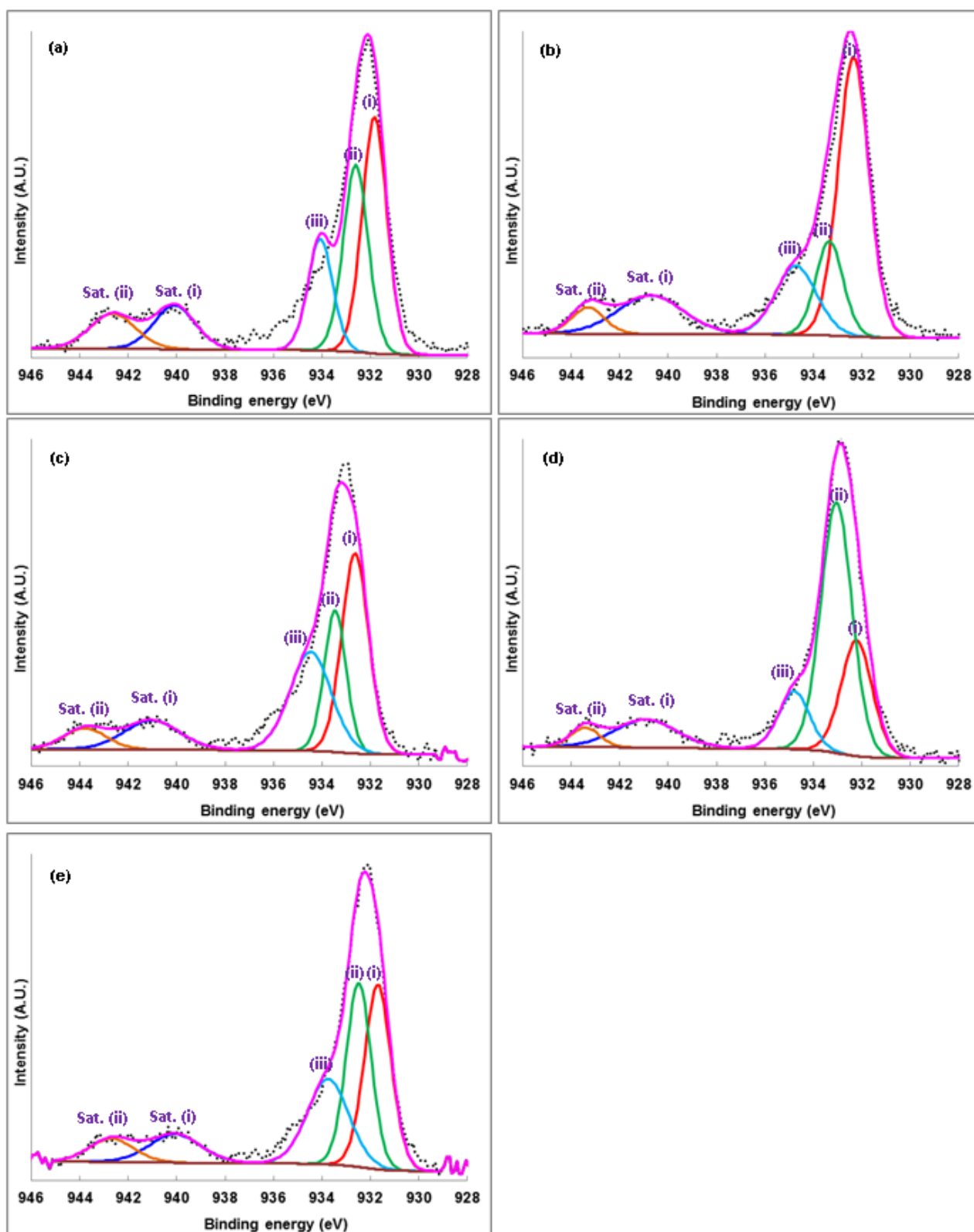


Figure 8.4: Decoupling of high resolution XPS spectra of $\text{Cu}2p_{3/2}$ peak of CuCo -oxide coatings (a) before annealing, and annealed at: (b) 200°C , (c) 300°C , (d) 400°C , and (e) 500°C .

Table 8.3: The deconvolution results of high resolution XPS spectra at Cu2p photoelectron line and its satellite.

Annealing temperature (°C)	Binding energy positions and percentage of bonding states				
	Cu2p photoelectron line			Satellites	
	i	ii	iii	iv	v
Before annealing	932.6 eV (35.5%)	933.5 eV (20.6%)	934.5 eV (27.0%)	941.0 eV (10.9%)	943.8 eV (6.0%)
200	931.7 eV (31.8%)	932.5 eV (29.4%)	933.7 eV (22.6%)	940.1 eV (9.4%)	942.7 eV (6.7%)
300	931.8 eV (35.1%)	932.7 eV (27.8%)	934.1 eV (16.6%)	940.1 eV (10.9%)	942.6 eV (9.6%)
400	932.3 eV (49.3%)	933.3 eV (9.33.3%)	934.7 eV (934.7%)	940.7 eV (940.7%)	943.3 eV (943.3%)
500	932.2 eV (23.2%)	933.1 eV (50.3%)	934.8 eV (11.6%)	940.9 eV (11.3%)	943.4 eV (3.6%)

Deconvolution curves of high resolution XPS profile and the corresponding satellite of Co2p_{3/2} photoelectron line, of CuCo-oxide coatings, before annealing and after annealing are presented in Figure 8.5. The manifestation of a typical satellite at high energy side of Co2p_{3/2} peak reveals the presence of Co^{II+} ions. Relatively low intensity of these satellites indicates a partial spinel-type lattice arrangement of cobalt ions. It is also predicted that lower intensity of these satellites might correspond to a mixer of Co^{III+} and Co^{II+} ions [462]. The deconvolution of Co2p_{3/2} peak and its satellite result in five curve fitting components. The first components seen at 778.8-779.7 eV are basically arising from the Co^{III+} ions in octahedral coordination. The second fitting curve is believed to be a contribution from the mixed Co^{III+} and Co^{II+} bonding states. The third fitting components in the binding energy range of 782.2-783.1 eV are the characteristic of Co^{II+} ions in tetrahedral coordination. The corresponding binding energy positions and the percentage of each component together with the satellite positions are set out in Table 8.4. From the Cu2p_{3/2} features, it is realized that the Cu^{III+} ions partially substitute the Co^{II+} ions thus forming a lower degree of crystallization of Cu^{II+}Co^{III+}O₄ spinel systems [462, 463]. The satellite peaks above 785.00 eV are well-known to be the contribution from cobalt oxide bonds. The gradual increases in annealing temperatures, generally, do not have any significant influence on bonding structure around the cobalt surface.

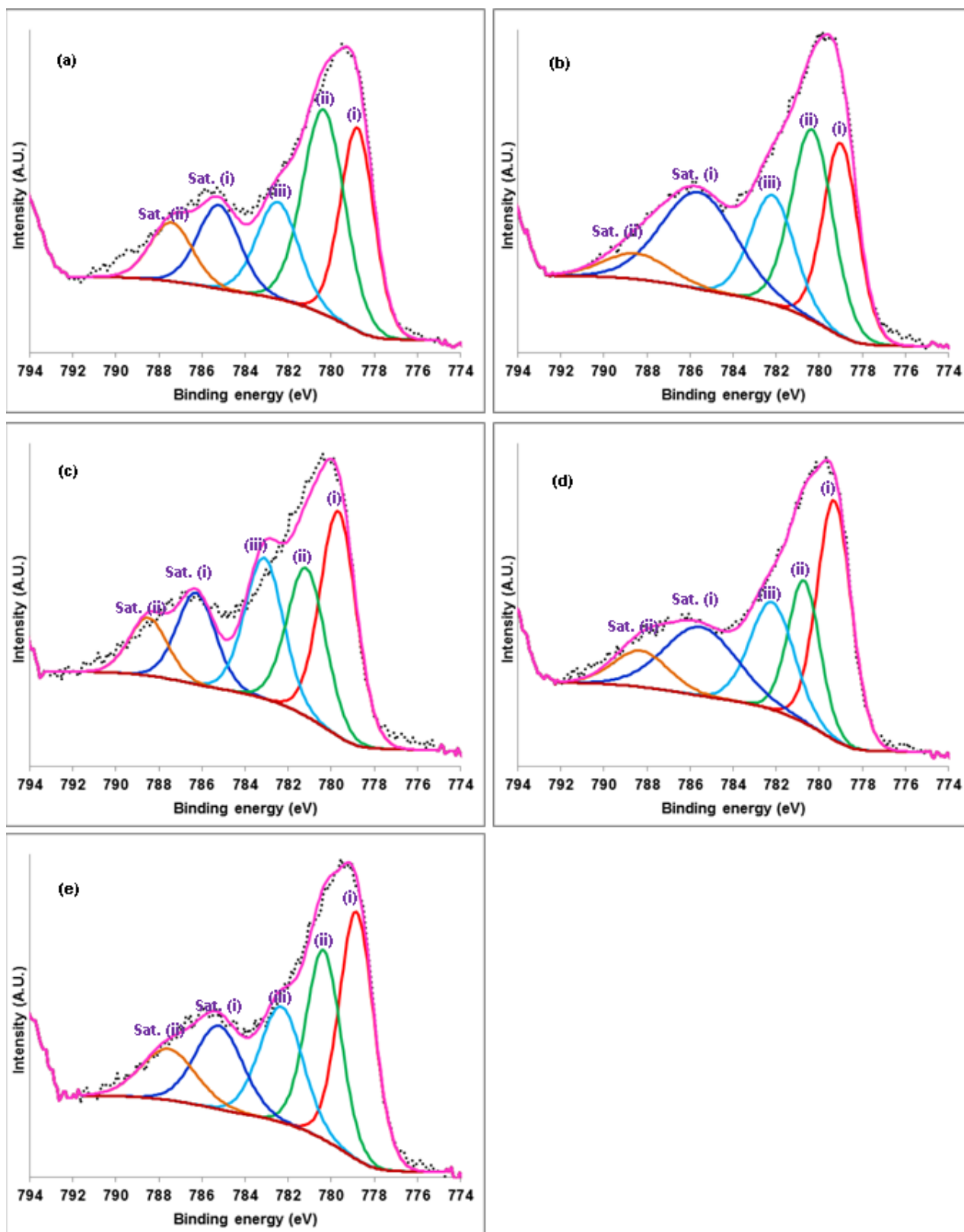


Figure 8.5: Decoupling of high resolution XPS spectra of $\text{Co}2p_{3/2}$ peak of CuCo-oxide coatings (a) before annealing, and annealed at: (b) 200°C , (c) 300°C , (d) 400°C , and (e) 500°C .

Table 8.4: The deconvolution results of high resolution XPS spectra at Co2p photoelectron line and its satellite.

Annealing temperature (°C)	Binding energy positions and percentage of bonding states				
	Co2p photoelectron line			Satellites	
	i	ii	iii	iv	v
Before annealing	779.7 eV (32.7%)	781.2 eV (22.7%)	783.1 eV (21.6%)	786.3 eV (14.0%)	788.5 eV (8.9%)
200	778.8 eV (32.0%)	780.3 eV (24.4%)	782.3 eV (18.4%)	785.2 eV (14.8%)	787.6 eV (10.4%)
300	778.8 eV (27.0%)	780.3 eV (33.7%)	782.5 eV (15.9%)	785.2 eV (13.8%)	787.4 eV (9.7%)
400	779.0 eV (23.7%)	780.2 eV (27.9%)	782.2 eV (16.9%)	785.6 eV (25.6%)	788.5 eV (5.9%)
500	779.3 eV (33.5%)	780.7 eV (18.4%)	782.2 eV (19.3%)	785.5 eV (20.6%)	788.3 eV (8.1%)

Figure 8.6 shows the deconvolution of O1s XPS spectra of CuCo-oxide coatings synthesized before annealing and after being annealed at different temperatures. In all five coatings, the O1s spectrum displays a prominent peak with a shoulder at the higher binding energy side above 530.0 eV. The curve-fitting of O1s photoelectron line gives out three fittings components. The first components at 528.6–529.6 eV (symbolized as ‘i’) is ascribed to lattice O²⁻ ions, while the second components at 529.1–530.1 eV (symbolized as ‘ii’) may be due to the surface oxygen originated from OH-like species such as hydroxyl, and carbonate groups [476, 490, 491]. The third and final component at 530.7–531.7 eV (symbolized as ‘iii’) is attributed to the sub-surface O⁻ species. The apparent are assumed to be the distinctive feature of the CuCo-oxide system which differentiates them from O1s on Co₃O₄ phase. However, there is no apparent alteration in the surface compositions of the CuCo-oxide coatings as they undergo at different annealing temperatures.

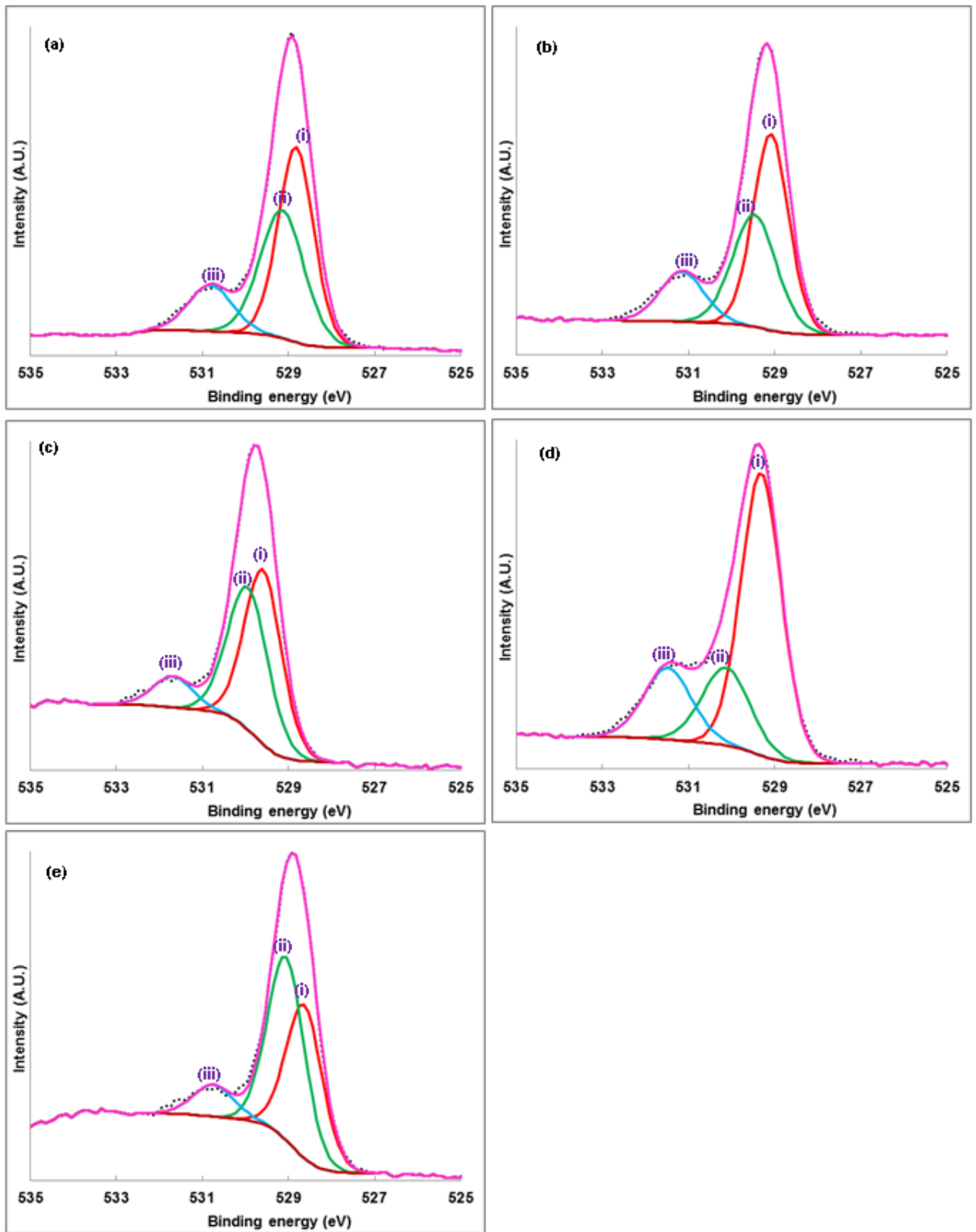


Figure 8.6: Decoupling of high resolution XPS spectra of O1s peak of CuCo-oxide coatings (a) before annealing, and annealed at: (b) 200°C, (c) 300°C, (d) 400°C, and (e) 500°C.

Table 8.5: The deconvolution results of high resolution XPS spectra at O1s photoelectron line and its satellite.

Annealing temperature (°C)	Binding energy positions and percentage of bonding states of O1s photoelectron line		
	i	ii	iii
Before annealing	529.6 eV (48.0%)	529.9 eV (42.7%)	531.7 eV (9.3%)
200	528.6 eV (40.7%)	529.1 eV (49.7%)	530.7 eV (9.6%)
300	528.8 eV (47.5%)	529.1 eV (38.6%)	530.8 eV (13.9%)
400	529.1 eV (49.5%)	529.5 eV (34.95)	531.2 eV (15.7%)
500	529.3 eV (61.5%)	530.1 eV (20.1%)	531.5 eV (18.4%)

8.4.3 FESEM Analysis of the Coatings

The impact of thermal treatment on the surface morphology of CuCo-oxide coatings was investigated *via* FESEM imaging. As observed from FESEM images shown in Figure 8.7.a-e, the annealing plays a significant role modifying the morphological features of the synthesized coatings. Before annealing the CuCo-oxide coatings were showing mould-like structures; after thermal treatment they were transformed into compact and smooth morphologies together with the homogeneously distributed particles. This might be due to the consequence of the grain size's change associated with amalgamation of grains. It is also expected that after consolidation of the grains, agglomerates are formed, and the new grains attain a certain specific shape (see Figure 8.7.e). Some of the particles shown well-defined grain boundaries and an average particle size of 25-70 nm were recorded. It was also confirmed that the average particle size of the coatings was monotonically increased with the gradual increase of annealing temperature of the coatings. The overall quality and morphology of the coating is quite impressive. Morphological studies on Cu₂O–CoO composites annealed at indicate the formation of dense nanostructured particles without any distinguishable landscapes. However, upon the increase of temperature to 500 °C, particles were agglomerated to irregularly shape larger sizes [492].

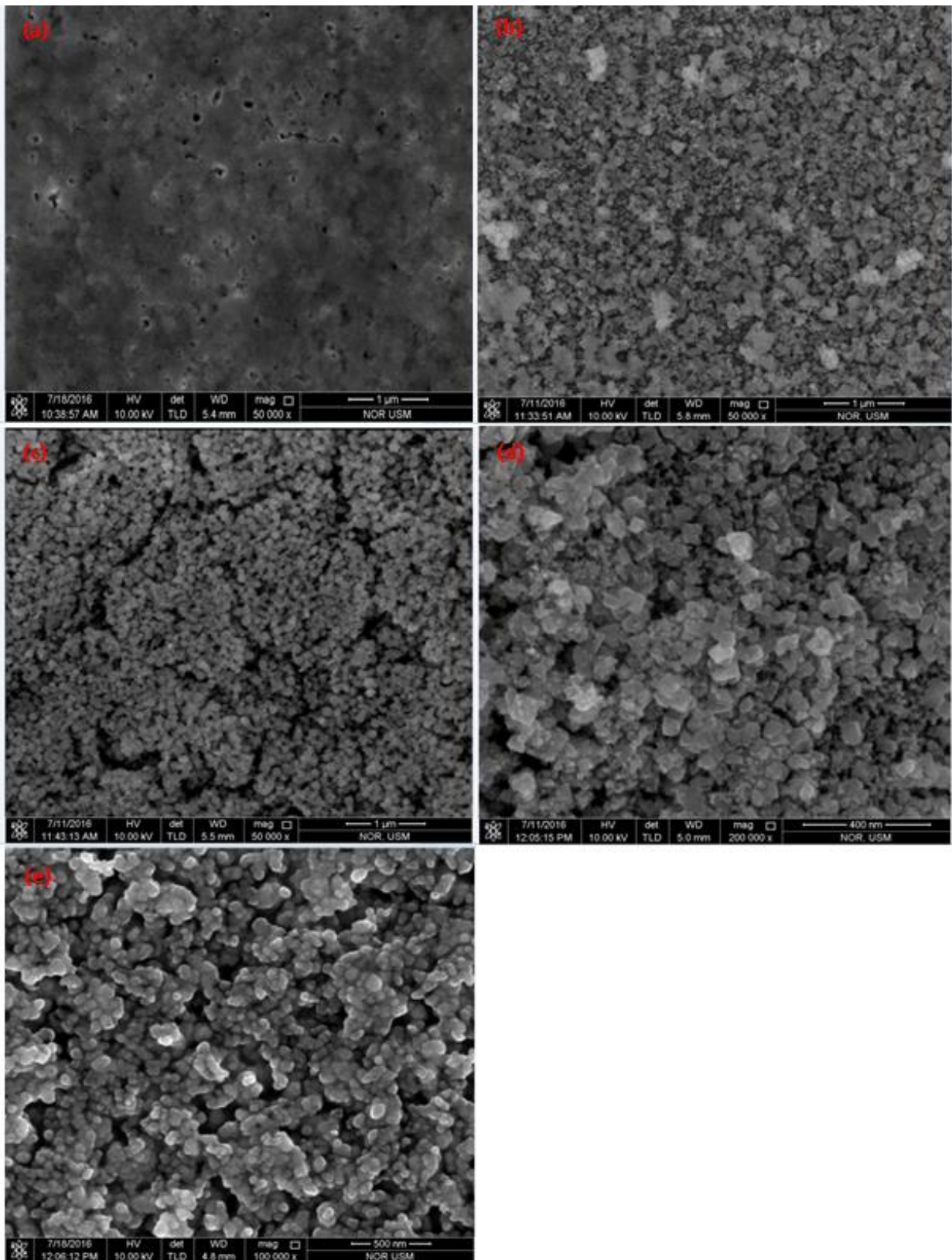


Figure 8.7: FESEM images of CuCo-oxide coatings (a) before annealing, and annealed at: (b) 200°C, (c) 300°C, (d) 400°C, and (e) 500°C.

8.4.4 AFM Analysis of the Coatings

Surface topographical features of the CuCo-oxide coatings imaged using AFM technique are presented in Figure 8.8. The estimated surface roughness values together with the image surface area of the CuCo-oxide coatings before and after annealing are presented in Table 8.6.

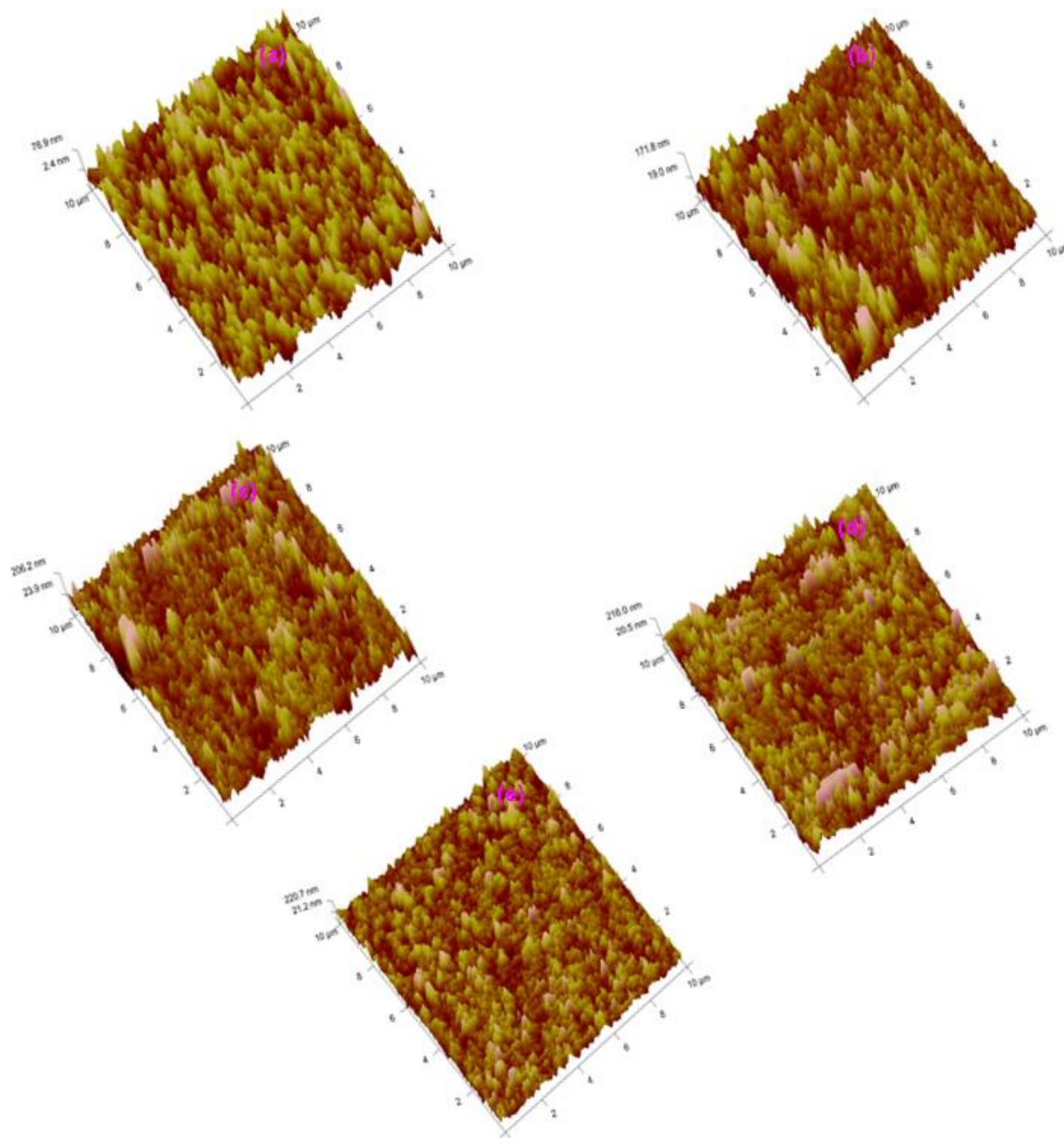


Figure 8.8: AFM images of CuCo-oxide coatings (a) before annealing, and annealed at: (b) 200°C, (c) 300°C, (d) 400°C, and (e) 500°C.

Table 8.6: Surface roughness parameters of CuCo-oxide coatings before and after annealing.

Annealing temperatures (°C)	Mean roughness, R_a (nm)	rms value of the surface roughness, R_q (nm)	z Scale (nm)	Image surface area (μm^2)
Before annealing	19.4	24.8	210	105
200	27.8	38.6	530	121
300	32.1	44.7	704	134
400	37.0	52.1	820	157
500	43.0	60.0	910	167

The R_a and R_q values of the CuCo-oxide coatings before annealing are found to be lower than the annealed ones. The mean surface roughness, R_a and the rms value of the surface roughness, R_q have been improved by 121 and 142%, respectively after the coatings been annealed, within an average image surface area of $117 \mu\text{m}^2$. This clearly indicates that annealing has remarkable impact on the surface topographical features of CuCo-oxide coatings. Annealing results in the occurrence of major grain growth around the coating surface which in turn is responsible for the enhanced surface roughness of the coatings. This is because as the annealing progresses, the atoms have adequate activation energy to occupy the correct site in the crystal lattice and grains. It is also assumed that, during annealing, due to the higher ionic mobility, and densification of the materials grains were growth on the z direction, perpendicular to the substrate surface and surface roughness of the coatings was increased. This is consistent with the crystalline properties of these coatings as seen in FESEM and XRD analysis of this manuscript. The peaks and valleys indicate the quantitative surface roughness and absorptance of these coatings. With close examination of images, grain-like particles are more obvious with sizes ranging from 20 to 80 nm which are embedded within pores. These grain-like particles morphologies were also reported by Amun *et al.* [463].

8.4.5 Solar Selectivity Studies

The solar selective properties of CuCo-oxide coatings before and after annealing were evaluated on the basis of solar reflectance spectra, acquired using UV-Vis and FTIR techniques in the wavelength range of 190-2500 nm and 2.5-15.4 μm , respectively shown in

Figures 8.9 and 8.10. Using the UV-Vis and FTIR reflectance spectra, the solar absorptance and thermal emittance values of these coatings were assessed by Duffie and Beckman method, as described [24]. The corresponding solar selectivity values of the coatings as computed using $s = \frac{\alpha}{\epsilon}$ are displayed in Table 8.7. The prepared coatings exhibit low to moderate reflectance together with interference peaks in the lower wavelength regions and sharp absorption edges that basically form solar selective absorber curve profiles surrounded by UV-Vis-NIR range of the solar spectrum. Gradual increase in annealing temperature, generally, has a tendency to shrink the interference peaks and the absorption edges. Consequently, the solar absorptance values are improved. Substantial reductions of the interference peak and the absorption edge were identified by the coatings annealed at 400 °C and 500 °C and the corresponding absorptance values reached to the maximum. It is, generally, assumed that the reflectance behaviors of CuCo-oxide coatings, in the NIR range, is governed by at three aspects [463, 493] thickness of the coatings, inherent properties of the coating materials, and the reflective nature of the substrates used to deposit the coatings. In the present case all the coatings having the similar thicknesses, the reflectance profiles are governed by the combined effect of solar absorptions/scattering by the coating materials and the back-reflections of the near-infrared radiations passed through the coatings by the substrate. Furthermore, high temperature annealing also boosts the crystallinity of the coatings material that consequently results increasing the scattering leading to enhance the absorption.

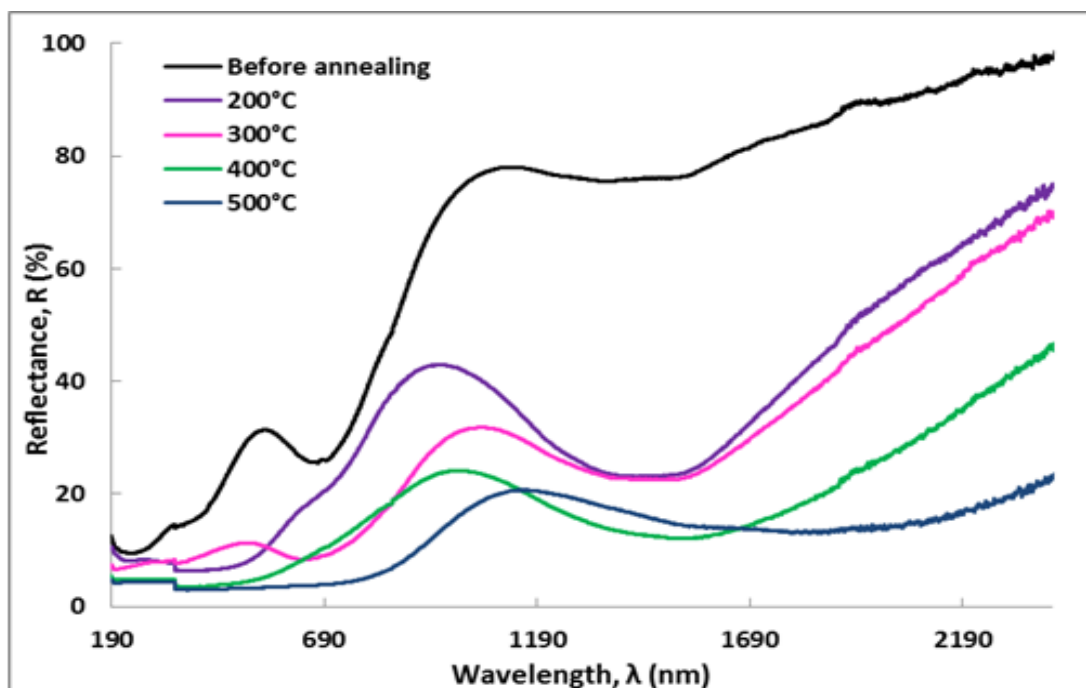


Figure 8.9: UV-Vis reflectance and absorptance spectra of CuCo-oxide coatings before annealing and after being annealed at different temperatures.

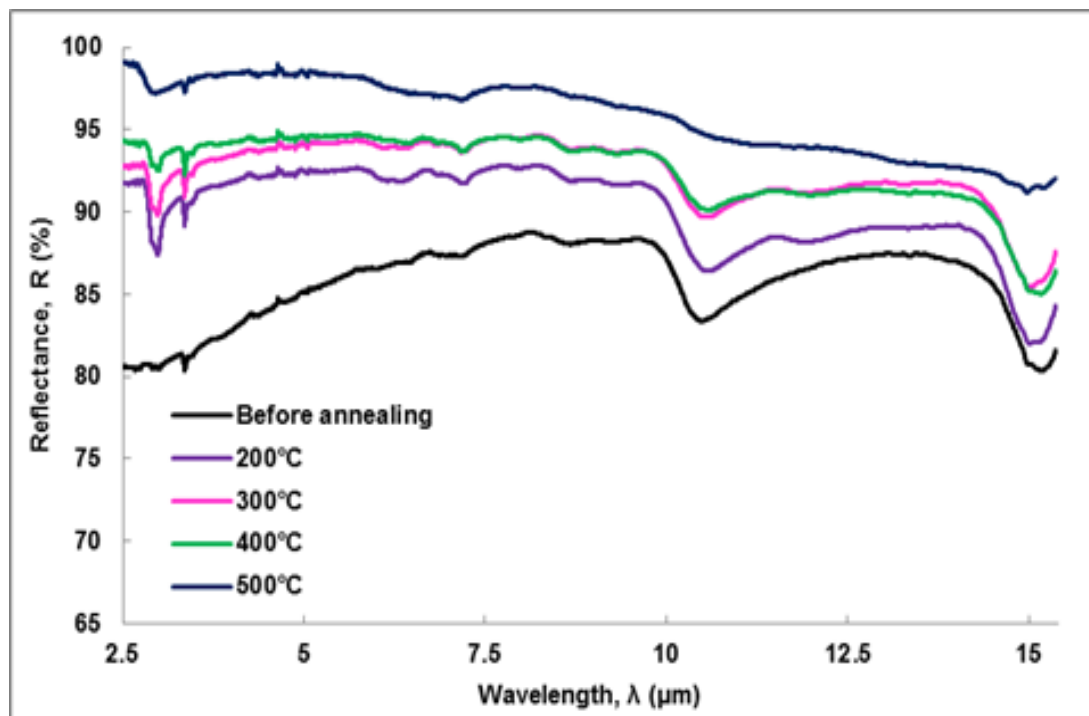


Figure 8.10: FTIR reflectance spectra of CuCo-oxide coatings before annealing and after being annealed at different temperatures.

Table 8.7: Solar absorbance, thermal emittance and solar selectivity values of CuCo-oxide coatings before annealing and after annealing at different temperatures in air for 1 hr.

Annealing condition	Solar absorbance (%)	Thermal emittance (%)	Solar selectivity
Before annealing	51.72	13.60	3.81
200 °C	74.45	9.72	7.66
300 °C	80.90	7.45	10.86
400 °C	86.30	6.49	13.30
500 °C	91.22	3.80	24.00

Following Beckman-Duffie method, using the FTIR reflectance data presented in Figure 8.10, the estimated thermal emittance values of CuCo-oxide coatings before and after annealing presented in Table 8.7 shows that the thermal emittance values are significantly reduced from 13.6 to 3.8% with the gradual increase in annealing temperatures. It is established that the solar absorbance and thermal emittance of coatings strongly depend on their corresponding band-gap. Annealing effectively modifies the overall band structure of these coatings and thereby the solar selectivity values are also improved. The selection of substrate materials also has a considerable impact on the reflective behavior of coatings. The longer the near-infrared wavelength, the more radiation will be transmitted through the coating due to the less energy preserved by the optical photons. As a result, it is easier for them to pass through to the coating without being absorbed and then reflected back by the substrate. This absorber–reflector tandem concept allows them to behave similar to a semiconducting object. The solar selectivity values of these coatings also depend on the materials used, synthesis conditions and techniques, coatings thickness, surface roughness of the coatings, and so on. It has been clearly seen that annealing leads to lattice and grain refinements (XRD results), modifications in residual stress and microstrain values (XRD data), formation of new bonding and changes in chemical bonding states (XPS results), microstructural modification (from FESEM studies), variations in surface roughness of the coatings (AFM studies), and band structure change (band-gap analysis data). All these factors substantially affect the scattering and the reflection of incident solar radiation and therefore the optical characteristics of the coatings are, in turn, are improved. Consequently, the solar selectivity values are boosted.

8.4.6 Bader's Charge Analysis

Table 8.8 lists Bader's charges on Cu, Co and O atoms in bulk $\text{Cu}_x\text{Co}_{3-x}\text{O}_4$ system. As seen from Table 8.8, the Cu and Co atoms in all the stoichiometries hold positive charges while the O atoms are associated with negative charges. Bader charge values also reveal a covalent character for Cu-Co bond in all the system that have both of these atoms and ionic character for Cu-O and Co-O bonds. Moreover, our results show that Co atoms loss more electrons when Cu is introduced into the system, while O atoms gains electrons less than what they did when Cu ratios increases.

Table 8.8 : Bader's charges on Cu, Co and O atoms in e on $\text{Cu}_x\text{Co}_{3-x}\text{O}_4$ ($x = 0, 0.75, 1.5, 2.25$ and 3) coatings.

Stoichiometry			Charge transfer (electrons)		
Cu_x	Co_{3-x}	O_4	Cu	Co	O
0	3	4	0	1.58	-1.18
0.75	2.25	4	1.10	1.61	-1.11
1.5	1.5	4	1.30	1.66	-1.11
2.25	0.75	4	1.28	1.66	-1.03
3	0	4	1.12	0	-0.84

8.5 Conclusions

The CuCo-oxide coatings, deposited on aluminum substrates, were investigated for their temperature dependent structural and solar selectivity analysis via XRD, XPS, FESEM, AFM, UV-Vis, and FTIR approaches. FESEM, AFM and XRD show increase in the crystalline domains of the coatings with increasing annealing temperatures while the residual stress systematically decreasing indicating mechanically stable material. XPS analysis determined (i) tetrahedral, octahedral and mixed states of Cu and Co ions, (ii) stable Co/Cu ratio, (ii) increasing surface C and O ratio and (iv) no metal-carbon bonding. Optical studies via UV-Vis and FTIR reflectance spectrum confirmed an excellent solar selectivity of 24 attained by the coating annealed at 500 °C.

Chapter 9 : Influence of the variation in the U parameters in the DFT + U methodology on activation and reaction energies

Paper IV

Miran, H.A., Jiang, Z-T, Jaf, Z.N., Rahman, M.M. and Altarawneh, M. Influence of the Variation in the Hubbard Parameter (U) on Activation Energies of CeO₂-Catalysed Reactions, Submitted to Catalysis Letters, August (2018).

9.1 Abstract

Accurate description of thermodynamic, structural and electronic properties for bulk and surfaces of ceria (CeO₂) necessitates the inclusion of the Hubbard parameter (U) in the density functional (DFT) calculations to precisely account for the strongly correlated $4f$ electrons. Such treatment is a daunting task when attempting to draw a potential energy surface for CeO₂-catalyzed reaction. This is due to the inconsistent change in thermodynamic/kinetics of the reaction in reference to the variation in the U values. As an illustrative example, we investigate herein the discrepancy in activation and reaction energies for steps underlying the partial and full hydrogenation of acetylene over the CeO₂ (111) surface. Overall, we find that both activation and reaction energies positively correlate with the increase in the U value. In addition to benchmarking against more accurate theoretical methodologies, we suggest that U values are better to be optimized against kinetics modelling of experimentally observed profiles of products from the catalytic reaction.

9.2 Introduction

Cerium oxide (CeO_2 , ceria) and their based materials are essential in many catalysis industries [74, 494, 495]. Because of being oxygen - storage ingredients [158], they are utilized in three-way catalysts (*TWCs*) technology [496]. In the latter, ceria act as an oxidizing and reducing agent for some pollutants (CO , NO_x , HC) emitted by cars and subsequently converting them to harmless materials. Another catalytic application of ceria is that the ceria- supported transition metals are being presently considered as active catalysts for the water- gas - shift reaction which converts CO and water to CO_2 and hydrogen [497]. The fact standing behind these and other applications of ceria is the two stable and extreme oxidation states [270] namely, Ce^{4+} , Ce^{3+} . As such cerium oxide may occupy different possible states between these two extreme states; CeO_x .

Accurate electronic, structural and thermo-mechanical properties of materials can now be readily acquired by density functional theory (DFT) calculations. However, plain DFT functional suffer from a serious shortcoming in describing the electronic structure of ceria. Excessive delocalization of the $4f$ electron wrongly result in a metallic behavior for CeO_2 in contrast to its semiconducting nature observed experimentally (band gap of ceria amounts to 6 eV [498]). To force localization and strong correlation in the $4f$ electrons in ceria, the DFT + U (Hubbard parameter) approach has been widely deployed. Unfortunately, there is a no single U value that can reproduce all materials attributes, such as geometries, thermodynamics and density of states. The U value for bulk CeO_2 is often optimized against its lattice constant, enthalpy of formation and band gap. The U value also displays sensitivity toward the deployed DFT functional. As such, an optimized U value for enthalpy of formation or band gap may not represent the optimum value for acquiring thermo-kinetic parameters for ceria-catalyzed reactions. Computing accurate activation energies is a central task in computational catalysis. Previous computational studies on catalytic reactions over ceria have mainly deployed the U value optimized for bulk's band gap. For instance, Chen, *et al.* [80] reported reaction pathways for the reduction of $\text{CeO}_2(111)$ and $\text{CeO}_2(110)$ surfaces via interaction with gaseous by H_2 molecules utilizing a U value of 7.1 eV based on the PW91 functional. Likewise, in recent study [499], we deployed a DFT + U functional to report reduction energies for pure CeO_2 and CeO_2 alloyed

with Zr and Hf at various loading ratios. We optimized our deployed U value against the experimental value for the complete reduction of ceria at 298.15 (2CeO₂ → Ce₂O₃ + 1/2O₂).

To this end, the aim of this chapter is to survey the change in reaction and activation energies for a set of well-studied systems of reaction when deploying different values of U . Herein, we limit our analysis to energy terms, however, it must also be noted that geometrical as well as electronic factors must also be taken into account when locating an optimal U value for a given reaction.

9.3 Methodology

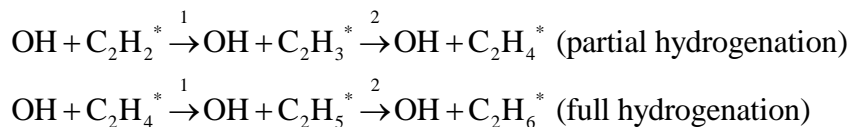
Herein, geometry optimizations and energy calculations were carried out at absolute zero via the plane wave DFT program of the Vienna ab initio simulation package (VASP) [381]. The calculations methodology comprises a spin-polarized PAW-PBE functional [219], van der Waals correction by the Grimme functional [500], and a Gaussian smearing. For Ce, it is necessary to apply on-site Coulomb interaction correction (DFT+ U), to account and correct f electron delocalization. The DFT+ U formalisms suggested by Dudarev *et al.* [214]. has been applied. This method was proven to yield band gap, lattice constant and heat of formation in a close agreement with the analogous experimental values. It has been shown including van der Waals corrections for species adsorption over ceria surfaces systematically increases adsorption energies [74]. Magnetic moment orientation has also been considered, but it is not sensitive to pristine CeO₂, as it is a nonmagnetic insulator material [501]. Integration over the Brillouin - zone was performed using Monkhorst - pack grids of $4 \times 4 \times 4$ and $4 \times 4 \times 1$ κ - points for the bulk and surface calculations, respectively [431]. Structural optimization calculations deploy a plane wave cut off energy of 400 eV, an energy tolerance of 0.1 meV and atomic force tolerance of 0.05 eV/Å. Nudged elastic band (NEB) utilized in transition state calculations uses the same plane wave cut off energy and energy tolerance.

9.4 Results and Discussions

The seminal work by Capdevila-Cortada *et al.* [502] has systematically analyzed the effect of the U parameter on the activation and reaction energy for the first hydrogen stripping of formaldehyde into adsorbed CHO and OH. Author finds that the influence of the variation in the U value is more evident when there is a reduction in the oxidation state of cerium surface atoms upon interaction/dissociative adsorption of gas phase species. Thus, the change in the U value exerts no change in the physisorption energy of formaldehyde over the CeO₂ (111) surface. Likewise, the change in activation and reaction energy when a small U value is employed was a rather very minimal. Indeed, at small values of U , the f electrons of Ce atoms are still delocalized. However, at higher values of U (3.0 – 6.0 eV), both activation and reaction energies vary almost linearly with the U value with a negative slope in both cases. The DFT (PBE) + U reproduces the activation and reaction energy of the computationally demanding hybrid DFT functional of HSE06 at U values of 3.33 eV and 4.32 eV; respectively. This follows the consensus that there is no universal U value that can produce all experimentally observed parameters such as band gap and lattice constant. The authors' proposed DFT + U methodology to locate transition states encompasses benchmarking the thermodynamic of the reaction against an accurate theoretical framework (*i.e.*, hybrid DFT functional), accurate accounting for f electrons localization, and rescaling the U value according to the perturbation of geometries between transition state, reactant and product. The authors argued that deploying a single U value along the entire reaction coordinate may induces significant in the overall kinetics of the reaction.

One of the most prominent catalytic applications of ceria is partial hydrogenation of alkyne cuts into their corresponding alkenes rather than alkanes. Carrasco *et al.* [73] carried out a combined experimental and DFT study to on the selective production of C₂H₄ from hydrogenation of C₂H₂. Catalytic tests were performed various H₂/C₂H₂ inlet ratios in the range of 10-30 within a temperature window of 423 – 623 K and a residence time of 0.12- 1.0 s. The selectivity toward ethylene attains a value of 80% and remains unchanged even at higher H₂/C₂H₂ inlet ratios. In order to model the experimentally observed selective formation of C₂H₄, Carrasco *et al.* adapted the DFT functional of PBE with the inclusion of a fixed U parameter at 4.5 eV for Ce atoms.

The underlying surface mechanism incorporates four hydrogen transfer reaction from the -OH site to the free carbon atom in the adsorbed C₂ adduct:



The authors attributed the occurrence of partial rather than full hydrogenation rests to lower activation for subsequent hydrogenation leading to gas phase C₂H₄ compared to those leading to with an adsorbed β -C₂H₄ adduct. Barriers for the first hydrogenation step in partial and full hydrogenation mechanism were considerably lower than those of the second step (0.09/0.41 versus 3.65/3.44 eV). We have also observed a similar trend in our recent study on hydrogenation of acetylene over Mo₂N (111) surface [503]. The objective of this chapter is to assess the influence of the U parameter on the activation reaction energies for these four reactions. The underlying aim herein are two-fold; to revisit conclusions made Capdevila-Cortada *et al.* and to assess the influence of the U parameter on the thermodynamic and kinetic orderings reported by Carrasco *et al.*

Table 9.1 and Figures 9.1- 9.4 enlist activation and reaction energies for the two hydrogenation steps in the partial and full hydrogenation routes for U values between 3.5 – 6.5 eV. Values obtained with a plain DFT (*i.e.*, $U = 0$) have also been included for comparison. Corresponding values obtained by Carrasco *et al.* ($U = 4.5$ eV) are highlighted. As displayed in Table 9.1, activation energies for the four-hydrogenation reaction increase with the U value. The first hydrogenation step in the partial hydrogenation route incorrectly incurs a negative value when the plain PBE functional is applied. The first hydrogenation step in both routes at all U values require considerably higher energy barriers than the first second step. The activation energy for the second step in the full hydrogenation route is more sensitive to the U treatment in reference to the three other reactions. The activation barrier for this step increases from 1.91 eV at $U = 0$ to 3.46 eV at a U value of 4.5 eV. Overall, the variation of the activation energies in reference to the deployed U value is very significant. The effect is more profound on the reaction rate constants. For instance, at 500 K, a difference of only 0.1 eV in the value of the activation

energy changes the reaction rate constant by a factor of ~ 10 . Activation barriers as large as 4.0 eV (~ 92.0 kcal/mol), most likely do not proceed at the relatively low temperature of the catalytic tests (423 – 623 K). Thus, we envisage here that an accurate benchmarking of the exact reaction barriers may stem from surveying *via* kinetics modelling the kinetic feasibility of the reaction at a given experimental operation conditions.

Table 9.1: Variation of activation barriers and reaction energies of acetylene hydrogenation into ethane over the CeO₂ (111) surface. Corresponding values by Carrasco *et al.* [73] are highlighted.

Reaction	U_values	Activation barrier (eV)	Reaction energy (eV)
R1 $C_2H_2^*+H^*\rightarrow C_2H_3^*$	U=0	-0.81	-1.26
	U=3.5	0.15	-1.65
	U=4.5	0.202 (0.09)	-1.42 (-1.45)
	U=5.5	0.205	-1.21
	U=6.5	0.296	-0.99
R2 $C_2H_3^*+H^*\rightarrow C_2H_4^*$	U=0	3.24	1.71
	U=3.5	3.50	1.95
	U=4.5	3.77 (3.65)	2.17 (2.13)
	U=5.5	3.99	2.38
	U=6.5	4.20	2.59
R3 $C_2H_4^*+H^*\rightarrow C_2H_5^*$	U=0	0.25	-0.63
	U=3.5	0.30	-0.59
	U=4.5	0.39 (0.41)	-0.99 (-1.03)
	U=5.5	0.50	-0.77
	U=6.5	0.66	-0.62
R4 $C_2H_5^*+H^*\rightarrow C_2H_6^*$	U=0	1.91	0.46
	U=3.5	3.00	0.88
	U=4.5	3.46 (3.44)	1.32 (1.20)
	U=5.5	3.89	1.75
	U=6.5	4.32	2.17

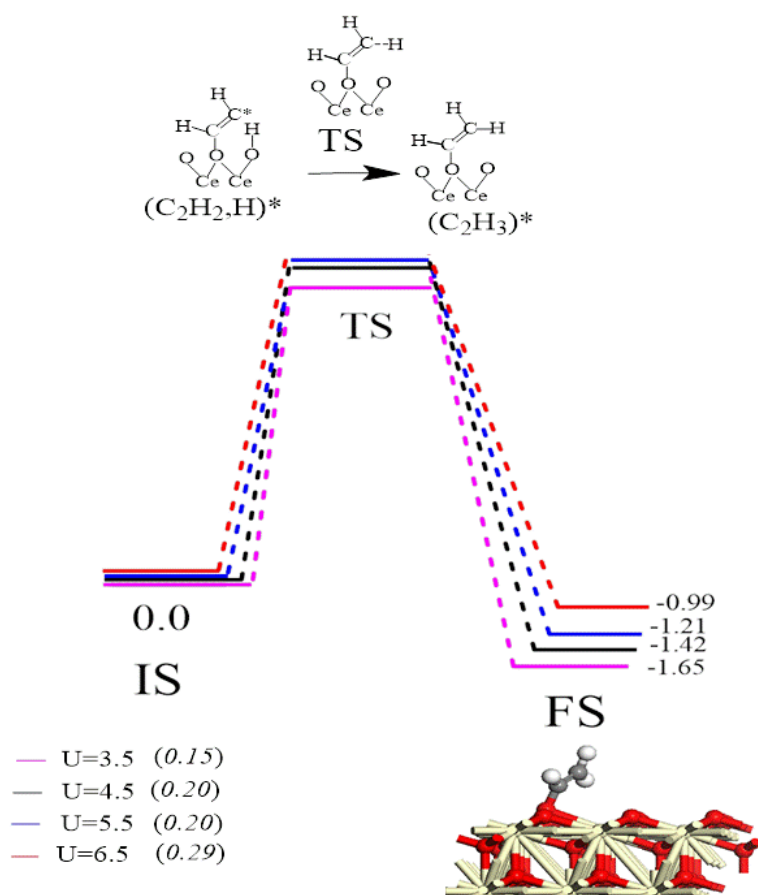


Figure 9.1: Energy profile for the first hydrogenation step in the partial hydrogenation route of acetylene over the CeO₂(111) surface at different U values. Values of activation barrier (tilted) and reaction energy are in kcal/mol with respect to the initial reactant. Red cream, gray, and white stand for atoms, oxygen, cerium, carbon, and hydrogen, respectively.

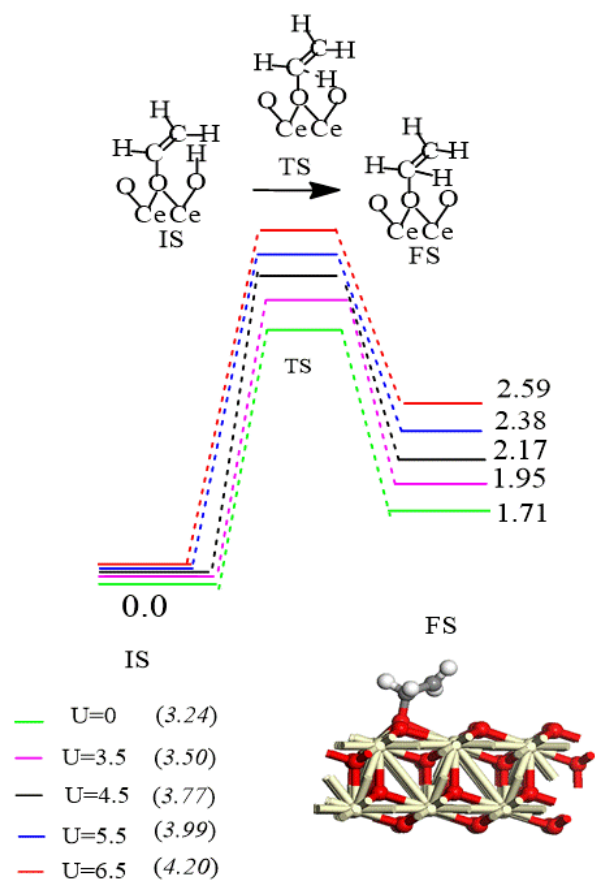


Figure 9.2: Energy profile for the second hydrogenation step in the partial hydrogenation route of acetylene over the CeO₂(111) surface at different U values. Values of activation barrier (tilted) and reaction energy are in kcal/mol with respect to the initial reactant.

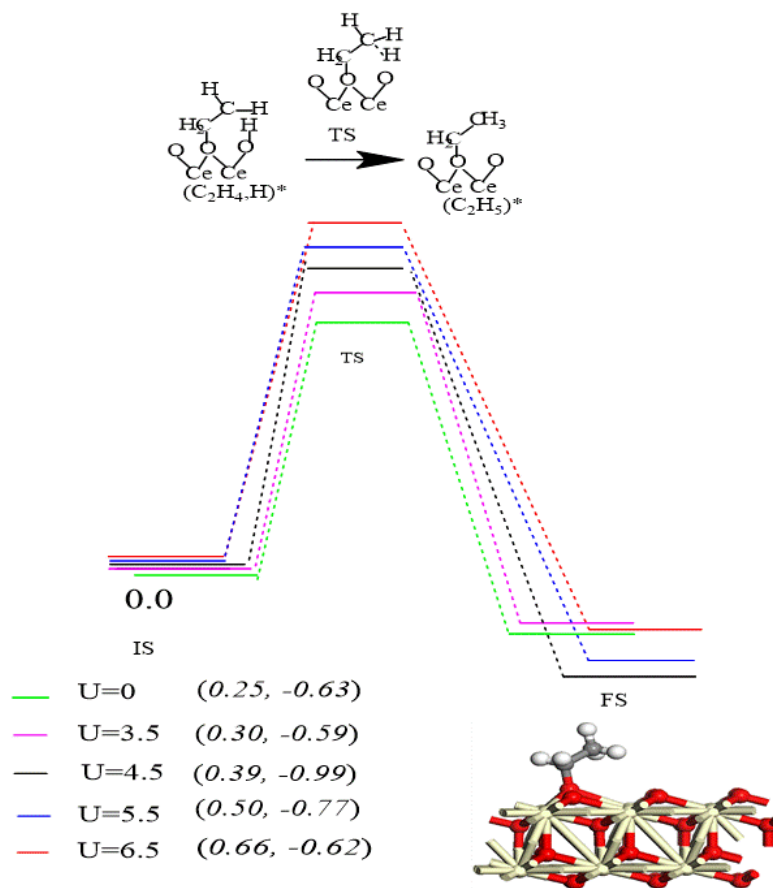


Figure 9.3: Energy profile for the first hydrogenation step in the full hydrogenation route of acetylene over the CeO₂(111) surface at different U values. Values of activation barrier (tilted) and reaction energy are in kcal/mol with respect to the initial reactant.

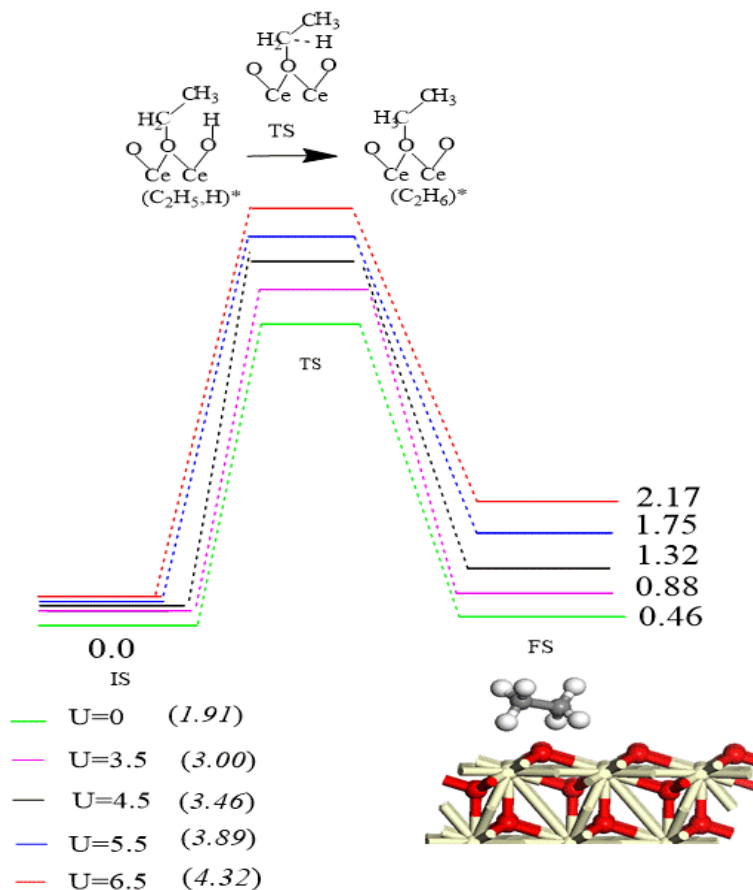


Figure 9.4: Energy profile for the second hydrogenation step in the full hydrogenation route of acetylene over the CeO₂(111) surface at different U values. Values of activation barrier (tilted) and reaction energy are in kcal/mol with respect to the initial reactant.

Inspection of the U -reaction energy variation displays an analogous thermodynamic sensitivity. Overall, the exothermicity of a given reaction correlates inversely with the U value. Finding the optimum U value for the reaction energy requires benchmarking against very accurate theoretical levels most notably, quantum Monte Carlo (QMC) and the random phase approximation (RPA) or even the relatively more computationally affordable hybrid DFT methods.

9.5 Conclusions

We are now in a position to convey the following concluding remarks and suggestions:

- As shown in previous studies, the variation in the U value induces a significant effect on computed activation and reaction energies for catalytic CeO_2 -assisted reactions.
- Higher U value tends to reduce the thermodynamic feasibility of the reaction and increases its activation energy.
- In addition to comparison with QMC, RPA and hybrid DFT method, detailed kinetic modelling can be utilized as a benchmarking tool in deriving the optimum U value.
- When feasible, clusters models at more accurate DFT methods (such as B3LYP) may give more accurate kinetics and thermochemical parameters for reaction involving CeO_2 than periodic systems.

Chapter 10 : Conclusions and Future Research Directions

This dissertation reports connected yet independent investigations onto structural, optical, thermo-mechanical and catalytic properties of rare earth metal oxides via synergetic experimental-theoretical approaches. Band gaps and lattice constants for the complete series of compounds in the sesquioxides family were reported in the first part of the thesis. Bader's atomic charges reveal an ionic nature for the Ln-O bonds in all Ln₂O₃ compounds. It was found that lanthanide sesquioxides obey the Born-Huang's criterion; and hence they are mechanically stable. In accordance with experimental trends, the Gibbs free energies for the reduction reaction of CeO₂ to Ce₂O₃ were found to exhibit endothermic behavior with a value of 740 kJ/mol-O₂ at the room temperature. The influence of temperature on the reduction energies of pure ceria was also elucidated. The reduction energy of ceria increases by 26 kJ/mol-O₂ upon reduction when the O/Ce atomic ratio decreases from 1.9 to 1.8. The findings illustrate that, adding Hf and Zr ions to the stoichiometric and reduced CeO₂ lattice reduces their reduction enthalpies. It has been demonstrated that alloying ceria with Zr or Hf leads to significant reduction in volume (in reference to pure ceria).

Ceria is a potent catalyst either when deployed as a stand-alone catalyst or when used as a support. In **Chapter 4**, modelling of experimental results relating to the decomposition of three chlorinated volatile organic compounds is performed; those being, chloroethene, chloroethane and chlorobenzene. We find that, the three titled compounds adsorb rather weakly in their physisorbed states over ceria. Activation energies deduced from the experimental conversion-temperature profiles match the estimated activation energies for the dissociative adsorption of these molecule over the CeO₂(111) surface, *via* fission of their C-Cl bonds. Hydrogen transfer from surface -OH sites to the radical center in adsorbed hydrocarbon radicals (vinyl, ethyl and phenyl radicals) liberates their corresponding stable hydrocarbon molecules; albeit via very sizable activation barriers. Pathways for the formation of benzene and 1,2-dichlorobenzene from the catalytic oxidative decomposition of 1-chlorobenzene molecule have also been proposed. The formation of the latter proceeds via chlorine transfer from an oxychloride structure. To the best of our knowledge, this suggested feasible pathway constitutes the first ever quantum

chemistry-confirmed pathway for a surface assisted chlorination pathway of an aromatic molecule in the literature. Dissociative adsorption of gas phase oxygen molecules vacant oxygen sites restores the catalytic activity of ceria by oxidizing adsorbed hydrocarbon adducts (for example, phenyl into phenoxy, o-benzoquinone). This process also results in the re-oxidation of the surface via filling in the oxygen vacant sites.

Terbium dioxide (TbO_2) is a promising material for prominent optical and catalytic applications. We found that bulk and surfaces of TbO_2 exhibit a semiconducting character based on their DOS curves. Thermo-elastic properties such as heat capacities, volume expansions, bulk modules and thermal expansions were obtained for a wide range of temperatures and pressures based on the quasi-harmonic approximation approach (QHA). The QHA approach relies on phonon density of states calculations at various atomic displacements within a 2×2 unit cell model. Using the Ab initio atomistic thermodynamics approach, surface free energies were calculated for all possible surface terminations as a function of the oxygen chemical potential. Two surfaces appear to be more stable in the accessible domain of oxygen chemical potential; namely, (111): Tb and (111): O+1V_O. The presence of an oxygen vacancy in the latter is expected to play a potent role in catalysis by TbO_2 .

CeO_2 films, prepared by Magnetron sputtering, deposited onto c-Si substrate as a function of oxygen/argon flow ratio, were comprehensively studied and characterized in this work by various structural and optical techniques such as XRD, XPS, FESEM, FTIR and UV-Vis. XRD spectra of all of the coatings showed a polycrystalline structure with cubic fluorite – structure for CeO_2 along (111), (200) and (222) orientations. From the survey scan obtained by XPS test, Ce, O, C elements were found in the studied films. Further analysis on survey scan spectra indicated to an increase in the Ce and O atomic percentages as the oxygen/argon flow ratio increases. At the lower oxygen/ argon mixture, high resolution XPS scans of the Ce 3d regions showed two oxidation states of CeO_2 and Ce_2O_3 in the films; while Ce_2O_3 oxidation state gradually vanished as the oxygen pressure increased. UV-Vis data was plotted to display the solar reflectance of the selected coating material and thereafter all optical and dispersion properties such as absorption coefficient (α), the real and imaginary parts of the dielectric function (ϵ_1 , ϵ_2), the refractive index

(n) and the extinction coefficient (k) were calculated. The analysis suggests that the CeO_2 films have indirect optical band gaps in the range of 2.25 - 3.1 eV. Plane wave DFT calculations were employed to report optical properties calculations of CeO_2 cluster at ground state. The band gap extracted from the plot of simulated density of state (DOSs) of the CeO_2 cluster is in agreement with the corresponding experimental value. The experimental absorption coefficient (α) and the analogous computed value show a similar trend and, to a degree, possess matching values in the wavelength range from 100 to 2500 nm. Overall, the theoretical results are shown to be consistent with the corresponding measured values

$\text{Cu}_x\text{Co}_{3-x}\text{O}_4$ coatings spinel oxides were prepared by sol-gel method and annealed at different temperature spanning from 200 to 500 °C with step size of 100 °C. Several characterization examinations were executed with the aim of highlighting their electronic, structural, optical and solar selectivity properties. Results derived by XRD demonstrate that with an increase in the annealing temperature, all coatings exhibit $\text{Cu}_{0.56}\text{Co}_{2.44}\text{O}_4$ structural phase (ICSD 78-2175) with favored direction along (400) peak. Solar selectivity of the thin films was observed to be significantly enhanced with the rise in the annealing temperatures. Atomic charge distributions were computed for the series of stoichiometries in $\text{Cu}_x\text{Co}_{3-x}\text{O}_4$ system ($x = 0, 0.75, 1.5, 2.25$ and 3). Charge density analysis revealed a covalent character for Cu-Co bond in the entire systems.

Finally, DFT + U , as a cost-effective method to describe the electronic structure ceria, was employed to investigate the effect of Hubbard parameter of U on the barrier and reaction energies for typical partial and total hydrogenation reactions over ceria surfaces. Analysis of the obtained results demonstrates that the barrier and reaction energies increase with the U value. The thermodynamic feasibility of the reactions clearly lessens as the U value increases. Nonetheless, accurate benchmarking of the U value still requires contrasting energies with analogous values obtained by the very computationally demanding hybrid methods.

Herein, potential future directions are discussed:

- Reactions steps governing catalytic-assisted reactions by ceria are still largely unknown for many systems. For example, this includes: conversion of propyne into propene; hydrogenation of benzene into cyclohexane and de-bromination of brominated hydrocarbons; and, most notably, brominated flame retardants.
- The shape Dependent Reactivity and Catalysis of Ceria Nanoparticles was investigated recently [504] and it was found that oxygen storage capacity (OSC) of ceria is very sensitive to the atomic environments of ceria. For instance, 2D ceria nanoplates, with an extended surface to volume ratio, displays higher OSC than bulk CeO₂. Thus, it will be insightful to study oxidation of Co into CO₂ and No into N₂ over nanoparticles and nanotubes of ceria.
- While thermodynamics dictates spontaneous occurrence of water splitting over TbO₂ [505], the eventual occurrence of this important chemical phenomena truly rests on kinetics factors. Thus, it is important to study mechanism for hydrogen production from water catalyzed by TbO₂.
- In **Chapter 9**, it was shown that kinetics modeling could be used to parametrize the U value. For example, the onset temperature for the occurrence of a chemical reaction at a given temperature depends primarily on the activation energy of the initial reaction. Kinetics modeling can accurately predict the required activation energy for a chemical reaction to commence at a given temperature. Knowing the activation energy from kinetics model will assist in benchmarking the U value against experimentally observed profiles of products.
- In **Chapter 4**, studies were limited to Hf and Zr ions as effective ceria dopants on lowering the reduction energies. In this regard, the effect of alloying with other atoms such as Tb can be investigated. The underlying aim is to acquire Gibbs free energies for Tb-Ce-O configurations at elevated temperatures pertinent to catalytic applications.

- In **Chapter 7**, the optical properties and dispersion parameters of Ce-oxide films were studied with the aim of evaluating the anti-reflection character of such films in the visible range. It is insightful to report potentially enhanced optical characteristic and anti-reflection properties of Ce-Oxides when alloying them with other transition metals such as Ti, Zr and Hf.
- In **Chapter 8**, a noticeable improvement was reported in the solar selectivity for CuCo-oxide coatings when annealed at different temperatures. As such, investigations into a likely improvement in solar selective materials for other spinal oxide would be warranted.

References

- [1] L. Petit, A. Svane, Z. Szotek, W.M. Temmerman, Electronic structure of rare earth oxides, *Rare Earth Oxide Thin Films*, Springer2007, pp. 331-343.
- [2] A. Bartos, K. Lieb, M. Uhrmacher, D. Wiarda, Refinement of atomic positions in bixbyite oxides using perturbed angular correlation spectroscopy, *Acta Crystallogr. B* 49 (1993) 165-169.
- [3] D. Richard, L. Errico, M. Rentería, Structural properties and the pressure-induced C→ A phase transition of lanthanide sesquioxides from DFT and DFT+ U calculations, *J. Alloys Compd.* 664 (2016) 580-589.
- [4] T. Montini, M. Melchionna, M. Monai, P. Fornasiero, Fundamentals and catalytic applications of CeO₂-based materials, *Chem. Rev.* 116 (2016) 5987-6041.
- [5] M. Yashima, D. Ishimura, Y. Yamaguchi, K. Ohoyama, K. Kawachi, High-temperature neutron powder diffraction study of cerium dioxide CeO₂ up to 1770 K, *Chem. phys. lett.* 372 (2003) 784-787.
- [6] M. Yashima, S. Kobayashi, Positional disorder of oxygen ions in ceria at high temperatures, *Appl. Phys. Lett.* 84 (2004) 526-528.
- [7] P. Knappe, L. Eyring, Preparation and electron microscopy of intermediate phases in the interval Ce₇O₁₂–Ce₁₁O₂₀, *J. Solid State Chem.* 58 (1985) 312-324.
- [8] M. Zinkevich, D. Djurovic, F. Aldinger, Thermodynamic modelling of the cerium–oxygen system, *Solid State Ion.* 177 (2006) 989-1001.
- [9] O.T. Sørensen, Thermodynamic studies of the phase relationships of nonstoichiometric cerium oxides at higher temperatures, *J. Solid State Chem.* 18 (1976) 217-233.
- [10] S. Ray, A. Nowick, D. Cox, X-ray and neutron diffraction study of intermediate phases in nonstoichiometric cerium dioxide, *J. Solid State Chem.* 15 (1975) 344-351.
- [11] E. Kümmerle, G. Heger, The structures of C–Ce₂O_{3+δ}, Ce₇O₁₂, and Ce₁₁O₂₀, *J. Solid State Chem.* 147 (1999) 485-500.
- [12] S. Ray, D. Cox, Neutron diffraction determination of the crystal structure of Ce₇O₁₂, *J. Solid State Chem.* 15 (1975) 333-343.
- [13] J. Conesa, Computer modeling of surfaces and defects on cerium dioxide, *Surf. Sci.* 339 (1995) 337-352.

- [14] H. Bärnighausen, G. Schiller, The crystal structure of A-Ce₂O₃, *J. Less Common. Met.* 110 (1985) 385-390.
- [15] D.J. Kim, Lattice Parameters, Ionic Conductivities, and Solubility Limits in Fluorite-Structure MO₂ Oxide [M= Hf⁴⁺, Zr⁴⁺, Ce⁴⁺, Th⁴⁺, U⁴⁺] Solid Solutions, *J. Am. Ceram. Soc.* 72 (1989) 1415-1421.
- [16] M. Mogensen, N.M. Sammes, G.A. Tompsett, Physical, chemical and electrochemical properties of pure and doped ceria, *Solid State Ion.* 129 (2000) 63-94.
- [17] S.J. Hong, A.V. Virkar, Lattice Parameters and Densities of Rare-Earth Oxide Doped Ceria Electrolytes, *J. Am. Ceram. Soc.* 78 (1995) 433-439.
- [18] R.T. Shannon, C.T. Prewitt, Effective ionic radii in oxides and fluorides, *Acta Crystallogr., Sect. B: Struct. Sci.* 25 (1969) 925-946.
- [19] M. Yashima, H. Takashina, M. Kakihana, M. Yoshimura, Low-Temperature Phase Equilibria by the Flux Method and the Metastable–Stable Phase Diagram in the ZrO₂–CeO₂ System, *J. Am. Ceram. Soc.* 77 (1994) 1869-1874.
- [20] M. Yashima, H. Arashi, M. Kakihana, M. Yoshimura, Raman scattering study of cubic–tetragonal phase transition in Zr_{1-x}Ce_xO₂ solid solution, *J Am Ceram Soc.* 77 (1994) 1067-1071.
- [21] M. Yashima, T. Mitsuhashi, H. Takashina, M. Kakihana, T. Ikegami, M. Yoshimura, Tetragonal—Monoclinic Phase Transition Enthalpy and Temperature of ZrO₂-CeO₂ Solid Solutions, *J. Am. Ceram. Soc.* 78 (1995) 2225-2228.
- [22] M. Yashima, T. Hirose, S. Katano, Y. Suzuki, M. Kakihana, M. Yoshimura, Structural changes of ZrO₂-CeO₂ solid solutions around the monoclinic-tetragonal phase boundary, *Phys. Rev. B* 51 (1995) 8018.
- [23] M. Yashima, K. Morimoto, N. Ishizawa, M. Yoshimura, Zirconia–ceria solid solution synthesis and the temperature–time–transformation diagram for the 1: 1 composition, *J. Am. Ceram. Soc.* 76 (1993) 1745-1750.
- [24] M. Yashima, S. Sasaki, Y. Yamaguchi, M. Kakihana, M. Yoshimura, T. Mori, Internal distortion in ZrO₂–CeO₂ solid solutions: neutron and high-resolution synchrotron x-ray diffraction study, *Appl. Phys. Lett.* 72 (1998) 182-184.
- [25] D.E. Vanpoucke, S. Cottenier, V. Van Speybroeck, I. Van Driessche, P. Bultinck, Tetravalent doping of CeO₂: The impact of valence electron character on group IV dopant influence, *J. Am. Ceram. Soc.* 97 (2014) 258-266.

- [26] S. Chavan, A. Tyagi, Investigations on ceria–hafnia system for phase analysis, and HT-XRD studies on a few cubic compositions, *Mater. Sci. Eng., A* 433 (2006) 203-207.
- [27] H. Fujimori, M. Yashima, S. Sasaki, M. Kakihana, T. Mori, M. Tanaka, M. Yoshimura, Internal distortion in ceria-doped hafnia solid solutions: High-resolution x-ray diffraction and Raman scattering, *Phys. Rev. B* 64 (2001) 134104.
- [28] Z. Hu, H. Metiu, Effect of dopants on the energy of oxygen-vacancy formation at the surface of ceria: Local or global?, *J. Phys. Chem. C* 115 (2011) 17898-17909.
- [29] M. Hegde, G. Madras, K. Patil, Noble metal ionic catalysts, *Acc. Chem. Res.* 42 (2009) 704-712.
- [30] L. Lefferts, K. Seshan, B. Mojet, J. van Ommen, Non-conventional oxidation catalysis, *Catal. Today* 100 (2005) 63-69.
- [31] Z. Yang, T.K. Woo, K. Hermansson, Effects of Zr doping on stoichiometric and reduced ceria: A first-principles study, *J. Chem. Phys.* 124 (2006) 224704.
- [32] Z. Yang, G. Luo, Z. Lu, K. Hermansson, Oxygen vacancy formation energy in Pd-doped ceria: A DFT+ U study, *J. Chem. Phys.* 127 (2007) 074704.
- [33] T. Vinodkumar, D. D NAGA, S. Maloth, B.M. Reddy, Tuning the structural and catalytic properties of ceria by doping with Zr^{4+} , La^{3+} and Eu^{3+} cations, *J. Chem. Sci.* 127 (2015) 1145-1153.
- [34] T. Kim, J.M. Vohs, R.J. Gorte, Thermodynamic Investigation of the Redox Properties of Ceria– Zirconia Solid Solutions, *Industrial & engineering chemistry research* 45 (2006) 5561-5565.
- [35] J. Kašpar, P. Fornasiero, N. Hickey, Automotive catalytic converters: current status and some perspectives, *Catal. Today* 77 (2003) 419-449.
- [36] J. Kašpar, P. Fornasiero, M. Graziani, Use of CeO_2 -based oxides in the three-way catalysis, *Catal. Today* 50 (1999) 285-298.
- [37] A.P. Amrute, C. Mondelli, M. Moser, G. Novell-Leruth, N. López, D. Rosenthal, R. Farra, M.E. Schuster, D. Teschner, T. Schmidt, Performance, structure, and mechanism of CeO_2 in HCl oxidation to Cl_2 , *J. Catal.* 286 (2012) 287-297.
- [38] R. Farra, M. Eichelbaum, R. Schlögl, L. Szentmiklósi, T. Schmidt, A.P. Amrute, C. Mondelli, J. Pérez-Ramírez, D. Teschner, Do observations on surface coverage-reactivity

correlations always describe the true catalytic process? A case study on ceria, *J. Catal.* 297 (2013) 119-127.

[39] M. Moser, C. Mondelli, T. Schmidt, F. Girgsdies, M.E. Schuster, R. Farra, L. Szentmiklósi, D. Teschner, J. Pérez-Ramírez, Supported CeO₂ catalysts in technical form for sustainable chlorine production, *Appl. Catal. B* 132 (2013) 123-131.

[40] E. Aneggi, M. Boaro, C. de Leitenburg, G. Dolcetti, A. Trovarelli, Insights into the redox properties of ceria-based oxides and their implications in catalysis, *J. alloys compd.* 408 (2006) 1096-1102.

[41] S. Scire, S. Minico, C. Crisafulli, C. Satriano, A. Pistone, Catalytic combustion of volatile organic compounds on gold/cerium oxide catalysts, *Appl. Catal. B* 40 (2003) 43-49.

[42] S.M. Saqer, D.I. Kondarides, X.E. Verykios, Catalytic activity of supported platinum and metal oxide catalysts for toluene oxidation, *Top. Catal.* 52 (2009) 517-527.

[43] M. Ousmane, L. Liotta, G. Di Carlo, G. Pantaleo, A. Venezia, G. Deganello, L. Retailleau, A. Boreave, A. Giroir-Fendler, Supported Au catalysts for low-temperature abatement of propene and toluene, as model VOCs: Support effect, *Appl. Catal. B* 101 (2011) 629-637.

[44] M. Huang, S. Fabris, CO adsorption and oxidation on ceria surfaces from DFT+ U calculations, *J. Phys. Chem. C* 112 (2008) 8643-8648.

[45] D.T. Shindell, G. Faluvegi, D.M. Koch, G.A. Schmidt, N. Unger, S.E. Bauer, Improved attribution of climate forcing to emissions, *Science* 326 (2009) 716-718.

[46] G. Myhre, D. Shindell, F.-M. Bréon, W. Collins, J. Fuglestvedt, J. Huang, D. Koch, J.-F. Lamarque, D. Lee, B. Mendoza, Anthropogenic and natural radiative forcing, *Clim. Change* 423 (2013) 658-740.

[47] L. Liotta, G. Di Carlo, G. Pantaleo, A. Venezia, G. Deganello, Co₃O₄/CeO₂ composite oxides for methane emissions abatement: relationship between Co₃O₄-CeO₂ interaction and catalytic activity, *Appl. Catal. B Environ.* 66 (2006) 217-227.

[48] W. Yang, D. Li, D. Xu, X. Wang, Effect of CeO₂ preparation method and Cu loading on CuO/CeO₂ catalysts for methane combustion, *J NAT GAS CHEM* 18 (2009) 458-466.

[49] D. Qiao, G. Lu, D. Mao, X. Liu, H. Li, Y. Guo, Y. Guo, Effect of Ca doping on the catalytic performance of CuO-CeO₂ catalysts for methane combustion, *Catal. Commun.* 11 (2010) 858-861.

- [50] B. Zhang, D. Li, X. Wang, Catalytic performance of La–Ce–O mixed oxide for combustion of methane, *Catal. Today* 158 (2010) 348-353.
- [51] S. Pengpanich, V. Meeyoo, T. Rirksomboon, K. Bunyakiat, Catalytic oxidation of methane over CeO₂-ZrO₂ mixed oxide solid solution catalysts prepared via urea hydrolysis, *Appl. Catal., A* 234 (2002) 221-233.
- [52] W. Yang, D. Li, D. Xu, X. Wang, Effect of CeO₂ preparation method and Cu loading on CuO/CeO₂ catalysts for methane combustion, *J NAT GAS CHEM* 18 (2009) 458-466.
- [53] C. Bozo, N. Guilhaume, J.-M. Herrmann, Role of the ceria–zirconia support in the reactivity of platinum and palladium catalysts for methane total oxidation under lean conditions, *J. Catal.* 203 (2001) 393-406.
- [54] S.M. Saqer, D.I. Kondarides, X.E. Verykios, Catalytic activity of supported platinum and metal oxide catalysts for toluene oxidation, *Top. Catal.* 52 (2009) 517-527.
- [55] G. Del Angel, J. Padilla, I. Cuauhtemoc, J. Navarrete, Toluene combustion on γ -Al₂O₃-CeO₂ catalysts prepared from boehmite and cerium nitrate, *J. Mol. Catal. A. Chem.* 281 (2008) 173-178.
- [56] J. Gaálová, P. Topka, L. Kaluža, O. Šolcová, Gold versus platinum on ceria–zirconia mixed oxides in oxidation of ethanol and toluene, *Catal. Today* 175 (2011) 231-237.
- [57] P.M. Heynderickx, J.W. Thybaut, H. Poelman, D. Poelman, G.B. Marin, The total oxidation of propane over supported Cu and Ce oxides: A comparison of single and binary metal oxides, *J. Catal.* 272 (2010) 109-120.
- [58] C. Hu, Q. Zhu, Z. Jiang, L. Chen, R. Wu, Catalytic combustion of dilute acetone over Cu-doped ceria catalysts, *Chem. Eng. J.* 152 (2009) 583-590.
- [59] X. Tang, Y. Li, X. Huang, Y. Xu, H. Zhu, J. Wang, W. Shen, MnO_x-CeO₂ mixed oxide catalysts for complete oxidation of formaldehyde: effect of preparation method and calcination temperature, *Appl. Catal., B* 62 (2006) 265-273.
- [60] X. Tang, J. Chen, Y. Li, Y. Li, Y. Xu, W. Shen, Complete oxidation of formaldehyde over Ag/MnO_x-CeO₂ catalysts, *Chem. Eng. J.* 118 (2006) 119-125.
- [61] M. Ousmane, L. Liotta, G. Di Carlo, G. Pantaleo, A. Venezia, G. Deganello, L. Retailleau, A. Boreave, A. Giroir-Fendler, Supported Au catalysts for low-temperature abatement of propene and toluene, as model VOCs: Support effect, *Appl. Catal. B* 101 (2011) 629-637.

- [62] H.-J. Sedjame, C. Fontaine, G. Lafaye, J. Barbier Jr, On the promoting effect of the addition of ceria to platinum based alumina catalysts for VOCs oxidation, *Appl. Catal. B* 144 (2014) 233-242.
- [63] M. Jeong, N. Nunotani, N. Moriyama, N. Imanaka, High methane combustion activity of PdO/CeO₂-ZrO₂-NiO/ γ -Al₂O₃ catalysts, *JAsCerS* 4 (2016) 259-262.
- [64] M. Alifanti, M. Florea, V.I. Pârvulescu, Ceria-based oxides as supports for LaCoO₃ perovskite; catalysts for total oxidation of VOC, *Appl. Catal., B* 70 (2007) 400-405.
- [65] G.J. Hutchings, C.S. Heneghan, I.D. Hudson, S.H. Taylor, Uranium-oxide-based catalysts for the destruction of volatile chloro-organic compounds, *Nature* 384 (1996) 341-343.
- [66] L. Lin, Y. Chai, B. Zhao, W. Wei, D. He, B. He, Q. Tang, Photocatalytic oxidation for degradation of VOCs, *Open Journal of Inorganic Chemistry* 3 (2013) 14.
- [67] S. Scirè, S. Minicò, C. Crisafulli, Pt catalysts supported on H-type zeolites for the catalytic combustion of chlorobenzene, *Appl. Catal., B* 45 (2003) 117-125.
- [68] R. Van den Brink, M. Krzan, M. Feijen-Jeurissen, R. Louw, P. Mulder, The role of the support and dispersion in the catalytic combustion of chlorobenzene on noble metal based catalysts, *Appl. Catal., B* 24 (2000) 255-264.
- [69] R. Van den Brink, R. Louw, P. Mulder, Increased combustion rate of chlorobenzene on Pt/ γ -Al₂O₃ in binary mixtures with hydrocarbons and with carbon monoxide, *Appl. Catal., B* 25 (2000) 229-237.
- [70] Q. Dai, X. Wang, G. Lu, Low-temperature catalytic destruction of chlorinated VOCs over cerium oxide, *Catal. Commun.* 8 (2007) 1645-1649.
- [71] S. Agarwal, J. Spivey, J. Butt, Deep oxidation of hydrocarbons, *Appl. Catal., A* 81 (1992) 239-255.
- [72] Q. Dai, X. Wang, G. Lu, Low-temperature catalytic combustion of trichloroethylene over cerium oxide and catalyst deactivation, *Appl. Catal. B* 81 (2008) 192-202.
- [73] J. Carrasco, G. Vilé, D. Fernández-Torre, R.n. Pérez, J. Pérez-Ramírez, M.V.n. Ganduglia-Pirovano, Molecular-level understanding of CeO₂ as a catalyst for partial alkyne hydrogenation, *J. Phys. Chem. C* 118 (2014) 5352-5360.
- [74] D. Fernández-Torre, K. Kośmider, J. Carrasco, M.V.n. Ganduglia-Pirovano, R.n. Pérez, Insight into the adsorption of water on the clean CeO₂ (111) surface with van der Waals and hybrid density functionals, *J. Phys. Chem. C* 116 (2012) 13584-13593.

- [75] A. Laachir, V. Perrichon, A. Badri, J. Lamotte, E. Catherine, J.C. Lavalley, J. El Fallah, L. Hilaire, F. Le Normand, E. Quéméré, Reduction of CeO₂ by hydrogen. Magnetic susceptibility and Fourier-transform infrared, ultraviolet and X-ray photoelectron spectroscopy measurements, *J. Chem. Soc., Faraday Transactions* 87 (1991) 1601-1609.
- [76] V. Perrichon, A. Laachir, G. Bergeret, R. Fréty, L. Tournayan, O. Touret, Reduction of cerias with different textures by hydrogen and their reoxidation by oxygen, *J. Chem. Soc., Faraday Transactions* 90 (1994) 773-781.
- [77] S. Overbury, D. Huntley, D. Mullins, K. Ailey, P. Radulovic, Surface studies of model supported catalysts: NO adsorption on Rh/CeO₂ (001), *J. Vac. Sci. Technol.* 15 (1997) 1647-1652.
- [78] H. Cordatos, R. Gorte, CO, NO, and H₂ Adsorption on Ceria-Supported Pd, *J. Catal.* 159 (1996) 112-118.
- [79] B. Chen, Y. Ma, L. Ding, L. Xu, Z. Wu, Q. Yuan, W. Huang, Reactivity of hydroxyls and water on a CeO₂ (111) thin film surface: the role of oxygen vacancy, *J. Phys. Chem. C* 117 (2013) 5800-5810.
- [80] H.T. Chen, Y.M. Choi, M. Liu, M. Lin, A theoretical study of surface reduction mechanisms of CeO₂(111) and (110) by H₂, *ChemPhysChem* 8 (2007) 849-855.
- [81] M.B. Watkins, A.S. Foster, A.L. Shluger, Hydrogen cycle on CeO₂(111) surfaces: Density functional theory calculations, *The Journal of Physical Chemistry C* 111 (2007) 15337-15341.
- [82] G. Vicario, G. Balducci, S. Fabris, S. de Gironcoli, S. Baroni, Interaction of hydrogen with cerium oxide surfaces: a quantum mechanical computational study, *J. Phys. Chem. B* 110 (2006) 19380-19385.
- [83] M.K. Alam, F. Ahmed, R. Miura, A. Suzuki, H. Tsuboi, N. Hatakeyama, A. Endou, H. Takaba, M. Kubo, A. Miyamoto, Study of reduction processes over cerium oxide surfaces with atomic hydrogen using ultra accelerated quantum chemical molecular dynamics, *Appl. Surf. Sci.* 257 (2010) 1383-1389.
- [84] T. Alessandro, *Catalysis by ceria and related materials*, World Scientific 2002.
- [85] G. Praline, B. Koel, R. Hance, H.-I. Lee, J. White, X-ray photoelectron study of the reaction of oxygen with cerium, *Journal of Electron Spectroscopy and Related Phenomena* 21 (1980) 17-30.

- [86] C. Helms, W. Spicer, Comparison of the oxidation process in strontium and cerium by ultraviolet photoelectron spectroscopy, *Appl. Phys. Lett.* 21 (1972) 237-239.
- [87] T.L. Barr, An ESCA study of the termination of the passivation of elemental metals, *J. Phys. Chem.* 82 (1978) 1801-1810.
- [88] D. Mullins, S. Overbury, D. Huntley, Electron spectroscopy of single crystal and polycrystalline cerium oxide surfaces, *Surf. Sci.* 409 (1998) 307-319.
- [89] Y. Choi, H. Abernathy, H.T. Chen, M. Lin, M. Liu, Characterization of O₂-CeO₂ Interactions Using In Situ Raman Spectroscopy and First-Principle Calculations, *ChemPhysChem* 7 (2006) 1957-1963.
- [90] Y. Zhao, B.-T. Teng, X.-D. Wen, Y. Zhao, Q.-P. Chen, L.-H. Zhao, M.-F. Luo, Superoxide and peroxide species on CeO₂ (111), and their oxidation roles, *J. Phys. Chem. C* 116 (2012) 15986-15991.
- [91] M. Nolan, Healing of oxygen vacancies on reduced surfaces of gold-doped ceria, *J. Chem. Phys.* 130 (2009) 144702.
- [92] D.R. Mullins, P.M. Albrecht, T.-L. Chen, F.C. Calaza, M.D. Biegalski, H.M. Christen, S.H. Overbury, Water dissociation on CeO₂ (100) and CeO₂ (111) thin films, *J. Phys. Chem. C* 116 (2012) 19419-19428.
- [93] V. Matolín, I. Matolínová, F. Dvořák, V. Johánek, J. Mysliveček, K. Prince, T. Skála, O. Stetsovykh, N. Tsud, M. Václavů, Water interaction with CeO₂ (1 1 1)/Cu (1 1 1) model catalyst surface, *Catal. Today* 181 (2012) 124-132.
- [94] L. Kundakovic, D. Mullins, S. Overbury, Adsorption and reaction of H₂O and CO on oxidized and reduced Rh/CeO_x(111) surfaces, *Surf. Sci.* 457 (2000) 51-62.
- [95] M.A. Henderson, C. Perkins, M.H. Engelhard, S. Thevuthasan, C.H. Peden, Redox properties of water on the oxidized and reduced surfaces of CeO₂ (1 1 1), *Surf. Sci.* 526 (2003) 1-18.
- [96] Y. Lykhach, V. Johánek, H.A. Aleksandrov, S.M. Kozlov, M. Happel, T.s. Skála, P.S. Petkov, N. Tsud, G.N. Vayssilov, K.C. Prince, Water chemistry on model ceria and Pt/ceria catalysts, *J. Phys. Chem. C* 116 (2012) 12103-12113.
- [97] G. Herman, Y. Kim, S. Chambers, C. Peden, Interaction of D₂O with CeO₂ (001) investigated by temperature-programmed desorption and X-ray photoelectron spectroscopy, *Langmuir* 15 (1999) 3993-3997.

- [98] S.D. Senanayake, D. Stacchiola, J. Evans, M. Estrella, L. Barrio, M. Pérez, J. Hrbek, J.A. Rodriguez, Probing the reaction intermediates for the water–gas shift over inverse CeO_x/Au (1 1 1) catalysts, *J. Catal.* 271 (2010) 392-400.
- [99] M. Fronzi, S. Piccinin, B. Delley, E. Traversa, C. Stampfl, Water adsorption on the stoichiometric and reduced CeO₂ (111) surface: a first-principles investigation, *Phys. Chem. Chem. Phys.* 11 (2009) 9188-9199.
- [100] D. Marrocchelli, B. Yildiz, First-principles assessment of H₂S and H₂O reaction mechanisms and the subsequent hydrogen absorption on the CeO₂(111) surface, *J. Phys. Chem. C* 116 (2012) 2411-2424.
- [101] M. Molinari, S.C. Parker, D.C. Sayle, M.S. Islam, Water adsorption and its effect on the stability of low index stoichiometric and reduced surfaces of ceria, *J. Phys. Chem. C* 116 (2012) 7073-7082.
- [102] M.A. Henderson, The interaction of water with solid surfaces: fundamental aspects revisited, *Surf. Sci. Rep.* 46 (2002) 1-308.
- [103] F. Esch, F. Esch, S. Fabris, L. Zhou, T. Montini, C. Africh, P. Fornasiero, G. Comelli, and R. Rosei, *Science* 309, 752 (2005), *Science* 309 (2005) 752.
- [104] M. Happel, J. Mysliveček, V. Johánek, F. Dvořák, O. Stetsovych, Y. Lykhach, V. Matolín, J. Libuda, Adsorption sites, metal-support interactions, and oxygen spillover identified by vibrational spectroscopy of adsorbed CO: A model study on Pt/ceria catalysts, *J. Catal.* 289 (2012) 118-126.
- [105] B. Chen, Y. Ma, L. Ding, L. Xu, Z. Wu, Q. Yuan, W. Huang, Reactivity of hydroxyls and water on a CeO₂ (111) thin film surface: the role of oxygen vacancy, *J. Phys. Chem. C* 117 (2013) 5800-5810.
- [106] R. Ferrizz, T. Egami, J. Vohs, Temperature programmed desorption study of the reaction of C₂H₄ and CO on Rh supported on α -Al₂O₃ (0001), YSZ (100) and CeO₂ thin films, *Surf. Sci.* 465 (2000) 127-137.
- [107] K.-i. Fukui, Y. Namai, Y. Iwasawa, Imaging of surface oxygen atoms and their defect structures on CeO₂(1 1 1) by noncontact atomic force microscopy, *Appl. Surf. Sci.* 188 (2002) 252-256.
- [108] H. Nörenberg, G. Briggs, Defect formation on CeO₂ (111) surfaces after annealing studied by STM, *Surf. Sci.* 424 (1999) L352-L355.

- [109] T.X. Sayle, S.C. Parker, C.R.A. Catlow, Surface oxygen vacancy formation on CeO₂ and its role in the oxidation of carbon monoxide, *J. Chem. Soc., Chem. Commun.* (1992) 977-978.
- [110] M. Nolan, S.C. Parker, G.W. Watson, The electronic structure of oxygen vacancy defects at the low index surfaces of ceria, *Surf. Sci.* 595 (2005) 223-232.
- [111] S. Overbury, D. Mullins, D. Huntley, L. Kundakovic, Chemisorption and reaction of sulfur dioxide with oxidized and reduced ceria surfaces, *J. Phys. Chem. B* 103 (1999) 11308-11317.
- [112] M. Waqif, P. Bazin, O. Saur, J. Lavalley, G. Blanchard, O. Touret, Study of ceria sulfation, *Appl. Catal. B* 11 (1997) 193-205.
- [113] P. Bazin, O. Saur, J. Lavalley, G. Blanchard, V. Visciglio, O. Touret, Influence of platinum on ceria sulfation, *Appl. Catal., B* 13 (1997) 265-274.
- [114] J.A. Rodriguez, T. Jirsak, A. Freitag, J.C. Hanson, J.Z. Larese, S. Chaturvedi, Interaction of SO₂ with CeO₂ and Cu/CeO₂ catalysts: photoemission, XANES and TPD studies, *Catal. Lett.* 62 (1999) 113-119.
- [115] M.Y. Smirnov, A.V. Kalinkin, A.V. Pashis, A.M. Sorokin, A.S. Noskov, K.C. Kharas, V.I. Bukhtiyarov, Interaction of Al₂O₃ and CeO₂ surfaces with SO₂ and SO₂ + O₂ studied by X-ray photoelectron spectroscopy, *J. Phys. Chem. B* 109 (2005) 11712-11719.
- [116] R.M. Ferrizz, R.J. Gorte, J.M. Vohs, TPD and XPS Investigation of the Interaction of SO₂ with Model Ceria Catalysts, *Catal. Lett.* 82 (2002) 123-129.
- [117] M. Happel, Y. Lykhach, N. Tsud, T.s. Skála, K.C. Prince, V. Matolín, J.r. Libuda, Mechanism of sulfur poisoning and storage: adsorption and reaction of SO₂ with stoichiometric and reduced ceria films on Cu (111), *J. Phys. Chem. C* 115 (2011) 19872-19882.
- [118] M. Polcik, L. Wilde, J. Haase, B. Brena, D. Cocco, G. Comelli, G. Paolucci, Adsorption and temperature-dependent decomposition of SO₂ on Cu (100) and Cu (111): A fast and high-resolution core-level spectroscopy study, *Phys. Rev. B* 53 (1996) 13720.
- [119] A.R. Alemozafar, X.-C. Guo, R.J. Madix, Adsorption and reaction of sulfur dioxide with Cu (110) and Cu (110)-p (2× 1)-O, *J. Chem. Phys.* 116 (2002) 4698-4706.
- [120] G. Liu, J.A. Rodriguez, J. Dvorak, J. Hrbek, T. Jirsak, Chemistry of sulfur-containing molecules on Au (1 1 1): thiophene, sulfur dioxide, and methanethiol adsorption, *Surf. Sci.* 505 (2002) 295-307.

- [121] R. Streber, C. Papp, M. Lorenz, O. Höfert, E. Darlatt, A. Bayer, R. Denecke, H.-P. Steinrück, SO₂ adsorption and thermal evolution on clean and oxygen precovered Pt (1 1 1), Chem. Phys. Lett. 494 (2010) 188-192.
- [122] R. Streber, C. Papp, M. Lorenz, O. Hofert, W. Zhao, S. Wickert, E. Darlatt, A. Bayer, R. Denecke, H.-P. Steinruck, Influence of steps on the adsorption and thermal evolution of SO₂ on clean and oxygen precovered Pt surfaces, J. Phys. Chem. C 114 (2010) 19734-19743.
- [123] J.A. Rodriguez, P. Liu, M. Pérez, G. Liu, J. Hrbek, Destruction of SO₂ on Au and Cu nanoparticles dispersed on MgO (100) and CeO₂ (111), J. Phys. Chem. A 114 (2009) 3802-3810.
- [124] J. Rodriguez, M. Perez, J. Evans, G. Liu, J. Hrbek, Reaction of SO₂ with Au/Ce O₂ (111): Importance of O vacancies in the activation of gold, AIP, 2005.
- [125] M. Happel, Y. Lykhach, N. Tsud, T.s. Skála, V. Johánek, K.C. Prince, V. Matolín, J.r. Libuda, SO₂ decomposition on Pt/CeO₂ (111) model catalysts: on the reaction mechanism and the influence of H₂ and CO, J. Phys. Chem. C 116 (2012) 10959-10967.
- [126] J.A. Rodriguez, T. Jirsak, A. Freitag, J.C. Hanson, J.Z. Larese, S. Chaturvedi, Interaction of SO₂ with CeO₂ and Cu/CeO₂ catalysts: photoemission, XANES and TPD studies, Catal. Lett. 62 (1999) 113-119.
- [127] M. Polčík, L. Wilde, J. Haase, B. Brena, G. Comelli, G. Paolucci, High-resolution XPS and NEXAFS study of SO₂ adsorption on Pt (111): Two surface SO₂ species, Surf. Sci. 381 (1997) L568-L572.
- [128] M. Polcik, L. Wilde, J. Haase, B. Brena, D. Cocco, G. Comelli, G. Paolucci, Adsorption and temperature-dependent decomposition of SO₂ on Cu (100) and Cu (111): A fast and high-resolution core-level spectroscopy study, Phys. Rev. B 53 (1996) 13720.
- [129] J. Stubenrauch, J. Vohs, Interaction of CO with Rh Supported on Stoichiometric and Reduced CeO₂ (111) and CeO₂ (100) Surfaces, J. Catal. 159 (1996) 50-57.
- [130] D. Mullins, K. Zhang, Metal–support interactions between Pt and thin film cerium oxide, Surface science 513 (2002) 163-173.
- [131] S.D. Senanayake, J. Zhou, A.P. Baddorf, D.R. Mullins, The reaction of carbon monoxide with palladium supported on cerium oxide thin films, Surf. Sci. 601 (2007) 3215-3223.
- [132] C. Müller, C. Freysoldt, M. Baudin, K. Hermansson, An ab initio study of CO adsorption on ceria (1 1 0), Chem. Phys. 318 (2005) 180-190.

- [133] B. Herschend, M. Baudin, K. Hermansson, CO adsorption on CeO₂ (1 1 0) using hybrid-DFT embedded-cluster calculations, *Chem. Phys.* 328 (2006) 345-353.
- [134] M. Nolan, G.W. Watson, The surface dependence of CO adsorption on ceria, *J. Phys. Chem. B* 110 (2006) 16600-16606.
- [135] D.R. Mullins, The surface chemistry of cerium oxide, *Surf. Sci. Rep.* 70 (2015) 42-85.
- [136] S.D. Senanayake, D.R. Mullins, Redox pathways for HCOOH decomposition over CeO₂ surfaces, *J. Phys. Chem. C* 112 (2008) 9744-9752.
- [137] Y. Lykhach, T. Staudt, R. Streber, M. Lorenz, A. Bayer, H.-P. Steinrück, J. Libuda, CO₂ activation on single crystal based ceria and magnesia/ceria model catalysts, *Eur. Phys. J. B* 75 (2010) 89-100.
- [138] T. Staudt, Y. Lykhach, N. Tsud, T. Skala, K. Prince, V. Matolín, J. Libuda, Ceria reoxidation by CO₂: A model study, *J. Catal.* 275 (2010) 181-185.
- [139] P.M. Albrecht, D.-e. Jiang, D.R. Mullins, CO₂ adsorption as a flat-lying, tridentate carbonate on CeO₂ (100), *J. Phys. Chem. C* 118 (2014) 9042-9050.
- [140] K.R. Hahn, M. Iannuzzi, A.P. Seitsonen, J.r. Hutter, Coverage effect of the CO₂ adsorption mechanisms on CeO₂ (111) by first principles analysis, *J. Phys. Chem. C* 117 (2013) 1701-1711.
- [141] Z. Cheng, B.J. Sherman, C.S. Lo, Carbon dioxide activation and dissociation on ceria (110): A density functional theory study, *J. Chem. Phys.* 138 (2013) 014702.
- [142] R. Ferrizz, T. Egami, G. Wong, J. Vohs, Reaction of NO on CeO₂ and Rh/CeO₂ thin films supported on α -Al₂O₃ (0 0 0 1) and YSZ (1 0 0), *Surf. Sci.* 476 (2001) 9-21.
- [143] S. Overbury, D. Mullins, D. Huntley, L. Kundakovic, Chemisorption and reaction of NO and N₂O on oxidized and reduced ceria surfaces studied by soft X-Ray photoemission spectroscopy and desorption spectroscopy, *J. Catal.* 186 (1999) 296-309.
- [144] M. Daturi, N. Bion, J. Saussey, J.-C. Lavalley, C. Hedouin, T. Seguelong, G. Blanchard, Evidence of a lacunar mechanism for deNO_x activity in ceria-based catalysts, *Phys. Chem. Chem. Phys.* 3 (2001) 252-255.
- [145] D. Castner, B. Sexton, G. Somorjai, Leed and thermal desorption studies of small molecules (H₂, O₂, CO, CO₂, NO, C₂H₄, C₂H₂ AND C) chemisorbed on the rhodium (111) and (100) surfaces, *Surf. Sci.* 71 (1978) 519-540.

- [146] L. Dubois, D. Castner, G. Somorjai, The chemisorption of acetylene and ethylene on Rh (111): a low energy electron diffraction (LEED), high resolution electron energy loss (ELS), and thermal desorption mass spectrometry (TDS) study, *J. Chem. Phys.* 72 (1980) 5234-5240.
- [147] A. Slavin, B. Bent, C.-T. Kao, G. Somorjai, Thermal fragmentation of ethylene on the Rh (100) single crystal surface in the temperature range of 200–800 K, *Surf. Sci.* 206 (1988) 124-144.
- [148] D. Mullins, K. Zhang, Interaction between NO and C₂H₄ on Rh-loaded CeO_x (111), *J. Phys. Chem. B* 105 (2001) 1374-1380.
- [149] R. Ferrizz, T. Egami, J. Vohs, The reaction of ethylene on a model automotive emissions control catalyst, *Catal. Lett.* 61 (1999) 33-38.
- [150] E. Wilson, R. Grau-Crespo, C. Pang, G. Cabailh, Q. Chen, J. Purton, C. Catlow, W. Brown, N. De Leeuw, G. Thornton, Redox behavior of the model catalyst Pd/CeO_{2-x}/Pt (111), *J. Phys. Chem. C* 112 (2008) 10918-10922.
- [151] T. Skála, N. Tsud, K.C. Prince, V. Matolín, Formation of alumina–ceria mixed oxide in model systems, *Appl. Surf. Sci.* 257 (2011) 3682-3687.
- [152] T. Skála, F. Šutara, M. Cabala, M. Škoda, K.C. Prince, V. Matolín, A photoemission study of the interaction of Ga with CeO₂(1 1 1) thin films, *Appl. Surf. Sci.* 254 (2008) 6860-6864.
- [153] Y. Zhou, J. Zhou, Ti/CeO_x (111) interfaces studied by XPS and STM, *Surf. Sci.* 606 (2012) 749-753.
- [154] G. Vilé, B. Bridier, J. Wichert, J. Pérez-Ramírez, Ceria in hydrogenation catalysis: high selectivity in the conversion of alkynes to olefins, *Angew. Chem. Int. Ed.* 51 (2012) 8620-8623.
- [155] D.R. Mullins, P.M. Albrecht, F. Calaza, Variations in reactivity on different crystallographic orientations of cerium oxide, *Top. Catal.* 56 (2013) 1345-1362.
- [156] D.R. Mullins, M.D. Robbins, J. Zhou, Adsorption and reaction of methanol on thin-film cerium oxide, *Surf. Sci.* 600 (2006) 1547-1558.
- [157] S.S. Lin, C.L. Chen, D.J. Chang, C.C. Chen, Catalytic wet air oxidation of phenol by various CeO₂ catalysts, *Water Research* 36 (2002) 3009-3014.
- [158] H. Yao, Y.Y. Yao, Ceria in automotive exhaust catalysts: I. Oxygen storage, *J. Catal.* 86 (1984) 254-265.
- [159] A.W. Peters, G. KIM, Rare earths in noncracking catalysts, ACS Publications 1981.

- [160] J. Cocking, J. Sprague, J. Reed, Oxidation behaviour of ion-implanted NiCrAl, *Surf. Coat. Technol.* 36 (1988) 133-142.
- [161] X. Yu, Y. Sun, The oxidation improvement of Fe₃Al based alloy with cerium addition at temperature above 1000 C, *Mater. Sci. Eng., A* 363 (2003) 30-39.
- [162] R. Thanneeru, S. Patil, S. Deshpande, S. Seal, Effect of trivalent rare earth dopants in nanocrystalline ceria coatings for high-temperature oxidation resistance, *Acta Materialia* 55 (2007) 3457-3466.
- [163] S.M.d.C. Fernandes, L.V. Ramanathan, Rare earth oxide coatings to decrease high temperature degradation of chromia forming alloys, *Materials research* 7 (2004) 135-139.
- [164] J. Huiming, L. Xiaojun, Z. Linnan, Influence of nanometric ceria coating on oxidation behavior of chromium at 900° C, *Journal of Rare Earths* 25 (2007) 63-67.
- [165] N. Özer, Optical properties and electrochromic characterization of sol-gel deposited ceria films, *Solar Energy Materials and Solar Cells* 68 (2001) 391-400.
- [166] M.-T. Ta, D. Briand, Y. Guhel, J. Bernard, J. Pesant, B. Boudart, Growth and structural characterization of cerium oxide thin films realized on Si (111) substrates by on-axis rf magnetron sputtering, *Thin Solid Films* 517 (2008) 450-452.
- [167] R.K. Jain, G. Kaur, S. Chauhan, Y.K. Gautam, R. Chandra, Study on structural, optical and wettability properties of CeO₂ thin films deposited by reactive DC magnetron sputtering, *AIP Conference Proceedings*, AIP, 2014, pp. 155-158.
- [168] V. Urusov, Interaction of cations on octahedral and tetrahedral sites in simple spinels, *Phys. Chem. Miner.* 9 (1983) 1-5.
- [169] E. Rios, J.-L. Gautier, G. Poillerat, P. Chartier, Mixed valency spinel oxides of transition metals and electrocatalysis: case of the Mn_xCo_{3-x}O₄ system, *Electrochim. Acta* 44 (1998) 1491-1497.
- [170] A. Tseung, B. Hobbs, Influence of oxygen partial pressure on the electrocatalytic activity of nickel-oxide oxygen electrodes, *Electrochim. Acta* 17 (1972) 1557-1562.
- [171] B. Chi, J. Li, X. Yang, H. Lin, N. Wang, Electrophoretic deposition of ZnCo₂O₄ spinel and its electrocatalytic properties for oxygen evolution reaction, *Electrochim. Acta* 50 (2005) 2059-2064.

- [172] R.N. Singh, J.F. Koenig, G. Poillerat, P. Chartier, Electrochemical Studies on Protective Thin Co_3O_4 and NiCo_2O_4 Films Prepared on Titanium by Spray Pyrolysis for Oxygen Evolution, *J. Electrochem. Soc.* 137 (1990) 1408-1413.
- [173] M. Hamdani, R. Singh, P. Chartier, Co_3O_4 and Co-based spinel oxides bifunctional oxygen electrodes, *Int. J. Electrochem. Sci* 5 (2010) 556-577.
- [174] N. Singh, J. Singh, R. Singh, Sol-gel-derived spinel Co_3O_4 films and oxygen evolution: Part II. Optimization of preparation conditions and influence of the nature of the metal salt precursor, *Int. J. Hydrog. Energy* 27 (2002) 895-903.
- [175] R.-N. Singh, M. Hamdani, J.-F. Koenig, G. Poillerat, J. Gautier, P. Chartier, Thin films of Co_3O_4 and NiCo_2O_4 obtained by the method of chemical spray pyrolysis for electrocatalysis III. The electrocatalysis of oxygen evolution, *J. Appl. Electrochem.* 20 (1990) 442-446.
- [176] B. Chi, J. Li, Y. Han, Y. Chen, Effect of temperature on the preparation and electrocatalytic properties of a spinel $\text{NiCo}_2\text{O}_4/\text{Ni}$ electrode, *Int. J. Hydrog. Energy* 29 (2004) 605-610.
- [177] R. Singh, D. Mishra, A. Sinha, A. Singh, Novel electrocatalysts for generating oxygen from alkaline water electrolysis, *Electrochem. Commun.* 9 (2007) 1369-1373.
- [178] M. De Koninck, S.-C. Poirier, B. Marsan, $\text{Cu}_x\text{Co}_{3-x}\text{O}_4$ Used as Bifunctional Electrocatalyst II. Electrochemical Characterization for the Oxygen Reduction Reaction, *J. Electrochem. Soc.* 154 (2007) A381-A388.
- [179] A. La Rosa-Toro, R. Berenguer, C. Quijada, F. Montilla, E. Morallón, J. Vázquez, Preparation and characterization of copper-doped cobalt oxide electrodes, *J. Phys. Chem. B* 110 (2006) 24021-24029.
- [180] N. Fradette, B. Marsan, Surface Studies of $\text{Cu}_x\text{Co}_{3-x}\text{O}_4$ Electrodes for the Electrocatalysis of Oxygen Evolution, *J. Electrochem. Soc.* 145 (1998) 2320-2327.
- [181] R. Bonchev, T. Zheleva, S. Sevov, Morphological and compositional characterization of copper-cobalt spinel made by mechanochemical reactions, *Chem. Mater.* 2 (1990) 93-95.
- [182] A. Sugier, E. Freund, Process for manufacturing alcohols, particularly linear saturated primary alcohols, from synthesis gas, Google Patents, 1978.
- [183] B. Chi, H. Lin, J. Li, Cations distribution of $\text{Cu}_x\text{Co}_{3-x}\text{O}_4$ and its electrocatalytic activities for oxygen evolution reaction, *Int. J. Hydrog. Energy* 33 (2008) 4763-4768.

- [184] E. Rios, J.-L. Gautier, G. Poillerat, P. Chartier, Mixed valency spinel oxides of transition metals and electrocatalysis: case of the $Mn_xCo_{3-x}O_4$ system, *Electrochim. Acta* 44 (1998) 1491-1497.
- [185] J. Häglund, G. Grimvall, T. Jarlborg, A.F. Guillermet, Band structure and cohesive properties of 3d-transition-metal carbides and nitrides with the NaCl-type structure, *Phys. Rev. B* 43 (1991) 14400.
- [186] D.S. Yadav, D.V. Singh, *Elastic Properties of Transition Metal Nitrides and Carbides*, *Elastic* 4 (2015).
- [187] M. Fronzi, A. Soon, B. Delley, E. Traversa, C. Stampfl, Stability and morphology of cerium oxide surfaces in an oxidizing environment: a first-principles investigation, *J. Chem. Phys.* 131 (2009) 104701.
- [188] Z. Lü, J. Zhou, Z. Sun, R. Chen, Effect of rare earth elements on the structures and mechanical properties of magnesium alloys, *Sci. Bull.* 58 (2013) 816-820.
- [189] S. Grieshammer, B.O. Grope, J. Koettgen, M. Martin, A combined DFT+ U and Monte Carlo study on rare earth doped ceria, *Phys. Chem. Chem. Phys.* 16 (2014) 9974-9986.
- [190] S. Tekumalla, S. Seetharaman, A. Almajid, M. Gupta, Mechanical Properties of Magnesium-Rare Earth Alloy Systems: A Review, *Metals* 5 (2014) 1-39.
- [191] S. Horoz, S. Simsek, S. Palaz, A.M. Mamedov, Electronic and Optical Properties of Rare Earth Oxides: Ab Initio Calculation, *World Journal of Condensed Matter Physics* 5 (2015) 78.
- [192] F. Grosse, T. Watahiki, W. Braun, Rare earth oxide alloys and stacked layers: An ab initio study, *Thin Solid Films* 518 (2010) 4747-4749.
- [193] M.B. Kanoun, A.H. Reshak, N. Kanoun-Bouayed, S. Goumri-Said, Evidence of Coulomb correction and spin-orbit coupling in rare-earth dioxides CeO_2 , PrO_2 and TbO_2 : An ab initio study, *J. Magn. Magn. Mater.* 324 (2012) 1397-1405.
- [194] I. Safi, Recent aspects concerning DC reactive magnetron sputtering of thin films: a review, *Surf. Coat. Techn.* 127 (2000) 203-218.
- [195] P. Kelly, R. Arnell, Magnetron sputtering: a review of recent developments and applications, *Vacuum* 56 (2000) 159-172.
- [196] P. Saikia, B. Kakati, B. Saikia, Study on the effect of target on plasma parameters of magnetron sputtering discharge plasma, *Physics of Plasmas* (1994-present) 20 (2013) 103505.

- [197] A. Nyaiesh, The characteristics of a planar magnetron operated at a high power input, *Thin Solid Films* 86 (1981) 267-277.
- [198] J. Musil, L. Bárdoš, A. Rajský, J. Vyskočil, B. Doležal, G. Lončar, K. Daďourek, V. Kubíček, TiN x coatings prepared by dc reactive magnetron sputtering, *Thin Solid Films* 136 (1986) 229-239.
- [199] B. Subramanian, K. Ashok, M. Jayachandran, Effect of substrate temperature on the structural properties of magnetron sputtered titanium nitride thin films with brush plated nickel interlayer on mild steel, *Appl. Surf. Sci.* 255 (2008) 2133-2138.
- [200] S. Kondo, K. Nanbu, A self-consistent numerical analysis of a planar dc magnetron discharge by the particle-in-cell/Monte Carlo method, *J. Phys. D* 32 (1999) 1142.
- [201] B. Window, N. Savvides, Charged particle fluxes from planar magnetron sputtering sources, *J. Vac. Sci. Technol. B* 4 (1986) 196-202.
- [202] A. Frisch, G. Trucks, H. Schlegel, G. Scuseria, M. Robb, J. Cheeseman, V. Zakrzewski, J. Montgomery Jr, R. Stratmann, J. Burant, *Exploring Chemistry with Electronic Structure Methods*, Frisch, JB Foresman,–Pittsburgh PA: Gaussian Inc 302 (1996).
- [203] R. Chimata, *Optical Properties of Materials Calculated from First Principles Theory*, (2010).
- [204] P.W. Atkins, R.S. Friedman, *Molecular quantum mechanics*, Oxford university press 2011.
- [205] R.J. Gillespie, P.L. Popelier, *Chemical bonding and molecular geometry*, New York, Oxford (2001).
- [206] R.G. Parr, W. Yang, *Density-functional theory of atoms and molecules*, Oxford university press 1989.
- [207] e. See, C. Cramer, *Essentials of Computational Chemistry: Theories and Models*, John Wiley & Sons Chichester, 2004.
- [208] R.G. Parr, W. Yang, *Density-Functional Theory of Atoms and Molecules*, vol. 16 of *International series of monographs on chemistry*, Oxford University Press, New York, 1989.
- [209] J. Kohanoff, *Electronic structure calculations for solids and molecules: theory and computational methods*, Cambridge University Press 2006.
- [210] F.W. Kutzler, G. Painter, First-row diatomics: Calculation of the geometry and energetics using self-consistent gradient-functional approximations, *Phys. Rev. B* 45 (1992) 3236.

- [211] D.C. Langreth, J.P. Perdew, Theory of nonuniform electronic systems. I. Analysis of the gradient approximation and a generalization that works, *Phys. Rev. B* 21 (1980) 5469.
- [212] D.C. Langreth, M. Mehl, Beyond the local-density approximation in calculations of ground-state electronic properties, *Phys. Rev. B* 28 (1983) 1809.
- [213] J.P. Perdew, M. Ernzerhof, K. Burke, Rationale for mixing exact exchange with density functional approximations, *J. Chem. Phys.* 105 (1996) 9982-9985.
- [214] S. Dudarev, G. Botton, S. Savrasov, C. Humphreys, A. Sutton, Electron-energy-loss spectra and the structural stability of nickel oxide: An LSDA+ U study, *Phys. Rev. B* 57 (1998) 1505.
- [215] N.J. Mosey, E.A. Carter, Ab initio evaluation of Coulomb and exchange parameters for DFT+ U calculations, *Phys. Rev. B* 76 (2007) 155123.
- [216] B. Himmetoglu, A. Floris, S. De Gironcoli, M. Cococcioni, Hubbard-corrected DFT energy functionals: The LDA+ U description of correlated systems, *Int. J. Quantum Chem.* 114 (2014) 14-49.
- [217] J.R. Rustad, Density functional calculations of the enthalpies of formation of rare-earth orthophosphates, *Am. Mineral.* 97 (2012) 791-799.
- [218] A. Bartos, K. Lieb, M. Uhrmacher, D. Wiarda, Refinement of atomic positions in bixbyite oxides using perturbed angular correlation spectroscopy, *Acta Crystallogr., Sect. B: Struct. Sci.* 49 (1993) 165-169.
- [219] J.P. Perdew, K. Burke, M. Ernzerhof, Generalized gradient approximation made simple, *Phys. Rev. Lett.* 77 (1996) 3865.
- [220] S.H. Vosko, L. Wilk, M. Nusair, Accurate spin-dependent electron liquid correlation energies for local spin density calculations: a critical analysis, *Can. J. Phys.* 58 (1980) 1200-1211.
- [221] J.P. Perdew, Y. Wang, Erratum: pair-distribution function and its coupling-constant average for the spin-polarized electron gas [*Phys. Rev. B* 46, 12 947 (1992)], *Phys. Rev. B* 56 (1997) 7018.
- [222] J.P. Perdew, K. Burke, M. Ernzerhof, D. of Physics and NOL 70118 J. Quantum Theory Group Tulane University, *Phys. Rev. Lett* 77 (1996) 3865-3868.
- [223] J.P. Perdew, K. Burke, Y. Wang, Generalized gradient approximation for the exchange-correlation hole of a many-electron system, *Phys. Rev. B* 54 (1996) 16533.

- [224] A.D. Boese, N.C. Handy, A new parametrization of exchange–correlation generalized gradient approximation functionals, *J. Chem. Phys.* 114 (2001) 5497-5503.
- [225] B. Hammer, L.B. Hansen, J.K. Nørskov, Improved adsorption energetics within density-functional theory using revised Perdew-Burke-Ernzerhof functionals, *Phys. Rev. B* 59 (1999) 7413.
- [226] A.D. Becke, A multicenter numerical integration scheme for polyatomic molecules, *J. Chem. Phys.* 88 (1988) 2547-2553.
- [227] N. Govind, M. Petersen, G. Fitzgerald, D. King-Smith, J. Andzelm, A generalized synchronous transit method for transition state location, *Comput. Mater. Sci.* 28 (2003) 250-258.
- [228] T.A. Halgren, W.N. Lipscomb, The synchronous-transit method for determining reaction pathways and locating molecular transition states, *Chem. Phys. Lett.* 49 (1977) 225-232.
- [229] G. Kresse, J. Furthmüller, Universität Wien, Sensengasse 8 (2005) 1130.
- [230] G. Kresse, J. Hafner, Ab initio molecular dynamics for liquid metals, *Phys. Rev. B* 47 (1993) 558.
- [231] P.E. Blöchl, C.J. Först, J. Schimpl, Projector augmented wave method: ab initio molecular dynamics with full wave functions, *Bull. Mater. Sci.* 26 (2003) 33-41.
- [232] P.E. Blöchl, Projector augmented-wave method, *Phys. Rev. B* 50 (1994) 17953.
- [233] M.C. Payne, M.P. Teter, D.C. Allan, T. Arias, J. Joannopoulos, Iterative minimization techniques for ab initio total-energy calculations: molecular dynamics and conjugate gradients, *Rev. Mod. Phys.* 64 (1992) 1045.
- [234] L. Kleinman, D. Bylander, Efficacious form for model pseudopotentials, *Phys. Rev. Lett.* 48 (1982) 1425.
- [235] D. Vanderbilt, Soft self-consistent pseudopotentials in a generalized eigenvalue formalism, *Phys. Rev. B* 41 (1990) 7892.
- [236] C. Stampfl, M.V. Ganduglia-Pirovano, K. Reuter, M. Scheffler, Catalysis and corrosion: the theoretical surface-science context, *Surface Science* 500 (2002) 368-394.
- [237] K. Reuter, M. Scheffler, Composition, structure, and stability of RuO₂ (110) as a function of oxygen pressure, *Phys. Rev. B* 65 (2001) 035406.
- [238] M.P. Rosynek, Catalytic properties of rare earth oxides, *Cat. Rev. Sci. and Eng.* 16 (1977) 111-154.

- [239] G. Azimi, R. Dhiman, H.-M. Kwon, A.T. Paxson, K.K. Varanasi, Hydrophobicity of rare-earth oxide ceramics, *Nature materials* 12 (2013) 315-320.
- [240] L. Gerward, J.S. Olsen, L. Petit, G. Vaitheeswaran, V. Kanchana, A. Svane, Bulk modulus of CeO₂ and PrO₂—an experimental and theoretical study, *J. Alloys Compd.* 400 (2005) 56-61.
- [241] Z. Yang, T.K. Woo, M. Baudin, K. Hermansson, Atomic and electronic structure of unreduced and reduced CeO₂ surfaces: A first-principles study, *J. Chem. Phys.* 120 (2004) 7741-7749.
- [242] N. Hirosaki, S. Ogata, C. Kocer, Ab initio calculation of the crystal structure of the lanthanide Ln₂O₃ sesquioxides, *J. Alloys Compd.* 351 (2003) 31-34.
- [243] B. Wu, M. Zinkevich, F. Aldinger, D. Wen, L. Chen, Ab initio study on structure and phase transition of A-and B-type rare-earth sesquioxides Ln₂O₃ (Ln= La–Lu, Y, and Sc) based on density function theory, *J. Solid State Chem.* 180 (2007) 3280-3287.
- [244] M. Zinkevich, Thermodynamics of rare earth sesquioxides, *Prog. Mater. Sci.* 52 (2007) 597-647.
- [245] M. Mikami, S. Nakamura, Electronic structure of rare-earth sesquioxides and oxysulfides, *J. Alloys Compd.* 408 (2006) 687-692.
- [246] T. Biljan, S. Rončević, Z. Meić, K. Kovač, Non-vibrational features in NIR FT-Raman spectra of lanthanide sesquioxides, *Chem. Phys. Lett.* 395 (2004) 246-252.
- [247] N. Dilawar, S. Mehrotra, D. Varandani, B. Kumaraswamy, S. Haldar, A. Bandyopadhyay, A Raman spectroscopic study of C-type rare earth sesquioxides, *Mater. Charact.* 59 (2008) 462-467.
- [248] H.R. Hoekstra, K.A. Gingerich, High-pressure B-type polymorphs of some rare-earth sesquioxides, *Science* 146 (1964) 1163-1164.
- [249] A. Trovarelli, *Catalysis by ceria and related materials*, World Scientific 2002.
- [250] A. Trovarelli, Catalytic properties of ceria and CeO₂-containing materials, *Cat. Rev.* 38 (1996) 439-520.
- [251] C. Xia, M. Liu, Microstructures, conductivities, and electrochemical properties of Ce_{0.9}Gd_{0.1}O₂ and GDC–Ni anodes for low-temperature SOFCs, *Solid State Ion.* 152 (2002) 423-430.

- [252] D. Richard, E. Muñoz, M. Rentería, L. Errico, A. Svane, N.E. Christensen, Abinitio LSDA and LSDA+ U study of pure and Cd-doped cubic lanthanide sesquioxides, *Phys. Rev. B* 88 (2013) 165206.
- [253] A. Prokofiev, A. Shelykh, B. Melekh, Periodicity in the band gap variation of Ln₂X₃ (X= O, S, Se) in the lanthanide series, *J. Alloys Compd.* 242 (1996) 41-44.
- [254] D. Richard, L. Errico, M. Rentería, Structural properties and the pressure-induced C→ A phase transition of lanthanide sesquioxides from DFT and DFT+ U calculations, *J. Alloys Compd.* 664 (2016) 580-589.
- [255] D. Templeton, C.H. Dauben, Lattice parameters of some rare earth compounds and a set of crystal radii, *J. Am. Chem. Soc.* 76 (1954) 5237-5239.
- [256] M. Dubau, J. Lavková, I. Khalakhan, S. Haviar, V. Potin, V.r. Matolín, I. Matolínová, Preparation of magnetron sputtered thin cerium oxide films with a large surface on silicon substrates using carbonaceous interlayers, *ACS Appl. Mater. Interfaces.* 6 (2014) 1213-1218.
- [257] M. Miritello, R.L. Savio, A. Piro, G. Franzo, F. Priolo, F. Iacona, C. Bongiorno, Optical and structural properties of Er₂O₃ films grown by magnetron sputtering, *J. Appl. Phys.* 100 (2006) 013502.
- [258] G. Adachi, N. Imanaka, Z.C. Kang, Binary rare earth oxides, Springer Science & Business Media 2004.
- [259] R. Gillen, S.J. Clark, J. Robertson, Nature of the electronic band gap in lanthanide oxides, *Phys. Rev. B* 87 (2013) 125116.
- [260] P.J. Hay, R.L. Martin, J. Uddin, G.E. Scuseria, Theoretical study of CeO₂ and Ce₂O₃ using a screened hybrid density functional, *J. Chem. Phys.* 125 (2006) 034712.
- [261] J.L. Da Silva, M.V. Ganduglia-Pirovano, J. Sauer, V. Bayer, G. Kresse, Hybrid functionals applied to rare-earth oxides: The example of ceria, *Phys. Rev. B* 75 (2007) 045121.
- [262] J.P. Perdew, Density functional theory and the band gap problem, *Int. J. Quantum Chem.* 28 (1985) 497-523.
- [263] A.J. Cohen, P. Mori-Sánchez, W. Yang, Insights into current limitations of density functional theory, *Science* 321 (2008) 792-794.
- [264] M.V. Ganduglia-Pirovano, J.L. Da Silva, J. Sauer, Density-functional calculations of the structure of near-surface oxygen vacancies and electron localization on CeO₂ (111), *Phys. Rev. Lett.* 102 (2009) 026101.

- [265] L. First-principles, U and GGA+ U study of cerium oxides: Dependence on the effective U parameter Loschen, Christoph; Carrasco, Javier; Neyman, Konstantin M.; Illas, Francesc, *Phys. Rev. B* 75 (2007) 035115.
- [266] L. Petit, A. Svane, Z. Szotek, W.M. Temmerman, First-principles study of rare-earth oxides, *Phys. Rev. B* 72 (2005) 205118.
- [267] H. Jiang, P. Rinke, M. Scheffler, Electronic properties of lanthanide oxides from the G W perspective, *Phys. Rev. B* 86 (2012) 125115.
- [268] S. Lutfalla, V. Shapovalov, A.T. Bell, Calibration of the DFT/GGA+ U method for determination of reduction energies for transition and rare earth metal oxides of Ti, V, Mo, and Ce, *J. Chem. Theory Comput.* 7 (2011) 2218-2223.
- [269] T. Zhu, L. Kundakovic, A. Dreher, M. Flytzani-Stephanopoulos, Redox chemistry over CeO₂-based catalysts: SO₂ reduction by CO or CH₄, *Catal. Today* 50 (1999) 381-397.
- [270] K. Sohlberg, S.T. Pantelides, S.J. Pennycook, Interactions of hydrogen with CeO₂, *J. Am. Chem. Soc.* 123 (2001) 6609-6611.
- [271] G. Qi, R.T. Yang, Characterization and FTIR studies of MnO_x-CeO₂ catalyst for low-temperature selective catalytic reduction of NO with NH₃, *J. Phys. Chem. B* 108 (2004) 15738-15747.
- [272] Q. Shen, G. Lu, C. Du, Y. Guo, Y. Wang, Y. Guo, X. Gong, Role and reduction of NO_x in the catalytic combustion of soot over iron–ceria mixed oxide catalyst, *Chem. Eng. J.* 218 (2013) 164-172.
- [273] H. Miran, M. Altarawneh, Z.-T. Jiang, H. Oskierski, M.H. Almatarneh, B.Z. Dlugogorski, Decomposition of Selected Chlorinated Volatile Organic Compounds on CeO₂, *Catal. Sci. Technol.* (2017).
- [274] M. Altarawneh, M.W. Radny, P.V. Smith, J.C. Mackie, E.M. Kennedy, B.Z. Dlugogorski, A. Soon, C. Stampfl, A first-principles density functional study of chlorophenol adsorption on Cu₂O (110): CuO, *J. Chem. Phys.* 130 (2009) 184505.
- [275] M. Altarawneh, B.Z. Dlugogorski, Formation of dibenzofuran, dibenzo-p-dioxin and their hydroxylated derivatives from catechol, *Phys. Chem. Chem. Phys.* 17 (2015) 1822-1830.
- [276] J.F. Nye, *Physical properties of crystals: their representation by tensors and matrices*, Oxford university press 1985.

- [277] H.J. Monkhorst, J.D. Pack, Special points for Brillouin-zone integrations, *Phys. Rev. B* 13 (1976) 5188.
- [278] R.F. Bader, Atoms in molecules, *Acc. Chem. Res.* 18 (1985) 9-15.
- [279] D. Jie, Z. Tong, Z. Li, D. Ji-Guang, J. Gang, W. Hong-Bin, Elastic properties and electronic structures of lanthanide hexaborides, *Chin. Phys. B* 24 (2015) 096201.
- [280] Y. You, C. Chun-Lin, Z. Guo-Dong, Z. Xiao-Lin, Z. Xing-Hua, Mechanical and Vibrational Properties of ZnS with Wurtzite Structure: A First-Principles Study, *Chin. Phys. Lett.* 31 (2014) 106301.
- [281] J.-W. Yang, T. Gao, Y.-R. Gong, The disproportionation reaction phase transition, mechanical, and lattice dynamical properties of the lanthanum dihydrides under high pressure: A first principles study, *SOLID STATE SCI.* 32 (2014) 76-82.
- [282] P. Ravindran, L. Fast, P.A. Korzhavyi, B. Johansson, J. Wills, O. Eriksson, Density functional theory for calculation of elastic properties of orthorhombic crystals: application to TiSi_2 , *J. Appl. Phys.* 84 (1998) 4891-4904.
- [283] A. Togo, F. Oba, I. Tanaka, First-principles calculations of the ferroelastic transition between rutile-type and CaCl_2 -type SiO_2 at high pressures, *Phys. Rev. B* 78 (2008) 134106.
- [284] W. Zachariasen, The crystal structure of the modification C of the sesquioxides of the rare earth metals, and of indium and thallium, *Norsk Geologisk Tidsskrift* 9 (1927) 82.
- [285] J. Blanusa, M. Mitric, D. Rodic, A. Szytula, M. Slaski, An X-ray diffraction and magnetic susceptibility study of $\text{Tm}_x\text{Y}_{2-x}\text{O}_3$, *J. Magn. Magn. Mater.* 213 (2000) 75-81.
- [286] F. Murnaghan, The compressibility of media under extreme pressures, *Proc. Natl. Acad. Sci. U.S.A.* 30 (1944) 244-247.
- [287] R. Wyckoff, pp. 1–22 in *Crystal Structures*, Vol. 2, Interscience, New York (1967).
- [288] S. Derbeneva, S. Batsanov, *WIDTH OF THE FORBIDDEN ZONE OF RARE-EARTH METAL OXIDES*, Inst. of Thermal Physics, Novosibirsk, USSR), 1967.
- [289] G. McCarthy, Crystal data on C-type terbium sesquioxide (Tb_2O_3), *J. Appl. Crystallogr.* 4 (1971) 399-400.
- [290] B. Zhu, Y. Cheng, Z.-W. Niu, M. Zhou, M. Gong, LDA+ U calculation of structural and thermodynamic properties of Ce_2O_3 , *Front. Phys.* 9 (2014) 483-489.

- [291] C. Loschen, J. Carrasco, K.M. Neyman, F. Illas, First-principles LDA+ U and GGA+ U study of cerium oxides: Dependence on the effective U parameter, *Phys. Rev. B* 75 (2007) 035115.
- [292] S. Fabris, S. de Gironcoli, S. Baroni, G. Vicario, G. Balducci, Taming multiple valency with density functionals: A case study of defective ceria, *Phys. Rev. B* 71 (2005) 041102.
- [293] R.F. Bader, *Atoms in molecules*, Wiley Online Library 1990.
- [294] Q. Guo, Y. Zhao, C. Jiang, W.L. Mao, Z. Wang, Phase transformation in Sm_2O_3 at high pressure: In situ synchrotron X-ray diffraction study and ab initio DFT calculation, *Solid State Commun.* 145 (2008) 250-254.
- [295] J.P. McClure, High pressure phase transitions in the lanthanide sesquioxides, (2009).
- [296] L. Bai, J. Liu, X. Li, S. Jiang, W. Xiao, Y. Li, L. Tang, Y. Zhang, D. Zhang, Pressure-induced phase transformations in cubic Gd_2O_3 , *J. Appl. Phys.* 106 (2009) 073507.
- [297] Y. Makino, S. Miyake, Estimation of bulk moduli of compounds by empirical relations between bulk modulus and interatomic distance, *J. Alloys Compd.* 313 (2000) 235-241.
- [298] D. Lonappan, N.C. Shekar, T. Ravindran, P.C. Sahu, High-pressure phase transition in Ho_2O_3 , *Mater. Chem. Phys.* 120 (2010) 65-67.
- [299] W. Manning, O. Hunter, Elastic Properties of Polycrystalline Yttrium Oxide, Holmium Oxide, and Erbium Oxide: High-Temperature Measurements, *J. Am. Ceram. Soc.* 52 (1969) 492-496.
- [300] P.C. Sahu, D. Lonappan, N.C. Shekar, High Pressure Structural Studies on Rare-Earth Sesquioxides, *Journal of Physics: Conference Series*, IOP Publishing, 2012, pp. 012015.
- [301] C. Meyer, J. Sanchez, J. Thomasson, J. Itie, Mössbauer and energy-dispersive x-ray-diffraction studies of the pressure-induced crystallographic phase transition in C-type Yb_2O_3 , *Phys. Rev. B* 51 (1995) 12187.
- [302] S. Jiang, J. Liu, C. Lin, L. Bai, W. Xiao, Y. Zhang, D. Zhang, X. Li, Y. Li, L. Tang, Pressure-induced phase transition in cubic Lu_2O_3 , *J. Appl. Phys.* 108 (2010) 083541.
- [303] G. Zhou, P.R. Shah, T. Montini, P. Fornasiero, R.J. Gorte, Oxidation enthalpies for reduction of ceria surfaces, *Surf. Sci.* 601 (2007) 2512-2519.
- [304] S. Park, J.M. Vohs, R.J. Gorte, Direct oxidation of hydrocarbons in a solid-oxide fuel cell, *Nature* 404 (2000) 265-267.

- [305] S. Park, R.J. Gorte, J.M. Vohs, Applications of heterogeneous catalysis in the direct oxidation of hydrocarbons in a solid-oxide fuel cell, *Appl. Catal. A* 200 (2000) 55-61.
- [306] R.J. Gorte, S. Park, J.M. Vohs, C. Wang, Anodes for direct oxidation of dry hydrocarbons in a solid-oxide fuel cell, *Adv. Mater.* 12 (2000) 1465-1469.
- [307] S. Park, R.J. Gorte, J.M. Vohs, Tape cast solid-oxide fuel cells for the direct oxidation of hydrocarbons, *J. Electrochem. Soc.* 148 (2001) A443-A447.
- [308] C. Lu, W. Worrell, C. Wang, S. Park, H. Kim, J. Vohs, R. Gorte, Development of solid oxide fuel cells for the direct oxidation of hydrocarbon fuels, *Solid State Ion.* 152 (2002) 393-397.
- [309] G. Zhou, P.R. Shah, T. Kim, P. Fornasiero, R.J. Gorte, Oxidation entropies and enthalpies of ceria-zirconia solid solutions, *Catal. Today* 123 (2007) 86-93.
- [310] F.B. Baker, E.J. Huber, C.E. Holley, N. Krikorian, Enthalpies of formation of cerium dioxide, cerium sesquicarbide, and cerium dicarbide, *J. Chem. Thermodyn.* 3 (1971) 77-83.
- [311] M. Huntelaar, A. Booi, E. Cordfunke, R. Van der Laan, A. Van Genderen, J. Van Miltenburg, The thermodynamic properties of Ce_2O_3 (s) from $T \rightarrow 0$ K to 1500 K, *J. Chem. Thermodyn.* 32 (2000) 465-482.
- [312] M. Chase, NIST—JANAF Thermochemical Tables (Journal of Physical and Chemical Reference Data Monograph No. 9), AIP (1998).
- [313] Y. Hao, C.-K. Yang, S.M. Haile, Ceria-Zirconia Solid Solutions ($\text{Ce}_{1-x}\text{Zr}_x\text{O}_{2-\delta}$, $x \leq 0.2$) for Solar Thermochemical Water Splitting: A Thermodynamic Study, *Chem. Mater.* 26 (2014) 6073-6082.
- [314] W.C. Chueh, S.M. Haile, A thermochemical study of ceria: exploiting an old material for new modes of energy conversion and CO_2 mitigation, *Philos. Trans. Royal Soc. A: Mathematical, Physical and Engineering Sciences* 368 (2010) 3269-3294.
- [315] G. Balducci, M.S. Islam, J. Kašpar, P. Fornasiero, M. Graziani, Bulk reduction and oxygen migration in the ceria-based oxides, *Chem. Mater.* 12 (2000) 677-681.
- [316] P.R. Shah, T. Kim, G. Zhou, P. Fornasiero, R.J. Gorte, Evidence for entropy effects in the reduction of ceria-zirconia solutions, *Chem. Mater.* 18 (2006) 5363-5369.
- [317] A. Bonk, A. Remhof, A.C. Maier, M. Trottman, M.V. Schlupp, C. Battaglia, U.F. Vogt, Low-Temperature Reducibility of $\text{MxCe}_{1-x}\text{O}_2$ ($\text{M} = \text{Zr}, \text{Hf}$) under Hydrogen Atmosphere, *J. Phys. Chem. C* 120 (2015) 118-125.

- [318] S. Bishop, D. Marrocchelli, W. Fang, K. Amezawa, K. Yashiro, G. Watson, Reducing the chemical expansion coefficient in ceria by addition of zirconia, *Energy & Environ. Sci.* 6 (2013) 1142-1146.
- [319] M. Altarawneh, B.Z. Dlugogorski, E.M. Kennedy, J.C. Mackie, Mechanisms for formation, chlorination, dechlorination and destruction of polychlorinated dibenzo-p-dioxins and dibenzofurans (PCDD/Fs), *Prog. Energy. Combust. Sci.* 35 (2009) 245-274.
- [320] S. Scirè, S. Minicò, C. Crisafulli, Pt catalysts supported on H-type zeolites for the catalytic combustion of chlorobenzene, *Appl. Catal., B.* 45 (2003) 117-125.
- [321] R. Van den Brink, M. Krzan, M. Feijen-Jeurissen, R. Louw, P. Mulder, The role of the support and dispersion in the catalytic combustion of chlorobenzene on noble metal based catalysts, *Appl. Catal., B.* 24 (2000) 255-264.
- [322] R. Van den Brink, R. Louw, P. Mulder, Increased combustion rate of chlorobenzene on Pt/ γ -Al₂O₃ in binary mixtures with hydrocarbons and with carbon monoxide, *Appl. Catal., B.* 25 (2000) 229-237.
- [323] S. Agarwal, J. Spivey, J. Butt, Deep oxidation of hydrocarbons, *Appl. Catal., A.* 81 (1992) 239-255.
- [324] S. Mosallanejad, B.Z. Dlugogorski, E.M. Kennedy, M. Stockenhuber, S.M. Lomnicki, N.W. Assaf, M. Altarawneh, Formation of PCDD/Fs in Oxidation of 2-Chlorophenol on Neat Silica Surface, *Environ. Sci. Technol.* 50 (2016) 1412-1418.
- [325] S. Jujjuri, F. Cárdenas-Lizana, M.A. Keane, Synthesis of group VI carbides and nitrides: application in catalytic hydrodechlorination, *J. Mater. Sci.* 49 (2014) 5406-5417.
- [326] J.D. Oxley, M.M. Mdleleni, K.S. Suslick, Hydrodehalogenation with sonochemically prepared Mo₂C and W₂C, *Catal. Today* 88 (2004) 139-151.
- [327] L. Delannoy, J.M. Giraudon, P. Granger, L. Leclercq, G. Leclercq, Group VI transition metal carbides as alternatives in the hydrodechlorination of chlorofluorocarbons, *Catal. Today* 59 (2000) 231-240.
- [328] Z.N. Jaf, M. Altarawneh, H.A. Miran, Z.-T. Jiang, B.Z. Dlugogorski, Mechanisms governing selective hydrogenation of acetylene over γ -Mo₂N surfaces, *Catal. Sci. Technol.* 7 (2017) 943-960.
- [329] F. Wang, M. Wei, D.G. Evans, X. Duan, CeO₂-based heterogeneous catalysts toward catalytic conversion of CO₂, *J. Mater. Chem. A.* 4 (2016) 5773-5783.

- [330] G. Vilé, P. Dähler, J. Vecchiotti, M. Baltanás, S. Collins, M. Calatayud, A. Bonivardi, J. Pérez-Ramírez, Promoted ceria catalysts for alkyne semi-hydrogenation, *J. Catal.* 324 (2015) 69-78.
- [331] K.-I. Maruya, A. Takasawa, M. Aikawa, T. Haraoka, K. Domen, T. Onishi, Mechanism of branched carbon-chain formation from CO and H₂ over oxide catalysts. Part 1. Adsorbed species on ZrO₂ and CeO₂ during CO hydrogenation, *J. Chem. Soc., Faraday Trans.* 90 (1994) 911-917.
- [332] F. Can, S.b. Berland, S.b. Royer, X. Courtois, D. Duprez, Composition-Dependent Performance of Ce_xZr_{1-x}O₂ Mixed-Oxide-Supported WO₃ Catalysts for the NO_x Storage Reduction–Selective Catalytic Reduction Coupled Process, *ACS Catal.* 3 (2013) 1120-1132.
- [333] C. Bonnelle, N. Spector, *Progress in Theoretical Chemistry and Physics, Rare-Earths and Actinides in High Energy Spectroscopy*, Springer2015.
- [334] M. Kanoun, S. Goumri-Said, M. Jaouen, Structure and mechanical stability of molybdenum nitrides: A first-principles study, *Phys. Rev. B* 76 (2007) 134109.
- [335] C. He, G. Men, Y. Yu, H. Pan, B. Xu, Chlorobenzene Destruction over Mesostructured CuO and MnO_x Co-Modified CeO₂ Catalyst: Activity and Activation Route, *Water Air Soil Pollut.* 226 (2015) 1-8.
- [336] Q. Dai, X. Wang, G. Lu, Low-temperature catalytic combustion of trichloroethylene over cerium oxide and catalyst deactivation, *Appl. Catal., B* 81 (2008) 192-202.
- [337] Y.-R. Luo, *Handbook of bond dissociation energies in organic compounds*, CRC press2002.
- [338] I.C. McNeill, L. Memetea, W.J. Cole, A study of the products of PVC thermal degradation, *Polym. Degrad. Stab* 49 (1995) 181-191.
- [339] B. Delley, From molecules to solids with the DMol₃ approach, *J. Chem. Phys.* 113 (2000) 7756-7764.
- [340] M. Fronzi, S. Piccinin, B. Delley, E. Traversa, C. Stampfl, Water adsorption on the stoichiometric and reduced CeO₂(111) surface: a first-principles investigation, *Phys. Chem. Chem. Phys.* 11 (2009) 9188-9199.
- [341] M. Capdevila-Cortada, Z. Łodziana, N. López, Performance of DFT+U Approaches in the Study of Catalytic Materials, *ACS. Catal.* 6 (2016) 8370-8379.
- [342] G. Henkelman, B.P. Uberuaga, H. Jónsson, Climbing image nudged elastic band method for finding saddle points and minimum energy paths, *J. Chem. Phys.* 113 (2000) 9901-9904.

- [343] F.L. Hirshfeld, Bonded-atom fragments for describing molecular charge densities, *Theor. Chem. Acc.* 44 (1977) 129-138.
- [344] K. Fukui, Role of Frontier Orbitals in Chemical Reactions, *Science* 218 (1982) 747-754.
- [345] J.A. Montgomery Jr, M.J. Frisch, J.W. Ochterski, G.A. Petersson, A complete basis set model chemistry. VI. Use of density functional geometries and frequencies, *J. Chem. Phys.* 110 (1999) 2822-2827.
- [346] M.J.T. Frisch, G. W.; Schlegel, H. B.; Scuseria, G. E.; Robb, M. A.; Cheeseman, J. R.; Scalmani, G.; Barone, V.; Mennucci, B.; Petersson, G. A.; et al. , *Gaussian 09*, Gaussian, Inc, Wallingford CT, 2009.
- [347] J. Yu, L. Sun, C. Ma, Y. Qiao, H. Yao, Thermal degradation of PVC: A review, *Waste Manag.* 48 (2016) 300-314.
- [348] N. Ahubelem, M. Altarawneh, B.Z. Dlugogorski, Dehydrohalogenation of ethyl halides, *Tetrahedron. Lett.* 55 (2014) 4860-4868.
- [349] N. Ahubelem, M. Altarawneh, B.Z. Dlugogorski, Kinetic and mechanistic study into emission of HCl in fires of PVC, *The Seventh International Seminar on Fire and Explosion Hazards (ISFEH7)* Providence, RI, USA, 2013, pp. 371-380.
- [350] M. Altarawneh, O.H. Ahmed, Z.-T. Jiang, B.Z. Dlugogorski, Thermal recycling of brominated flame retardants with Fe₂O₃, *J. Phys. Chem. A.* 120 (2016) 6039-6047.
- [351] S. Biswas, A. Pramanik, P. Sarkar, Computational studies on the reactivity of alkyl halides over (Al₂O₃)_n nanoclusters: an approach towards room temperature dehydrohalogenation, *Nanoscale* 8 (2016) 10205-10218.
- [352] M.B. Watkins, A.S. Foster, A.L. Shluger, Hydrogen Cycle on CeO₂ (111) Surfaces: Density Functional Theory Calculations, *J. Phys. Chem. C.* 111 (2007) 15337-15341.
- [353] W. Cen, Y. Liu, Z. Wu, J. Liu, H. Wang, X. Weng, Cl Species Transformation on CeO₂(111) Surface and Its Effects on CVOCs Catalytic Abatement: A First-Principles Investigation, *J. Phys. Chem. C.* 118 (2014) 6758-6766.
- [354] M. Bhasin, J. McCain, B. Vora, T. Imai, P. Pujado, Dehydrogenation and oxydehydrogenation of paraffins to olefins, *Appl. Catal., A* 221 (2001) 397-419.
- [355] M. Fronzi, S. Piccinin, B. Delley, E. Traversa, C. Stampfl, CH_x adsorption (x= 1– 4) and thermodynamic stability on the CeO₂(111) surface: a first-principles investigation, *RSC Adv* 4 (2014) 12245-12251.

- [356] F. Battin-Leclerc, Detailed chemical kinetic models for the low-temperature combustion of hydrocarbons with application to gasoline and diesel fuel surrogates, *Prog. Energy. Combust. Sci.* 34 (2008) 440-498.
- [357] W.-C. Ding, X.-K. Gu, H.-Y. Su, W.-X. Li, Single Pd atom embedded in CeO₂(111) for NO reduction with CO: a first-principles study, *J. Phys. Chem. C.* 118 (2014) 12216-12223.
- [358] P. Trogadas, J. Parrondo, V. Ramani, CeO₂ Surface Oxygen Vacancy Concentration Governs in Situ Free Radical Scavenging Efficacy in Polymer Electrolytes, *ACS Appl. Mater. Interfaces*, 4 (2012) 5098-5102.
- [359] M. Alaydrus, M. Sakaue, H. Kasai, A DFT+U study on the contribution of 4f electrons to oxygen vacancy formation and migration in Ln-doped CeO₂, *Phys. Chem. Chem. Phys.* 18 (2016) 12938-12946.
- [360] M. Bowker, Catalysis resolved using scanning tunnelling microscopy, *Chem. Soc. Rev.* 36 (2007) 1656-1673.
- [361] J.V. Lauritsen, M. Reichling, Atomic resolution non-contact atomic force microscopy of clean metal oxide surfaces, *J. Phys. Condens. Matter* 22 (2010) 263001.
- [362] M. Altarawneh, B.Z. Dlugogorski, Thermal Decomposition of 1,2-Bis(2,4,6-tribromophenoxy)ethane (BTBPE), a Novel Brominated Flame Retardant, *Environ. Sci. Technol.* 48 (2014) 14335-14343.
- [363] M. Altarawneh, B.Z. Dlugogorski, Mechanism of Thermal Decomposition of Tetrabromobisphenol A (TBBA), *J. Phys. Chem. A.* 118 (2014) 9338-9346.
- [364] X.-P. Wu, X.-Q. Gong, G. Lu, Role of oxygen vacancies in the surface evolution of H at CeO₂(111): a charge modification effect, *Phys. Chem. Chem. Phys.* 17 (2015) 3544-3549.
- [365] N.R. Peela, J.E. Sutton, I.C. Lee, D.G. Vlachos, Microkinetic Modeling of Ethane Total Oxidation on Pt, *Ind. Eng. Chem. Res.* 53 (2014) 10051-10058.
- [366] Y. Xin, H. Wang, C.K. Law, Kinetics of catalytic oxidation of methane, ethane and propane over palladium oxide, *Combust. Flame* 161 (2014) 1048-1054.
- [367] A.D. Mayernick, M.J. Janik, Methane oxidation on Pd–Ceria: A DFT study of the mechanism over Pd_xCe_{1-x}O₂, Pd, and PdO, *J. Catal.* 278 (2011) 16-25.
- [368] M.D. Krcha, M.J. Janik, Catalytic propane reforming mechanism over Mn-Doped CeO₂ (111), *Surf. Sci.* 640 (2015) 119-126.

- [369] M.D. Krcha, M.J. Janik, Catalytic propane reforming mechanism over Zr-doped CeO₂ (111), *Catal. Sci. Technol.* 4 (2014) 3278-3289.
- [370] Q. Dai, S. Bai, X. Wang, G. Lu, Catalytic combustion of chlorobenzene over Ru-doped ceria catalysts: Mechanism study, *Appl. Catal., B* 129 (2013) 580-588.
- [371] R. Farra, S. Wrabetz, M.E. Schuster, E. Stotz, N.G. Hamilton, A.P. Amrute, J. Perez-Ramirez, N. Lopez, D. Teschner, Understanding CeO₂ as a Deacon catalyst by probe molecule adsorption and in situ infrared characterisations, *Phys. Chem. Chem. Phys.* 15 (2013) 3454-3465.
- [372] M. Altarawneh, B.Z. Dlugogorski, Formation and Chlorination of Carbazole, Phenoxazine, and Phenazine, *Environ. Sci. Technol.* 49 (2015) 2215-2221.
- [373] H.-F. Wang, H.-Y. Li, X.-Q. Gong, Y.-L. Guo, G.-Z. Lu, P. Hu, Oxygen vacancy formation in CeO₂ and Ce_{1-x}Zr_xO₂ solid solutions: electron localization, electrostatic potential and structural relaxation, *Phys. Chem. Chem. Phys.* 14 (2012) 16521-16535.
- [374] H.S. Fogler, *Essentials of Chemical Reaction Engineering*, 1st ed., Prentice Hall New York, 2011.
- [375] D.Y. Murzin, T. Salmi, *Catalytic Kinetics*, 2nd ed., Elsevier, London, 2016.
- [376] H.A. Al-Madfa, M.M. Khader, M.A. Morris, Reduction kinetics of ceria surface by hydrogen, *Int. J. Chem. Kinet.* 36 (2004) 293-301.
- [377] S.V. Belaya, V.V. Bakovets, I.P. Asanov, I.V. Korolkov, V.S. Sulyaeva, MOCVD Synthesis of Terbium Oxide Films and their Optical Properties, *Chem. Vap. Deposition* 21 (2015) 150-155.
- [378] S. Bernal, G. Blanco, M.A. Cauqui, P. Corchado, J.M. Pintado, J.M. Rodríguez-Izquierdo, Oxygen buffering capacity of mixed cerium terbium oxide: a new material with potential applications in three-way catalysts, *Chem. Commun.* (1997) 1545-1546.
- [379] S. Bernal, G. Blanco, M. Cauqui, M. Corchado, C. Larese, J. Pintado, J. Rodríguez-Izquierdo, Cerium–terbium mixed oxides as alternative components for three-way catalysts: a comparative study of Pt/CeTbO_x and Pt/CeO₂ model systems, *Catal. Today* 53 (1999) 607-612.
- [380] R. Bhosale, A. Kumar, F. AlMomani, Solar thermochemical hydrogen production via terbium oxide based redox reactions, *Int. J. Photoenergy* 2016 (2016).
- [381] G. Kresse, J. Furthmüller, Efficient iterative schemes for ab initio total-energy calculations using a plane-wave basis set, *Phys. Rev. B* 54 (1996) 11169.

- [382] Y. Wang, K. Burke, J. PERDEW, Generalized gradient approximation for the exchange-correlation hole of a many-electron system, *Phys. Rev. B* 54 (1996) 16533-16539.
- [383] R. Zeller, Spin-polarized dft calculations and magnetism, *Computational Nanoscience: Do It Yourself* 31 (2006) 419-445.
- [384] M. Altarawneh, A. Marashdeh, B.Z. Dlugogorski, Structures, electronic properties and stability phase diagrams for copper (i/ii) bromide surfaces, *Phys. Chem. Chem. Phys.* 17 (2015) 9341-9351.
- [385] H. Widjaja, H.A. Miran, M. Altarawneh, I. Oluwoye, H.N. Lim, N.M. Huang, Z.-T. Jiang, B.Z. Dlugogorski, DFT+ U and ab initio atomistic thermodynamics approach for mixed transitional metallic oxides: A case study of CoCu_2O_3 surface terminations, *Mater. Chem. Phys.* 201 (2017) 241-250.
- [386] M.M. Branda, R.M. Ferullo, M. Causa, F. Illas, Relative stabilities of low index and stepped CeO_2 surfaces from hybrid and GGA+ U implementations of density functional theory, *J. Phys. Chem. C* 115 (2011) 3716-3721.
- [387] A. Prokofiev, A. Shelykh, B. Melekh, Periodicity in the band gap variation of Ln_2X_3 (X= O, S, Se) in the lanthanide series, *J. Alloys Compd.* 242 (1996) 41-44.
- [388] J. Yan, J.S. Hummelshøj, J.K. Nørskov, Formation energies of group I and II metal oxides using random phase approximation, *Phys. Rev. B* 87 (2013) 075207.
- [389] A. Togo, I. Tanaka, First principles phonon calculations in materials science, *Scr. Mater.* 108 (2015) 1-5.
- [390] V.G. Baonza, M. Taravillo, M. Cáceres, J. Núñez, Universal features of the equation of state of solids from a pseudospinodal hypothesis, *Phys. Rev. B* 53 (1996) 5252.
- [391] S. Baroni, P. Giannozzi, E. Isaev, Densityfunctional perturbation theory for quasiharmonic calculations, *Rev. Mineral Geochem.* 71 (2010) 39.
- [392] M. Woolfson, *Solid state physics 3. Theory of lattice dynamics in the harmonic approximation* by AA Maradudin, EW Montroll, GH Weiss and IP Ipatova, IUCr, 1973.
- [393] E. Mohammadpour, M. Altarawneh, Z.-T. Jiang, N. Mondinos, B.Z. Dlugogorski, Electronic properties and stability phase diagrams for cubic BN surfaces, *MOL. SIMULAT.* 43 (2017) 267-275.
- [394] S.A. Saraireh, M. Altarawneh, Electronic structure of the CuCl_2 (100) surface: A DFT first-principle study, *J. Nanomater* 2012 (2012) 78.

- [395] M. Chase, NIST-JANAF Thermochemical Tables, (Melville, NY: AIP), J. Phys. Chem. Ref. Data, Monograph (1998).
- [396] J. MacChesney, H. Williams, R. Sherwood, J. Potter, Preparation and Low-Temperature Magnetic Properties of the Terbium Oxides, J. Chem. Phys. 44 (1966) 596-601.
- [397] A. Erba, J. Maul, R. Demichelis, R. Dovesi, Assessing thermochemical properties of materials through ab initio quantum-mechanical methods: the case of α -Al₂O₃, Phys. Chem. Chem. Phys. 17 (2015) 11670-11677.
- [398] Z.N. Jaf, Z.-T. Jiang, H.A. Miran, M. Altarawneh, Thermo-elastic and optical properties of molybdenum nitride, Can. J. Phys. 94 (2016) 902-912.
- [399] S.A. Saraireh, M. Altarawneh, Thermodynamic stability and structures of iron chloride surfaces: A first-principles investigation, J. Chem. Phys. 141 (2014) 054709.
- [400] T.X. Sayle, S.C. Parker, C.R.A. Catlow, Surface oxygen vacancy formation on CeO₂ and its role in the oxidation of carbon monoxide, J. Chem. Soc., Chem. Commun. (1992) 977-978.
- [401] H. Dai, C. Ng, C. Au, SrCl₂-promoted REO_x (RE= Ce, Pr, Tb) catalysts for the selective oxidation of ethane: A study on performance and defect structures for ethene formation, J. Catal. 199 (2001) 177-192.
- [402] D. Devaiah, D. Jampaiah, P. Saikia, B.M. Reddy, Structure dependent catalytic activity of Ce_{0.8}Tb_{0.2}O_{2- δ} and TiO₂ supported Ce_{0.8}Tb_{0.2}O_{2- δ} solid solutions for CO oxidation, J. IND. ENG. CHEM. 20 (2014) 444-453.
- [403] H.A. Miran, M. Altarawneh, Z.-T. Jiang, H. Oskierski, M. Almatarneh, B.Z. Dlugogorski, Decomposition of selected chlorinated volatile organic compounds by ceria (CeO₂), Catal. Sci. Technol. 7 (2017) 3902-3919.
- [404] R.F. Bader, Atoms in Molecules: a quantum theory, International series of monographs on chemistry, 22, Oxford University Press, Oxford Henkelman G, Arnaldsson A, Jónsson H (2006) A fast and robust algorithm for Bader decomposition of charge density. Comput. Mater. Sci. 36 (1990) 354-360.
- [405] H.-T. Chen, First-principles study of CO adsorption and oxidation on Ru-doped CeO₂ (111) surface, J. Phys. Chem. C 116 (2012) 6239-6246.
- [406] N. Lu, L. Li, P. Sun, M. Wang, Q. Liu, H. Lv, S. Long, M. Liu, A novel method of identifying the carrier transport path in metal oxide resistive random access memory, J. Phys.D 48 (2015) 065101.

- [407] N. Lu, L. Li, P. Sun, M. Wang, Q. Liu, H. Lv, S. Long, W. Banerjee, M. Liu, Carrier-transport-path-induced switching parameter fluctuation in oxide-based resistive switching memory, *Materials Research Express* 2 (2015) 046304.
- [408] M. Altarawneh, Z.-T. Jiang, B.Z. Dlugogorski, The structures and thermodynamic stability of copper (II) chloride surfaces, *Phys. Chem. Chem. Phys.* 16 (2014) 24209-24215.
- [409] J. Rogal, K. Reuter, M. Scheffler, Thermodynamic stability of PdO surfaces, *Phys. Rev. B* 69 (2004) 075421.
- [410] J.R. González-Velasco, M.A. Gutiérrez-Ortiz, J.-L. Marc, J.A. Botas, M.P. González-Marcos, G. Blanchard, Contribution of cerium/zirconium mixed oxides to the activity of a new generation of TWC, *Appl. Catal. B* 22 (1999) 167-178.
- [411] S. Kumar, S. Gautam, T. Song, K.H. Chae, K. Jang, S. Kim, Electronic structure study of Co doped CeO₂ nanoparticles using X-ray absorption fine structure spectroscopy, *J. Alloys Compd.* 611 (2014) 329-334.
- [412] F. Varsano, F. Decker, E. Masetti, F. Cardellini, A. Licciulli, Optical and electrochemical properties of cerium–zirconium mixed oxide thin films deposited by sol–gel and rf sputtering, *Electrochim. Acta* 44 (1999) 3149-3156.
- [413] I. Hotovy, V. Rehacek, P. Siciliano, S. Capone, L. Spiess, Sensing characteristics of NiO thin films as NO₂ gas sensor, *Thin Solid Films* 418 (2002) 9-15.
- [414] Z. Al-Dhhan, C. Hogarth, Electrical conduction in thin films of CeO₂/GeO₂, *J. Mater. Sci.* 23 (1988) 2205-2212.
- [415] A. Frangoul, K. Sundaram, P. Wahid, The fabrication of metal–oxide–semiconductor transistors using cerium dioxide as a gate oxide material, *J. Vac. Sci. Technol.* 9 (1991) 181-183.
- [416] D. Mitzi, *Solution processing of inorganic materials*, John Wiley & Sons 2008.
- [417] C. Granqvist, A. Azens, L. Kullman, D. Rönnow, Progress in smart windows research: Improved electrochromic w oxide films and transparent Ti - Ce oxide counter electrodes, *Renewable energy* 8 (1996) 97-106.
- [418] C. Misiano, E. Simonetti, 4.4 Co-sputtered optical films, *Vacuum* 27 (1977) 403-406.
- [419] R.P. Netterfield, W.G. Sainy, P.J. Martin, S.H. Sie, Properties of CeO₂ thin films prepared by oxygen-ion-assisted deposition, *Appl. Opt.* 24 (1985) 2267-2272.
- [420] M. Angadi, K. Nallamshetty, Heat mirrors using CeO₂/Cu/CeO₂ multilayer films, *J. Mater. Sci. Lett.* 8 (1989) 391-394.

- [421] I. Porcheras, C. Person, C. Corbella, M. Vives, A. Pinyol, E. Bertran, Characteristics of e-beam deposited electrochromic CeO₂ thin films, *Solid State Ion.* 165 (2003) 131-137.
- [422] S. Debnath, M. Islam, M.S. Khan, Optical properties of CeO₂ thin films, *Bull. Mater. Sci.* 30 (2007) 315-319.
- [423] K. Sundaram, P. Wahid, P. Sisk, Characterization and optimization of cerium dioxide films deposited by rf magnetron sputtering, *Thin Solid Films* 221 (1992) 13-16.
- [424] Z. Shi, P. Shum, Z. Zhou, L.K.-Y. Li, Effect of bias voltage on the properties of CeO_{2-x} coatings prepared by magnetron sputtering, *Surf. Coat. Technol.* (2016).
- [425] Z. Shi, Z. Zhou, P. Shum, L.K.-Y. Li, Thermal stability, wettability and corrosion resistance of sputtered ceria films on 316 stainless steel, *Appl. Surf. Sci.* (2017).
- [426] H.A. Miran, M.M. Rahman, Z.-T. Jiang, M. Altarawneh, L.S. Chuah, H.-L. Lee, E. Mohammedpur, A. Amri, N. Mondinos, B.Z. Dlugogorski, Structural and optical characteristics of pre-and post-annealed sol-gel derived CoCu-oxide coatings, *J. Alloys Compd.* 701 (2017) 222-235.
- [427] M.M. Rahman, Z.-T. Jiang, Z.-f. Zhou, Z. Xie, C.Y. Yin, H. Kabir, M.M. Haque, A. Amri, N. Mondinos, M. Altarawneh, Effects of annealing temperatures on the morphological, mechanical, surface chemical bonding, and solar selectivity properties of sputtered TiAlSiN thin films, *J. Alloys Compd.* 671 (2016) 254-266.
- [428] D. Arndt, R. Azzam, J.M. Bennett, J. Borgogno, C.K. Carniglia, W.E. Case, J. Dobrowolski, U.J. Gibson, T.T. Hart, F. Ho, Multiple determination of the optical constants of thin-film coating materials, *Appl. Opt.* 23 (1984) 3571-3596.
- [429] M.M. Rahman, H.A. Miran, Z.-T. Jiang, M. Altarawneh, L.S. Chuah, H.-L. Lee, A. Amri, N. Mondinos, B.Z. Dlugogorski, Investigation of the post-annealing electromagnetic response of Cu-Co oxide coatings via optical measurement and computational modelling, *RSC Advances* 7 (2017) 16826-16835.
- [430] M. Segall, P.J. Lindan, M.a. Probert, C. Pickard, P.J. Hasnip, S. Clark, M. Payne, First-principles simulation: ideas, illustrations and the CASTEP code, *J. Phys. Condens. Matter* 14 (2002) 2717.
- [431] H. Monkhorst, J. Pack, Special points for Brillouin-zone integrations, (2005).

- [432] Y. Mao, X. Liu, F. Zhang, C. Ren, S. Zou, Ion beam assisted deposition of biaxially textured cerium dioxide films on polycrystalline nickel based alloy, *Surf. Coat. Technol.* 103 (1998) 78-82.
- [433] K. Ellmer, Magnetron sputtering of transparent conductive zinc oxide: relation between the sputtering parameters and the electronic properties, *J. Phys. D* 33 (2000) R17.
- [434] M. Ashokkumar, S. Muthukumaran, Cu doping effect on optical, structural and morphological properties of $\text{Cd}_{0.9}\text{Zn}_{0.1}\text{S}$ thin films, *JOL* 145 (2014) 167-174.
- [435] W. Liu, Z. Liu, F. Yan, T. Tan, H. Tian, Influence of O_2/Ar flow ratio on the structure and optical properties of sputtered hafnium dioxide thin films, *Surf. Coat. Technol.* 205 (2010) 2120-2125.
- [436] S. Ershov, M.-E. Druart, M. Poelman, D. Cossement, R. Snyders, M.-G. Olivier, Deposition of cerium oxide thin films by reactive magnetron sputtering for the development of corrosion protective coatings, *Corros. Sci.* 75 (2013) 158-168.
- [437] S. Durrani, M.F. Al-Kuhaili, I.A. Bakhtiari, M.B. Haider, Investigation of the carbon monoxide gas sensing characteristics of tin oxide mixed cerium oxide thin films, *Sensors* 12 (2012) 2598-2609.
- [438] J. Holgado, G. Munuera, J. Espinós, A. González-Elipe, XPS study of oxidation processes of CeO_x defective layers, *Appl. Surf. Sci.* 158 (2000) 164-171.
- [439] E. Preisler, O. Marsh, R. Beach, T. McGill, Stability of cerium oxide on silicon studied by x-ray photoelectron spectroscopy, *J. Vac. Sci. Technol. B: Microelectronics and Nanometer Structures Processing, Measurement, and Phenomena* 19 (2001) 1611-1618.
- [440] G. Ingo, E. Paparazzo, O. Bagnarelli, N. Zacchetti, XPS studies on cerium, zirconium and yttrium valence states in plasma-sprayed coatings, *Surf. Interface Anal.* 16 (1990) 515-519.
- [441] R. Bel Hadj Tahar, T. Ban, Y. Ohya, Y. Takahashi, Tin doped indium oxide thin films: Electrical properties, *J. Appl. Phys.* 83 (1998) 2631-2645.
- [442] H.-H. Huang, M.-C. Wang, C.-Y. Chen, N.-C. Wu, H.-J. Lin, Effect of deposition parameters on the growth rate and dielectric properties of the $\text{Ba}(\text{Sn}_x\text{Ti}_{1-x})\text{O}_3$ thin films prepared by radio frequency magnetron sputtering, *J. Eur. Ceram. Soc.* 26 (2006) 3211-3219.
- [443] P. Singh, D. Kaur, Influence of film thickness on texture and electrical and optical properties of room temperature deposited nanocrystalline V_2O_5 thin films, *J. Appl. Phys.* 103 (2008).

- [444] Z.-T. Jiang, K. Ohshimo, M. Aoyama, T. Yamaguchi, A study of Cr–Al oxides for single-layer halftone phase-shifting masks for deep-ultraviolet region photolithography, *Jpn. J. Appl. Phys.* 37 (1998) 4008-4013.
- [445] P.Y. Dave, K.H. Patel, K.V. Chauhan, A.K. Chawla, S.K. Rawal, Examination of zinc oxide films prepared by magnetron sputtering, *Procedia Technology* 23 (2016) 328-335.
- [446] P. Lei, J. Zhu, Y. Zhu, C. Jiang, X. Yin, Yttrium oxide thin films prepared under different oxygen-content atmospheres: microstructure and optical properties, *J. Appl. Phys. A* 108 (2012) 621-628.
- [447] F. Abelès, *Optical properties of solids*, (1972).
- [448] S. Morgan, Two types of dielectric polarization, *Transactions of The Electrochemical Society* 65 (1934) 109-118.
- [449] J. Sun, X.-F. Zhou, Y.-X. Fan, J. Chen, H.-T. Wang, X. Guo, J. He, Y. Tian, First-principles study of electronic structure and optical properties of heterodiamond BC₂N, *Phys. Rev. B* 73 (2006) 045108.
- [450] A. Rahman, A. Rahman, Z. Rahaman, First-principles calculations of structural, electronic and optical properties of HfZn₂, *J. Adv. Phys.* 5 (2016) 354-358.
- [451] A. Hagfeld, M. Grätzel, Light-induced redox reactions in nanocrystalline systems, *Chem. Rev.* 95 (1995) 49-68.
- [452] A. Henglein, Small-particle research: Physicochemical properties of extremely small colloidal metal and semiconductor particles, *Chem. Rev.* 89 (1989) 1861-1873.
- [453] M.E. Davis, Ordered porous materials for emerging applications, *Nature* 417 (2002) 813-821.
- [454] Y. Wan, D. Zhao, On the controllable soft-templating approach to mesoporous silicates, *Chem. Rev.* 107 (2007) 2821-2860.
- [455] R.J. Wu, J.G. Wu, T.K. Tsai, C.T. Yeh, Use of cobalt oxide CoOOH in a carbon monoxide sensor operating at low temperatures, *Sens. Actuator B-Chem.* 120 (2006) 104-109.
- [456] A. Amri, X. Duan, C.Y. Yin, Z.T. Jiang, M.M. Rahman, T. Pryor, Solar absorptance of copper-cobalt oxide thin film coatings with nano-size, grain-like morphology: Optimization and synchrotron radiation XPS studies, *Appl. Surf. Sci.* 275 (2013) 127-135.

- [457] A. Amri, Z.T. Jiang, X. Zhao, Z. Xie, C.Y. Yin, N. Ali, N. Mondinos, M.M. Rahman, D. Habibi, Tailoring the physicochemical and mechanical properties of optical copper-cobalt oxide thin films through annealing treatment, *Surf. Coat. Technol.* 239 (2014) 212-221.
- [458] J.F. Marco, J.R. Gancedo, M. Gracia, J.L. Gautier, E.I. Rios, H.M. Palmer, C. Greaves, F.J. Berry, Cation distribution and magnetic structure of the ferrimagnetic spinel NiCo_2O_4 , *J. Mater. Chem.* 11 (2001) 3087-3093.
- [459] T.J. Yoon, J.S. Kim, B.G. Kim, K.N. Yu, M.H. Cho, J.K. Lee, Multifunctional nanoparticles possessing a "magnetic motor effect" for drug or gene delivery, *Angew. Chem. Int. Ed.* 44 (2005) 1068-1071.
- [460] S. Xiong, C. Yuan, X. Zhang, B. Xi, Y. Qian, Controllable synthesis of mesoporous Co_3O_4 nanostructures with tunable morphology for application in supercapacitors, *Chem. Eur. J.* 15 (2009) 5320-5326.
- [461] E.K. Brechin, Using tripodal alcohols to build high-spin molecules and single-molecule magnets, *Chem. Commun.* (2005) 5141-5153.
- [462] A. Amri, Z.T. Jiang, P.A. Bahri, C.Y. Yin, X. Zhao, Z. Xie, X. Duan, H. Widjaja, M.M. Rahman, T. Pryor, Surface electronic structure and mechanical characteristics of copper-cobalt oxide thin film coatings: Soft X-ray synchrotron radiation spectroscopic analyses and modeling, *J. Phys. Chem. C* 117 (2013) 16457-16467.
- [463] A. Amri, Z.T. Jiang, T. Pryor, C.Y. Yin, Z. Xie, N. Mondinos, Optical and mechanical characterization of novel cobalt-based metal oxide thin films synthesized using sol-gel dip-coating method, *Surf. Coat. Technol.* 207 (2012) 367-374.
- [464] M. Beekman, J. Salvador, X. Shi, G.S. Nolas, J. Yang, Characterization of delafossite-type CuCoO_2 prepared by ion exchange, *J. Alloys Compd.* 489 (2010) 336-338.
- [465] M. De Koninck, S.C. Poirier, B. Marsan, $\text{Cu}_x\text{Co}_{3-x}\text{O}_4$ Used as bifunctional electrocatalyst, *J. Electrochem. Soc.* 153 (2006) A2103-A2110.
- [466] A. La Rosa-Toro, R. Berenguer, C. Quijada, F. Montilla, E. Morallón, J.L. Vázquez, Preparation and characterization of copper-doped cobalt oxide electrodes, *J. Phys. Chem. B* 110 (2006) 24021-24029.
- [467] W.M. Shaheen, A.A. Ali, Characterization of solid-solid interactions and physico-chemical properties of copper-cobalt mixed oxides and $\text{Cu}_x\text{Co}_{3-x}\text{O}_4$ spinels, *Mater. Res. Bull.* 36 (2001) 1703-1716.

- [468] R. Bayón, G. San Vicente, C. Maffiotte, A. Morales, Preparation of selective absorbers based on CuMn spinels by dip-coating method, *Renewable Energy* 33 (2008) 348-353.
- [469] G. Katumba, L. Olumekor, A. Forbes, G. Makiwa, B. Mwakikunga, J. Lu, E. Wäckelgård, Optical, thermal and structural characteristics of carbon nanoparticles embedded in ZnO and NiO as selective solar absorbers, *Sol. Energy Mater Sol. Cells* 92 (2008) 1285-1292.
- [470] M.M. Rahman, Z.-T. Jiang, C.-Y. Yin, L.S. Chuah, H.-L. Lee, A. Amri, B.-M. Goh, B.J. Wood, C. Creagh, N. Mondinos, M. Altarawneh, B.Z. Dlugogorski, Structural Thermal Stability of Graphene Oxide-Doped Copper–Cobalt Oxide Coatings as a Solar Selective Surface, *J. Mater. Sci. Technol.* 32 (2016) 1179-1191.
- [471] C. Gattinoni, A. Michaelides, Atomistic details of oxide surfaces and surface oxidation: the example of copper and its oxides, *Surf. Sci. Rep.* 70 (2015) 424-447.
- [472] S. Sun, D. Zhang, C. Li, Y. Wang, DFT study on the adsorption and dissociation of H₂S on CuO (111) surface, *RSC Advances* 5 (2015) 21806-21811.
- [473] J.G. McAlpin, T.A. Stich, C.A. Ohlin, Y. Surendranath, D.G. Nocera, W.H. Casey, R.D. Britt, Electronic structure description of a [Co (III) 3Co (IV) O₄] cluster: a model for the paramagnetic intermediate in cobalt-catalyzed water oxidation, *J. Am. Chem. Soc.* 133 (2011) 15444-15452.
- [474] W. Piskorz, F. Zasada, P. Stelmachowski, A. Kotarba, Z. Sojka, Decomposition of N₂O over the surface of cobalt spinel: A DFT account of reactivity experiments, *Catal. Today* 137 (2008) 418-422.
- [475] A. Soon, M. Todorova, B. Delley, C. Stampfl, Thermodynamic stability and structure of copper oxide surfaces: A first-principles investigation, *Phys. Rev. B* 75 (2007) 125420.
- [476] J.L. Gautier, E. Trollund, E. Ríos, P. Nkeng, G. Poillerat, Characterization of thin CuCo₂O₄ films prepared by chemical spray pyrolysis. Study of their electrochemical stability by ex situ spectroscopic analysis, *J. Electroanal. Chem.* 428 (1997) 47-56.
- [477] M. Hamid, A.A. Tahir, M. Mazhar, K.C. Molloy, G. Kociok-Köhn, Copper-cobalt heterobimetallic ceramic oxide thin film deposition: Synthesis, characterization and application of precursor, *Inorg. Chem. Commun.* 11 (2008) 1159-1161.
- [478] R.N. Singh, J.P. Pandey, N.K. Singh, B. Lal, P. Chartier, J.F. Koenig, Sol-gel derived spinel M_xCo_{3-x}O₄ (M = Ni, Cu; 0 ≤ x ≤ 1) films and oxygen evolution, *Electrochim. Acta* 45 (2000) 1911-1919.

- [479] G. Sberveglieri, *Gas Sensors: Principles, Operation and Developments*, Kluwer Academic Publishers, The Netherlands, 1992.
- [480] A.A. Taysioglu, A. Peksoz, Y. Kaya, N. Derebasi, G. Irez, G. Kaynak, GMI effect in CuO coated Co-based amorphous ribbons, *J. Alloys Compd.* 487 (2009) 38-41.
- [481] A. Millar, M.M. Rahman, Z.-T. Jiang, Review of Sol-Gel Derived Mixed Metal Oxide Thin Film Coatings with the Addition of Carbon Materials for Selective Surface Applications, *J. Adv. Phys.* 3 (2014) 179-193.
- [482] M.M. Rahman, Z.-T. Jiang, P. Munroe, L.S. Chuah, Z.-f. Zhou, Z. Xie, C.Y. Yin, K. Ibrahim, A. Amri, H. Kabir, Chemical bonding states and solar selective characteristics of unbalanced magnetron sputtered $Ti_xM_{1-x-y}N_y$ films, *RSC Advances* 6 (2016) 36373-36383.
- [483] J.P. Perdew, J. Chevary, S. Vosko, K.A. Jackson, M.R. Pederson, D. Singh, C. Fiolhais, Atoms, molecules, solids, and surfaces: Applications of the generalized gradient approximation for exchange and correlation, *Phys. Rev. B* 46 (1992) 6671.
- [484] H.J. Monkhorst, J.D. Pack, Special points for Brillouin-zone integrations, *Phys. Rev. B* 13 (1976) 5188.
- [485] R. Bader, W. Atoms in molecules, *Acc Chem Res* (1990) 9-15.
- [486] M. Ashokkumar, S. Muthukumaran, Cu doping effect on optical, structural and morphological properties of $Cd_{0.9}Zn_{0.1}S$ thin films, *J. Lumin.* 145 (2014) 167-174.
- [487] J.B. Cohen, I.C. Noyan, *Residual Stresses: Measurement by Diffraction and Interpretation*, Springer Verlag, New York, USA, 1987.
- [488] L.B. Freund, S. Suresh, *Thin Film Materials: Stress, Defect Formation and Surface Evolution*, Cambridge University Press, Sydney, Australia, 2003.
- [489] A.P. Boresi, R.J. Schmidt, *Advanced Mechanics of Materials*, John Wiley and Sons Inc., New York, USA, 2003.
- [490] G. Tyuliev, D. Panayotov, I. Avramova, D. Stoichev, T. Marinova, Thin-film coating of Cu-Co oxide catalyst on lanthana/zirconia films electrodeposited on stainless steel, *Mater. Sci. Eng. C* 23 (2003) 117-121.
- [491] A. La Rosa-Toro, R. Berenguer, C. Quijada, F. Montilla, E. Morallón, J.L. Vázquez, Preparation and Characterization of Copper-Doped Cobalt Oxide Electrodes, *J. Phys. Chem. B* 110 (2006) 24021-24029.

- [492] M. Sultan, A.A. Tahir, M. Mazhar, M. Zeller, K.G.U. Wijayantha, Hexanuclear copper-nickel and copper-cobalt complexes for thin film deposition of ceramic oxide composites, *New J. Chem.* 36 (2012) 911-917.
- [493] P.W. De Oliveira, C. Becker-Willinger, M.H. Jilavi, Sol-gel derived nanocomposites for optical applications, *Adv. Eng. Mater.* 12 (2010) 349-351.
- [494] A. Trovarelli, C. de Leitenburg, M. Boaro, G. Dolcetti, The utilization of ceria in industrial catalysis, *Catal. Today* 50 (1999) 353-367.
- [495] Z. Chafi, N. Keghouche, C. Minot, DFT study of Ni-CeO₂ interaction: adsorption and insertion, *Surf. Sci.* 601 (2007) 2323-2329.
- [496] A. Diwell, R. Rajaram, H. Shaw, T. Truex, The role of ceria in three-way catalysts, *Stud. Surf. Sci. Catal.* 71 (1991) 139-152.
- [497] G. Vicario, G. Balducci, S. Fabris, S. de Gironcoli, S. Baroni, Interaction of hydrogen with cerium oxide surfaces: a quantum mechanical computational study, *J. Phys. Chem. B* 110 (2006) 19380-19385.
- [498] E. Wuilloud, E. Wuilloud, B. Delley, W.-D. Schneider, and Y. Baer, *Phys. Rev. Lett.* 53, 202 (1984), *Phys. Rev. Lett.* 53 (1984) 202.
- [499] H.A. Miran, Z.-T. Jiang, M. Altarawneh, J.-P. Veder, Z.-f. Zhou, M.M. Rahman, Z.N. Jaf, B.Z. Dlugogorski, Influence of DC magnetron sputtering reaction gas on structural and optical characteristics of Ce-oxide thin films, *Ceram. Int.* (2018).
- [500] S. Grimme, Semiempirical GGA-type density functional constructed with a long-range dispersion correction, *J. Comput. Chem.* 27 (2006) 1787-1799.
- [501] T. Jarlborg, B. Barbiellini, C. Lane, Y.J. Wang, R. Markiewicz, Z. Liu, Z. Hussain, A. Bansil, Electronic structure and excitations in oxygen deficient CeO_{2- δ} from DFT calculations, *Phys. Rev. B* 89 (2014) 165101.
- [502] M. Capdevila-Cortada, M. García-Melchor, N. López, Unraveling the structure sensitivity in methanol conversion on CeO₂: A DFT+ U study, *J. Catal.* 327 (2015) 58-64.
- [503] Z.N. Jaf, M. Altarawneh, H.A. Miran, Z.-T. Jiang, B.Z. Dlugogorski, Mechanisms governing selective hydrogenation of acetylene over γ -Mo₂N surfaces, *Catal. Sci. Technol.* 7 (2017) 943-960.
- [504] A. Trovarelli, J. Llorca, Ceria catalysts at nanoscale: how do crystal shapes shape catalysis?, *ACS Catal.* 7 (2017) 4716-4735.

- [505] R. Bhosale, A. Kumar, F. AlMomani, Solar thermochemical hydrogen production via terbium oxide based redox reactions, *INT J PHOTOENERGY* 2016 (2016).
- [506] L.B. Freund, S. Suresh, *Thin film materials: stress, defect formation and surface evolution*, Cambridge University Press 2004.
- [507] M. Ohring, *Materials science of thin films*, Academic press 2001.
- [508] G.L. Hornyak, J.J. Moore, H. Tibbals, J. Dutta, *Fundamentals of nanotechnology*, CRC press 2008.
- [509] R.A. Powell, S.M. Rossnagel, *PVD for microelectronics: sputter deposition applied to semiconductor manufacturing*, Elsevier 1999.

Appendices

Appendix A

Coating Deposition Techniques

Recently, great strides have been made in the field of thin films industry due to thin films having increasing applications in versatile technologies such as in optical, decorative, electrical, thermal, and protective areas. Thin film layers possess a thickness ranging from nanometers to few micrometers which is applied to a surface of material to improve its desired properties. In fact, these new obtained properties are different than that of bulk materials or substrate on which the film is formed. A variety of methods have been used for film depositions. In principle they are considered as vapor deposition processes. Depending on the vapor source to be deposited they are divided into physical vapor deposition (PVD) and chemical vapor deposition (CVD). Vapor deposition refers to a process in which a solid immersed becomes larger in mass due to the transference of a material from the vapor onto the solid surface. PVD is the most widely used technique for thin film deposition and a high vacuum is required for almost their types. If the vapor is formed using physical means without chemical reactions, then the process is classified as a physical vapor deposition. In contrast, if the vapor is created using chemical reactions then the process is called chemical vapor deposition. The vapor source is different in each kind of PVD process, it can be developed through resistive heating, atomic sputtering, ion plating, magnetron sputtering or lasers, or hybrid processes combining all of these sources. For CVD process vapors, they can be achieved from gas, liquid, or solid precursors and a chemical reaction is required for the film formation[506]. Below is explanation for some of the main CVD and PVD processes:

Chemical Vapor Deposition (CVD)

Chemical vapor deposition involves a variety of methods that aim to produce films having high purity and desirable properties films and coatings of metals, semiconductors, and amorphous or crystalline compounds. In this process, the substrate is located inside a vacuum chamber to which gases are provided. The main principle of the deposition using this process is that a chemical reaction between a volatile compounds of a material to be deposited, with other gases is

happened, to produce a nonvolatile solid resulted in the deposition of a solid material on a substrate surface [507].

Furthermore, an important advantage of using this technique is that it does not require high vacuum or any special conditions of electrical power as well as it is with low cost of the equipment. On the other hand, high substrate temperature (higher than 600°C) and the relatively slow deposition rate are the main drawback seen with this process. Amendments should therefore be applied to overcome these limitations. There are three classifications of CVD techniques namely as the Low-Pressure CVD (LPCVD), Plasma Enhanced CVD (PECVD) and laser-enhanced (LECVD) chemical vapor deposition.

Physical Vapor Deposition (PVD)

Physical vapor deposition (PVD) processes have long been used to deposit thin layers on substrates. In this process the material to be deposited is physically moved onto the substrate and that means there is no chemical reaction occurred. However, the substantial difference between the deposition using this process and chemical vapor deposition process is that it takes place at lower deposition temperature. In other words, the substrate deposition temperature is in the range of 150-550 °C and the substrate tends not to be damaged [508]. Moreover, physical vapor deposition (PVD) processes are nowadays preferred for industrial applications such as, coating tool steel. In industrial applications the trends have shifted towards PVD in coating different components for instance aerospace, automotive, surgical or medical equipment, and cutting tools *etc.*

Sputtering is the most dominant physical vapor deposition - based process. It takes place when a substrate to be coated is placed in a vacuum chamber containing an inert gas - usually argon - then a negative charge is applied to a target source material that will be deposited onto the substrate causing the plasma to glow. As a result of the bombarding particles hitting the target material in a vacuum, atoms will be ejected from the target directing to be deposited on the substrate [509].

Appendix B

This appendix includes supporting information for **Chapter 5** and reports the Vibrational frequencies for the transition states.

TS1

-269.3400000	255.5400000	227.1300000
31.0400000	258.6500000	231.7800000
32.4500000	259.4300000	235.7700000
34.7600000	260.7400000	239.9300000
36.1300000	265.8500000	242.7500000
37.5300000	267.5100000	247.7300000
39.4200000	269.0500000	248.8900000
40.9100000	273.4500000	250.4300000
48.4900000	275.5100000	252.9000000
48.8500000	275.6500000	253.3600000
52.6300000	277.9400000	253.8100000
55.7700000	279.8400000	255.0100000
60.3000000	281.9500000	290.2100000
61.5100000	283.9100000	292.1300000
62.6000000	285.6900000	381.5200000
62.7900000	287.2100000	383.7200000
62.8800000	287.8900000	393.9700000

63.79000000	289.01000000	397.10000000
67.44000000	296.11000000	397.53000000
70.75000000	299.19000000	403.03000000
73.85000000	302.87000000	404.32000000
294.44000000	303.58000000	654.35000000
74.63000000	307.80000000	680.84000000
77.18000000	308.64000000	829.08000000
80.52000000	330.91000000	972.75000000
81.04000000	331.45000000	214.59000000
81.71000000	333.26000000	215.88000000
82.60000000	333.67000000	216.93000000
82.91000000	335.69000000	220.79000000
84.00000000	336.48000000	222.18000000
88.05000000	337.92000000	127.48000000
88.39000000	338.22000000	127.78000000
95.59000000	351.66000000	132.57000000
96.38000000	355.15000000	136.68000000
98.02000000	357.43000000	138.22000000
104.18000000	358.54000000	148.33000000
113.14000000	364.25000000	151.58000000
113.56000000	365.07000000	161.16000000
120.24000000	367.18000000	163.01000000
120.85000000	367.28000000	166.34000000

125.85000000	370.97000000	167.56000000
125.94000000	226.46000000	200.29000000
224.16000000	210.13000000	212.26000000

TS2

-828.59000000	126.67000000	288.53000000
16.87000000	127.08000000	289.25000000
28.87000000	128.51000000	295.94000000
30.51000000	131.30000000	296.59000000
32.63000000	137.26000000	298.53000000
33.65000000	148.20000000	300.31000000
33.96000000	153.86000000	302.72000000
34.90000000	155.37000000	303.79000000
38.83000000	159.09000000	309.08000000
43.05000000	165.82000000	311.15000000
44.44000000	166.30000000	312.42000000
46.67000000	168.26000000	318.84000000
52.84000000	204.55000000	320.25000000
62.93000000	207.22000000	323.60000000
63.61000000	211.06000000	325.44000000
63.68000000	212.34000000	328.73000000
65.15000000	215.08000000	342.27000000
66.27000000	215.75000000	343.93000000
67.87000000	216.50000000	345.30000000

73.85000000	218.74000000	346.73000000
74.90000000	222.13000000	348.47000000
81.43000000	224.70000000	352.42000000
83.38000000	228.66000000	358.23000000
84.05000000	233.11000000	360.29000000
85.06000000	233.84000000	361.27000000
85.66000000	234.42000000	362.72000000
86.24000000	238.39000000	364.05000000
87.60000000	248.81000000	366.19000000
88.29000000	252.06000000	366.57000000
90.33000000	266.54000000	368.18000000
92.14000000	270.14000000	375.98000000
97.08000000	273.17000000	377.78000000
97.29000000	273.60000000	378.89000000
98.86000000	275.77000000	379.70000000
100.3400000	276.43000000	382.05000000
100.78000000	279.84000000	382.85000000
104.11000000	282.70000000	383.75000000
105.79000000	283.15000000	385.83000000
108.88000000	286.67000000	386.67000000
111.16000000	287.41000000	389.67000000
114.09000000	424.21000000	397.36000000
114.26000000	425.62000000	409.67000000

423.65000000	428.93000000	413.54000000
--------------	--------------	--------------

TS3

-1056.910000	119.30000000	264.42000000
254.76000000	122.46000000	268.64000000
134.0900000	125.22000000	270.29000000
68.76000000	125.63000000	270.69000000
13.23000000	127.06000000	274.81000000
16.13000000	127.37000000	275.65000000
19.53000000	132.11000000	277.02000000
34.05000000	136.25000000	277.04000000
35.11000000	137.90000000	277.68000000
36.47000000	147.50000000	278.66000000
38.01000000	151.12000000	281.70000000
41.31000000	161.70000000	283.62000000
48.29000000	165.34000000	285.42000000
48.71000000	167.09000000	286.83000000
52.61000000	181.38000000	287.67000000
55.56000000	201.72000000	288.71000000
60.02000000	208.45000000	292.16000000
61.52000000	213.41000000	295.35000000
62.47000000	215.42000000	296.90000000

62.55000000	217.88000000	299.09000000
62.72000000	218.51000000	299.95000000
64.23000000	220.00000000	301.40000000
73.25000000	223.29000000	307.54000000
74.19000000	224.22000000	311.24000000
76.23000000	225.63000000	330.65000000
79.78000000	226.67000000	331.99000000
80.63000000	230.20000000	333.11000000
81.59000000	232.05000000	334.02000000
82.30000000	239.13000000	335.13000000
82.51000000	244.86000000	335.57000000
83.11000000	249.11000000	337.52000000
87.72000000	250.20000000	338.03000000
88.62000000	251.21000000	349.44000000
94.96000000	255.92000000	354.15000000
96.34000000	256.87000000	354.99000000
97.54000000	257.63000000	356.71000000
101.76000000	257.75000000	360.94000000
106.47000000	260.04000000	361.70000000
112.35000000	262.10000000	363.14000000
112.97000000	262.62000000	364.55000000
374.64000000	398.38000000	366.89000000
381.88000000	401.44000000	371.76000000

391.17000000	511.19000000	613.31000000
393.32000000	571.47000000	3.100560e+003
395.75000000	1.540560e+003	3.166090e+003

TS5

-440.6	167.6	337.1
36.9	214.8	338.6
37.4	217.7	342.8
46.4	219.9	343.3
50.4	221.8	344.2
51.1	222.4	347.5
61.5	224.0	348.4
62.2	227.3	349.2
62.8	230.0	351.2
64.1	233.0	352.4
64.5	235.0	353.0
66.7	236.3	354.3
67.0	239.4	356.7
68.9	241.6	357.8
71.0	244.4	360.8
71.2	249.2	362.8
72.1	251.9	367.4
77.5	253.7	373.2

77.9	260.1	384.9
79.4	261.2	385.2
80.4	263.2	391.8
81.5	263.4	392.9
84.4	264.2	394.0
85.0	266.7	491.4
85.9	267.7	701.4
86.0	269.4	847.5
88.4	270.1	1019.7
88.6	271.1	1090.0
103.2	271.6	1245.6
104.6	273.0	1277.7
105.7	273.7	1309.9
107.4	276.3	1336.9
112.0	278.9	2781.7
112.1	280.5	2867.0
122.0	282.7	3042.4
123.9	284.1	3156.5
125.1	285.7	3316.8
125.8	286.9	308.3
128.8	287.2	309.2
129.3	289.1	312.3
135.1	290.4	329.9

137.8	291.9	164.6
138.2	293.5	167.0

TS6

-716.4	220.1	339.3
0.9	222.1	341.7
20.4	222.6	343.5
35.4	223.2	344.3
37.9	224.9	344.7
49.6	229.5	346.0
51.2	233.9	348.3
53.8	234.5	349.0
60.2	236.4	350.5
61.9	236.6	351.6
62.9	239.5	352.5
64.0	241.5	353.1
65.2	245.0	355.0
66.4	247.9	356.9
66.8	248.9	360.3
68.8	251.0	361.1
71.3	253.5	366.1
71.4	260.6	367.5
76.7	261.4	369.9

77.0	263.2	382.5
79.2	265.0	385.7
79.6	267.4	392.1
81.2	267.9	392.6
84.1	268.0	393.3
84.8	269.9	662.8
85.3	271.3	736.1
86.9	273.1	778.8
87.9	273.7	823.8
89.1	274.8	1089.5
103.4	275.2	1220.3
105.1	282.3	1321.9
105.5	284.3	1438.6
106.8	285.4	2814.0
110.0	286.3	2880.0
111.3	287.3	2981.4
119.5	288.2	3115.1
123.7	292.7	306.6
124.7	293.2	310.8
125.7	295.6	311.5
127.9	298.3	316.4
129.1	302.6	317.5
134.9	302.8	329.6

135.7	303.4	153.8
-------	-------	-------

TS8

-227.2	210.7	338.7
--------	-------	-------

17.1	211.2	339.7
------	-------	-------

27.1	214.7	341.4
------	-------	-------

31.4	216.2	345.5
------	-------	-------

32.4	220.8	347.7
------	-------	-------

34.0	222.9	353.1
------	-------	-------

36.7	224.8	355.1
------	-------	-------

40.2	227.5	357.7
------	-------	-------

46.4	231.3	370.5
------	-------	-------

48.1	231.8	374.7
------	-------	-------

49.8	235.9	378.3
------	-------	-------

55.4	238.2	381.0
------	-------	-------

57.7	241.9	386.6
------	-------	-------

61.4	245.4	389.0
------	-------	-------

62.5	247.2	391.1
------	-------	-------

63.0	249.0	393.9
------	-------	-------

64.1	253.5	409.5
------	-------	-------

65.3	256.0	413.6
------	-------	-------

73.6	258.3	592.8
------	-------	-------

74.8	259.5	684.5
------	-------	-------

75.9	260.1	690.5
76.5	261.7	937.1
79.1	263.9	1255.2
80.8	264.6	1453.5
81.4	266.2	2994.0
83.2	269.1	3060.4
84.7	270.2	3083.4
87.0	273.1	331.7
87.4	275.1	333.8
93.8	276.3	334.6

TS16

-370.5	114.4	370.0
11.9	122.0	374.4
27.8	123.6	382.3
37.4	124.6	385.9
37.5	125.0	387.4
50.7	129.1	393.2
50.9	129.7	393.7
61.4	135.6	395.4
62.0	138.0	500.4
62.4	138.9	532.7
64.2	153.6	571.0

64.8	154.0	594.7
66.5	165.1	671.8
66.7	167.1	683.6
68.9	167.5	763.1
70.6	200.3	874.5
71.1	213.1	949.3
77.1	217.0	978.0
78.7	220.5	1017.5
79.0	222.5	1086.7
79.6	223.6	1181.2
81.0	226.0	1278.0
84.3	227.9	1306.0
84.5	232.6	1355.9
85.9	234.3	1404.5
85.9	235.4	1433.0
88.1	238.6	2977.0
88.4	241.1	2990.3
102.4	244.7	2994.5
103.9	247.3	3001.2
105.2	248.2	301.4
105.8	255.7	303.4
110.3	256.3	304.7
111.7	261.1	305.9

271.9	262.6	306.7
273.5	264.9	308.6
274.3	265.3	313.0
277.0	266.2	329.6
278.6	267.1	335.6
280.2	269.1	336.8
281.9	269.6	343.6
283.1	270.7	344.9
285.0	271.5	345.4
285.3	347.6	356.0
286.0	348.4	357.1
287.4	350.2	357.4
289.0	353.2	362.3
290.7	354.0	364.5
292.4	354.5	299.0

TS21

-678.4	335.5	223.0
35.3	338.5	223.8
39.2	339.2	224.7
47.5	340.9	225.5
49.7	341.4	226.4
52.8	343.4	231.8

59.9	346.7	234.3
60.2	347.6	235.0
62.6	348.2	237.4
63.5	353.3	237.8
64.4	356.5	241.0
65.2	357.4	243.3
66.6	360.0	248.8
68.4	364.4	250.2
70.3	369.2	254.6
70.9	373.2	255.4
73.4	376.3	256.9
76.3	380.7	261.3
77.2	388.5	264.8
78.8	390.1	265.9
79.7	391.8	266.5
81.8	393.1	267.3
83.7	399.7	269.4
84.9	405.8	270.4
86.7	425.1	271.0
88.7	456.5	271.9
88.9	510.9	272.8
96.0	568.3	275.3
98.7	599.3	277.2

103.0	654.8	281.3
105.2	708.2	282.4
107.3	781.1	283.5
109.5	804.3	285.0
112.8	841.8	285.7
117.0	920.6	287.3
123.5	983.9	289.3
124.7	1058.6	290.0
125.2	1117.7	291.2
128.7	1129.1	294.4
130.5	1223.4	296.7
130.7	1297.4	298.4
133.0	1335.5	302.4
137.5	1402.0	305.3
140.2	1414.6	305.6
140.5	1445.6	306.9
155.1	1472.6	318.0

TS19

-39.9	305.3	234.6
30.2	306.9	235.1
36.4	310.8	236.3
37.5	312.5	238.5

41.7	315.3	239.6
48.7	317.6	246.1
50.3	322.8	246.8
51.0	328.7	255.2
60.4	336.3	257.0
61.1	340.2	257.4
62.3	341.1	259.3
63.8	344.9	261.9
64.5	346.2	265.6
64.9	348.0	266.2
66.2	349.1	267.0
68.6	351.0	267.3
70.6	351.9	268.6
71.5	353.0	270.7
73.0	353.8	271.5
77.4	354.8	271.9
78.1	355.7	273.2
79.5	357.1	273.9
80.5	361.5	276.9
82.1	363.0	278.0
83.5	364.9	281.7
85.0	365.7	284.8
85.8	369.9	285.4

88.2	384.4	286.9
89.0	387.3	288.4
95.1	392.9	290.2
103.5	393.9	291.3
104.4	394.8	293.7
105.6	502.5	294.8
106.2	514.6	298.5
111.3	531.8	300.8
113.4	564.8	303.5
120.1	584.4	234.6
123.5	604.2	235.1
124.8	642.7	236.3
126.7	713.8	238.5
128.0	763.3	239.6
129.7	790.8	246.1
132.1	933.5	246.8
134.6	962.1	255.2
138.6	979.3	257.0
140.2	1013.1	257.4
141.7	1095.3	259.3
153.7	1096.0	261.9
154.2	1230.0	265.6
165.3	1352.3	266.2

168.1	1366.6	267.0
169.5	1412.4	267.3
190.1	1449.4	268.6
209.7	1464.0	270.7
218.0	2987.3	271.5
221.4	2991.8	271.9
223.6	2998.6	273.2
224.3	3005.9	273.9
227.1	3007.3	276.9
229.9	3234.0	278.0

TS17

-187.4	306.6	167.1
9.4	309.7	173.1
15.0	310.8	218.9
28.1	317.2	221.8
33.7	321.2	223.7
37.3	324.8	227.2
44.0	326.5	228.0
47.3	330.7	229.4
49.2	333.5	231.3
51.7	337.5	233.2
59.3	338.1	233.9

61.0	340.0	236.8
61.8	343.8	240.6
63.5	344.3	244.5
64.0	346.4	247.8
64.4	347.8	251.0
66.8	354.8	253.9
68.5	355.5	254.4
69.3	360.4	256.7
70.9	361.3	261.7
74.4	363.1	264.0
75.2	369.2	267.1
76.1	373.7	268.2
77.6	377.4	268.5
79.4	386.7	270.0
81.9	393.0	271.4
83.1	393.8	273.0
84.5	398.0	276.7
85.1	403.9	278.4
87.6	521.4	279.8
88.9	525.9	281.8
92.2	541.5	285.4
97.5	602.4	286.9
98.8	652.0	289.1

102.6	709.0	290.8
105.4	783.6	295.1
108.0	813.3	295.6
109.1	864.2	297.6
111.7	929.3	301.6
112.7	975.9	302.8
118.4	991.6	305.1
123.6	1076.2	138.4
125.4	1089.6	139.4
126.7	1195.2	146.7
129.6	1302.8	150.7
130.8	1313.9	161.5
132.3	1375.8	163.2
137.7	1382.2	2890.5
2980.2	1526.6	2978.3

TS22

-388.5	323.0	220.6
26.6	330.7	223.6
38.0	334.6	225.4
43.8	335.7	226.9

48.0	338.8	230.5
49.9	340.5	232.2
59.6	341.9	234.3
61.7	342.9	234.6
62.6	346.2	236.7
64.3	347.0	240.8
64.7	350.6	242.7
65.3	353.4	249.2
66.1	355.7	251.8
68.4	356.6	254.8
69.0	363.1	257.7
70.9	370.3	260.5
74.4	373.0	261.2
75.8	375.4	262.9
78.5	379.1	265.2
79.6	381.7	266.9
81.3	389.7	268.1
82.7	392.7	269.6
84.4	398.1	270.3
85.2	404.7	272.2
86.6	410.1	274.1
88.3	418.9	275.6
88.9	456.3	276.2

99.6	508.9	278.2
100.4	544.4	282.2
103.1	574.2	283.4
105.0	608.1	284.5
108.2	613.3	285.9
113.2	696.4	287.7
114.9	752.4	289.9
118.2	800.4	291.0
121.1	802.8	293.5
123.9	941.7	296.1
128.5	978.0	296.8
129.1	1027.7	299.1
131.4	1097.3	302.4
132.3	1105.9	303.6
138.6	1203.6	307.1
140.2	1244.6	310.6
143.1	1357.5	2982.4
153.3	1392.0	2992.3
156.0	1421.4	2997.3
161.6	1465.9	3004.5

Appendix C

This appendix provides supplementary information for chapter 7.

Table S1. The deconvolution results of high-resolution XPS spectra at O1s photoelectron line.

Argon/oxygen flow rate ratio %	Photoelectron line	Bonding states	Binding energy (eV)	FWHM (eV)	Percentages of the component (%)
0	O1s	CeO ₂	529.0	1.0	60.2
		organic O	531.1	1.9	39.7
7	O1s	CeO ₂	529.0	1.0	65.3
		Organic O	530.9	2.1	34.6
14	O1s	CeO ₂	528.9	1.1	82.3
		Organic O	530.9	2.2	17.6
28	O1s	CeO ₂	529.0	1.0	83.9
		Organic O	530.9	2.0	16.1
42	O1s	CeO ₂	529.0	1.0	83.0
		Organic O	530.9	2.1	16.9
56	O1s	CeO ₂	528.9	1.0	83.3
		Organic O	530.9	2.0	16.6

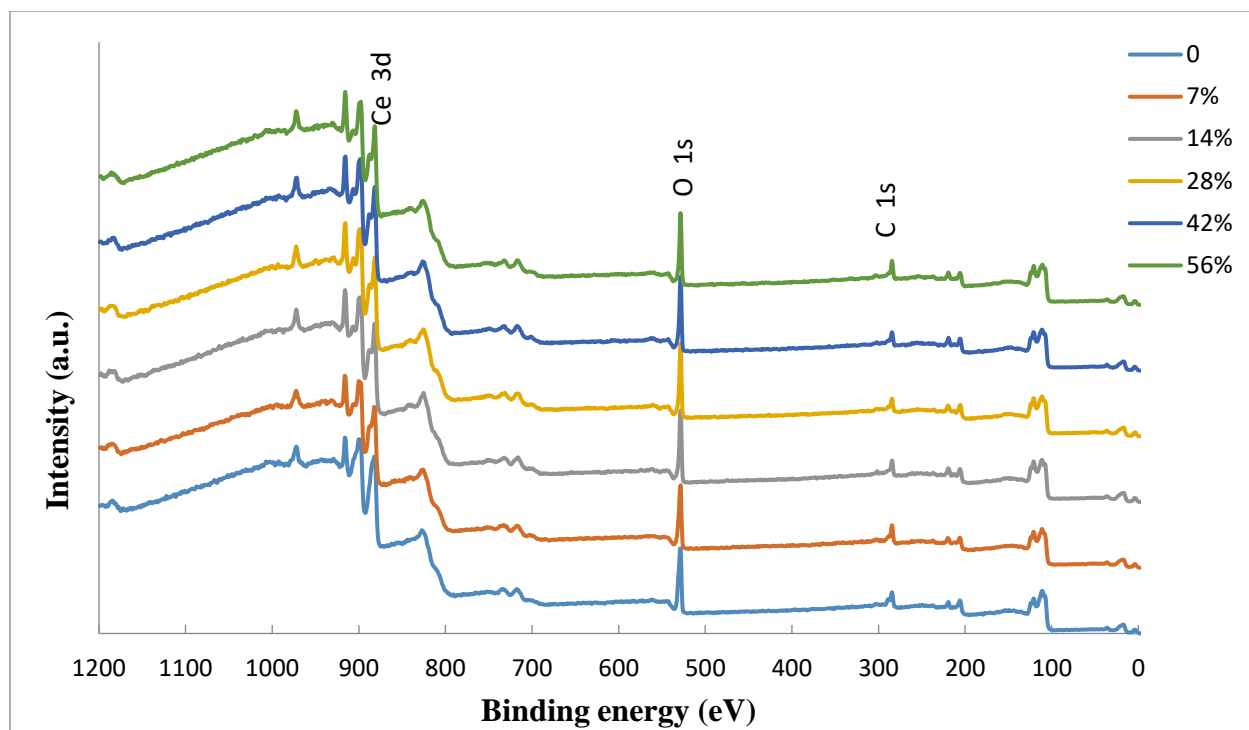


Figure S1. XPS survey scan of CeO_x coatings at the selected argon/ oxygen flow ratios.

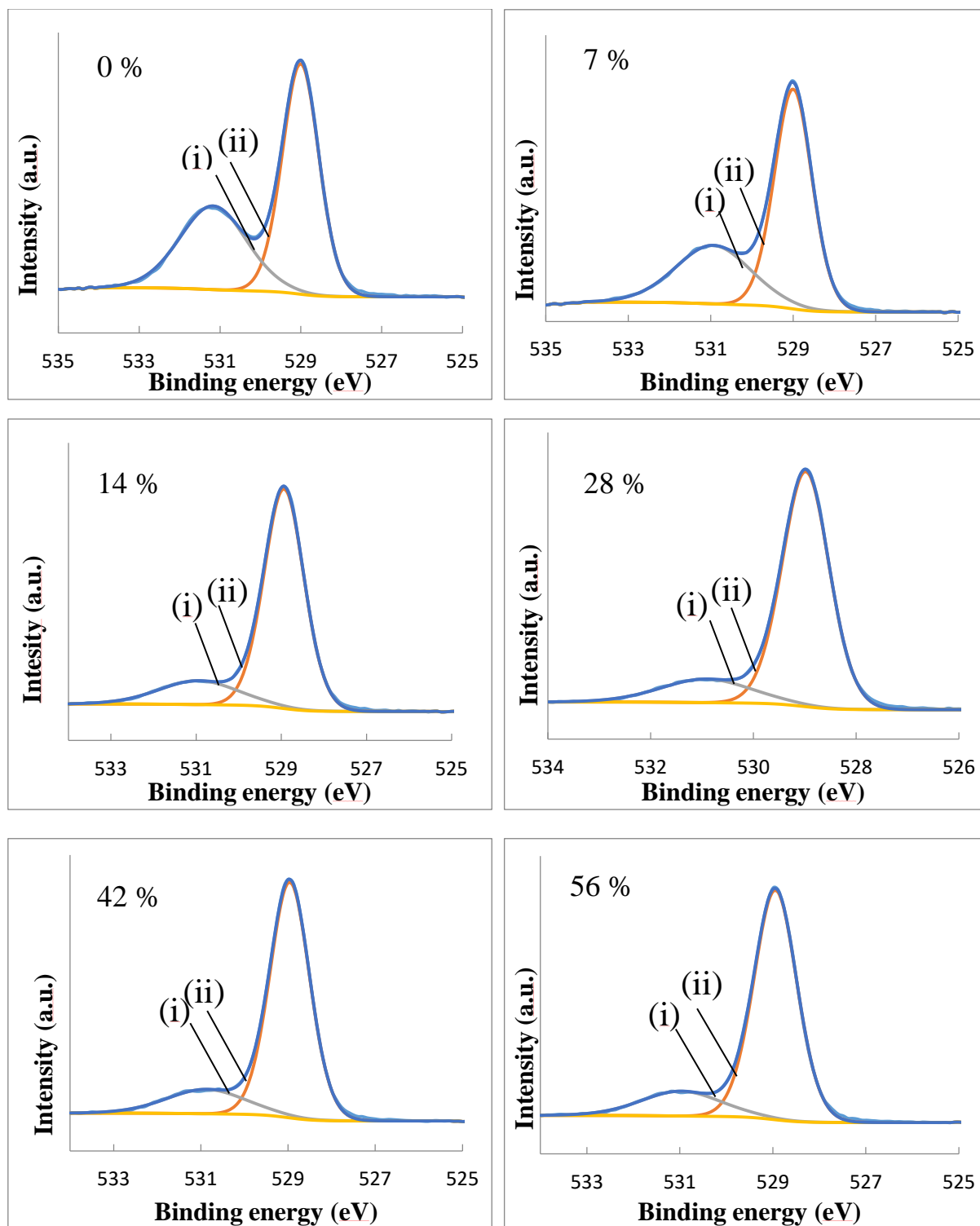


Figure S2. Typical fitting curves of O1s XPS spectra of sputtered CeO_x films at the selected argon/ oxygen flow ratios.

Appendix D

This appendix contains supporting information for Chapter 8

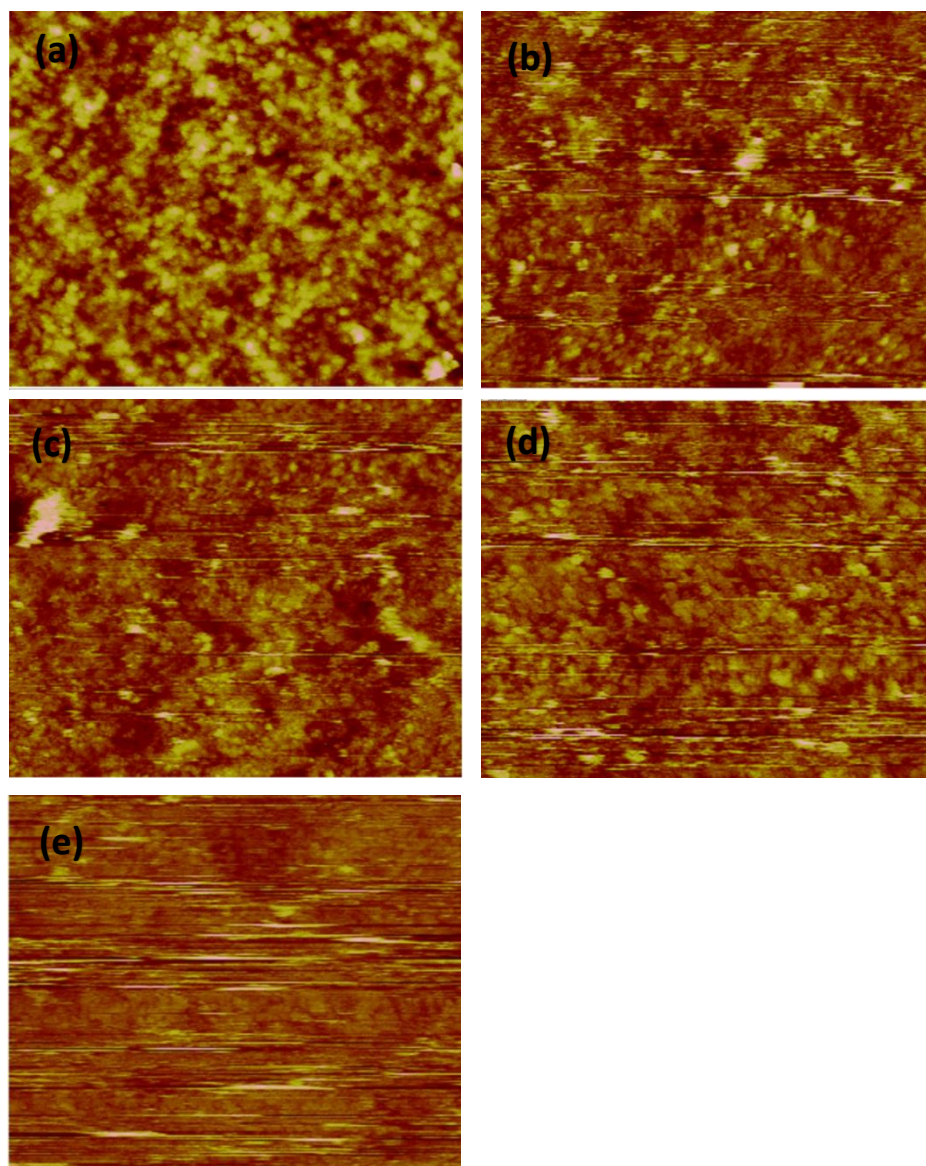


Fig. S4. 2D AFM images of CuCo-oxide coatings (a) before annealing, and annealed at: (b) 200°C, (c) 300°C, (d) 400°C, and (e) 500°C.

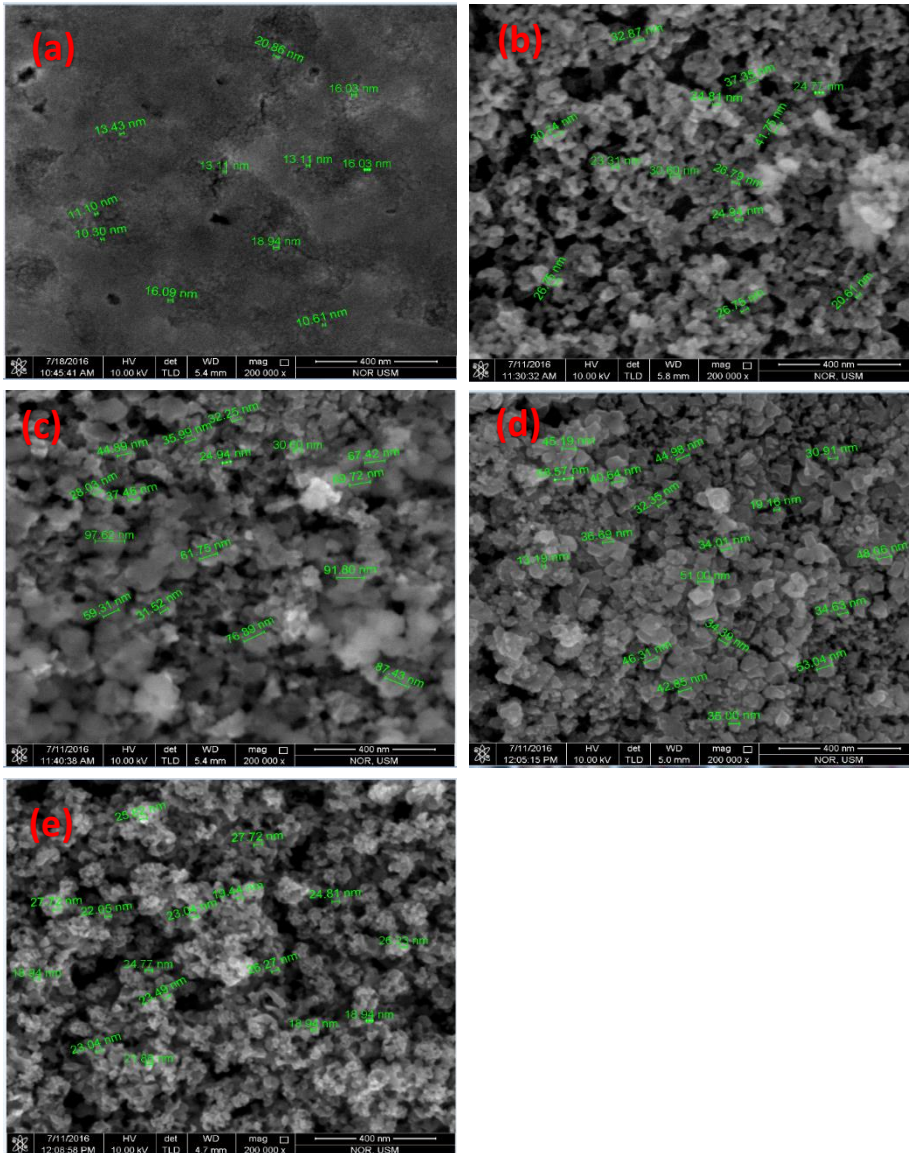


Fig. S5. Average particle size of CuCo-oxide coatings (a) before annealing and annealed at: (b) 200°C, (c) 300°C, (d) 400°C, and (e) 500°C, estimated from FESEM imaging.